NATO Science for Peace and Security Series - B:
Physics and Biophysics

Advanced Sensors for Safety and Security

Edited by
Ashok Vaseashta
Surik Khudaverdyan

Springer

This publication is supported by:

The NATO Science for Peace and Security Programme

Advanced Sensors for Safety and Security

NATO Science for Peace and Security Series

This Series presents the results of scientific meetings supported under the NATO Programme: Science for Peace and Security (SPS).

The NATO SPS Programme supports meetings in the following Key Priority areas: (1) Defence Against Terrorism; (2) Countering other Threats to Security and (3) NATO, Partner and Mediterranean Dialogue Country Priorities. The types of meeting supported are generally "Advanced Study Institutes" and "Advanced Research Workshops". The NATO SPS Series collects together the results of these meetings. The meetings are co-organized by scientists from NATO countries and scientists from NATO's "Partner" or "Mediterranean Dialogue" countries. The observations and recommendations made at the meetings, as well as the contents of the volumes in the Series, reflect those of participants and contributors only; they should not necessarily be regarded as reflecting NATO views or policy.

Advanced Study Institutes (ASI) are high-level tutorial courses to convey the latest developments in a subject to an advanced-level audience

Advanced Research Workshops (ARW) are expert meetings where an intense but informal exchange of views at the frontiers of a subject aims at identifying directions for future action

Following a transformation of the programme in 2006 the Series has been re-named and re-organised. Recent volumes on topics not related to security, which result from meetings supported under the programme earlier, may be found in the NATO Science Series.

The Series is published by IOS Press, Amsterdam, and Springer, Dordrecht, in conjunction with the NATO Emerging Security Challenges Division.

Sub-Series

A.	Chemistry and Biology	Springer
B.	Physics and Biophysics	Springer
C.	Environmental Security	Springer
D.	Information and Communication Security	IOS Press
E.	Human and Societal Dynamics	IOS Press

http://www.nato.int/science
http://www.springer.com
http://www.iospress.nl

Series B: Physics and Biophysics

Advanced Sensors for Safety and Security

edited by

Ashok Vaseashta
Norwich University Applied Research Institutes
Herndon, VA, USA

VTT/AVC U.S. Department of State
Washington, DC, USA

and

Surik Khudaverdyan
State Engineering University of Armenia
Yerevan, Republic of Armenia

Published in Cooperation with NATO Emerging Security Challenges Division

Proceedings of the NATO Advanced Study Institute on
Technological Advances in Chemical, Biological, Radiological, Nuclear, Explosives – (CBRNE) Sensing and Detection for Safety, Security, and Sustainability
Yerevan, Republic of Armenia
29 September – 01 October 2012

Library of Congress Control Number: 2013944681

ISBN 978-94-007-7017-1 (PB)
ISBN 978-94-007-7002-7 (HB)
ISBN 978-94-007-7003-4 (e-book)
DOI 10.1007/978-94-007-7003-4

Published by Springer,
P.O. Box 17, 3300 AA Dordrecht, The Netherlands.

www.springer.com

Printed on acid-free paper

Preface

The primary objective of the NATO Advanced Research Workshop (ARW) titled "Technological Innovations in CBRNE Sensing and Detection for Safety, Security, and Sustainability" was to discuss and exchange views as to how fusion of advanced technologies can lead to improved sensors/detectors in support of defense, security, and situational awareness. The ubiquitous presence of sensors provides enhanced situational awareness of pollution and contaminants – anthropogenic, inadvertent, and intentional.

The current geopolitical landscape is quite complex, dynamic, and unpredictable. From security viewpoint, notwithstanding the unparalleled level of military/ technological dominance that the United States and NATO Allies have demonstrated within several war-theatres, the evolving asymmetric, kinetic, and unconventional threats from non-aligned terrorist groups continue to grow and evolve. Adversaries and terrorist groups have demonstrated a strong will and interest to wage unconventional war against Western targets despite their limited technological capabilities and lack of sophistication in conducting such operations. In fact, the unsophisticated compositions of Chemical Biological Radiological Nuclear high-yield Explosives (CBRNE) threats pose more technical challenges in countermeasures. Rapid advances in both science and technology (S&T) coupled with universal internet ramp access have inspired both state and non-state-sponsored actors to new levels of creativity in the development of novel and non-traditional threat agents. It is apparent that asymmetric threats have changed the traditional nature of the battlefield, where conventional rules of engagement are not followed. Accompanying the evolution of asymmetric threats is the relative ease of their transport and employment, thus broadening the potential battlefield and virtually eliminating the generally accepted premise of homeland as a safe haven from catastrophic and man-made disasters. Finally, the terrorist toolkit includes direct attacks against persons, basic human values, economic and critical infrastructure, and the environment in pursuit of their own personal and political agendas.

In the current financially austere environment, it is prudent to employ a nexus of technological innovations to find appropriate solutions and strategies that are consistent with the Smart Defense program of NATO. One such technology

is nanotechnology, where materials approaching nanoscale dimensions exhibit characteristics that uniquely enable novel characteristics in unprecedented ways. Advances in synthesis of such materials in reduced dimensions and characterization methods allow the means to study, understand, control, and even manipulate the transitional characteristics between isolated atoms and molecules and bulk materials. Technological advances arise from the potential of nanoscale materials to exhibit properties that are attributable to their small size, physical characteristics, and chemical composition. In addition, the nanoscale geometrical dimensions are comparable to the smallest engineered entity, the largest molecules of living systems, and several fundamental physical quantities. This allows development of application specific materials. Recent functional and architectural innovations in nanoscale materials have initiated applications in chem.-bio agents' interrogation, environmental pollution sensing, monitoring, mitigation and remediation, energy harvesting and storage devices, plasmonics, *in-vivo* analysis of cellular processes, and nano-biotechnology based futuristic health and clinical medicine platforms. A nanotechnology-based sensor platform enables direct detection of chemical and biological agents in a label-free, highly multiplexed format over a broad dynamic range. Nucleic acid layers combined with nanomaterials-based electrochemical or optical transducers produce affinity biosensors for converting hybridization events into analytical signals for obtaining sequence-specific information. Examples further include commission of quantum dots (QDs) for remote detection of threat vectors. The field is very active and rapidly developing, and covers a wide range of disciplines.

The subject of clean water is critical. The contamination in water can range from classical to non-traditional chemical agents, toxic industrial chemicals (TICs), and/or toxic industrial materials (TIMs). Conventional methods employed to sense/detect contaminants use commercial off -the-shelf (COTS) systems and broad-spectrum analytical instruments with interpretive algorithms. The current threat environment requires detection of complex contaminant signatures in addition to recycled pharmaceuticals present in water supplies. Hence it is critical to seek revolutionary solution pathways to such challenges, by using advanced sciences convergence (ASC) involving inter-/trans-disciplinary nexus of science and technologies.

The ARW aimed to address several important and relevant issues related to enhancing security using advanced technological solutions. The ARW was attended by participants from 23 countries, thus exemplifying the international vision of NATO Science for Peace for Security endeavours. Lectures covering the basic principles and state-of-the-art applications of nanostructured and advanced materials for chemical-biological sensors were conducted by experts widely recognized for advances in nanotechnology. Focused seminar sessions, poster sessions, and interactive feedback sessions stimulated extended interactions between participants and subject matter experts. As a venue for collaborative learning, the interactive lectures and sessions drew enthusiastic response and sharing of information and ideas from all participants.

The ARW was held at the Golden Tulip in Yerevan, the capital and largest municipality in the Republic of Armenia. The facility supported formal and informal settings for structured and spontaneous learning and sharing of ideas. The meeting lasted 3 days. The sessions were packed with agenda. The meals were arranged in the city – walking distance from hotel. This provided a much needed break from the conference room environment and most everyone stayed engaged despite the inevitable post-lunch slowdown. The unique balance of technical and social interactions materialized in alliances among participants, which have been evidenced by continued correspondence in the months following the ARW. The co-directors interpret the ongoing interaction and positive feedback from participants as an affirmation of a successful ARW.

Such a constructive ARW is the outcome of efforts by participants, speakers, and co-directors in addition to a host of caring individuals who supported their work. Much appreciation is extended to Golden Tulip management who ensured gracious hospitality to all participants. We would like to acknowledge tireless logistics support by Anne Stammwitz, Aleksandra Buha, Didem Demir, Luiza Gevorgyan, David Khudaverdyan, and Ashot Khudaverdyan and editorial support provided by Yulia Mutafchieva and Didem Demir.

We offer our gratitude to Dr. Deniz Beten, the director of the NATO Emerging Security Challenges Division and Ms. Alison Trapp for their resolute encouragement and support of the ARW. Ms. Annelies Kersbergen with the NATO Publishing Unit of the Springer Publishers has provided us with much appreciated expertise in publishing this workshop proceeding.

Thanks are due to the Vaseashta Foundation for several travel and poster awards to support the scientific community. We also thank the State Engineering University of Armenia and State Committee of Science of Armenia for generous support and many efforts to make the ARW successful.

The co-directors are confident that ARW participants will continue research collaborations that began in Yerevan in the advancement of nanotechnology and ASC to enhance safety and security for all mankind in support of NATO mission. The ARW was supported by NATO–Emerging Security Challenges division of Science for Peace and Security program.

- **Organizational Support**
  Reshef Tenne, Anatolie Sidorenko, Brian Nordmann, and Eric Braman
- **Directors**
  Ashok Vaseashta (Herndon, VA; Northfield, VT; and Washington, DC, USA)
  Surik Khudaverdyan (Yerevan, Armenia)

Herndon, VA, USA — Ashok Vaseashta
Yerevan, Republic of Armenia — Surik Khudaverdyan

Contents

Part I Invited and Key Lectures – Challenges and Opportunities

1 Ecosystem of Innovations in Nanomaterials Based CBRNE Sensors and Threat Mitigation 3
Ashok Vaseashta

2 New Terahertz Security Opportunities Based on Nanometric Technology 27
Hans L. Hartnagel

3 Structured Inorganic Oxide-Based Materials for the Absorption and Destruction of CBRN Agents..... 43
Matteo Guidotti, Massimo C. Ranghieri, Fabio Carniato, and Chiara Bisio

4 The Quirra Syndrome: Matter of Translational Medicine..... 55
A.M. Gatti, S. Montanari, and F. Capitani

Part II Policy, Diplomacy, Verification, Compliance, Implementation

5 The Yin and Yang of Countering Biological Threats: Public Health and Security Under the International Health Regulations, Biological Weapons Convention, and the U.N. Security Council Resolution 1540 67
D. Perkins

6 Timely Detection of Outbreaks in the Public Health Surveillance System of the Republic of Moldova 75
S. Gheorghita and N. Caterinciuc

7 Advanced Sciences Convergence to Analyze Impact of Nanomaterials on Environment, Health and Safety 83
Jack E. Smith and Ashok Vaseashta

8 Conversion Disorders in Patients with Discogenic Radiculopathy 93
Svetlana Sidorenko, Ludmilla Sidorenko, Ion Moldovanu, Irina Sidorenko, and Ashok Vaseashta

Part III Chemical-Biological Sensors

9 Use of Metaloxide, Porous Silicon and Carbon Nanotube Gas Sensors for Safety and Security 105
Vladimir Aroutiounian

10 Chemical Sensors Based on Nano-hexagonal Tungsten Oxide: Synthesis and Characterization 125
Csaba Balázsi, István Endre Lukács, and Katalin Balázsi

11 Noise Reduction in (Bio-) Chemical Sensors Functionalized with Carbon Nanotube Multilayers 139
F.V. Gasparyan

12 Polymer Nanocomposite Films as a Potential Sensor 151
A. Grozdanov, A. Tomova, and A. Dimitrov

13 Carboxyhemoglobin in Blood of Smokers and Non-smokers Determined by Gas Chromatography with Thermal Conductivity Detector 163
A. Buha, A. Vaseashta, Z. Bulat, and V. Matović

14 Electron Emission Standed Nanodosimetry and Gas Detection 173
Yu. Dekhtyar, D. Krumpane, K. Perovicha, R. Reisfeld, M. Romanova, T. Saraidarov, and I. Surkova

Part IV Optical Sensors

15 Photoelectric Properties of Selectively Sensitive Sensors for the Detection of Hazardous Materials 183
Surik Khudaverdyan, A. Avetsiyan, D. Khudaverdyan, and Ashok Vaseashta

16 Portable Point-of-Care Optical Device to Detect Brain Injury 193
Adkham Paiziev

17 Absorbance Control of Liquids Employing Transmission Sub-wavelength DLC Diffraction Grating 203
Tomas Tamulevičius, Ieva Gražulevičiūtė, and Sigitas Tamulevičius

18 Detection and Monitoring of Surface Deformations in Armenia Using INSAR Satellite 213
G.M. Aleksanyan and M.A. Grigoryan

19 Applications of an Effect Based on Electromagnetic Field-Matter Interactions for Investigations of Water 225
O. Ivanov, Y. Mutafchieva, and Ashok Vaseashta

Part V Water Security and Water Contaminations Sensors

20 Real-Time Monitoring of Water Contaminants for Situation Awareness Using Electromagnetic Field Sensing System ... 233
O. Korostynska, K. Arshak, A. Arshak, A. Mason, Ashok Vaseashta, and A. Al-Shamma'a

21 Development of Polymeric Cryogels as Potential Matrices for Removing Antibiotics from Wastewater 243
Nimet Bolgen, Didem Demir, and Ashok Vaseashta

Part VI Radiation Sensors

22 On the Concept of System to Detect Unclaimed Inclusions of Fissile and Radioactive Materials in Hand Luggage and Cargo Trucking 253
A. Lobko, A. Fedorov, M. Korjik, V. Mechinski, and G. Drobychev

23 New Model of Spectral Analysis of Integral Flux of Radiation 261
Surik Khudaverdyan, M. Khachatryan, D. Khudaverdyan, S. Caturyan, and Ashok Vaseashta

24 Cyclic Amino Acid Derivatives as New Generation of Radioprotectors 271
A. Boyajyan, A. Poghosyan, T. Hovsepyan, E. Arakelova, L. Zhamharyan, V. Ayvazyan, M. Malakyan, S. Bajinyan, V. Matosyan, and V. Tonoyan

25 New Polymeric Materials for Medicine and Rehabilitation of Buildings and Different Surfaces Exposed to Radioactive Contamination 279
V. Sargsyan, L. Hayriyan, G. Harutyunyan, N. Tavakalyan, and P. Voskanyan

26 Application of New Heavy Scintillation Crystals for Remote Detection of Fissile Materials 287
G.Yu. Drobychev, A.E. Karneyeu, and V.A. Mechinsky

Part VII Synthesis/Processing

27 Inorganic Nanotubes and Fullerene-Like Nano-particles: From the Lab to Applications 299
R. Tenne

28 Porous Silicon by Galvanostatic Electrochemical Anodisation of Epitaxial Silicon, Polycrystalline Silicon and Silicon on Insulator Layers 303
M. Ivanda, M. Balarin, O. Gamulin, V. Đerek, D. Ristić, S. Musić, M. Ristić, and M. Kosović

29 Advanced Materials for IR Sensors 321
A.I. Belogorokhov, I.A. Denisov, A.G. Milvidskaya, S.N. Knyazev, K.E. Anoshin, and A.B. Danilin

30 Small Carbon Molecules and Quasi-Fullerenes as Products of New Method of Hydrocarbons Pyrolysis 329
Oleksii Kharlamov, Ganna Kharlamova, Marina Bondarenko, and Veneamin Fomenko

31 Hetero-Carbon: Heteroatomic Molecules and Nano-structures of Carbon 339
Ganna Kharlamova, Oleksii Kharlamov, Marina Bondarenko, Nadezhda Gubareni, and Veneamin Fomenko

32 A Preliminary Analysis of Wind-Hydrogen System in Bulgaria 359
M. Ali, D. Kirova, and K. Petrov

Photographs 367

Index 373

Part I
Invited and Key Lectures – Challenges and Opportunities

Chapter 1
Ecosystem of Innovations in Nanomaterials Based CBRNE Sensors and Threat Mitigation

Ashok Vaseashta

Abstract Recent developments in science and technology (S&T), coupled with universal access to content information via internet have inspired both state- and non-state-sponsored actors to new levels of creativity in the development of unconventional and non-traditional weapons. Remote access to critical infrastructure, global links using faster means of transport, and unmanned aerial vehicles have decentralized the traditional nature of battlefield. Threat vectors have become increasingly asymmetric, highly kinetic, undefined and randomly non-linear. Implementation of effective countermeasures necessitates an advanced understanding of emerging security challenges and transformational concepts conjoining nexus of S&T and their full potential beyond traditional capabilities. Recent progress in reduced and multi-dimensional materials coupled with advanced synthesis methods have significantly contributed to sensor platforms capable of direct detection of chem.-bio agents in a label-free, parallel, and multiplexed format with broad dynamic range, allowing *in-situ* and accurate detection of multiple agents with high sensitivity and specificity. Furthermore, the use of bio-mimetic materials is a game-changing technology as it provides ultra-sensitive reconnaissance and remote maneuverability for missions in combat theatres. The development of integrated solution pathways using ecosystem of technological innovations provides tactical superiority in support of effective countermeasures and opportunities in identifying emerging and unconventional threats vectors.

Keywords Nanotechnology • Convergence • Synthetic-biology • Biomimetic • Counter-measures • Ecosystem of innovations • Technology nexus • Emerging security challenges

A. Vaseashta (✉)
Norwich University Applied Research Institutes, Herndon, VA, USA

VTT/AVC U.S. Department of State, Washington, DC, USA
e-mail: prof.vaseashta@ieee.org

A. Vaseashta and S. Khudaverdyan (eds.), *Advanced Sensors for Safety and Security*,
NATO Science for Peace and Security Series B: Physics and Biophysics,
DOI 10.1007/978-94-007-7003-4_1, © Springer Science+Business Media Dordrecht 2013

1.1 Situational Awareness – Threat Environment

The current geopolitical landscape is exceedingly complex, dynamic, and capricious. Recent developments in S&T coupled with universal access to the information ramp have fueled both state- and non-state-sponsored actors to new levels of creativity in the development of unconventional and non-traditional weapons. Cyber access/control to critical infra-structure, global links using faster means of transport, dual-use technologies, and unmanned aerial vehicles (UAVs) have decentralized the traditional nature of battleground. Threat vectors have become increasingly asymmetric, highly kinetic, and undefined randomly non-linear. Traditional rules-of-engagement no longer apply or have different interpretation. Figure 1.1 shows many ways by which adversaries can launch overt/covert attacks. Such operations range from psychological operations (PSYOPS), Chemical, biological, radiological, nuclear (CBRN), improvised explosive devices (IEDs), non-traditional agents (NTA), cyber-attacks, or non-traditional fund raising (*hawala*) to commit such acts. Notwithstanding unparalleled level of technological sophistication, the evolving asymmetric threat from terrorist groups continues to grow and evolve.

Effective countermeasures use essentially the same tools, viz. advances in S&T, information, and an advanced knowledge base with an understanding of transformational emerging sciences, concepts and theories, and their potential applications in support of defense and security. Numerous technological advances arise from the potential of nanoscale materials to exhibit unique properties that

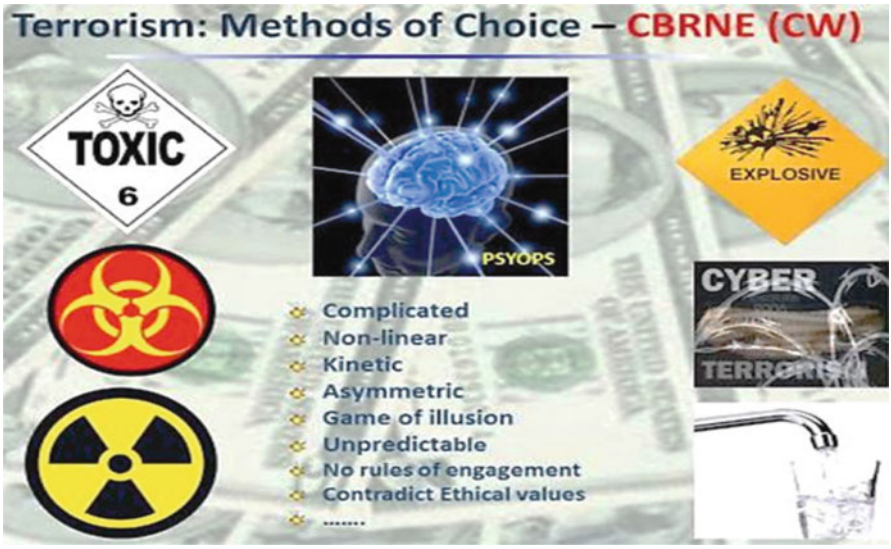

Fig. 1.1 Methods of terrorism including CBRNE, cyber, water, and *hawala*

are attributable to their reduced dimensions. Furthermore, advances in material synthesis, device fabrication and characterization have provided the means to study, understand, control, or even manipulate the transitional characteristics between isolated atoms and molecules, and bulk materials. Consequently, various "designer" materials capable of producing devices and systems with remarkable, tunable, and specific properties have recently been fabricated. Such advances coupled with information technology, cognitive sciences, biotechnology, artificial intelligence, and genetics offer an ecosystem of innovations and potential pathways to counter threat vectors in ways never imagined possible earlier, such as deployment of systems with enhanced and remote maneuverability capabilities, remote interrogation and mitigation, enhanced information gathering, and thwarting threats at the point-of-origin (PO2).

This report provides many examples of innovative countermeasures that use advanced and nanomaterials, such as sensors/detectors employing materials, phenomena, and effects including multilayer semiconductor structures, specially formulated interfaces, and exploiting different regions of the electro-magnetic (e.m.) spectrum to provide various functionalities. Mechanisms such as refractive and nonlinear effects, absorption of electromagnetic radiation, fluorescence, avalanche phenomena for the detection of small fluxes of optical radiation, remote detection by neutron radiation, etc., provide additional sensing capabilities, in conjunction with algorithms for complex processing of information, and provide end-to-end strategic assessments and modeling of mixed and complex hazardous environments to delineate signal from noise and background interactions.

Securing life-sustaining critical infrastructures presents dynamic challenge for local, state, federal, scientific and defense communities. Tactically, the unsophisticated nature of such threats poses significantly more technical challenges in both point and stand-off detection. These threats are growing due to increased globalization and mobility within society, the explosion in chemical and biotech expertise and the relative ease with which chemical weapons can be prepared at offsites, and the means by which pathogens can be covertly engineered, transported and released or dispersed.

Furthermore, drinking water distribution systems are vulnerable to intentional and/or inadvertent contamination with classic and non-traditional chemical agents, toxic industrial chemicals (TICs), and/or toxic industrial materials (TIMs), in addition to recycled pharmaceuticals. Conventional methods employed to sense/detect such contaminants use commercial-off the shelf (COTS) systems and broad-spectrum analytical instruments with interpretive algorithms.

This report and many chapters in this book result from a NATO Advanced Research Workshop (ARW) held in 2012 in Yerevan, Armenia. The objective of the ARW was to examine new generation of sensors/detectors that utilize an ecosystems of innovation in nanomaterials, biomimetics, plasmanoics, ASC, bioinformatics, hyper-spectral imagery, etc. in support of effective counter-measures against CBRNE threats.

1.2 Threat Vectors – Emerging, Persistent, Dual Use and *Avant Garde*

Understanding the emerging security challenges (ESC), nature and potential of threats may prevent or minimize a potentially catastrophic occurrence. Most potential threats have been characterized by a severity of hazard (SH) ranking based on toxicity, flammability, and/or reactivity. Notwithstanding many conventional and well characterized TICs/TIMs, there are many other emerging, persistent, dual-use, and unconventional threat vectors that must be identified and mitigated using advanced technology platforms. Genetically modified organisms (GMO) refer to those organisms whose genetic material have been altered using genetic engineering, such as recombinant DNA (rDNA) or DNA molecules derived from different sources, rendering modified genes with many applications ranging from pharmaceutical, regenerative medicine, agriculture, transgenic microbes for human performance enhancement (HPE) treating certain complex medical conditions, transgenic animals for phenotypic and many similar experimental endeavors. Despite its many useful applications, research on GMO coupled with recent advances in nucleic acid synthesis, lack of *in-situ* detection, reference materials and standards have caused public and scientific concerns.

Synthetic biology (syn-bio), likewise, is modifying the DNA of an organism to change its information contents, such as selecting desired mutations, inducing mutagenesis, altering genes or regulatory elements, cloning, designing biological components and systems that otherwise do not exist naturally. Syn-bio provides the tools to "redesign" the genomes of existing microbes to increase their efficacy or provide new functionalities. The successful "redesign" of the bacterium Mycoplasma genitalium, which has the smallest known bacterial genome, yet possessing all of the bio-chemical functionality needed to metabolize, grow, and reproduce, has been readily available in open literature and on the Internet [citation withheld]. Synthetic genomics refers to the set of technologies that make it possible to construct any specified gene (or full genome) from synthesis to a custom designed base pair series, e.g. short strands of synthetic DNA, a.k.a. "oligonucleotides", which are produced chemically and are generally between 50 and 100 base-pairs in length. Syn-bio is subject to potential misuse, in terms of its enhanced virulence, resistance to control agents, altering host defense, and increasing environmental stability and/or dispersal. Similar to GMO, limited detection methods exist for emerging syn-bio threats requiring countermeasures using advanced technology innovations platforms. Dual-use is a term often used in the political and diplomatic context to state that a technology can be used for both peaceful and military ambitions. Although used primarily in context of nuclear proliferation, the use of GMO and (bio) weaponized syn-bioagents pose a major concern. Use of functionalized nanomaterials has been identified as a potential dual-use concern and is currently under investigation by the author, as a part of a defense contract.

Water is fundamental to sustaining life. Despite its essential nature, drinking water distribution systems are vulnerable to intentional and/or inadvertent introduction

of contamination. Such contaminants can be known traditional and non-traditional agents/compounds/chemicals. The current threat environment requires detection of complex contaminant signatures in addition to recycled pharmaceuticals present in water supplies. A growth in human population and associated increased demands on water poses a significant challenge in maintaining adequate, yet acceptable water quality for various sectors. Emergence of mega-cities and regions has caused severe water-stress levels accompanied by global water shortage. The problem is becoming more widespread with population growth, drought, and industrial expansion. There are increasing concerns about the availability of usable water, and many communities and industries alike are faced with dramatic reductions in fresh water supplies and deteriorating water quality from contaminated wells, aquifers, runoffs, and sources of ground water supplies. Global water scarcities increase the urgency for the preservation of fresh water resources and increased water reclamation efforts, viz. management of global water resources is critical to creating sustainable water supplies for residential, agricultural, commercial, energy conservation, and improved quality of life. It is critical to observe the association between the basic need for clean drinking water and water resources, and national security concerns and policy, generally referred to as eco-terrorism – defined by the Federal Bureau of Investigation (FBI) as "the use or threatened use of violence of a criminal nature against people or property by an environmentally oriented, subnational group for environmental-political reasons, or aimed at an audience beyond the target, often of a symbolic nature". Ecological sabotage (ecotage) is often seen as indistinguishable from ecoterrorism. In the context of challenges, ecological terrorism and ecotage are used as intentional contamination of the environment to cause harm to the population, infrastructure, and/or denial-of-service.

Use of technological innovation platforms to sensors/detectors and remediation of contaminations strategies are likely to provide situational awareness in support of safety, security, and sustainability.

1.3 Response Posture – *Recta Ratio Speculabilium – Recta Ratio Agibilium*

The origin of war and weapons dates as far back as the invention and growth of agriculture coupled with domestication of animals and use of stone and Bronze around 4000 B.C. in Egypt and Mesopotamia. Over time, the mechanism of cultural development as well as the conduct of war has evolved as a legitimate social function supported by an extensive institutional infrastructure. It became an indispensable characteristic to maintain/sustain a social order if individuals were to survive the predatory behavior of others. With the emergence of social, political, economic, psychological, and military technologies that made the conduct of war a relatively normal part of social existence, the response posture has changed significantly.

The principle of retributive justice, viz. *an eye for an eye* (or *a tooth for a tooth*), or principle of equivalent retaliation – *tit for ta*t, seemed appropriate at the time, even a few short years ago. While in ancient Hindu culture, leaving justice and response to higher moral authority and doctrine of "passive acceptance of injustice and oppression" by Mahatma Gandhi (and also according to Matthew 5:39–41) – *if any one strikes you on the right cheek, turn the other also*, seemed an appropriate and astute response.

Presently, there is a divide between those who play by the rules and those who are not bound by any rules, rendering response posturea new level of complexity. *Phronesis* is a term used for the virtue of practical wisdom, the capacity for moral insight, the capacity, in a given set of circumstances, to discern what moral choices or course of action (COA) is the most advantageous response. *Phronesis* is the intellectual virtue that disposes us habitually to attain for the sake of action, as compared to speculative wisdom or *sophia*. Prudence takes into account the full breadth of Aristotelian *phronesis,* including virtues of faith, hope, and charity – as well as moral and intellectual virtues. Thus, prudent perspective on the Aristotelian notion of "practical wisdom" is one which asserts -*recta ratio speculabilium; recta ratio agibilium* – the right measure of knowledge to compel the right measure of actions.

This prudence is best achieved with the nexus of technological innovations and the tools currently available and as described in this chapter. Mitigating threat at the point of origin, interrogating level of threat remotely and assembling an appropriate response posture, isolating cause from effect, are only a few paradigm-shift examples of accomplishments resulting from nexus of innovations and the latest technological tools that allows an appropriate response posture, consistent with human values, rules of engagement, United Nations Security Council Resolutions (UNSCRs), and many other treaties and bi/tri/multi-lateral agreements among countries.

1.4 Countermeasures Using Advanced Technologies

1.4.1 Nanotechnology: Materials in Reduced Dimensions

Solids in reduced dimensions have reduced coordination number; hence the electrons have less opportunity to hop from site to site; thus reducing kinetic energy of electrons. A higher Coulomb interaction/bandwidth ratio at a site enhances electron correlation and Mott-transition leading to the appearance of magnetism. Furthermore, the symmetries of the system are lowered and the appearance of new boundary conditions leads to surface and interface states. A change of the quantization conditions alters the Eigen value spectrum and transport properties of the solid. Below a certain critical size $\sim$ comparable with the double space-charge layer thickness of the semiconductors, there is a marked change in physical characteristics

along with high surface area/volume ratio. Thus, systems in reduced dimensional instigates novel characteristics due to their reduced dimensionality. Furthermore, nanomaterials have geometrical dimensions comparable to the smallest engineered unit and the largest living organism molecules, and fundamental physical quantities, they offer uniqueness due to enhanced surface activity, more so with target specific functionalization. Furthermore, advances in material synthesis, device fabrication and characterization techniques have provided the means to study, understand, control, or even manipulate the transitional characteristics between isolated atoms and molecules, and bulk materials, providing additional sensing/detection capabilities. Typically, reduced dimensional systems are characterized, in which one or more dimensions are reduced (in nm.) such that material begins to display quantifiable novel characteristics. The onset of deviation from bulk to reduced dimensions has resulted in many exceptional characteristics [1–4]. Studies to calculate surface elastic constants using MD simulations, the curvature effect by the Cauchy-Born rule, and electronic effects by effective nuclei-nuclei interaction DFT calculations provide superior understanding of surface and interface effects. Size and surface collectively control interactions of nanoscale materials due to existence of large boundaries in its surroundings and thus interplay of physico-chemical interactions. The surface free-energy is size-dependent and hence increases almost inversely with the decreasing feature sizes of the material. The collective response of a nanomaterial-medium system that is attributable to reduced dimensions is vital to developing a scientific model that dictates its response as a novel sensor element.

1.4.2 Requirement for Critical Technologies

The nature of modern warfare has changed. The "newbattlespace" is asymmetric, unconventional, distributed, unstructured, low-intensity, hybrid and decentralized. Conflicting requirements of retaining necessary critical military readiness, asymmetric and covert nature of warfare, and financially austere research environment, all necessitate incremental use of technology in support of countermeasures. It is instructive to note that adversaries also rely on the same technology that the civilized societies use as countermeasures. However, there are some pros and cons. Pros – the civilized nations have access to more research base and capabilities. Cons – the civilized nations play by the rules while adversaries do not abide by the same rules. The civilized nations are bound by ethics and must use cautions before exercising any counter measures. Adversaries, on the other hand, do not have that burden, viz. one single "successful" attack on their part is sufficient to inflict severe financial, psychological, and other consequences. Furthermore, since adversaries have access to the same infrastructure and are homogenized in the same and common environment, the task "*is no longer to find a needle in a haystack . . . instead it is – finding hay in a haystack*". Hence, the requirements are complex and different. Some (selected) of the critical requirements requiring that a platform using nexus of technological innovations are provided in the following sections.

For sensing/detection, it is always preferable to interrogate environment via stand-off detection, e.g. optical or high frequency electromagnetic field – such as THz. Alternatively, for sampled collection, a.k.a. point-contact, it can be accomplished in person or by a UAV. Remote controlled UAVs also allow situational awareness by visually inspecting the sample, object, or device under surveillance. Robotic animals are also used for sampled collection, such as from IEDs. A conceptual schematic of robotic animal (SA3) equipped with moisture absorbing fibers is shown in a later section to gather air samples from an IED. In some cases, point or sampled collection is necessary and in those cases, a methodology which can provide *in-situ* verification of contaminants is preferable. Lethal dose at 50 % (LD_{50}) is available for many chemicals and *in-situ* analysis assists a quick-decision making, based on the lethal dose of the chemicals present. However, the threat is not always a "knownfactor". Hence, capabilities for complex processing of information and to provide end-to-end strategic assessments and modeling of mixed and complex hazardous environments to delineate signal are very useful. Distributed nature of wireless sensor networks along with communication devices provide latest trends in identifying and mitigating threat at the point of origin. High performance nanofibers loaded with different compounds have been used by the author for sensing/detection, communication, force protection, and several other features desirable in soldier uniform [5]. Plasmonics or nanophotonics is considered for an invisible soldier program where simply by an appropriate illumination, the light "rounds around" rendering asset invisible. Similarly, fibers embedded with antibiotics and analgesics (including anti-inflammatory and anticonvulsants) are used as a patch for wounds in the battlefield and provide anti-biotic and disambiguation protection, in addition to preventing formation of post injury fibrotic bands. The fibers are also used for nano-filtration to provide filtered water in austere environments of battle fields. There are many similar requirements for critical technologies and a complete scope is beyond the scope of this report and can be found in different critical technology requirement reports.

1.4.3 Sensor Platforms

Nanotechnology based sensor platforms enable direct detection of chem.-bio agents in a label-free and multiplexed format over a broad dynamic range [6]. For instance, nanoscale resonators [7] have allowed detection of mass of molecules by detecting shift in resonance frequency [8]. Surface effect may play a key role in resonant frequency shift, if the thickness of the biomolecular layer becomes comparable to the resonator's thickness. Devices using surface plasmon resonance (SPR) and surface enhanced Raman spectroscopy (SERS) [9] provide optical response [10] as a function of biological molecule interactions resulting from adsorbate-substrate bonding. Several other platforms based on quantum effects in biological systems (QeBS), flexoelectricity [11], electrochemical sensing [12, 13], biomimetic [14], catalysis [15, 16], carbon-filled polymers [2], nanomagentics [17], and cantilever

[18] based platforms have been reported. A full potential and complexity of tasks performed by such a platform can be extrapolated by advanced sciences convergence (ASC) and some of the foresight tools described in a later section and in this volume [19].

Various nanoscale materials with new architectures and improved functionalities in support of chem.-bio sensing [1], environmental pollution sensing/monitoring [2, 20, 21], mitigation/remediation [22], and *in-vivo* analysis of cellular processes and development futuristic integrated platforms in support of health and clinical medicine [18, 23], and safety and security [24, 25] have been reported. Chemical and biological agents and high-yield explosives – a.k.a. improvised explosive devices (IEDs) – display characteristic features which may preferably be interrogated by remote and sampled detection, discrimination, and identification techniques. Several commonly employed technologies for point and/or stand-off detection methods include Mass Spectrometry [26], Ion Mobility Spectrometry [27], Surface Acoustic Waves [28], Fourier Transform Infrared Spectrometry [29], Differential Absorption LIDAR [30], Laser-Induced Fluorescence (LIF) [31], (SPR) [10, 20], SERS [32], Immunoassay [33], Polymerase Chain Reaction (PCR) [34], Laser-Induced Breakdown Spectroscopy [35] and LIDAR Backscatter systems [36]. For chem.-bio sensing, nucleic acids serve as powerful tools for recognition and monitoring of many compounds. Recent advances in molecular biology allow study of the effects of proteins and drugs on gene expression, e.g. gel mobility shift, filter binding, DNA foot-printing and fluorescence-based assays [37].

Electrochemical based biosensors play a vital role for clinical, pharmaceutical, environmental and forensic applications, as they provide rapid, simple and low-cost point-of-care detection of specific nucleic acid sequences [2, 10] by using different chemistries and interactions between target, recognition layer and electrode. Direct electrochemical sensors use DNA-mediated charge transport chemistry. The analysis is based on a guanine signal where a base-pairing interaction recruits a target molecule to the sensor, allowing monitoring of drug/biological molecule-DNA interactions. It is vital to develop sensing strategies to maintain critical dynamics of target capture to generate a sufficient recognition signal. Standard electrochemical techniques, such as differential pulse voltammetry (DPV), potentiometric stripping analysis (PSA), square-wave voltammetry (SWV), etc. are used as genosensors. Since genosensors are compatible with existing micro and nanofabrication technologies, they enable design of low-cost devices that offer potential for detection and diagnosis of diseases and potential for detecting pathogenic bacteria, tumors, and genetic disease by credit card-sized sensor arrays, and may be used for disease surveillance program described later in this report.

A study of functionalized self-assembled monolayer (SAM) consists of organized layer of amphiphilic molecules that use molecules – usually enzymes, antibodies, or nucleic acids to recognize simple bio-molecules of interest. Investigations using SAM based SPR and Atomic Force Microscopy (AFM) techniques detect several pathogens [38]. The SPR detection technique is rapid, real-time, and requires no labeling, and involves immobilizing antibodies by a coupling matrix on the surface of a thin film of precious metal, such as nanoparticles of gold deposited

on the reflecting surface of an optically transparent wave-guide. The precise angle at which SPR occurs depends on several factors. A main response is the refractive index of the metal film, to which target molecules are immobilized using specific capture molecules or receptors along the surface, causing a change in the SPR angle, which is monitored in real-time by detecting changes in the intensity of the reflected light and producing a sensorgram. When the antigens interact with antibodies, the refractive index of the medium surrounding the sensor changes; thus, producing a shift in the angle of resonance proportional to the change in the concentration of antigens bound to the surface.

To detect gas and vapors, response of a nanomaterials based gas sensor is studied based on the reactions of replacement atoms at the sensing surface of these materials, which in-turn relies on change of the resistance of the oxide. Depending on the free electron density in the space charge layer, the depletion region is increased. Since electric properties are influenced by the depletion layer, variation in electrical conductivity indicates sensor response. Similarly, moisture can influence the resistance or conductivity of oxide materials via two pathways: first, the adsorption of monolayer/s of water molecules at the surface; and second, the process of formation of a parallel resistance path by capillary condensation of water via adsorption of the water molecules as protons and hydroxyl groups within pores. The sensitivity and response of nanomaterials of metal-oxide sensors is highly dependent on the roughness of the substrate, which is caused by the increasing surface area and porosity of the film surface modifications in the film surface morphology. The sensitivity (and selectivity) of a sensor can be improved by parameters such as decreasing the crystallite size, the valence control, and using noble metal catalysts.

A combination of these platforms is recommended for chemical, biological, and gas phase thereat vectors. In fact, bioterrorism remains an attractive option for terrorists to choose and deploy as it is relatively easy and cheap to procure and process raw materials, allows effortless dissemination with little to no detection due to time-phased incubation, and if and when detected, there is ensuing wide spread anxiety and panic beyond the actual physical damage. Categories and characteristics of some of the biological agents are shown in Table 1.1.

Carbon Nanotubes (CNTs) are conducting, can act as electrodes, generate electro-chemiluminescence (ECL) in aqueous solutions, and can be derivatized with a functional group that allows immobilization of biomolecules. CNTs have high surface/volume ratios for adsorption, and have surface/weight ratios ~ 300 m^2/g. The uniform chemical functionalization of CNTs is a key to the formation of biosensors. Oxidation of nanotubes with HNO_3-H_2SO_4 leads to high concentrations of carboxylic, carbonyl, and hydroxyl groups on a surface and removal of the tip to expose the tube interior. Carboxyl groups can readily be derivatized by a variety of reactions allowing linking of biomolecules such as proteins, enzymes, DNA, or even metal nanoparticles. The covalent modification of nanotubes facilitates the creation of well-defined probes, which are sensitive to specific intermolecular interactions of many chemical and biological systems. Covalent modification of single wall CNTs (SWNTs) offers mapping of functional groups at a molecular

Table 1.1 Categories and characteristics of biological agents

Category	Priority rating	Characteristics	Biological agents
A	Agents that pose a threat to national security because –	Can be easily disseminated or transmitted person-to-person Cause high mortality, with potential for major public health impact Might cause panic and social disruption Require special public health	Variola major (smallpox), Bacillus anthracis (anthrax), Yersinia pestis (plague), Clostridium botulinum toxin (botulism), Francisella tularensis (tularemia), Filoviruses, Ebola hemorrhagic fever, Marburg hemorrhagic fever, Arenaviruses, Lassa (Lassa fever), Junin (Argentine hemorrhagic fever), . . .
B	Second highest priority agents that –	Are moderately easy to disseminate Cause moderate morbidity and low mortality Require specific enhancements of CDC's diagnostic capacity and enhanced disease surveillance	Coxiella burnetti (Q fever), Brucella species (brucellosis), Burkholderia mallei (glanders), Alphaviruses, Venezuelan equine encephalomyelitis eastern/western equine encephalomyelitis, Ricin toxin from Ricinus communis (castor bean), Epsilon toxin of Clostridium perfringens, Staphylococcus enterotoxin B. Food and water borne – Salmonella species, Shigella dysenteriae, Escherichia coli O157:H7, Vibrio cholerae Cryptosporidium parvum
C	Third highest priority agents include emerging pathogens that could be engineered for mass dissemination in the future because of –	Availability Ease of production and dissemination Potential for high morbidity and mortality and major health impact	Nipah virus, Hantaviruses, Tick borne hemorrhagic fever viruses, Tick borne encephalitis viruses, Yellow fever, Multidrug-resistant tuberculosis, and others not listed here

resolution. Furthermore, chemical processes to link catalysts, such as transition-metal complexes, to the ends of CNTs are useful in creating or modifying the structures at a molecular scale, creating interconnections for electronic devices, and even developing new classes of materials. During interaction with the polymer

coatings, the electrical properties of the nanotubes are altered, enabling detection of the molecules leading to a very sensitive sensing mechanism.

In addition to nanotubes, novel materials such as porous silicon [39] and porous carbon [40], with porosities of comparable dimensions to those of the biomolecules have been used for biosensor applications. The mesoporous carbon matrix is used for stable immobilization of the biological molecule, and C_{60} serves as an electron mediator. Both C_{60} and NTs are good electron mediators when used with a mesoporous carbon matrix or modified metal electrodes. CNT-based transducers, however, show a significant advantage over porous silicon due to defect free structures, and also because the NTs promote homogenous electron transfer reactions.

Satellites play a major role in communication, navigation, climatology, surveillance, and environmental monitoring, and support many applications. Nanophotonics and micro/nano electromechanical systems (MEMS/NEMS) hold the potential to revolutionize the field of satellite design for environmental pollution monitoring.

The eradication of waterborne diseases is an overwhelming challenge. However, the devastating effects of infectious microorganisms may be minimized and controlled through efficient methods of monitoring and detection. Direct pathogen identification and isolation is difficult if not impossible. Indirect "indicator organism" based inferences have been used for decades as indicators of contaminated water. Traditional and standard bacterial detection methods for identifying waterborne pathogens are often not suitable for routine monitoring due to their high cost, inadequate sensitivity, or lengthy processing time. Moreover, all conventional methods require *a priori* knowledge of the pathogen. There is a growing global public health concern about the emergence and reemergence of waterborne microbial pathogens that occur through a complex interaction of social, economic, and ecological factors. Currently, indicators for water quality do not take into account new and emerging microbes. Astoundingly, only $\sim$1 % of microorganisms have actually been characterized; the spectrum of new disease is expanding, antimicrobial resistance is increasing, and waterborne diseases once believed to have been done away with are re-emerging. Clearly, more effective methodologies are needed for monitoring and detection.

The advancement of molecular biology and its application in environmental microbiology will significantly advance rapid detection of waterborne microbial pathogens. Molecular biology-based alternative methods have improved the speed of detection from multiple days, as required for cell culture methods, down to a few hours. For example, real-time PCR allows for rapid (4–6 h) and specific detection of target genome and also yields quantitative estimation of the concentration of the microorganism in the water environment. Hand-held nucleic acid analyzers, miniaturized real-time thermal cycler, have been developed for real-time PCR detection of waterborne pathogens, such as *Cryptosporidium parvum* and *E. coli O157:H7*, with the cell culture-PCR to detect waterborne pathogens. The methods are relatively specific and will not detect all pathogens. However, molecular methods, coupled with high-throughput parallel process may detect microorganisms over a greater range.

1.4.3.1 Point and Stand-Off Detection/Sensor Platforms

Given the complex environment described above, the challenges at subsystem levels occur to evaluate overall effectiveness and efficacy of the sensor systems. Nanotechnology based sensor platforms enable multiple sensing mechanisms to be incorporated on a platform – typically in a lab-on-chip (LOC) format. In addition to common sensing functions, the sensor and transduction system must demonstrate capabilities in the following areas: logistics, response to interference, response to unknown agents, low power consumption, weight/size, reagentless/low-reagent consumption, cross-validated response, ubiquitous presence, and secure signal transmission capability. Achieving such an autonomous system will require some additional advances in both nano and biotechnologies, particularly in the areas of energy storage and smart or self-healing materials to produce rugged, reliable, and effective response in the field. Critical technical challenges arise from the integration of self-healing materials and systems/platform integration.

Point Detection Platforms: Most of the platforms discussed here require analysis based on sampling, hence are point contact. The analysis is accurate, real-time (in most cases), and conform to sensor metrics of specificity, selectivity, and sensitivity. However, due to the extreme nature of some chemical-biological agents, it is not always feasible to have either a direct or close contact with such environments. In such cases, stand-off detection systems are necessary.

Stand-Off Detection/Sensing Platforms: Ideally, a set of methodologies adopted to detect CBRNE agents and contamination should be amenable to both field and laboratory analysis, and provide fast, reliable, and real-time detection and differentiation of chemical, biological (e.g., bacteria, virus, pathogens), VOC, TIC/TIM, pharmaceuticals, and other contaminants at a distance. Generally, optical properties of nanomaterials are considered for stand-off detection/sensing applications when combined with biotechnology and quantum mechanics. Several other approaches include use of nanoparticles, more specifically, quantum dots for catalysis or carriers to enable transduction. A few stand-off detection examples are using surface-enhanced Raman spectroscopy (SERS) and localized surface plasmon resonance. Yet another application is in metamaterials or negative refractive index materials for potential applications in satellite imaging elements. Potential challenges arise in that the source of illumination must have sufficient light intensity with minimum power consumption. Further, intensity based measurements are susceptible to intensity-based noise in signals and require appropriate signal extraction software. Yet another stand-off detection methodology is generation of THz regime electromagnetic waves using carbon nanotubes (CNTs) that identify signatures in reflected/scattered beam of potential chemical-biological agents. Significant challenges still remain in the generation of high frequency using CNTs and also producing CNTs of same chirality. In almost all cases, signal transduction is one of the areas where revolutionary advances could be generated by leveraging NBIC convergence. Technologies that exploit the unique optical, electrical, and mechanical properties of nanomaterials, and find ways to efficiently couple those nanomaterials to sensing elements will be critical. Integration of the following functionalities of stand-off

detection will further enhance their utility: multiplex, parallel processing sensors/actuators interface; battle space suits interface; war fighters status, alerts, and warnings; biotechnologies integration: antidote, prophylaxis, HPE administration; bioinformatics – multi-source fusion, machine learning and recognition; adaptive and self-reflective systems. Some additional technologies, currently in-use are based on smart-phone technology where applications (commonly known as *apps*) use "what is trending", internet-of-things (IOT), and crowd sourcing to sense/detect information and by way of instantaneous transmission assist response deployment by appropriate response unit to mitigate such theat.

1.4.4 Bio-inspired Systems, Biomimickry, Opto/Bio-cloaking

Nature offers a diverse wealth of responsive and multifunctional surfaces, whose properties are unmatched by current artificial materials. As we observe nature closely, many characteristics such as hydrophobic nature of lotus leaf, adhesive force of gecko, camouflage by animals, mechanical strength of spider web, etc., combined with better understanding of the characteristics of advanced and nanomaterials; it is feasible that nanomaterials may present some characteristics allowing us to mimic nature by the synergistic effect of materials formation and further complemented with surface functionalization. By the synergistic effect of laser induced texturing surface functionalization schemes, 3D structures exhibiting controlled dual-scale roughness which mimics the hydrophobic nature of the Lotus leaf, and also depending on the functional entities attached to the structures pH-, Photo-, Electro-, and Chemo- responsiveness can be obtained for microfluidic applications. By creating biomimetic siderophore analogues, Shanzer et al. [14] studied effects of iron-sequestering siderophores to extract scarce iron (III) and hence microorganisms from their environment, that involved arranging the hydroxamic acid moieties arranged along a linear chain, such as ferrioxamine B on three identical side arms in a tripodal arrangement such as ferrichrome, or more complex arrangements such as coprogen. The biomimetic siderophore analogues can also be designed for a particular bacterium to distinguish between related uptake systems of different microorganisms. Also, by employing "drop-on-demand" multiscale biotechnical engineering, three dimensional cell structures of organotypic cell in conjunction with nanomaterials to replenish or replace certain protein compounds are likely to mimic cells the in-vivo environment allowing study of extracellular matrix (ECM), intercellular and cell-to-matrix interactions, and soluble factors and mechanical forces including microfluidic perfusion. Furthermore, by integration of proteins with synthetic membrane materials, provides basis for bio-cloaking films for mimicry of cellular membrane surfaces toward the enhancement of implant biocompatibility. Example of invisible soldier program cited earlier is based on optical cloaking, where plasmonics and suitable incoming light source causes light to "round about" rending object invisible. Such concepts are experimented in battlefield to optically render assets invisible, providing tactical superiority.

1.4.5 Persistent Surveillance of Emerging Diseases

The Term "Bio surveillance" is commonly referred to as the process of data gathering with appropriate analysis and interpretation of biosphere data that might relate to disease activity and threats to human or animal health – whether infectious, toxic, metabolic, or otherwise, and regardless of intentional or natural origin – in order to achieve early warning of health threats, early detection of health events, and overall situational awareness of disease activity. Because of international trade, travel, and migration patterns; pathogens can spread contagious diseases fairly rapidly. Hence, early warning and persistent surveillance to monitor any new infections or diseases, unintentional or otherwise, to map emerging patterns is a key security imperative to containment and remediation with minimum loss. Persistent surveillance requires increased CB, Zoonotic and infectious disease detection/diagnostic capabilities in fielded systems, large pathogen collection and reference materials library, and the ability to integrate existing biosurveillance tools and data fusion capability to include medical and environmental information. Nanomaterials based sensors/detectors in conjunction with bioinformatics and other "omics" provide full-spectrum capability to ensure sustained public health and medical readiness to prepare against bioterrorism and infectious disease outbreaks.

1.4.6 Advanced Sciences Convergence

Advanced Sciences Convergence refers to the early monitoring and identification of emerging scientific advances across multiple disciplines that create revolutionary, integrated and cross-cutting technologies to break through existing solution paradigms. The process of ASC is to understand how different disciplines, focusing on discrete problems and applications, can coalesce into an integrated solution pathway to solve a seemingly intractable problem. It requires understanding of far-reaching end goal that is described in terms of desired actions or qualities of the eventual system. Multiple approaches, some of which may be high risk research, can be pursued simultaneously to create components of the system. The first step in this high-level analysis is to identify the specific requirements and design a strategic approach based on the intersection of global cutting edge scientific advances with the most critical operational requirements identified in collaboration with the user community. These data mining operations are focused in areas identified through the strategic planning process as having a high potential for meeting some desired characteristic of the solution system (Fig. 1.2).

The ASC process requires the sharing of findings to determine if theoretical constructs can be applied to a different discipline. The data mining operations and analysis require both human data mining and human domain expertise. The overall process starts with strategic planning to describe the solution system supported by data mining and investigation of emerging science. Brainstorming and cross pollination assist the ASC process by identifying potential emerging additions to the solution

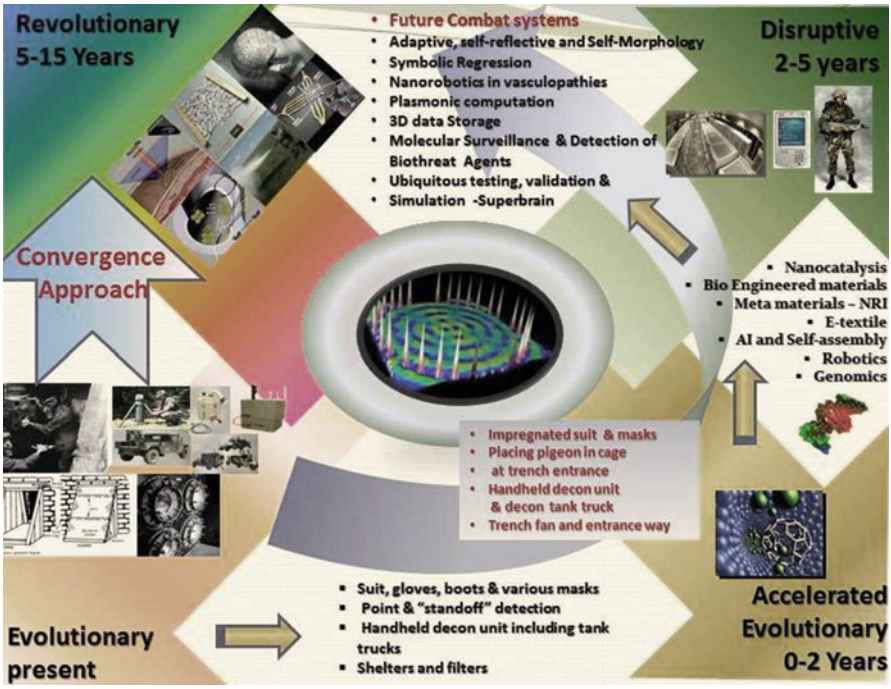

Fig. 1.2 Approaches and strategy used in future trends analysis

system. Due diligence is required to verify the viability of a research entity and feasibility of the scientific effort. Using ASC, three tools were developed viz. Technology Foresight and Roadmapping (TechFARM^{TM}) [41], Automated Data Mining, Analysis, and Surveillance (ADAMS^{TM}) [42], and New and Emerging S&T Trends Surveillance (NESTTS^{TM}) [43]. Details of these tools are described elsewhere [44].

In addition to advance and nanotechnology, we used the ASC approach along with TechFARM^{TM}, ADAMS^{TM} and NESTTS^{TM} to study chemical and biological sensors/detectors to equip war fighters with capabilities that are mostly transparent in operation; fully capable in the event of a chemical-biological attack; detect multiple agents in real-time with high specificity, selectivity, and sensitivity; transmit data to central location for situational awareness; and have the capability to re-generate themselves. The overall goal is to develop an integrated system consisting of many sub-systems (some already developed) to sense/detect multiple chem.-bio agents simultaneously. There are several challenges that must be overcome to bring such a system to reality: systems integration between nano/micro/macro; the possibility of synthetic biomolecules for which complex algorithms must be employed to decipher a complex environment; and dosage level issues, below which chemical agents do not produce noticeable effects. The two most important metrics for the sensing and transduction systems are time to detect concentration to enable appropriate response and response consistent with the species detected.

Using electrospinning, we have investigated nanofibers prepared from high performance polymer composites embedded with metal oxides, glasses coated with rare earth metals, and biocompatible compounds for sensing, and even controlling electrical, optical, and chemical and biological response in support of force protection, health and medicine, and safety and security (Fig. 1.3).

1.5 Fusion of Technologies – Ecosystem of Innovation

As a consequence of convergence of multiple disciplines and technologies, new and innovative solution pathways have emerged leading to smarter, with more precision, cost effective, threat mediation at point of origin (PO2), and with least collateral damage. Such innovations are abundant and progressing at rapid rate. For sensors and detectors – nano-taggants have been identified as technology with can tag, track, and authenticate a threat as it propagates from a point of origin. Optical [45], magnetic [46], and biological [47] tags have been reported in literature, while some companies are working on lab-on-chip (LOC) nano-tags for watermarking, tracking, and communication of multiple threats simultaneously. Biomimicking has also proved an effective tool in threat identification as an orthogonal approach to reduce false positives. The concept of dial-a-beacon is to use remote finger printing and many variations of SERS [48] have been used for that purpose. THz imaging and sensing is a promising technology for identification of concealed weapons, chem.-bio agents, and sub-surface defects. This now can be accomplished with the help of mid-infra-red quantum cascade lasers [49]. Moisture absorbing nanofibers are used as sensors for IEDs when used in conjunction with Transcranial magnetic stimulation (TMS) apparatus, as shown in Fig. 1.3d. For effective surveillance and reconnaissance; the use of high resolution, multi-spectral and polarimetric imaging systems consisting of photon to plasmon conversion is used, as part of plasmonics. For force protection, many variations of ceramers-loaded nanofibers [5] are tested for the Army Combat Uniform (ACU), Battle Dress Uniform (BDU), and Desert Camouflage Uniform (DCU) to provide multiple functionalities, ranging from light weight, breathable, impact-resistant, color-coded sensors arrays, physiological condition based drug-delivery system, embedded GPS, WAN and RFID, and power harvesting capabilities. With the recent advances in plasmonics, the ACU, BDU, and DCU are now part of "invisible soldier" program to optically cloak military assets in the battleground. Another project that is in progress at the author's institute is to provide soldiers with hand-held portable water filtration unit which will reduce soldiers' dehydration considerably. Electrical shielding of sensitive electronics is often necessary as a part of electronic warfare. Metal-impregnated fibers provide necessary electro-magnetic shielding for UAVs, sensitive electronics, and other assets that may require such shielding.

Due to enhanced features resulting from reduced dimensionality, nanomaterials offer unprecedented advantage to offer "materials and devices by design". The spectrum of innovations for predictive design is a set of parallel, inter-woven

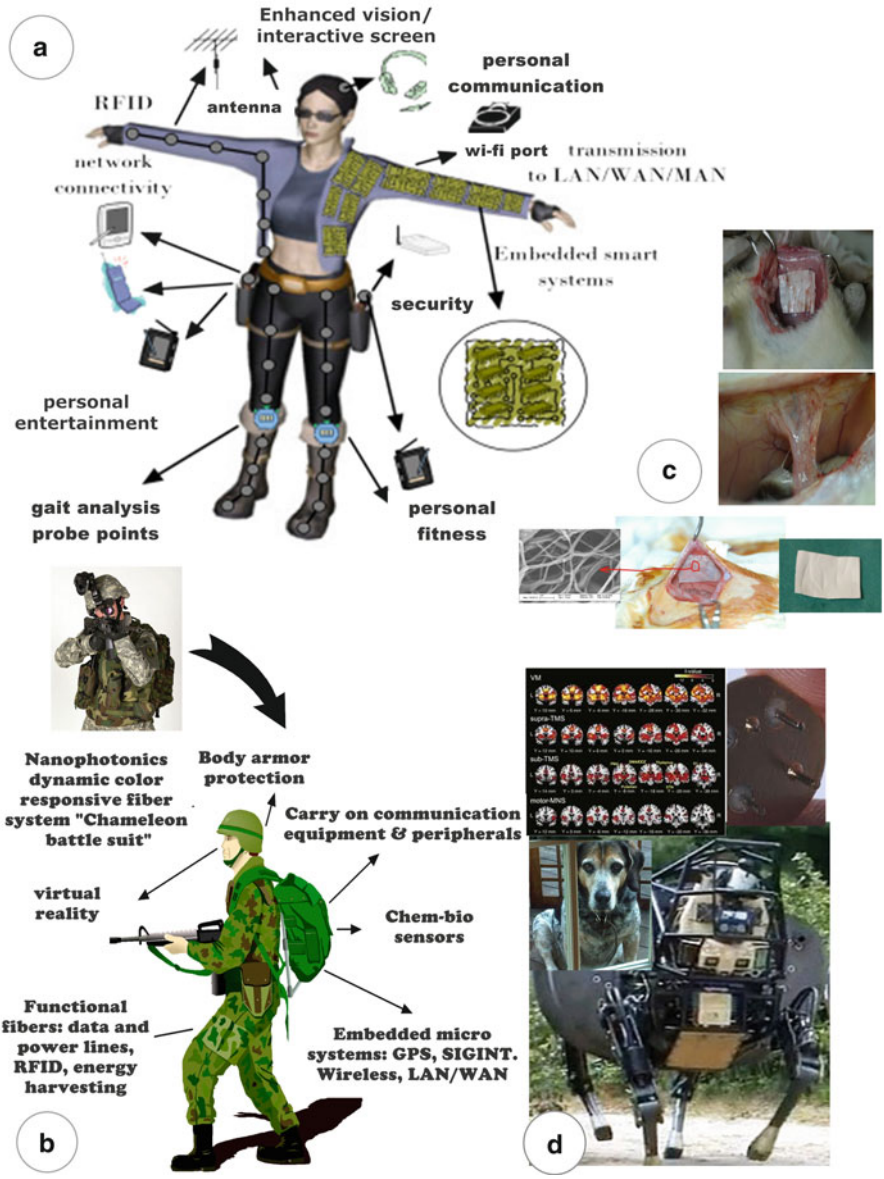

Fig. 1.3 Use of electrospinning for (**a**) force protection, (**b**) chem.-bio sensors, (**c**) health and medicine and (**d**) security

activities oriented towards providing unique capabilities to counter such threats with far more accuracy at POO in terms of sensing/detection, mitigation, communication, pathogen ID and characterization, disease surveillance, novel vaccines development, therapeutics, and human performance enhancement to name a few. Due to the

sensitive nature of many other similar recent discoveries, a comprehensive list is beyond the scope of this report; however, it should suffice to state that nexus of technological innovations play a major role in situational awareness, threat mitigation, and effective countermeasures supporting defense against terrorism.

1.6 Ethical Consideration

An ecosystem of innovations, as described above, offers countermeasures, calculated response, and potential solution pathways in ways never imagined possible earlier. However, coupled with every enhanced capability, there comes an added responsibility of using the capability with a sense of judgment, which may often be perceived as fiduciary. In a conventional battlefield, conventional "rules of engagements" apply. However, in current asymmetric, kinetic, and unconventional warfare, the rules of engagement from adversaries are non-existent, in part due to undefined battlefield, enemy and end justifying means approach by adversaries. While the "societal" burden mostly rests on the civilized society to be protective "all the time", adversaries escape that responsibility, and perhaps may even be perceived as "underdogs". The axiomatic goal of national security and the *Jus ad Bellum*is the protection of the population by all means possible, hence in this convoluted milieu and to somehow justify "*political correctness*", it is indispensable to revisit definition of ethics and view it through S&T lenses.

Ethical issues related to use of S&T usually in the current context focus on military (counter terrorism, weapons of mass destruction, chemical warfare, Lysergic acid diethylamide (LSD), nuclear testing, etc.), medicine (human subjects in military experiments, human performance enhancement (HPA), biotechnology – cloning, gene therapy/alteration/mutation), and decision making, viz. teleology (Consequence Ethics), deontology (Duty Ethics), and personal ethics. Barring ethical conflicts such as violation of established world orders or exception-less moral principles, infliction of harm or exposure to significant risks of harm without prior consent, counter-terrorism and respect for human rights are not mutually exclusive.

Terrorism is an assault on human rights and states have a right and obligation to protect their population from terrorist attacks. States must respect the basic human rights of terrorist suspects as well, as – everyone is equal before the law – SCR 1373 (2001). Furthermore, the U.N. Security Council often argues how its powers should be exercised when the U.N. Charter offers no specific criteria, i.e. when different States see their interest differently and exercise more powers than the others. The UN High-level Panel on Threats, Challenges and Change proposed in its 2004 report the following criteria to guide the Council's decision on recourse to armed forces: seriousness of threat; proper purpose; last resort; proportional means; and balance of consequences [50].

States are required to ensure that legislation is not vague or too broad and due process and human rights safeguards are in place. Any measure taken to

prevent and combat terrorism must comply with international law of Armed Conflict (ILOAC), in particular human rights law, refugee law and international humanitarian law. Effective counter-terrorism measures and the protection of human rights are complementary and mutually reinforcing. A detailed scope of protection of victim/human rights and states obligation to afford ethico-legal issues is beyond the scope of this chapter, it is instructive, nevertheless, to mention that criteria for using technologies in national security settings must engage technical and ethical concepts to revise/develop pertinent laws to ethico-legally govern use of S&T. There is less harm done to the subject by using the latest technology, i.e. if an individual poses a realistic and immediate threat of severe harm to others. Hence while choosing the most effective technology, the least harmful (or may be termed as the most appropriate) of among such options should be utilized. The use of such technologies must be admissible in a court of law. Using these technologies in a preventative or predictive manner is still practically problematic and should not be implemented until further development and adequate ethical frameworks are addressed and/or generated.

It is an acknowledged position that asserting advanced forms and applications of S&T should not be used and/or experimented with as a potential viability in warfare. Further, in an ideal world, this would not be the case, but recognize the pitfalls of the "is/ought" dichotomy, and the realities that any other forms of advanced S&T historically have, can, and will be employed in such agenda. Moreover, the current and future iterations of combat will not adhere to conventional Napoleonic doctrine, and will become ever more hybrid and irregular. Thus, in order to provide accurate intelligence, surveillance, preparedness and interdiction of such combative postures, nexus of technological innovations and advanced S&T may be employed, so as to remain aware, alert and actively ready for any/all such contingencies, and in support of both technical and ethico-legal efforts to sustain a prudent, responsible stance of S&T preparedness.

1.7 Conclusion, Discussion, and Path Forward

The report provides an overview of how novel phenomena arising due to reduced dimensions of nanomaterials and device/system configurations are used address some of the grand challenges for the twenty-first century. Although, addressing all of the challenges is beyond the scope of this report, the focus is on safety, security, and sustainability. Discussion includes novel sensing platforms, sensors/detectors for monitoring pollution, contamination, and interrogating hybrid threat-vectors, especially in war theaters; personal protection equipment; information and communication technologies; disease surveillance; water-borne threats and contamination remediation strategies; etc. Furthermore, sensors are increasingly used in augmenting human capabilities at the neural-digital interface, thus providing technological base for future sustainability. Sensors/actuators systems consisting of additional

components, such as nanoantennas will demonstrate massive connectivity. To achieve "ideal" sensor platforms, many questions remain at the material level. In view of ever increasing complexity and unpredictable nature of threat vectors, it is crucial to utilize advanced technologies in conjunction with ASC, as countermeasures. Use of innovations of technologies also provide ethical and legal basis to adjudicate an appropriate response posture.

References

1. Vaseashta A, Dimova-Malinovska D, Marshall J (2005) Nanostructured and advanced materials. Springer Science and Business Media, Dordrecht
2. Vaseashta A, Mihailescu I (2007) Functionalized nanoscale materials, devices, and systems. Springer Science and Business Media, Dordrecht
3. Magarshak Y, Sergey K, Vaseashta A (2009) Silicon versus carbon. Springer Science and Business Media, Dordrecht
4. Vaseashta A (2012) The potential utility of advanced sciences convergence. In: Advances in neurotechnology – ethical, legal, and social issues. CRC Press, Boca Raton, pp 15–36. ISBN 978-1-4398-2586-0
5. Vaseashta A, Braman E, Susmann P, Bolgen N (2012) Loaded nanofibers for force protection, filtration, decontamination. In: Proceedings of the nanotechnology for defense (NT4D), chem.-bio defense & medical applications, nanotechnology for defense (NT4D/ITAR restricted and military critical), Summerlin, Aug 2012
6. Erdem A (2008) Electrochemical sensor technology based on nanomaterials for bimolecular recognition. In: Vaseashta A, Mihailscu IN (eds) Functionalized nanoscale materials, devices, and systems. Springer Science and Business Media, Dordrecht
7. Pokropivny V, Pokropivny P, Vaseashta A et al (2005) Ideal nano-emitters and panel nano-devices based on 2D crystals of superconducting nanotubes. In: Vaseashta A (ed) Nanostructured and advanced materials. Springer, Dordrecht, pp 367–370
8. Denkbas E et al (2012) Nanoplatforms for detection, remediation, and protection against chem.-bio-warfare. In: Vaseashta A, Braman E, Susmann P (eds) Technological innovations in sensing and detection of chemical, biological, radiological, nuclear threats and ecological terrorism. Springer Science and Business Media, Dordrecht. ISBN 978-94-007-2488-4
9. Kawai NT, Spencer KM (2004) Raman spectroscopy for homeland defense applications. Raman Technology for Today's Spectroscopists, pp 54–58
10. Vaseashta A, Stamatin I (2007) Electrospun polymers for controlled release of drugs, vaccine delivery, and system-on-fibers. JOAM 9(6):1506–1613
11. Petrov A (2012) Disposable membrane sensors for biohazardous substances. In: Vaseashta A, Braman E, Susmann P (eds) Technological innovations in sensing and detection of chemical, biological, radiological, nuclear threats and ecological terrorism. Springer Science and Business Media, Dordrecht. ISBN 978-94-007-2488-4
12. Erdem A (2012) Nanomaterials based sensor development towards electrochemical sensing of biointeractions. In: Vaseashta A, Braman E, Susmann P (eds) Technological innovations in sensing and detection of chemical, biological, radiological, nuclear threats and ecological terrorism. Springer Science and Business Media, Dordrecht. ISBN 978-94-007-2488-4
13. Wang J (2003) Nanoparticle-based electrochemical DNA detection. Anal Chem Acta 500:247–257
14. Shanzer A, Felder CE, Barda Y (2009) Natural and biomimetic hydroxamic acid based siderophores. In: Rappoport Z, Liebman JF (eds) The chemistry of hydroxylamines, oximes and hydroxamic acids. Patai's Chemistry of Functional Groups Ltd/Wiley, Chichester

15. Guidotti M et al (2012) Nano-structured solids and heterogeneous catalysts: powerful tools for the reduction of CBRN threats. In: Vaseashta A, Braman E, Susmann P (eds) Technological innovations in sensing and detection of chemical, biological, radiological, nuclear threats and ecological terrorism. Springer Science and Business Media, Dordrecht. ISBN 978-94-007-2488-4
16. Guidotti M (2013) Structured inorganic oxide-based materials for the absorption and destruction of CBRN agents. In: Vaseashta A (ed) Advanced sensors for safety and security. NATO 2012. Springer, Dordrecht, pp 43–52
17. Gould P (2006) Nanomagnetism shows in-vivo potential. Nanotoday 1(4):34–39
18. Vaseashta A, Riesfeld R, Mihailescu I (2008) Green nanotechnologies for responsible manufacturing. In: MRS proceedings, 1106, 1106-PP03-05. San Francisco, CA, USA. doi:10.1557/PROC−1106-PP03-05
19. Smith J, Vaseashta A (2013) Advanced sciences convergence to analyze impact of nanomaterials on environment, health and safety. In: Vaseashta A (ed) Advanced sensors for safety and security. NATO 2012. Springer, Dordrecht, pp 81–89
20. Vaseashta A, Erdem A, Stamatin I (2006) Nanobiomaterials for controlled release of drugs and vaccine delivery. In: MRS proceedings, 920, 0920-S06-06. San Francisco, CA, USA. doi: 10.1557/PROC-0920-S06-06
21. Pumakaranchana O, Phonekeo V, Vaseashta A (2008) In: Vaseashta A, Mihailescu I (eds) Functionalized nanoscale materials, devices and systems. Springer, Dordrecht
22. Vaseashta A et al (2007) Nanostructures in environmental pollution detection, monitoring, and remediation. Sci Technol Adv Mater 8:47–59
23. Tripathi RD et al (2007) Arsenic hazards: strategies for tolerance and remediation by plants. Trends Biotechnol 25:158–165
24. Vaseashta A, Braman E, Susmann P, Dekhtyar Y, Perovicha K (2012) Sensors for water safety and security. Surf Eng Appl Electrochem 48:478–486
25. NATO, North Atlantic Treaty Organization (2003) AJP-3.8 – Doctrine for the NBC Defense of NATO Forces
26. Hagan NA, Smith CA, Antoine MD, Lin JS, Feldman AB, Demirev P (2012) Enhanced in-source fragmentation in MALDI-TOF-MS of oligonucleotides using 1,5-diaminonapthalene. J Am Soc Mass Spectrom 23(4):773–777
27. Krebs MD, Zapata AM, Nazarov EG, Miller RA, Costa IS, Sonenshein AL, Davis CE (2005) Novel technology for rapid species-specific detection of Bacillus spores. IEEE Sens J 5(4):696–703
28. Khuri-Yakub et al (2007) The capacitive micromachined ultrasonic transducer (CMUT) as a Chem/Bio sensor. In: IEEE ultrasonics symposium, New York, 2007, pp 472–475
29. Swim CR (2004) Sources for standoff chem.-bio detection. Unclassified report, U.S. Army Edgewood Chemical Biological Center, Aberdeen Proving Ground
30. Saito Y, Weibring P, Edner H, Svanberg S (2001) Possibility of hard-target lidar detection of a biogenic volatile organic compound, alpha-pinene gas, over forest areas. Appl Opt 40(21):3572–3574
31. Killinger D (2003) Optics in chemical and biological weapons detection. Defense section of optics report, on-line Journal: www.opticsreport.com. 19 Aug 2003
32. Sun L, Yu C, Irudayaraj J (2007) Surface enhanced Raman scattering based nonfluorescent probes for multiplex detection. Anal Chem 79(11):3981–3988
33. Wild D (2005) The immunoassay handbook. Elsevier, Kidlington/Oxford
34. Erdem A, Karadeniz H, Caliskan A, Vaseashta A (2008) Electrochemical DNA sensor technology for monitoring of drug–DNA interactions. NANO Br Rep Rev 3(4):229–232
35. Barbini R et al (2000) In: Proceedings of EARSeL-SIG-LIDAR, Dresden/FRG, 1, 122. Dresden, Germany
36. Tamer F et al (2008) Lidar backscatter signal recovery from phototransistor systematic effect by deconvolution. Appl Opt 47(29):5281–5295
37. Eccleston JF et al (2005) Fluorescence-based assays. Prog Med Chem 43:19–48

38. Vaseashta A, Irudayaraj J (2005) Nanostructured and nanoscale devices and sensors. J Optoelectron Adv Mater 7(1):35–42
39. Sailor M, Schmedake T, Cunin F, Link J (2002) Standoff detection of chemicals using porous silicon "smart dust" particles. Adv Mater 14:1270
40. Lee J, Kim J, Hyeon T (2006) Recent progress in the synthesis of porous carbon materials. Adv Mater 18(16):2073–2094
41. TechFARM™: NUARI Trademark: TechFARM, serial # 85287943, Commissioner for Trademarks
42. ADAMS™: NUARI Trademark: ADAMS, serial # 85287846, Commissioner for Trademarks
43. NESTS™: NUARI Trademark: NESTTS, serial # 85287940, Commissioner for Trademarks
44. Vaseashta A et al (2011) NBIC, GRAIN, BANG, and TechFARM– ASC for surveillance of emerging S&T trends. In: Proceedings of the 4th international seville conference on future oriented technology analysis, May 2011. Seville, Spain
45. Hyun B et al (2008) Electron injection from colloidal PbS quantum dots into TiO2 nanoparticles. ACS Nano 2(11):2206–2212
46. http://www.bnl.gov/bnlweb/pubaf/pr/PR_display.asp?prID=1448
47. Peng X, Draney D (2004) Near IR fluorescent dyes for biological applications. LPI April/May 2004
48. Andrade GFS, Fan M, Brolo AG (2010) Multilayer silver nanoparticles-modified optical fiber tip for high performance SERS remote sensing. Biosens Bioelectron 25(10):2270–2275
49. Yao Y, Hoffman AJ, Gmmachi CF (2012) Nature photonics, mid-infrared quantum cascade lasers. Nat Photonics 6:432–439
50. Report of the High-level Panel on Threats, Challenges and Change (2004) A more secure world: our shared responsibility. UN Doc A/59/565 [207]

Chapter 2
New Terahertz Security Opportunities Based on Nanometric Technology

Hans L. Hartnagel

Abstract To identify weapons hidden under the apparel of people walking through entrance gates it is important to use THz illumination of sufficient power levels and fast image detection and processing. Various approaches of THz generation by nanometric dimensions are under studies in connection with semiconductor structures as well as electron beam systems. The issues of a THz camera are discussed. Power-level increases require paralleling many sources such as those of two-laser optical mixing in suitable non-linear materials or those of ballistic resonances in heterostructures of nanometric dimensions. In particular heat-sinking optimization is required so that THz-illuminating sources can be distributed along the frame of the entrance door for efficient employment of imaging facilities. THz detection is then using optical mixing so that phase and amplitude data can be derived by a matrix of pixels for ultrafast imaging. These pixels need to have antennas with low side lobes to avoid ghost images, produced by transverse resonances of the pixel matrix. The THz frequencies employed are initially aimed at narrow-band facilities of 830 GHz to identify metal and dielectric objects. This means that the required antennas for sending and detection can be based on dipole schemes. The ultimate wide-band possibility to identify the chemical compositions of explosive materials needs the wide-band antennas, such as half-spherical Si lenses.

Keywords THz • Optical mixing • Ballistic electron resonance • Field-emission • Security

H.L. Hartnagel (✉)
Institute for Microwave Electronics and Optics, Technical University Darmstadt,
64283 Darmstadt, Germany
e-mail: hartnagel@mwe.tu-darmstadt.de

A. Vaseashta and S. Khudaverdyan (eds.), *Advanced Sensors for Safety and Security*,
NATO Science for Peace and Security Series B: Physics and Biophysics,
DOI 10.1007/978-94-007-7003-4_2,

2.1 Introduction

Electromagnetic signals at Terahertz frequencies have the advantage that their photon energies are in the low meV range and therefore not capable to break up organic molecules of living cells. Therefore they have been considered for many applications such as airport surveillance. Such scanners can detect metals such as those of weapons hidden under clothing from a distance of several meters, without exposing the persons to harmful radiation. There are many other applications, such as identifying the validity of documents by identifying THz metallic thin-film structures covered by only optically in transparent paints. THz spectroscopy is used to characterize many materials, including packaging, explosives and drugs. A recent application has been to characterize single-wall nanotube thin film electrodes. In another approach, using a separate pump beam to excite charge carriers in a material shortly before the THz analysis is carried out; information about ultrafast carrier dynamics may be obtained. A recent example of such time-resolved THz measurement deals with poly (3-hexylthiophene) and methanofullerene blended films.

THz radiation can pass through clothing and packaging, but they are strongly absorbed by metals and many other inorganic substances. THz sources use a number of basic techniques, namely either harmonic extraction from the mm-waves or using various methods from the optical signals. The possibility of deep-infrared lasers by quantum-cascading reaches the low THz frequencies of interest only by cooling to liquid nitrogen or below.

Here then several approaches are described as developed by the research team of the author and his international research partners, together with an assessment of the capability for wide-spread applications. Of course a decision is made here to not base the approach on such techniques as quantum cascade lasers, where low-temperature usage appears to be required for the generation of lower THz frequencies as required for the security issues under consideration.

2.2 Ballistic Electron Wave Swing (BEWAS)

A new type of THz source is presented, which can provide relatively large signal powers up to 2 THz. It is based on an electron resonance structure formed by a semiconductor heterojunction structure. The electrons in n-layer need to be accelerated by V_e – applied alternating voltage. They reach the barrier of the widegap semiconductor and are reflected without any loss of kinetic energy. They then travel ballistically towards the opposite barrier, where they are reflected again. When V_e changes the polarity, this process continues. The resulting electron resonance produces THz signals. The new concept is based on room-temperature reflection of ballistic electrons in a short (length L typically 150 nm) high-mobility n-type semiconductor terminated at both ends by wide band gap materials. The length L is sufficiently short for ballistic electron resonance to occur at room temperature. The reflection occurs at the edge of the heterojunctions without any loss of kinetic

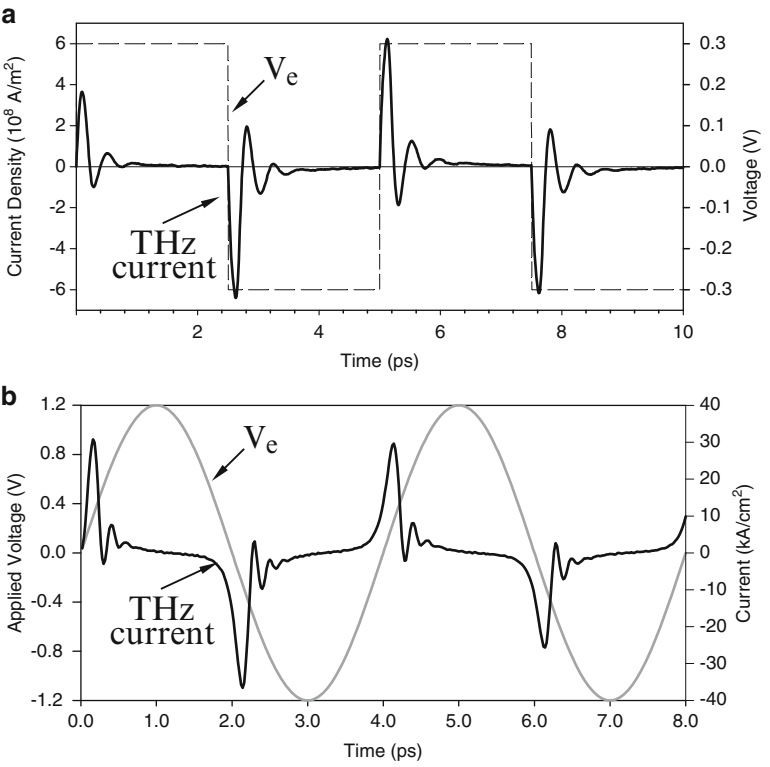

Fig. 2.1 Temporal evolution of current density in response to (**a**) square-wave and (**b**) sinusoidal signal

energy. The electrons are accelerated towards the barrier by an energizing RF voltage V_e, (of typically 100 GHz) sinusoidal or pulse-shaped voltage. The electrons are reflected several times with gradual loss of energy due to occasional scattering. They then need to be accelerated again by the opposite phase of the voltage of V_e. The material to be selected needs to exhibit good ballistic properties and InGaAs is considered here, although there are possibly even better materials.

Monte Carlo simulation, undertaken by Prof. D. Sheng Ong [1] under Humboldt Fellowship with the author in Darmstadt, has shown that this device gives an efficiency of more than 40 % of a suitably designed 1 THz device (Fig. 2.1). This device is not a harmonic generator for V_e (say the 100 GHz input), but generates the THz signal by electron resonance. The device is therefore an electron wave device which can be considered to be equivalent to the electromagnetic wave resonator, i.e. the well-known laser. The energy is provided by the applied V_e. The fabrication of an n++InGaAs–InAlAs–n InGaAs–InAlAs-n++InGaAs structure with ohmic contacts at both ends is performed by the research student Ion Oprea [2] in Darmstadt (Figs. 2.2 and 2.3).

Fig. 2.2 Epitaxial layers of the wafer used

Layer	Thickness(nm)	Doping(cm^{-3})
n^{++}-$In_{0.53}Ga_{0.47}As$ contact	150	$1x10^{19}$
$In_{0.52}Al_{0.48}As$ barrier	15	undoped
$In_{0.53}Ga_{0.47}As$ spacer	3	undoped
n^{+}-$In_{0.53}Ga_{0.47}As$	144	$1.5x10^{16}$
$In_{0.53}Ga_{0.47}As$ spacer	3	undoped
$In_{0.52}Al_{0.48}A$ barrier	15	undoped
n^{++}-$In_{0.53}Ga_{0.47}As$ contact	2000	$1x10^{19}$
InP substrate S.I.		

CST Microwave Studio solver was used to design and calculate the microstrip circuitry. The microstrip circuitry was fabricated on a ceramic thermoset polymer composite substrate and the devices were flip-chip soldered on it. The measurements were performed with the setup consisting of an Anritsu MG3692A signal generator, the microstrip circuitry embedded in a microstrip test fixture and an HP 8565E spectrum analyzer. The results are presented in Fig. 2.3b. These depend of course on the frequency dependence of the terminating network. An optimization should be possible for a selected output frequency by employing electronic resonance terminations. To enhance the effect, several of these resonant structures can be operated in series, provided that the electron charges in several neighboring swings do not interfere with each other to affect the operation negatively. The series connection has also the benefit of enhancing the impedance of this device as required for suitable incorporation in an electronic structure.

2.3 Double Step-Recovery Diodes for Diffusive Electron Resonance a Further New Concept for THz Signal Generation

A heterostructure equivalent to the well-known step recovery diode principle, arranged as a double structure gives a new nonlinear device for highly efficient harmonic THz signal generation. Like in the case of step recovery diodes, these devices exhibit promising performance especially for the generation of higher order harmonics. Theoretical and experimental results are presented. The well-known

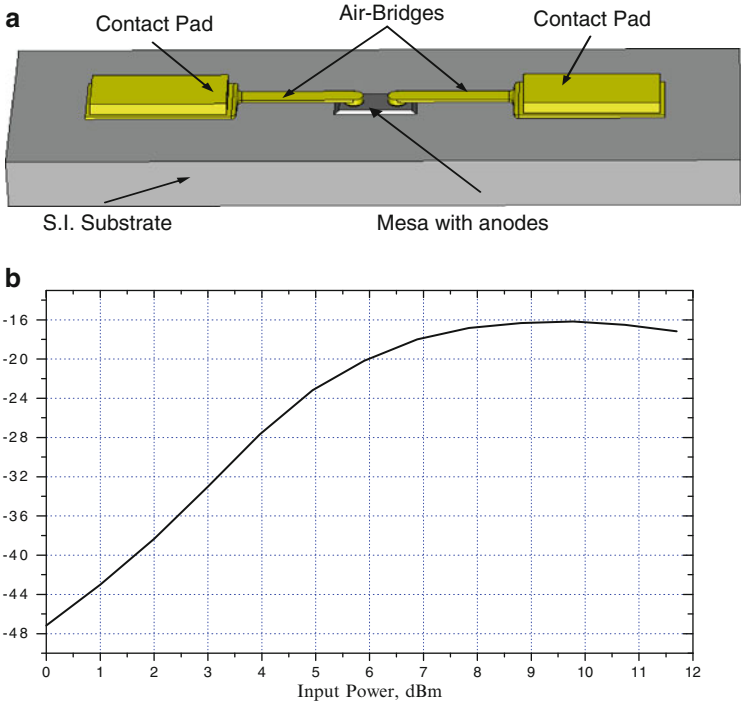

Fig. 2.3 (**a**) Test structure employed and (**b**) preliminary measurements of the output power from a two barrier BEWAS (the vertical scale is the uncalibrated output power, and the correct values were not determined. The output frequency was around 0.06 THz and the input at about 15 GHz, therefore this represents only a feasibility of the effect and not yet a try THz source)

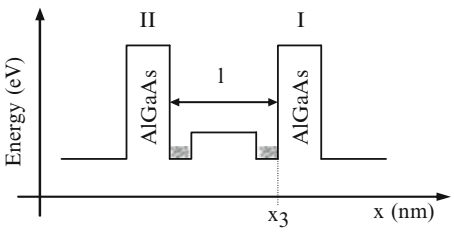

Fig. 2.4 Schematic illustration of the energy band profile for enhanced THz harmonic output by diffusive transport

step recovery effect of pn-junctions can be realized in a highly improved way by transferring the basic principle to heterojunctions. In fact, two barriers opposing each other via a narrow-gap semiconductor such as AlGaAs/GaAs/AlGaAs or InAlAs/InGaAs/InAlAs with a suitable n-doping can be considered as two step-recovery-diode junctions in opposition, which operate without any dc bias requirement. There are several types of structurization. One has a localized bile electron source in front of the barriers, as shown by Fig. 2.4. Here a suitable doping is employed (see Fig. 2.4).

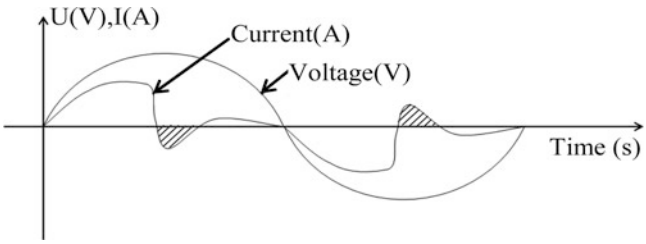

Fig. 2.5 Variation of the output harmonic signal as function of the input RF versus time for equivalent double step recovery diode

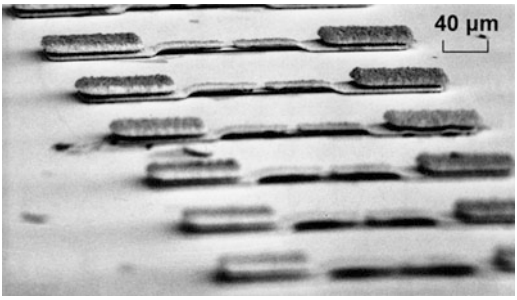

Fig. 2.6 SEM picture of two fabricated devices connected in planar approach

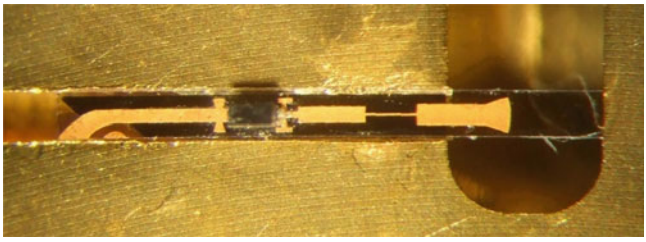

Fig. 2.7 Microscope picture of the fabricated circuitry with the device mounted on a gap of the microstrip line

When the fundamental wave voltage is applied, the electrons from the higher potential trough travel towards the lower potential barrier by diffusive transport. When the electrons reach the opposite barrier, they are stationary there so that the current is abruptly terminated. When the opposite phase of the fundamental takes place, these electrons are travelling to the opposite barrier until they are stationary there (see Fig. 2.5). This step-recovery type of behavior produces sharp interruptions of current, ideally-depending on the design –half through the phase. Such current interruptions have a considerable harmonic constant, which can be taken out by filtering. Experimental realizations [3] are shown by Figs. 2.6 and 2.7.

The cut-off frequency of the new types of devices was estimated to exceed 1 THz. Therefore, and for ease of manufacturing and measurement, frequency multiplication from W-Band frequencies (75–110 GHz) to approximately 300 GHz was chosen as a first step to validate the theoretically found results. The fabrication approach included a planar tripler circuit on a quartz substrate and the growth and dicing of two of the structures shown in Fig. 2.4, connected in series configuration. The device was flip-chip mounted on a 50 μm thick substrate with the microstrip circuitry developed and optimized by simulation for sufficient impedance match and low transmission losses. Figure 2.7 shows a microscopic view of the planar circuitry. Using WR-03 and WR-10 waveguides as input and output in split-block technology provided a fully waveguide based tripler setup with the possibility of TRL-calibration and error correction. A geometrical model of the device was used within full 3D field simulation software to include parasitic effects of the device structure. When feeding the input waveguide of the resulting split-block with a frequency of 102 GHz the output signal around 306 GHz was clearly detectable proving that the theoretical approaches hold. The measured efficiency, however, did not reach the simulated values up to now. Higher input power and improved circuit design with tunable elements are expected to raise the efficiency for tripling operation to higher values.

2.4 Optical Pulsed Techniques and Continuous Wave Methods

To generate THz radiation using suitable materials such as some of the compound semiconductor materials as targets, the optical excitation can be provided [4] by typically a 12-fs mode-locked Ti:sapphire laser of center frequency 790 nm and repetition rate 75 MHz. The emitted THz radiation is then detected either using a pneumatic Golay cell (incoherent detection) or in a conventional time-domain spectroscopy arrangement using electro-optic (coherent) detection.

An extension of the ballistic device is the use of simultaneous dc biasing and the generation of mobile electrons in a short quantum well of smaller gap values by a pulsed optical signal. The optical pulses can be longer than half of the THz period due to space charge limited effect of electron bunch transfer. Therefore, this approach can be extended also to the involvement of low-cost femtosecond laser pulsers together with a dc bias voltage. Instead of solid-state ballistics, corresponding laser-pulse initiated field emission of electron bunches in a THz vacuum resonator can be employed, too [5]. Another approach was also recently published, where resonant tunneling structures were employed to sharpen the electron energies of the ballistic electrons [6], see Fig. 2.8.

By using two laser emissions with frequency differences in the THz range, continuous wave sources can be obtained for very convenient application conditions. A considerable effort is under way in Darmstadt, as can be seen by a large range of recent publications (see [7–11]).

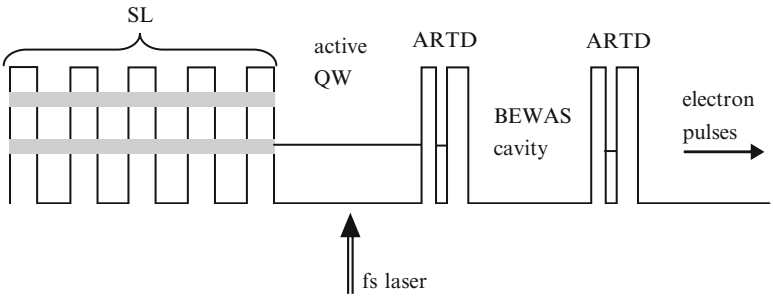

Fig. 2.8 Schematic representation of the conduction band of the THz source

The dominant cw optoelectronic technology here is *photomixing employing materials with short mobility lifetimes and charge-carrier lifetimes* (corresponding to ultrafast trapping and ultrafast recombination, respectively). The most successful and until recently the only available material is LTG-GaAs (LTG: Low-Temperature-Grown) with a carrier trapping time constant of about 0.3 ps and a recombination time constant of several ps. Antenna-coupled photomixers on the basis of LTG-GaAs have proven to be versatile emitters and detectors of THz radiation providing for high signal-to-noise ratios in optoelectronic systems. And this is despite the fact that the emitters even of these workhorses of cw THz optoelectronics have output powers of not more than 1–2 μW. While LTG-GaAs for a long time has been the only useful choice for cwphotomixing, more recently new ultrafast GaAs-based materials and growth/preparation techniques have emerged such as GaAs with ErAs island and ion-implanted GaAs. In synchrony with the development of a wider material basis and inspired by an improved understanding of the material-science aspects concerning ultrafast materials, attempts to develop ultrafast materials also for wavelength ranges other than 0.8 μm, and namely for the 1.55-μm telecom window, finally begin to look promising. Materials with short lifetimes, high mobility of the photo-generated charge carriers and the required high dark-resistivity emerge (among others, LTG-GaAsSb at TU Darmstadt) thus gradually establishing a potential for THz optoelectronics based on 1.55 μm lasers.

There is a long-established consensus in the community that it is highly desirable to establish 1.55 μm THz optoelectronics and move away from the 0.8-μm wavelength regime. The first reason is the superior properties of the relevant semiconductor materials as compared with GaAs, notably the higher electron mobility, which promises a larger sensitivity of THz detectors and, together with the better thermal conductivity, let us expect the generation of more output power of the THz emitters. The second reason is the possibility to link THz optoelectronics with the 1.55 μm telecommunications technologies. This by itself brings with it a number of advantages, the first and foremost being that of the much more advanced performance status of high-power semiconductor lasers and (fiber) amplifiers with operation at a single lateral and longitudinal mode. Costs of these lasers are also significantly lower and the lifetimes longer. In addition, with the fact in mind that

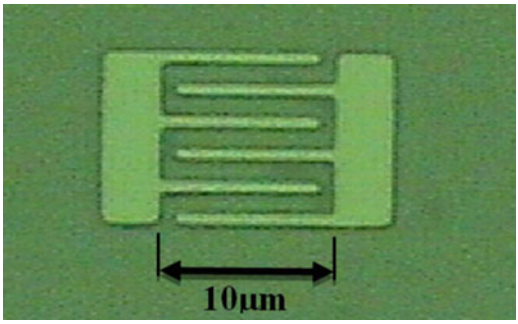

Fig. 2.9 First step product photomixer (Ni Material 93 nm above **N^+i GaAs**)

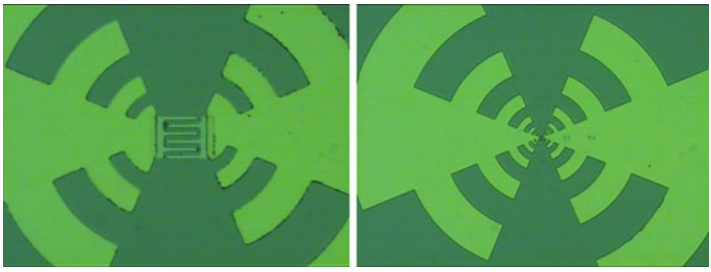

Fig. 2.10 Second step complete antenna with photomixer (Cr 20 nm + Au 105 nm above N+i GaAs)

the significance of the 1.55-μm wavelength regime arose from fiber, one would like to draw on the vast available fiber technologies there in order to enable the building of robust, hands-off and eye-safe THz systems where the optical power is delivered through fibers and where the THz unit of the system can be spatially separated by many meters from the optical unit containing the light source. An advantage not to be forgotten is the sustained advance of the telecommunications components technology which would also feed and support technological advances in THz optoelectronics in the future. The N^+i GaAs was developed (TU Darmstadt Laboratory) into complete photoconductive devices by using the Lithography, Photoresists and Developers and by using the specific Lithography Mask (log-periodic antenna) for photomixers and antennas suitable for THz wavelengths (see the figures below) (Fig. 2.9).

Photomixing can be very generally defined as the optical heterodyne down conversion of two laser beams with detuned frequencies (here in the THz range). The "photoconductive mixer" or photomixer consists therefore of a current source, able to deliver a current modulated at high frequencies, connected to a planar distributed circuit such as a planar antenna or a coplanar waveguide. The active element, i.e. the photomixer is essentially a photoconductor (Fig. 2.10).

The photoconductance of the switch is modulated by the optical beating of the two CW laser sources (each assumed to be single mode), producing a THz current

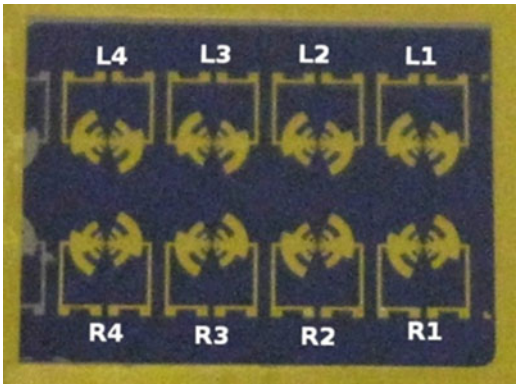

Fig. 2.11 Complete sample with 8-antenna with photomixer

which when feed into a planar antenna generates electromagnetic radiation in the THz frequency range. The advantages and novelty introduced by the usage of $\mathbf{N^{+}i}$ **GaAs** as the photoconductive material resides in the extremely short carrier trapping time (suitable for modulation of the photocurrent at very high frequencies) and also the high dark resistivity and the relatively high mobility (Fig. 2.11).

2.5 Field Emitters of Electrons in Vacuum to Generate THz Signals

New types of Terahertz generators are proposed which is based on field emission of electrons into vacuum. Here are vacuum travelling-wave structures used to generate such signals, as well as revisited triode type tubes such as the dynatron. A particular suggestion is a heterostructure field emitter of electrons involving laser pulses [12].

Electron beam based sources promise great efficiency. A novel miniaturized tunable, portable THz source use the Dynatron oscillator concept [12]. Electron beam based sources promise there the great efficiency required. Presently 200 GHz radiation sources are employed in airport body scanners which are several dm^3 in size. Industry requires a miniaturized source to enhance speed and resolution of the scanning process. A portable THz source for this frequency range uses the Dynatron oscillator concept. This is composed of a triode tube with a grid voltage higher than the anode voltage. This configuration accelerates secondary electrons from the anode to the grid, which makes the dynatron to act as a negative resistance. A serial or parallel oscillator circuit is connected between the anode and a working point potential source with a value lower than the extraction grid. The primary electron beam charges the oscillator capacitance to self-excited oscillations, see Fig. 2.1.

In the presented system a miniaturized triode with field electron emitter is employed, having a cathode to grid capacitance of $24{\cdot}10^{-18}$ F and a total beam

Table 2.1 Dimensions for IR-sources in the 0.2–10 THz range

Frequency (THz)	Wavelength (μm)	Resonator E0 (μm)	1 electron pulse at 100 V travels (μm)	
			IR window (μm)	S/N at 1 mA DC
0.2	1,500	750	15	173
0.5	600	300	6	77.5
1	300	150	3	54
5	60	30	0.6	24.6
10	30	15	0.3	17

length of 1 μm. EBID field emitters can emit up to 1 mA at an extractor voltage of 20 V. EBID electron emitters can provide at an anode voltage of 100 V a beam power of 0.1 W using the miniaturized focusing optics. Such sources render a very high brightness. As a series oscillator is chosen, this charges the capacitor at the resonance frequency up to Q times the applied fixed anode voltage (Q quality factor of the resonance circuit). The oscillator signals control two miniaturized field emitter electron beam sources, which emit charge pulses in each half wave's time to fly across a resonator, however through opposite apertures with opposite directions, see Fig. 2.2. The amplified signal which controls the left electron beam is reversed by a capacitor (C12) to send the pulse of the second half wavelength from the right side. The signals must be adjusted to be in phase by circuit CAD design. Generating IR-dipole radiation with free flying charges avoids energy loss by resistive energy loss and Joule heating in the emitter wire of an emitter antenna system. Such pulsed free flying beams can couple directly a high percentage of the beam energy into the THz radiation. They suffer no resistive loss like wire transmitters do. If a higher extractor voltage is needed for a more powerful field emission, the oscillator voltage can be amplified with miniaturized triodes with field emission cathodes.

The usable voltage is limited in miniaturized beam sources, due to stability requirements of electrostatic elements. Experimentally 100 V can be used in a safe way in vacuum, especially at metal line distances as small as 1 μm. Electrons reach by acceleration at 100 V a speed of 6 μm/ps. The oscillator voltage cuts the DC beam in charge pulses of half a wavelength in length, which corresponds to half the time span of a period. For example: at 500 GHz the pulse length is 1 psec. To clearly separate the two electric fields each beam must pass an aperture of 6 μm diameter located in the center of the resonator through which the electric and the magnetic field of the Hertz Dipole radiation is delivered into the resonator having a dimension of half a wavelength, which is 300 μm at 500 GHz. The required dimensions for sources in the 0.2–10 THz range are listed in Table 2.1. The radiation emitted from the resonator to both sides is aligned by reflectors and focused by lenses. Our simulation using CST Software (Particle and Microwave Studios) shows that this can be beneficial for the technical realization of the miniaturized THz source (Figs. 2.12 and 2.13).

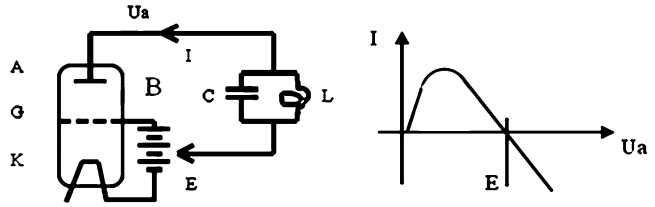

Fig. 2.12 *Left*: Dynatron oscillator circuit with series resonator, *Right*: I–V curve, and work-point E for symmetric oscillation around I = 0 A. A 2 THz oscillator could be obtained with C = 10^{-16} F and L = 10^{-11}H

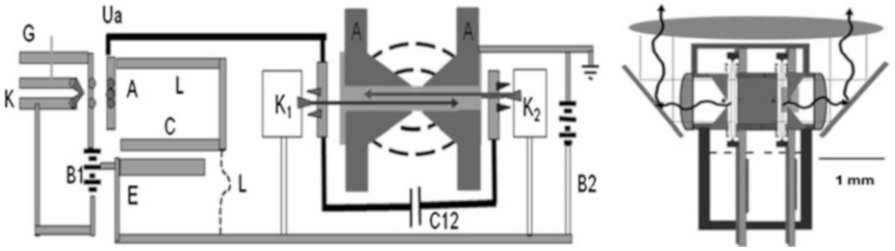

Fig. 2.13 *Left*: Layout of the THz-source. *Right*: 200 GHz source for body-scanner in safety survey applications

2.6 Various Application Areas for Security

2.6.1 Reading Secured Data of Matrix of Metal Squares by THz Wave Reflection

It is common practice to have relevant information stored in optical patterns such as the well-known bar or matrix codes as commonly experienced in supermarkets carrying data like prices as useful for accounting both with the customer as well as with the company administration. There exists an interest to realize this also for THz-wave reading, particularly since this pattern can be covered by a THz transparent, but optically non-transparent paint for security reasons. The information content can then not be recognized in particular by any outside person not having the relevant THz detection equipment. It is even possible to work with flexible substrates and corresponding THz patterns of flexible metal materials as is being developed by a number of laboratories. In fact, instead of metal matrix bars, polymer bars of suitable material for THz interaction might be possible. The pattern might even be optically transparent but THz effective due to its dielectric or conductive properties [13]. Indeed, even money notes are produced by using flexible paints, which often contain THz affecting metals.

Here then a matrix of THz-reflecting metal antennas can be employed, where the presence or absence of such structures carries corresponding confidential digital information. It is then required to read this by identifying the far-field reflection pattern by an array of receiving antennas above the structure after it is illuminated by a centrally positioned THz source. An interesting question concerns the use of THz RFID's on flexible substrates, including liquid crystal structures.

2.6.2 THz Camera for Security Issues

Here, in particular, the development of THz power sources out of laser mixing is a primary interest. This concerns non-linearity effects with various types of materials or with semiconductor structures, which initially need to be simulated by using permissible approximations. An important issue is the handling of waste heat in electronic structures introducing new ideas of heat sinking.

The illumination of individual mixers of an array is undertaken by fibres from the output of two lasers operating at the difference frequency of the THz signal to be generated. The mixer array needs to be composed of mixers which are separated from each other by distances as required for good heat sinking. Such schemes are designed by us now on the basis of a heat-conducting thick metal grid. The THz antennas coupling out the electromagnetic waves are designed by us such that a narrow main lobe with only minimal side arms occurs [14, 15].

Work was undertaken towards a photonic Vector Network Analyzer for THz heterodyne phase-coherent measurements [16]. This is based on the combination of a continuous wave (CW) THz photonic transmitter and a CW THz photonic front-end receiver that serve as THz interface extensions for a radiofrequency Vector Network Analyzer (VNA). The proposed PVNA would be able to perform measurements in the THz range, where both magnitude and phase are directly measured, eliminating all the delays associated with typical time-domain schemes, by adding phase control and measurement to existing photonic THz heterodyne receivers. The proposed scheme makes use of commercial, low cost components to achieve a compact and cost-effective system. This approach is the first scheme for vectorial measurements of THz radiation using a photonic approach for both generation and detection, combining in a single scheme the RF, THz and optical frequency regions. This study was presented at the European Microwave Week in Amsterdam.

Imaging techniques are important issues towards the realization of a THz camera. To obtain Continuous Wave (CW) operation the main issue is power handling via suitable heat sinking strategies [17]. Regarding a maximization of THz illumination, a new design structure and a first experimental approach is introduced by using Nitrogen implanted GaAs (N + i GaAs) material as a photoconductive material. Here in particular the continuous interaction, mostly via e-mail, with a doctoral assistant in Darmstadt, Shihab Al-Daffaie, has been continuing. He is pursuing

this work technologically and experimentally. The issue of CW operation requires careful heat transfer designs. Here a study is presented regarding multiple source interconnections in a matrix structure. This is aimed at broad illumination schemes.

The image detection is then based on an array of photoconductive antenna heterodyne receivers illuminated with two phase-locked optical wavelengths obtained from an Optical Frequency Comb Generation (OFCG) for CW operation. This architecture allows for an efficient, phase controlled, Local Oscillator (LO) distribution with low losses intrinsic to the use of optical fibers, as well as amplitude and phase recovery due to the coherence of the LO distributed. Tunable operation is achieved using the different lines of the OFCG and broadband design for the photoconductive antenna.

A design involvement concerns the opportunities of nanometric electronics. The assessment of the fabrication techniques are to be studied. The outcome of such work was an invitation by the University of Shizuoka in Hamamatsu, Japan, to present an "Invited Plenary Paper" entitled "Nanoelectronic Technology" on 23rd January, 2012. In connection with these studies a further invited presentation took place at the 22nd International Conference "Radioelektronika 2012" in Brno, Czech Republic, from 17th to 18th April, 2012 with the title: "The New Age: After Microelectronics – now Nanoelectronics".

2.7 Conclusion

It can be concluded that it is most promising with all these miniature nanometric approaches to achieve general security for the many occasions in modern life, where weapons or explosives have to be identified when large numbers of people enter a facility. There are indeed a number of options as described here. The security issue requires of course small dimensions in order to be implemented easily and reliably. Additionally, the overall cost needs to be acceptable for wide-spread usage.

References

1. Ong DS, Hartnagel HL (2008) Enhanced THz frequency multiplier efficiency by quasi-ballistic electron reflection in double-heterojunction structures. EPL 81:48004
2. Hartnagel HL, Ong DS, Oprea I (2009) Ballistic Electron Wave Swing (BEWAS) to generate THz-signal power. Frequenz 63:60–62
3. Nicolae B, Ruf M, Schür J, Schmidt L-P, Hartnagel HL (2008) A heterostructure barrier charge swing device for frequency multiplication at 306 GHz. IEEE MTT-S, Atlanta, GA, USA, June 2008, pp 1545–1548
4. Hargreaves S, Bignell L, Lewis R, Schoenherr D, Saglam M, Hartnagel H (2008) Investigation of p-GaAsSb as a new candidate THz emitter. J Electrochem Soc ECS 155:H734–H737
5. Hartnagel H, Dragoman M (2010) Heterostructure field emitter of electrons to generate THz signals by laser pulses. In: Proceedings of the IVNC 2010, Palo Alto, 26–30 July

6. Dragoman D, Dragoman M, Hartnagel H (2010) Terahertz generation based on an optically pumped ballistic electron wave swing device. J Appl Phys 108:026103
7. Göbel T, Schoenherr D, Sydlo C, Feiginov M, Meissner P, Hartnagel HL (2008) Continuous-wave terahertz system with electro-optical terahertz phase control. Electron Lett 44(14):863–864 (3 July 2008)
8. Schönherr D, Hartnagel HL, Hargreaves S, Lewis RA, Henini M (2008) Time-domain THz spectroscopy using acceptor-doped GaAs photoconductive emitters. Semicond Sci Technol 23:105012 (7 pp)
9. Göbel T, Schönherr D, Sydlo C, Feiginov M, Meissner P, Hartnagel HL (2009) Single-sampling-point coherent detection in continuous-wave photomixing terahertz systems. Electron Lett 45(1):65
10. Sigmund J, Lampin JF, Ivannikov V, Sydlo C, Feiginov M, Pavlidis D, Meissner P, Hartnagel HL (July 2008) Low-temperature grown GaAsSb with sub-picosecond photocarrier lifetime for continuous-wave terahertz measurements. IEICE Trans Electron E91-C(7):1058–1062
11. Park I, Sydlo C, Fischer I, Elsässer W, Hartnagel HL (2008) Generation and spectroscopic application of tunable continuous-wave terahertz radiation using a dual-mode semiconductor laser. Meas Sci Technol 19:065305 (9 pp)
12. Koops HWP, Al-Daffaie S, Hartnagel HL (2012) Portable source with free electron beams for 0.1 to 10 THZ. In: Proceedings of "WOCSDICE-EXMATEC 2012", Island of Porquerolles/France
13. Hartnagel HL, Schönherr D, Osman NH, Free C (2010) Optically hidden, secured data of matrix of metal squares by THz wave interaction. Frequenz 64:5–6
14. Criado Serrano AR, Montero-de-Paz J, Ugarte-Muñoz E, de Dios C, García LE, Acedo P, Hartnagel HL (2013) Heterodyne photonic receiving antenna in the microwave and millimeter regime. In: IEEE Antennas and Wireless Propagation Letters, Manuscript ID AWPL-06-12-0724
15. Montero-de-Paz J, Ugarte-Muñoz E, Garcia-Muñoz LE, Segovia-Vargas D, Schoenherr D, Oprea I, Amrhein A, Cojocari O, Hartnagel HL (2012) Millimeter-wave receiver based on a folded dipole antenna and Schottky diode for maximum power transfer. In: Conference EuCAP in Prague 2012, 26–30 March 2012
16. Criado AR, de Dios C, Acedo P, Hartnagel HL (2012) New concepts for a photonic vector network analyzer based on THz heterodyne phase-coherent techniques. In: European microwave week, Amsterdam, Holland, 28 Oct–3 Nov 2012
17. Al-Daffaie S, Acedo P, Hartnagel H (2012) Simulation of a CW THz camera scheme. In: Presentation at the conference WOCSDICE in France, Porquerolles, France, 29–30 May 2012

Chapter 3
Structured Inorganic Oxide-Based Materials for the Absorption and Destruction of CBRN Agents

Matteo Guidotti, Massimo C. Ranghieri, Fabio Carniato, and Chiara Bisio

Abstract Absorption and destruction of chemical and biological (CBRN) hazardous agents can be required on the field (decontamination after warfare or terrorist use) as well as in laboratories, pilot plants and chemical agent destruction sites (abatement of CBRN weapons). Inorganic metal oxides, in all forms and formulations, constitute a large class of materials that are suitable for such purposes. They are robust under usual working conditions, rich in specific surface sorption sites, active in the degradation of hazardous compounds via catalytic or photocatalytic mechanisms and, in most cases, relatively cheap. In addition, thanks to the recent advances in the nanosciences, structured nanosized inorganic solids show promising performances because of their high activity and selectivity, even at very low catalyst to toxic agent ratios.

Keywords Heterogeneous catalysis • inorganic oxides • porous and layered materials • Decontamination • Absorption • CBRN agents

M. Guidotti (✉)
CNR-Istituto di Scienze e Tecnologie Molecolari, Via G. Venezian, 21, 20133 Milan, Italy

1st Field Unit, EI-ACISMOM Military Corps, Milan, Italy
e-mail: m.guidotti@istm.cnr.it

M.C. Ranghieri
1st Field Unit, EI-ACISMOM Military Corps, Milan, Italy

F. Carniato • C. Bisio
DISIT and Nano-SiSTeMI Center, Università del Piemonte Orientale "A. Avogadro",
Via T. Michel 11, 15121 Alessandria, Italy

A. Vaseashta and S. Khudaverdyan (eds.), *Advanced Sensors for Safety and Security*,
NATO Science for Peace and Security Series B: Physics and Biophysics,
DOI 10.1007/978-94-007-7003-4_3,

3.1 Introduction

3.1.1 Historical Context

Weapons of mass destruction have been the major source of threat at worldwide level since the beginning of twentieth century. Chemical, biological, radiological and nuclear (CBRN) warfare agents have been considered, in various situations in contemporary history, the most deadly tools humankind have ever invented [1]. Nevertheless, the *perception of threat* related to this sort of non-conventional weapons has not been constant in the last decades. If one considers the period starting from second World War (WWII) until today, the trend of threat perception can be depicted as in Fig. 3.1. During WWII no use of chemical or biological warfare agents was recorded. At the final part of the war, the dramatic events in Hiroshima and Nagasaki marked the beginning of the ever-increasing threat escalation for a possible nuclear holocaust that reached a maximum in the Cold War period, during which both USA and Soviet Union collected huge stockpiles of CBRN weapons.

In 1989, the sudden change in global equilibria caused a partial diminution of the perceived threat. In fact, most of conflicts in the 1990s had a regional nature (Yugoslavia, Rwanda, Middle East) and were carried out at local (non-global) scale with conventional weapons and with a remote risk of a diffuse use of mass destruction weapons. Then, in 2001, the facts of 9/11 and the following wave of terrorist attacks in several countries led to an abrupt increase of the threat perception. The risk of use of CBRN weapons is therefore in these times back again, for terrorist purposes, rather than for explicit warfare aims.

In addition to that, it is necessary to consider the ubiquitous and ever-present risk of accidental and unintentional releases of hazardous and highly toxic CBR(N) agents. The disasters in Seveso (1976) and Bhopal (1984), the risk of pandemic spreads for SARS (2003) and H1N1 (2009) as well as severe accident in Chernobyl

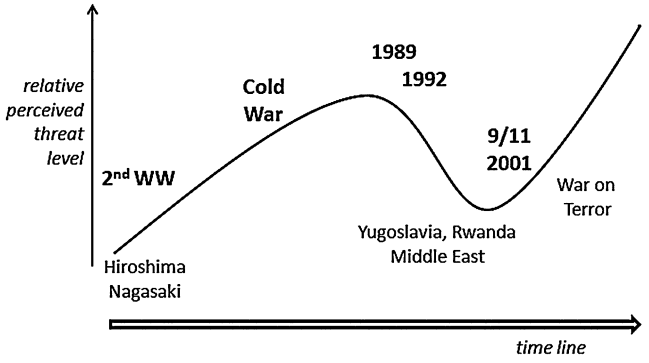

Fig. 3.1 The relative perception of threat from CBRN mass-destruction weapons in last decades

(1986) and the recent case of Fukushima (2011) show that the threat is not necessarily linked to illicit deliberate use of hazardous materials and, therefore, to a particular global political situation.

The need for a constant CBRN Defense preparedness plan is therefore always valid and, as mentioned in the NATO guidelines, it requires the development and employment of policies, plans, doctrine, procedures and equipment designed to defend against attacks with nuclear, biological and chemical or radiological weapons or hazards arising from ROTA (Release Other Than Attack) events [2]. With this objective, the use of appropriate tools for a physical protection against the noxious agents (protection) and for a proper management of the hazard (decontamination) is two main elements of a modern and effective CBRN defense planning.

3.1.2 Protection and Decontamination on Reactive Sorbents

The two actions of protection and decontamination can be performed simultaneously by means of *reactive sorbents* [3]. Indeed, decontamination is intended as the action of making any person, object or area safe and clean absorbing, making harmless or removing chemical or biological agents. In the case of radioactive contaminants (R agents) the only possible action is removal and disposal. When the decontamination action is performed at the same time as the protection and shielding action, it is possible to get an active protection and a tool for *in situ* abatement of the noxious agent [4].

The addition or insertion of catalytically active sites into/onto a porous support is one of the better strategies to obtain materials with marked adsorption properties together with abatement and decontamination capabilities. Structured porous inorganic oxides are optimal materials for these purposes as they show a noteworthy chemical, physical and mechanical robustness and they are suitable supports for obtaining an even dispersion of active metal sites (*e.g.* V, Ag, W, Mo), thus producing useful catalysts for the abatement of non-conventional warfare agents [5]. In addition, nanostructured inorganic metal oxides (*i.e.* Al_2O_3, ZnO, TiO_2, Fig. 3.2a) were largely proposed and studied in the literature.

More recently, other oxides possessing structured and ordered array of nanometer-sized channels, pores or cavities were proposed for CBRN adsorption and abatment. Among them, the three classes featuring the most promising capabilities in CBRN decontamination or abatement are porous and layered solids (*clays*) (Fig. 3.2b, c).

A schematic representation of the structure of different classes of materials proposed for CBRN adsorption and decontamination is reported in Fig. 3.2.

Porous materials are well known for their particles of variable size, their tunable pore architecture and high specific surface area: these properties render porous solids suitable for adsorption of large amounts of hazardous chemical or biological agents and eventually their decomposition. Among porous solids, materials with

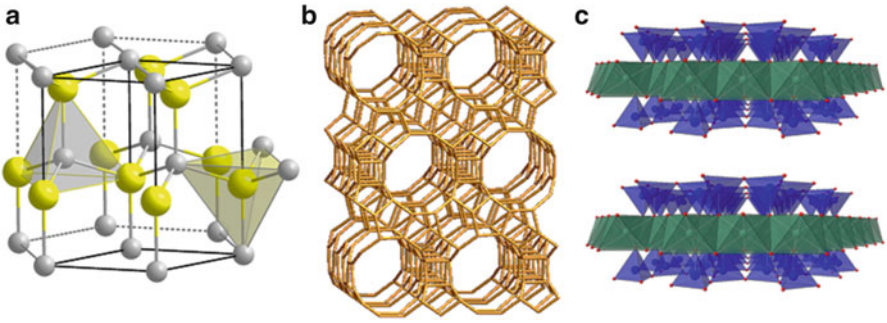

Fig. 3.2 A schematic representation for the structure of different classes of nanostructured oxides; (**a**) ZnO with wurtzite structure; (**b**) zeolite; (**c**) neutral layered material

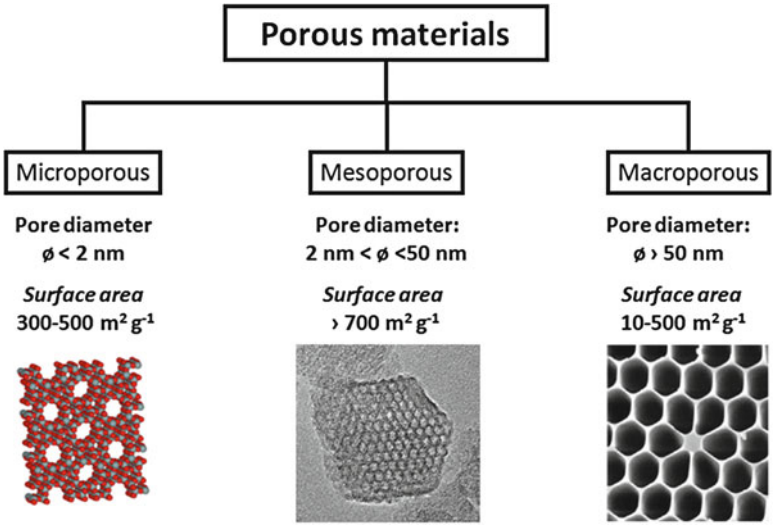

Fig. 3.3 Porous inorganic-oxide materials classified according their pore size

micro-, meso- and macroporosities can be prepared by using different synthetic approaches (vide infra). Zeolites are microporous frameworks (0.2 nm < pore diameter < 2 nm) of aluminosilicates with a crystalline structure (Fig. 3.3). They can be extracted from natural sources, but are now produced synthetically at large scale via cheap preparation methods. They possess unique properties as ion exchangers, molecular sieves, adsorbent materials and they are optimal host solids to accommodate catalytically active sites.

When materials with a network of wider and larger pores are required, mesoporous materials are the solids of choice (Fig. 3.3). They are able to accommodate bulkier molecules (*i.e.* molecules of higher molecular weight as many organic compounds are) and they present arrays of broad channels suitable to accommodate

a large variety of chemical functionalities and to obtain functional materials. Their synthesis and preparation are, nonetheless, currently more expensive than the ones of zeolites.

For this reason, clay solids are been considered for absorption and abatement of hazardous agents. Clays belong to the broad class of aluminum phyllosilicates. They are layered materials and can be of natural or synthetic origin. The modification of the interlayer space and/or inorganic framework via introduction of redox-active species or acid/basic centers leads to catalytically-active clays which find application in several selective transformations, as oxidations, hydrogenations, acid-catalyzed rearrangements, industrial scale, etc.

3.2 Synthesis of Inorganic Oxide-Based Materials

The development and optimization of synthetic methods is one of the fundamental aspects to obtain functional materials whose properties can be tuned in relation to desired applications. Numerous synthetic approaches were explored allowing control over parameters such as particle size, shape, size distributions and chemical composition. In the last years, nanosized oxides attracted special interest due to their peculiar physico-chemical properties arising from their nanometer-scale dimensions. Two principal approaches to the preparation of nanostructured materials are possible: a *bottom-up* and a *top-down* method. While *top-down* preparations involve approaching the nanometer scale by breaking down larger starting materials, in the *bottom-up* approach, solids are obtained by chemical assembly of fundamental building blocks (*i.e*. atoms or molecules). Typically, synthetic chemists follow a *bottom-up* approach, starting from simple and cheap inorganic and/or organic precursors. Several methods were reported for the synthesis of nanosized oxide particles including co-precipitation [6], thermochemical decomposition of metal–organic precursors [7–9], sol-gel [10] and solvothermal methods [11].

Co-precipitation is one of the conventional synthesis pathways to prepare nanosized particles of oxides: this method involves the precipitation of soluble precursors from aqueous solutions, followed by thermal decomposition of those products to oxide [6, 12]. The precursors are the starting materials for the formation of the corresponding metal oxides or hydroxides that are precipitated in water by the addition of a basic solution. If hydroxides are produced, a calcination step is needed to obtain metal oxide. Very often, fast and uncontrolled precipitation takes place, resulting in the formation of large particles with low specific surface area. In order to overcome this shortcoming, some new co-precipitation methods have been developed, such as sonochemical and microwave-assisted co-precipitation.

Another approach largely used for the preparation of nanostructured materials is represented by *sol-gel technique* (Fig. 3.4a). Sol-gel processes are generally performed in liquid media and at low temperature ($T < 100$ °C). The process is typically used to prepare metal oxides via hydrolysis of reactive precursors (usually alkoxides) in an alcoholic solution, resulting in the corresponding hydroxide

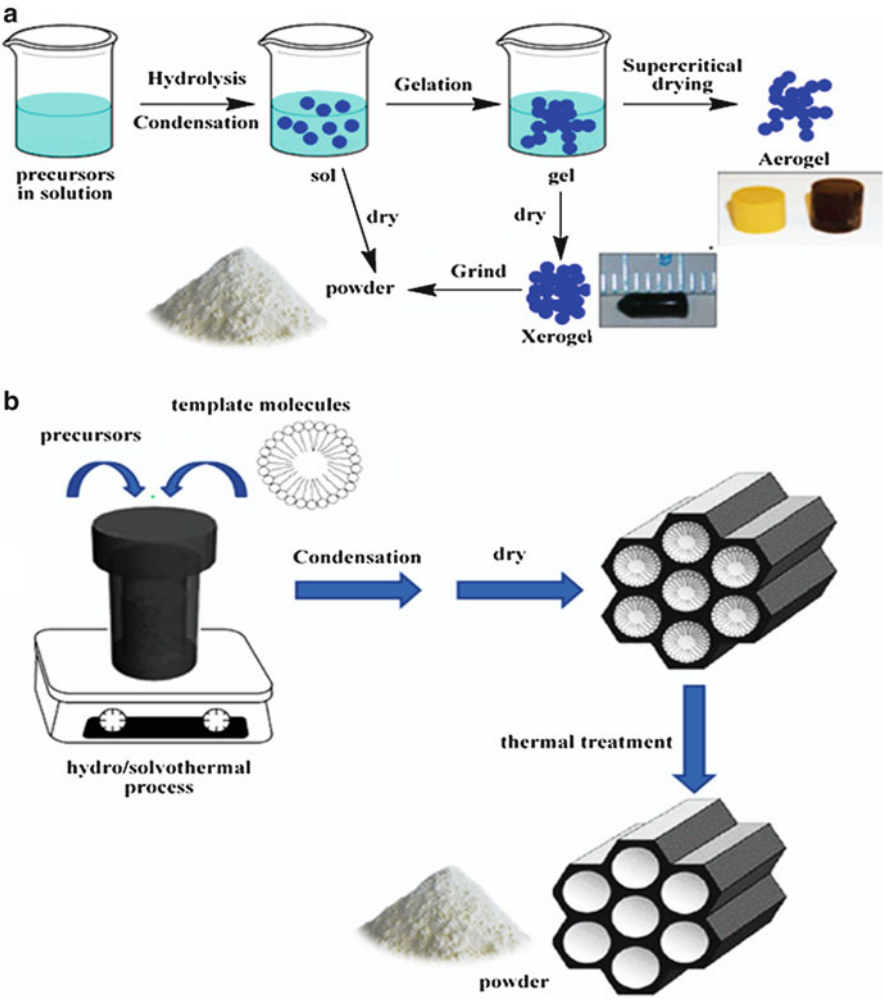

Fig. 3.4 Schematic view of (**a**) sol-gel reaction and (**b**) solvo/hydrothermal synthesis of nanostructured metal oxides samples

(*sol* phase). Condensation of the hydroxide species with loss of water leads to the formation of a gel phase. Removal of the solvents and appropriate drying of the gel are important steps that result in an ultrafine powder of the metal hydroxide. Heat treatment of the hydroxide is a final step that leads to the corresponding metal oxide. Depending upon the heat treatment procedure, the final product may be in the form of a nanometric-scale powder, bulk material or xero- and aero-gels metal oxide.

Metal oxides can be also prepared by using solvothermal methods (Fig. 3.4b). As a general feature, the synthetic approach is conducted in water (hydrothermal processes) [11, 13] or solvents (solvothermal methods) at elevated temperature and under autogenous pressure in a closed system (i.e. in autoclaves). Under solvo

(hydro) thermal conditions, certain properties of the solvent, such as density, viscosity and diffusion coefficient, change dramatically and the solvent behaves much differently from what is expected under ambient conditions [13]. Consequently, the solubility, the diffusion process and the chemical reactivity of the reactants are greatly increased or enhanced, enabling the reaction to take place at a far lower temperature than normal. The method has been widely applied and adopted for crystal growth of many inorganic materials such as quartz, metal carbonates, synthetic clays, phosphates and other oxides and halides [14–16]. As a matter of fact, this method is largely used for the preparation of zeolite and porous solids: in such cases, proper organic template molecules (i.e. amines and ammonium ions, surfactants molecule or, block co-polymers) are added to the synthesis gel in order to promote the formation of a structured porous network.

3.3 Absorption and Abatement of CBR(N) Agents

Many research papers and patents are related to the decontamination of hazardous chemical warfare agents (CWAs) by using chemical adsorption of toxic molecules and their consequent abatement through catalytic steps, normally carried out at low temperatures. Different classes of nanostructured materials were used for this purpose because of their high activity due to the presence of a high number of surface defects (*i.e.* the ideal loci for active sites) and high specific surface area.

Numerous examples dealing with the exploitation of inorganic metal oxides, porous materials and layered solids are given in the literature. As a general feature, metal oxide particles (*i.e.* Al_2O_3, SiO_2, α-Fe_2O_3) adsorb and decompose CWA trough hydrolysis and oxidation steps promoted by the presence of surface Lewis-acid centers. For instance, CuO nanoparticles were found to be promising for the adsorption and decomposition of nerve agent simulants. Singh et al. studied the effect of preparation steps on the catalytic performances of CuO towards the abatement of sulphur mustard, allowing optimizing the condition to obtain CuO catalysts with high performances in CWA degradation [17].

More recently, TiO_2 nanoparticles were successfully explored as photocatalysts to decompose nerve agents. Photocatalysis is a promising approach for decontamination of water tainted with organophosphorus compounds. When a semiconductor material is irradiated with UV light, whose energy is greater than the band gap, electron–hole pairs are generated. These pairs react with water and surrounding oxygen species to form hydroxyl radicals ($OH^{\bullet}$) and superoxide anion($O_2^{-\bullet}$) radicals. The CWA agents are thus converted into relatively non-toxic products, like H_3PO_4, CO_2, H_2O, etc.

TiO_2 has been the most investigated photocatalyst and it was found to be capable of degrading a wide variety of pollutants in both liquid and gas phases. Recently, it was used to degrade photocatalytically organophosphorous pesticides such asmalathion, diazon, fenitrothion, and parathion [18, 19].

As an alternative to metal oxide catalysts, zeolites were also investigated for the adsorption and hydrolysis of organophosphonate (OP) agents. Different from

simpler metal-oxo species, zeolites are well-known for their particles of variable size and the presence of a regular array of channels and/or cavities thus giving an excellent overall contact area with the toxic agent.

The most recent interests have been in the adsorption and hydrolysis of OP in clay, soil components and zeolites [20]. For example, VX nerve agent (*ortho*-ethyl-S-[2-(diisopropylamino)ethyl]methylphosphonothioate) was reported to be hydrolyzed on Na-Y and Ag-Y zeolites at room temperature, through cleavage of the P-S bond [21]. Decomposition of dimethylmethylphosphonate (DMMP) to methylphosphonate in sodium X zeolite (Na-X) by nucleophilic zeolite reactions was reported, together with the multiple effects of water on the nucleophilic substitution reaction. However, the size limitation to diffusion into active supercage sites presented by the microporous Na-X faujasite supercage was evident and there is a strong need to enlarge the pore size from microporous to mesoporous to enhance adsorption. In 2011, commercial NaX zeolite and its mesoporous derivative (Meso-X) where selected as adsorbents for trimethylphosphate (TMP). A careful physico-chemical characterization of zeolites after adsorption of contaminants demonstrate that zeolites with mesoporous channels are the most effective in the nucleophilic substitution and subsequent hydrolysis reactions of organophosphate molecules, supporting the hypothesis that slow or incomplete diffusion in zeolite microporosity limits organophosphate decomposition [22].

To overcome the limits of microporous materials, mesoporous solids were exploited for CWA adsorption and decomposition. It was recently demonstrated that vanadium oxide supported on mesoporous silicas is an effective catalyst for the oxidation of mustard gas analogue (chloroethyl ethyl sulfide, CEES) at room temperature and using molecular oxygen in the presence of aldehydes. The material act as a heterogeneous catalyst and, in fact, no leaching of vanadium ions was observed during the reaction. The key-role of vanadium centers as single sites involved in the degradation mechanism was also fully elucidated [23].

Beside porous materials, layered solids such as clays can be considered as good absorbents as well as useful components of barrier protective equipment because of their high specific surface area, chemical stability and high cation exchange capacity. Many organic molecules with polar functional groups and hydrated ions can be easily intercalated in the interlayer space of clays and then decomposed. It is well known that clays such as montmorillonite and kaolinite accelerate the degradation of insecticides such as paraoxon, chloropyrifos, etc.

In 2011, Hatton and coworkers [24] prepared organo-modified clay with nucleophilic character due to the presence in the interlayer space of pyridine aldoximemethiodide (PAM), that is highly active in the hydrolysis of toxic organophosphates. It was found that the clay and the PAM act in a synergic way enhancing each other's ability to chemisorb and degrade the toxic compounds.

Multifunctionalized zeolitic materials have found recently an interesting application as photoactive hybrid nanomaterial for targeting, labeling and killing antibiotic-resistant bacteria and thus as an active countermeasure against biological (B) agents [25]. The nanocrystals of L zeolite (LTL type) are loaded with *N*,*N*′-bis(2,6-dimethylphenyl)perylene-3,4,9,10-tetracarbodiimide (DXP) as a dye emitter

and the zeolite surface is functionalized with a phthalocyanine derivative and with amino groups. Aminofunctionalities provide non-covalent binding of the hybrid nanomaterial to the bacterial surface, while phthalocyanine pendants assure an efficient photoassisted production of singlet-oxygen $^1O_2$ with antibacterial activity. The hybrid nanomaterial is able to adhere to bacterial surfaces and to produce *in situ* singlet oxygen, leading to a targeted attack and photo inactivation of the bacteria. This kind of system can be therefore considered a nano-sized equivalent of "smart bombs". The photobiological activity was tested on antibiotic-resistant *Escherichia coli* and a pathogenic strain of tetracycline-resistant *Neisseria gonorrhoeae* by suspending the cells with the hybrid nanomaterial and irradiating the sample for 2 h in the wavelength range between 570 and 900 nm. The photodynamic inactivation was complete (95 %) after 2 h on both kind of microorganisms.

Finally, the remarkable cation exchange capability of zeolitic materials can be exploited in the removal of radiological (R) contamination. Macroporous monoliths of LTA zeolite has been applied to the in-flow removal of radioactive strontium from aqueous effluents and tested on marine water samples with a composition similar to the fluids found on the site of Fukushima disaster [26]. Simulated R-contaminated seawater contained high amount of Na^+ (9.6 g L^{-1}), Ca^{2+} (0.4 g L^{-1}), Mg^{2+} (1.28 g L^{-1}), K^+ (0.5 g L^{-1}) and Sr^{2+} (7.8 mg L^{-1}), together with radioactive $^{90}Sr^{2+}$ (5.5 ng L^{-1}, 28 kBq L^{-1}). Thanks to its high mechanical robustness and optimal exchange capacity, LTA-monolith showed an in-flow decontamination capacity four times higher than powder-based batch processes (*e.g.* free LTA zeolites, titanates). Furthermore, LTA-monoliths can be directly used as systems for concentration and storage of radioactive cations without any further solidification process.

3.4 Final Remarks

An *ideal* inorganic-oxide based sorbent material for decontamination and abatement possesses a series of specific characteristics: it neutralizes all C, B (and R) agents; it is safe (non-toxic, non-corrosive); it is compatible with human beings and the environment (life cycle assessment); it is easily available and usable; it acts rapidly; it produces no toxic by-products; it is stable and affordable; it is cheap and it is easily disposable. Before designing and preparing a new material, a scientist should clearly take into account these guidelines.

For these purposes, zeolites and clays are among the most promising active porous materials. The scientific capabilities are already available. Further efforts in the field of technological scale-up and industrial development are, on the contrary, now necessary. A proper CBRN defense planning and strategy is based on these materials too. Improved protection and decontamination equipment indeed means improved preparedness and CBRN counteracting capabilities. In fact, sources of non-conventional threat can be found not only in warfare and terrorist actions, but also in unintentional releases of hazardous CBR(N) materials that may always occur, notwithstanding the global sociopolitical situation.

Acknowledgements M. G. gratefully thanks Prof. A. Vaseashta and Prof. S. Khudaverdyan for the kind invitation to the NATO Advanced Research Workshop held in Yerevan, Armenia. M.G. also thanks the Italian Ministry of Education, University and Research for financial support through the Project "ItalNanoNet" (Rete Nazionale di Ricerca sulle Nanoscienze; prot. no. RBPR05JH2P).

References

1. Nwanna GI (2004) Weapons of mass destruction. Library of Congress, Washington, DC
2. NATO, North Atlantic Treaty Organization (2003) AJP-3.8 – Doctrine for the NBC Defence of NATO Forces
3. Guidotti M, Rossodivita A, Ranghieri MC (2012) Nano-structured solids and heterogeneous catalysts: powerful tools for the reduction of CBRN threats. In: Vaseashta A, Braman E, Susmann P (eds) Technological innovations in detection and sensing of CBRN agents and ecological terrorism, NATO science for peace and security series – A: chemistry and biology. Springer, Amsterdam, pp 89–97
4. Netherlands Organization for Applied Scientific Research (2007) Present state of CBRN decontamination methodologies, TNO report, pp 1–27
5. Kim K, Tsay OG, Atwood DA, Churchill DG (2011) Destruction and detection of chemical warfare agents. Chem Rev 111:5345–5403
6. Gao L, Wang HZ, Hong JS, Miyamoto H, Miyamoto K, Nishikawa Y, Torre SDDL (1999) SiC-ZrO_2(3Y)-Al_2O_3 nanocomposites superfast densified by spark plasma sintering. Nanostruct Mater 11(1):43–49
7. Xu CH, Shi SQ, Surya C, Woo CH (2007) Synthesis of antimony oxide nano-particles by vapor transport and condensation. J Mater Sci 42:9855–9858
8. Ulrich GD, Riehl JW (1982) Aggregation and growth of submicron oxide particles in flames. J Colloid Interface Sci 87(1):257–265
9. Skandan G, Chen YJ, Glumac N, Kear BH (1999) Synthesis of oxide nanoparticles in low pressure flames. Nanostruct Mater 11(2):149–158
10. Khaleel A, Richards RM (2001) Ceramics. In: Klabunde KJ (ed) Nanoscale materials in chemistry. Wiley Interscience, New York, pp 85–114
11. Rabenau A (1985) The role of hydrothermal synthesis in preparative chemistry. Angew Chem Int Ed 24:1026–1040
12. Rama Mohana Rao K, PrasadaRao AV, Komarneni S (1996) Bismuth titanate from nanocomposite and sol-gel processes. Mater Lett 28(4–6):463–467
13. Laudise RA (1987) Hydrothermal synthesis of crystals. Chem Eng News 65(39):30–43
14. Corbett JD (1985) Polyatomic Zintl anions of the post-transition elements. Chem Rev 85: 383–397
15. Haushalter RC, Strohmaier KG, Lai FW (1989) Structure of a three-dimensional, microporous molybdenum phosphate with large cavities. Science 246:1289–1291
16. Haushalter RC, Mundi LA (1992) Reduced molybdenum phosphates: octahedral-tetrahedral framework solids with tunnels, cages, and micropores. Chem Mater 4(1):31–48
17. Mahato TH, Singh B, Srivastava AK, Prasad GK, Srivastava AR, Ganesan K, Vijayaraghavan RJ (2011) Effect of calcinations temperature of CuO nanoparticle on the kinetics of decontamination and decontamination products of sulphur mustard. J Hazard Mater 192(3):1890–1895
18. Prasad GK, Ramacharyulu PVRK, Praveen Kumar J, Srivastava AR, Singh B (2012) Photocatalytic degradation of paraoxon-ethyl in aqueous solution using titania nanoparticulate film. Thin Solid Films 520:5597–5601
19. Sato K, Hirakawa T, Komano A, Kishi S, Nishimoto CK, Mera N, Kugishima M, Sano T, Ichinose H, Negishi N, Seto Y, Takeuchi K (2011) Titanium dioxide photocatalysis to decompose isopropyl methylphosphonofluoridate (GB) in gas phase. Appl Catal B Environ 106(3–4):316–322

20. Seger MR, Maciel GE (2006) NMR investigation of the behavior of an organothiophosphate pesticide, chlorpyrifos, sorbed on montmorillonite clays. Environ Sci Technol 40:797–802
21. Wagner GW, Bartram PW (1999) Reaction of VX, HD, and their simulants with NaY and AgY zeolites. Desulfurization of VX on AgY. Langmuir 15:8113–8118
22. Meng Q, Doetschman DC, Rizos AK, Lee M-H, Schulte JT, Spyros A, Kanyi CW (2011) Adsorption of organophosphates into microporous and mesoporous NaX zeolites and subsequent chemistry. Environ Sci Technol 45:3000–3005
23. Livingston SR, Landry CC (2008) Oxidation of a mustard gas analogue using an aldehyde/O_2 system catalyzed by V-doped mesoporous silica. J Am Chem Soc 130:13214–13215
24. Bromberg L, Straut CM, Centrone A, Wilusz E, Hatton TA (2011) Montmorillonite functionalized with pralidoxime as a material for chemical protection against organophosphorous compounds. ACS Appl Mater Interfac 3:1479–1484
25. Strassert CA, Otter M, Albuquerque RQ, Hoene A, Vida Y, Maier B, De Cola L (2009) Photoactive hybrid nanomaterial for targeting, labeling, and killing antibiotic-resistant bacteria. Angew Chem Int Ed 48:7928–7931
26. Sachse A, Merceille A, Barré Y, Grandjean A, Fajula F, Galarneau A (2012) Macroporous LTA-monoliths for in-flow removal of radioactive strontium from aqueous effluents: application to the case of Fukushima. Microporous Mesoporous Mater 164:251–258

Chapter 4
The Quirra Syndrome: Matter of Translational Medicine

A.M. Gatti, S. Montanari, and F. Capitani

Abstract The study deals with the military firing range of Perdasdefogu (Sardinia–Italy) called PISQ, the activities there performed and the impact that some activities could have on human and animal health. The research started from some occurrences of evidence of diseases (a.k.a. Quirra Syndrome) among a population of 2,500 human inhabitants and an unknown number of animals, and proposes a novel type of investigation to verify whether the effects of military activities can trigger pathologies in humans. The investigation takes as starting point the analyses of the pathological tissues of inhabitants who developed cancers of the blood and the soft tissues. This was done by means of a Field Emission Gun Environmental Scanning Electron Microscope equipped with an X-ray microprobe of an Energy Dispersion System in order to detect micro- and nano-sized foreign bodies and identify their chemical composition. This method indicates the exposure the patients underwent by inhaling polluted air or ingesting polluted food. The investigation is based on the fact that the explosion of weapons hitting a target implies a temperature rise within the volume involved. The higher the temperature, the thinner are the particles (bomb + target) produced and aerosolized, thus allowing a higher possibility of particle internalization in the body. So, the study of the internalized particles compared with those produced by the different military activities through an environmental 1-year-long survey carried out by the Italian Ministry of Defense can give an idea if there is a coincidence of chemical composition. The pollution detected in the urban area of Mantua (Italy) is taken as a reference or control. The results indicate that in the pathological tissues of ten civilians, two soldiers who

A.M. Gatti (✉)
ISTEC-CNR, Faenza (RA), Italy
e-mail: gatti@nanodiagnostics.it

S. Montanari • F. Capitani
Nanodiagnostics srl, Italy

A. Vaseashta and S. Khudaverdyan (eds.), *Advanced Sensors for Safety and Security*,
NATO Science for Peace and Security Series B: Physics and Biophysics,
DOI 10.1007/978-94-007-7003-4_4,

worked in the PISQ and five malformed lambs born of ewes that pastured in the firing range that there is the presence of nano-sized foreign bodies with chemical compositions that can be the results of bomb explosions and not of a usual urban environmental pollution.

Keywords Military firing range • Nanoparticles • Combustion • Leukaemia • Hodgkin's lymphoma

4.1 Introduction

Quirra is a small village located in the Italian island Sardinia, close to an interforce firing range where soldiers are trained and other military activities are performed such as tests on ballistic missiles, missile engines and other weapons. Also the regular activities usual in any small civilian community occur there.

Recently, the population living in the territory reported an increase in the number of lethal diseases among civilians and among animals as well as among some soldiers who served sometime in the firing range. The media indicated the use of Depleted Uranium (DU) weapons as the possible cause of the diseases. Since the type of diseases is shared with the soldiers who served in peace-keeping missions in the Balkans, the identification of this pathogenic agent seemed to be valid at first sight. Specific investigations on radioactivity carried out by CISAM (Interforce Centre for the Study of Military Applications) in the firing range verified that no zones exist in that territory where radioactivity is higher than is considered normal. Besides, the Italian Ministry of Defense declared that no DU was ever used there. For these reasons, a new scenario opens on the origin of these illnesses and the study of environmental pollution.

The military firing range has been in use since 1957 and occupies an area of 12,700 km^2. The range is divided into two parts where specific activities are carried out. Figure 4.1 shows two grey areas (one at the seaside and another, larger area, at an altitude of 600 m) where the activities are actually performed. The "sea range" contains launching areas for SAM (Surface-to-Air-Missiles) and paying industries are sometimes permitted to test solid fuels and propulsion systems for rockets. In the "mountain range", the normal activity of training soldiers occurs and the disposal or destruction of obsolete weapons are performed. The dry seal of gas pipelines is also tested with the consequent final blast of the tube. All these activities involve explosions that develop gases, vapours and dust that contaminate the environment.

A few epidemiological and environmental studies [1–6] were carried out but their results were contradictory. Only recently, a study carried out on the field by local veterinaries who investigated directly on the shepherds and the cattle (oxen and sheep), demonstrated that 65 % of the shepherds working in the two areas developed either leukaemia or non-Hodgkin lymphoma, while a substantial number of animals were malformed and died just after being born [7]. The direct observation on the

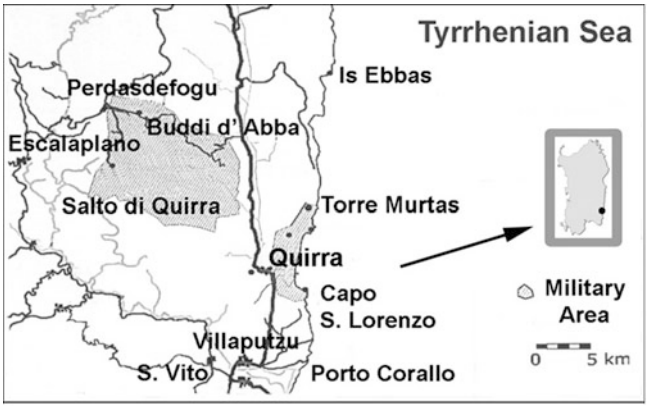

Fig. 4.1 The image shows the map of the Eastern part of Sardinia island where the firing range is located. The *gray areas* show the parts where the military activity is performed

"crime scene" verified a simultaneous onset of pathologies (cancer in humans and miscarriages or malformations in animals) within the perimeter of the military firing range.

The present article proposes a new approach to the problem of these illnesses, starting from the pollution generated by the different military activities and considering its dispersion in the surrounding areas, in the air and in the soil, but, above all, looking for its traces inside pathological tissues.

4.2 Materials and Methods

Thirteen samples of pathological tissues from humans who lived in the village and developed diseases were obtained from hospital archives, while samples of internal organs (liver, kidney, brain, lung) of four malformed lambs (Fig. 4.2) and other animals (two sheep, two goats, three cows [8]) pasturing in the area were given directly by shepherds and by the Prosecutor of the Tribunal of Lanusei who is investigating on the environmental contamination as possible origin of diseases.

The samples were fixed in 10 % formalin, dehydrated in ascending concentration alcohols and embedded in paraffin. Table 4.1 shows the list of the cases analyzed. 5–10-μm-thick sections were cut by means of a microtome (Leica RM 2125RT, Nussloch, Germany). The sections were deposited on an acetate sheet, de-paraffined with xylol and mounted on an Aluminum stub. After that they were inserted in the chamber of a Field Emission Gun-Environmental Scanning Electron Microscope (ESEM Quanta 200 and FEG-ESEM Quanta 250, by FEI Company, Eindhoven, The Netherlands) equipped with an Energy Dispersive System (EDS by EDAX, Mahwah, NJ, USA) to identify the elemental chemical composition of the foreign bodies found trapped in the tissues [9, 10].

Table 4.1 List of the pathologies analyzed of the human samples of inhabitants of Quirra and their anatomical location

Disease	Location
1 Melanoma	Skin
2 Spinocellular carcinoma	Skin
2 Non-Hodgkin's lymphoma	Lymph node
1 Tyroid papillar carcinoma	Lymph node
1 Chronic mieloid leukaemia	OMB (osteomedullary biopsy)
1 Leukaemia	OMB
1 Mielo-proliferative syndrome	OMB
1 Thrombocythemia	OMB
1 Ductal carcinoma	Breast
1 Lobular carcinoma	Breast
1 Adenocarcinoma	Uterus

Fig. 4.2 Malformed lamb died immediately after birth

With the same technique we analyzed environmental samples:

1. dust collected by air-pump in the mountain and sea section of the firing range after military activities;
2. dust collected on personal garments after a full-day walk in the fire range area;
3. small metallic debris found on the ground;
4. leaves of small plants growing in the area.

The above-mentioned samples were collected in order to identify the air-borne particles generated by the activities. Their analyses gave a notion of the air-and-soil contamination even if they were not exhaustive. We are conscious that the military and industrial activities carried out in the territory can vary over time and, as an obvious consequence, the pollution generated can be different in terms of quantity,

chemical composition, morphology and size. The study verified the compatibility of the dust identified in the environment and the one trapped in the pathological tissues of humans and animals.

4.3 Results

The investigations carried out on all the animal and human samples showed the constant presence of micro- and nanosized foreign bodies, mostly metallic and spherically-shaped. In the late 1990s we discovered that micro- and nanosized inorganic particulate matter can contaminate the body by reaching virtually any anatomical district, even far from its possible entrance site in the organism which can be the nose for inhalation and the mouth for ingestion. In every pathological sample collected in the area of the firing range analyzed we found many debris, often nanosized and with a spherical morphology, a feature that identifies them as generated by high-temperature combustive processes.

Figure 4.3 shows spherical 800-nm-sized Antimony-Cobalt particles found in the brain (a), in the liver (b) and in the testicle (c) of a malformed lamb that died

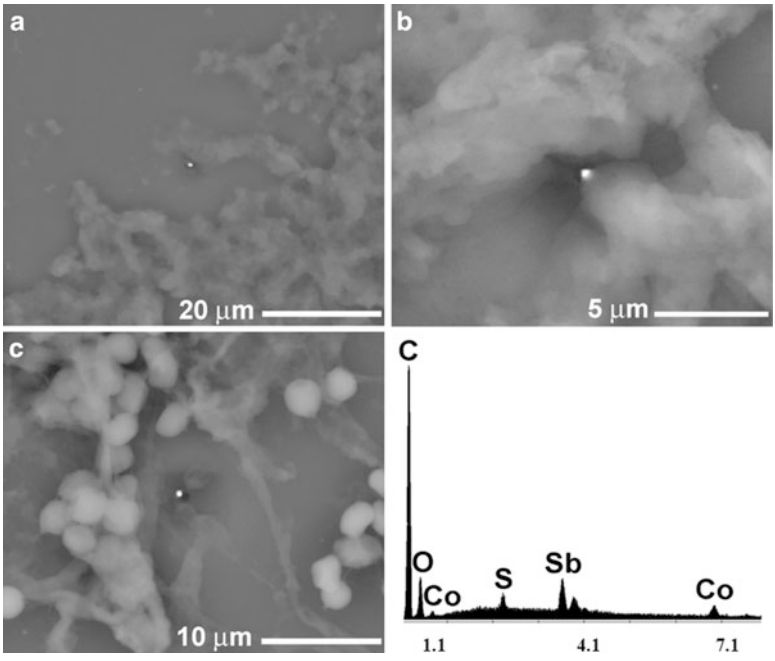

Fig. 4.3 The image shows Antimony-Cobalt nanoparticles found respectively in the brain (**a**), in the liver (**b**) and in the testicle of a malformed lamb, who died after being born. The last inset (**c**) two sections show SEM image (*left pane*) and the chemical composition (*right pane*) of the nanoparticles found in the different organs

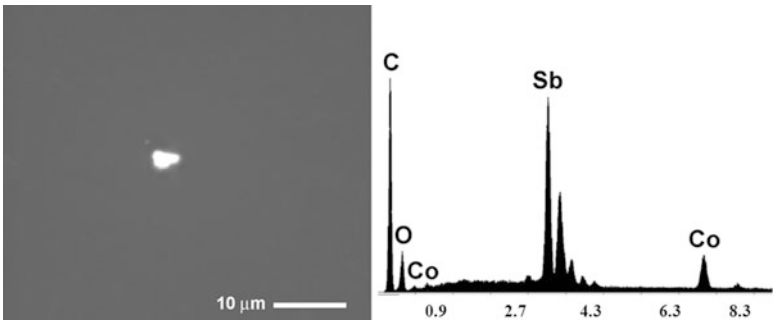

Fig. 4.4 The image shows an Antimony-Cobalt spherical nanoparticle close to a spermatozoon (*white arrows*). The seminal fluid belongs to a soldier who served in the Quirra firing range

immediately after being born. Figure 4.4 shows a similar Antimony-Cobalt particle found in the seminal fluid of an ill soldier who served in the firing range. Figure 4.5 shows a cluster of Stainless steel (Iron-Chromium-Nickel alloy) found in autoptic samples of a 6-year old goat that have pastured in the area for many years. Similar steel nanoparticles were found in lymph nodes of a citizen of Quirra who suffered of non-Hodgkin's lymphoma (Fig. 4.6).

In a cow's internal tissues Lead-compound particles were found (Fig. 4.7) and similar compounds were also identified in a pathological tissue of a Quirra's citizen affected by non-Hodgkin's lymphoma (Fig. 4.8). Lead-based particles with unusual composition were also identified in the soil, in the area of the military activity (Fig. 4.9).

4.4 Discussion and Conclusions

The results indicate that both civilians and animals presented showed foreign particulate matter embedded in their biological tissues as an evidence of their exposure to certain environmental pollution. The analyses of the samples taken from the environment confirmed the presence of pollutants whose origin is beyond any possible doubt anthropogenic. In some cases those findings were similar to those detected that were embedded in the pathological tissues analyzed. Of course, in some cases we did not found the same chemical compositions, since some combinations like, for instance, Sb-Co were generated by a single, spot test of explosion of a particular weapon. The pollution thus generated was limited in time and only the soldiers, shepherds and animals present at that very time close to the spot were exposed, so they had the possibility to inhale or to ingest those particular environmental pollutants. Another example is given by the contamination generated by the tests on the propellants of the missiles (Ariane first, and Zephir after) that before 2006 contained Lead and then Aluminum.

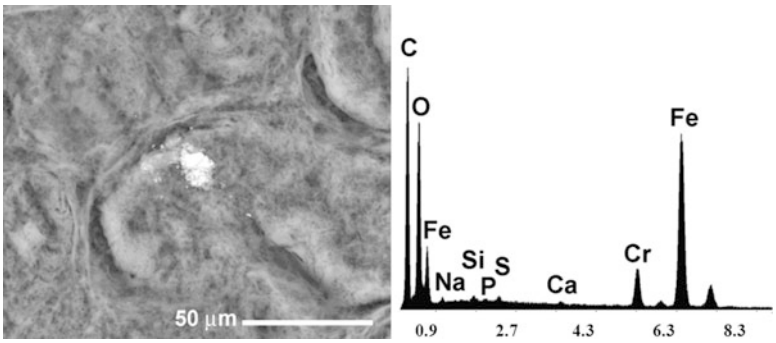

Fig. 4.5 The image shows a cluster of stainless-steel nanoparticles embedded in the testicle tissue of a 6-year old goat that lived in the territory of the firing range

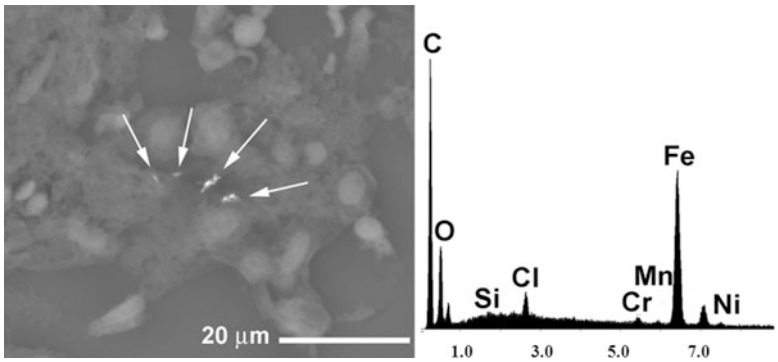

Fig. 4.6 The image shows stainless-steel particles embedded in the biological tissue of a patient who lived close to the firing range and died of a non-Hodgkin's lymphoma

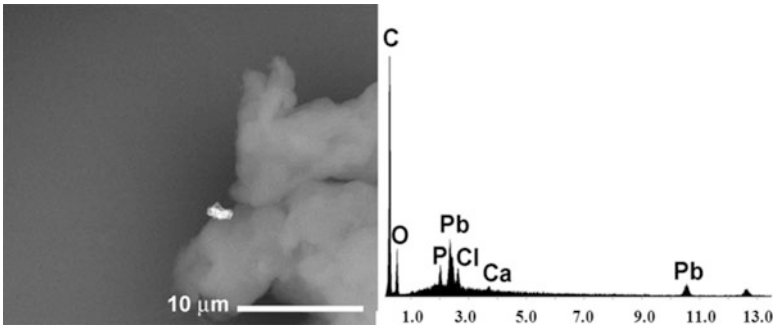

Fig. 4.7 The image shows a Lead particle found in cow's lung

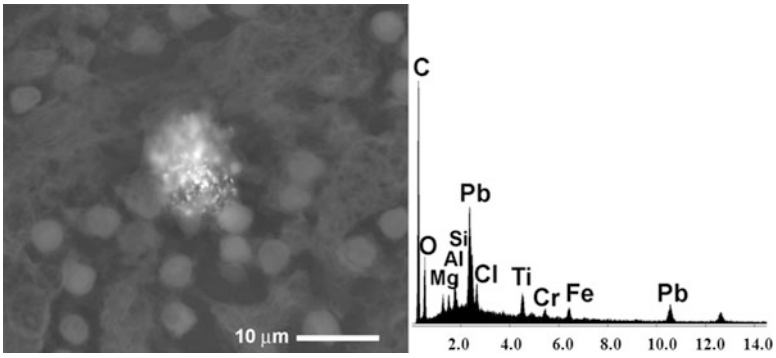

Fig. 4.8 The image shows a cluster of Lead-alloy nanoparticles embedded in a pathological tissue of a subject who lived at Quirra and died of non-Hodgkin's lymphoma

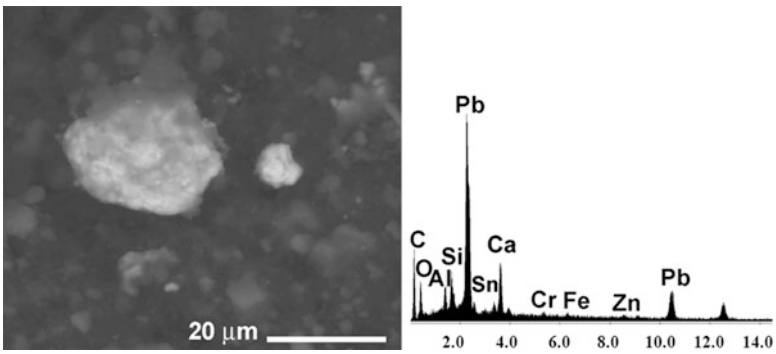

Fig. 4.9 The image shows unusual Lead-compound debris found in the environmental pollution

The post-mortem samples of animals showed an ample dispersion of the environmental contamination in the gonads, in the brain and in the bone marrow. That means that, when those pollutants get into the body, they can reach all its anatomical districts negotiating any physiological barrier. The chemical composition is sometimes characterized by never-seen before element aggregations that cannot be found in any handbooks of materials, since they are due to uncontrolled combustions. In the course of the explosion of a weapon, gases and aerosols are generated containing all the elements making up the weapon itself, the target and the environment involved (often soil). All those elements take part in the formation of solid particles whose size is roughly inversely proportional to the temperature at which the explosion occurred.

The chemical compositions we identified, mostly made up of heavy metals, suggest an origin of that pollution from ammunition explosions, since some elements are typical of weapons and are not generally found elsewhere. The airborne particles generated during the firing-range activity (soldiers' training,

destruction of obsolete weapons, test activity, etc.) contaminated air and soil, so people and animals spending time for years in that area had a high probability to be contaminated through inhalation and/or ingestion. As a matter of fact, micro- and, especially, nanoparticles can remain suspended in the atmosphere for a long time and, at least for some aspects, behaving like a gas, they can be inhaled and, if small enough, reach the alveoli whence they enter the blood and are thus carried virtually to any tissue. After a while, a considerable part of airborne particles falls to the ground, so contaminating grass, vegetables and cereals that are food for men and animals. Another issue that should be considered is the capability of particles to pass from mother to fetus, thus inducing miscarriages or malformations and their further capability to enter cell nuclei, thus interfering with the DNA. It was demonstrated that [11] 100-nm-sized particles, if inhaled, can negotiate the pulmonary barrier in 60 s and in 1 h can reach the liver. Also the blood–brain and the fetal barrier can be crossed [12, 13]. In the former case, their possibility to trigger not only cancer [14] but also neurological diseases ought to be considered. In the latter, they may disturb and damage the development of the embryo inducing malformations.

Humans eating contaminated animals, their dairy products or their eggs can be exposed to an indirect contamination that adds to the direct one. There is also the possibility that water gets contaminated, since in the higher part of the firing range many springs are located, particularly active during the winter months. The metal debris left on the ground can corrode and release compounds and ions that can pollute the ground water tables. These interdisciplinary investigations offer an objective support to an evidence-based medicine, the basis for a translational medicine and the knowledge obtained can be the foundations for prevention measures to be adopted for the health of humans, animals, and the environment.

References

1. Biggeri A et al (2006) Report on health status of residents with industrial, mining or military sites in Sardinia, Italy. Epidemiologia e Prevenzione Italia 30(Suppl 1):5–95
2. Broccia G, Cocco P, Casula P (2001) Incidence of non-Hodgkin's lymphoma and Hodgkin disease in Sardinia, Italy: 1974–1993. Haematologica 86:58–63
3. Broccia G, Longinotti M, Ginnico B, Porcu C, Chessa E (2011) Haematological malignancies on the island of Sardinia, 1974–1993: a geographical study. J Open Hematol 5:4–9
4. Zucchetti M (2006) Environmental pollution and population health effects in the Quirra area, Sardinia island (Italy) and the depleted uranium case. J Environ Prot Ecol 7:82–88
5. Zucchetti M, Coraddu M, Littarru B, Cristaldi M (2011) Environmental pollution and health effects in the Quirra area, Sardinia (Italy). Fresenius Environ Bull 20:810–817
6. Gramiccioni L (2004) Caso Sindrome di Quirra, Report Istituto Superiore di Sanità (ISS) n. 33619, Roma
7. Mellis G, Lorrai S (2012) Monitoraggio ambientale al PISQ. Analisi chimiche su matrici fisiche e biologiche (Lotto 3-Fase veterinaria), Internal Report Italy, pp 1–48
8. Final Report (2013) Commissione parlamentare di inchiesta sui casi di morte e di gravi malattie che hanno colpito il personale Italiano ... del senato del 16 marzo 2010- Relazione sulle risultanze delle indagini svolte dalla commissione. http://www.senato.it/service/PDF/PDFServer/DF/288867.pdf.

9. Gatti AM, Montanari S, (2005) Handbook of nanostructured biomaterials and their applications in nanobiotechnology. Capitolo 12: risk assessment of microparticles and nanoparticles and human health. American Scientific Publishers, Stevenson Ranch, California USA, pp 347–367
10. Gatti AM, Montanari S (2008) Nanopatology: the health impact of nanoparticles. Pan Stanford Publishing, Singapore
11. Nemmar A, Hoet PHM, Vanquickenborne B, Dinsdale D, Thomeer M, Hoylaerts MF, Vanbilloen H, Mortelmans L, Nemery B (2002) Passage of inhaled particles in to the blood circulation in humans. Circulation 105(4):411–417
12. Oberdörster G, Sharp Z, Atudorei V, Elder A, Gelein R, Kreyling W, Cox C (2004) Translocation of inhaled ultrafine particles to the brain. Inhal Toxicol 16(6–7):437–445
13. Gatti AM, Bosco P, Rivasi F, Bianca S, Ettore G, Gaetti L, Montanari S, Bartoloni G, Gazzolo D (2011) Heavy metals nanoparticles in fetal kidney and liver tissues. Front Biosci (Elite edition E3) 1:221–226
14. Gatti AM, Quaglino D, Sighinolfi GL (2009) A morphological approach to monitor the nanoparticle-cell interaction. J Imaging 2(S09, Editorial 1):2–21

Part II
Policy, Diplomacy, Verification, Compliance, Implementation

Chapter 5
The Yin and Yang of Countering Biological Threats: Public Health and Security Under the International Health Regulations, Biological Weapons Convention, and the U.N. Security Council Resolution 1540

D. Perkins

Abstract The objective of this report is present the inter-governmental dynamics when considering a deliberate biological incident. In such an event, the epidemiological data may be incorporated into a larger investigation or intelligence analysis framework and may be showcased for legal or national security decision making. While in many countries, the civilian public health and security communities (broadly including in the latter the intelligence, law enforcement and the military) are not *de facto* partners in countering biological threats, there is a significant, upward global trend of pursuing inter-ministerial collaboration and a "*whole of government*"/"*whole of society*" national approach in that regard. Illustrative examples of blending these "*yin and yang*" areas of countering biological threats also exist at the international level under the WHO International Health Regulations (IHRs), Biological Weapons Convention (BWC), and the U.N. Security Council Resolution 1540 (UNSCR 1540) as well as in several bilateral engagements between inter-governmental organizations. By identifying the synergy and convergence of public health and security under the BWC, IHRs, and UNSCR 1540, countries could maximize the use of limited national resources by establishing inter-ministerial, regional and international partnerships in order to strengthen the core capacities required by the WHO IHRs as well as the existing national measures consistent with their obligations under the BWC and UNSCR 1540 to deter, prevent, and respond to biological incidents or threats.

Keywords International Health Regulations • Biological Weapons Convention • UN Security Council Resolution 1540

D. Perkins (✉)
U.S. Department of Health and Human Services, Office of the Assistant Secretary for Preparedness and Response, Washington, DC 20201, USA
e-mail: doctor.perkins@gmail.com

A. Vaseashta and S. Khudaverdyan (eds.), *Advanced Sensors for Safety and Security*, NATO Science for Peace and Security Series B: Physics and Biophysics,
DOI 10.1007/978-94-007-7003-4_5,

5.1 The Yin and Yang: Public Health and Security

Fundamentally, the medical and public health response to a natural, accidental, or deliberate biological incident is basically identical since it is aimed at saving lives and alleviating human suffering. In countering biological threats, the public health and security communities may have different objectives, and terminology as well as distinct methods. However, their overlapping missions and common goal of protecting public health and safety, serve to address holistically the entire spectrum of risk, thus the "*yin and yang*" of countering biological threats – whether they are due to state-level biological weapons (BW) programs, rapid global spread of infectious disease driven by international transportation and commerce, or the empowerment of non-state actors by technological advances.

In this context, epidemiological investigations focus on determining the source of an outbreak in order to contain it and prevent the spread of the disease to vulnerable populations. These public health investigations do not aim to find the perpetrator of an attack in order to prosecute him or her in a court of law. That is ultimately the job of the law enforcement community. However, in the case of a deliberate terrorist or biological weapon attack, these epidemiological data may be incorporated into a larger investigation or intelligence analysis framework and may be showcased for legal or national security decision making. The response to a public health emergency (whether a natural outbreak, laboratory accident, or a criminal or terrorist incident) begins with the recognition of the event by the public health systems. Public health agencies will work to protect the public and the first responders by implementing specific interventions (such as medical countermeasures and/or vaccine distribution, health education, and medical surveillance) in order to determine the causative pathogen, save lives, and prevent the spread of disease.

The security community (whether law enforcement or intelligence agencies or both) will work to prevent criminal or terrorist acts as well as subsequent attacks, and identify, apprehend, and prosecute the perpetrators. The deliberate nature of biological events is difficult to ascertain in a situation when the first indicator of a bioterrorism incident that occurred may be people or animals showing symptoms of an unusual disease or an unusual pattern of disease (i.e. non-endemic causative agent or large number of victims in relation to a particular time and geographic location, or other criteria[1]).

[1]Confidence-Building Measure (CBM) "B" under the BWC (on "Exchange of information on outbreaks of infectious diseases and similar occurrences caused by toxins") identifies specific reporting criteria for "outbreaks that seem to deviate from the normal pattern"- when the cause of the outbreak cannot be readily determined or the causative agent is difficult to diagnose; when the disease may be caused by organisms which meet the criteria for risk groups III or IV, according to the classification in the latest edition of the WHO Laboratory Biosafety Manual; when the causative agent is exotic to a given geographical region; when the disease follows an unusual pattern of development; when the disease occurs in the vicinity of research centres and laboratories subject to exchange of data under CBM A; when suspicions arise of the

Thus, the protection of public health and safety is best served if the public health and security communities establish a working relationship at the local and national levels so that relevant information, evidence collected, and threat assessments are shared early in the course of an incident. The Joint Investigation Model established by the Centers for Disease Control and Prevention (CDC) and the Federal Bureau of Investigation (FBI) in the U.S. [1] shows that such collaboration and partnership between the public health and security communities are possible. Specific limitations and exemptions may exist in each country with regard to joint investigations, especially in countries where an intelligence agency not the law enforcement has the legislative authority to prevent and respond to bioterrorism attacks (Romania, as an example) [2]. However, the recognition of the benefits of such collaboration and the decision to work jointly, are first steps to effectively tackle biological threats across the entire spectrum of risk (natural, accidental or deliberate) at the national level.

5.2 International Regimes at the Health and Security Nexus

At the inter-governmental level, the "*yin and yang*" of countering biological threats converged into the nexus of health and security of International Health Regulations (IHRs), Biological Weapons Convention (BWC), and the U.N. Security Council Resolution 1540 (UNSCR 1540), as they apply to all WHO Member States, BWC Member States, and all UN Member States, respectively.

The IHRs, as revised in 2005,[2] aim to "*prevent, protect against, control and provide a public health response to the international spread of disease in ways that are commensurate with and restricted to public health risks, and which avoid unnecessary interference with international traffic and trade*" and they legally bind the WHO and its 193 Member States (which is also the total number of UN Member States) to new standards of global responsibility. The eight core capacities required for implementation of IHRs (National legislation, policy and financing; Coordination and National Focal Point communications; Surveillance; Response; Preparedness; Risk communication; Human resources; and Laboratory) assume an effective inter-ministerial approach (including *inter-alia* between public health and security communities). For instance, a country level indicator of achieving Core Capacity 2 ("Coordination and National Focal Point communications") refers to "*a mechanism . . . established for the coordination of relevant sectors in the implementation of IHR*" with the specific outcome of "*multi-sectoral and multi-disciplinary coordination and communication mechanisms are tested and updated regularly through exercises or through the occurrence of an actual event*" and

possible occurrence of a new disease. See: http://www.unog.ch/80256EE600585943/. (httpPages)/E5DF7E4EB547D5ACC1257AC40056A030?OpenDocument

[2]WHO IHRs website at: http://www.who.int/ihr

"*annual updates on status of IHR implementation to stakeholders across all relevant sectors conducted*" [3]. Similarly, the IHRs requirements on Core Capacities for Responding to public health emergencies at Points of Entry (PoE) refer to the capability of designated PoEs to "*apply entry or exit controls for arriving and departing travelers and other recommended public health measures*" (Ibid) which include entry or exit controls for arriving and departing travelers, and measures to disinfect, decontaminate or otherwise treat baggage, cargo, containers, conveyances, goods or postal parcels including, when appropriate, at locations specifically designated and equipped for this purpose. Needless to say, effective implementation of such measures at any point of entry (be it a port, airport or border crossing point) would require multi-sectorial and multi-disciplinary collaboration and partnership between the public health authorities and other governmental agencies including those responsible for border security; law enforcement; transportation; environmental, water, and food safety; nuclear, radiological and chemical disciplines, etc.

Civil society (including non-governmental and professional organizations), academia, and industry play an increasingly important role in public health and security through their contribution with technical, human, financial, and institutional resources [4, 5], and thus in assisting Member States with meeting their IHRs obligations.

Significantly, the IHRs (2005) apply to any diseases and public health events (biological, chemical, radiological), including those from new or unknown causes, irrespective of origin or source, that could present significant harm to humans. There are no formal enforcement mechanisms or sanctions for failing to comply with the IHRs but compliance relies on each government's recognition that mitigating public health threats (whether of biological, chemical or radiological/nuclear nature and due to natural, accidental or deliberate causes) and working cooperatively with other nations in that regard, serves all countries' mutual interests.

Similarly, implementation of UNSCR 1540 spans the biological, chemical, and radiological/nuclear spectrum of risk and there are no formal enforcement mechanisms or sanctions for failing to comply with the resolution.

Resolution 1540 was adopted by the Security Council on 28 April 2004 under Chapter VII of the UN Charter. It was the first formal decision ever taken by the Security Council to address the weapon of mass destruction (WMD) proliferation as a global threat to international peace and security and it imposes far reaching obligations on all States to take a series of steps to prevent proliferation of WMDs, their means of delivery, and related materials to non-state actors. UNSCR 1540 aimed to enhance the capacity of all States to respond effectively to the threats posed by the proliferation of WMD; prevent the proliferation of WMDs, their means of delivery and related materials; and fill the existing gaps in international law by preventing and deterring any non-State actor from manufacturing, acquiring, possessing, developing, transporting, transferring, or using WMD and their means of delivery, in particular for terrorist purposes. UNSCR 1540 is binding on all UN Member States and specifies obligations States have to meet with regard to national legislation on WMD prohibitions; domestic controls and enforcement

(on accounting for, securing, physical protection of materials; border controls; and export and trans-shipment controls); assistance; promotion and implementation of multilateral treaties; promotion of dialogue and cooperation; and reporting.[3]

The Security Council also established a subsidiary body, known as "*the 1540 Committee*"[4] to monitor the UNSCR 1540 implementation. The 1540 Committee is aided by a Group of Experts [established per Security Council resolutions 1977 (2011) and 2055 (2012)] to assist the Committee in carrying out its mandate. The 1540 Committee and its Experts Receive and examine reports to monitor implementation; promote greater awareness of UNSCR 1540, including by outreach and dialogue with Member States; and facilitate capacity building and assistance by providing a "*clearing house*" function.

A primary tool used by the 1540 Committee and its Experts to monitor UNSCR 1540 implementation, is the 1540 Matrix.[5] The Matrix for each country is prepared by the 1540 Committee and its Experts with information which originates primarily from national reports as complemented by official government information, including that made available to inter-governmental organizations. National matrices are used as a reference tool for facilitating technical assistance and the Committee's constructive dialogue with States on their implementation of UNSCR 1540. The 1540 Matrix template has 382 "fields" covering national activities related to the 1540 operative paragraphs. With regard to BWs, related materials, and means of delivery, the Matrix records the UNSCR 1540 implementation in the following areas:

- Measures to account for/secure production, use, storage, and transport;
- Regulations for physical protection of facilities/materials/transports;
- Licensing/registration of facilities/people handling biological materials;
- Reliability check of personnel;
- Measures to account for secure/physically protect means of delivery;
- Regulations for genetic engineering work;
- Other legislation/regulation related to safety and security of biological materials.

These areas show significant overlap with the IHRs core capacity requirements related to biological risk management and similarly, the effective implementation of UNSCR 1540 at the national level requires a "*whole of government*" approach.

While the implementation of UNSCR 1540 is the responsibility of each UN Member State, civil society, academia, and industry, have already demonstrated in many areas that they are important partners in strengthening the global implementation of resolution 1540 (2004) and they have a critical role to play in identifying effective practices on implementing resolution UNSCR 1540 and relevant technology governance. As Mr. VukJeremić, President of the 67th Session

[3] 1540 Committee website at: http://www.un.org/en/sc/1540

[4] *Ibid.*

[5] National 1540 Matrices are posted online at: http://www.un.org/en/sc/1540/national-implementation/1540-matrix/committee-approved-matrices.shtml

of the United Nations General Assembly, stated, "*We live in an increasingly volatile and unpredictable world. One of the most alarming aspects of the new global reality is that capabilities once thought to be exclusively in the hands of states such as the ability to inflict harm on a massive scale could become more easily accessible to non-state actors*". While the 1540 Committee meetings are not open to the public, civil society, academia, and industry, had an opportunity to provide their perspectives to the 1540 Committee during the 2009 Comprehensive review.[6] The comprehensive review of 2009 acknowledged the significant number of measures that States have taken to implement obligations under resolution 1540(2004), but identified some areas in which States have adopted fewer measures, such as BWs, means of delivery, national control lists, access to related materials and financing of prohibited or illicit proliferation activities. Civil society could continue to be the driver for strengthening national implementation of UNSCR 1540 by *inter-alia*:

- Increasing awareness of the resolution 1540 obligations and existing gaps in Member States' legislation and enforcement programs
- National Action Plan needs
- Sharing "success stories", and
- Participating in delivering assistance on capacity building with their respective governments.

In addition, civil society, academia, and industry could put forward ideas on how the 1540 Committee can more effectively contribute to implementing UNSCR 1540, including by:

- Analyzing its current tools and methods for their relevance and "user-friendliness",
- Thematic outreach on specific areas identified by the 2009 Comprehensive review as "low compliance" and
- Way forward toward the next Comprehensive review scheduled for 2016.

Arguably, the international regime that provides most opportunities for strengthening the ties between public health, science, security, and civil society, is the Biological Weapons Convention.[7] Its inter-sessional program of work, with Meetings of Experts and Meetings of States Parties organized during a 4 year period between the review conferences, showed innovation and inspiration at work, with poster sessions and other informative side events organized by civil society, intergovernmental organizations, and Member States; speed networking and other opportunities for informal interaction and outreach; employment of social networking tools (such as webcasts, Twitter, and Facebook). The BWC forum also demonstrates currently an unprecedented openness and transparency, with invited observers, civil society, industry, and academia guests (who provide statements

[6] 1540 Committee website dedicated to the 2009 Comprehensive review, at: http://www.un.org/en/sc/1540/comprehensive-review/2009.shtml

[7] BWC Implementation Support Unit website, at: http://www.unog.ch/bwc

and briefings and participated in seminars and panel discussions), open working sessions, and posting of all national papers, statements, and all other BWC meeting-related documents available online on the BWC Implementation Support Unit's website at http://www.unog.ch/bwc.

Of note, the BWC Seventh Review Conference in December 2011, called upon States Parties "*to adopt, in accordance with their constitutional processes, legislative, administrative, judicial and other measures, including penal legislation*" to enhance domestic implementation and ensure the safety and security of microbial or other biological agents or toxins. To strengthen the implementation of BWC, States Parties agreed upon the value of specific measures, showing a large overlap with the requirements of IHRs and UNSCR 1540, such as:

- Implementing voluntary management standards on biosafety and biosecurity
- Encouraging the promotion of awareness of obligations to the Convention as well as relevant national legislation amongst those working in the biological sciences and related professionals in the private and public sectors
- Encouraging the development of education programs and voluntary codes of conduct to promote a culture of responsibility for those with access to biological agents and toxins relevant to the Convention
- Strengthening methods and capacities for surveillance and detection of outbreaks of disease at the national, regional and international levels.

The BWC Seventh Review Conference also noted "*the contribution by the WHO, FAO, OIE and other relevant international organizations, as well as scientific and academic institutions and nongovernmental organizations, to the meetings of States Parties and meetings of experts*" and that "*the International Health Regulations (2005) are important for building capacity to prevent, protect against, control and respond to the international spread of disease; such aims are compatible with the objectives of the Convention.*" [6]. The Conference also noted that "*information provided to the United Nations by states in accordance with Resolution 1540 may provide a useful resource for States Parties in fulfilling their obligations under this Article [IV]*" (Ibid).

5.3 Conclusion

Our shared goal of a safer and healthier world could only be achieved through a smart, long-term engagement of health and security communities to build global preparedness to prevent, detect, and respond to all health hazards. Effective national implementation of the International Health Regulations, Biological Weapons Convention, and the UN Security Council Resolution 1540 requires "*whole of government*" and "*whole of society*" approach and they are critical instruments for achieving global health security. Global health security (that is, the measures societies and governments take to minimize the vulnerability of populations against high-impact public health risks and emergencies and mitigate the consequences of

biological incidents that endanger public health, affect multiple sectors of society, and may impact national and global security) requires the power of inter-sectoral collaborations that not only save and enhance lives but also bolster the security of all nations.

Disclaimer The views, opinions, findings, and conclusions expressed in this paper are those of the authors and do not necessarily represent the views or the official policy or position of the Department of Health and Human Services, the U.S. Government, or the United Nations. At the time of publication of this manuscript, the author serves in a U.S. Government-seconded position as a member of the UN Security Council 1540 Committee's Group of Experts (http://www.un.org/en/sc/1540/committee/expert-group.shtml).

References

1. Public Health and Law Enforcement Emergency Preparedness Workgroup (2008) Joint Public Health – law enforcement investigations: model memorandum of understanding (MOU). Available online at: http://www.nasemso.org/Projects/DomesticPreparedness/documents/JIMOUFinal.pdf. Accessed on 19 Jan 2013
2. Perkins D, Sârbu E (2011) Bioterrorism emergency preparedness and response in Romania-implications for the NATO strategic concept. Acad Rom Sci Ann Mil Sci 3(1):52–65
3. IHR Core Capacity Monitoring Framework: checklist and indicators for monitoring progress in the development of IHR core capacities in States Parties, WHO/HSE/IHR/2010.1.Rev.1. Available online at: http://www.who.int/ihr/IHR_Monitoring_Framework_Checklist_and_Indicators.pdf. Accessed on 19 Jan 2013
4. Ford N, Wilson D, Bunjumnong O, von Schoen Angerer T (2004) The role of civil society in protecting public health over commercial interests: lessons from Thailand. Lancet 363(9408):560–563
5. Understanding Civil Society Issues for WHO, Civil Society Initiative External Relations and Governing Bodies, Discussion paper no. 2 CSI/2002/DP2. Available online at: http://www.who.int/civilsociety/documents/en/understanding_en.pdf. Accessed on 19 Jan 2013
6. Final Document of the seventh review conference, Geneva, 5–22 Dec 2011, BWC/CONF.VII/7. Available online at: http://www.unog.ch/80256EDD006B9C2E/(httpNewsByYear_en)/925929F5F28485EAC125796E0064AD82?OpenDocument. Accessed on 11 Mar 2013

Chapter 6
Timely Detection of Outbreaks in the Public Health Surveillance System of the Republic of Moldova

S. Gheorghita and N. Caterinciuc

Abstract This study analyses the structure and functions of a surveillance system for communicable diseases and public health events, exploited by using information technologies in support of facilitating early detection of outbreaks and Chemical, Biological, Radiological and Nuclear (CBRN) risks in the Republic of Moldova. Functioning public health surveillance system in the Republic of Moldova (RM) is provided by the international (International Health Regulation (IHR), 2005) and national (Law on Surveillance System in Public Health, governmental decisions and Ministry of Health orders) legal framework and the availability of trained human resources, finance and technical equipment at all levels of health sector. In the context of strengthening national surveillance system required by IHR(2005), electronic system on surveillance of communicable disease and public health events (biological, chemical, radiological) ensures early detection of the public health threats at various community levels in order to organize timely and coordinated public health response.

Keywords Health surveillance • Emergency system • Electronic alert

6.1 Introduction

A public health emergency may refer to a single case of infectious disease, a cluster of cases of the same disease occurring in the same time and place, epidemics, or pandemics. An outbreak is defined as a situation when diseases or health events occur at a greater frequency than normally expected in a period of time and place [4]. An effective public health surveillance system should ideally detect outbreaks early

S. Gheorghita • N. Caterinciuc (✉)
National Center of Public Health, 67A, Gh. Asachi str., Chisinau MD-2028, Republic of Moldova
e-mail: ncaterinciuc@mail.ru

A. Vaseashta and S. Khudaverdyan (eds.), *Advanced Sensors for Safety and Security*,
NATO Science for Peace and Security Series B: Physics and Biophysics,
DOI 10.1007/978-94-007-7003-4_6,

in the course of monitoring the trends of infectious diseases, thus allowing for a timely response and containment of disease. The surveillance system may also be used for damage and need assessment in case of emergency situations and for the evaluation of the effectiveness of prevention and intervention measures. Early risk detection requires the implementation of sensitive systems for routine surveillance, including electronic systems which allows for automated analysis and visualization tools. Such information systems are essential for improving the performance of public health services, managing data quality and optimizing the decision-making process. Public health informatics differs from other fields because it has to be focusedon the application of information to promoting the health of population rather than individuals; disease prevention, rather than treatment; on interventions at all vulnerable points in the chain of events leading to diseases, injury, or disability; and on measures within the governmental, rather than private context [7]. Timely detection of outbreaks in the public health system ensures that epidemiological investigations are started as soon as possible in order to implement appropriate measures to prevent future outbreaks [4] and can be improved by implementing electronic tools. The essential components of outbreak investigations include:

1. Establishing case definition(s);
2. Confirming that cases are "real" (i.e. validation of cases);
3. Establishing the background rate of disease;
4. Identifying cases and deciding ifan outbreak is occurring (and also what are the potential consequences);
5. Examining the epidemiologic features of the cases;
6. Generating hypotheses;
7. Testing hypotheses;
8. Collecting and test clinical and/or environmental samples;
9. Implementing control measures; and
10. Interacting with the press, informing the public [4, 9].

6.2 National Legislative Context and Responsibilities

In the Republic of Moldova, the responsibilities of Chemical, Biological, Radiological and Nuclear (CBRN) risk management team are shared among various state authorities (i.e. justice, law enforcement, health, agriculture, environment, etc.) according to their statutory roles and responsibilities. The Ministry of Health (MoH) is responsible for ensuring the heath security (including biosafety and biosecurity) and is partly responsible for ensuring the chemical and radiological safety and security. The surveillance and control of communicable diseases and public health emergencies (includingoutbreaks of infectious disease) are implemented by the State Public Health Surveillance Service in accordance with Law #.10-XVI of 03.02.2009.

The national legal framework of the Republic of Moldova includes provisions for the risk prevention and management, based on an all hazard approach, and addresses *inter-alia* the risk of bioterrorism, public health emergencies, and requirements for handling dangerous or potentially dangerous biological materials, microorganisms or toxins, chemicaland radiological materials. Ensuring public health security is accomplished through *inter-alia*, systematic surveillance and identification of potential risks (e.g. natural, environmental, industrial), laboratory biosafety and biosecurity, early detection of threats in order to ensure timely and coordinated public health response. The National and Territorial Extraordinary Public Health Commission was established at the national and territorial level to integrate and coordinate prevention, management of the threats and hazard to public health and the multi-sectorial response and consequence management [8].

Our national surveillance system is capable of notifying a list of 72 communicable diseases lists based on standard case definitions. Moreover, recently the list of reportable diseases has been extended to 102, in accordance with international requirements (viz., pathogenic *E. coli*, giardiasis, avian influenza, SARS, are also included). The surveillance of communicable diseases encompasses information-gathering activities relevant for the detection of biological threats utilizing a routine – nominal case-based and event-based system. Through the MoH order # 368/2004, the algorithm of detection and reporting of the outbreaks at early stageswas. For selected diseases with seasonal manifestation (diarrheic diseases, respiratory infection) a weekly surveillance system was set up which allows monitoring the specific indicators for trend evaluation and forecasting epidemiological situations. The sentinel surveillance system offers data and indicators for influenza, cholera, etc.

6.3 Identification of the Public Health Threatsat Various Community Levels

The surveillance system on communicable disease and public health events is structured by functional levels: local, intermediate and national levels. This functional structure was maintained when the electronic tool was designed and developed (Fig. 6.1).

In case of suspicion of infectious disease and/or a public health event, the public health personnel from the primary, emergency and hospital facilities have to report the cases by completing the electronic reporting form. Primary- care physicians at the local/community level and emergency medical-care specialists have to detect early events, including diseases or deaths above expected levels for the particular time, place and population. Data of nominal infectious diseases and outbreaks are reported during the 12–24 h-time frame, using approved standard forms. Detection and intervention in outbreaks are ensured by medical care specialists using standard national protocol (for diarrheic diseases, food-borne pathogen diseases, etc.).

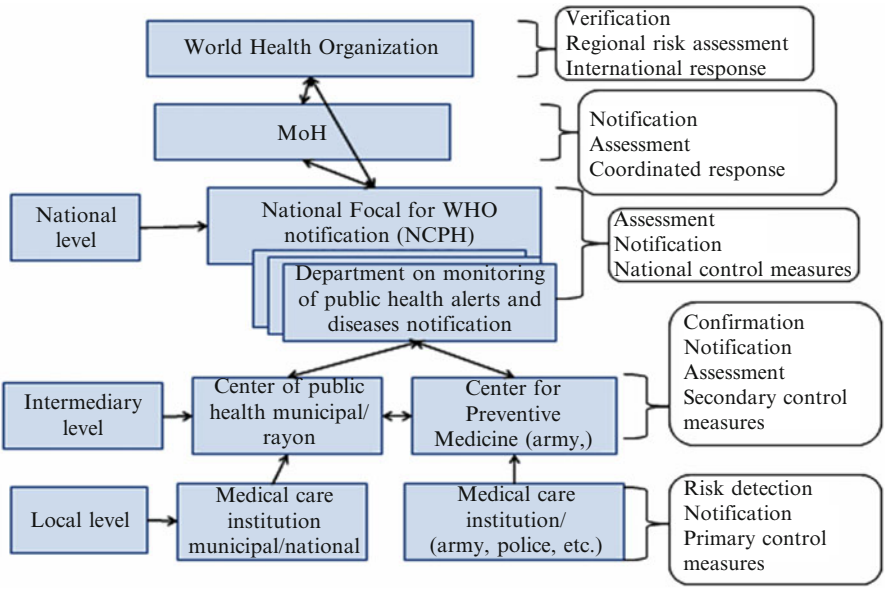

Fig. 6.1 Levels and functions of the surveillance system for communicable diseases and public health events in Republic of Moldova

Implementation of primary response measures at the lowest level in the community represents the critical step for containing and limiting the spread of communicable diseases.

Data which come from traditional indicator-based surveillance system involving different kind of systems (i.e. sentinel, laboratory surveillance, health care activity monitoring) are more robust and reliable than that obtained based on events; however, the latter effectively complements the indicator-based surveillance system. At the intermediate levels, there is a the network of public health centers and laboratories for confirmation of public health events and the upper next level – is the national level (for assessment and complex interventions).

6.4 Structure and Functions of the Electronic Surveillance System

In 2008, a national team of epidemiologistsfrom the National Center for Public Health and information technology specialists within the "Control avian influenza and preparedness in the event of a human pandemic and response activities" funded by the World Bank initiated development of the current electronic surveillance system in the Republic of Moldova. The electronic platform for the surveillance of communicable disease and public health events is capturing the data flow of

reported cases of infectious disease and public events that may affect adversely the health of human populations and it is also analyzing data by aggregating them into tables, graphs, and is developing information and dissemination (feedback) to all medical institutions in order to implement appropriate containment measures and timely intervention.

In the Republic of Moldova, the national surveillance electronic system (ES) for communicable diseases and public health events facilitates standardized reporting as well early notification of infectious diseases cases and public health events. Nominal cases reporting are facilitated by downloading data from the national registers (demographic, medical care institution, primary care physicians).

In order to assure the data quality management during notification, the data are selected from established standardized lists (clinical symptoms, epidemiologic data – risk factors, mechanism of transmission, etiological agents, laboratory data – list of methods, agents, antimicrobial resistance). A logical control and data validation mechanisms of entering of cases, laboratory results and events, are also included. Protection of personal data is ensured by specifying the roles and levels of access. The automatic registries in the historical order of users' access to electronic platform are maintained at the National Center of Public Health.

ES allows the real time monitoring, analysis and assessment of public health indicators and events in the country. The electronic disease surveillance system routinely collects data about occurrence of diseases on the national territory, and it is complemented by an event monitoring component where the information on potential threats is routinely searched for and assessed with the system generating emergency alerts (based on the events' temporal and spatial occurrence and clustering). This electronic tool automatically alerts specialists from public health centers at the rayon and national level about any potential outbreaks.

The outbreak notification or electronic alert allows the initiation of the risk assessment at the community and/or national levels as well as the commencement of the epidemiological investigation. At the national and territorial centers of public health there are rapid response teams which consist of epidemiologists, microbiologists, hygienists, etc. Outbreak' cases are reported in accordance with approved standard case definition [1–3, 6]. A public health event is evaluated by epidemiologists from community level using the decision instrument for the assessment and notification of events that may constitute a public health emergency of international concern (Annex 2, International Health Regulation, IHR 2005) [10]. At the national level, the assessment of public health event is provided by a national rapid response team within 48 h of notification [1, 5] which is using again the same IHR making decision instrument for the assessment and notification considering the following criteria: the seriousness of public health impact, whether the event is unusual or unexpected, whether is a significant risk for international spread, and whether there is a sufficient risk for trade or travel restrictions.

In accordance with the approved regulations, the Ministry of Agriculture is responsible for the regulatory framework of the agriculture sector including national food safety. The veterinary service of the Ministry of Agriculture is responsible for animal health, zoonotic and vector-borne diseases (rabies, anthrax, brucellosis,

salmonellosis, Avian, and H5N1 etc.) and food safety of animal products that can also affect human health. In case of zoonotic diseases, the specialists from the veterinary service will report data through the electronic surveillance system of animal traceability which automatically exchanges data with the public health electronic surveillance system or/and will inform the local public health authority by phone or mail. At the territorial level, the investigation of zoonotic and food borne diseases is conducted by an epidemiologist and a specialist from the veterinary services. Clinical and environmental (food, water, vectors etc.) samples are tested in public health microbiological laboratories.

The electronic disease surveillance system in the Republic of Moldova integrates human and veterinary disease surveillance and allows statistics and GIS analysis as well as the generation of specific or general reports. Strengthening national early warning systems will enable timely confirmation of alerts and the detection of public health threats thus the prompt implementation of mitigation measures to prevent the national and international spread of the disease.

6.5 Conclusions

Based on the national experience of the Republic of Moldova, the implementation of electronic reporting tools in the public health service allows for the improvement of the quality and accessibility of data on the situation and trends in morbidity, the optimization of surveillance and control of communicable diseases and public health events, and it leads to an increase in the efficiency of outbreak response and effective financial and human resources management. Such a routine electronic surveillance system of communicable diseases and public health events is critical for the timely and qualitative detection of outbreaks, the effective implementation of the International Health Regulations, and strengthening the health security in the Republic of Moldova.

References

1. Case definitions for the four diseases requiring notification to WHO – under the IHR 2005–2009, WER/REH 2009, 84:49–56. http://www.who.int/wer/2009/wer8407.pdf
2. Commission Decision of 19 March 2002 laying down case definitions for reporting communicable diseases to the Community network under Decision Nr. 2119/98/EC of the European Parliament and of the Council (notified under document number C(2002) 1043) (2002/253/EC), Off J Eur Commun 3.4.2002, L 86/44
3. Decision # 2119/98/EC of the European Parliament and of the Council of 24 September 1998 setting up a network for the epidemiological surveillance and control of communicable diseases in the Community. Off J Eur Commun 3.10.98, L 268/1
4. Detels R, McEwen J, Beaglehole R, Tanaka H (2004) Oxford textbook of public health. Oxford University Press, Oxford, pp 529–581

5. International Health Regulation (2005) II, WHO, Geneva, 2008. http://whqlibdoc.who.int/publications/2008/9789241580410_eng.pdf
6. Ministry of Health ordernr. 385 from 12.10.2007 'on approving case definition for surveillance and reporting system of communicable diseases in the Republic of Moldova', Chisinau, 38 p
7. O'Carroll PW, Yasnoff WA, Ward ME et al (2003) Public health informatics and information systems. Springer Science – Business Media, Inc, New York
8. Perkins D, Gheorghita S (2011) After-action report trilateral (US-Romania-Moldova) civilian-military forum and tabletop exercise on outbreak response and bioterrorism investigation, createSpace
9. Reingold AL (1998) 'Outbreak Investigations – a perspective', Emerg Infect Dis 4(1):21–27
10. WHO guidance for the use of annex 2 of the International Health Regulation (2005) – decision instrument for the assessment/notification of events that may constitute a public health emergency of international concern – 2010. http://www.who.int/ihr/annex_2_guidance/en/index.html

Chapter 7
Advanced Sciences Convergence to Analyze Impact of Nanomaterials on Environment, Health and Safety

Jack E. Smith and Ashok Vaseashta

Abstract We present Advanced Sciences Convergence (ASC) to develop a risk assessment methodology of nanomaterials towards environmental health and safety from an applications perspective. This enables nanomaterials to be examined more effectively because applications depend on risk assessments by potential users who are likely to display a range of risk thresholds. Results of certain tools, such as TechFARM™, ADAMS™, and NESTS™ are discussed in the context of societal benefits that nanotechnology may offer. Strategic decision-making requires a knowledge base, analytical capability, foresight, risk-assessment, and optimization. The methodology and results presented here will assist strategic policy implications of the use of nanomaterials and their environment, health, and safety (EHS) implications. The basic premise of the methodology is to provide a vision into the future by scientific and cross-validated models that can address the contingent nature of many of these applications, and thereby help us prepare for and so help to mitigate whatever risks or be more ready to act on opportunities that may arise.

Keywords Science convergence • Risk-assessment • Nanomaterials • Foresight

7.1 Introduction

Advanced Sciences Convergence is one of the methods that unify the divergent methods and several overlapping fields in science and technology (S&T) employed for Technology Futures Analysis (TFA) and techniques of futures studies.

J.E. Smith
Telfer School of Management, University of Ottawa, Ottawa, Canada

A. Vaseashta (✉)
Norwich University Applied Research Institutes, Herndon, VA, USA

VTT/AVC U.S. Department of State, Washington, DC, USA
e-mail: prof.vaseashta@ieee.org

A. Vaseashta and S. Khudaverdyan (eds.), *Advanced Sensors for Safety and Security*,
NATO Science for Peace and Security Series B: Physics and Biophysics,
DOI 10.1007/978-94-007-7003-4_7,

The process of ASC is to understand how advances in different disciplines and focusing on discrete problems and applications can coalesce to solve a seemingly obdurate problem. The synergy arising from the convergence of nanotechnology, biotechnology, information processing and cognitive sciences (NBIC) and other fields offers great potential for transformational and revolutionary opportunities with many applications. Within these interacting systems, or resulting convergent applications, it may be difficult or just not practical or useful to even try to discern the role or precise contribution played by any one element of the convergent system. More importantly, the applications provide new capabilities to understand natural world, human society & scientific research as closely coupled, complex & hierarchal systems.

Recent advances in both sciences and technologies have provided the means to study, understand, control, and articulate and precisely control transitional characteristics between isolated atoms and molecules and bulk materials. Materials exhibiting desired characteristics and devices and systems designed with specific and targeted applications have been fabricated. Notwithstanding realization of such advances, a key issue concerning nanotechnology is how to best protect human health, safety, and the environment as nanoscale materials and products are researched, produced, manufactured, used, and discarded. As the natural sciences have evolved into a wider variety of specialties, with biology for example, including biophysics and synthetic biology, plus many other subspecialties, and new capabilities are emerging in materials with reduced dimensions through the addition of new and powerful linkages.

While the rapidly emerging field of nanotechnology offers significant economic and societal benefits, there are some indications by way of research about the potential and perceived adverse EHS implications. In addition many of these impacts are still more prospective than actual insofar as they are only beginning to be developed and yet in the spirit of preparedness and health and safety, it is both timely and essential that we use techniques such as foresight to anticipate, analyze and understand how convergent systems may affect us and any risks and uncertainties they may carry with them. It is thus critical to evaluate potential detrimental effects of nanoscale materials and devices – both real and perceived – to enable an effective cost-benefit analysis.

Using nexus of technologies and ASC, the systemic properties of these adjoining and intersecting scientific approaches are enabling new insights and new ways of analyzing prospective societal impacts of the products of these same forces such as nano-materials and nano devices, as shown conceptually in Fig. 7.1. Conjoining the nexus of technologies and ASC that enables creation of this system-of-systems approach, we employ the same set of tools to develop a risk assessment methodology of nanomaterials with applications in EHS. This is important because ASC addresses the “nano” challenge from an applications perspective (prospective and currently available) which enables nanomaterials to be examined more effectively because applications are more grounded in real risk judgments by potential users who are likely to display a range of risk thresholds. A successful introduction of nanomaterials in product development is based on exhaustive, evolving, and

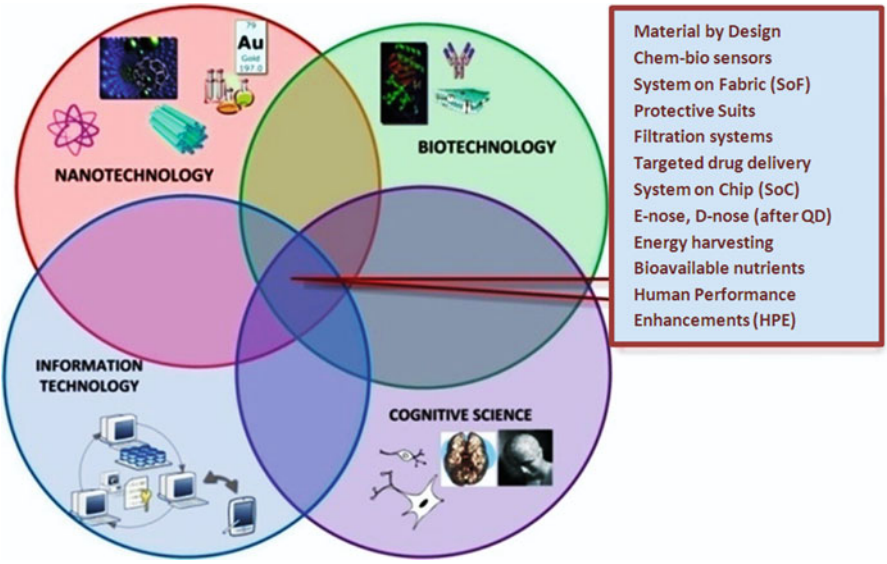

Fig. 7.1 A conceptual framework displaying Convergence of Nanotechnology Biotechnology Cognitive Sciences & Information Technology [1]

innovative approaches of objective risk assessment. The study includes incidental as well as engineered nanomaterials, to ensure an inclusive database for investigation. Study further includes fate and transport and ontological modality of nanomaterials.

The study is intended to be used by strategic decision-makers on policies relating to EHS. Foresight in S&T involves examining the properties and capabilities of derived knowledge and asking three basic kinds of questions:

- *What if*....these capabilities are able to develop-produce effects, viz. x or y; or $x + y = z$;... *then what?*
- *How might these capabilities evolve from here forward,* within a systemic context of developments in related sciences, such as: ecology, neuro-science, systems biology, or nano-scale molecular manipulation and advanced informatics?
- *How wide or narrow and how far out in time should our kaleidoscope of socio-economic and policy perspectives be framed?* -given systemic forces and our (or our clients and stakeholders) need for reasonably confident – but still contingent -anticipatory knowledge of prospective applications that would affect policy or economic actions.

7.2 Exploring ASC as Foresight Tool

Some of the most familiar tools to explore foresight include environmental scanning, scenario planning, technology mapping, road-mapping, expert technical panels, robust factor analysis, strategies development, web virtual conferences, computerized

modeling, and dynamic simulation. To explore this realm, a methodology termed "Technology Foresight, Assessment, and Road-Mapping" (TechFARM™) [1, 2] – a multi-dimensional futures-oriented modality that identifies and manages emerging and/or disruptive science and technology trends is articulated in context of interaction of nanomaterials with human, toxicity, and fate and transport of nanomaterials in environment.

ASC essentially originated in the 1980s with the developments of advanced-networked computation methodology that was enabled largely by personal computers and nanotechnology "discovery" and have accelerated since 2000 with advances in systems and synthetic biology made possible by speed and capacity growth in computation. The examples below illustrate how these three intersecting domains are revolutionizing science through the new capabilities they can deliver individually and collectively.

Example 1: Trends in Nanotechnology – Smart materials with integration of functions and structure in membranes;, self-powered and healing fabrics and fibers; biomimetic materials; contamination specific water filtration and purification [3] – biocides, pathogens, and pharmaceutical remediation/decontamination; sensor networks with tracking capacities; NEMS – nano-electro-mechanical systems (NEMS);wearable personalized flexible sensors with data/communications capabilities; energy and power harvesting capabilities; battery power management; smart dust capability for wide area surveillance; functional, programmable, and targeted structures for controlled drug delivery, performance prostheses; climate responsive building materials.

Example 2: Trends in Biotechnology – Control/improvements in organisms; sensing at the micro/nano level, integration with wireless/RFID/nano-photonics; tissue engineering, artificial organs, implants and prostheses; targeted drug delivery; *in-vitro* diagnostics capabilities, regenerative medicine; medical diagnosis and forensics; personalized medicine using large data sets of patient information, disease statistics, gene sequences and genotypes; genetically modified insects to counter pathogen carriers; *in-silico* testing&comprehensive modeling for drug characteristics, side effects and receptor simulation; lab on chip (LOC) and system on fibers (SoF).

Example 3: Trends in Information Technology – Progress toward ubiquitous access and embededness; Open source collaborative tools and deeper peer- to peer functionality; pervasive social networks; migration towards functional convergence; claytronics for distributed fabrication; object based nodes and networks for smart and ubiquitous connectivity; pervasive sensor networks with dynamic simulation and modeling; gaming for personal and organizational decisions, risk abatement and learning; emerging horizons for faster, exponentially more powerful encryption, quantum information; sustained information growth for surveillance, sensor networks, and tracking capacities.

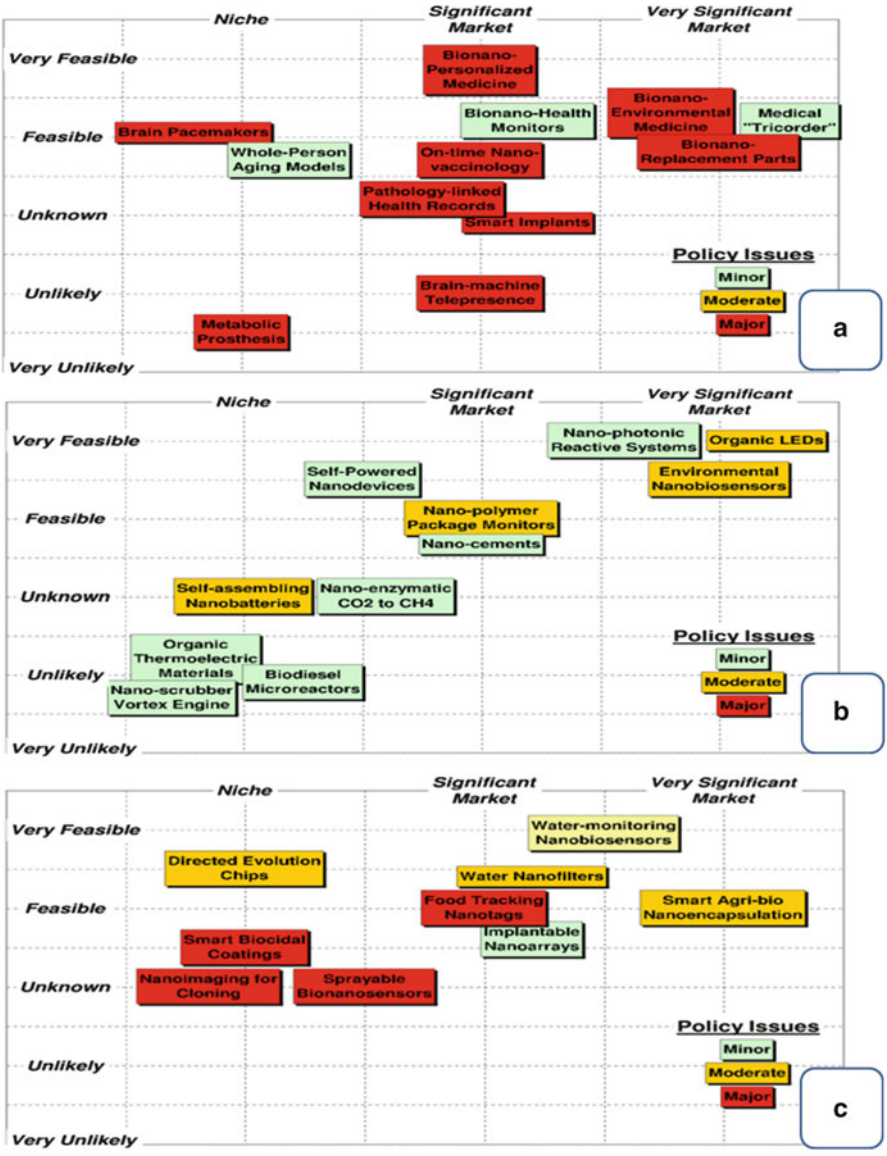

Fig. 7.2 Domain intersection matrix approach for (**a**) health and life sciences, (**b**) energy and environment, (**c**) water, food, and bio-fuels

To examine some of these intersecting capabilities and trends further in terms of domains of application, technologies that could or would be created to identify potentially transformative applications, we developed a series of matrix analytical tables to portray this process and its initial results. Figure 7.2a–c demonstrate domains and technologies can evolve using such intersections.

Adapted from the Rand Corporation, these matrix tables rely upon experts to evaluate prospective applications on the basis of three attributes – market appeal and commercial potential; technical readiness and feasibility; and the perceived degree of complexity-barriers in terms of how the applications may be publically received, impact or stir up (or not) strong public policy concerns, issues and debates. This complexity can be tied into foresight of any desired technology or innovation outcome, in this case, the application being the EHS aspects of nanomaterials.

With the addition of cognitive sciences, the convergence is then critical towards understanding the human mind that imagines-designs-creates-evaluates-decides, and eventually approves or executes actions. Emergence of incorporation of cognitive is demonstrated in autonomous and self-learning designs and we await full implementation of these new capabilities– at least for a few more years until the arrival of – what is termed as the Singularity- that would likely transform this aspect of convergence enormously.

7.2.1 Challenges and Complexities

In a foresight context, as these new capabilities begin to be more rigorously investigated, described, and examined, it undoubtedly requires a comprehensive paradigm and new integrated modalities capable of advanced simulations for the future analysis. An initial need will be for a more iconoclastic and futuristic scanning coupled with – what if – questions, termedhere as "provocative scanning".

A second applicable technique is the Protean or Proteus project approach – a series of intelligence insights, lenses or perspectives that have emerged from many focus groups of US intelligence professionals and military strategists. The Proteus approach offers an elaborative description of the uncertainties and the resulting implications and environments that are being shaped by the emerging new challenges and realities. Proteus is a set of foresight tools and insights premised upon asymmetries of action, intent and impacts, aimed at exploring unforeseen implications and consequences of actions undertaken under conditions of threat, surprise, disruption and disorder.

This dynamic and algorithmic set of tools relies upon real-time human group simulation wherein complexity is built into the fabric and structure through ten key insights which have been codified into the Proteus Critical Thinking Game [4, 5] as 'forces' that are available to participants. It is a foresight game in which there are no clear winners – just choices, actions and consequences as revealed by the game record and evident and/or steal the strategies that can be analyzed in after-action reviews for insights into the complexity of the serious behavior and game play exhibited.

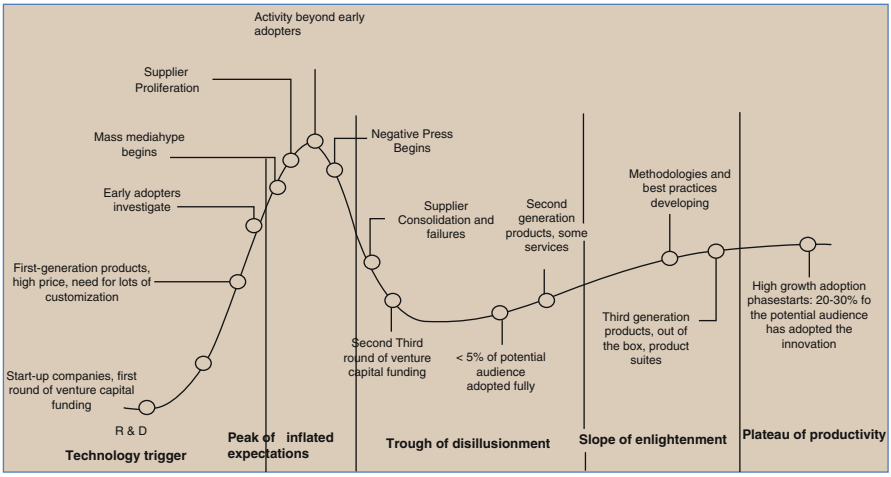

Fig. 7.3 S-curve of macro-economic context

7.2.2 Characterizing Innovations Involving Convergence

There are many ways to evaluate how well positioned a particular technology or application may be for public acceptance and/or commercial success i.e. to be regarded as an innovation. And while most innovations can be described as incremental, many, especially those derived from advanced S&T sources like our convergence methodology [1], could be characterized as disruptive, radical or potentially transformative. By distinguishing what type of market situation an application-innovation is aimed at changing, we developed "Technology Assessment Matrices (TAM)" for specific sectors. Another set of characterization criteria can be employed to focus on Technology Gaps and by using TAM 9 [6, 7], at least a rudimentary comparative insight into which ones might be the most accessible and practical from a strategic choice perspective, or where further analyses might be focused. Finally – it is also important not to forget that all technologies are not only positioned in time but also against other technologies in cycles of S-curve development which in turn can be subjected to hype, maturity and macro-economic context, as demonstrated in Fig. 7.3 below.

7.3 Challenge – Nanomaterials and EHS Related Issues

We use the foresight methodology described above in the context of nanomaterials and its possible impact on environment, health and safety, after a brief synopsis of the issue.

Reduced dimensional aspect attributes that provide novel characteristics are also believed to be responsible for bioadverse response pathways for toxicity of nanomaterials. Consequently, nanoparticle toxicity is studied in context of its ability to induce tissue damage through the generation of oxygen radicals, electron–hole pairs, and oxidant stress by abiotic and cellular responses resulting in pro-inflammatory, mitochondrial injury and pro-apoptotic cellular effects in the lung, cardiovascular system and brain [4]. It is further believed that nanoparticles absorb cellular proteins which could induce protein folding and thiol cross-linking; leading to neuro-toxicity and reduced enzymatic activity.

Nanoparticles which are cationic in nature are also believed to induce toxicity via acidifying endosomes that lead to cellular toxicity and apoptosis in epithelial lung through endosomal rupture through proton sponge mechanism (PSM), mitochondrial targeting, and cytosolic deposition. Nanomaterials composed of redox-active elements are particularly reactive and can possibly provoke potentially damaging chemical transformations. Furthermore, even chemically benign nanoparticles may become activated by light absorption. It is thus essential to investigate the long-term consequences of NPs upon crossing blood–brain-barrier (BBB) and its distribution in cortex and hippocampus over time to ensure their safety using a set of tools termed as Nanopathology, such as x-ray fluorescence microscopy (XFM) for distribution, magnetic resonance imaging (MRI) to measure metal concentrations in cerebrospinal fluid, etc. One approach to determining the safe application of nanomaterials in biology is to obtain a deep mechanistic understanding of the interactions between nanomaterials and living systems (bio-nano-interactions).

7.4 Recommendation, Conclusions, and Path Forward

As described earlier that S&T Foresight involves systematic attempts to look into the longer-term future of S&T and their potential impacts on society, with a view to identifying the emerging change factors, and the source areas of scientific research and technological development likely to influence change and yield the greatest economic, environmental and social benefits during the next 10–25 years. The approach we are taking relies upon consulting a wide range of expertise, with the expectation that through our collective experience, imaginative abilities and interactive knowledge of technological development pathways, we can begin to construct a coherent view of some of the major developments that can be anticipated within a 10–25 time horizon. Foresight is therefore research that can inform planning, policy and strategic choice amidst uncertainty. By employing the ASC approach, inconjunction with TAM and Protean approaches, the following recommendations are provided.

1. It is critical to evaluate the exposure pathways of engineered, incidental, and nanomaterials produced in nature.

2. Study of fate and transport of nanomaterials via a matrix of parameters such as exposure routes, chemical composition, distribution, metabolism, and agglomeration and excretion rate provide a comprehensive overview of interaction pathways.
3. An ontological modality to identify its relationship to other items in the lexicon; viz. to enable information retrieval from various sources, databases, and via expert elicitation.
4. Studying other contributing factors that range from biodegradation and bioaccumulation, thermodynamic properties, interfaces, and free energy of nanoparticles as a function of particle size, composition, and phase and crystallinity influence particle dissolution in a biological environment. The accumulation, dispersion, and functional surface groups play an important role in cytotoxicity and in evaluating pathways of cellular uptake, subcellular localization, and targeting of subcellular organelles.

A fundamental understanding of a nanomaterial-surrounding medium is vital to sustaining technological advances of nanoscale materials as catalyst for new scientific and technological avenues. Use of ASC and foresight methods described will assist researchers, policy-makers, and end-users in responsible use, discard, and recycle of nanomaterials based products.

References

1. Vaseashta A (2012) The potential utility of advanced sciences convergence. In: Giordano J (ed) Advances in neurotechnology – ethical, legal, and social issues. CRC Press, Boca Raton, pp 15–36. ISBN 978-1-4398-2586-0
2. TechFARM™: NUARI Trademark: TECHFARM, SERIAL #: 85287943, Commissioner for Trademarks
3. Vaseashta A, Braman E, Susmann P, Dekhtyar Y, Perovicha K (2012) Sensors for water safety and security. Surf Eng Appl Electrochem 48:478–486
4. Cote MC, Miller RE (2012) Stimulating innovation: is Canada pursuing the right policies? Available at SSRN: http://ssrn.com/abstract=2057923 or http://dx.doi.org/10.2139/ssrn.2057923. 1 May 2012
5. Smith JE (2008) S&T foresight: a tool for prospecting the security and prosperity implications of convergent technologies 2010–2025. In: IT revolutions, 2008 first conference, Venice, Italy, pp 17–19. 10.4108/ICST.ITREVOLUTIONS2008.5122
6. ADAMS™: NUARI Trademark: ADAMS, SERIAL #: 85287846, Commissioner for Trademarks
7. NESTTS™: NUARI Trademark: NESTTS, SERIAL #: 85287940, Commissioner for Trademarks

Chapter 8
Conversion Disorders in Patients with Discogenic Radiculopathy

Svetlana Sidorenko, Ludmilla Sidorenko, Ion Moldovanu, Irina Sidorenko, and Ashok Vaseashta

Abstract Conversion disorder is one of the most mysterious diseases since it was first described as "hysteria" centuries ago. The term "conversion" comes from the observation that psychological distress is being converted into a physical symptom, such as loss of muscle control, blindness, deafness, seizures or even apparent unconsciousness (Schönfeldt-Lecuona C, Connemann BJ, Höse A, Spitzer M, Walter H, Der Nervenarzt 75:619–627, 2004). For soldiers in combat theater, operating in a stressful environment due to asymmetric warfare is a routine requirement. Staying alert is critical to situational awareness and readiness. The objective of this investigation is to identify and find solution pathways for conversion disorders in patients, so as to enhance combat alertness. The preliminary data presented here is consistent with some of the initial investigations by other physicians, viz. Sydenham, Charcot, Breuer, Shapiro, Freud and many others (Semke VY, Sketches about hysteria. Publishing House of Tomsk University, Tomsk, 2008). Much work remains to be done to resolve hysteria's enigma and conversion disorders, which still remain a mystery in approximately 16 % patients, notwithstanding many medical and technological advances. A brief discussion of regenerative nanotechnology

S. Sidorenko (✉) • L. Sidorenko
Department of Neurology, Universitatea De Stat De Medicina Si Farmacie "Nicolae Testemitanu", bd. Stefan cel Mare si Sfant 165, MD-2004 Chisinau, Republic of Moldova
e-mail: svetlana.sidorenko@yahoo.com; anatoli.sidorenko@kit.edu

I. Moldovanu
Department of Neurology, Institute of Neurology and Neurosurgery, Str. Korolenco 2, MD-2028 Chisinau, Republic of Moldova

I. Sidorenko
Medical Center "Gesundheit", Str Kogalniceanu 45/2, MD-2009 Chisinau, Republic of Moldova

A. Vaseashta
Norwich University Applied Research Institutes, Herndon, VA, USA

VTT/AVC U.S. Department of State, Washington, DC, USA
e-mail: prof.vaseashta@ieee.org

A. Vaseashta and S. Khudaverdyan (eds.), *Advanced Sensors for Safety and Security*, NATO Science for Peace and Security Series B: Physics and Biophysics,
DOI 10.1007/978-94-007-7003-4_8, © Springer Science+Business Media Dordrecht 2013

based platforms to enhance brain-machine interface is introduced. This investigation is intended to enhance awareness of the subject matter in PTSD and mTBI patients, as well.

Keywords Conversion disorder • Discogenic radiculopathy • mTBI • PTSD

8.1 Introduction

Conversion disorder (DSM-IV 300.11) is a condition in which psychological stress is manifested in physical ways. The phenomenon is the "transformation" of internal unsolved psychological conflict in a seeming "somatic disease" involving the motor and sensory system, causing involuntary display of physical symptoms, such as twitching, blindness, deafness, loss of muscle control, seizures or even apparent unconsciousness. The indications of characteristic for organic illness are present, but neuro-visual investigations of such patients do not confirm the presence of organic changes [1]. Recent investigations with Positron Emission Tomography (PET), Single Photon Emission Computerized Tomography (SPECT) and functional Magnetic Resonance Imaging (fMRI) show functional changes in organism [2–5]. It is for this reason; conversion disorders are also called "somatoform" or "functional diseases". Irreconcilable conflicts, chronic stress and traumatic psychological impact on the patient is a trigger, and the subconscious "gain" from the presence of the disease interfere patient's healing, representing an innate coping mechanism [1, 6]. The "gain" may not be particularly evident to an outside observer. Patient generally converts a psychological conflict or problem into his/her inability to move specific parts of his/her body or to "use senses" in a normal manner. Hence, patients unconsciously displace their unsolved internal conflict "out" as the organism tries to solve it by somatoform symbolic manifestation. The physical symptoms are not under the patient's conscious control, hence it is neither purposeful intention nor to complicate the diagnostic process. Somatoform disorders are generally "expensive" proposition for the health care system, overusing medical services and resources. Currently, patients with somatoform disorders, according to World health Organization (WHO), consume up to 20 % of all expenses spent on health care.

Manifesting in dramatic body reactions and appearing in various strata of society and profession, conversion disorders causes significant problems, limiting the everyday life, routine job functions and significantly add to patient's mental and physical suffering. They may begin at any age, with a peak of incidence from 25 to 30 years and then after 40–55 years, and it does not appear to be hereditary. The prevalence in general population is estimated between 11/100 K and 330/100 K (DSM-IV-Literature), with significant regional difference, but the disorder is more likely to occur among less educated or sophisticated sectors of society [7]. Conversion disorder is not usually persistent over years or develops as a chronic disturbance. The majority of patients recover within less than a month, at the peak of distress, seldom with recurrences, but in some cases it last over several

years. The female-to-male ratio is between 2:1 and 5:1 [7, 8]. Female patients are predisposed, because of the frequent emotional liability and inadequate coping-strategies. Male patients are likely to develop conversion disorders in occupational settings or stressful situations such as military service.

A frequent phenomenon is the "combat neurosis" that was observed in soldiers and prisoners of war during the World War I (1914–1918) and World War II (1939–1945), then again in Afghanistan, and Iraq. A common symptom of extended rotation in military conflict is the state of being "shell-shocked" for soldiers, which is identical to the "hysterical" behavior. For soldiers, combat readiness is crucial in war theatre. Operating in stressful environment is routine and any lapse in split-second judgment due to stress can cost their lives or of fellow soldiers. Disorders related to post traumatic stress disorder (PTSD) and mild traumatic brain injury (mTBI) is a post combat theatre symptom and may likely interferes with full performance, if a soldier is rotated into the combat fields without significant treatment. However, with conversion disorder, such symptoms are previously unknown and hence it is critical to understand and diagnose before deployment.

8.2 DSM-IV Criteria for Conversion Disorder [9]

Criteria for conversion are listed as follows:

- One or more symptoms or deficits are present that affect voluntary motor or sensory function suggestive of a neurologic or other general medical condition.
- Psychological factors that could be associated with the symptom or deficit because conflicts or other stressors precede the initiation or exacerbation of the symptom or deficit.
- The symptom or deficit is not intentionally produced or feigned.
- The symptom or deficit, after appropriate investigation, cannot be explained fully by a general medical condition, the direct effects of a substance, or as a culturally sanctioned behavior or experience.
- The symptom or deficit causes clinically significant distress or impairment in social, occupational, or other important areas of functioning or warrants medical evaluation.
- The symptom or deficit is not limited to pain or sexual dysfunction, and also does not occur exclusively during the course of somatization disorder. Further, it is not accounted for by other mental disorder.

The most frequent symptoms of conversion disorders affecting the sensory system are the following symptoms or deficits:

- Impaired vision (hysterical blindness),
- Double vision,
- Impaired hearing (deafness),
- Loss or disturbance of touch or pain sensation.

The following symptoms or deficits are among the most common affecting the motor system:

- Impaired coordination or balance
- Weakness/paralysis of a limb or the entire body (hysterical paralysis or motor conversion disorders)
- Impairment or loss of speech (hysterical aphonia)
- Difficulty swallowing or a sensation of a lump in the throat
- Urinary retention
- Psychogenic non-epileptic seizures or convulsions
- Fixed dystonia unlike normal dystonia
- Tremor, myoclonus or other movement disorders
- Gait problems (Astasia-abasia)
- Syncope (fainting)

With the exclusion of feigning, the condition for diagnosis for conversion disorders is the presence of certain physical symptoms that cannot be fully explained by a medical condition, such as substance abuse and mental disorders. The most difficult diagnostic situation seems to appear when conversion disorders are accompanied by organic diseases and painful states [7]. To explain the mechanism of conversion in patients with pain, the following scheme is suggested. Permanent pain leads to constant suffering, which reduces the quality of life. Patients cannot realize themselves in their daily lives, so that the pain grows over into an internal conflict, which may seem to be unsolvable. Additionally external stress-factors translate a physical condition into psychological. If there seems to be no possible solution, the problem gets "converted" in somatoform disorder. Impossibility of return to normal life causes fear and it leads to a feeling of being trapped in a vicious circle. It was shown in a representative study [10], that back pain is one of the primary reasons for exaggerate somatoform reactions, and as a result patients with discogenic radiculopathy were chosen for this study.

The objective of the abovementioned study was to identify conversion phenomena in patients with discogenic radiculopathy (DRP) by;

- Conducting clinical trials to identify psychogenic factor in the development of conversion in patients with DRP.
- Application of questionnaires to identify somatoform disorders in patients with DRP.
- Consider the possibility of clinical application of techniques employing the objectives of study of somatoform disorders in patients with organic pathology.

In clinical trials, two main groups of patients (32 persons) and one control group of healthy individuals (8 persons) in the age range of 25–65 were selected. The study group consisted of patients diagnosed with discogenic radiculopathy with moderate/severe pain syndrome, as confirmed by computer tomography (CT) and magnetic resonance imaging (MRI). After initial screening and primary investigation, three groups, structured as follows were formed:

Table 8.1 The average data of these questionnaires of the three studied groups

	Screener SFD WHO	Scale for somatoform reactions	SCL 90 – SOM	Quantity of patients
DRP with somatoform disorders	4.39 ± 0.41	46.65 ± 1.27	2.71 ± 0.73	23
DRP without somatoform disorders	1.63 ± 0.38	13.5 ± 1.21	1.44 ± 0.78	10
Control	0.5 ± 0.59	7.5 ± 0.93	0.39 ± 0.33	8

- Group 1: DRP with somatoform disorders (23).
- Group 2: DRP without somatoform disorders (10).
- Group 3: control group with healthy individuals.

For the initial screening, the patients were tested using Screener for Somatoform Disorders (SSD) [11], on which results were divided primary the clinical groups. Additionally, Somatoform Reaction scale S and the Symptomatic Checklist SCL-90 were used.

To determinate conversion phenomenon in patients with "pain paresis", caused by discogenic radiculopathy was tested using the Hoover test – the most common test for the differentiation of organic paresis from psychogenic weakness [12, 13]. The Hoover test is performed during the straight leg test: As the patient tries to lift the leg, he or she will put pressure on the heel of the opposite foot (lack of pressure is suggestive that the attempt to raise the leg was not genuine). The sign relies on the principle of synergistic contraction. Involuntary extension of the "paralyzed" leg occurs when flexing the contra-lateral leg against resistance. It has been neglected, although it is a useful clinical test. Essentially, you hold your hand under the "weak" limb and ask the patient to flex the contra-lateral hip against resistance. If you feel pressure from the weak leg, the weakness is likely non organic. This is a positive outcome of the Hoover's sign. If no pressure is felt, this is more likely organic limb weakness.

- Group 1: Patients with DRP and (somatoform disorders) SFD. Average for this group was – 4.39 of the minimum 3.
- Group 2: DRP without SFD. Average for this group was – 1.63. – Indicated in the questionnaire 2 or fewer symptoms.
- Group 3: Consisted of healthy persons also tested for control. Average for this group was – 0.5.

Based on results of the SSD, persons were divided into three groups. The criteria of selection was that persons have three or more symptoms for 3 months or more. Scale for Somatoform reactions and SCL 90 additionally confirmed the division into groups with and without somatoform disorders (Fig. 8.1 and Table 8.1).

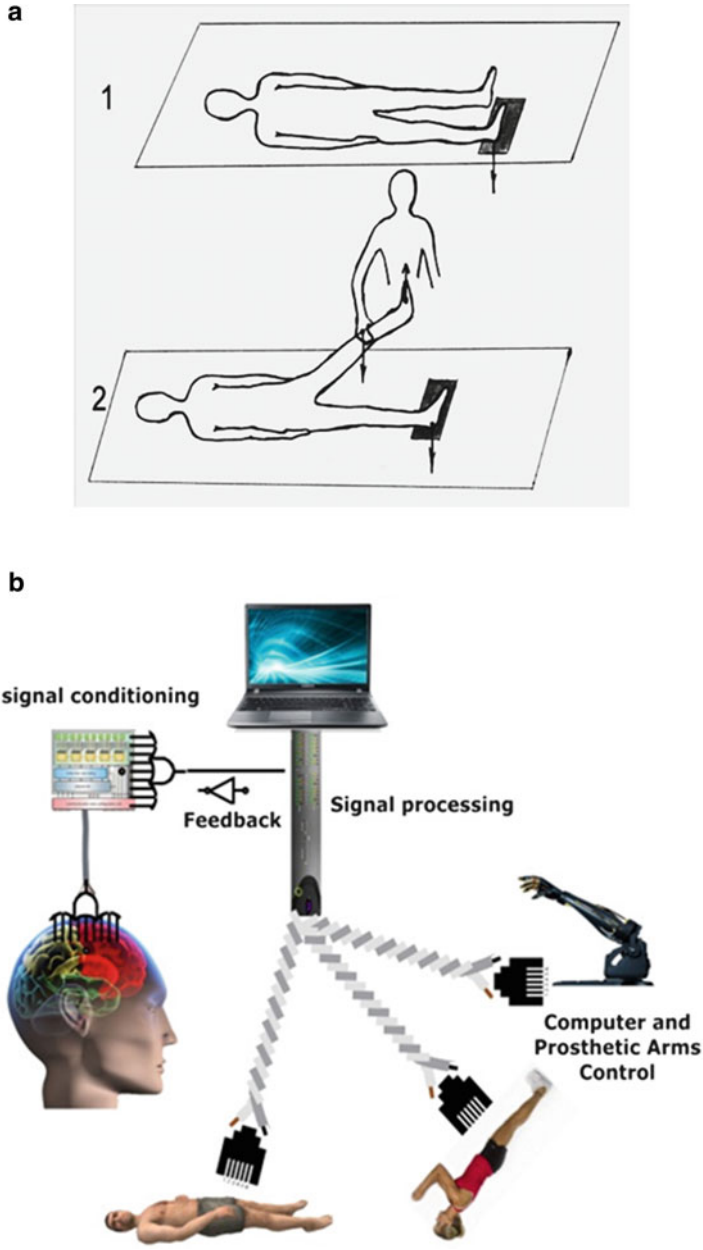

Fig. 8.1 (**a**) Administering Hoover test using an electronic balance to measure the force of pressure from healthy feet and the limb with "pain paresis" to register the difference of force in units, (**b**) brain-machine interface for Hoover test administration

Table 8.2 Results of Hoover test with electronic balance force measure in kg

Limb – h-healthy, p-with pain paresis, rep-repause (weight of limb, without force), f-force fe-females, ma-males	DRP with somatoform disorders 23 (14 fe/9 ma)	DRP without somatoform disorders 10 (6 ma/4 fe)	Control 8 (4 fe/4 ma) healthy
h Rep (kg)	3.92 ± 0.46	3.67 ± 0.52	3.53 ± 0.22
h. f, (kg repause + kg of force)	8.33 ± 1.26	10.51 ± 1.05	14.11 ± 1.23
Applied force (N)	43.25	67.08	103.75
p. rep (kg)	3.21 ± 1.12	3.47 ± 1.03	
p. f (kg repause + kg of force)*1	6.86 ± 1.87	8.66 ± 1.79	–
*1 Applied force (N)	35.79	50.90	
h. f Hoover sign (involuntary force in kg)*2	7.63 ± 0.38	8.97 ± 1.46	12.01 ± 1.12
*2 Applied force (N)	36.38	51.98	83.16
p. f Hoover sign (involuntary force in kg)*3	8.71 ± 1.12	6.74 ± 1.35	–
*3 Applied force (N)	53.94	32.07	
*kg was used for better visualization of obtained results			$p < 0.05$

8.3 Interpretation of Hoovers Test

In group 1 patients with DRP and Somatoform disorders was recorded with a significant difference of the pressure force of "healthy feet" and the leg with "pain paresis." This difference is much smaller in the group – 2. The pressure of the "healthy feet" was less than the corresponding pressure in groups 2 and 3. Pressure force of "bad leg" in group 1, produced by patient gently and was a few units lower than the pressure of patients in group 2.

It is interesting to note that unintentional pressure of the "bad feet" on the balance, measured under the heel, while the resistance force of the examiner, was greater than the force applied in the same conditions, patients in group 2 (group without SFD). Based on the results of Hoover test, it is assumed that the "pain paresis" in patients in Group 1 shows a predominance of psychogenic nature.

8.4 Results, Discussion, and Path Forward

In 10–30 % of patients who consulted neurologists with claims about conversion disorder symptoms, there exists no clear pathophysiological explanation [10] (Table 8.2).

Among the functional symptoms, back pain seems to be the dominant symptom, thus verifying the conversion mechanism with DRP. Organic disorders cause pain and change the patient's behavior resulting in excess use of medical services and resources. Patients with somatoform disorders primarily use maladaptive strategies to overcome stress (inadequate coping strategies) focused at micro-social negative influence. It is necessary to help patients overcome the internal conflict to improve the quality of life. Physicians' should not neglect the importance of alternate technological solutions to find solutions for unresolved conflicts in complex treatment in patients with organic disease.

Nature offers a diverse wealth of responsive and multifunctional surfaces, whose properties are unmatched by current artificial materials. Also, by employing "drop-on-demand" multi-scale biotechnical engineering, three dimensional cell structures of organotypic cell in conjunction with nanomaterials to replenish or replace certain protein compounds are likely to mimic cells the in-vivo environment allowing study of extracellular matrix (ECM), intercellular and cell-to-matrix interactions, and soluble factors and mechanical forces including microfluidic perfusion. Many of these materials display regenerative medicinal characteristics.

Although the scope of such regenerative nano-pharmacogenomics is beyond the scope of this chapter, however many advances in tissue engineering and nanomaterials based therapy finds many applications in finding cure for mTBI and PTSD. Some of these applications are considered for controlling and managing neurotransmitters allowing establishing link between brain-machine interfaces [14].

8.5 Conclusions

The following conclusion can be drawn.

1. Internal picture of the disease in patients with psychogenic background and somatoform disorders show the dominance of organic disease model in minds.
2. Inadequate internal picture of the disease in the SFD promotes chronic illness behavior in various forms, such as "attention-seeking" hysterical behavior.
3. With the help of the testing and questionnaires, the SFD can be identified in patients with organic diseases. The methodology will further improve the effectiveness of treatment strategy which will allow considering the pain of radiculopathy as a syndrome accompanied with somatoform component.
4. The disorder must be looked into as a-priori condition in soldiers' in advance of their deployment in stressful environment.

References

1. Noll-Hussong M, Henningsen P (2009) Zur Neuro-Psychosomatik der Konversion. Schweiz Arch Neurol Psychiatr 160(8):356–361
2. Marshall IC, Halligan PW, Fink GR, Wade DT, Frackowiack RSJ (1997) The functional anatomy of hysterical paralysis. Cognition 64:B1–B8
3. Vuilleumier P, Chicherio C, Assal F, Schwartz S, Slosmen D, Landis T (2001) Functional neuroanatomical correlates of hysterical sensorimotor loss. Brain 124:1077–1090
4. Spence SA, Crimlisk HL, Cope H, Ron MA, Grasby PM (2000) Discrete neurophysiological correlates in prefrontal cortex during hysterical and feigned disorder of movement. Lancet 355:1243–1244
5. Stone J, Zeman A, Simonotto E, Meyer M, Azuma R, Flett S, Sharpe M (2007) FMRI in patients with motor conversion symptoms and controls with simulated weakness. Psychosom Med 69(9), Epub 2007 Nov 8
6. Reuber M, Mitchell AJ, Howlett SJ, Crimlisk HL, Grünewald RA (2005) Functional symptoms in neurology: questions and answers. J Neurol Neurosurg Psychiatry 76:307–314
7. Schönfeldt-Lecuona C, Connemann BJ, Höse A, Spitzer M, Walter H (2004) Konversionsstörungen – Von der Neurobiologie zur Behandlung. Der Nervenarzt 75:619–627
8. Semke VY (2008) Sketches about hysteria. Publishing House of Tomsk University, Tomsk, pp 20–32. ISBN 978-5-7511-1878-5
9. American Psychiatric Association (1994) Diagnostic and statistical manual of mental disorders (DSM-IV). APA, Washington, DC
10. Rief W, Hessel A, Braehler E (2001) Somatization symtomps and hypochondrical features in the general population. Psychosom Med 63:595–602
11. WHO. Screener for somatoform disorders (SSD). Developed for the WHO International Study of somatoform disorders study protocol and instruments by Dr. M. Isaac, Dr. G. Tacchini and Dr. A. Janca. http://whqlibdoc.who.int/hq/1994/MNH_MND_94.1.pdf
12. Stone J, Zeman A, Sharpe M (2002) Functional weakness and sensory disturbance. J Neurol Neurosurg Psychiatry 73:241–245
13. Okun MS, Koehler PJ (2004) Babinski's clinical differentiation of organic paralysis from hysterical paralysis. Arch Neurol 61:778–783
14. Moxon KA, Kalkhoran NM, Markert M, Sambito MA, McKenzie JL, Webster JT (2004) Nanostructured surface modification of ceramic-based microelectrodes to enhance biocompatibility for a direct brain-machine interface. IEEE Trans Biomed Eng 51(6):881–889

Part III
Chemical-Biological Sensors

Chapter 9
Use of Metaloxide, Porous Silicon and Carbon Nanotube Gas Sensors for Safety and Security

Vladimir Aroutiounian

Abstract There is an urgent need to detect explosives, dangerous and toxic gases for general safety of people at home and at work – which may be office, industry, mines, and transport or even battle-field. We investigated different semiconductor gas sensors which were manufactured elsewhere. Most of these gas sensors are made of metal-oxide and do not show appreciable response to gases without pre-heating, which results in increased cost due to power consumption and poor response and recovery of sensors thus complicates their safe use. Therefore main strategy in the manufacture of metal-oxide sensors is to decrease their working temperature and increase in the performance. Results of development of different gas sensors in Yerevan State University (YSU) are reported by using very promising sensors made from porous silicon and carbon nanotubes (CNTs) without pre-heating. The sensors reported here overcome such shortcomings.

Keywords Gas sensor • Hydrogen • Toxic gas • Metal-oxide • Porous silicon • CNTs

9.1 Introduction

Gas, smoke and ion-selective sensors were investigated and developed at YSU. Different gas sensors were made from Bi_2O_3, SnO_2, ZnO, TiO_2, In_2O_3, Ga_2O_3 and Fe_2O_3 thin films and many other ceramic materials [1, 2]. Earlier we realized several gas sensors without pre-heating the sensor (i.e. working near room temperature) and developed their theoretical basis. As for example, in case of sensors made of Bi_2O_3, $NaBiTi_2O_6$, $LaAlO_3$-$CaTiO_3$, Fe_2O_3 and $Bi_2V_4O_{11}$, operating temperature

V. Aroutiounian (✉)
Department of Physics of Semiconductors and Microelectronics, Yerevan State University, 1 Alex Manoukian Str., Yerevan 0025, Republic of Armenia
e-mail: kisahar@ysu.am; aroutiounv1@yahoo.com

A. Vaseashta and S. Khudaverdyan (eds.), *Advanced Sensors for Safety and Security*, NATO Science for Peace and Security Series B: Physics and Biophysics,
DOI 10.1007/978-94-007-7003-4_9,

was 20–70 °C. Sensors working at room temperatures were sensitive to smoke, ethanol and sulphur vapors as well as humidity. Our Bi_2O_3 smoke detectors are competitive with photoelectric (optical) and ionization detectors of smoke, which currently are widely used in fire-alarm systems [3, 4]. Independent testing in the U.S. of our adsorptive type smoke detectors yielded fairly promising results. We also investigated simple and mixed metal oxide photo-electrodes for photo-electrochemical conversion of solar energy [5]. Investigations of metal oxide, porous silicon and CNT sensors were carried out recently and are reported below.

9.2 Metal Oxide Hydrogen Sensors

Hydrogen (H_2) is the lightest of all gases, has relatively wide flammability limits (4–75 vol. % in air) and, at certain concentrations, an extremely low ignition energy. The USA Department of Energy targets H_2 safety with sensor having specification – measurement range 0.1–10 %; operating temperature 30–80 °C; work in ambient air, 10–98 % RH; accuracy 5 % of full scale; lifetime 10 years; and interference resistance to hydrocarbons. The technical requirements and performance targets are specified by sensor users for automotive, fuel cells and stationary applications. At present, commercial H_2 detectors are too bulky, expensive and sometimes dangerous. From the standpoint of the safety with the global environment, it is necessary today to develop new semiconductor H_2 gas sensors working at or near room temperature without pre-heating. In addition, they should be small, cheap and easy to be inserted into microelectronic ICs.

There are many types of H_2 sensors – see, for example, review-papers [6–8]. We will consider below only properties of semiconductor metal oxide H_2 sensors. After invention of the phenomenon of sensitivity of SnO_2 to different gases, many efforts were made, which led to bringing such metal oxide gas sensors into practice. Beside detection of H_2, SnO_2, ZnO, In_2O_3, TiO_2, WO_3, Zr_2O_3 and other oxides are used as active material for other gas sensing. State semiconductor metal oxides sensors generally operate at temperatures well above ambient. The literature shows that the operating temperature of the best gas sensors usually made of SnO_2 lies in the range 250–400 °C, below and above of which the gas response dramatically decreases. We avoided use of high operating temperature due to its operating cost and difficult and expensive large-scale use and production.

We consider below H_2 sensors made from metal oxide semiconductors. The physical and gas-sensing behavior of semiconductor sensors depends directly on their preparation methods and conditions. One of the main objectives for research at YSU is to develop nanoparticles, because decreasing in the particle size raises the effective surface area for gas adsorption. The nanosized particles, porosity of the films, and the large surface/ volume ratio ensure high sensitivity. On the other hand, below a certain critical nano-crystallite size, the sensitivity of the gas sensor increases sharply. This occurs when the nano-crystallite size becomes comparable with the double space-charge layer thickness of the semiconductors

under consideration. Nano-crystalline SnO_2 thin film is a well-known n-type semiconductor gas-sensing material. For such film or powder, the calculated value of the space-charge layer thickness is ≈3 nm.

There are different methods for getting nanoparticles with required sizes. The sol-gel techniques are among these methods; the sol-gel process has many advantages with respect to other processes. These advantages include low processing temperatures and the possibility of chemically tailoring the starting solutions, resulting in new compositions and better control of the final microstructure as well as high specific area of the sensing layer. Our efforts were mainly focused on developing and improving the nanocrystalline SnO_2 processing technique with the goal of developing sensors with very high response and selectivity for H_2 with lower operating temperatures. The results of our R&D work are presented in [9–11]. Na_2SnO_3 was used as precursor for SnO_2 sol preparation. It gives us highly thermally stable mesoporous SnO_2 films. The technology is based on adding phosphoric acid to Na_2SnO_3 aqueous solution until its neutralization. In this case, absolutely transparent and very stable solution is obtained. This is evidence of the small sizes of the nanoparticles contained in the colloidal solution. The solution was purified by means of electro dialysis in a rectangular cell. As a result of a sharp decrease in the electrolyte concentration during purification, most of the SnO_2 precipitated near the anode as a transparent gel. Adding up to 1 % ammonium to purified sol causes the dissolving of the gel. Acquired sol mixed with the same quantity of 2 % polyvinyl alcohol was spin-on coated onto alumina and other substrates over preliminary formed thin film comb-like electrodes. The specimens were dried after which the next layer was deposited. This procedure was repeated several times. After that, different samples were exposed to annealing at various temperatures ranging from 500 to 750 °C. Nanocrystallites sizes did not exceed 10 nm even after the calcinations at 750 °C. The temperature of final annealing was selected higher than the temperatures of previous annealing processes with sol-gel layers as it is known that the re-crystallisation of sputtered or evaporated Pt catalyst layer occurs at 700–750 °C. This leads to formation of Pt nanoclusters covering the sensitive layer which apparently significantly increases the catalytic activity of Pt layer and, hence, to increase gas sensitivity and lowering of sensor operation temperature. As a result, we obtained a homogeneous film without cracks and with satisfactory adhesion to the substrate. Correct selection of electrodes, heater materials, their configurations, and on reliable adhesion to the substrate was realized. Both the inter-digitized contacts and the heater were formed in a single vacuum sputtering process work cycle. To improve the long-term stability and reliability of our thin-film H_2 sensors, taking into account how the sensor parameters drift with time, we conducted subsequent adjustment of the SnO_2 sol-gel processing to improve conditions for electron-beam deposition of the Ti sub-layer, as well as upper layer from Pt to maximize adhesion of Pt and SnO_2 to substrates, and for stable functioning of the sensors [9].

To quickly and reliably measure and test the semiconductor gas sensor performances and parameters in real time, the automated measurement setup was developed (Fig. 9.3 in [11]). We studied the response of sensors to detect the

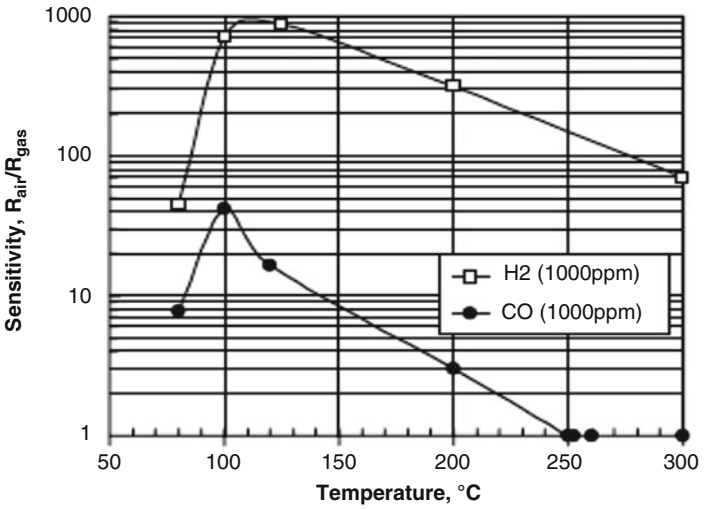

Fig. 9.1 Response to 1,000 ppm – concentration of H_2 or CO versus sensor operation temperature [9]

presence of H_2 in air at various temperatures (25–300 °C). As a result, the maximal response is registered in the 80–130 °C range of operating temperatures; although rather high sensitivity to H_2 gas at RT was observed.

The measurements were carried out at different concentrations of H_2 and carbon monoxide (CO) in air to check selectivity of sensors. The dependence of the gas sensitivity on operating temperature for 1,000 ppm H_2 and CO concentration in air is shown in Fig. 9.1. Response of sensors is determined by the ratio R_{air}/R_{gas}, where R_{air} and R_{gas} are resistance of the sensor measured in clean or synthetic air and in the air/gas mixture, respectively. The comparison of these dependencies shows that H_2 and CO gas sensitivity maxima of the sensor appear close to the operating temperatures (120 and 100 °C, respectively). The CO gas response is much lower and disappears at temperatures higher than 250 °C. At the same time, the response to H_2 remains high (up to two orders of magnitude). This means that the selectivity of the sensors to H_2 is ensured by selection of corresponding operating temperatures. The response time of the sensors functioning at a constant 125 °C operating temperature was also studied. We established that the response time to the H_2 concentration change is ≈ 1 s, while the response time to the CO concentration change reaches several minutes.

We used pulsed heating to minimize the humidity influence on the sensor parameters. The sensor signal should be measured when the sensing film temperature is ≈ 120 °C (the temperature of the best sensitivity). Short heating pulses diminish the humidity influence during the time interval between the heating pulses, since full recovery of the sensor's initial state takes place after each "annealing" pulse. The difference in sensor performance parameters under high humidity conditions (up to

100 % RH) compared with 52 % RH is negligible especially for H_2 concentrations lower than 300–400 ppm. To understand how the catalytic Pt layer influences the parameters of the studied gas sensors, samples without any catalytic layer were made and tested. The result of 5,000 ppm H_2 exposure on the samples at 125 °C is a slow decrease in the sample resistances, about ten times. The parameters' recovery in clear air also occurs slowly. Increasing the operating temperature improves the response time only up to 10 s. Thus, the thin Pt catalytic layer improves both sensitivity and reaction times. The peak sensitivity of the samples was observed at lower *(*∼50 °C*)* temperatures. However, these characteristics are influenced not only by the deposition of a thicker catalytic layer but by also by the substrate material. Doping of the SnO_2 with 1.7 % Si leads to a decrease in the operating temperature. The sensitivity drops as the operating temperature increases, and stabilizes at about 10. So, the operating temperature of developed sensors is low enough (not exceeding 150 °C). The results of our investigation devoted to find ways for stabilization of SnO2 based thin-film H_2 sensors fabrication using sol-gel are presented below.

The measurements of the gas sensitivity to 1,000 ppm H_2 as well as 90 % response and recovery times at different operation temperatures were carried out for both as-prepared and aged sensors. Response and recovering times remarkably increased with decrease in operating temperature. In order to stabilize the sensitivity and time performance of the sol-gel derived thin-film H_2 sensors, we carried out relatively long-term aging of the as-prepared samples in 0.5 % H_2 in air at 150 °C with continuous measurements of the sensor resistance and temperature changes. As-prepared samples of thin-film H_2 sensors were placed in the measurement chamber under standby state conditions in air at operating temperature (150 °C). After initial inlet of 1,000 and 5,000 ppm H_2 in the chamber, relatively low response was observed ($S_{1000} = 5$ and $S_{5000} = 100$). The sensor operation is entailed with significant increase in its substrate temperature despite of the fact that the power consumption of the sensors still remains constant. This fact indicates that catalytic exothermic reaction of H_2 oxidation takes place on the surface. The decrease in temperature takes place concurrently with rise in sensor resistance. It is predicated on the consumption of H_2 in the chamber, as shown by the decrease in the concentration of H_2 in the chamber. After proper air blowing of the chamber, during the next H_2 inlet, this process runs again. This procedure of chamber air purging and allowing H_2 in with the same concentration, was repeated several times. Analyzing the results of this long-term aging and testing, we can conclude that the catalytic combustion rate decreases in time, reaching almost zero after fifth day (sensor response and H_2 concentration in the chamber remains constant). The described process of sensors aging led sensor sensitivity rise up to 2×10^4 to the end of the aging process mainly due to decrease in the R_{gas} value and holds out during further sensors operations. The measurement of response and recovery times immediately after the aging shows that the long-term exposure under H_2-containing atmosphere leads to some slowing of sensor reaction. The similar effect is observed when the sensors were placed in air during a long time. However, this effect disappears after short-term exposure to H_2/air mixture in the operation conditions or short 10 min heating up to 300 °C. Good reliability and reproducibility were obtained

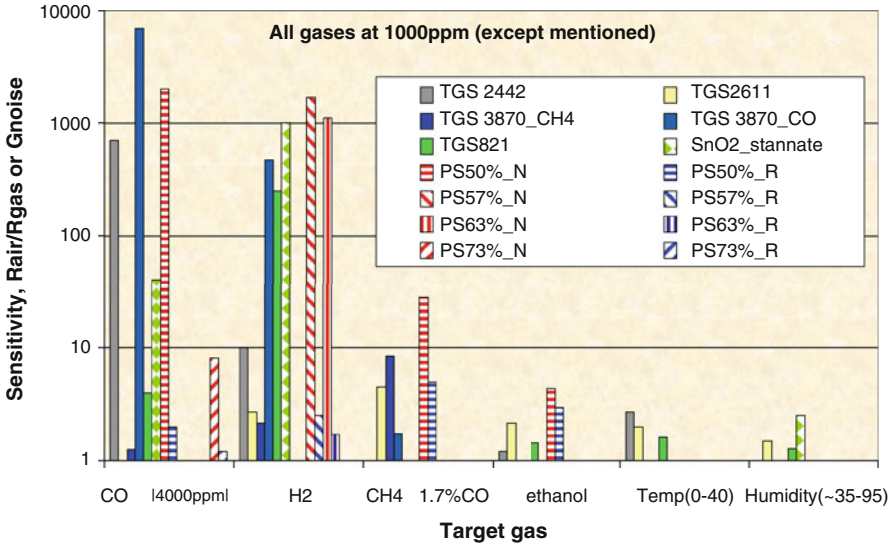

Fig. 9.2 Sensitivity of different sensors to gases

Fig. 9.3 Portable Pen Type H_2 Leak Detector

at different concentrations of H_2. Another SnO2 thin film processing technology reported here is based on the reactive ion-plasma assisted sputtering in the presence of Ar/O2 gas mixture and sol-gel deposition. This leads to an improvement of the sensitive films adhesion with the substrate and thus reliability and long-term stable operation of these gas sensors. Analysis was shown that freshly prepared sputtered films consist partly of metallic Sn and tin suboxides, where the SnO2 thin films were obtained by reactive ion-plasma assisted sputtering. As a result, the superposition of technologies allowed obtaining both double layer structures of SnO2 ensuring good adhesion with the substrate and highly gas sensitive SnO2 one-dimensional nanostructures. The comparison of data for Figaro sensors #TGS 2442, 2611, 3870, and 821 as well as our SnO_2 stannate sol-gel H_2 and porous silicon sensors was carried out in Fig. 9.2 [12]. We realized also the Portable Pen Type H_2 Leak Detector worked in autonomous regime from battery (14 h) from the battery charger (including ones for cell phone) (see Fig. 9.3). Comparison of electrical characteristics of our tin dioxide H_2 sensor and other commercial ones (Table 9.1) shown that our sensors have better characteristics.

Table 9.1 *YSU thin-film H2 sensor; ** (1) and (2) commercial sensors by Synkera Technologies Inc. (Trace H_2 Sensor P/N 701) and Figaro Inc. (TGS 821–H_2 sensor)

Property	Symbol	YSU sensor*	Remarks	(1)**	Remarks	(2)**	Remarks
Heater power consumption	P_H	120 mW	At $V_H = 3.5$ V	~600 mW	At $V_H = 5.4$	660 mW	At $V_H = 5.0$ V
Heater voltage	V_H	3.5 V_{DC}	120 °C	5.4 V_{DC}	T_{sensor} ~240 °C	5.0 ± 0.2 V	AC or DC
Heater resistance	R_H	75 Ω	At room temp.	$32\ \Omega \pm 2\ \Omega$	At room temp.	$38.0 \pm 3.0\ \Omega$	At room temp.
Sensing voltage	V_C	5.0	Recom.	5.0 V_{DC}	Recom.	Max 24 V	DC only
Sensitivity at 1,000 ppm H_2	S (R_S/R_G)	$\sim 10^3$	–	~10	–	$1.6 \cdot 10^2$	–
Response time at 100 ppm	τ_{res}	<7 s	(90 % response)	15 s	(90 % response)	–	–

9.3 Porous Silicon Gas Sensors

Porous silicon (PSi) can be used as an alternative material for gas sensors, operating at relatively lower temperature of pre-heating of sensor element [13]. Usually, PSi is electrochemically formed by anodic dissolution of silicon in a hydrofluoric solution. Passing an electric current between the acid electrolyte and the Si sample produces an array of deep narrow pores. Pores with diameters from nanometers up to micrometers deep have been achieved. PSi exhibits strong visible luminescence at room temperature [14, 15]. This discovery of L. Canham opened possibilities to develop silicon-based optoelectronic device, fabricating Si quantum wires and pillars of crystalline Si only a few nanometers wide [16, 17]. Depending on the electrolysis conditions and the illumination level, a porous texture with pore diameters varying from 2 to 15 nm and a density varying from 20 to 80 % can be realized [18]. Beside luminescence sensors, the following PSi gas sensors are developed: conductivity, capacitance, photovoltaic and other different sensors [13]. Noise PSi gas sensors developed by us are briefly reported below.

The sensitivity of gas sensors is mainly measured by classical method, viz. comparison of the resistance of sensors in gas media and air. Results of the experimental study of low-frequency noise characteristics of sensors were compared with data for different sensors. The sensitivity evaluated from the spectral dependence of noise to gas concentration is higher in comparison with the sensitivity obtained by classical method of the measurements of gas sensing by the change in the Ohmic resistance part of current-voltage characteristics of samples. In [19, 20] the phenomenon of a reduction in the heat of adsorption was taken into account using results of the Langmuir's theory. The noise for oxygen and other type of gases was calculated.

We studied experimentally samples of PSi-layered structures like Au/PSi/SCS/Al with SCS being single crystal silicon [21–24]. The PSi layer was formed by electrochemical etching on a substrate made of heavily doped p^+-type silicon with the orientation (100) and resistivity 0.01 $\Omega \cdot$cm. The samples were $\sim$2 μm thick. The back side of the wafer was coated with a 20–30 nm thick Al film. The top contact of gold sprayed on the surface of PSi had a diameter of 1.5 mm. Conductive glue on the basis of silver "Conductive Epoxy" was used for the top contact. The porosity of PSi films was fixed (50 and 73 %).

Measurements of current-voltage characteristics (CVCs) of above-mentioned structures were carried out at room temperatures in air and in mixtures of air with different concentrations of carbon monoxide. Typical CVC of samples with porosity of 73 % in all environments has a nonlinear behavior. CVC is nonlinear for low back bias, but with an increase in the latter it becomes linear. The behavior of CVC for PSi of 73 % porosity, both in air and in air + 0.4 % CO, has a rectifying character, but, as compared with corresponding characteristics of samples with 50 %-PSi, a sharp decrease in conductivity and absence of current saturation took place. The factor of ideality m was estimated from initial part of the direct branch. The barrier height was determined from the linear part of the reserve branch of CVC.

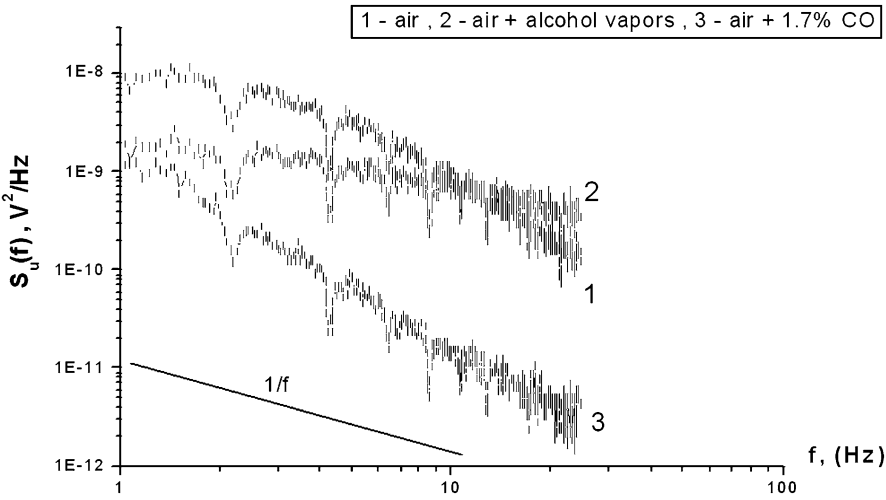

Fig. 9.4 Noise spectra for samples with the 50 %-porosity PSi layers exposed to the indicated gases at a current of 0.1 mA. The straight line refers to "classical" 1/*f* noise. Samples were placed in air (*1*), air + ethyl alcohol vapor (*2*), and air + 1.7 % CO (*3*)

A model where the resistance R_s of the heterojunction interface PSi/Si-single crystal is connected in series with the base resistance of the PSi layer was applied for the study of CVC. The initial part of the direct branch is approximated by the exponential dependence of current J on voltage U with a large factor of ideality m. We obtained that a change in the structure of environment results in the change of CVC both in the direct displacement region and in the region of backward displacement. The current grows essentially in both regions at the same displacement with introduction of CO into air. Reduction of the height of a heterojunction barrier took place because of migration of CO molecules into pores of the heterojunction interface. This is one of the reasons of the high gas response of the heterostructure containing a nanosize porous film. However, the mechanism of the high gas sensitivity of porous structures is not yet completely understood. The performed analysis of experimental data has shown that the gas adsorption of CO molecules led to a decrease in the height of heterojunction barrier. It is accompanied by the reduction of the PSi layer base resistance which is connected in series with the heterojunction. The degree of decrease in the barrier height depends on the amount of CO in air.

Sharp drop, by several orders of magnitude, of S_U (f)/U^2 with the change in concentration of CO in air suggests a possibility to estimate precisely the gas content in air. S_U is the spectral density of the noise voltage. Corresponding noise spectra for PSi layers placed in different gas media are shown in Figs. 9.4 and 9.5. Results of our measurements are shown that we can offer a new method of estimation of the concentration of gases in environment – the noise spectroscopy. So, the value grows with the increase in porosity of silicon and in the concentration of

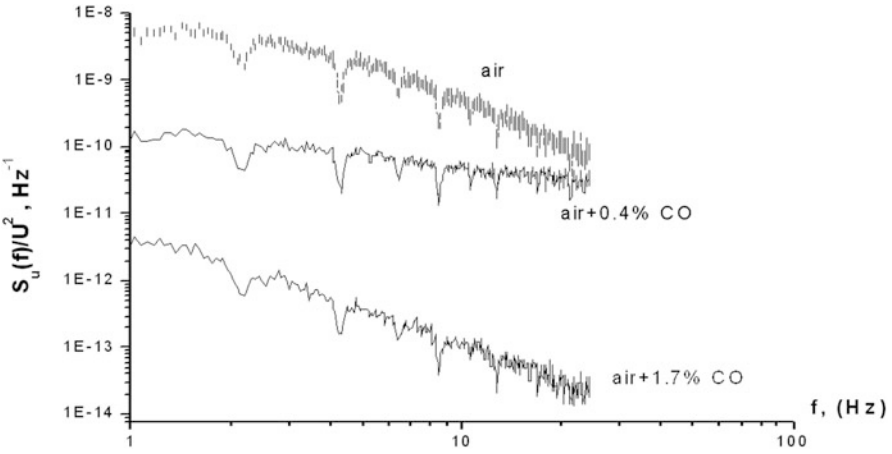

Fig. 9.5 Normalized noise spectra for samples with the 50 % porosity PSi layers exposed to the indicated gases at a current of 0.1 mA. Samples were placed in air, air + 0.4 % CO, and air + 1.7 % CO

polar CO molecules in air. Noise spectra of the structures investigated in various gas media in the low frequency range were different quantitatively and displayed different characteristics. The physics of the noise phenomena in a system containing a gas-semiconductor structure is rather complicated is beyond the scope of this investigation.

The possible reasons of large values of γ for PSi samples in air and their increase in the gas chamber are discussed below. As seen from our measurements, value of the spectral density of the noise voltage is remarkably changed when samples are placed in different gas media and air. Therefore, we decided to compare the gas response of sensors made by using of different technologies. We compared data for Figaro TGS 2443, 2511, 3870, and 821 sensors as well as our sol-gel H_2 and PSi sensors [19, 20]. The response of above-mentioned sensors was measured earlier by classical method, i.e. comparison of the resistance of sensors in gas media and air. Here we report the results of our study of low-frequency noise characteristics of the metal–PSi–silicon single crystal – metal structure with different porosity of PSi. The study was performed in dry air and in a mix of dry air with carbon monoxide, H_2 and alcohol of different concentrations. Calculation of the response of the investigated porous structures was carried out using results obtained during experiment for changes in target gas media and air of resistance $G_{dc} = R_{sa}/R_{tg}$ (in the Ohmic part of CVC) and of the spectral density of noise (SND) due to voltage fluctuations

$$G_{NOISE} = \frac{S(f)_{SA}/{U_{sa}}^2}{S(f)_{tg}/{U_{tg}}^2} \tag{9.1}$$

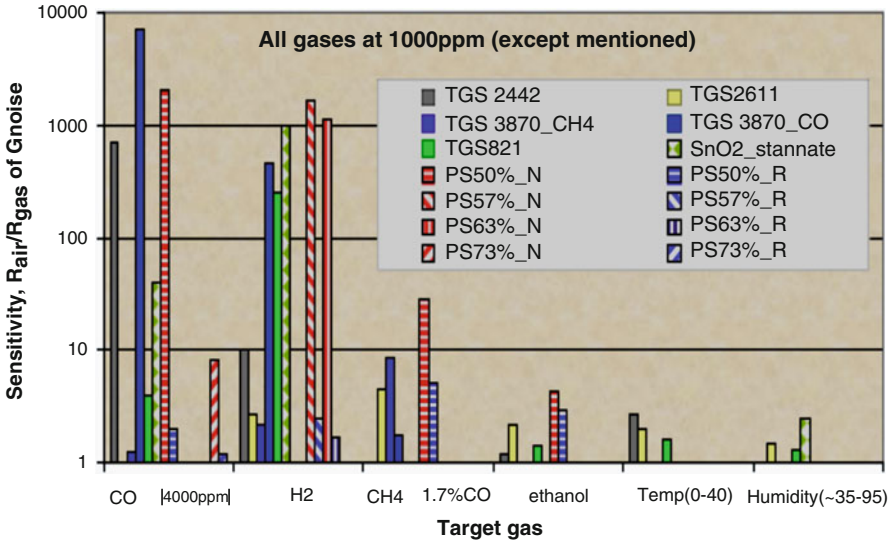

Fig. 9.6 Response of different sensors to gases. We compares data for Figaro sensors TGS 2442, 2611, 3870 and 821 as well as our sol-gel H_2 and porous silicon sensors

Here $R_{I\,is}$ the sensor resistance, $S(f)_{noise}$ is the spectral density of the noise of the sensor. We introduce results of our measurements of the response of the Figaro sensors and our samples made of SnO_2 and PSi (Figs. 9.6 and 9.7) [12, 13]. We observe that the dc resistance response G_{dc}, which is measured by classical method of measurement, gives lesser values in comparison with the SND sensitivity. It allows carrying out fluctuation-enhanced measuring of the response of sensors.

The heterojunction barrier' height at gas adsorption decreases with increase in the adsorbate concentration. Therefore, the effect of a potential barrier, in comparison with increasing concentration of surface traps, becomes less important.

In conclusion, using PSi gas sensors detection of H_2, CO, CO2, Cl_2, Br_2, J_2, O_2, NH_3, H_2S, HCl, halogens, amines, ethanol, butanol, methanol, isopropanol, benzene, toluene, xylene, Freon, ethers, chlorinated carbons, linear aliphatic alcohols, organic vapors and many other gases and vapors is now possible [13].

9.4 Manufacturing and Investigations SnO_2 MWCNTs Gas Sensor

Carbon nanotubes (CNTs) have a large surface-to-volume ratio and special electrical properties, which make them a promising material for the development of new sensors for the detection of different gases [25–28]. Gas i-butane is widely used for domestic purposes, in the cooling plant, and as a fuel, being a part of LPG. Vapors of

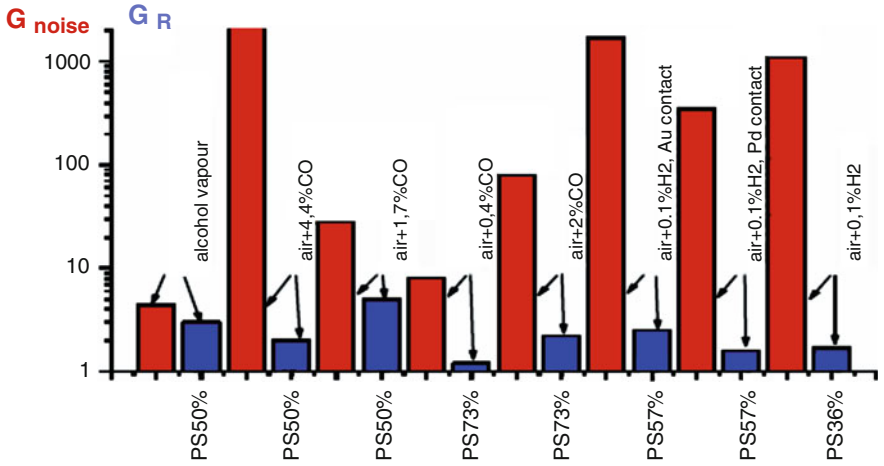

Fig. 9.7 Comparison of the sensitivity of different sensors obtained by measurements by classical resistivity and noise methods

this gas are hazardous to the human health. Note that i-butane cannot be detected by our sensors made of pure SnO_2 and pure CNTs. We investigated that the response and selectivity of sensors can also be improved by developing a nanocomposite consisting of both non-functionalized CNT and inorganic nanoparticles like SnO_2, ZnO or similar metal-oxides.

Multiwall carbon nanotubes (MWCNT) were prepared at EPFL (Switzerland), Szeged University and YSU [29–34]. Millimeter long MWCNT grown by CVD were used to prepare membranes by vacuum filtration from a suspension in isopropanol. We used CNT membrane for the preparation of the nanocomposite SnO_2/MWCNT powder by the sol-gel method. A uniform functionalization was applied to as-grown CNTs in order to improve their dispersion and surface reactivity. MWCNTs were heated in the HNO_3/H_2SO_4 acid mixture then rinsed and dried. Tin chloride pentahydrate ($SnCl_4 \cdot 5H_2O$) powder was subsequently added into the suspension of CNTs, the solution was processed by ultrasound again. SnO_2 precipitated on the CNT surface after the stirring. The 0.5 M $SnCl_4$ solution was added to CNTs. The resulting solution was treated by ultrasound. Diluted solution of NH_4OH was dropped in the solution CNTs to keep a final constant pH of 8.3. After precipitation, the sediment is aged, filtered, and rinsed in distilled water, so that chlorine-ions were removed, and dried at 120°C for several hours. CNTs (0.1 wt %) with functionalized surface have been added to prepare CNT/SnO_2 powder. The mix was grinded and the resulting powder was annealed in the air. The prepared nanocomposite SnO_2/MWCNT powder was divided into three parts after calcinations. Tablets were pressed from one part of the powder. Some tablets were sensitized at the 0.01 and 0.03 M $Ru(OH)Cl_3$ water solution and in the Mg $(NO_3)_2$ solution. Then all the tablets were exposed to the second heat treatment in

the air. Polypropylene powder (2.5–3 wt %) was added as a binder to the second part of nanocrystalline SnO_2/MWCNT powder with the aim of manufacturing samples with sufficient density and consequently for stabilization of sensors parameters. After stirring, this mix was pressed into tablets, which were exposed to second annealing in the air. Further these tablets were sensitized by immersing in the 0.01 and 0.03 M $Ru(OH)Cl_3$ water solution and then exposed to heat treatment in the air. The third part of the nanocomposite powder was used to develop thick films by the spray pyrolysis method. First, two solutions were prepared: the 0.5 g SnO_2/MWCNT powder in 10 ml absolute dimethyl formamide and 0.5 g SnO_2/MWCNT powder + 0.42 % $RuOHCl_3$ in 10 ml absolute dimethyl formamide. Both solutions were processes by ultrasound, and then the spray pyrolysis of these solutions was carried out. Three layers were precipitated consistently on the substrate for preparing of samples. They were exposed to heat treatment in the nitrogen atmosphere. After annealing, the samples were presoaked in the 0.01 M and 0.03 M $Ru(OH)Cl_3$ water solution and exposed to the subsequent heat treatment in the air. Pd catalytic nanoparticles and gold inter-digital ohmic contacts have been manufactured on the surface of tablets and films made of the nanocomposite SnO_2/MWCNT powder using the ion-plasma sputtering method. The subsequent annealing of samples in the air was carried out for improving the adhesion of contacts and releasing any possible mechanical stress.

The gas sensing properties of the fabricated sensors made of the nanocomposite MWCNT/SnO_2/Pd structures were tested in the presence of isobutane and H_2. Main attention was given to i-butane sensors due to their higher response in comparison with H_2-sensors. Changes in the sensor resistance were registered at operating 100–350 °C. The response to H_2 and i-butane of the sensors made of the MWCNT/SnO_2/Pd nanocomposite was investigated. It was determined as usually by (R_{air}/R_{gas}). The results of these investigations have shown that response appears only after sensitizing the samples of the MWCNT/SnO_2 nanocomposite in the $Ru(OH)Cl_3$ water solution. For example, sensors made of the MWCNT/SnO_2/Pd nanocomposite sensitized with the 0.03 M $Ru(OH)Cl_3$ solution have rather high response to H_2 and isobutane already at 120 °C. The resistance of sensor was equal ∼700 kΩ at this temperature. It decreased ten times in ∼10 and ∼30 s after the injection of isobutane and H_2, respectively. The recovery time was equal ∼30 at 120 °C.

We think that oxygen is adsorbed on the surfaces of the structure and the influencing gas reacts with oxygen species releasing electrons. The increase in the electrons concentration in the semiconductor conduction band leads in its turn to the reduction of structure resistance. It is known that Ru is a sensitizer for SnO_2 and thus allows enhancing the sensor response and selectivity to hydrocarbons [9, 31]. Ruthenium stimulates an increase in rate of oxidation and other surface reactions, involving adsorption of oxygen from the air on the structure surface which causes an increase in depletion layer of semiconductor near-surface region and hence leads to the enhancement of the sensor response. The measurements of the sensor response to i-butane at higher temperatures have shown that characteristics become stable. The recovery time decreases down to ∼10 min.

The comparison of characteristics of the sensors sensitized with ruthenium has shown that sensors made of the MWCNT/SnO_2 nanocomposite sensitized with the 0.03 M Ru $(OH)Cl_3$ solution were the most sensitive. However, the response time was lower for the samples, sensitized in the 0.01 M $Ru(OH)Cl_3$ solution. For these sensors, it was equal to ∼30–40 s while the response time for the samples sensitized in the 0.03 M $Ru(OH)Cl_3$ solution was equal to ∼2–3 min. A limitation of the sensor is its slow recovery after the gas supply is stopped.

In order to develop samples with sufficient density, we used as a binder the polypropylene (2.5–3 wt %) powder. Sensors made of SnO_2/MWCNT nanocomposite were also prepared with this binder and presoaked in two $Ru(OH)Cl_3$ (0.01 and 0.03 M) solutions. The results of the measurements of response to isobutane for these sensors at different temperatures and concentrations of the gas are shown that sensors sensitized with the 0.03 M $Ru(OH)Cl_3$ solution are more sensitive when the sensor temperature is lower than 250 °C. However, the largest response was observed for the sensors sensitized with the 0.01 M $Ru(OH)Cl_3$ solution at 300 °C. The dependence of the response on the concentration of isobutane is almost linear for the sensors made of the MWCNT/SnO_2/Pd nanocomposite. For these sensors, almost the same times of response and recovery were observed. They are equal ∼30–40 s at low concentrations of the gas. Parameters of these structures remained stable at its long-term testing (about 1 year).

Many applications have CNTs in the form of thin film. There are several methods of manufacturing films made of CNTs. We developed thick films made of the MWCNT/SnO_2 powder nanocomposite by the spray coating method. The sensors prepared with these films have shown sufficient response to isobutane at temperatures higher than 200 °C. The sensitization of films in the 0.01 M $Ru(OH)Cl_3$ solution leads to the best response at the temperature of the work body at 250 °C. Despite the fact that values of response are not so high, the characteristics of these sensors are steady enough and the system response and recovery times are equal to ∼30 s.

We reported above that surface modification of the CNTs/metal-oxide hybrid gas sensors and sensors based on the nanocomposites components with noble metals (Pt, Pd, Au, Ru, Rh) promotes increasing in sensitivity and improvement of the gas sensors sensitivity and selectivity because of these metals or theirs oxides are the catalysts for chemical reactions taking place on the surface. In hybrid material metal oxides and CNTs can be connected with each other by different ways, namely: CNTs filled or coated by metal oxide as well as metal oxide doped with CNTs. In all these cases we can expect an increase in sensitivity to certain gases as well as lowering the operating temperature.

We expect that coating of functionalized MWCNTs with SnO_2 nanoparticles with such sizes should provide further improvement of the gas sensor performance and lowering of its operating temperature. We prepared and studied thick-film gas-sensor structures using various precursors for wet chemical processes. The choice of corresponding treating conditions and regimes for CNTs functionalization were focused on obtaining response to such target gases as H_2, ethanol, methanol and i-butane.

We further obtained and studied hybrid MWCNTs/SnO_2 surface-modified with Ru thick films. MWCNT and SnO_2 mixed nanopowders samples were studied by us both with and without Ru catalyst. For ruthenium plating, in our research works, we used ruthenium (IV) chloride hydroxide ($RuOHCl_3$) as precursor material. MWCNTs/SnO_2 nanopowders for thick film preparation were made by the following two ways: using sol-gel preparation technique (obtaining samples with MWCNTs/SnO_2 ratio 1:50, further marked as ECS7) as well as hydrothermal synthesis (samples with MWCNTs/SnO_2 ratio 1:4 and 1:8, further marked as KCS1 and KCS2, respectively). MWCNTs membranes made in EPFL (Lausanne, Switzerland) were used for preparation of nanocrystalline MWCNTs/SnO_2 powder by wet chemical method. Millimeter long MWCNT grown by CVD were used to prepare membranes by vacuum filtration form a suspension in isopropanol. To make a functionalization of nanotube walls with oxygen-containing hydroxyl (OH), carbonyl (C = O), and carboxylic (COOH) functional groups, MWCNTs from the membranes were transferred to slurry in HNO_3/H_2SO_4 acids mixture. Later, tin chloride pentahydrate ($SnCl_4 \cdot 5H_2O$) was added to obtained suspension in the ratio of 1:7. The thick films were obtained on the base of ECS (1:50) MWCNTs/SnO_2 composite powder (ECS7 and ECS7Ru samples). The paste for thick film deposition was obtained by mixing with α-terpineol ("Sigma Aldrich"), and then printed on chemically treated surface of the substrate over the ready-made Printer digitized electrodes. Thin-film heater was formed on the back side of the substrate. For samples preparation by hydrothermal synthesis in both cases $SnCl_2 \cdot 2H_2O$ was chosen as a precursor material. After annealing and cooling the MWCNTs/SnO_2 thick films was surface-ruthenated by dipping them into 0.01 M $RuOHCl_3$ aqueous solution.

The crystallization of the MWCNTs/SnO_2 composite samples with components ratio of 1:4 and 1:8 takes place adequately. The electrical resistance of ECS7 samples in air at 20 °C was about 10^6 Ohm while the resistance of KCS set of samples measured at the same conditions was as large as 10^9 Ohm. Nevertheless, the resistance values for the all samples obtained by the both used technologies equalize to10^6–10^7 Ohm at 200 °C operating temperature. As a result of numerous testing of gas response of the samples containing CNTs carried out at various temperatures and target gas concentrations, the optimal operating temperatures were estimated for each type of the sensor. The results of these investigations are summarized in the bar chart presented in Fig. 9.8.

The analysis of the results of testing the ECS7 and KCS set of samples made without any catalysts revealed relatively high response to methanol and ethanol vapors. From the point of view of improvement of sensitivity and selectivity of these sensors to alcohols vapors, we sensitized the set of MWCNTs/SnO_2 nanocomposites with Ru catalyst. Such sensitization leads to sharp rise in response to methanol and ethanol vapor up to 10^3 and higher for both set of samples. At that, the cross-sensitivity to other gases decreases or remains on the same level. The response to methanol and ethanol vapors appears at the operating temperature of 200 °C and decreases exponentially with temperature rise up to 300 °C. It should be also noted that the functionalization of ECS7 set of samples with Ru leads to

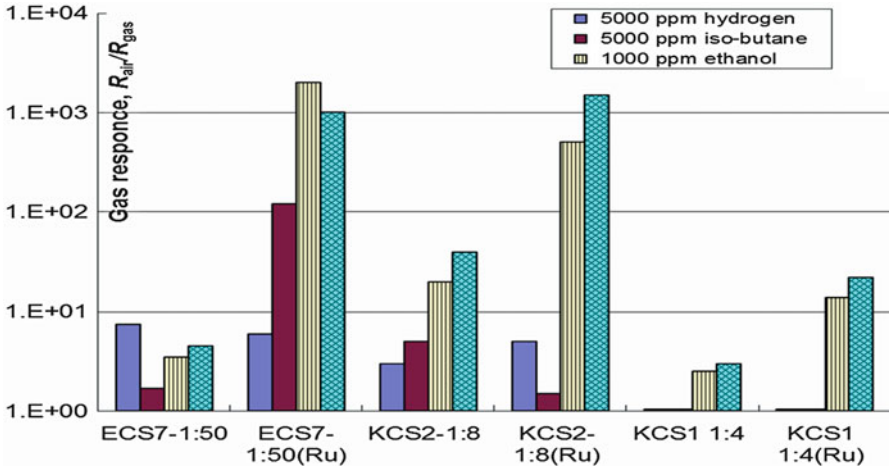

Fig. 9.8 Responses to affecting gases for the studied structures Symbol Ru points to the test of same set of samples but sensitized by ruthenium catalyst. The optimal operating temperature 200 °C acceptable for all under study affecting gases is chosen

appreciable increase in response to i-butane together with rise in response to ethanol and methanol vapors. We can note that noticeable response to i-butane is observed beginning from 50 ppm gas concentration. The typical response and recovery times of the ECS7 i-butane sensors measured on the 90 % level of the signal amplitude and at operating temperature of 200 °C are 5–7 s and about 1 min, respectively. It is also interesting to note that increase in operating temperature up to 250 °C leads to sharp decrease in both response and recovery times down to 1–2 s and 10 s, respectively. At that, the sensitivity remains practically the same. Therefore, if priority is given to faster response behavior, slightly elevated 250 °C operating temperature can be selected. With the following increase in operating temperature ($\geq$300 °C), adsorbed oxygen desorbs increasingly from the surface. As a result, the response to i-butane sharply decreases.

The formation of the surface-ruthenated MWCNTs/SnO_2 nanocomposite hybrid structure leads to high response to alcohols and i-butane at certain (1:50) ratio of the nanocomposite components as well as decrease in operating temperature. As can be seen from Fig. 9.8, different effects caused by the weight ratio of the components of nanocomposite are found. So, the surface-ruthenated nanocomposite containing large amount of SnO_2 (1:50) nanocrystallites shows high response both to methanol and ethanol vapors. Simultaneously, relatively high response to i-butane is also observed. Approximately the same sensitivity to alcohols (about 10^3) remains at the 1:8 ratios of the nanocomposite components but the response to i-butane sharply decreases. The responses to H_2 and i-butane disappear completely with the following decreasing of SnO_2 part in the nanocomposite (at the 1:4 weight ratios of the components). At that, the response to alcohols also has a little fall. It should be noted that the samples prepared without formation of the CNTs frame within

the SnO_2 matrix exhibit much smaller response to i-butane (2–3 times) only at more elevated operating temperatures (>300 °C) and higher gas concentrations. The samples based on surface-ruthenated nanocrystalline SnO_2 structures without CNTs also have smaller response (not more than 5) to methanol and ethanol vapors exposure at similar conditions (1,000 ppm and 200 °C operating temperature). Negligible sensitivity only to saturated ethanol vapor was observed for pure SnO_2 thick-film samples without CNTs and RuO_2 sensitizing layer.

The mechanism of high responses to alcohols and i-butane is still not understood completely. Getting more insight in this issue needs further thorough research work. Due to polar COOH groups attached onto the nanotubes sidewalls as a result of purification and sonication in sulfuric and nitric acids, the sensors have stronger responses to methanol and ethanol vapors. It occurs because the absorption efficiency of these volatile organic molecules increases due to dipole-dipole interactions between COOH groups and polar organic molecules. It is presumed that the response to alcohols is higher since COOH groups are capable to form H_2 bonds with ethanol and methanol molecules at low temperatures close to room temperature whereas hydrocarbons are chemisorbed on the SnO_2 nanoparticles surface only at higher temperatures. High response to i-butane was detected for heavily ruthenated SnO_2-MWCNTs samples. Nevertheless, in the case of the samples with 1:8 and 1:4 weight ratio of the components (with low content of SnO_2); there is a lack of oxygen sites for complete dehydrogenisation reaction under i-butane influence. The response to alcohols vapors is noticeably higher even under much smaller concentrations in comparison to i-butane. At smaller portions of SnO_2 in nanocomposites, the number of adsorption centers is lesser; therefore responses to alcohols decreases, but responses to i-butane and H_2 gases are not revealed at al. Relatively stronger responses towards the alcohol vapors in this case are conditioned mainly by the dipole-dipole interactions between the COOH groups attached onto the not covered by SnO_2 nanotubes sidewalls and the polar organic molecules of methanol and ethanol [35]. Results of our investigations on SnO2/MWCNT sensors are published recently [36–38]. These investigations can be expanded to detection of chemical warfare agents.

9.5 Conclusion

The use of the sol-gel technology with increasing Pt catalyst layer thickness, led to realization of the best thin-film H_2 sensors with no to lower temperature pre-heating and improvement of many parameters of H_2 sensors such as consumed power, long-term stability as well as selectivity. Theoretical and experimental investigations of noise phenomena in gas sensors allow proposing method of estimation of the concentration of gases in environment – the noise spectroscopy-can be more effective in the case of porous Si and other sensors, which are sensitive to many gases.We would like to report that we did not detect any response of pure SnO_2 and CNTs to isobutane, but such response was detected by using our sensors

made of the SnO_2/MWCNT nanocomposite and SnO_2/MWCNT/Pd nanostructures. The sensitization of the SnO_2/MWCNT nanocomposite in the $Ru(OH)Cl_3$ water solution leads to rather high response to isobutane and H_2 already at 120 °C. Maximal response reached about 50 at 5,000 ppm. The response dependence on the isobutane concentration has almost linear character for the ceramic sensors made of the MWCNT/SnO_2/Pd nanostructure. The thick film sensors made of the MWCNT/SnO_2/Pd had the response to isobutane more than 5–7 at a rather low temperature of the work body (250 °C). These sensors recovered well, times of the response and recovery were almost identical and equal 30 s.

Functionalization by Ru leads to increase in gas response of studied MWCNT structures particularly to methanol and ethanol vapors. It was also established that from all concerned MWCNTs/SnO_2/Ru powders the powder with weight ratio of MWCNTs to SnO_2 1:8 and 1:50 is the most interesting from the point of view of responses to these vapors. Relatively low sensor operating temperature as well as short response and recovery times are realized. Moreover, surface-ruthenated samples exhibit the highest response to i-butane in comparison with other studied set of samples. But sensors with 1:4 ratio of the components have exhibited good selectivity to ethyl and methyl alcohols vapors. By means of certain choice of the gas sensor processing technique, weight ratio of the nanocomposite components and the best operating temperature, as well as by impregnating the sensor structures with Ru catalyst, it is possible adjusting surface-ruthenated MWCNT/SnO_2 nanocomposite sensors response and selectivity as well as response and recovery times.

Acknowledgment I express my deep gratitude to co-authors of our joint papers from YSU, the USA, Sweden, France, Italy, Hungary, Germany and Switzerland.

References

1. Seiyama T (ed) (1981) Chemical sensors. Kodasha Ltd./Elsevier, Tokyo
2. Aroutiounian VM (1991) Microelectronic technologies – the main way for obtaining of chemical sensors. Sov Microelectron 20(4):337–355
3. Aroutiounian VM, Abovian HV, Adamyan ZN et al (1995) Method of making smoke detector. Patent USA N 5382341, 17 Jan 1995
4. Adamian AZ, Adamyan ZN, Aroutiounian VM (2003) Smoke sensor with overcoming of humidity cross sensitivity. Sens Actuator B 93:416–421
5. Aroutiounian VM, Arakelyan VM, Shahnazaryan GE (2005) Metal oxide photoelectrodes for hydrogen generation using solar radiation-driven water splitting. Sol Energy 78:581–592
6. Aroutiounian V (2012) Hydrogen sensors. In: Dekker encyclopedia of nanoscience and nanotechnology, 2nd edn. Taylor and Francis, New York, pp 1–10. Published online 25 June 2012, doi:10.1081/E-ENN2-120048385
7. Aroutionian V (2007) Metal oxide hydrogen, oxygen, and carbon monoxide sensors for hydrogen setups and cells. Int J Hydrog Energy 32:1145–1158
8. Huebert T et al (2011) Hydrogen sensors. Sens Actuator B 157:329–352
9. Adamyan AZ, Adamyan ZN, Aroutiounian VM et al (2007) Sol–gel derived thin-film semiconductor hydrogen gas sensor. Int J Hydrog Energy 564(32):4101–4108

10. Adamyan AZ, Adamyan ZN, Aroutiounian VM (2009) Study of sensitivity and response kinetics changes for SnO_2 thin-film hydrogen sensors. Int J Hydrog Energy 34:8438–8443
11. Adamyan AZ (2010) Nanostructured semiconductor gas sensors. Lambert Academic Publishing, Saarbruecken (in Russian)
12. Aroutiounian V, Mkhitaryan Z, Adamyan A et al (2009) Fluctuation-enhanced gas sensing. Proced Chem 1:216–219
13. Aroutiounian V (2013) Porous silicon gas sensors. In: Jaaniso R, Tan OK (eds) Semiconductor gas sensors, Series in electronic and optical materials. Woodhead Publishing Ltd., Cambridge. ISBN 0857092367
14. Canham LT (1990) Silicon quantum wire array fabrication by electrochemical and chemical dissolution of wafers. Appl Phys Lett 57:1046–1048
15. Canham L (1999) Properties of porous silicon. INSPEC IEE, London
16. Pavesi L, Lockwood DJ (eds) (2004) Silicon photonics, vol 94, Topics in applied physics. Springer, New York
17. Ossicini S, Pavesi L, Priolo F (2003) Light emitting silicon for microphotonics, vol 194, Springer tracts in modern physics. Springer, Berlin/Heidelberg, pp 75–122
18. Foucaran A, Pascal-Delannoy F, Giani A et al (1997) Porous silicon layers used for gas sensor applications. Thin Solid Film 297:317–320
19. Paremuzyan VG, Aroutiounian VM (2012) Porous silicon layers used for gas sensor applications. Inform Technol Electron Radio Eng 15:62–69
20. Paremuzyan VG, Aroutiounian VM (2012) Influence of reduction in the heat of adsorption on noise characteristics of sensors. Sens Transducer J 137:95–103
21. Mkhitaryan ZH, Shatveryan AA, Aroutiounian VM et al (2007) Current–voltage and low-frequency noise characteristics of structures with porous silicon layers exposed to different gases. Physica E 38:160–163
22. Mkhitaryan ZH, Shatveryan AA, Aroutiounian VM et al (2007) Low-frequency noise in structures with porous silicon in different gas media. Phys Status Sol C 4:2063–2067
23. Mkhitaryan ZH, Shatveryan AA, Aroutiounian VM et al (2008) Noise spectroscopy of gas sensors. IEEE Sens J 8(6):786–790
24. Aroutiounian V, Arakelyan V, Galstyan V et al (2009) Hydrogen sensor made of porous silicon and covered by TiO_2-x or ZnO<Al> thin film. IEEE Sens J 9(1):9–12
25. Varghese OK, Kichambre PD, Gong D et al (2001) Gas sensing characteristics of multi-wall carbon nanotubes. Sens Actuators B 81:32–41
26. Cao Q, Rogers JA (2009) Ultrathin films of single-walled carbon nanotubes for electronics and sensors: a review of fundamental and applied aspects. Adv Mater 21:29–53
27. Liu Y-L, Yang H-F, Yang Y (2006) Gas sensing properties of tin dioxide coated carbon nanotubes. Thin Solid Film 497:355–360
28. Hieu NV, Duc NAP, Trung T et al (2010) Gas-sensing properties of tin oxide doped with metal oxides and carbon nanotubes: a competitive sensor for ethanol and liquid petroleum gas. Sens Actuators B 144:450–456
29. Smajda R, Andresen JC, Duchamp M et al (2009) Synthesis and mechanical properties of carbon nanotubes produced by the water assisted CVD process. Phys Status Sol B 246: 2457–2460
30. Aroutiounian VM, Arakelyan VM, Khachaturyan EA et al (2011) Manufacture and investigation of gas sensor made of carbon nanotube. In: Proceedings of 8th international conference semiconductor micro-and nano electronics, Yerevan, Armenia, pp 14–18
31. Adamyan AZ, Adamyan ZN, Aroutiounian VM et al (2009) Improvement and stabilization of thin-film hydrogen sensors parameters. Armen J Phys 2(3):200–212
32. Magrez A, Seo JW, Smajda R, Mionić M, Forro L (2010) Catalytic CVD synthesis of carbon nanotubes: towards high yield and low temperature growth. Materials 3(11):4871–4891
33. Seo JW, Couteau E, Umek P et al (2003) Synthesis and manipulation of carbon nanotubes. New J Phys 5:120.1–120.22
34. Hernadi K, Ljubovic E, Seo JW, Forro L (2003) Synthesis of MWNT-based composite materials with inorganic coating. Acta Mater 51:1447–1452

35. Sin MLY, Chow GCT, Wong GMK et al (2007) Ultralow-power alcohol vapor sensors using chemically functionalized multiwalled carbon nanotubes. IEEE Trans Nanotechnol 6(5): 571–577
36. Aroutiounian VM, Mnatsakanyan BV (2012) IMCS 2012: in the 14th international meeting on chemical sensors, Nuremberg, pp 1025–1027. doi:10.5162/IMCS2012/P1.5.1
37. Aroutiounian VM, Arakelyan VM, Khachaturyan EA et al (2012) Manufacturing and investigations of i-butane sensor made of SnO_2/multiwall-carbon-nanotube nanocomposite. Sens Actuators B 173:890–896
38. Aroutiounian VM, Adamyan AZ, Khachaturyan EA et al (2012) IMCS 2012: the 14th international meeting on chemical sensors, Nuremberg, pp 1085–1088. doi:10.5162/IMCS2012/P1.7.10

Chapter 10
Chemical Sensors Based on Nano-hexagonal Tungsten Oxide: Synthesis and Characterization

Csaba Balázsi, István Endre Lukács, and Katalin Balázsi

Abstract Tungsten oxide based materials have received a great attention in the fabrication of semiconducting oxide based gas sensor devices. In the present work the preparation of nanocrystalline hexagonal WO_3 (hex-WO_3) from sodium tungstate solution by acidic precipitation as a nanocrystalline processing route is presented. Metal decorated carbon nanotubes (CNTs) were added to hex-WO_3 nanopowder with the aim to further lower the operating temperature of sensors. Hex-WO_3/Au-decorated MWCNTs composites were able to detect as low as 100 ppb of NO_2, with no need to heat the sensors substrates during operation, which demonstrates the high potential of our new gas sensors. The developed porous tungsten oxide nanofibers might be find application on a special chip designed for gas sensorics.

Keywords Hexagonal tungsten oxide • Carbon nanotube • Gas sensor

10.1 Introduction

During the last years, in the materials science, great emphasis has been placed on the nanosized materials in order to study the unique physical properties [1, 2]. Grain-size reduction is one of the main factors in enhancing the gas sensing properties of semiconducting oxides. The adsorption of gases basically occurs at the surface level of a sensing film, and an increase in the active surface area of the semiconductor

C. Balázsi (✉) • I.E. Lukács • K. Balázsi
Institute for Technical Physics and Materials Science, Research Centre for Natural Sciences, Hungarian Academy of Sciences, Konkoly-Thege út 29-33, Budapest 1121, Hungary

Institute for Materials Science and Technology, Bay Zoltán Nonprofit Ltd. for Applied Research, Fehérvári út 130, Budapest H-1116, Hungary
e-mail: balazsi.csaba@ttk.mta.hu

A. Vaseashta and S. Khudaverdyan (eds.), *Advanced Sensors for Safety and Security*, NATO Science for Peace and Security Series B: Physics and Biophysics,
DOI 10.1007/978-94-007-7003-4_10,

oxide would enhance the properties of the materials used for gas sensors. The mechanism of the electrical conductivity change of the oxide under gas exposure is understood in terms of adsorption–desorption reactions involving surface oxygen vacancies [3]. Among many other candidates, oxides of tungsten oxides are the most used materials in electro-, photo- and gasochromic devices and have been commonly applied as sensing layers for hazardous gas detection [4–6].

Tungsten oxide based materials have received a great deal of attention in the fabrication of semiconducting oxide based gas sensor devices. Several semiconducting metal oxide sensor based on WO_3 [7–9] and WO_3 modified with various metal composites [10–12] have been used for potential NO_x sensors. The reactivity of WO_3 based sensors was found to be highly dependent on the deposition process and testing protocol [7–9]. Various crystalline forms of tungsten oxides can be prepared by thermal evaporation of WO_3 powder [13, 14], by Radio-Frequency-sputtering from metallic W [15] or WO_3 targets [16] in Ar_2/O_2 atmosphere, by chemical vapor deposition [17] and by wet chemistry such as the sol-gel process [18].

In the present work the preparation of nanocrystalline hexagonal WO_3 (hex-WO_3) from sodium tungstate solution by acidic precipitation as a nanocrystalline processing route is presented. Metal decorated CNTs were added to hex-WO_3 nanopowder with the aim to further lower the operating temperature of sensors [19]. The sensing properties of the hex-WO_3 and hex-WO_3/Au-decorated MWCNTs composites were tested under normal testing conditions. Detection of hazardous gases, e.g. NO_2 which results from combustion and automotive emissions, is very important for the environmental protection and human health. The adsorption of gases basically occurs at the surface level of a sensing film, and an increase in the active surface area of the semiconductor oxide would enhance the properties of the materials used for gas sensors [20, 21]. In addition to this emerging field the tungsten oxides and tungsten oxide hydrates are among the most used materials in electro-, photo- and gasochromic applications [22].

Structural and electrochemical performances of thin films have been determined by XRD and atomic force microscopy. Sensing properties of the prepared tungsten oxides have been tested to gaseous nitrogen dioxide and ammonia at various temperatures. Sensor films showed a decrease in resistance on exposure to ammonia as is characteristic of an n-type semiconductor. The hex-WO_3 layers were found to be sensitive in the concentration range of 50–500 ppm at the temperature of 300 °C and the hex-WO_3/CNT layers were sensitive to nitrogen dioxide gas at the concentration range of 100 ppb–1 ppm at room temperature.

10.2 Experimental

10.2.1 Hexagonal Tungsten Oxide Processing

The following scheme describes the processing route to obtain nanocrystalline hex-WO_3 powder:

$$Na_2WO_4 \cdot 2H_2O \text{ (solution)} \rightarrow H_2WO_4 \cdot H_2O \text{ (gel)} \rightarrow WO_3 \cdot 1/3H_2O$$
$$\text{(suspension)} \rightarrow WO_3 \cdot 1/3H_2O \text{ (powder)} \rightarrow \text{hex-}WO_3 \text{ (powder)}$$

$H_2WO_4 \cdot H_2O$ gel samples were prepared according by HCl precipitation from sodium tungstate solution [23]. According to these methods, the precipitated gels should be washed several times. However, as a modification of these processes, an overnight cooling of the freshly precipitated gel was carried out before washing the gel. The resulted gels were washed and centrifuged 3–5 times depending on the process. Suspensions of the washed gels underwent hydrothermal dehydration. The hydrothermal reaction was carried out in Parr acid digestion bombs at autogenous pressure at 125 °C ± 5 °C. After hydrothermal dehydration, the obtained products were dried at room temperature or used as "as-received" suspensions. Droplet(s) of the "as-received" suspension were deposited onto ITO conductive transparent glass and (110) oriented silicon wafers. The silicon wafers covered with the deposit and the resulted powder was then passed to final dehydration (furnace temperature: 330–340 °C, annealing time: 90 min under ambient air).

10.2.2 Measurements

Structural characterization was conducted using X-ray diffraction (Bruker AXS D8 Discover X-ray diffractometer with CuKα radiation). The morphology of the samples was studied by scanning electron microscopy (LEO 1540XB field emission SEM). The structure of samples was investigated further by conventional transmission electron microscopy (TEM) using a Philips CM-20 microscope and by high resolution transmission electron microscopy (HREM) with a JEOL 3010 microscope. AFM measurements of $WO_3 \cdot 1/3H_2O$ layers deposited onto 5×5 μm corning glass (2947) substrates were also carried out.

The sensing gases were NH_3 and NO_2. The flow rate of the gases in the presence of either NH_3 was maintained at 1000 sccm. Sensing layers have been produced by spin coating 10 mg powder/5 ml n-butanol suspensions on Al_2O_3 substrates with Au-metallization. Sensing experiments were carried out at r.t. (room temperature), 250 and 300 °C. The tungsten oxide and hybrid composite films were tested in the presence of very low concentrations of NO_2. To perform the measurements, the gas sensors were placed inside a 5.3 dm^3 test chamber, and the desired concentrations of NO_2 (ranging from 100 ppb to 1 ppm) or NH_3 (50–500 ppm) were introduced by the direct injection method using a gas-tight chromatographic syringe. An Agilent 34970A multimeter was used for continuously monitoring the electrical resistance of the sensors during the measurement process. The data acquired were stored in a PC for further analysis Sensing experiments were carried out at room temperature and at various temperatures up to 300 °C.

10.3 Results and Discussion

10.3.1 Materials Properties

XRD measurement was used to analyze the sample structure and confirmed that the resulted film after heat treatment in air atmosphere is WO_3. It was observed from XRD that the films present an orthorombic WO_3 phase until 300 °C annealing. After heat treatment at 330 °C for 90 min the phase changed to hexagonal phase as demonstrated on Fig. 10.1.

In conclusion the phase change during the heat treatment (330 °C, 90 min in air) from orthorhombic to hexagonal was observed. The SEM observation supported all the above results and it was consistent with the XRD investigations. XRD patterns were compared and checked with the Joint Committee on Powder Diffraction Standards files, $WO_3 \cdot 1/3H_2O$, (JCPDS card 35-270) and hex-WO_3 (JCPDS card 33-1387).

The morphology of the $WO_3 \cdot 1/3H2O$ nanograins as resulted from the hydrothermal process is presented in Fig. 10.2. The structural characterization of tungsten oxide hydrate nanopowders by SEM is showing sticking powder consisting of columnar grains. This orthorhombic $WO_3 \cdot 1/3H_2O$ phase (Fig. 10.2) appearing after hydrothermal preparation is so called mother phase of hex-WO_3. The powder in this state consists from columnar crystallites which lengths are ∽200 nm and their thicknesses are ∽50 nm.

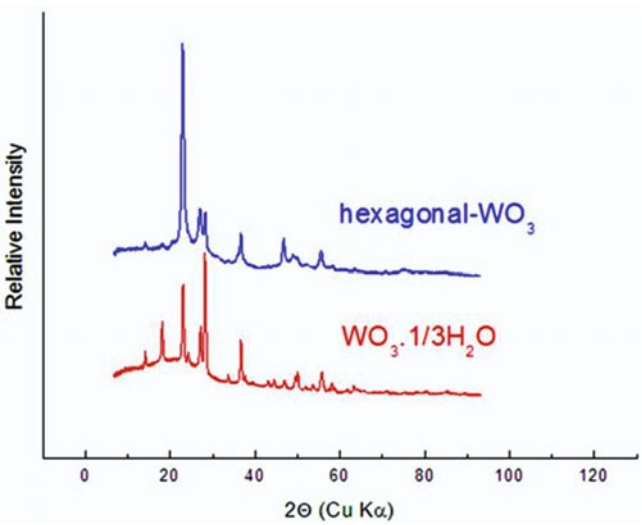

Fig. 10.1 XRD patterns of $WO_3 \cdot 1/3H_2O$ and h-WO_3

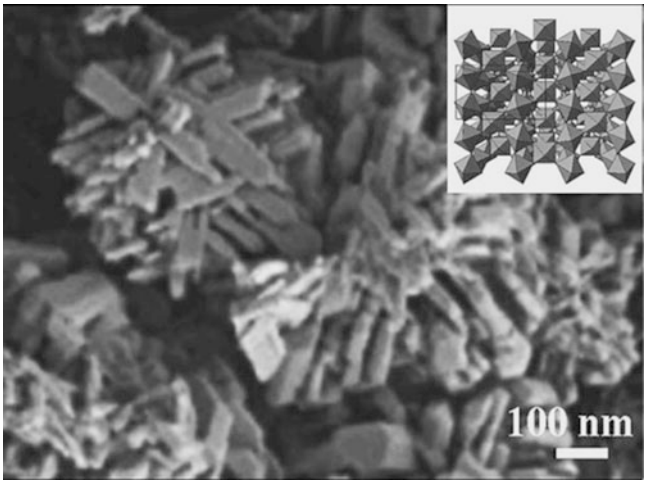

Fig. 10.2 Structure of orthorombic $WO_3 \cdot 1/3H_2O$. SEM image of structure shows that the average size of $WO_3 \cdot 1/3H_2O$ grains is about 200 nm, *inset* shows schematic image

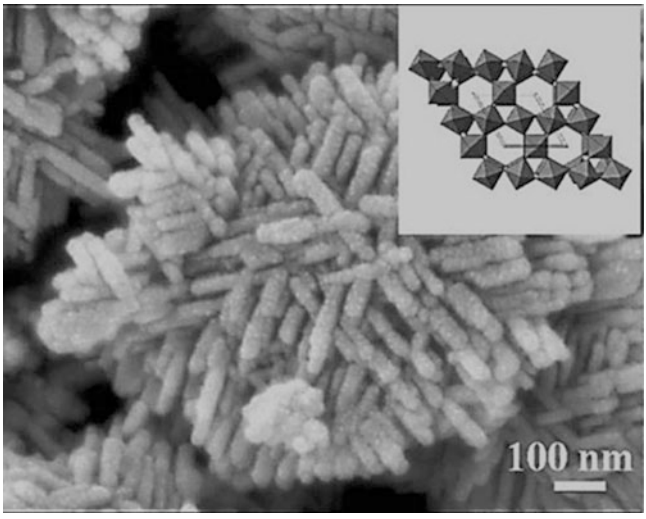

Fig. 10.3 Structure of hexagonal WO_3. SEM image of structure shows that the average size of $WO_3 \cdot 1/3H_2O$ grains is about 200 nm, *inset* shows schematic image

The structure and morphology change occurred after heat treatment at 330 °C for 90 min in air. The average size of hex-WO_3 crystallites was found to be ∽100 nm (length) and ∽30 nm (thickness) (Fig. 10.3).

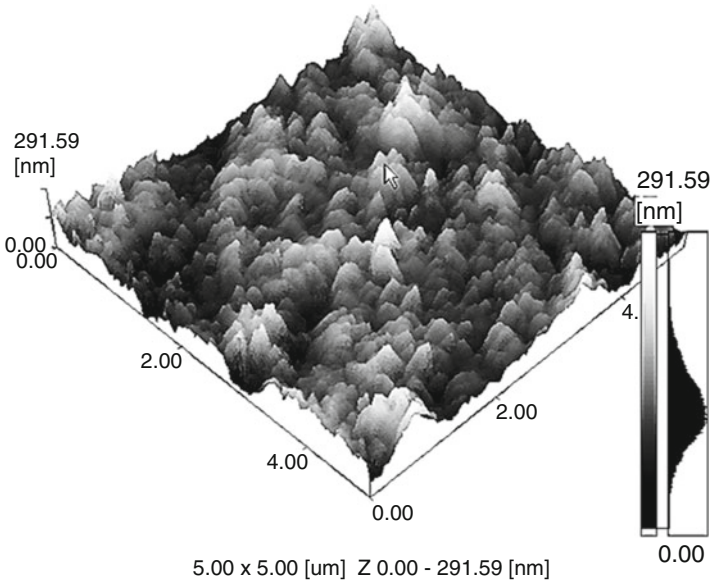

Fig. 10.4 AFM images of $WO_3 \cdot 1/3H_2O$ nanocrystalline film after two washing processes

Figure 10.4 presents the AFM images of the $WO_3 \cdot 1/3H_2O$ films derived from the mother phase shown in Fig. 10.2. The grain size is uniform with grains packed together to form a nanocrystalline film. TEM and HRTEM investigations of $WO_3 \cdot 1/3H_2O$ films reveal more details on the morphology (see Fig. 10.5). The electron diffraction showed the orthorhombic phase of $WO_3 \cdot 1/3H_2O$ crystallites.

To improve the room temperature sensing properties, the Au-decorated MWCNTs were added to hex-WO_3 nanopowder (Fig. 10.6a). The used ratio of MWCNTs in hex-WO_3 was 1/500 wt%. The tungsten oxide crystallites are bonded by Au-decorated MWCNTs. The average diameter of nanotubes is $\backsim$25 nm and their lengths are $\backsim$ few hundred nanometers (Fig. 10.5b).

10.3.2 Sensing Characterization

Hex-WO_3 had a good response to NH_3 at 300 °C (Fig. 10.7). The resistance of the sample decreased in accordance with the n-type character of semiconducting hex-WO_3. At increasing NH_3 concentration, the response time was about 20–100 s. However, the recovering time was longer, 200–300 s. Figure 10.8a shows the response of a hex-WO_3 sensor to increasing concentration of NO_2. This result was recorded for the sensor operated at 250 °C.

When the operating temperature was lowered below 250 °C (in this paper not shown), the conductivity change drastically decreased (more than a factor of 4 at

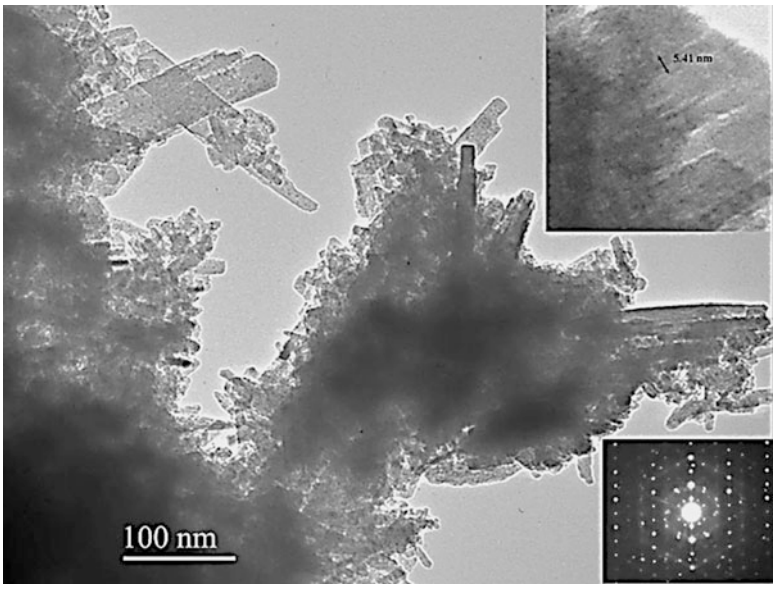

Fig. 10.5 Plan view TEM image of $WO_3 \cdot 1/3H_2O$ film

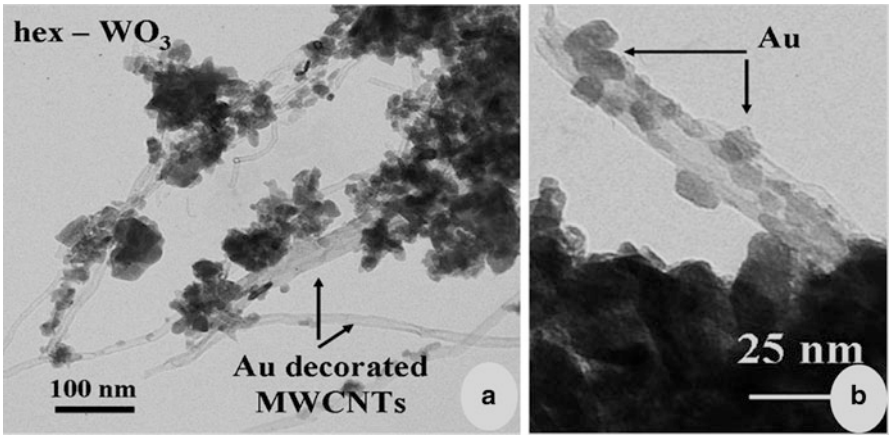

Fig. 10.6 Structure of hex-WO_3/Au-decorated MWCNTs composite. (**a**) TEM image of composite show the MWCNTs between nanosized hex-WO_3 grains, (**b**) TEM detail of Au - decorated MWCNT

150 °C, while at room temperature it lose completely its property to sense NO_2 at concentrations range up to 1 ppm). It was found that the CNT networks provide good response to low NO_2 concentrations. The pretreatment period, sensor response, and recovery times were all found to be temperature dependent.

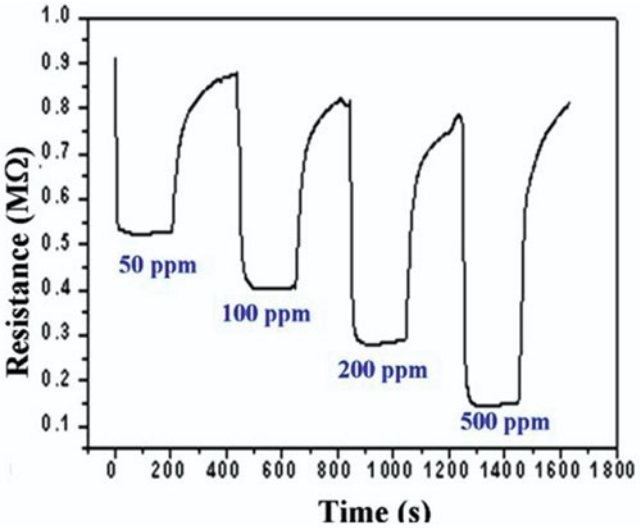

Fig. 10.7 Sensing responses of hex-WO_3 to NH_3 gas at 300 °C

The sensing properties of hex-WO_3/MWCNTs composite materials were also studied. Figure 10.8b shows the response of a hex-WO_3/Au-decorated MWCNTs sensor to increasing concentration of NO_2. This response, recorded for the sensor operated at room temperature, demonstrates that the addition of a low amount of MWCNTs to the original hex-WO_3 matrix can improve the sensing potential in terms of room temperature NO_2 detection. Importantly, the quantity of MWCNTs embedded into the hex-WO_3 matrix plays a crucial role, and it depends on the type of metal used to decorate the carbon nanotubes.

10.3.3 Porous Tungsten Oxide Nanofibers for Gas Sensors

We report on a technique for fabrication of porous tungsten oxide nanofibers with a diameter under 200 nm and a macroscopic length. The decisive method of the production is electrospinning. A technique has been developed to evenly disperse tungsten oxide nanoparticles in polymer solution for electrospinning. The ideal mass ratio of solvents, polymer and the maximum amount of tungsten oxides have been determined by a series of experiments. A solution of polymer (polyvinyl alcohol) and dopant is put in a syringe, which is controlled by a stepper motor. The solution leaves the needle, and flies to the target (metal plate) driven by the high voltage switched between the target and the needle. A microchip specially developed for gas sensing is fixed on the target. At this state the hexagonal tungsten oxide nanoparticles are coated with polymer, we developed methods for eliminate the polymer whilst the nanofibers remain and the tungsten oxide nanoparticles form porous nanofibers on the surface of gas sensor chip.

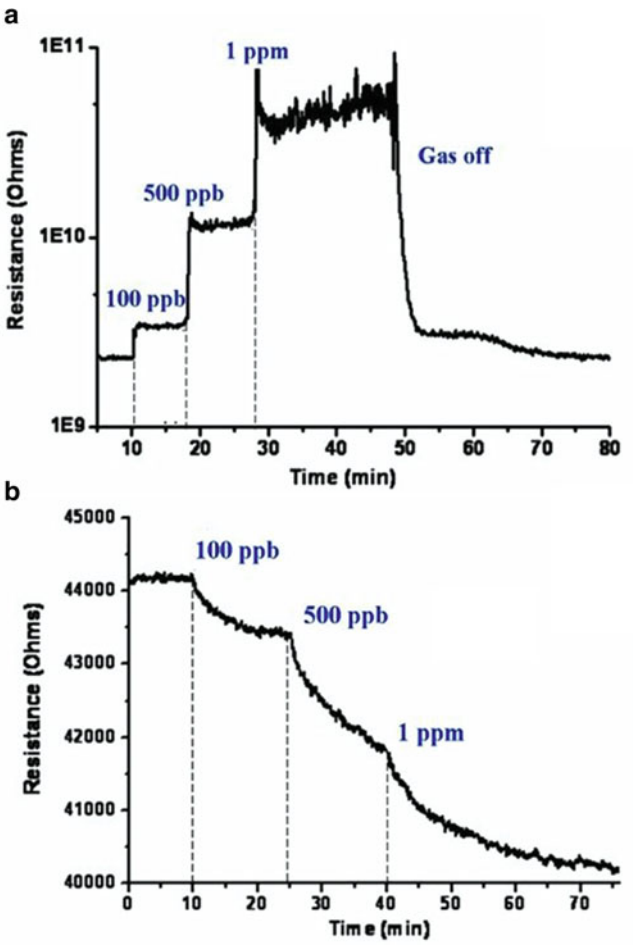

Fig. 10.8 Resistance change experienced by the gas sensors exposed to increasing concentrations of NO_2. (**a**) hex-WO_3 film operated at 250 °C, (**b**) hex-WO_3/Au-MWCNTs (500/1 wt%) film operated at room temperature

The electrospinning process (Fig. 10.9) operates on the basis that the application of a high voltage to a viscous polymeric based solution results in the accumulation of charges on the solution which forces the solution to stretch and form a jet of charged fibrous structures as a direct consequence of repulsion forces. In parallel an electrostatic field is created between the needle and the collector, as seen in Fig. 10.9, and is used to direct the charged fibers to the selected area. The applied voltage is usually in the range from 7 to 30 kV. In this range the voltage is high enough to break the surface tension of a droplet of the composite solution formed at the end of the syringe including the formation of a fiber jet. Electrostatic forces between the collector plate and the tip of the needle direct the flow of the fibers

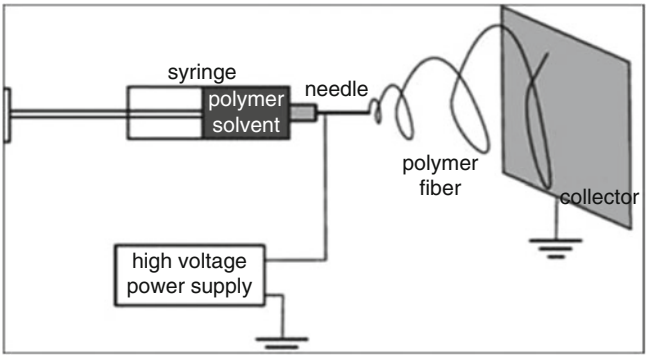

Fig. 10.9 Electrospinning apparatus

Table 10.1 Compound of solvents for electrospinning

Cellulose acetate solvents							
Spl. Nr	CA [g]	Water [g]	2-propanol [g]	Acetic acig [g]	Tungsten oxide [g]	Acetone [g]	Tungsten oxide content in fibers [wt%]
1	2	1.5	0	11	0.4	0	16.6
2	2	0	2	0	0.35	8	14.9
3	2	0	2	0	0.5	8	20

Polyvinyl alcohol advents					
Spl.Nr	PVA [g]	Water [g]	Tungsten oxide [g]	PVA content in water [wt%]	Tungsten oxide content in fibers [wt%]
4	0.172	2.655	0.173	6.1	50.1
5	0.19	2.501	0.309	7.1	61.9
6	0.14	2.545	0.315	5.2	69.2
7	0.16	2.528	0.312	6.0	66.1
8	0.22	2.474	0.306	8.2	58.2
9	0.229	2.651	0.120	8.0	34.3
10	0.199	2.653	0.147	7.0	42.5
11	0.14	2.658	0.201	5.0	58.9

from the needle to the collector. While in the air, the solvent evaporates, and the dry matter forms tissue or dust depending on the recipe.

Our aim was to maximize the concentration of $WO_3 \cdot 1/3H_2O$ content in the produced polymer fibers. Experiments were performed with varied recipes of different solvents and a high range of ratios (Table 10.1). A good solvent of cellulose acetate is acetone or acetic acid, whereas of good solvent of polyvinyl alcohol is water. At sample 2 the water content of sol were changed to propanol by several cycles of centrifuging and diluting. The tungsten oxide sol was dried and re-dispersed by ultrasonic unit for sample 3.

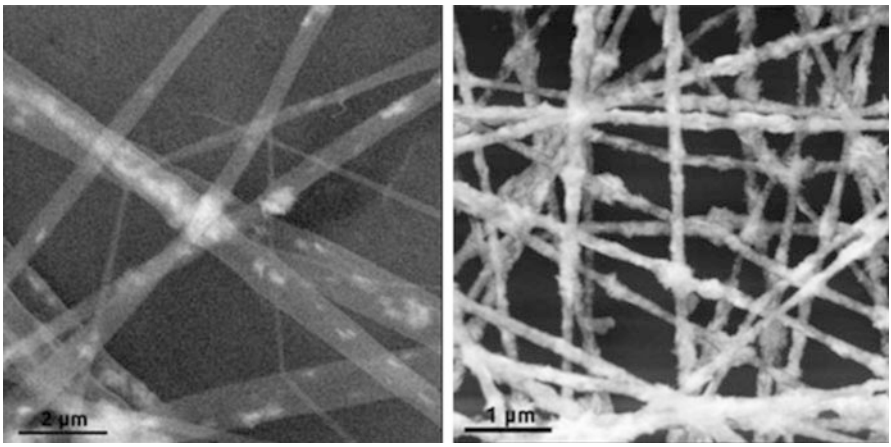

Fig. 10.10 Scanning electron microscope images of doped cellulose acetate and PVA fibers

The typical needle-collector voltage during electrospinning was 7–8 kV at the samples 1–3, 11 kV at sample 4, 16–17 kV at samples 5–10 and 13 kV at sample 11. The flow rate was 60 μl/min at samples 1–3, and 5–7 μl/min at samples 4–11. The distance between the needle and collector was 16 cm. For sensoric application the polymer must be eliminated to provide the tungsten oxide conduction and the NO_x absorption onto the surface of the nanofibers. After electrospinning the polymer was burned by heat treatment at 400 °C 4 h in tube furnace or oxygen stripping at 300 W RF power 1 h in vacuum, and UV tube generated ozone 24 h. Finally the samples were heat-treated in air at 330 °C 3 h to obtain porous hexagonal tungsten oxide nanofibers. In Fig. 10.10a there is electron microscope images of doped cellulose acetate fibers. The typical diameter of these fibers is 1 μm.

It is clearly seen that the $WO_3 \cdot 1/3H_2O$ nanoparticles are cohered producing large clusters. For better results we changed the cellulose acetate to polyvinyl alcohol increased the tungsten oxide concentration. Note that in cellulose acetate fibers the maximum tungsten oxide content was 22 wt%. More tungsten oxide prohibits the electrospinning process. Figure 10.10b shows the SEM images of the $WO_3 \cdot 1/3H_2O$ doped PVA nanofibers.

Figure 10.11 shows the morphology of samples after the polymer calcination. All three methods eliminate the most of the polymer, but the heat treatment changes the morphology of the crystal particles. The XRD measurement demonstrated that the heat treatment converts the lattice structure of WO_3 to monoclinic (not shown). The FTIR measurements show that all three methods reduce the amount of the polymer (Fig. 10.12).

$WO_3 \cdot 1/3H_2O$ doped polymer composite nanofibers were fabricated by electrospinning. The polymer content was eliminated/reduced by several methods. The porous tungsten oxide nanofibers can be produced on a special chip designed for gas sensor.

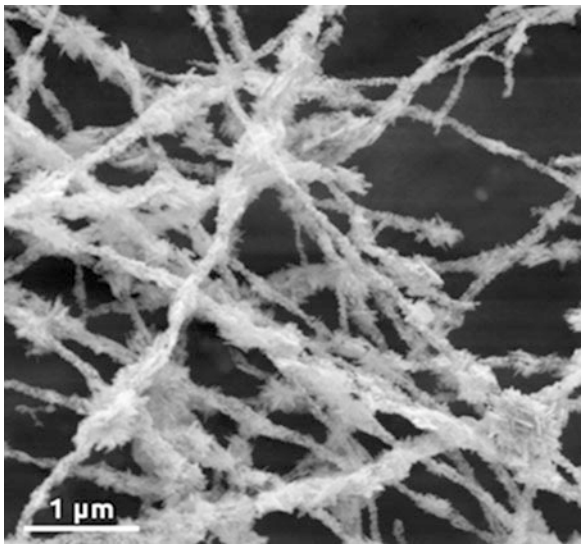

Fig. 10.11 Morphology of the oxidized polymer

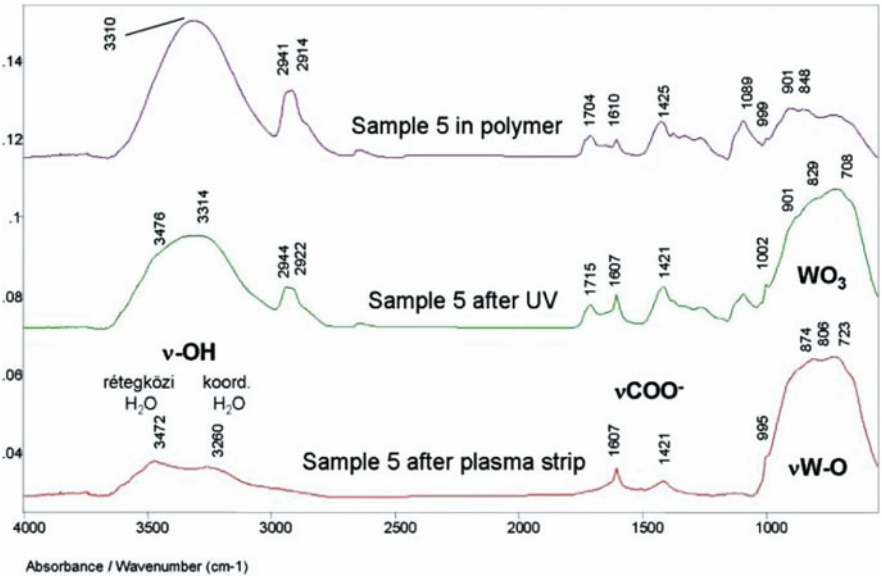

Fig. 10.12 FTIR measurement of oxidized polymer mats

10.4 Conclusion

The preparation of nanosized hexagonal WO_3 powder by acidic precipitation from sodium tungstate solution was shown. The morphological (from ∽200 to ∽50 nm) and phase change (from orthorhombic to hexagonal) was obtained after

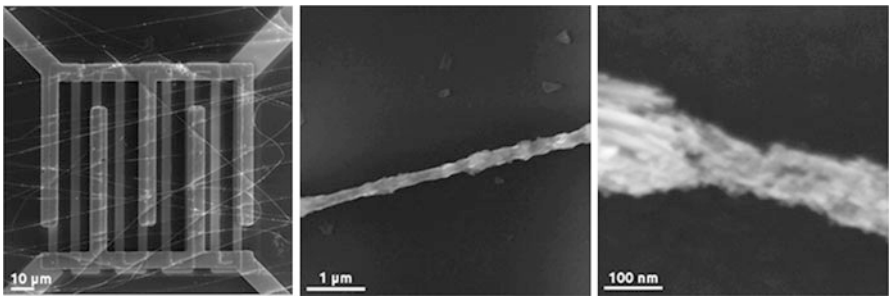

Fig. 10.13 Porous tungsten oxide nanofibers as a special chip designed for gas sensor

heat treatment at 300 °C, 90 min, in air. For the better sensing properties, the Au-decorated MWCNTs were added to hex-WO_3 nanopowder. Chemical gas sensors based on hex-WO_3 operating at 250 °C showed a good potential to detect very low amounts of NO_2 and at 300 °C showed the good sensitivity on NH_3, but they significantly lose this sensing characteristic at lower operating temperatures, while at room temperature they could not detect NO_2 at all. Hex-WO_3/Au-decorated MWCNTs composites were able to detect as low as 100 ppb of NO_2, with no need to heat the sensors substrates during operation. The detected concentration level is very close to the ambient air quality standard for nitrogen dioxide established by the North Carolina Department of Environment and Natural Resources, USA (i.e., 53 ppb [24]), which demonstrates the high potential of our new gas sensors. The porous tungsten oxide nanofibers can be applied on a special chip designed for gas sensor.

Acknowledgements The work was supported by the bilateral NSF-OTKA-MTA co-operation, contract # MTA:96 OTKA: 049953. The authors are grateful to Felten and Pireaux for providing to this study the metal decorated CNTs. Many thanks to Tóth for SEM, Ionescu and Prof. Gouma for sensor measurements. We acknowledge the financial help from NIH-DST Hungarian-Indian program.

References

1. Solonin YM, Khyzhun OY, Graivoronskaya EA (2001) Nonstoichiometric tungsten oxide based on hexagonal WO_3. Cryst Growth Des 1:473
2. Kim G-S, Lee YJ, Kim D-G, Kim YD (2008) Consolidation behavior of Mo powder fabricated from milled Mo oxide by hydrogen-reduction. J Alloy Compd 454:327
3. Gillet M et al (2007) Growth, structure and electrical conduction of WO_3 nanorods. Appl Surf Sci 254:270–273
4. Stankova M, Vilanova X, Llobet E, Calderer J, Bittencourt C, Pireaux JJ, Correig X (2005) Influence of the annealing and operating temperatures on the gas sensing properties of rf sputtered WO_3 thin-film sensors. Sens Actuator B 105:271–277

5. Choi YG, Sakai G, Shimanoe K, Yamazoe N (2004) Wet process-based fabrication of WO_3 thin film for NO_2 detection. Sens Actuator B 101:107–111
6. Balazsi C, Sedlackova K, Llobet E, Ionescu R (2008) Novel hexagonal WO_3 nanopowder with metal decorated carbon nanotubes as NO_2 gas sensor. Sens Actuator B 133(1):151–155
7. Boulova M, Gaskov A, Lucazeau G (2001) Tungsten oxide reactivity versus CH_4, CO and NO_2 molecules studied by Raman spectroscopy. Sens Actuator B 81:99–106
8. Vallejos S, Khatko V, Calderer J, Gracia I, Cané C, Llobet E, Correig X (2008) Micro-machined WO_3-based sensors selective to oxidizing gases. Sens Actuator B 132:209–215
9. Yang J-C, Dutta PK (2009) Solution-based synthesis of efficient WO_3 sensing electrodes for high temperature potentiometric NOx sensors. Sens Actuator B 136:523–529
10. Comini E, Ferroni M, Guidi V, Faglia G, Martinelli G, Sberveglieri G (2002) Nanostructured mixed oxides compounds for gas sensing applications. Sens Actuator B 84:26–32
11. Yang J-C, Dutta PK (2007) Promoting selectivity and sensitivity for a high temperature YSZ-based electrochemical total NOx sensor by using a Pt-loaded zeolite Y filter. Sens Actuator B 125:30–39
12. Reyes LF, Hoel A, Saukko S, Heszler P, Lantto V, Granqvist CG (2006) Gas sensor response of pure and activated WO_3 nanoparticle films made by advanced gas reactive gas deposition. Sens Actuator B 117:128–134
13. Mohammed AA, Gillet M (2002) Phase transformations in WO_3 thin films during annealing. Thin Solid Film 408:302–309
14. Akiyama M, Zhang Z, Tamaki J, Miura N, Yamazoe N, Harada T (1993) Tungsten oxide-based semiconductor sensor for detection of nitrogen oxides in combustion exhaust. Sens Actuator B 14:619–620
15. Xu Z, Vetelino JF, Lee R, Parker DC, Vac J, Tracy CE, Benson DK (1986) Preparation of amorphous electrochromic tungsten oxide and molybdenum oxide by plasma enhanced chemical vapor deposition. Sci Technol A 4:2377
16. Kaneko H, Nishimoto S, Miyake K, Suedomi N (1986) Physical and electrochemichromic properties of rf sputtered tungsten oxide films. J Appl Phys 59:2526–2534
17. Pal S, Jacob C (2007) The influence of substrate temperature variation on tungsten oxide thin film growth in an. HFCVD system. Appl Surf Sci 253:3317–3325
18. Shieh J, Feng HM, Hon MH, Juang HY (2002) WO_3 and W-Ti-O thin film gas sensors prepared by sol-gel dip coating. Sens Actuator B 86:75–80
19. Espinosa EH, Ionescu R, Chambon B, Bedis G, Sotter E, Bittencourt C, Felten A, Pireaux J-J, Correig X, Llobet E (2007) Hybrid metal oxide and multiwall carbon nanotube films for low temperature gas sensing. Sens Actuator B 127:137–142
20. Balázsi C, Kalyanasundaram K, Ozkan Zayim E, Pfeifer J, Tóth AL, Gouma PI (2006) Tungsten oxide nanocrystals for electrochromic and sensing applications. In: Freiman S (ed) Proceedings of the 1st international congress on ceramics. Wiley, Toronto, pp 1–6
21. Balázsi C, Farkas-Jahnke M, Kotsis I, Petrás L, Pfeifer J (2001) The observation of cubic tungsten trioxide at high temperature dehydration of tungstic acid hydrate. Solid State Ion 141–142: 411–416
22. Balázsi C, Özkan Zayim E (2007) Preparation and characterisation of $WO_3.1/3H_2O$ thin films. Mater Sci Forum 537–538:113–120
23. Pfeifer J, Balázsi C, Kiss BA, Pécz B, Tóth AL (1999) The influence of residual sodium on the formation and reductive decomposition of hexagonal tungsten oxide. J Mater Sci Lett 18: 1103–1105
24. http://daq.state.nc.us/rules/rules/D0407.pdf

Chapter 11
Noise Reduction in (Bio-) Chemical Sensors Functionalized with Carbon Nanotube Multilayers

F.V. Gasparyan

Abstract Low frequency noise's investigation in (bio-)chemical sensors on the base of electrolyte-gate field-effect devices, such as capacitive electrolyte-insulator-semiconductor (EIS) structures functionalized with single-walled carbon nanotubes (SWCNT) were carried out. At frequencies below 10 Hz, noise-reduction effect has been revealed in a functionalized EIS structure. This effect depends on the applied gate voltage and is stronger in the depletion regime. The presence of an additional SWCNT multilayer leads to essential reduction (by the factor of up to 100) of the 1/f-noise in comparison to bare EIS structure. A modified charge fluctuation noise model is developed. The model is successfully used for the explanation of noise peculiarities of p-Si/SiO_2/Ta_2O_5/electrolyte and p-Si/SiO_2/Ta_2O_5/dendrimer/SWCNT/electrolyte bio-chemical sensors. The results of noise spectra investigation should be taken into account for sensitivity enhancement of capacitive EIS biosensors, especially to improve the lower detection limit.

Keywords Electrolyte-insulator-semiconductor • Sensor • Charge fluctuation

11.1 Introduction

The functionalization of electrolyte-gate field-effect devices (FED), like ion-sensitive field-effect transistors (ISFET), capacitive EIS structures with the nano- and biomaterials is one of the most attractive approaches for the development of (bio-)chemical sensors and biochips. Since FEDs are charge sensitive devices, each (bio-)chemical reaction leading to chemical or electrical changes at the gate insulator/electrolyte interface can be detected by coupling the gate with respective

F.V. Gasparyan (✉)
Department of Physics of Semiconductors and Microelectronics, Yerevan State University,
1 Alex Manoogian St., 0025 Yerevan, Republic of Armenia
e-mail: fgaspar@ysu.am

A. Vaseashta and S. Khudaverdyan (eds.), *Advanced Sensors for Safety and Security*,
NATO Science for Peace and Security Series B: Physics and Biophysics,
DOI 10.1007/978-94-007-7003-4_11,

chemical or biological recognition elements. These devices were shown to be versatile tools for detecting pH, ion concentrations, enzymatic reactions, charged macromolecules (DNA-deoxyribonucleic acid, proteins, polyelectrolytes), cellular metabolism and action potentials of living cells, as well as for bio-computing logic gates (see e.g., [1, 2]). More recently, nanoparticles, silicon nanowires (NW) and carbon nanotubes (NT) have attracted significant interest as promising materials for novel nanoscale bioelectronic devices and gas sensors [3–8], due to their excellent mechanical, electronic and chemical properties, leading to an enhanced sensor performance. SWCNT employed in a FET layout can be used as sensors for molecular adsorption. ChemFETs based on silicon NWs, CNTs, and other nanomaterials have already proved to be very useful in detection of macromolecular complexes such as proteins, biomolecules and toxic gases [9–12]. These nanosensors can also be useful in nanomedicine, which refers to highly specific medical inventions at the molecular scale, enabling detection of proteins and other biomolecules released by cancer cells. The physical properties limiting sensor devices in planar semiconductors can be readily overcome by exploiting nanoscale devices. Binding to the surface of a NT or NW can lead to depletion or accumulation of carriers in the bulk of the nanometer diameter structure and increasing sensitivity to the point that single molecule detection.

Noise investigations in functionalized FEDs are especially important in the case of an application of FEDs for the measurement of low analyte concentrations, for the detection of biomolecules by their intrinsic molecular charge, as well as for the monitoring of action potential of living cells, where the sensor output signal can be very small. Moreover, development of noise spectroscopy in functionalized FEDs can give additional insight into the detection mechanisms of the biosensors. On the other hand, noise measurements could be very sensitive method for the analysis of semiconductor/other media (e.g. metal, insulator, semiconductor, electrolyte, gaseous) interface quality as well as for the quantitative determination of an analyte concentration, as it has been shown for H_2 gas sensors in [13, 14].

The combination of operation in aqueous solution, high sensitivity, and the unique 1D geometry with a critical dimension in the size range of individual biomolecules makes CNTs outstanding biosensors. A next challenge in the use of NTs as biosensors is to push the sensitivity down to the lowest analyte concentrations [15] and ultimately down to single molecule sensitivity. In this context, optimizing the signal-to-noise ratio (SNR) is a crucial aspect, which has been given little attention to date. Low frequency (LF) noise of CNT transistors, which exhibits a 1/f-type spectrum [16] reveals a strong gate dependence [17, 18] consistent with a recently proposed charge noise model [17, 19]. The well-established high sensitivity of SWNT FETs as bimolecular detectors demonstrates that various fluctuating entities in the environment lead to a high level of noise in these devices. In [17] the mechanism responsible for the LF noise in liquid-gated SWNT-FETs and its scaling with the length of the NT channel down to the nanometer scale was investigated. It is shown that the gate dependence of the noise amplitude provides strong evidence for charge-noise model. It is find that spectral density of the charge noise scales as the inverse of the channel length of the SWNT-FET. Measurements show that the ionic

strength of the surrounding electrolyte has a minimal effect on the noise magnitude in SWNT-FETs. The observation reported in [18] shows 1/f-noise in CNTFETs as a function of gate potential. In order to avoid additional LF noise contribution from SiO_2-NT interactions, the measurements were carried out in conducting liquid. In [20] demonstrated the drastic improvement of sensitivity (SNR) in CNTFET sensors. Authors of [20] also investigated the sensing operations of CNTFET pH sensors and biosensors using A.C. Sensing performances in CNTFET sensors were dramatically improved. The SNR of pH sensors measured by A.C. was six times higher than that by D.C. measurement.

Experiments on various types of nanochannels and nanopores, both biological and artificial, showed random fluctuations of the channel conductivity. The fluctuations result from random transitions between different conductivity states of the channel. It is now widely accepted that LF noise is produced by fluctuations in sample conductance. In general, if diffusive transport is assumed, the conductance σ is proportional to both carrier mobility μ and carrier concentration n:

$$\sigma = e\mu n.$$

In principle, both n and μ can contribute to the 1/f-noise. Numerous LF noise models have been proposed for different types of materials [21] and they usually divide into two general categories, namely, number (Δn) and mobility ($\Delta\mu$) fluctuations models. Besides, a combination and modification of both models applicable for many types of conventional FETs and other semiconductor devices was proposed [17, 22, 23]. The LF noise of liquid-gated SWNT-transistors reveals a 1/f-type spectrum, where the noise power is inversely proportional to the length, L, of the SWNT [17, 18, 24]. As shown by Tersoff [19], the LF noise is described by an augmented charge-noise model. Results of LF noise in functionalized EIS sensors and peculiarities of corresponding noise model are investigated and presented.

11.2 pH Sensitivity and LF Noise in EIS Sensors

Before the noise experiments, the pH sensitivity of bare and functionalized pSi-SiO_2-Ta_2O_5 sensors has been tested in buffer solutions of pH 3–11. The EIS sensors with bare Ta_2O_5 gate-insulator showed a pH sensitivity of about 56–57 mV/pH, that is in good agreement to values typically reported for a Ta_2O_5 layer [25]. The presence of the PAMAM/SWNT film did not affect significantly the pH sensitivity of the EIS structure (54.5 mV/pH). The behavior may be attributed to high porosity of the PAMAM/SWNT film allowing penetration of H^+- or OH^--ions to the Ta_2O_5 surface. Noise spectra in bare and functionalized EIS sensors were measured in a buffer solution of pH 3, 7, and 11 in a frequency range from 0.03 to 100 Hz using the experimental setup shown in Fig. 11.1.

A voltage from battery E was applied to the EIS structure via load resistance ($R = 10$ MΩ) and an Ag/AgCl liquid-junction reference electrode (RE). The

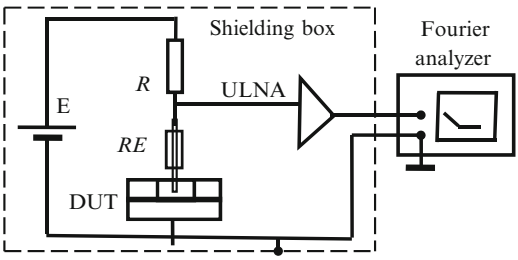

Fig. 11.1 Experimental setup for noise measurements. *E* battery, *R* load resistance, *DUT* device under test, *ULNA* ultra low noise amplifier

EIS sensor was coupled to a ultra-low noise current amplifier (ULNA). The ULNA-output was connected to an HP 35670A dynamic signal analyzer that records the noise signal. The measuring cell with the EIS sensor, reference electrode and ULNA were placed in a shielding box for protecting from external electromagnetic influences. The gate leakage current and LF noise spectra were measured in accumulation, depletion and inversion regions by applying different gate voltages. The gate leakage current was in nA range (accumulation range) or less (depletion and inversion range). As an example, Fig. 11.2 demonstrates the gate-voltage noise spectral density (NSD, S_V) as a function of frequency for the bare (a) and functionalized EIS structures (b), recorded in pH7 buffer solution at the applied gate voltages, V_G, of −1.5, −1.2, −0.4, 0, and 0.5 V. The measured NSD exhibits $1/f^{\gamma}$ dependence with an exponential slope of $\gamma \approx 0.8$ and $0.8 \leq \gamma \leq 1.8$ for the bare and functionalized EIS sensor, respectively. The pH value of the buffer solution did not affect significantly the NSD. It has previously been reported that the gate-referred 1/f-noise in pH ISFETs is also independent of pH, which may suggest that the interface between the solution and the gate insulator does not contribute to 1/f-noise and the origin of LF noise in these ISFET devices is trapping-detrapping of carriers at the Si-SiO_2 interface [26]. The noise in bare EIS structure shows clear dependence on the applied gate voltage in the accumulation and depletion ranges (see Fig. 11.2a).

Moreover, the LF noise is higher in the accumulation range. Similar effect has been reported for an Al-SiO_2-Si metal-oxide-semiconductor capacitor [27] and explained by the gate-voltage dependent changes of the relative position of the Fermi level and in the occupancy of the oxide trap levels, resulting in a modulation of the current paths or charge carriers passing through the device. This suggestion is supported by the fact that gate leakage current in our EIS structures was much higher in the accumulation range. In contrast to the bare EIS structure, the gate-voltage referred effects in the LF noise of a functionalized EIS sensor are suppressed (Fig. 11.2) that could be attributed to the presence of the PAMAM/SWNT multilayer. Surprisingly, at frequencies of $f < 10$ Hz, noise-reduction effect has been revealed in a functionalized EIS structure. This effect depends on the applied gate voltage and is stronger in the depletion regime. As can be seen in Fig. 11.2, the presence of an additional PAMAM/SWNT multilayer leads to essential reduction (by the factor of up to 100) of the 1/f-noise in the depletion mode in comparison to bare EIS structure.

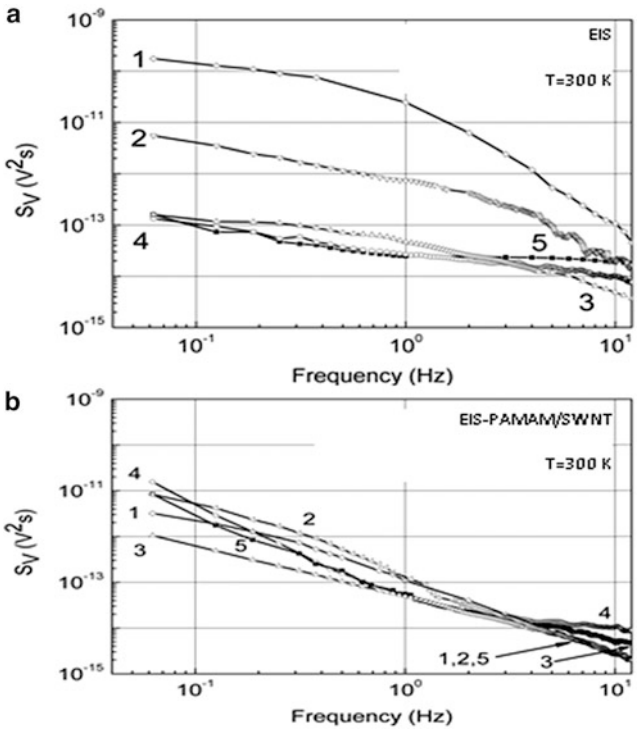

Fig. 11.2 NSD S_V vs. frequency for (**a**) bare and (**b**) functionalized EIS structure, measured at V_G (V): (*1*) −1.5, (*2*) −1.2, (*3*) −0.4, (*4*) 0, and (*5*) 0.5 V

11.3 Charge Fluctuation LF Noise Model for the Capacitive EIS Sensor

EIS sensor consists of a RF, electrolyte, insulator, and semiconductor structure. LF-noise is primarily caused by the fluctuation of the number of carriers (ions and molecules) trapped to and de-trapped from the traps located at the oxide-electrolyte interface by semiconductor surface potential fluctuation and semiconductor bulk generation-recombination (g-r) processes due to the carriers number, mobility and unified number-mobility fluctuations in the semiconductor [21, 22, 28–30]. The physical origin of LF noise in EIS sensors is the result of a collective effect of several processes (see Fig. 11.3). According to the trapping-detrapping model, known also as the number fluctuation model [22, 30], the electrolyte exchanges ions with the oxide traps. It is shown [22] that the flicker noise in MOS transistors can be described using the trap-charge fluctuation mechanism, which produces a mobile carrier number fluctuation and is correlated with the surface mobility fluctuation. In [31, 32], an alternative model for 1/f-noise is considered in solid-state nanopores in which the LF noise originates from surface charge fluctuations.

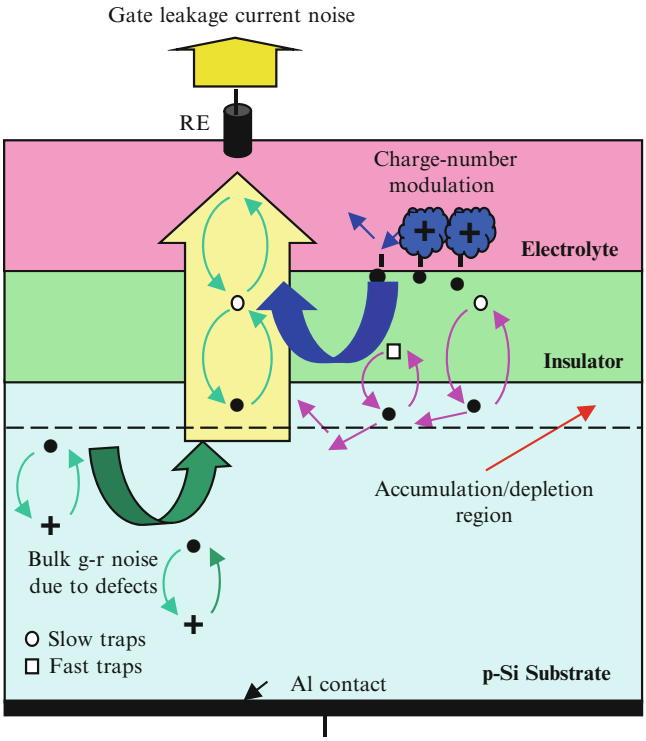

Fig. 11.3 Schematic presentation of EIS sensor structure showing main trapping-de-trapping processes

Recently, for explanation of the LF noise behavior of a sandwich-type structure of Al/p-Si-/SiO_2/Ta_2O_5/Ag the model of charge fluctuation is used [32]. Experimental studies of the dependence of the excess noise on pH and electrolyte concentration indicate that the noise arises from surface (interface) charge fluctuations. There are several types of transitions, which depend on the nature and density of the traps. Usually one is assumed that oxide traps are uniformly distributed in space and energy. Noise emerging from electrochemical processes at the electrolyte-dielectric interface is additional to the expected noise level for chemical and biosensors. For an electrode-electrolyte interface noise can arise from charge transfer in the bulk electrolyte. Noise models for charge transfer across the electrode/electrolyte interface and trapping-detrapping on the oxide/electrolyte interface are described in [28, 32]. These are composed of noise components caused by the resistance at the interface (due to diffuse region) and redox-generated noise. All noise sources for purely passive resistances can be considered by white noise sources.

The electrolyte can be considered as an efficient capacitor, and the total gate capacitance is the combination of the quantum capacitance and electrochemical double-layer capacitance. Thus, fluctuation of number of charge carriers (protons

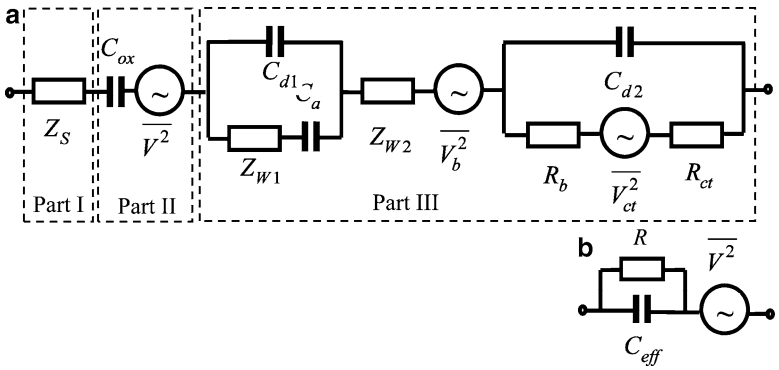

Fig. 11.4 Equivalent scheme of the EIS sensor structure: (**a**) build-up, (**b**) simplified

and ions) in the electrolyte (that also causes a variation of the semiconductor surface potential) can result in a change of the carriers' number near to the semiconductor/insulator interface in the oxide and can be suggested as the main source for the 1/f-noise, where the trapping-detrapping of the charges results in a surface potential and consequently voltage fluctuations.

For detailed noise analyses of EIS and ISFET biosensors it is convenient to use a noise equivalent scheme [28, 33]. For the electrical equivalent scheme for EIS noise analysis one can present the following components (see, Fig. 11.4a: built-up scheme, (Fig. 11.4b): simplified scheme): Part I–"Semiconductor", Part II–"Insulator" (SiO_2), Part III–"Electrolyte". In Fig. 11.4a, Z_S is the semiconductor impedance (including its resistance and capacitance effects), C_{ox} is the capacitance of the insulator layer (SiO_2), Z_{W1} and Z_{W2} are the Warburg impedances, C_a is the capacitance associated with the adsorbed charge at the oxide-electrolyte interface, $C_{d1(2)} = C_{H1(2)}C_{D1(2)} \big/ (C_{H1(2)} + C_{D1(2)})$ are double-layer capacitances, $C_{H1(2)}$ and $C_{D1(2)}$ are capacitances of the Helmholtz and diffusion layers, respectively, $R_b = \frac{1}{K}\sqrt{\frac{\pi}{wl}}$ is the electrolyte bulk resistance, K is the electrolyte conductivity, w and l are the gate sizes, R_{ct} is the charge transfer-resistance of the electrode, $\overline{V_{ct}^2} = 4kTR_{ct}$ is the thermal noise source of the R_{ct} resistance fluctuations, k is the Boltzmann's constant, and T is the absolute temperature. $\overline{V_b^2} = 4kTR_b$ is the thermal noise source of the R_b resistance fluctuations, and $\overline{V^2}$ is the noise source due to the charge trapping-detrapping in the oxide-electrolyte interface.

For the LF noise analysis one can neglect the influence of Z_{W1}, also for non-Faradaic processes usually $Z_{W2} = 0$ [28]. After neglecting the Warburg impedances and thermal white noise sources, and presenting Z_S as parallel-connected semiconductor bulk resistance (R_{Sb}) and capacitance of the depletion layer (C_d), the equivalent scheme can be simplified (see Fig. 11.4b, where R is the equivalent resistance related with the leakage current), and other parameters, such as C_{eff} and C_d are described as follows.

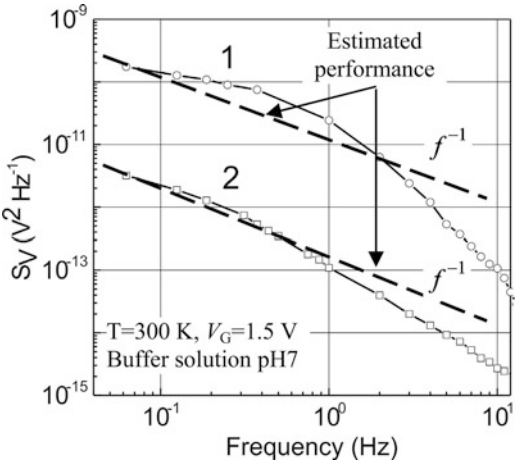

Fig. 11.5 Measured (*open circles*) and calculated (*dashed curves*) according to Eq. (11.6) voltage NSD as a function of frequency for bare (*plot 1*) and functionalized (*plot 2*) EIS structures for case: $A = 0.5\,\mathrm{cm}^2$, $\rho = 5\,\Omega - \mathrm{cm}$, $C_{ox} \approx 30$ nF, $\varepsilon_S = 3.9$, $N_{ot} = 6 \times 10^8\,\mathrm{cm}^{-2}$ ($N_{ot,\,NT} = 4 \times 10^8\,\mathrm{cm}^{-2}$) for C_d using Eq. (11.1)

$$C_{eff} = \frac{C_{ox}C_d}{C_{ox}+C_d}, C_d = \frac{\varepsilon_S}{\sqrt{2}L_D}\frac{1-e^{-\beta\varphi}+\xi\left(e^{\beta\varphi}-1\right)}{\sqrt{e^{-\beta\varphi}+\beta\varphi-1+\xi\left(e^{\beta\varphi}-\beta\varphi-1\right)}}$$
$$\beta = \frac{e}{kT}, \quad \xi = \frac{n_p}{p_p}, \quad L_D = \sqrt{\frac{kT\varepsilon_S}{e^2 p_p}}. \tag{11.1}$$

Here, ε_S is the semiconductor permittivity, φ is the semiconductor surface potential, L_D is the Debye length, e is the electron charge, p_p and n_p are the equilibrium majority and minority carrier concentrations in the semiconductor, respectively, and $\overline{V^2}$ is the noise source.

Note that the simplified scheme in Fig. 11.4b includes processes on the semiconductor/insulator and insulator/electrolyte interfaces, as well as on the semiconductor surface: via C_{eff} and surface potential φ. We consider that these are main processes which are responsible for the leakage current noise. It should be also noted that bulk thermal noise in the semiconductor, insulator and electrolyte can be neglected.

There are several models for the 1/f-noise description in EIS, MOS, MOSFET and ISFET structures: the Hooge's model of mobility fluctuations [21, 22, 29, 34], the McWhorter model of number fluctuations, including its different modifications such as the correlated number-mobility fluctuation model [30, 33], and the charge fluctuation model [22, 31, 32]. We show that only the modified charge fluctuation model can be applied to describe the case of the EIS structures. For discussion, we use two experimental curves from Fig. 11.2 presented in Fig. 11.5 NSD for bare EIS-Al/p-Si/SiO_2/Ta_2O_5/electrolyte/RE (plot 1) and functionalized EIS-Al/p-Si/SiO_2/Ta_2O_5/dendrimer/CNT/RE (plot 2) structures. Details concerning fabrication of EIS structures, measurements technique and results can be found in [7, 8].

One can consider the 1/f-noise source, $\overline{V^2}$ (see Fig. 11.4a), via fluctuation of the oxide trap charge density. The charge density of occupied traps can be described as

$$Q_{ot} = \frac{eN'_{ot}}{wl}, \tag{11.2}$$

where N'_{ot} is the number of occupied traps. Then, the spectral density of the charge fluctuations of occupied traps is

$$S_{Qot}(f) = \left(\frac{e}{wl}\right)^2 S_{N'_{ot}}(f) \tag{11.3}$$

Spectral density of the number fluctuations of occupied traps can be determined as [9]:

$$S_{N'_{ot}}(f) = \frac{wlN_{ot}}{f} \tag{11.4}$$

Substitution of Eq. (11.4) into Eq. (11.6) results in

$$S_{Qot}(f) = \left(\frac{e}{wl}\right)^2 \frac{wlN_{ot}}{f} = \frac{e^2 N_{ot}}{wl}\frac{1}{f} \tag{11.5}$$

The voltage-fluctuation NSD can be calculated using the expression

$$S_V(f) = \frac{S_{Qot}(f)}{C_{eff}^2} = \frac{e^2 N_{ot}}{AC_{eff}^2}\frac{1}{f} \tag{11.6}$$

Here, $A = wl$ is the gate area, N_{ot} is the equivalent density of traps per unit area at the SiO_2/electrolyte interface. It should be emphasized that an increase of the 1/f-noise level with decreasing gate area is a typically registered behavior [22, 28, 31].

11.4 Results and Discussion

According to Eq. (11.6), the noise spectral density S_V strongly depends on the magnitude C_{eff}. In the bare EIS structure a number of binding sites of the insulator surface actively takes part in trapping-detrapping processes with ions and molecules in the electrolyte. Usually, these processes are very slowly. The capacitance C_{ox} and captured charge will slowly fluctuate. On the other hand, the capacitance of the depletion region C_d also depends on charge fluctuations of insulator/semiconductor

and insulator/electrolyte interfaces and fluctuates due to such changes via the surface potential φ. Generally, noise is determined by the modulation of the capacitance of the semiconductor depletion region and surface potential due to charge fluctuations at the insulator/electrolyte interface.

As a result, the level of 1/f-noise has to be relatively high.

The equivalent trap density at the insulator/electrolyte interface can be calculated using Eq. (11.6) and the method of calculation of effective trap density proposed in [32]. Thus, using the noise measurement results, one can estimate the magnitude of the equivalent density of traps per unit area at the insulator/electrolyte interface. In Fig. 11.5; the gate-voltage NSD as a function of frequency for bare (plot 1) and functionalized (plot 2) EIS structures at an applied gate voltage of −1.5 V are shown [7]. The dashed curves are calculated according to Eq. (11.6). At a gate voltage $V \approx -1.5$ V it is: for $f = 0.5$ Hz, $N_{ot} \approx 9 \times 10^8\,\mathrm{cm}^{-2}$ and $N_{ot,FL} \approx 4 \times 10^8\,\mathrm{cm}^{-2}$; for $f = 2$ Hz, $N_{ot} \approx 4.6 \times 10^8\,\mathrm{cm}^{-2}$ and $N_{ot,FL} \approx 1.9 \times 10^8\,\mathrm{cm}^{-2}$. Here, "*FL*" is the functionalized layer. Thus, using noise measurements results one can estimate the magnitude of the equivalent density of traps per unit area for the dendrimer/CNT ensemble, too. Its value is in the range of $N_{ot,FL} \approx (2 \div 4) \times 10^8\,\mathrm{cm}^{-2}$. For comparison, note that for SiO_2, the number of traps is in the same order of magnitude ($10^7\,\mathrm{cm}^{-2}$).

The dashed lines in Fig. 11.5 are plotted according to Eq. (11.6) using the following data and parameters [7, 8]: $d_{ox} = d_{SiO_2} + d_{Ta_2O_5} = 30 + 55 = 85$ nm, $C_{ox} \approx C_d \approx 40 - 50$ nF, $A \approx A_{FL} = 0.5\,\mathrm{cm}^2$, the thickness of three dendrimer/CNT layers is about $d_{FL} \approx 60.5$ nm, $\varepsilon_{FL} \approx 10$, $C_{FL} \approx 1.5 \times 10^{-7} \times A_{NT}$ F. In this case, for the cumulative capacitance, Eq. (11.1) is used.

A modified charge fluctuation noise model is developed. The model presented here is successfully used for the explanation of noise peculiarities of p-Si/SiO_2/Ta_2O_5/electrolyte and p-Si/SiO_2/Ta_2O_5/dendrimer/CNT/electrolyte bio-chemical sensors. The obtained results of noise spectra investigation should be taken into account for sensitivity enhancement of capacitive EIS biosensors, especially with respect to improve the lower detection limit.

References

1. Lee C-S, Kim SK, Kim M (2009) Ion-sensitive field-effect transistors for biological sensing. Sensors 9:7111–7131
2. Fromherz P (2006) Three levels of nanoelectronic interfacing: silicon chips with ion channels, nerve cells, and brain tissue. Ann N Y Acad Sci 1093:143–160
3. Katz E, Willner I, Wang J (2004) Electroanalytical and bioanalytical systems based on metal and semiconductor nanoparticles. Electroanalysis 16:19–44
4. Gun J, Schöning MJ, Abouzar MH, Poghossian A, Katz E (2008) Field-effect nanoparticle-based glucose sensor on a chip: amplification effect of co-immobilised redox species. Electroanalysis 20:1748–1753
5. Patolsky F, Zheng G, Lieber CM (2006) Nanowire-based biosensors. Anal Chem 78:4260–4269

6. Balasubramanian K, Burghard M (2006) Biosensors based on carbon nanotubes. Anal Bioanal Chem 385:452–468
7. Gasparyan FV, Poghossian A, Vitusevich SA, Petrychuk MV, Sydoruk VA, Surmalyan AV, SiqueirJR Jr, Oliveira ON Jr, Offenhausser A, Schöning MJ (2009) Low frequency noise in electrolyte-gate field-effect devices functionalized with dendrimer/carbon-nanotube multilayers. In: Proceedings of the 20th international conference noise and fluctuation, ICNF, Pisa, Italy, 14–19 June 2009, pp 133–136
8. Gasparyan FV, Poghossian A, Vitusevich SA, Petrychuk MV, Sydoruk VA, Siqueira JR Jr, Oliveira ON Jr, Offenhäusser A, Schöning MJ (2011) Low-frequency noise in field-effect devices functionalized with dendrimer/carbon-nanotube multilayers. IEEE Sens J 11:142–149
9. Cui Y, Wei Q, Park H, Lieber CM (2001) Nanowire nanosensors for highly sensitive and selective detection of biological and chemical species. Science 293:1289–1292
10. Chen RJ, Bangsaruntip S, Drouvalakis KA, Kam NWS, Shim M, Li Y, Kim W, Utz PJ, Dai H (2003) Monovalent functionalization of carbon nanotubes for highly specific electronic biosensors. Appl Phys Sci 100:4984–4989
11. Park S, Taton TA, Mirkin CA (2002) Array-based electrical detection of DNA with nanoparticle probes. Science 295:1503–1506
12. Star A, Gabriel J-C, Bradley K, Gruner G (2003) Electronic detection of specific protein binding using nanotube FET devices. Nano Lett 3:459–463
13. Aroutiounian VM, Mkhitaryan ZH, Shatveryan AA, Gasparyan FV, Ghulinyan MZ, Pavesi L, Kish LB, Granquist C-G (2008) Noise spectroscopy of gas sensors. IEEE Sens J 8:786–790
14. Mkhitaryan Z, Gasparyan F, Surmalyan A (2009) Low frequency noises of hydrogen sensors. Sens Transducer 104:58–67
15. Sheehan PE, Whitman LJ (2005) Detection limits for nanoscale biosensors. Nano Lett 5:803–807
16. Collins PG, Fuhrer MS, Zettl A (2000) 1/f noise in carbon nanotubes. Appl Phys Lett 76:894–896
17. Mannik J, Heller I, Janssens AM, Lemay SG, Dekker C (2008) Charge noise in liquid-gated single-waal carbon nanotube transistors. Nano Lett 8:685–688
18. Briman M, Bradley K, Gruner G (2006) Source of 1/f noise in carbon nanotube devices. J Appl Phys 100:013505
19. Tersoff J (2007) Low-frequency noise in nanoscale ballistic transistors. Nano Lett 7:194–198
20. Yamamoto Y, Ohno Y, Maehashi K, Matsumoto K (2008) Carbon nanotube field-effect transistor biosensors with high signal-to-noise ratio using alternating current measurement. In: Nicolini C (ed) Proceedings of the IASTED international conference on nanotechnology and applications (NANA 2008). Acta Press, A Scientific and Technical Publishing Company, Crete, Track 615–043, pp 21–26
21. Hooge FN, Kleinpenning TGM, Vandamme LKJ (1981) Experimental studies on 1/f noise. Rep Prog Phys 44:479–532
22. Hung K, Ko P, Hu C, Cheng Y (1990) A unified model for the flicker noise in metal-oxide-semiconductor field-effect transistors. IEEE Trans Electron Dev 37:654–665
23. Gasparyan FV, Asriyan HV, Melkonyan SV, Corman CE (2010) Method of 1/f noise reduction and noise level manipulation in semiconductor based devices. US Patent Application for Letters Patent of the United States No. 61/332,408, 7 May 2010
24. Behnam A, Ural A, Bosman G (2009) Modeling and measurements of low frequency noise in single-walled carbon nanotube films with bulk and percolation configurations. In: Proceedings of the 20th international conference on noise and fluctuations, ICNF, Pisa, 14–19 June 2009, pp 79–84
25. Lin Y-M, Appenzeller J, Knoch J, Chen Z, Avouris P (2006) Low-frequency current fluctuations in individual semiconducting single-wall carbon nanotubes. Nano Lett 6:930–936
26. Jacobson CG, Nemirovsky Y (1999) 1/f noise in ion sensitive field effect transistors from subthreshold to saturation. IEEE Trans Electron Dev 46:259–261
27. Chim WK, Leong KK, Choi WK (2001) Random telegraphic signals and low-frequency noise in rapid-thermal-annealed silicon-silicon dioxide structures. Jpn J Appl Phys 40:1–6

28. Hassibi A, Navid R, Dutton RW, Lee TH (2004) A comprehensive study of noise processes in electrode-electrolyte interfaces. J Appl Phys 96:1074–1082
29. Hooge FN (1969) 1/f noise is no surface effect. Phys Lett A 29:139–140
30. Tian H, Gamal AE (2001) Analysis of 1/f noise in switched MOSFET circuits. IEEE Trans Circuit Syst-II Analog Digit Signal Process 48:151–157
31. Smeets RM, Dekker NH, Dekker C (2009) Low-frequency noise in solid-state nanopores. Nanotechnology 20(9):095501
32. Gasparyan FV, Mkhitaryan ZH, Surmalyan AV (2009) Basis structure of (bio-) chemical sensors: comparative analysis of CVC and noises. In: Proceedings of the 7th international conference on semiconductor micro- and nanoelectronics, Tsakhcadzor, 3–5 July 2009, pp 101–104
33. Snow ES, Novak JP, Lay MD, Perkins FK (2004) 1/f noise in single-walled carbon nanotube devices. Appl Phys Lett 85:4172–4174
34. Melkonyan SV, Aroutiounian VM, Gasparyan FV, Asriyan HV (2006) Phonon mechanism of mobility equilibrium fluctuation and properties of 1/f-noise. Phys B Phys Condens Matter 382:65–70

Chapter 12
Polymer Nanocomposite Films as a Potential Sensor

A. Grozdanov, A. Tomova, and A. Dimitrov

Abstract Polymer composites using carbon nanotubes (CNTs) are fast growing class of materials since CNTs exhibit a high aspect ratio, unique electrical, mechanical and structural properties which contribute to novel characteristics for engineering applications such as actuators, hydrogen storage, chemical sensors and nanoelectronic devices. Several papers have been published utilizing CNTs as the sensing material in pressure, flow, thermal, gas, optical, mass, strain, stress, chemical and biological sensors. Amongst many of its superior electro-mechanical properties, piezoresistive effect in CNTs is attractive for sensor design. When CNTs are subjected to a mechanical strain, a change in its chirality leads to modulation of its conductance. For this investigation, biocompatible polymer matrices prepared using PMMA and PCL were used to provide good interfacial bonding between VNTs. MWCNT mixed in 0.2, 0.5 and 1.0 % w/w content were used for the preparation of polymer nanocomposites. PMMA-based nanocomposites were prepared via the mixing of the MWCNT and polymer in a dichloromethane solution, while for the PCL-based nanocomposites as a solvent tetra-hyrofurane was used. Characterization of the nanocomposite films was performed by DSC, TGA, WAX, FTIR and SEM, as well as electrical measurements. Sensor activity was followed through the changes in the electrical conductivity of the nanocomposite films indicating that MWCNT into polymer matrix significantly changes their properties.

Keywords Carbon nanotubes • Nanocomposites • Sensors

A. Grozdanov (✉) • A. Tomova • A. Dimitrov
Faculty of Technology and Metallurgy, University Ss Cyril and Methodius, Rugjer Boskovic 16, 1000 Skopje, Republic of Macedonia
e-mail: anita@tmf.ukim.edu.mk; anita.grozdanov@yahoo.com

A. Vaseashta and S. Khudaverdyan (eds.), *Advanced Sensors for Safety and Security*,
NATO Science for Peace and Security Series B: Physics and Biophysics,
DOI 10.1007/978-94-007-7003-4_12,

12.1 Introduction

Chemical and mechanical multi-nanosensors can be described as devices composed of a sensitive part which, interacting with the surrounding environment, collects and concentrates molecules and structural elements at or within the surface which thereupon undergoes physical changes. A transducer converts these changes in the sensing part into an interpretable and quantifiable signal. The heart of a multi(functional) – nanosensor is a sensitive element, which is the interface between transducer and external environment, such that the nature and the selectivity of the sensor depend upon these interactive materials. An ideal sensor must have high sensitivity (ppb detection), high selectivity (chemical and biological), fast response time (< seconds), fast recovery time (< minutes), and inexpensive. The list of most promising materials for multi-nanosensors includes polymers, ceramics, metals, nanostructured materials and nanocomposites, molecular sieves, sol-gels, biomaterials and their combinations [1–7]. Thus, for design and development of multi-nanosensors and their performances, proper and detailed physical, chemical and structural characterization of the sensing materials are essential for a complete understanding of their properties.

New research directions in the area of nanostructured materials science, device engineering and circuits are facilitating the design of novel multi-nanosensors based on carbon nanotubes (CNTs). Amongst many of their superior electro-mechanical properties, the great adsorptive capacity of CNTs due to the larger surface area-to-volume ratio that contributes to high sensitivity and fast response time. The gas detection principle is based on the change in electrical resistance of the thin films due to the presence of organic vapors. Most of the sensors based on CNTs are field effect transistors (FETs), since in the past great interest has been focused on the study of the changes in their electrical properties as a consequence of the interaction with gaseous species; these electrical properties are extremely sensitive to the effects of charge transfer and chemical doping by various molecules (Fig. 12.1). Another advantage of CNTs based sensors is the fact that they operate at room temperatures compared to the other solid-state sensors that operate at higher temperatures (T > 400 °C).

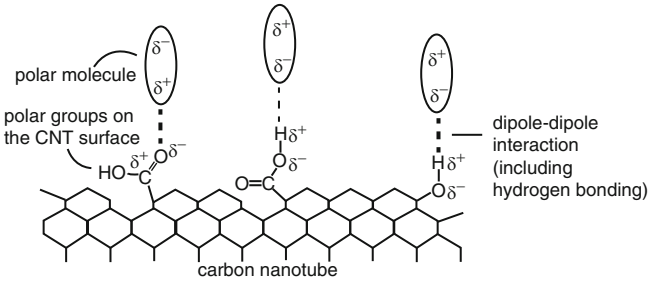

Fig. 12.1 Interactions of gas molecules with carbon nanotubes

Table 12.1 Summary of sensing performance of organic polymer/MWCNT sensors as chemiresistor

Organic polymer	Targeted analytes	Detection limit	Response time [s]	Reversibility	Reference
PMMA	Acetone, Chloroform	N/S	2–5	Reversible	Abraham et al. [8]
Poly(3-methyl-thiophene)	CH_2Cl_2 $CHCl_3$ CCl_4 CH_4	N/S	60–120	Reversible	Santhanam et al. [9]
Poly (vinyl acetate)	Ethanol, Cyclohexane, Tetrahydrofuran	N/S	1,200	Reversible	Wei et al. [10]
Polyaniline	Triethylamine	500 ppb	200–400	Reversible	Li et al. [11]

Note: *N/S* not-stated

To prepare CNT/polymer nanocomposites, several problems had to overcome, viz. to obtain uniform dispersion of CNTs in a polymer matrix despite the insolubility of CNTs and inherently poor compatibility between the CNTs and polymers. In direct blending of CNTs and polymers, the nanotubes tend to aggregate; and such nonuniform dispersions in the polymer matrix often results in deleterious effects. The second main approach is the utilization of biodegradable and biocompatible polymeric materials such as Poly Methyl Methacrylate (PMMA), Polylactide (PLA), Poly(-caprolactone) (PCL) and Poly(3-hydroxybutyrate) (PHB).

Biocompatible nanocomposites based on CNTs and biopolymer matrices are still subject of great research interest, especially with respect to the effects of carbon nanotubes on the thermal and mechanical behavior of the composites, as well as the utilization of piezoresistive effects in CNT/polymer nano-composites, which opens up the field of biomedical/biomechanical applications of these hybrids (Table 12.1).

Fujiware et al. studied adsorption properties of CNT bundles using the N_2 and O_2 and their structures [2]. The effect of the adsorption of several gases on CNTs was also described by Zahab et al. [3]. Sumanasekera et al. have created a thermoelectrical chemical sensor to measure reversibly thermoelectrical power changes of carbon nanotubes in contact with He, N_2 and H_2 [4]. Kang et al. [5] have worked on polymethylmethacrylate (PMMA) based CNT/PMMA strain sensors for structural health monitoring, such as the Florida Advanced Center for Composite Technologies. Here MWCNT/PMMA strain sensors were studied, comparing solution prepared sensors with dry-blended ones. Dharap et al. [6] studied MWNT/polycarbonate strain sensors and published gauge factors 3.5 times larger than that of typical strain gauges (5 % MWNTs).

In this report, novel CNTs/biocompatible polymer nanocomposite films were investigated to develop a bio-nano gas sensor utilizing the effect of a MWCNTs/polymer nanocomposites chemiresistor for the detection of organic vapors. Multi-walled carbon nanotubes were used because they can be grown longer than

single wall carbon nanotubes, are stiffer, more resistant, and have larger diameter (∼70 nm). MWCNTs were also select in order to reduce the cost for real application. They can be integrated into the material (composite) and serve both sensor and structural functions.

12.2 Experiment

The PMMA/MWCNT nanocomposite films were prepared by the solution casting method, via ultrasonic mixing of the MWCNT and the polymer matrix in a dichloromethane solution (Fig. 12.2), while for the PCL-based nanocomposites, tetrahydrofurane solvent was used. MWCNT (d = 30–50 nm, purity > 95 %), untreated and thermally oxidized, were used for preparation of Poly(Methyl Metacrylate) and Poly(ε-caprolactone) based nanocomposites. The main reason why this solution casting method was used is because of the satisfied dispersion (dispersion is consistent and reproducible) obtained due to the low viscosity of the mixture and this method works with small sample sizes. MWCNT-surface was modified by thermal oxidation at 490 °C for 40 min and thermogravimetric analysis (TGA) of thermally oxidized CNTs are presented in Fig. 12.3.

Characterization of the polymer/MWCNTs nanocomposite films was performed by differential scanning calorimetry (DSC), TGA, Fourier-transform infrared (FTIR) and Raman spectroscopy, X-ray analysis and scanning electron microscopy (SEM).

DSC measurements were performed with a DSC system (Mettler Star) under nitrogen atmosphere in the non-isothermal regime (heating rate = 10 K/min, cooling rate = 10 K/min). All specimens were weighted to be in the range of 8–9 mg. TGA was performed in the range of 50–800 °C with heating rate of 20 K/min (in nitrogen) using a Perkin Elmer Pyris DIAMOND TGA/DTA system. FTIR spectroscopy

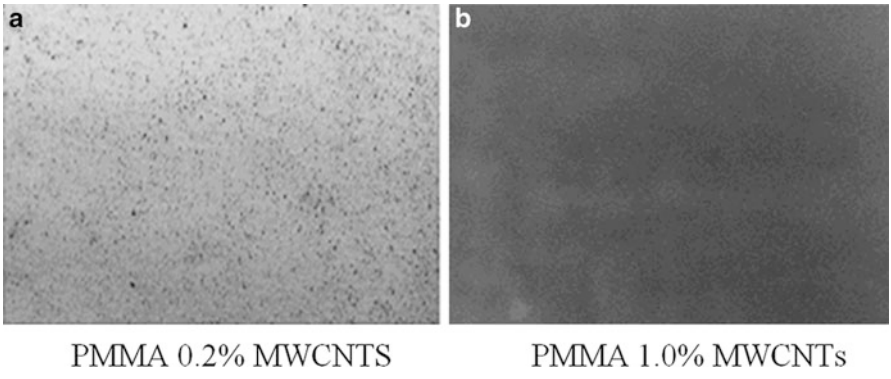

Fig. 12.2 Cast films of PMMA/MWCNTs nanocomposites (**a** − 0.2 % MWCNTS, **b** − 1 % MWCNTs)

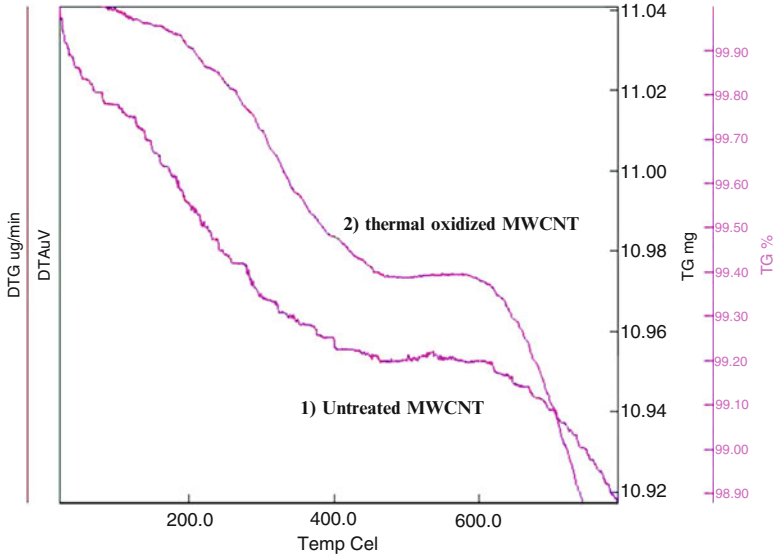

Fig. 12.3 Characteristic TGA/DTA thermograms of untreated and thermally oxidized MWCNTs

was used to characterize the structure of the PMMA/MWCNT and PCL/MWCNT nanocomposites. FTIR spectra were recorded with a Perkin Elmer Paragon 500 analyzer, using 64 scans and a resolution of 2 cm^{-1}. SEM microphotographs were recorded with a FA SEM microscope.

X-Ray diffraction spectra of PMMA and PMMA/MWCNTs nanocomposite films were recorded using a PAN-anlytical X'Pert Pro diffractometer using CuKα radiation between 2 and 40 2. Raman spectra were collected using a 785 nm (Titan sapphire laser), Jobin-Yvon HR640 spectrometer fitted with an Andor Technology CCD detector. The changes in the nanocmposite resistance were followed after exposure of PMMA/MWCNTs nanocomposite films to different gases (chloroform, acetone, toluene, hexane) where the pressure of all solvents was controlled at 25 °C.

12.3 Results

Characteristic thermal data such as the onset temperature T_o, and the glass transition temperature T_g, were determined from DSC curves and the results are shown in Table 12.2. It is evident that as the MWCNT content increased, both transition temperatures (T_o and T_g) were shifted to lower temperatures which indicate on changes in the elastic behavior. The PMMA/MWCNT nano-composites have lower T_g values than the pure PMMA.

Using the DSC technique, characteristic non-isothermal crystallization data such as T_o – the onset crystallization temperature, T_c – the end temperature of

Table 12.2 Characteristic thermal data for PMMA/MWCNT nanocomposites

Sample	T_G [°C]	T_{ONSET} [°C]	ΔC_p [J/GK]
PMMA	116.8	110.9	0.288
PMMA/0.2 % MWCNT	114.8	110.5	0.233
PMMA/0.5 % MWCNT	113.9	109.5	0.295
PMMA/1.0 % MWCNT	112.6	108.7	0.296

Table 12.3 The nonisothermal parameters for PCL and PCL/MWCNT nanocomposites determined by DSC exotherms

Cooling rate [c/min]	Crystallization parameter [°C]	PCL	PCL 0.25 % MWCNT	PCL 0.5 % MWCNT	PCL 1.0 % MWCNT
5	*To*	34.2	39.7	40.0	44.6
	Tc	26.1	32.1	29.5	34.9
	Tp	30.3	36.7	36.0	39.9
10	*To*	31.2	37.2	37.7	42.3
	Tc	20.8	26.7	23.9	29.6
	Tp	27.4	33.3	31.7	36.9
20	*To*	28.8	34.1	35.1	39.7
	Tc	15.4	19.2	16.3	21.9
	Tp	24.9	28.9	27.2	33.3
40	*To*	26.8	30.5	31.8	37.1
	Tc	8.0	7.7	5.4	9.3
	Tp	22.7	28.9	21.6	28.3

crystallization and T_p – the exothermic peak temperature of the crystallization were determined. The results are shown in Table 12.3. It is evident that as the cooling rate increased, all the parameters (T_o, T_c and T_p) were shifted to lower temperatures. The lower the cooling rate, the earlier the crystallization starts. It was noted that the PCL/MWCNT nanocomposites have higher T_p values than the pure PCL at all cooling rates (except for PCL/0.5 % MWCNT at 40 K/min).

This phenomenon could be explained by the heterogeneous nucleation of the MWCNTs suggesting that the melted PCL macromolecule segments can be easily attached to the surface of the rigid nanotubes, which leads to the crystallization of PCL macromolecules at higher temperature.

For the PCL/MWCNT nanocomposites prepared as described above, the linear growth G and the activation energy Ea were determined (Table 12.4). Generally, for increasing MWCNT contents, the values of both parameters increase. A higher content of MWCNTs means more steric hindrance and a reduction of the transportation ability of the polymer chains (higher Ea).

Themogravimetric analysis was used to study thermal stability of the MWCNTs and PMWCNTs/Polymer based nanocomposites (Table 12.5). Characteristic TGA/DTA thermograms of untreated and thermally oxidized MWCNTs are shown in Fig. 12.3, while the characteristic thermograms of PMMA/1.0 % MWCNT are

Table 12.4 Linear growth rate G and activation energy ΔE_a for PCL and PCL/MWCNT nanocomposites

Parameter	PCL	PCL/0.25 % MWCNT	PCL/0.5 % MWCNT	PCL/1.0 % MWCNT
ΔE_a [kJ/mol]	308.6	250.2	257.9	317.0
G [min^{-1}]	3.60×10^3	1.19×10^3	2.06×10^3	3.01×10^3

Table 12.5 Degradation temperatures for PMMA/MWCNT nanocomposites

Sample	*Td* [°C]
PMMA	334.2
PMMA/0.2 % MWCNT	338.2
PMMA/0.5 % MWCNT	338.8
PMMA/1.0 % MWCNT	339.0

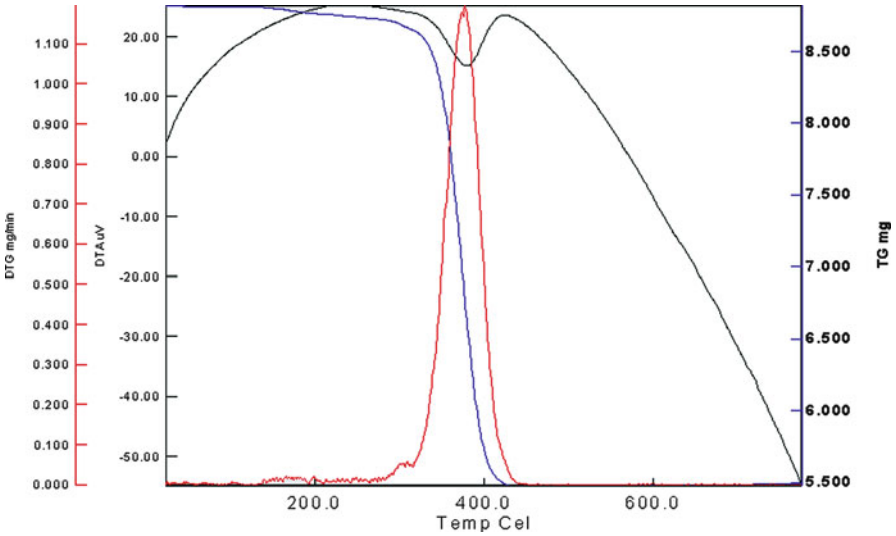

Fig. 12.4 Characteristic TGA/DTA thermograms of PMMA/1 % MWC nanocmposites

shown in Fig. 12.4. It was shown that MWCNTs improved the thermal stability of nanocomposites based on PMMA. Td was shifted by 5°. For the MWCNT/PCL system it was found that temperature of thermal decomposition for MWCNT/PCL nanocomposites was slightly shifted to lower temperatures compared to the pure PCL ($Td_{PCL/1\ \%MWCNT} = 393$ °C, $Td_{PCL} = 395$ °C) probably due to the lower level of dispersion of the MWCNTs in semi-crystalline polymer matrix.

Characteristic diffraction curves for PMMA and PMMA/MWCNT are present in Fig. 12.5. The curve for PMMA (series 2) has shown wider diffraction peak in the range of $2\Theta = 14°$ which suggest that it is amorphous PMMA. Decreased intensity of this peak in the X-Ray analysis of the nanocomposite film (series 1) suggests that it is a compatible nanocomposite system, with compatible mixing of the polymer matrix and MWCNT. Also, some shifting of the diffraction peaks to the lower values was registered for the nanocomposite films indicating changes in

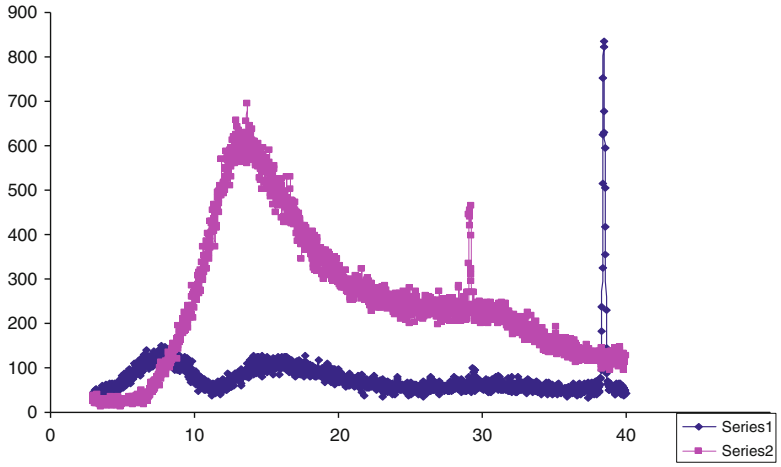

Fig. 12.5 WAX-analysis of PMMA/MWCNT nanocomposite film (*series 1* – PMMA/MWCNT; *series 2* – PMMA)

the interlayer distance. For the PMMA also, sharp peak is registered at $2\Theta = 29°$ which is shifted to $2\Theta = 39°$ in the nanocomposite film. The results achieved show an agreement with the literature data [8].

To evaluate the degree of dispersion of MWCNTs within the polymer matrix, the nanocomposites films have been observed by scanning electron microscopy. The characteristic morphology of the PMMA based nanocomposites was presented in Fig. 12.6 (a: pure PMMA, b: MWCNT, c:PMMAL/1.0 % MWCNT, d: PMMA/0.5 % MWCNT), while in Fig. 12.7 the obtained morphology of PCL based nanocomposites was shown (a: pure PCL, b: PCL/0.5 % CNT, c: PCL/1 % CNT). The SEM images clearly show that homogeneous dispersions of MWCNTs (well-dispersed bright dots) throughout the PMMA matrix are achieved at all CNT contents, although at higher MWCNT content of 1 % smaller aggregates are also formed.

The FTIR spectra of the pure PMMA matrix and PMMA/MWCNT nanocomposites are shown in Fig. 12.8. Besides small peak shifts, there is only one significant change in the compared FTIR peaks of pure PMMA and PMMA/MWCNTs nanocomposites. Namely the C—O stretching bands in pure PMMA matrix at 1,583 cm^{-1} and 1,611 cm^{-1} remarkably decreased in the PMMA/MWCNTs nanocomposites which indicate the changes induced by the presence of MWCNTs in the polymer structure.

The response and the changes of the resistance due to the PMMA/MWCNTs nanocomposite film exposure to gas vapors (for chloroform $\Delta R = 939$, for acetone $\Delta R = 90$, for methanol $\Delta R = 45$) shown that each solvent had its own impact on the resistance and it is good parameter for detection and identification of gases. According to Abraham et al. [8] the electrical response of the PMMA/MWCNTs nanocomposite based gas sensors to organic solvents could be explained by the

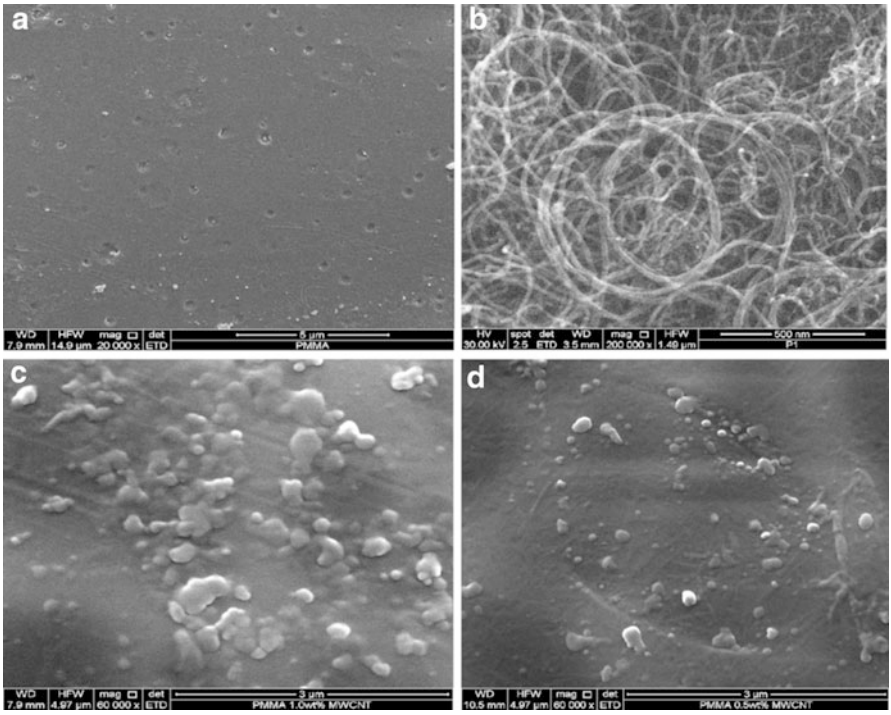

Fig. 12.6 SEM microphotographs of PMMA/MWCNT nanocomposites: (**a**) pure PMMA (×20,000), (**b**) MWCNT (×200,000) (**c**) PMMA/1 % MWCNT (×60,000), (**d**) PMMA/0.5 % MWCNT (×60,000)

following mechanism. Namely, the conducting paths were formed inside the CNT/polymer composites due to quantum mechanical tunneling effects, where the distance among the conducting sticks was such that electron hopping can occur. The contact resistance between CNTs increased due to the distance increase among adjacent CNTs. Swelling of the polymer matrix due to the absorption of organic vapors may also increase the volume and those increase the distance among the nanotubes, thereby increasing the contact resistance. The extent of swelling and hence the electrical response depends on the solubility of the polymer in the solvents.

12.4 Conclusions

The results presented above indicate that introducing MWCNTs into PMMA and PCL significantly changes the properties of the obtained nanocomposite films. Structural changes were shown by X-ray and FTIR spectroscopy. Elastic behaviour

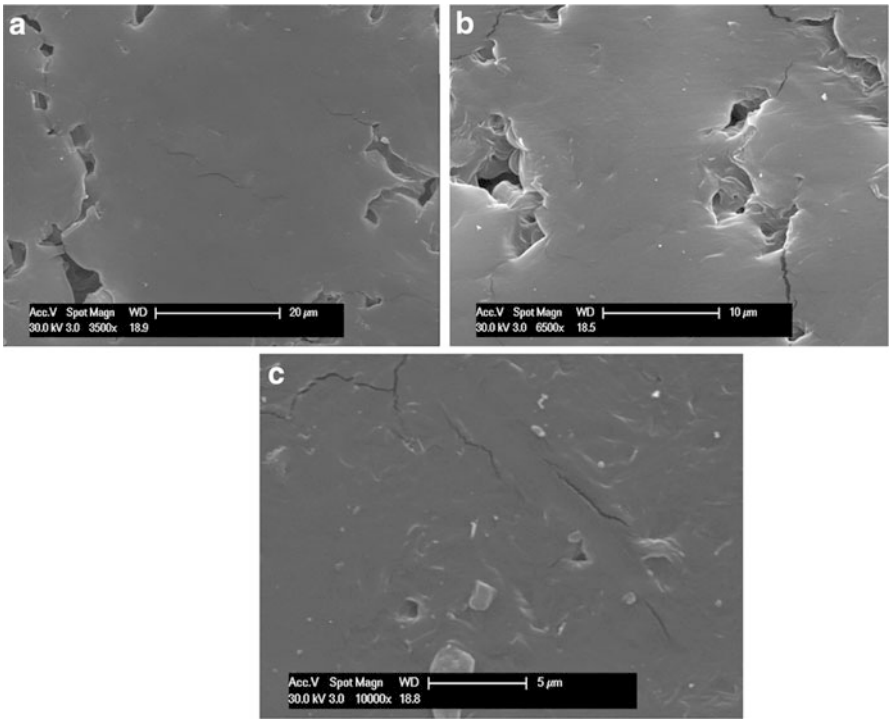

Fig. 12.7 SEM microphotographs of the prepared PCL/CNT nanocomposites; (**a**) pure PCL (×3,500), (**b**) PCL/0.5 %CNT (×6,500), (**c**) PCL/1 %CNT (×10,000)

is evident as exhibited by DSC data for changes of T_g temperature. TGA/DTA analysis as shown improved thermal stability. SEM images shown that a homogeneous dispersion of MWCNT was achieved throughout the PMMA and PCL matrices at all CNT contents. The resistance changes of PMMA/MWCNTs nanocomposites is a good indicator for detection and identification of different gases. So, the potential application of these nanocomposite films could be extended to develop many different types of accurate gas sensors for CO detection, indoor air quality monitoring, automobile exhaust monitoring, gas leak detectors, home food spoilage monitors.

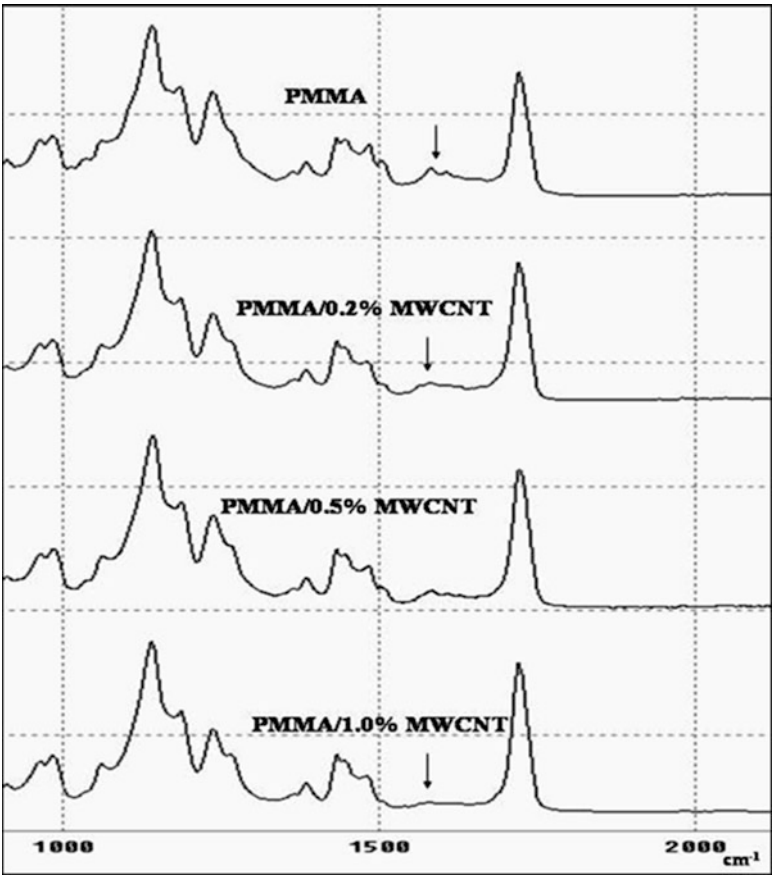

Fig. 12.8 FTIR spectra of PMMA and PMMA/MWCNT nanocomposites

References

1. Sinha N, Ma J, Yeow JT (2006) Carbon nanotube-based sensors. J Nanosci Nanotechnol 6:573–590
2. Fujiware A, Jshii K, Suematsu H, Kataura H, Maniwa Y, Suzuki S, Achiba Y (2001) Gas adsorption in the inside and outside of single-walled carbon nanotubes. Chem Phys Lett 336:205–211
3. Zahab A, Spina L, Poncharal P, Marliere C (2000) Water-vapor effect on the electrical conductivity of a single-walled carbon nanotube mat. Phys Rev B 62:10000–10003
4. Sumanasekera GU, Pradhan BK, Romero HE, Adu CKW, Foley HC, Eklund PC (2002) Thermoelectric chemical sensor based on single wall carbon nanotubes. Mol Cryst Liquid Cryst 387:31–37
5. Kang WP, Wong YM, Davidson JL, Wisitsora A, Soh KL (2003) A novel microelectronic gas sensor utilizing carbon nanotubes for hydrogen gas detection. Sens Actuators B 93:327–332
6. Dharap P, Li Z, Nagarajaiah S, Barrera EV (2004) Nanotube film based on single-wall carbon nanotubes for strain sensing. Nanotechnology 15:379–382

7. Shandas R, Lanning C (2003) Development and validation of implantable sensors for monitoring function of prosthetic heart valves: in vitro studies. Med Biol Eng Comput 41: 416–424
8. Abraham JK, Philip B, Witchurch A, Varadan VK, Reddy CC (2004) A compact wireless gas sensor using a carbon nanotube/PMMA thin film chemiresistor. Smart Mater Struct 13: 1045–1049
9. Santhanam KSV, Sangoi R, Fuller L (2005) A chemical sensor for chloromethanes using a nanocomposite of multiwalled carbon nanotubes with poly(3-methylthiophene). Sens Actuator B106:766–771
10. Wei C, Dai L, Roy A, Tolle TB (2006) Multifunctional chemical vapor sensors of aligned carbon nanotube and polymer composites. J Am Chem Soc 128:1412–1413
11. Li Y, Wang H, Cao X, Yuan M, Yang M (2008) A composite of polyelectrolyte-grafted multi-walled carbon nanotubes and in situ polymerized polyaniline for the detection of low concentration triethylamine vapor. Nanotechnology 19:015503. doi:10.1088/0957-4484/19/01/015503

Chapter 13
Carboxyhemoglobin in Blood of Smokers and Non-smokers Determined by Gas Chromatography with Thermal Conductivity Detector

A. Buha, A. Vaseashta, Z. Bulat, and V. Matović

Abstract The aim of this study was to determine Carboxyhemoglobin (COHb) levels in the blood of smokers and non-smokers using gas chromatography; evaluate the impact of smoking habits; and determine whether living environment has influence on COHb blood content in non-smokers. Blood samples were collected from 127 Belgrade residents of different age and gender and smoking disposition (39 smokers and 88 non-smokers). The samples were analyzed by an Agilent Technologies 6890N gas chromatograph with molecular sieve packed column with thermal conductivity detector. A median value of COHb levels in non-smokers was 0.81 % and in smokers 5.33 %. Strong negative correlation (Pearson's $r = -0.529$) was obtained between COHb levels and time interval between last smoked cigarette and moment of blood sampling with significantly higher COHb levels in smokers who had their last cigarette ≤ 30 min before blood sampling. Statistically significant difference in COHb levels was obtained between residents living in the center of Belgrade, as compared to residents living in suburbs and outskirts of Belgrade with median values of 1.06 and 0.53 %, respectively. The obtained results suggest risk associated with first and second hand CO exposure. The method has greater applicability to test harmful exposure in polluted industries and detonation byproducts in battlefield and subject of nano-toxicity.

Keywords Smokers • Gas chromatography • Carboxyhemoglobin • Nano-toxicity • Blood-sampling

A. Buha (✉) • Z. Bulat • V. Matović
Department of Toxicology Akademik Danilo Soldatović, Faculty of Pharmacy, University of Belgrade, Vojvode Stepe 450, Belgrade, Serbia
e-mail: aleksandra@pharmacy.bg.ac.rs; sandrabuha@gmail.com

A. Vaseashta
Norwich University Applied Research Institutes, Herndon, VA, USA

VTT/AVC U.S. Department of State, Washington, DC, USA
e-mail: prof.vaseashta@ieee.org

A. Vaseashta and S. Khudaverdyan (eds.), *Advanced Sensors for Safety and Security*, NATO Science for Peace and Security Series B: Physics and Biophysics,
DOI 10.1007/978-94-007-7003-4_13,

13.1 Introduction

Carbon monoxide (CO) is one of the most abundant anthropogenic pollutants humans have been exposed to, since the earliest history. This odorless, tasteless and nonirritating gas is a product of the incomplete combustion of carbon-containing materials. Tens of millions of people are exposed to at least one source of CO exposure daily, hundreds of thousands are exposed to at least two sources, and perhaps many thousands are exposed to three or more sources of CO. Literature indicates that chronic exposure to CO can cause serious health problems, not only to people who are exposed to this gas as a result of their profession but also to general population. Smokers are considered to be especially at risk since mainstream tobacco smoke contains high amount of this compound. However, recent studies have proved that non-smokers living in highly polluted areas can be also exposed to high concentrations of CO from car exhaust and second hand smoke. COHb is an adduction product of hemoglobin and CO and can be used as an integral biomarker of human exposure to CO.

Acute inhalation of high concentrations of CO will lead to increased levels of dissolved CO and subsequently to the formation of COHb. When bound to hemoglobin, it displaces oxygen and also shifts the oxygen dissociation curve to the left making the process of oxygen releasing in the body harder. It is also toxic in mitochondria since it alters cytochrome c oxidase (EC 1.9.3.1) in the respiratory chain [1].

Acute inhalation of high amounts of CO can lead to pathological conditions and death. However, recent studies have shown that chronic exposure to CO can also cause serious health problems not only in people exposed to this gas in their profession, but also in general population-smokers and non-smokers living in highly polluted areas [2]. This raised an issue of the slightly but constantly elevated CO levels in blood of people who are exposed to CO from external sources. The exposure of general population to possibly hazardous levels of CO includes exposure to this substance via cigarette smoke which outweighs all the other sources, although car combustion in polluted areas is considered another major source of CO.

To verify the exposure of CO gas to persons, it is essential to measure percent of COHb in blood [3]. Various methods are used for determination of COHb in blood micro-diffusion, viz. colorimetric, infrared absorption, spectrophotometric methods after release of CO from COHb [4]. However, gas chromatography (GC) has been claimed to be the commonly used method for determination of lower COHb concentrations (<5 %) [5]. Detection of CO is possible by using thermal conductivity detector (TCD) [6, 7] or by using flame ionization detection (FID) [8, 9]. Recent studies have introduced using of GC with mass spectrometry [10]. In this paper, we established slightly modified GC method utilizing a thermal conductivity detector (TCD) for determination of COHb levels in blood.

13.2 Materials and Methods

13.2.1 Blood Samples

Blood samples were collected from 127 Belgrade residents of different age, gender and smoking disposition (39 smokers and 88 non-smokers). After providing written and informed consent, they completed a questionnaire about age, smoking history and living environment to include traffic as a possible source for CO contamination. Elapsed time between cigarette smoking and blood donation was also assessed in the questionnaire. Response is provided below in Table 13.1. Samples were collected in 4.5 ml tubes (Vacutte, Greiner Bio-One International AG) containing sodium-citrate.

13.2.2 Analysis

Blood samples (1 ml) were put in headspace vial and were added 0.5 ml releasing agent containing saponin and conc. sulfuric acid [11]. After 24 h, gas phase was

Table 13.1 Demographic over the studied population

Total participants	
	Number (%)
Smokers	30.71
Non-smokers	69.29
Smokers	
Gender	
Male	40.77
Female	59.23
Smoking history	
<10 years	45.64
>10 years	54.36
Time elapsed between last cigarette and blood sampling	
Recent smoking (< = 3 h)	51.28
Late smoking (> 6 h)	48.72
Non-smokers	
Gender	
Male	48.64
Female	51.36
Living areas	
Centre	51.02
Suburbs	48.98

injected and analyzed using gas chromatograph (Agilent Technologies 6890N) with TCD under the following conditions: oven temperature 40 °C, detector temperature 200 °C, carrier gas helium at flow of 4.3 ml/min and molecular sieve packed column. The retention time was 6.3 min. This assay had low limits of detection (0.1 %) and quantification (0.3 %). Calculated calibration curve showed linear relation between concentrations and peak areas ($y = 17.688x + 17.038, R^2 = 0.9933$). The GC/TCD method described is a modified version of the one described by [7].

13.2.3 Statistical Analysis

For statistical analysis we used SPSS (ver.11.5 for Windows). The Kolmogorov-Smirnov test was used to test normality, and since *P* value was less than 0.05, null hypothesis of normal distribution was rejected. Since COHb concentrations do not follow normal distribution, Mann-Whitney non-parametric test was used in all statistical calculations. Furthermore, Pearson correlation analysis was used to determine the relationship between time interval between cigarette smoking and blood sampling and COHb levels in blood. *P* values of <0.05 were considered significant. Carboxyhemoglobin levels are expressed as a percentage of total hemoglobin.

13.3 Results and Discussion

13.3.1 Carboxyhemoglobine Levels-Relation to Smoking

Median value of COHb levels in non-smokers was 0.81 % and in smokers was 5.33 % (Fig. 13.1). Statistically higher levels of COHb were observed in blood of

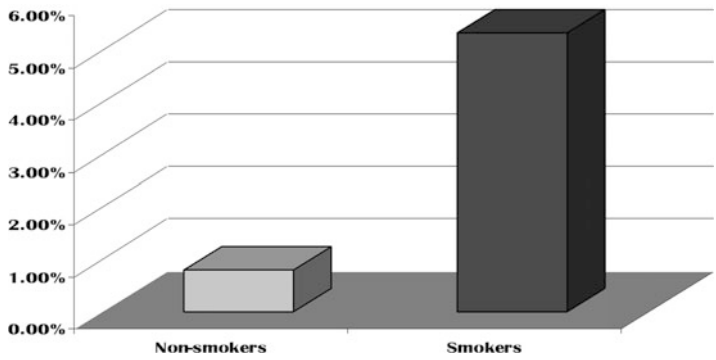

Fig. 13.1 COHb levels in blood of smokers and non-smokers from Belgrade

smokers ($P < 0.01$) confirming that cigarette smoking is the main factor of increased blood concentration of CO in general population. The mean concentrations of COHb in smokers were reported to be 4–7 % and in non-smokers were between 1 and 2 % which is agreement with the results obtained in previous study [12, 13]. The highest measured levels of COHb in blood of smokers in this studies was 9.01 % which is in agreement with the results obtained in heavy smokers that had levels of COHb > 12 % [14].

These high levels of COHb oversees the physiological levels of COHb and can lead to headache, dizziness, weakness, shortness of breath, muscle cramping and other symptoms of acute CO poisoning. Furthermore, significant myocardial changes were seen in patients with COHb levels exceeding 6 % [15].

It has been known for decades that cigarette smoke contains CO in far larger concentrations than any other potentially hazardous ingredients such as nicotine and polycyclic aromatic hydrocarbons. Carbon monoxide yields in mainstream smoke of cigarettes vary widely and are dependent on the extent of filter efficacy, paper porosity and moisture content. Modern cigarettes range from 0.5 to 13 mg/cigarette corresponding to 0.2–4.5 % CO in mainstream smoke [16]. The recent Tobacco Directive of the European Union passed in 2001 and revised in 2012 sets a guidance limit of CO in mainstream smoke of max. 10 mg/cigarette.

13.3.2 Carboxyhemoglobine Levels-Relation to Gender

Measured COHb fractions did not reveal any significant gender based differences either in smokers or non-smokers group. Median level of COHb in blood of female was 4.91 % and in male smokers was 5.79 % while in female non-smokers were 0.9 % and in male non-smokers 0.83 %. We expected higher levels of COHb in women, since women have higher CO endogenous production [17] and since Hb levels are higher in man. However these results are in accordance with the results obtained by [11] who also did not find any statistically significant differences in COHb levels in blood of females and males from both smokers' and non-smokers' groups.

13.3.3 COHb Levels in Smokers-Relation to Smoking Habits

No statistically significant difference was observed between smokers with regard to smoking duration (shorter/longer than 10 years). The median concentrations were 5.58 % for those who smoked less than 10 years and 5.44 % for those who have been smoking for more than 10 years. In accordance with the hypothesis that CO could have second slower elimination phase, some authors even showed that former smokers had higher COHb fraction than non-smokers [18]. Therefore, we expected higher levels in smokers that have been smoking longer than 10 years. However, our

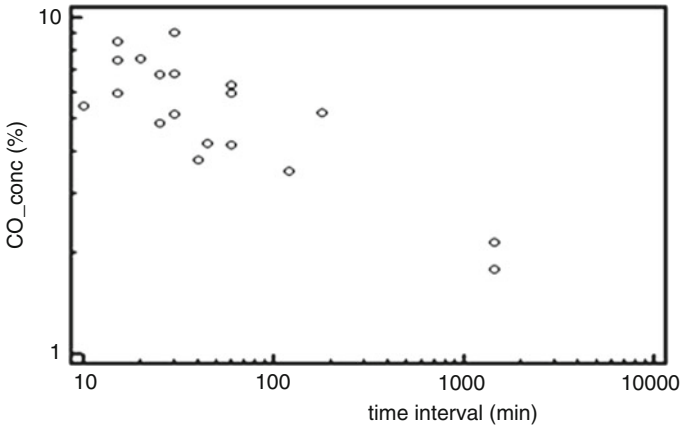

Fig. 13.2 The relation between COHb levels in blood and time interval between last cigarette and blood sampling

result indicated that smoking duration has no significant influence on COHb levels. This perhaps can be explained by the fact that there is a non-steady-state exposure pattern for COHb in smokers [14].

However, time interval between last cigarette and blood sampling seems to be particularly important factor. Strong negative correlation was observed between these parameters ($r = -0.529$, $P < 0.05$) with significantly higher COHb levels in smokers who had their last cigarette $\leq$30 min before blood sampling (Fig. 13.2). Carbon monoxide levels in those who smoked 30 min or less than 30 min before blood sampling was 6.38 %, while in those who smoked more than 30 min before sampling was 4.15 %.

This observation is in accordance with studies that have shown that blood donors should avoid smoking 24 h before blood donation [19] and with the results of the study conducted on smokers' blood donors that showed higher COHb levels in those who had their last cigarette 1 h before the blood donation [11]. Possible explanation for this phenomenon can be explained by the short half-life of COHb which ranges from 36 to 131 min [20] and which may be affected by gender differences, age, and lung function [21].

13.3.4 COHb Levels in Non-smokers-Relation to Living Environment

Although lower than in smokers, median COHb level in non-smokers living in the center of Belgrade can be considered as upper physiological level. Statistically significant difference was obtained between residents living in the center of

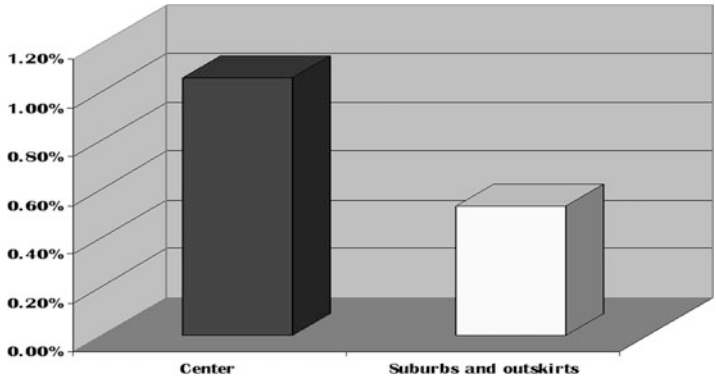

Fig. 13.3 COHb levels in blood of non-smokers from Belgrade

Belgrade if compared with residents living in suburbs and outskirts of Belgrade with median values of 1.06 and 0.53 %, respectively (Fig. 13.3). This can be explained by higher levels of outdoor pollution in the center of Belgrade, as a result of heavier city traffic.

The CO concentration in urban areas is quite variable and localized depending on human and meteorological activity. People are involved in the community exposure to motor vehicle exhaust resulting in an average blood level concentration of COHb < 2 % [22] which is in accordance with our results. Values of COHb in non-smokers living in the center of Belgrade can also lead to manifestation of some mild symptoms of CO poisoning. Bearing in mind that heavy traffic is a persistent problem in parts of Belgrade, these values of COHb are most probably constantly present in blood of people living in these parts of city. It was observed that the severity of CO poisoning depends more on the duration of exposure than on the inhaled CO levels [23].

13.4 Conclusion

The obtained high COHb levels in smokers' blood indicate that CO inhaled from tobacco smoke can significantly contribute to smoking-induced diseases, especially cardiovascular diseases. Higher COHb content in non-smoker residents living in the city center suggests that this part of general population can also be at risk from developing symptoms of CO poisoning. Carbon monoxide level in blood can be used as a biomarker of exposure and biological effects not only in smokers, but also in non-smokers living in urban polluted areas. We further argue that although methods are used for CO based study based on anthropogenic pollution by smokers and traffic, the model and methodology is equally applicable to industrial workers and even soldiers in battle ground as they experience significant foreign gases and matter inhalation.

Acknowledgment This work was partly supported by the Ministry of Education, Science and Technological Development of Serbia (Project III 46009).

References

1. Alonso J, Cardellach F, Lopez S, Casademont J, Miro O (2006) Carbon monoxide specifically inhibits cytochrome C oxidase of human mitochondrial respiratory chain. Pharmacol Toxicol 93(3):142–146
2. Vreman HJ, Wong RJ, Stevenson DK, Smialek JE, Fowler DR, Li L et al (2006) Concentration of carbon monoxide (CO) in postmortem human tissues: effect of environmental CO exposure. J Forensic Sci 51(5):1182–1190
3. Seto Y, Kataoka M, Tsuge K (2001) Stability of blood carbon monoxide and hemoglobins during heating. Forensic Sci Int 121(1–2):144–150
4. Commins BT (1975) Measurement of carbon monoxide in the blood: review of available methods. Ann Occup Hyg 18(1):69–77
5. Johansson M, Wollmer P (1989) Measurement of carboxyhaemoglobin by spectrophotometry and gas chromatography. Clin Physiol 9(6):581–586
6. Goldbaum LR, Chace DH, Lappas NT (1986) Determination of carbon monoxide in blood by gas chromatography using a thermal conductivity detector. J Forensic Sci 31(1):133–142
7. Van Dam J, Daenens P (1994) Microanalysis of carbon monoxide in blood by head-space capillary gas chromatography. J Forensic Sci 39(2):473–478
8. Cardeal ZL, Pradeau D, Hamon M, Abdoulaye I, Pailler FM, Lejeune B (1993) New calibration method for gas chromatographic assay of carbon monoxide in blood. J Anal Toxicol 17(4): 193–195
9. Sundin A, Larsson JE (2002) Rapid and sensitive method for the analysis of carbon monoxide in blood using gas chromatography with flame ionisation detection. J Chromatogr B 766(1):115–121
10. Oritani S, Zhu B, Ishida K, Shimotouge K, Quan L, Fujita MQ, Maeda H (2000) Automated determination of carboxyhemoglobin contents in autopsy materials using head-space gas chromatography/mass spectrometry. Forensic Sci Int 113(1–3):375–379
11. Aberg A, Sojka BN, Winsö O, Abrahamsson P, Johansson G, Larsson JE (2009) Carbon monoxide concentration in donated blood: relation to cigarette smoking and other sources. Transfusion 49(2):347–353
12. Heinemann G, Schievelbein H, Richter F (1984) Analytical and diagnostic validity of the determination of carboxyhemoglobin in blood and carbon monoxide in the breath of smokers and non-smokers. J Clin Chem Clin Biochem 22(3):229–235
13. Wald NJ, Watt HC (1997) Prospective study of effect of switching from cigarettes to pipes or cigars on mortality from three smoking related diseases. Br Med J 314(7098):1860–1863
14. Scherer G (2006) Carboxyhemoglobin and thiocyanate as biomarkers of exposure to carbon monoxide and hydrogen cyanide in tobacco smoke. Exp Toxicol Pathol 58(2–3):101–124
15. Ayres SM, Giannelli S Jr, Mueller H (1970) Myocardial and systemic responses to carboxyhemoglobin. Ann N Y Acad Sci 174(1):268–293
16. Rickert WS (1997) Partial characterization of 10 “common” brands of American cigarettes. Project report prepared for Massachusetts Department of Public Health. LABSTAT Incorporated 30:1–20. http://legacy.library.ucsf.edu/tid/ydr66c00. 1 Dec 2012
17. Longo LD (1977) The biological effects of carbon monoxide on the pregnant woman, fetus, and newborn infant. Obstet Gynecol 129(1):69–103
18. Hart CL, Smith GD, Hole DJ, Hawthorne VM (2006) Carboxyhaemoglobin concentration, smoking habit, and mortality in 25 years in the Renfrew/Paisley prospective cohort study. Heart 92(3):321–324

19. Aronow WS, O'Donohue WJ Jr, Freygang J, Sketch MH (1984) Carboxyhemoglobin levels in banked blood. Chest 85(5):694–695
20. Weaver LK, Howe S, Hopkins R, Chan KJ (2000) Carboxyhemoglobin half-life in carbon monoxide-poisoned patients treated with 100% oxygen at atmospheric pressure. Chest 117(3):801–808
21. Deller A, Stenz R, Forstner K, Konrad F (1992) The elimination of carboxyhemoglobin (COHb) – sex-specific and circadian influences in healthy volunteers. Infusionsther Transfusionsmed 19(3):121–126
22. Goldsmith JR (1970) Contribution of motor vehicle exhaust, industry, and cigarette smoking to community carbon monoxide exposures. Ann N Y Acad Sci 174(1):122–134
23. Sokal JA, Kralkowska E (1985) The relationship between exposure duration, carboxyhemoglobin, blood glucose, pyruvate and lactate and the severity of intoxication in 39 cases of acute carbon monoxide poisoning in man. Arch Toxicol 57(3):196–199

Chapter 14
Electron Emission Standed Nanodosimetry and Gas Detection

Yu. Dekhtyar, D. Krumpane, K. Perovicha, R. Reisfeld, M. Romanova, T. Saraidarov, and I. Surkova

Abstract Photoelectron (PE) and thermostimulated exoelectron (TE) emission spectroscopies were explored for gas sensing and electron radiation nanodosimetry. Silicon substrates were in use as the working matter for benzene and isopentane sensing. PbS nanocrystals embedded in ZrO_2 thin-films were employed to absorb electron radiation. Both PE and TE influenced by gas absorption and radiation deliver promising approaches for gas sensing and nanodosimetry.

Keywords Gas and radiation sensor • Nanodosimetry • Electron emission

14.1 Introduction

Gas sensing and ionizing radiation are correspondingly employed for cancer diagnostics and therapy. According to medical research, patients with cancer, diabetes and chronic obstructive pulmonary disease have very specific volatile organic compounds (VOC) in their exhaled gases [1–3]. Pathologically increased concentrations of VOCs such as benzene, acetone, toluene, pentane and hexane, which are the metabolites of cancer cells, are very specific for oncology patients. As for examples, isopentane and benzene gases are typical for lung cancer patients [1–3]. Concentration of the exhaled gases is not high; therefore, they can be accumulated by an absorber changes in properties of which will be measured.

Y. Dekhtyar (✉) • D. Krumpane • K. Perovicha • M. Romanova • I. Surkova
Institute of Biological Engineering and Nanotechnology, Riga Technical University, Kalku Str. 1, Riga 1050, Latvia
e-mail: dekhtyar@latnet.lv

R. Reisfeld • T. Saraidarov
Faculty of Science, Institute of Chemistry, Hebrew University of Jerusalem, Edmond J. Safra Campus, Givat Ram, Jerusalem 91904, Israel

A. Vaseashta and S. Khudaverdyan (eds.), *Advanced Sensors for Safety and Security*, NATO Science for Peace and Security Series B: Physics and Biophysics,
DOI 10.1007/978-94-007-7003-4_14,

Radiation therapy is aimed at delivery of a dose of ionizing radiation to the targeted organ. Nanodosimetry (ND) is a cutting edge technology which aim is to measure the absorbed dose in a nanovolume of the irradiated substance. There are several reasons why ND is of a great importance: (i) biological effects caused by radiation depend on dose absorbed by nanosized DNA units; (ii) there is a trend in radiation therapy to apply high dose gradients (several Gy per nm or μm), survival of the cells depends on the gradient value; (iii) nanoparticles as radiation scattering centers are expected to reach local micro- nano-scaled treatment that minimally influences risk organs/cells; and (iv) radiation sensitive nanoparticles have ability to penetrate from the environment to human body. However, still there are no detectors that measure radiation in nanovolumes. To fix the problem, a nanosized detector is a great candidate to get a reliable readout. Also, detection must not be independent of the measurement process and contactless technologies are preferable.

One of the contactless technologies is to measure emission of low energy electrons (LEE) escaping from a solid surface layer with depth ~10–100 nm. Pre-threshold photoelectron emission (PE) stimulated by photons ~5 eV could be employed to induce LEE. Typically, PE current (I) depends on the difference between photon energy ($h\nu$) and electron work function (φ) of the emitter in accordance with the parabolic law [4]. In such case, absorption of gas molecules or radiation that alters φ provides a high response of I.

LEE could be also reached due to thermostimulated exoelectron emission (TE) when electrons escape from the solid because of the heat induced interactions of molecules absorbed on the emitter and its surface [5]. In case of semiconductor, φ is influenced by the thermodesorbed electrically active molecules [4, 5]. The research demonstrates novel results on application of LEE emission via the PE and TE approaches to identify isopentane and benzene gases and dose of electron radiation that is in use for radiation therapy.

14.2 Gas Detection

14.2.1 Materials and Methods

Crystalline silicon wafers (Si) having n- or p-type conductivity were selected as absorbers of gas molecules (Table 14.1). The wafers were fabricated mechanically from Si crystals (cutting, grinding, polishing) till reaching mirror-like surface. The specimens were cut from the wafers and had sizes 1×1 cm^2, thickness 0.2 mm. The specimens were cleaned with lint free cloth soaked in 96 % ethanol. After cleaning the specimens were placed in the PE spectrometer. PE current I was detected in vacuum 10^{-5} Pa at room temperature, energy of hν was 4.5–6 eV. Some bends on I(hν) spectra were displeasing. After PE measurements, the specimens were annealed in the same spectrometer in vacuum 10^{-5} Pa at +600 °C. This procedure removed the bends and the spectra became smooth. These spectra were assumed as the native ones for the PE experiments.

Table 14.1 Electrical resistance of Si wafers

Si	Electrical resistance, Ω cm	Legend for the Figs. 14.1, 14.2, and 14.3 below
p-Si, doped with boron	0.0005	SHB-0.0005
	1	SHB-1
n-Si, doped with phosphorus	0.0014	SEP-0.0014
	5	SEP-5

TE was also measured from the specimens annealed as described above. TE detection was performed in vacuum 10^{-5} Pa. The specimens were heated from room temperature till +400 °C with heating rate 0.3 °C/s. The specimens which underwent the procedures described above were assumed as the native ones for further TE experiments.

To absorb gases, the Si specimens were placed into Petri dishes (volume 0.08 cm^3). 125 μl of liquid benzene (dipole moment D = 0 D) or isopentane (dipole moment D = 0.29 D) was dripped inside the Petri dishes near Si specimens using single-channel pipette. Then the dishes were sealed with their covers. The liquids evaporated completely in less than 10 min. Si specimens were exposed in the closed dishes to the gas vapors for longer than those 10 min. After the specimens were exposed, they were again positioned in the spectrometer to measure LEE. Differences between measured emission current before and after exposure were calculated as ΔI and ΔI_T for PE and TE, correspondingly. Next, exposure-dependent increments of total emitted charges Q and Q_T were numerically calculated as:

$$Q = \int_{4.5eV}^{6eV} \Delta I(h\nu) d(h\nu), \tag{14.1}$$

$$Q_T = \int_{20C}^{400C} \Delta I_T(T) dT \tag{14.2}$$

14.2.2 Results and Discussion

Figures 14.1 and 14.2 demonstrate increments I and I_T of the PE and TE currents after 30 min exposure of the Si specimens to benzene and isopentane gases.

Figure 14.1 demonstrates that the PE responds on exposures to benzene and isopentane. Exposure to benzene (left graph) provides higher ΔI, when Si is characterized with lower resistance (lines 2, 3). This could be connected to the shorter Debye length of Si in contrast with specimens provided the lines 1, 3. In this case the emitted electron is stronger influenced by the surface electrical potential subjected to the attached gas molecules. The greatest ΔI is observed for the p-Si

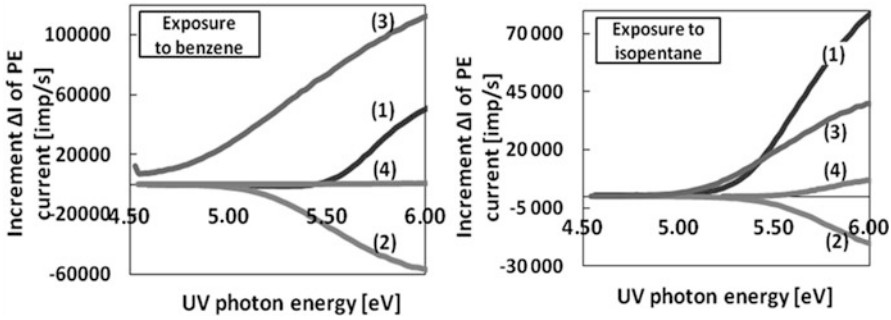

Fig. 14.1 ΔI because of exposure to benzene and isopentane, exposure time 30 min: *1* – SEP-5, *2* – SEP-0.0014, *3* – SHB-0.0005, *4* – SHB-1

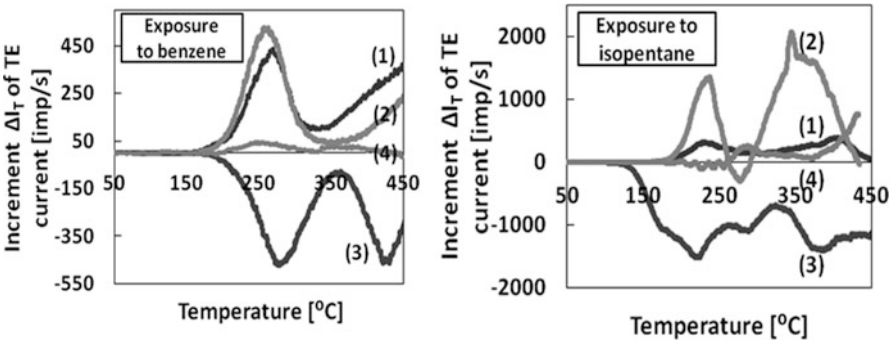

Fig. 14.2 ΔI_T because of exposure to benzene and isopentane, exposure time 30 min: *1* – SEP-5, *2* – SEP-0.0014, *3* – SHB-0.0005, *4* – SHB-1

(line 3). This shows that benzene decreases φ of the p-Si. The dipole moment of the benzene molecule is zero, therefore, one could assume that influence on φ was provided by the strongly polarized C-H couple of the benzene ring, the proton perhaps connecting the surface of Si.

Exposure to isopentane (right graph) gives evidence that lower resistance gives higher signal of emission current in case of p-Si (lines 3, 4). However ΔI of the n-Si is higher when the resistance is higher (lines 1, 2). The above cannot be considered as the fact that the resistance clearly contributes ΔI by the same way as in case of benzene. However, because the dipole moment of isopentane molecule is not zero in contrast with benzene, isopentane delivers electrical filed that has an influence on emission of the electron. The later to leave the emitter travels across both the electric field of the Debye (ED) layer and isopentane molecule (E_{is}). If $ED << E_{is}$, the latter contributes emission of the electron significantly. The Si having higher resistance is characterized with a thicker Debye layer. On the other hand the density of the Si surface charge is provided by its nature and does not vary a lot in dependence on the resistance. Therefore, ED is lesser, when the resistance if higher. This could explain higher ΔI detected from the Si characterized with higher resistance (line 1 in contrast with line 2).

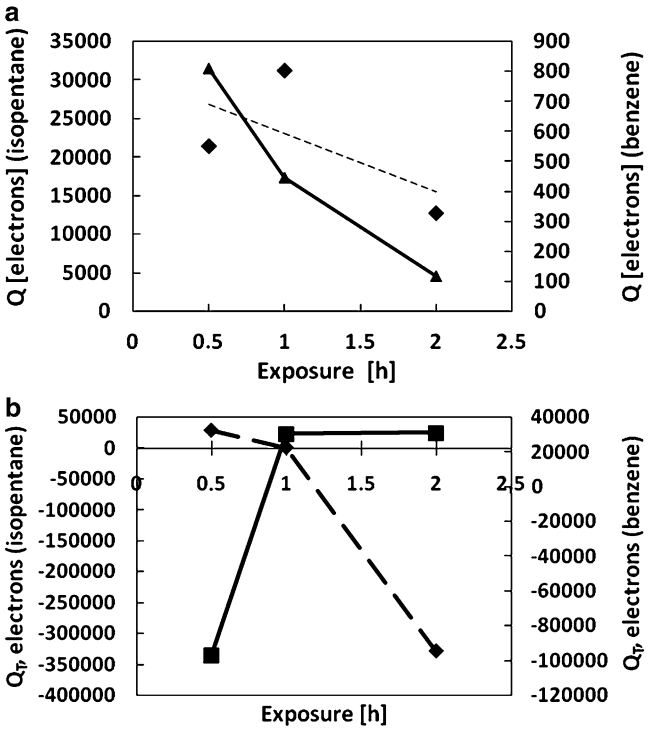

Fig. 14.3 Value of Q (**a**) and QT (**b**) in dependence on expose to benzene (- - - - -) and isopentane (——): (**a**) benzene (SHB-0.0005), isopentane (SEP-5); (**b**) benzene (SEP-5), isopentane (SHB-0.0014)

Figure 14.2 demonstrates that TE responds to benzene and isopentane exposures. Exposure to benzene (left graph) provides high ΔI_T, for n-Si, and for low resistance p-Si (lines 1, 2, 3). Low signal (line 4) from high resistance p-Si could evidence that the molecules were strongly connected to the surface and heat did not desorb them.

Exposure to isopentane (right graph) gives evidence that lower resistance of Si provides higher emission current (lines 2, 3). However, low ΔI_T from Si with higher resistance (lines 1, 4) evidences that the molecules were pinned stronger to the specimens surface. Figure 14.3 demonstrates Q and Q_T in dependence on exposure for the highest signals from Figs. 14.1 and 14.2, correspondingly. The value of Q_T depends on the exposure stronger than Q and therefore TE approach could be recommended for further investigation.

To identify a sensitivity of Q and Q_T to respond to attachment of the benzene and isopentane to Si, the specimens similar to the above, a couple of cm square of the surface was weighed before and after the gas exposure. The latter was provided in the same gas evaporation conditions as the above. The balance ACCULAB (accuracy 0.1 mg) was employed to weight. The Q and Q_T detection threshold corresponded to the density $\sim$10 μg/cm^2 of the benzene/isopentane on the Si surface.

14.3 Nanodosimetry

14.3.1 Materials and Methods

ZrO_2: PbS films consisting of PbS nanoparticles embedded in ZrO_2 matrix were explored for purposes of nanodosimetry of electron radiation. PbS nanodots were supposed to be radiation-sensitive and electron emission active centers because they have emission and absorption lines in large spectral region [6–8]. The signal from such thin-film dosimeter could be read by measuring LEE.

ZrO_2:PbS films were fabricated using sol-gel technique [8] with 20 % concentration of PbS nanoparticles. The films were deposited on a glass substrate. Thickness of the films was 0.1–1 μm. Typical size of PbS nanodot was 2–4 nm. To verify the size of the nanodots, atomic force microscope Solver P-47 PRO was employed. ZrO_2:PbS films were irradiated with 9 MeV electrons that supplied the doses 3, 7 and 10 Gy using medical linear accelerator. PE current was recorded before (I_0) and after (I_{Gy}) irradiation in the same conditions as described above.

14.3.2 Results and Discussion

Radiation decreased PE current of ZrO_2:PbS films ($I_0 > I_{Gy}$). Figure 14.4 demonstrates relative increment (δI) of the current:

$$\delta I = \frac{I_{Gy} - I_0}{I_0} \cdot 100\,\% \tag{14.3}$$

Figure 14.4 indicates that radiation has influence on PE of ZrO2:PbS. To investigate dose -dependent peculiarities of the PE spectra, derivatives dI/d(hv) of the PE current were calculated from the I(hv) spectra. The maximums of dI/d(hv) were found at 5.65 ± 0.03 eV and 5.75 ± 0.03 eV (Fig. 14.5). Radiation decreased

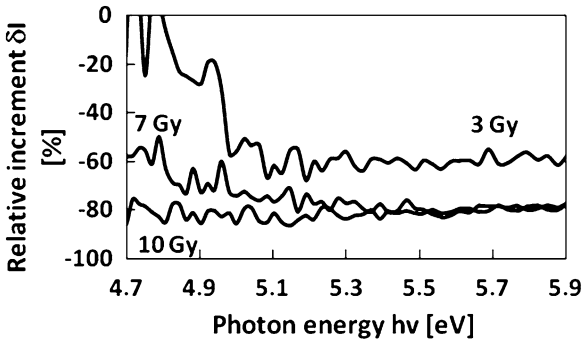

Fig. 14.4 Relative increment δI of PE current of ZrO_2:PbS films for different doses of electron radiation

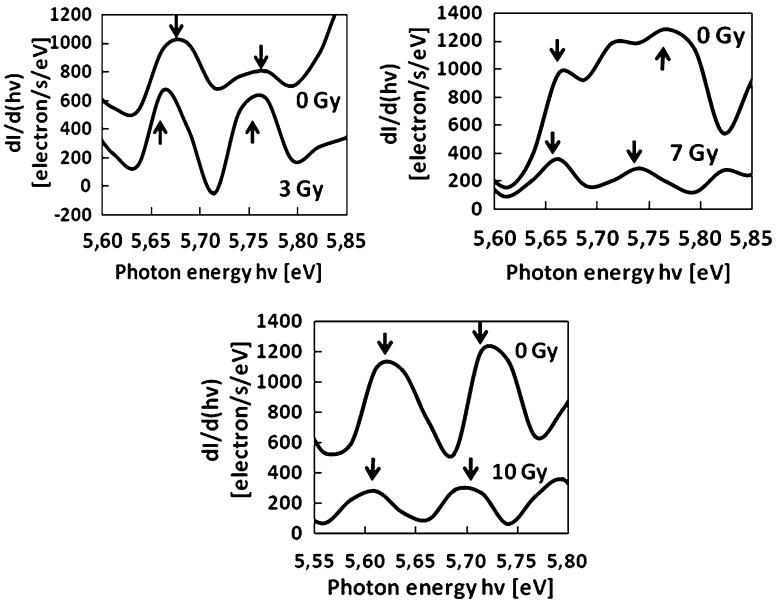

Fig. 14.5 dI/d(hν) of PE spectra of ZrO_2:PbS films for different electron radiation dose

amplitudes of the maximums. This decrease could be due to loss of the emission active centers under influence of radiation.

To verify contribution of PbS nanodots to PE, emission was measured for ZrO_2 film without PbS nanoparticles. In this case the maximums observed above were not detected. This gave evidence that the analyzed maximums were provided by the electron emission from PbS dots. To estimate possibility to use ZrO_2:PbS films for dosimetry, relative increment Δ(dI/d(hν)) of the maximums at 5.65 and 5.75 eV was correlated to the dose:

$$\Delta\left(\frac{dI}{dh\nu}\right) = \frac{\left(\frac{dI}{dh\nu}\right)_{Gy} - \left(\frac{dI}{dh\nu}\right)_0}{\left(\frac{dI}{dh\nu}\right)_0} \cdot 100\,\% \tag{14.4}$$

Figure 14.6 demonstrates linear correlation between Δ(dI/d(hν)) and dose of electron radiation.

14.4 Conclusions

The PE and TE approaches have potential to provide readout from Si wafers to detect isopentane and benzene gases and to detect the signal from ZrO2, PbS nanodotted film to measure doses of electron radiation employed in radiation therapy. To reach Si based sensor sensitive to isopentane and benzene gases, TE

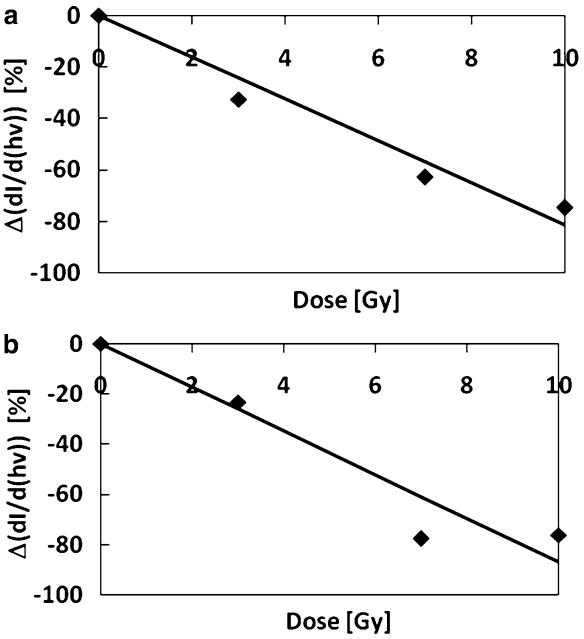

Fig. 14.6 Linear correlation between Δ(dI/d(hν)) and dose of electron radiation: (**a**, **b**) for maximums at 5.65 and 5.75 eV, correspondingly

mode of LEE is preferable. The increments (dI/d(h)) at 5.65 and 5.75 eV observed after irradiation of ZrO2:PbS films with 9 MeV electrons are correlated to the absorbed dose. To achieve Si based sensor sensitive to isopentane and benzene gases, TE mode of LEE is preferable.

References

1. Wang C, Sahay P (2009) Breath analysis using laser spectroscopic techniques: breath biomarkers, spectral fingerprints, and detection limits. Sensors 9:8230–8262
2. Shirau M, Touhaza K (2011) The scent of disease volatile organic compounds of the human body related to disease and disorder. J Biochem 3:257–266
3. Mandis A (1983) The diagnostic potential of breath analysis. Clin Chem 29:5–15
4. Kane E (1962) Theory of photoelectric emission from semiconductor actors. Phys Rev 127: 131–141
5. Kortov VS, Shifrin VP, Gaprindashvili AI (1975) Exoelectron spectroscopy of semiconductors and insulators. Microelectronics 8:28–49 (in Russian)
6. Reisfeld R, Saraidarov T (2006) Innovative materials based on sol-gel technology. Opt Mater 28(1–2):64–70. Polish–French–Israeli symposium on spectroscopy of modern materials in physics, Bedlewo
7. Saraidarov T, Reisfeld R, Sashchiuk A, Lifshitz E (2005) NanoCrystallites of lead sulfide in hybrid films prepared by sol–gel process. J Sol–Gel Sci Technol 34:137–145
8. Sashchiuk A, Lifshitz E, Reisfeld R, Saraidarov T, Zelner M, Willenz A (2002) Optical and conductivity properties of PbS nanocrystals in amorphous zirconia sol–gel films. J Sol-Gel Sci Technol 24:31–38

Part IV
Optical Sensors

Chapter 15
Photoelectric Properties of Selectively Sensitive Sensors for the Detection of Hazardous Materials

Surik Khudaverdyan, A. Avetsiyan, D. Khudaverdyan, and Ashok Vaseashta

Abstract The objective of this investigation is to evaluate a new model of a portable photodetector for remote interrogation of spectral signature analysis using optical information and its feasibility for identification and quantitative analysis of hazardous mixtures. Electromagnetic waves have different absorption depths and the selection is made by changing of the width of the registration area via step-by-step change of external voltage applied to the photodetector.

Keywords Spectral sensitivity • Photogeneration • Photodetector

15.1 Introduction

In modern photonics systems, ultraviolet and visible spectroscopy is widely used in medical diagnostics, drug manufacturing, environmental protection, study of nano-bio-systems [1–3]. For a variety of reasons, there is an urgent need for the development of hand-held, portable, and decentralized systems for environmental monitoring. There is a current body of research wherein the selection of electromagnetic spectrum is carried out by their spatial separation [4, 5]. The filter less, selectively sensitive photo-detectors [4] require complex fabrication, data processing, and an identical lighting on all surfaces of multi-stage structures,

S. Khudaverdyan (✉) • A. Avetsiyan • D. Khudaverdyan
Faculties Radio Engineering and Communication Systems, Department Design and Production of Radio Devices, State Engineering University of Armenia, 105, Teryan str., Yerevan 0009, Armenia
e-mail: xudaver13@mail.ru

A. Vaseashta
Norwich University Applied Research Institutes, Herndon, VA, USA

VTT/AVC U.S. Department of State, Washington, DC, USA
e-mail: prof.vaseashta@ieee.org

A. Vaseashta and S. Khudaverdyan (eds.), *Advanced Sensors for Safety and Security*, NATO Science for Peace and Security Series B: Physics and Biophysics,
DOI 10.1007/978-94-007-7003-4_15,

whereas for spectrally sensitive "color separation by depth" photocells [5], the proper disposition of "Blue-Green" and "Green-Red" "color separating" p + -Si barriers is dictated by both the spectral dependent absorption coefficient in silicon, coupled with a necessity for color-channels spectral response to conform to the CIE 1931 XYZ Color space. An additional requirement of identical intensities and wavelengths further complicates the analysis. The current research is thus aimed at studying a viable model of a portable photo-sensor for identification and quantitative analysis of hazardous mixtures in the environment. The spatial selection of optical signatures is carried out by means of new physical principles.

15.2 Method of Investigation

For the structure under investigation, the cross-section and energy band diagram are presented in Fig. 15.1a, b respectively.

The structure consists of regions I and II: a thin high-resistance photosensitive n-Si layer (with thickness d) which covers the unified space of the surface metal-n-Si and the rear p + -n junction of potential barriers, and region III: a highly doped p + -Si active layer (with thickness w 1(b)) which provides Ohmic contact. On the surface of the n layer with thickness d (base), a semi-transparent metal semiconductor Schottky barrier (with thickness x_m) is created. As a result of drift and diffusion, photogenerated electrons are stored in the potential well of the conduction band during Maxwellian relaxation, and then move into the metal contact over low potential barrier. A part of electrons recombine with the holes incoming from the first region of Fig. 15.1b.

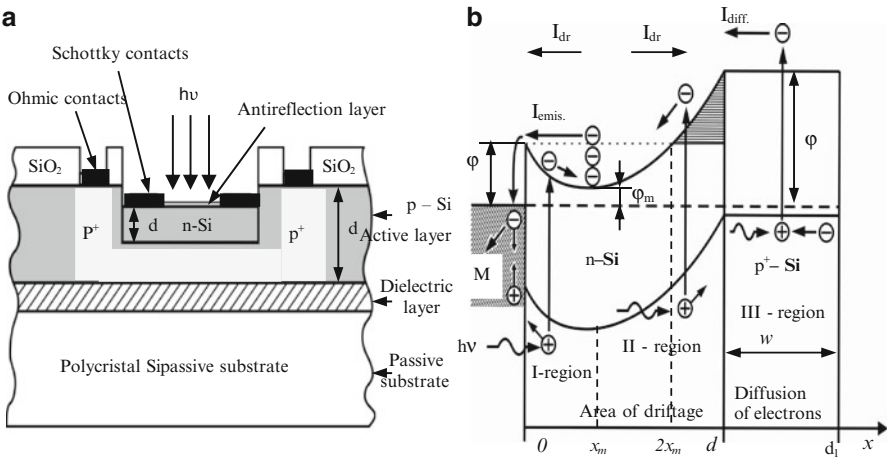

Fig. 15.1 (**a**) Cross-section of the structure and (**b**) energy-band diagram of the structure and potential distribution for electrons in n – base

Thus, the first region does not create any external current. The remaining electrons move into the p + region through the external circuit and create external photocurrent via recombination with photogenerated holes in the II and III regions (see Fig. 15.1b). With any variation in external voltage, absorption spectrum varies in the first and second regions. An appropriate algorithm allows selection of individual waves and their intensities from the integral of flux radiation.

To model the physical processes of such structures, a system of mathematical expressions are used. The equations include dependence among the characteristic parameters of the structure [6].

$$I_{emiss} = qSn_f v_T e^{-\left(\frac{\varphi_1-\varphi_m}{kT}\right)} = qF_0S\left(1-e^{-\alpha d_1}\right) \tag{15.1}$$

$$2\frac{\varphi_1-\varphi_m}{kT} + 2\frac{n_f}{N_d}\left[1-e^{-\left(\frac{\varphi_1-\varphi_m}{kT}\right)}\right] = \left[\left(\frac{\varphi_2-\varphi_1+qV}{kT}\right)\cdot\frac{L_s}{d-2x_m} - \frac{d-2x_m}{L_s}\right]^2 \tag{15.2}$$

$$\int_0^{\frac{\varphi_1-\varphi_m}{kT}} \frac{dy}{\left[y+\frac{n_f}{N_d}\left(1-e^{-y}\right)\right]^{1/2}} = \frac{\sqrt{2}x_m}{L_s}, \qquad y=\frac{\varphi-\varphi_m}{kT} \tag{15.3}$$

F_o, d, α and V are given values for simulation purpose.

It connects the main parameters of the structure: the position of the minimum point of the potential energy of the electron x_m in the base, the total flow of incident photons F_o, the width of the base d, the absorption coefficient α, the bias voltage V, the density of photocarriers n_f at the point x_m and the heights of both potential barriers φ_1 and φ_2. L_s is the shielding distance, N_d is the concentration of donor impurities, v_T is the thermal velocity of carriers, S is the photosensitive area, q is the electron charge.

The set of equations (15.1, 15.2, and 15.3) allow us to determine changes in the energy and spatial position of x_m, depending on the external bias voltage. With the help of the law of radiation absorption and the expression for the photocurrent (as in equation (15.4) provided later in text) we can determine the absorption coefficient α and intensity of a given wavelength.

The results of these studies are demonstrated below.

15.3 Results and Discussion

In the system of equations (15.1, 15.2, and 15.3) x_m, φ_m and n_f are the unknown quantities which are dependent on V, F_0 and α. By solving the system of equations, the inter-dependence of these parameters can be studied.

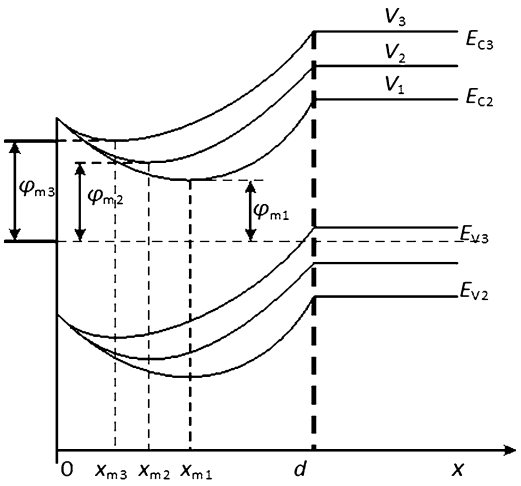

Fig. 15.2 The Position of x_m at different bias voltage. $V_1 < V_2 < V_3$. $x_{m3} < x_{m2} < x_{m1}$

We list below the results of these studies using following parameters of the structure: the concentration of donors in the n region $N_d \approx 3.36 \cdot 10^{15} \text{cm}^{-3}$, and of acceptors in the p region $N_a \approx 8 \cdot 10^{16} \text{cm}^{-3}$. The potential barriers metal/n-Si and n-Si/p-Si create the potential for electrons $\varphi_1/q = 0.826\ V$ and $\varphi_2/q = 0.926\ V$, respectively (see Fig. 15.1). The depletion regions of junctions cover the whole base of the structure with thickness d. The point of contact of these regions x_m has a potential energy φ_m and shifts from zero to d by varying external voltage. The thickness of depleted region varies according to the expressions above. It leads to the change of the values of the drift and diffusion photocurrents $I_{dr.1}$ and $I_{dr.2} + I_{diff}$ created by these junctions (see Fig. 15.1).

With the increase of voltage, there is an increase of the rear barrier and a decrease of the surface barrier (see Fig. 15.2), the increase of φ_m is observed (Figs. 15.2 and 15.3), and the point of minimum of potential energy of electrons x_m shifts linearly towards the surface barrier at a constant radiation intensity F_0 (Fig. 15.4).

Figure 15.5 shows that the dependence of position of the minimum point x_m on the intensity of absorbed radiation is weak, and when F_0 changes by three orders, x_m changes by 7.5 nm, which can be ignored as compared with the thickness of the base 1 μm.

The dependence of the minimum of the potential energy of electrons on the intensity of radiation is relatively stronger (Fig. 15.6). The studies further show that under all radiation intensities the number of absorbed quanta decreases with the increase of the emission wavelength (because of passing through the structure). Consequently, we observe a decrease of φ_m [6].

The point of minimum of the potential energy of electrons does not depend on the spectral distribution, and decreases slightly with the increase of radiation intensity. This can be explained by the fact that electrons are accumulated in the potential well of the conduction band symmetrically, and they increase φ_m and change x_m only

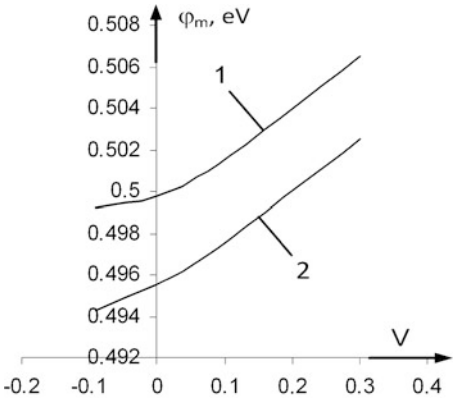

Fig. 15.3 Dependence of the minimum of potential energy of electrons on voltage at wavelengths: *1* – 400 nm, *2* – 500 nm (the specified voltage sign is applied to Schottky barrier)

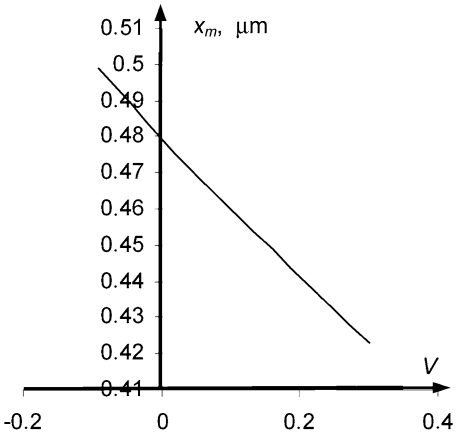

Fig. 15.4 Dependence of the minimum point of potential energy of electrons on voltage (the specified voltage sign is applied to Schottky barrier)

slightly. The mentioned laws allow us to carry out spatial selection of optical waves. In the spatial selection of UV and visible light in silicon structures, the parameters defining the absorption length are the depth and the radiation intensity F_0.

This can be determined by means of the absorption law,

$$F(\lambda_i) = F_0(\lambda_i)\, e^{-\alpha_i x_m}$$

and the values of the photocurrent for specified values of x_m or V (bias voltage). From the law of absorption,

$$\alpha_i = \frac{1}{\Delta x_m} \ln n$$

Where α_I is the absorption coefficient, $\Delta x_m = x_{m1} - x_{m2}$ (see Fig. 15.7) is the minimum change of the position x_m (the most deeply penetrated waves that we

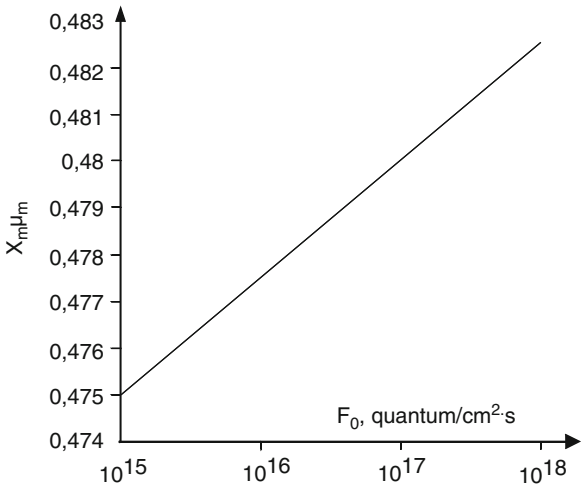

Fig. 15.5 Dependence of the point of minimum of potential energy of electrons on the intensity of radiation at V = 0 V and λ = 400 nm

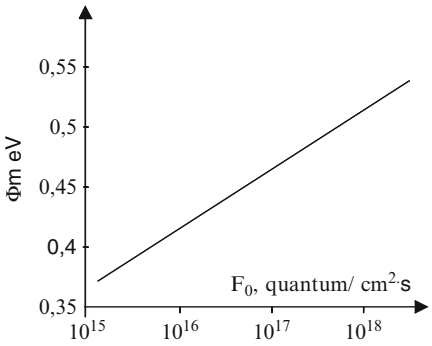

Fig. 15.6 Dependence of the minimum of the potential energy of electrons on the intensity of radiation (λ = 400 nm, V = 0 V)

calculated to reach that region) and n (> 1) is the multiplier. The smaller is the value of n, the smaller is Δx_m, and thus, the more accurate is the calculation. The threshold sensitivity determines the extreme accuracy of calculations.

It is evident that the second wave that we identify will reach x_{m2} and will be defined in the minimum area $\Delta x_m = x_{m2} - x_{m3}$, etc. At the given structural parameters and the determined absorption coefficients α_i, we can determine the intensity of the given wave by means of the value of the photocurrent:

$$\sum_{i,j} I_{Ph.i,j} = \sum_{i,j} I_{dri,j} + \sum_{i,j} I_{diff\ i,j} = S\,q \sum_{i} \sum_{j} F_0(\lambda_i) \left(e^{-\alpha_i x_{mj}} - \frac{e^{-\alpha_i d}}{1 + \alpha_i\ w} \right) \tag{15.4}$$

In Eq. (15.4), variation in (i = 1,2,3, ...) in the integral flux with the change of radiation wavelength, and variation in (j = 1,2,3, ...) with the change of bias

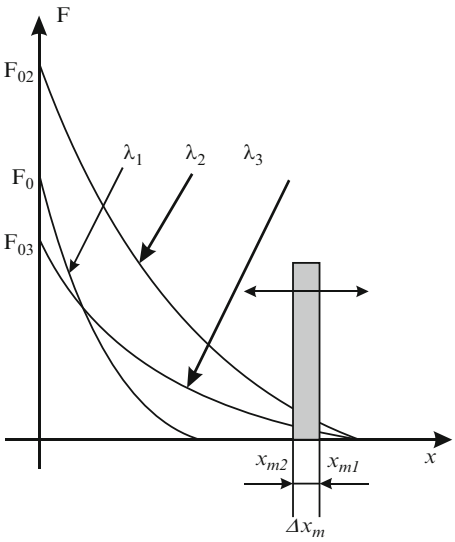

Fig. 15.7 The absorption depth of different waves at different radiation intensities

Table 15.1 Number of molecules of explosives/cm^3 of air

Types of explosives	Number of molecules of explosives per cm^3 of air
Nitroglycerine (NG)	10^{13}
Trotyl (TNT)	10^{11}
ТЭН* (PETN)	10^8–10^9
Cyclonite (RDX)	10^8
Ethylene glycol dinitrate (EGDN)	10^{15}

voltage; F(λ_i) is the total flow of incident photons with wavelength λ_i, the width of p-region w is smaller than the diffusion length L_n of electrons in the p^+-region. For this reason, the value L_n can be replaced by w. After finding α_1, $I_{Ph} = f(\alpha_1)$ can be determined and withdrawn from the dependence of the summed photocurrent as a function of the position x_m : $\sum I_{Phi} = f(x_{mi})$. Thereafter, the length and the intensity of the second wave can be determined, then of the third, and so on. All operations are carried out automatically employing a program and that we developed. Thus, the dependence $F_0 = f(\alpha_i)$ and $F_0 = f(\lambda_i)$ can be obtained.

The studies show that the proposed photodetector may be applied in different spheres, for instance, for stand-off detection of explosives by way of their vapors which are present in different amounts near or on the surface of explosive devices. The number of molecules of explosives/cm^3 of air is presented in Table 15.1 [7].

The table shows that it is possible to detect some of the specified explosives under the design threshold sensitivity of the proposed photodetector 10^5 quantums/cm^2 and using relevant structure of the sensor.

Table 15.2 Wavelength, current and voltage under solar spectrum

Wavelength range, nm	Current spectral photosensitivity, A/nm	Voltage spectral photosensitivity, mV/nm
225–280	$5.836*10^{-8}$	1.42
280–284	$1.0*10^{-8}$	0.56
284–300	$1.65*10^{-7}$	3.89
300–310	$1.1*10^{-7}$	3.35
310–357	$4.6*10^{-8}$	1.8
357–370	$8.8*10^{-8}$	9.88
370–374	$2*10^{-7}$	38.51
374–380	$4*10^{-7}$	67.49

For identification and quantitative determination of, for instance, of cyclonite on the basis of its ability to absorb UV radiation and laser-induced fluorescence of NO-fragments [7], it is necessary to carry out the spectral analysis within the range of wavelengths 225–240 nm. While determining the impurity of water, the maximum absorption often falls on the wavelength interval 350–354 nm and may be changed as a function of time depending on, for instance, the composition of natural water according to the concentration of dissolved organic impurities [8]. Based on this aforementioned analysis, the current and voltage spectral photosensitivity of the proposed photodetector (which leads to the change of the position of x_m – Fig. 15.1) was studied within the range of wavelengths 225–380 nm. A complicated extra-atmospheric solar spectrum [9] was also used. The results of studies are presented in Table 15.2.

The table shows high spectral sensitivity of the photodetector. Since the range of wavelengths is determined by the position of x_m caused by external voltage, the changes in the energy position of the potential minimum φ_m (Figs. 15.2 and 15.3) by bias voltage for wavelengths 225–380 nm have the same effect as that for the rest of the region (e.g. 400, 500 nm etc.). But, for each individual case, the width of the base of the structure and the intensity of the registered wave must be taken into account.

15.4 Conclusion

As a result of the studies conducted here, the influence of optical radiation on the parameters and properties of a small-size spectro-photometrical photodetector, it is determined that the position of the point of minimum of the potential energy of electrons x_m depends on the intensity of the absorbed optical radiation, and x_m changes linearly with the change of the external voltage. These observations confirm that the proposed structures can be used as spectrophotometric photodetectors and will have utility in detection of hazardous materials remotely – i.e. stand-off detection. Remote measurements are highly preferred over point-contact measurements.

References

1. Ensell G (2008) UK silicon photonics. EPSRC Reference: EP/F001894/1
2. Bercu M, Zhou X, Lee A, Poenar D, Heng C, Tan S (2006) Spectral characterization of cell with an epitaxy – based UV – VIS optical sensor. Biomed Microdevices 8:177–185
3. Ligler F (2009) Perspective on optical biosensors and integrated sensor systems. Anal Chem 81(2):519–526
4. Nader K, Fereydoon N (2004) Filterless Si-based ultraviolet-selective photodetectors. Spire Corp. for Stennis Space Center, Mississippi, Refer to SSC-00072
5. Vanyushin I, Gergel V, Zimoglyad V, Tishin Y (2005) Adjusting the spectral response of silicon photodiodes by additional dopant implantation. Russ Microelectron 34(3):155–159
6. Khudaverdyan S, Dokholyan J, Arustamyan V, Khudaverdyan A, Clinciu D (2009) On the mechanism of spectral selective sensitivity of photonic biosensors. Nuclear Instrum Methods Phys Res A 610:314–316, ELSEVIER
7. Evgeny G (2005) Development and research method vapor detection of explosives in the atmosphere with the help of a laser. Unpublished, available: http://iao.ru/data/iao_data/thesis_abstr/abstract_31pdf
8. Mosin O (2011) Methods for rapid analysis of water quality. Unpublished, available: http://www.o8ode.ru/article/answer/method/metody_ekcpreccanaliza_ka4ectva_pitevoi_ody.htm
9. National Renewable Energy Laboratory (NREL) U.S. department of energy, alliance for sustainable energy, LLC, Wehrli 1985 AM0 Spectrum are available http://rredc.nrel.gov/solar/spectra/am0/wehrli1985.new.html

Chapter 16
Portable Point-of-Care Optical Device to Detect Brain Injury

Adkham Paiziev

Abstract To improve diagnosis of brain injury (BI), it is critical to identify its symptoms early. We describe here a portable and cost effective device that may be able to detect BI in field. This report includes our recent publications devoted to devices based on near infra-red spectroscopy (NIRS) that can objectively detect, quantify, and record exposures that may cause BI as well capable of measuring changes in brain activity, physiology, or function that may be associated with BI. Another important task is to determine which devices are appropriate for use in the combat zone and civil environment, device size and ease of use. The results of the review revealed that empirical data characterizing BI in humans early after injury are lacking, making it difficult to critically evaluate and compare different devices and the measures they provide. Detailed consideration of many papers indicate that there is a critical need to determine the sensitivity and specificity of diagnostic devices in detecting BI, compare their ability to discriminate BI, and provide a better understanding of brain pathology and physiology immediately following injury.

Keywords Near infra-red spectroscopy • Brain injury • Point-of-care

16.1 Introduction

BI is frequent disease especially in combat zone and difficult to detect and diagnose because of lack of objective diagnostic tools. Early diagnosis of BI promotes early intervention and may improve outcomes. First, trans-illumination of the human head, as described in [1] was considered. Use of visible light provides information to reveal several types of neonatal brain pathologies [2, 3], but it was not ideal for

A. Paiziev (✉)
Biophotonics Laboratories, Institute of Ion-Plasma & Laser Technologies, Durmon Yuli 33, Tashkent 100125, Uzbekistan
e-mail: adkhanpaiziev@gmail.com

A. Vaseashta and S. Khudaverdyan (eds.), *Advanced Sensors for Safety and Security*,
NATO Science for Peace and Security Series B: Physics and Biophysics,
DOI 10.1007/978-94-007-7003-4_16,

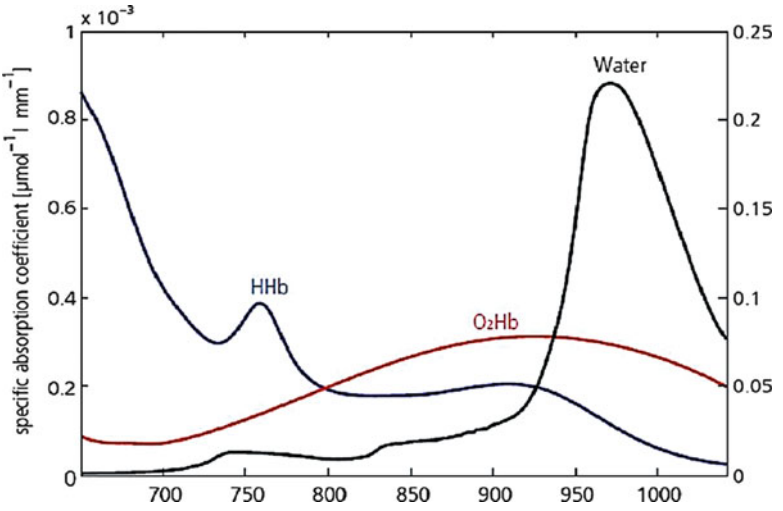

Fig. 16.1 Specific absorption coefficients for oxyhemoglobin (*O_2Hb*) and deoxyhemoglobin (*HHb*) solutions (plotted against the *left* ordinate) and of pure water (plotted against the *right* ordinate) [5]. The optical density (*OD*) is defined as the base-10 logarithm of the light attenuation i.e. $OD = \log_{10}(1/10)$

penetrating the thick skull and tissues of the adult head. In 1977, Jobsis [4] proposed using light in the NIR range (700–1,000 nm) for optical imaging of the head. Light in the NIR spectrum is able to penetrate biologic tissue and bone because it does not absorb significant energy in the NIR range. Over the past several decades, a variety of NIR-based brain monitoring methods have been developed, with some providing basic cerebral hemodynamic measures, such as blood oxygen saturation, while others attempt to measure more complex aspects of brain function. In terms of BI, most of the relevant research has employed NIR spectroscopy to assess deoxyhemoglobin (HHb) and oxyhemoglobin (HbO_2).

In NIR spectroscopy devices that send and receive light, called *optodes*, are attached to the scalp. These *optodes* transmit light in the NIR wave range to the underlying tissue. Portions of the light are absorbed, diffusively scattered, or reflected back based on the composition and respective absorption characteristics of the underlying tissue and on the wavelengths of the transmitted light. NIRS protocols generally transmit wavelengths of light that target the characteristic absorption spectra of the chromophores, HbO_2, HHb, and, in some cases, cytochrome c oxidase (see Fig. 16.1).

Because of the low absorption of bone and tissue, changes in intracranial chromophore concentration cause measurable changes in the amount of transmitted light that is absorbed and scattered back. By transmitting multiple NIR wavelengths, some of which are better absorbed by HbO_2 and others that are better absorbed by HHb, blood flow and tissue oxygenation can be estimated. It is important to recognize that the NIRS signal represents a *local* oxygenation index from arterial, venous, and capillary compartments.

NIRS has been used for neonatal clinical applications [6] but has been less successful for adult evaluation. Because older children and adults have relatively large heads, trans-illumination is not feasible. Reflectance-mode NIRS was developed to overcome this issue [7]. In reflectance-mode NIRS, NIR light is transmitted through the head in a localized area, and the light that is reflected back is measured at the scalp. Original reflectance-mode NIRS, however, was plagued by the probable extracranial contamination of the NIRS signal [8]. To mitigate the contribution of extracranial blood, spatially and time-resolved spectroscopy methods were developed [8, 9] and have since been implemented in commercially available NIRS devices.

16.2 Principles of NIRS Devices. Basic Model

The Beer-Lambert Law represents the mathematical relationship between the absorbance and the concentration of the material that is absorbing light and describes the exponential decay of the light intensity with the growing tissue depth d, attenuation caused by the concentration of the chromophores e.g. [HHb] denoted as (I_a and additional parameters DPF and G) can be discerned from Eq. 16.1 [5, 10].

$$I = I_0 \exp(\mu_a DPF d + G) \tag{16.1}$$

whereas:

Io – the intensity of a narrow-bandwidth light source
I – the detected intensity after the light has interacted with the tissue
$\mu_\alpha = c_{O_2Hb}\alpha_{O_2Hb} + c_{HHb}\alpha_{HHb}$ – the absorption coefficient of the tissue
α_{O_2Hb} *and* α_{HHb} – absorption coefficient of the oxy and deoxyhemoglobin,
d – the distance between source and detector,
DPF – the differential path length factor that accounts for the increase of travelling distance of photons due to scattering,
G – geometry dependent factor that compensates for the photons that miss the detector.

Some parameters of Eq. 16.1 remain unknown such as I_o and G. The intensity of the emitted light I_o can only be controlled indirectly by controlling the current of the light emitting diode (LED) that produces the I_o. Thus the light intensity is subject to the manufacturing tolerance of the LED and the associated electronic circuits. Similarly the G is unknown for the unknown efficiency of the light coupling to the tissue [5]. The calibration of the said parameters is a rather complex issue. However in many applications there is no need for such a calibration since only the relative changes in O_2Hb and HHb are observed. Thus the terms I_o and G can be eliminated by differentiation of the Eq. 16.1 with respect to time. For more detail consideration of Eq. 16.1, is provide in [10]. Two carefully selected wavelengths are mathematically sufficient for back-calculation of concentrations of [O_2Hb] and [HHb], as shown below.

$$-\frac{\partial}{\partial t}\begin{bmatrix}\ln I_{\lambda_1}\\ \ln I_{\lambda_2}\end{bmatrix}=\begin{bmatrix}DPF_{\lambda_1} & 0\\ 0 & DPF_{\lambda_2}\end{bmatrix}\times\begin{bmatrix}\alpha_{HHb,\lambda_1} & \alpha_{O_2HHb,\lambda_1}\\ \alpha_{HHb,\lambda_2} & \alpha_{O_2HHb,\lambda_2}\end{bmatrix}\times\frac{\partial}{\partial t}\begin{bmatrix}[HHb]\\ [O_2Hb]\end{bmatrix}\times d$$

Solving the above equation for [O_2Hb] and [HHb] allows for the determination of the oxygen saturation of arterial blood [10], which is calculated as

$$SaO_2=\frac{\Delta\,[O_2Hb]}{\Delta[O_2Hb]+\Delta[HHb]}$$

The oxygen saturation is the ratio of oxygenized hemoglobin to total hemoglobin and is clinically widely measured value by pulse-oxymeters. The equation makes use of measurements at two points in time, namely at systole and at diastole [10].

16.3 Difference Among NIRS Devices and Methods

It is important to note that spatially resolved, continuous-wave NIRS methods vary among devices. Key differences include specific modifications to the Beer-Lambert Law, the number and spacing of the light-emitting and receiving *optodes*, and the algorithms used to produce an output value. For example, in one method, light detectors are positioned at two different distances from the light-emitting *optode*. The detector close to the emitting *optode* is assumed to measure light reflected by the superficial tissue layers and extracranial blood, whereas the far detector presumably measures more of the cerebral light reflectance. An algorithm is then used to subtract the "extracranial signal." This method can be compared to one that uses three emitting and detecting diodes separated by different distances. HbO_2 and HHb are calculated from the regression line between the three values from the three detectors. This method does not directly subtract extracranial contamination but instead attempts to mitigate it through the use of algebraic calculations [8, 11]. Currently, most protocols are consistent with the general positioning of *optodes*, which are usually attached to the forehead and presumably provide a local measure of frontal lobe cerebral oxygenation.

The impact of methodological differences on study results is illustrated by a comparison of two relatively common NIRS devices: the NIRO 300 (Hamamatsu Photonics, Hamamatsu City, Japan) and the INVOS 5100 (Somanetics, Troy, Michigan, USA). The two devices differ significantly in several aspects, including their output. The NIRO 300 measures a "tissue oxygen index" (TOI), whereas the INVOS 5100 measures "regional cerebral oxygenation saturation" (rSO_2). The study found that rSO_2 values were 2.1 % lower than TOI values (SD of the difference between them = 7.5 %; ± 1.96 SD limit of agreement = 14.7 %), with results from the NIRO 300 having less variability. This is consistent with questions raised by others over the reliability of the INVOS 3100 [12–14]. Furthermore, there were

large inter- and intra-individual differences between the outputs of the two monitors. Despite the apparent imprecision of the rSO_2 and TOI values, both recorded an increase in cerebral oxygen (O_2) following hyperoxia and a significant reduction during hypocapnia. Other studies comparing different NIRS devices have also found variability in and among devices. For example, a study comparing INVOS 4100 and NIRO 300 during a CO_2 challenge test in anaesthetized patients found differences between the devices similar to those reported in [15].

The factors underlying variation in NIRS device measures are not fully understood, but they likely stem from multiple sources. For example, evidence suggests that the type of light emitter and *inter-optode* distance may influence output. Furthermore, even when using the same NIRS data, different published analysis methods produce different results [16]. Thus, the sensitivity and specificity of NIRS measures for BI diagnosis may be device dependent.

16.4 Some Medical Applications of NIRS Devices

16.4.1 NIRS and Ischemia

Overall, NIRS has good sensitivity and specificity for detecting ischemia. For example, in a large study that included 167 patients [17] undergoing carotid endarterectomy, TOI changes occurring during internal carotid artery clamping were compared with intracranial blood flow and cerebral function monitoring to identify and quantify periods of cerebral ischemia. Blood flow velocity and TOI changes were significantly correlated on clamping. Of the patients having TOI above −13, none showed evidence of ischemia on clamping. This threshold provided to have a sensitivity and specificity of 100 % and 93.2 %, respectively, for patients satisfying the preset criteria for cerebral ischemia [17].

16.4.2 NIRS and Hematoma

Relatively few clinical studies have examined the relationship between NIRS measures and BI of any severity. Of those that have included BI patients, most have focused on the ability of NIRS to detect subdural and epidural hematomas or predict delayed intracranial hematoma in head-injured patients (For example, NIR light at 760 nm was able to detect hematomas in head-injured patients [18]). In a more recent study, results comparing NIRS to CT findings suggest that NIRS may be useful in screening BI patients because it has good sensitivity, though the authors also noted that NIRS produced false positives [19].

16.4.3 Characterization of Atherosclerotic Plaque

The use of NIR spectroscopy for characterization of atherosclerotic plaque was initiated in 1993 by Cassis and Lodder [20] and reviewed in [21]. It was first shown that NIR spectra could accurately characterize low-density lipoprotein cholesterol accumulation in hyper-cholesterolemic rabbit aortas [20]. Near-infrared spectroscopy was then used in humans to image lipid content in carotid plaques exposed at the time of surgery [22]. After surgery, *ex-vivo* NIR scanning was performed on the excised plaque, and spectra were shown to predict lipoprotein composition as determined by gel electrophoresis. The early reports that NIR spectroscopy could be useful for characterizing plaque have been supported by similar findings from other groups. In 1999, Jaross et al. [23] compared cholesterol content determined by NIR spectroscopy versus that determined by reversed-phase, high pressure liquid chromatography in human aorta specimens. A high correlation coefficient (0.96) was observed. The same group later reported that the cholesterol-to-collagen ratio could also be accurately quantified by NIR [24]. In a study of recently excised human carotid plaque samples, Wang et al. [25] found a high correlation between direct *ex-vivo* measurements of lipid/protein ratios and results obtained with a NIR spectrometer fitted with a fiber-optic probe.

16.4.4 Neuronal Activity Measured by NIRS

The NIRS is suitable for non-invasive studies of oxygenation, perfusion and function of the tissue. Hence the NIRS is applied to observe the neuronal brain activity by observing the associated changes in concentrations of [O_2Hb] and HHb that take place in the stimulated regions of the brain. The local adaptation of the nutritional and oxygen demands of the stimulated regions in brain or other tissue has been observed for the first time by Roy and Sherrington in 1890. The described mechanism is called neurovascular coupling. The neurovascular coupling refers to changes in cerebral blood flow (CBF) as a consequence of the neuronal activity [26]. The neuronal activity involves various cellular processes, such as the restoration of ionic gradients and neurotransmitter recycling [26]. The said processes require energy in the form of adenosine triphosphate (ATP), whose synthesis can take place in anaerobic or aerobic manner. In the brain, about 90 % of glucose is metabolized by the oxidative glucose metabolism, which underlines the importance of CBF for supply of oxygen and glucose [26]. The alterations in neural activity and metabolism are correlated with changes in CBF, however mechanisms linking these processes are a matter of debate [26]. Knowing that the neuronal activity causes variations of ionic and molecular metabolic byproducts (K+, NO and CO_2 and arachidonic acid metabolites), the existence of a feedback mechanism sensitive to the said variations could be assumed. A further assumption is that the said by-products may directly or indirectly alter blood flow by depolarizing

(or hyperpolarizing) the vascular smooth muscle cells, which trigger vasodilatation [26] (or vasoconstriction). However, the assumed feedback mechanism appears to be oversimplified and an alternative feed-forward mechanism involving signaling via neurotransmitters and a dedicated role of the astrocytes is discussed [26]. Also some evidence on direct neuronal innervation of smooth muscle cells has been found [26]. To sum up, it can be said that there are some unknowns in functioning of the neurovascular coupling. Nevertheless, it is known that in regions of increased neuronal activity a hemodynamic change takes place causing the [O_2Hb] and [HHb] to change accordingly. These changes are measurable by NIR devices and provide some information about the underlying neuronal activities. It is reasonable to use the NIRS for its excellent temporal resolution to better understand the neuronal activities and possibly help in demystifying the discussed unknowns of the neurovascular coupling.

16.5 Strengths and Weaknesses of the NIRS as a Medical Technology

The NIRS technology is promising and there is hope that it will find its way into the clinical practice. As with every medical innovation, NIRS technology has its own advantages and disadvantages, which is discussed in this section. NIRS is not an imaging technology, thus the anatomical structures are all missing, which is a disadvantage. Further disadvantages encompass the inability to acquire measurements from the tissue depths below 2–3 cm [27], a rather poor spatial resolution and a not yet available detailed knowledge on meaning and interpretation of the acquired signals. On the other hand there are the advantages, which become apparent depending on the concrete applications. In neurology, it is increasingly important to detect unfavorable changes such as e.g. the insufficient supply of oxygen and nutrients to the brain possibly resulting in an apoplectic stroke, even before the anatomical change manifests and becomes visible with e.g. the CT 4–12 h thereafter. The NIRS provides excellence in temporal resolution regarding the information on tissue oxygenation above the ROI, which in many cases may present a significant contribution for staying within the therapeutic window [28]. For a reason of being small in dimensions the NIRS technology turns out to be practicable at the bedside or in even more ubiquitous settings such as incubators for pre-term infants or measurement of muscle oxygenation during exercise on adults [4]. The NIRS-technology exhibits absence of ionizing radiation that can harm the cells or the DNA, which is of particular importance when treating infants or young patients in general. Finally NIRS devices are quite inexpensive (see Table 16.1). Changes in cerebral hemodynamic and oxygenation can be measured by several techniques. For example, positron emission tomography (PET) has been used to measure changes in regional cerebral blood flow (CBF). These methods, however, are expensive, not widely available, associated with injection of radioactive compounds, and have a low temporal resolution [28].

Table 16.1 Comparison of difference methods in-vivo analysis of human brain function

Methods	Hemodynamic	Neuronal activity	Time resolution	Spatial resolution	Tracer	Bedside	Cost
NIRS	Yes	Yes	ms	10 nm	No	Yes	Low
MRI	Yes	No	s	1 mm	No	No	High
PET	Yes	No	min	5 mm	Yes	No	High
MEG	No	Yes	ms	cm	No	No	High
EEG	No	Yes	ms	cm	No	EMI	Low

Transcranial Doppler (TCD) sonography has been used to monitor changes in blood flow velocity in the large cerebral arteries. This method is relatively cheap, has a good temporal resolution, but does not provide information about regional changes in cerebral oxygen supply or metabolism [29]. Functional MRI provides high-spatial resolution imaging of cerebral [HHb] changes overtime due to exploitation of the difference in magnetic susceptibility between oxyhemoglobin and deoxyhemoglobin. Disadvantages of the fMRI method include its high expenses, contraindications in cases of ferrous implants such as vascular clips and pacemakers, claustrophobia, liability to movement artifacts, inability to detect changes in oxygenation parameters other than [HHb], and limitations in monitoring changes in cerebral oxygenation during assuming a different position. Finally, fMRI availability in clinical centers for research purposes is often limited. NIRS is a simple, inexpensive bedside technique that permits specified monitoring of changes in [O_2Hb], [HHb], and total hemoglobin ([tHb]) with high temporal resolution. Disadvantages of NIRS are the relatively low spatial resolution and low cerebral penetration depth. In addition, *optode* positioning over specific cerebral cortical areas depends on external anatomical landmarks and on determining the area of optimum signal responses by trial-and-error positioning. NIRS and fMRI can be considered as complementary methods for cerebral cortical oxygenation monitoring. Because we often encounter cerebral symptomatology during posture changes or an inability to lie completely still in elderly patients, NIRS may be an easier method than fMRI for investigating cerebral oxygenation responses in an elderly population, e.g. for investigating cerebral oxygenation responses to orthostatic stress [30, 31].

16.6 Conclusion

In summary, even though some of the disadvantages are imposed by the law of physics such as the penetration depth or the spatial resolution, there are quite a few applications, where the mentioned constraints are not predominant but can beneficially be traded for the advantages of e.g. the temporal resolution or the transportability. Other disadvantages such as the lack of anatomical information can possibly be ameliorated by use of multiple NIRS devices or repositioning a single

NIRS device, while searching for regions that may have caused an apoplectic stroke. Transportability and absence of ionizing radiation allows for the almost ubiquitous use of NIRS devices, which makes them particularly interesting for clinical research and understanding of brain processes in e.g. the neonates. This research on the other hand will hopefully improve the mathematical models and provide for better understanding of acquired signals.

References

1. Bright R (1831) Reports of medical cases selected with a view of illustrating the symptoms and care of diseases by a reference to morbid anatomy, vol 2, Diseases of the brain and nervous system. Longman, London, pp 431–435
2. Barozzino T, Sgro M (2002) Trans-illumination of the neonatal skull: seeing the light. J De l'Assoc Med Can 167(11):12717–12727
3. Cope M, Delpy DT (1988) System for long-term measurement of cerebral blood and tissue oxygenation on newborn infants by near infra-red transillumination. Med Biol Eng Comput 26(3):289–294
4. Jobsis FF (1977) Noninvasive, infrared monitoring of cerebral and myocardial oxygen sufficiency and circulatory parameters. Science 198(4323):1264
5. Matcher SJ, Elwell CE, Cooper CE, Cope M, Delpy DT (1995) Performance comparison of several published tissue near-infrared spectroscopy algorithms. Anal Biochem 227:54–68. doi:10.1006/abio.1995.1252
6. Brazy JE, Lewis DV, Mitnick MH, vander Vliet FF (1985) Noninvasive monitoring of cerebral oxygenation in preterm infants: preliminary observations. Pediatrics 75(2):217
7. Young AE, Germon TJ, Barnett NJ, Manara AR, Nelson RJ (2000) Behaviour of near-infrared light in the adult human head: implications for clinical near-infrared spectroscopy. Br J Anaesth 84(1):38
8. Al-Rawi PG (2005) Near infrared spectroscopy in brain injury: today's perspective. Acta Neurochir Suppl 95:453–457
9. Calderon-Arnulphi M, Alaraj A, Slavin KV (2009) Near infrared technology in neuroscience: past, present and future. Neurol Res 31(6):605–614
10. Muhlemann TL (2010) A novel wireless near- infrared spectrophotometer applied to measure cortical haemodynamics in humans and sheep. ETH (Swiss Federal Institute of Technology) dissertation no 19051
11. Al-Rawi PG, Smielewski P, Kirkpatrick PJ (2001) Evaluation of a near-infrared spectrometer (NIRO 300) for the detection of intracranial oxygenation changes in the adult head. Stroke 32(11):2492
12. Colier W, Haaren N, Oeseburg B (1995) A comparative study of two near infrared spectrophotometers for the assessment of cerebral haemodynamics. Acta Anaesthesiol Scand 39(s107):101–105
13. Grubhofer G, Tonninger W, Keznickl P, Skyllouriotis P, Ehrlich M, Hiesmayr M, Lassnigg A (1999) A comparison of the monitors INVOS 3100 and NIRO 500 in detecting changes in cerebral oxygenation. Acta Anaesthesiol Scand 43(4):470
14. McKeating EG, Monjardino JR, Signorini DF, Souter MJ, Andrews PJD (1997) A comparison of the Invos 3100 and the Critikon 2020 near-infrared spectrophotometers as monitors of cerebral oxygenation. Anaesthesia 52(2):136–140
15. Thavasothy M, Broadhead M, Elwell C, Peters M, Smith M (2002) A comparison of cerebral oxygenation as measured by the NIRO 300 and the INVOS 5100 near-infrared spectrophotometers. Anaesthesia 57(10):999–1006

16. Matcher SJ, Elwell CE, Cooper CE, Cope M, Delpy DT (1995) Performance comparison of several published tissue near-infrared spectroscopy algorithms. Anal Biochem 227(1):54–68
17. Al-Rawi PG, Kirkpatrick PJ (2006) Tissue oxygen index: thresholds for cerebral ischemia using near-infrared spectroscopy. J Cereb Circ 37(11):2720–2725
18. Gopinath SP, Robertson CS, Grossman RG, Chance B (1993) Near-infrared spectroscopic localization of intracranial hematomas. J Neurosurg 79(1):43–47
19. Ghalenoui H, Saidi H, Azar M, Yahyavi ST, Borghei Razavi H, Khalatbari M (2008) Near-infrared laser spectroscopy as a screening tool for detecting hematoma in patients with head trauma. Prehosp Disaster Med 23(6):558–561, The Official Journal of the National Association of EMS Physicians and the World Association for Emergency and Disaster Medicine in Association with the Acute Care Foundation
20. Cassis LA, Lodder RA (1993) Near-IR imaging of atheromas in living arterial tissue. Anal Chem 65:1247–1256
21. Caplan JD, Waxman S, Nesto RW, Muller JE (2006) Near-infrared spectroscopy for the detection of vulnerable coronary artery plaques. J Am Coll Cardiol 47(8s1):C92–C96
22. Dempsey RJ, Davis DG, Buice RG et al (1996) Biological and medical applications of near-infrared spectroscopy. Appl Spectrosc 50:18A–34A
23. Jaross W, Neumeister V, Lattke P et al (1999) Determination of cholesterol in atherosclerotic plaques using near infrared diffuse reflection spectroscopy. Atherosclerosis 147:327–337
24. Neumeister V, Scheibe M, Lattke P, Jaross W (2002) Determination of the cholesterol-collagen ratio of arterial atherosclerotic plaques using near infrared spectroscopy as a possible measure of plaque stability. Atherosclerosis 165:251–257
25. Wang J, Geng YJ, Guo B et al (2002) Near-infrared spectroscopic characterization of human advanced atherosclerotic plaques. J Am Coll Cardiol 39:1305–1313
26. Pasley BN, Freeman RD (2008) Neurovascular coupling. Scholarpedia 3(3):5340, Brain Corporation
27. Wolf M, Greisen G (2009) Advances in near-infrared spectroscopy to study the brain of the preterm and term neonate. Clin Perinatol 36:807–834
28. Villringer A (1997) Understanding functional neuroimaging methods based on neurovascular coupling. Adv Exp Med Biol 413:177–193
29. Vernieri F, Rosato N, Pauri F, Tibuzzi F, Passarelli F, Rossini PM (1999) Near infrared spectroscopy and transcranial Doppler inmonohemispheric stroke. Eur Neurol 41:159–162
30. Delpy DT, Cope M, van der Zee P, Arridge S, Wray S, Wyatt J (1988) Estimation of optical path length through tissue from direct time of flight measurement. Phys Med Biol 33:1433–1442
31. Mehagnoul-Schipper DJ, Vloet LCM, Colier WNJM, Hoefnagels WHL, Jansen RWMM (2000) Cerebral oxygenation declines in healthy elderly subjects in response to assuming the uprightposition. Stroke 31:1615–1620

Chapter 17
Absorbance Control of Liquids Employing Transmission Sub-wavelength DLC Diffraction Grating

Tomas Tamulevičius, Ieva Gražulevičiūtė, and Sigitas Tamulevičius

Abstract This research focuses on the application of transmission sub-wavelength diffraction grating, consisting of dry etched in SiO_x doped amorphous diamond like carbon (DLC) films for real time monitoring of complex refractive index of liquid analytes. The 428 nm period diffraction was fabricated employing holographic lithography and dry etched utilizing CF_4/O_2 gas mixture plasma in 230 nm DLC film synthesized from the hexamethyldisiloxane vapor employing direct ion beam deposition. Sensor chip fabricated here was placed in contact with different concentration Methylene Blue (MB) aqueous solutions was applied in the automated motorized angular white polarized light reflectivity measurement setup. From complex refractive index sensitive to peak positions in the reflection spectra, information about model analyte solutions was extracted. It was demonstrated that the sensor is sensitive to $>1{\cdot}10^{-5}$ mol/l concentration changes of the MB aqueous solution. The grating solver based on rigorous coupled wave analysis was used to explain the experimental behavior of the peaks in the reflection spectra. Comparing the experimental and simulation results, parameters such as grating height and thickness of waveguiding layer were defined.

Keywords DLC • MB • Diffraction grating • Complex refractive index

17.1 Introduction

It was demonstrated that application of the regular optical structures, e.g. transmission diffraction gratings [1], long period gratings (LPG) [2], Bragg gratings [3] etc., can be applied for the determination of real or/and imaginary part of refractive

T. Tamulevičius (✉) • I. Gražulevičiūtė • S. Tamulevičius
Institute of Materials Science, Kaunas University of Technology, Savanorių Ave. 271, LT-50131 Kaunas, Lithuania
e-mail: tomas.tamulevicius@ktu.lt; Ieva.Grazuleviciute@ktu.lt; sigitas.tamulevicius@ktu.l

A. Vaseashta and S. Khudaverdyan (eds.), *Advanced Sensors for Safety and Security*, NATO Science for Peace and Security Series B: Physics and Biophysics,
DOI 10.1007/978-94-007-7003-4_17,

index of liquids. Refractive index of liquid is closely related to its concentration and density [4]. It was shown that measuring the diffraction efficiencies of the monochromatic light diffracted from the total internal reflection diffraction grating that is in contact with analyte, one can characterize the absorbance of the medium [5]. It was also demonstrated that monitoring spectral composition (peaks/dips) of the white polarized light reflection spectra obtained from the transmission diffraction grating that is in contact with the analyte, one can simultaneously obtain information about the real and imaginary parts of the refractive index of the liquid under investigation [1].

Applications of the regular structures for the refractive index, absorbance or biological reaction sensing require compatibility of the construction material with the microlithography techniques, low absorbance in the utilized wavelength range, and resistance together with bio-compatibility for the different analytes. Diamond like carbon (DLC) films received considerable interest due to their outstanding mechanical, chemical, optical and electrical properties making them useful for a wide range of contemporary applications [6, 7]. As for example, deposition of the high refractive index DLC coating on optical fiber with LPG improved the sensitivity of the refractive index sensor by 15 times compared with the uncoated one [8, 9].

In our recent work we have demonstrated that the sub-wavelength diffraction gratings in photoresist, photoresist coated with DLC or etched in DLC can be applied for determination of the dispersion curve of the liquid analytes and substrate of the sensor chip itself [10]. Moreover it was demonstrated that the DLC sensor chips can be applied for monitoring of the refractive index kinetics including temperature and concentration changes of aqueous glucose solution or biological reactions [11]. It was shown that by monitoring the amplitude and peak position in the reflection [11], transmission or wave-guided light spectra [12] one can control the refractive index changes with the uncertainty down to 10^{-4} [11]. It was also demonstrated that application of the DLC for the sensor chip fabrication as the high refractive index material broadens the detection range of the refractive index [11]. In the current work, we demonstrate that the transmission sub-wavelength diffraction grating dry etched in DLC doped with SiO_x can be applied for the determination of absorbance of the model analytes i.e. MB aqueous solutions. We simulated the reflection spectra of the sensor chip employing grating solver based on rigorous coupled wave analysis and explained positions of the peaks in the spectra.

17.2 Experimental

17.2.1 Deposition of the DLC Film

The SiO_x doped amorphous hydrogenated carbon (a-C:H:SiO_x, DLC) films were deposited employing a modified Ion-beam etcher on chemically cleaned fused silica (FS) and crystalline silicon substrates. The film deposition was carried employing

hexamethyldisiloxane (HMDSO – $(CH_3)_3SiOSi(CH_3)_3$) vapor as a source of the hydrocarbon and silicon oxide utilizing hydrogen (H_2) as a transport gas. The total flux of gases was 30–40 sccm (standard cubic centimeters/minute). The residual pressure was 2×10^{-4} Pa, work pressure $1–2 \times 10^{-2}$ Pa, ion beam energy was 500 eV, and current density – 60 μA/cm^2.

17.2.2 Characterization of the DLC Film

Transmittance and reflectance spectra of the DLC film deposited on fused silica substrates (and absorption coefficient of the liquid analytes) were evaluated employing UV/VIS/NIR Avantes AvaSpec-2048 spectrometer (spectral range (SR): 172–1,100 nm, resolution 1.4 nm) and a light source AvaSpec-DHc (SR: 200–2,500 nm). The thickness ($t = 230$ nm) and refractive index ($n_{DLC} = 1.85$) of the DLC film (deposited on Si) were measured by a laser ellipsometer Gaertner L115 ($\lambda = 632.8$ nm).

17.2.3 Fabrication of the Diffraction Grating in DLC Film

The fused silica substrates with DLC films were spin-coated with a positive tone photoresist maP-1205 and baked on the hotplate. The photoresist was exposed employing a custom built holographic lithography setup. The optical setup consists of the HeCd laser (442 nm), beam expanding and collimating optics, beam splitter, and mirrors directing the two interfering beams on the sample surface at the selected angle of incidence. After the appropriate exposure dose, the samples were developed in the MF-26A developer. Residuals of the photoresist in the grating grooves were removed employing reactive ion beam etching utilizing modified Usi-ionic ion beam etching unit with a multi-cell closed drift Hall-current ion source. Typical processing parameters: oxygen ion beam energy 300 eV, ion current density 0.15 mA/cm^2, processing duration 3 min, pressure in vacuum chamber $1 \cdot 10^{-2}$ Pa.

DLC films were dry etched in a plasma deposition system PK-2430PD. The structures were etched employing CF_4/O_2 (80 %/20 %) feedstock gas mixture RF (13.56 MHz) plasma at 60–67 Pa pressure, total flux of gases was 300 sccm and 0.75 W/cm^2 RF power density, processing durations 3 min. The period of the resulting structure $d = 427.76 \pm 0.83$ nm was determined from the FEI Quanta 200 FEG scanning electron microscope micrograph and was also estimated by optical means measuring the angles of diffraction with a laser diode ($\lambda = 405$ nm).

17.2.4 Automated Optical Responds Measurement Setup

The white polarized light angular reflectance from the sensor chip was obtained employing a custom built motorized angular reflectance measurement stand and

CCD spectrometer AvaSpec-2048 (SR: 360–860 nm, resolution 1.2 nm). The angles of incidence and detection were controlled via motorized stages with 0.6 arcmin full step resolution. The sensor chip was fixed together with a fluid cell for the liquid analytes. The white light emitted from the incandescent lamp was collimated employing set of lenses and polarized employing Glan-Taylor prism driven by a motorized stage. The reflected light was coupled to the spectrometer fiber employing a lens. The motorized stages and spectrometer were controlled via custom software.

Normalizing the specular reflection data to the lamp spectrum and taking into account the different integration time we have estimated the reflectance spectra for the different angles of incidence. To enhance the peaks detected in the specular reflection spectra, first derivative of the reflection coefficient ($dR(\lambda)/d\lambda$) was calculated employing Savitzky–Golay Smoothing (SGS) procedure, where the data was fitted by the second order polynomial expansion and derivative was obtained using 51 point filter [13]. Reflectance measurements of the TM polarized light were performed at different angles of incidence: 10°, 15°, 20° for different analytes including air, water and three different molar concentration MB aqueous solutions – $1{\cdot}10^{-5}$ mol/l, $5{\cdot}10^{-5}$ mol/l, $1{\cdot}10^{-4}$ mol/l. The absorbance of the MB solutions was estimated employing transmission measurements described in Sect. 17.2.2.

17.2.5 Simulations

The reflectance spectra from the DLC sensor chips were simulated employing commercially available grating solver software "GSolver" [14] based on Rigorous Couples Wave Analysis (RCWA) [15]. The sinusoidal profile diffraction grating was approximated by 21 layers and in total 10 reflections and transmission diffraction orders were taken into account. Optical properties of the DLC [16], fused silica [17], air [18], water [19] and MB solutions [1] where taken from the literature.

17.3 Results and Discussions

The absorption coefficient of the DLC film (see Fig. 17.1) was calculated employing Eq. 17.1 taking into account the reflectance and transmittance of the film:

$$abs = \frac{1}{t} \ln\left(\frac{1-R}{T}\right) \tag{17.1}$$

where abs – absorption coefficient (cm^{-1}), t – thickness of the film (cm), R – reflection coefficient, T – transmission coefficient.

From Fig. 17.1 one can see that the DLC film is transparent in the visible range covered by the employed light source and spectrometer detector therefore it can be utilized as a constructional material for the grating sensor chip.

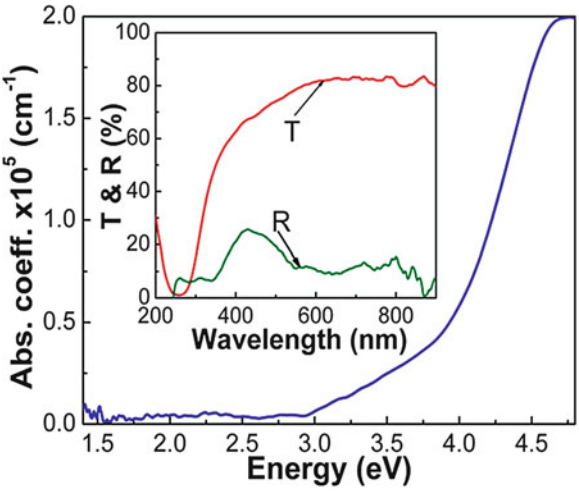

Fig. 17.1 Absorption coefficient of the DLC film deposited on fused quartz substrate. The inset shows reflection (R) and transmission (T) spectra obtained from the film

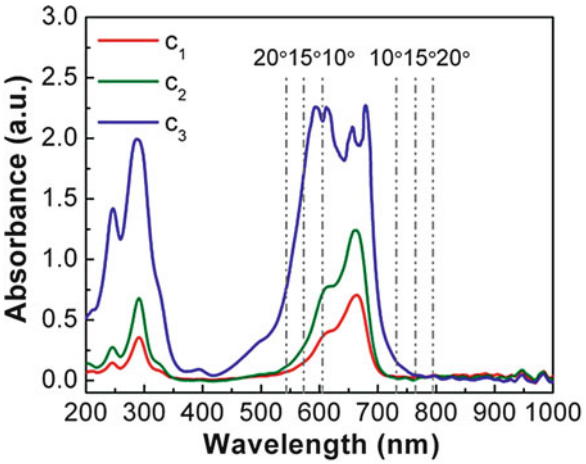

Fig. 17.2 Absorbance of MB aqueous solutions of the different molar concentration ($c_1 = 1{\cdot}10^{-5}$ mol/l, $c_2 = 5{\cdot}10^{-5}$ mol/l, $c_3 = 1{\cdot}10^{-4}$ mol/l). Truncated lines represent the positions of the peaks that emerge in the reflection spectra obtained from the sub-wavelength diffraction grating at different angles of incidence (10°, 15°, 20°)

The absorbances of different molar concentration MB aqueous solutions are shown in Fig. 17.2. One can see that the absorbance of the solution is increasing together with the molar concentration of MB. Truncated lines (see Fig. 17.2) represent the complex refractive index sensitive peak positions in the reflection spectra obtained at different angles of incidence.

The reflectance spectra from the sensor chip in contact with different analytes at different angles of incidence of light were obtained. In Fig. 17.3 the optical response from the grating sensor when it is in contact with water is presented. One can see that the positions (critical wavelengths) of the double peaks in the reflection spectra change with the angle of incidence. Therefore by scanning the angle one can obtain the dispersion curve of the complex refractive index or select the wavelength region of interest. In Fig. 17.4 the first derivative of the reflection spectra obtained from

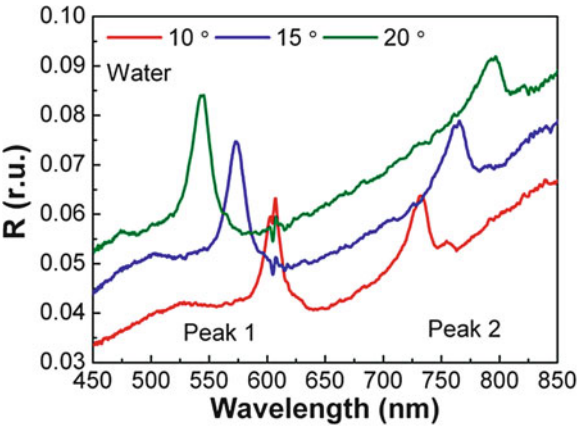

Fig. 17.3 Reflectance spectra obtained at different angles of incidence (10°, 15°, 20°). Analyte water. "Peak 1, 2" represents the peak number used later on in the text

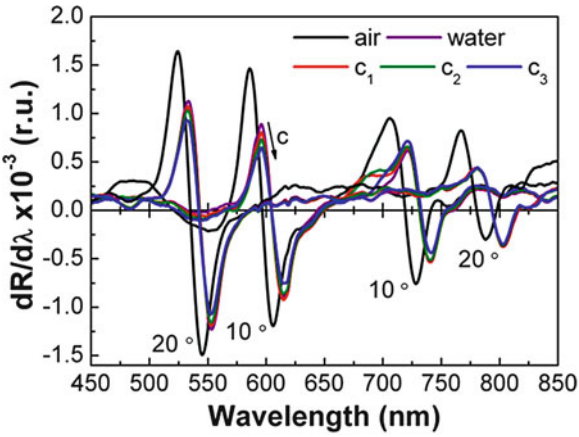

Fig. 17.4 First derivate of the reflectance spectra calculated employing SGS smoothing obtained from different analytes (air, water, MB solutions of different concentration) at two different angles of incidence (10°, 20°). The *arrow* indicates the direction of the increasing concentration (*c*)

different analytes at two different angles of incidence calculated employing SGS procedure is shown. One can see that the critical wavelength positions are red shifted in the case of the liquid analytes compared to the case of air. This can be addressed to the change in the real part of the analyte refractive index. Whereas decrease of the first derivative amplitude is more pronounced for the different liquid analytes as compared with the peak shift. It should be noted that this decrease is related to the increase of the imaginary part of the refraction index similarly like in [1].

In Fig. 17.5 one period of the diffraction grating structure used for modeling with GSolver is presented. The period of the diffraction grating and total thickness of the DLC film was obtained from the measurements (see Sect. 17.2.3) while the depth of the sine profile etched in DLC film and the thickness of the residual wave guiding layer was determined varying the grating model and comparing the calculated peak positions with the experimental ones. In Fig. 17.6 one can see the principle example of the peak position dependence on the height of the diffraction grating. The increase in the grating height at the same time decreases the residual film (wave guiding)

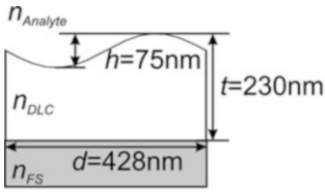

Fig. 17.5 One period of the grating model employed in the GSolver software

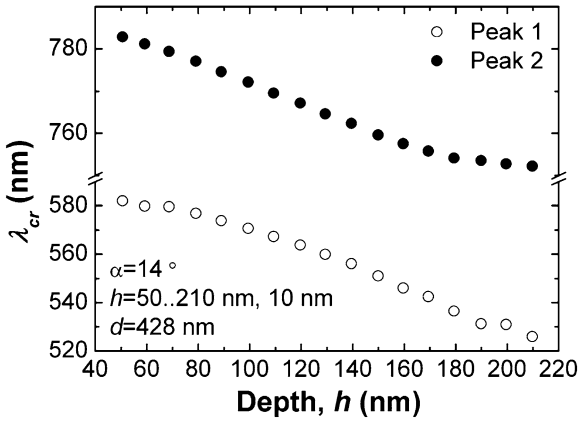

Fig. 17.6 Peak positions vs. depth of the grating in fixed thickness DLC film. Analyte air

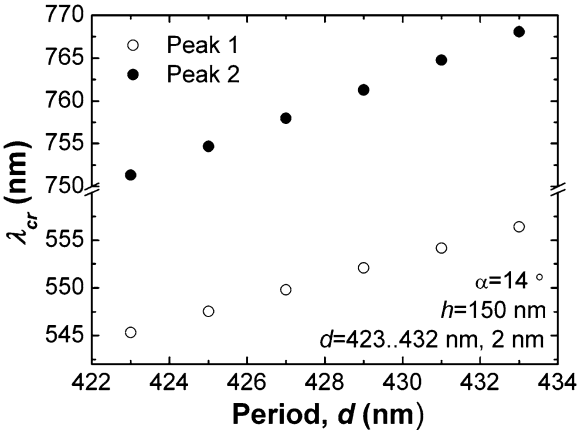

Fig. 17.7 Peak positions vs. period of the fixed depth grating in the DLC film. Analyte air

layer and results in the blue shift of the peaks in the reflection spectra. While the variation of the period in the vicinity of the determined value shows red shift of the peaks with the increase of the period (see Fig. 17.7).

In this way, comparing the simulation and experimental results one can characterize linear dimensions of the sensor chip. The simulated spectra at the angle of incidence of 14° were compared with the experimental results that are not presented in this work. The simulation results presented later on in the text were calculated employing the obtained geometrical parameters depicted in Fig. 17.5.

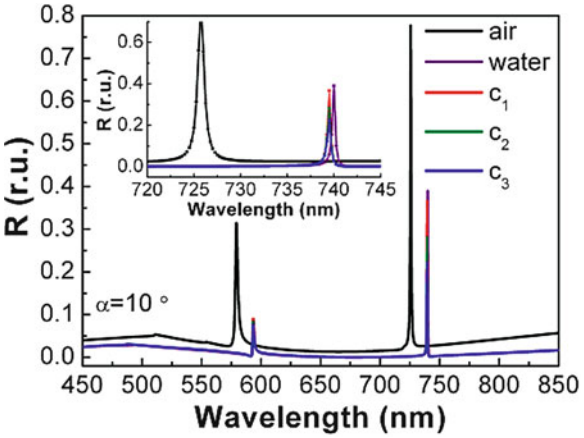

Fig. 17.8 Reflection spectra from the grating in contact with different analytes simulated employing GSolver for 10° angle of incidence

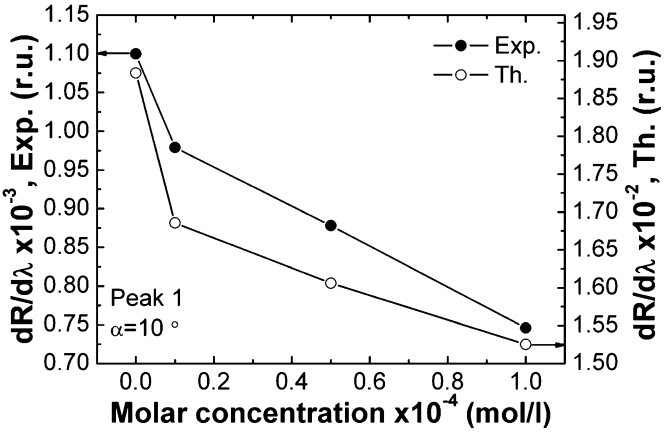

Fig. 17.9 Experimental and simulated dependence of the amplitude height of the first derivative of reflection spectra vs. concentration of the MB in water. *Lines* are for guiding the reader's eye

In Fig. 17.8 the simulated reflectance spectra from the diffraction grating when it is in contact with different analytes are presented. Comparing the simulated spectra with the experimental results, i.e. first derivative of the reflection spectra (see Fig. 17.4) one can see that the simulated results demonstrate the same peak behavior dependent on the analyte that is in contact with the diffraction grating. In Figs. 17.9 and 17.10 the analysis of the peak amplitude and position on the MB concentration is presented. From Fig. 17.9 one can see that the amplitude of the first derivative of the reflection spectrum at the peak position decreases with increasing concentration of the MB in water i.e. increasing absorption similarly like in [1].

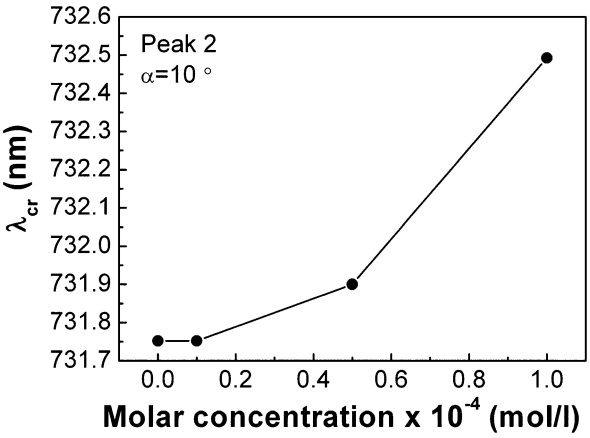

Fig. 17.10 Experimental dependence of the peak position vs. concentration of the MB in water. *Lines* are for guiding the reader's eye

One can also see that the trend of the experimental results agrees with the simulated data obtained from Fig. 17.8. Successively the peak positions are also sensitive to the increasing real part of the refractive index (or MB concentration) that emerges as a red shift of the peak (see Fig. 17.10) like in [1, 10, 11]. In this case the simulation results are not shown because only two theoretical refractive index points were known for the accurate calculations.

17.4 Conclusions

We have demonstrated experimentally that the sub-wavelength DLC diffraction grating can be applied for monitoring of the absorbance changes in the Methylene Blue aqueous solutions. It was shown that the method is sensitive to at least $1{\cdot}10^{-5}$ mol/l change in the MB concentration. The simulation of the reflectance spectra enabled us to determine the geometrical parameters of the waveguiding structure and to explain the nature of the peaks together with their response to the model analytes.

Acknowledgments I.G. acknowledges Student Research Fellowship Award from the Research Council of Lithuania. Authors are grateful to Dr. Š. Meškinis and V. Kopustinskas for their help in thin film technologies. This research was performed within COST action MP0803.

References

1. Anderson BB, Brodsky AM, Burgess LW (1996) Threshold effects in light scattering from a binary diffraction grating. Phys Rev E 54:912–923
2. Smietana M, Bock WJ, Mikulic P, Ng A, Chinnappan R, Zourob M (2011) Detection of bacteria using bacteriophages as recognition elements immobilized on long-period fiber gratings. Opt Express 19:7971–7978

3. Simoni F, Castagna R, Criante L, Lucchetta DE, Vita F (2008) Method and apparatus for measuring the refractive index of a material with Bragg gratings. Patent Pub. No. WO/2008/129580, International Application No. PCT/IT2008/000257
4. Guo WP, Xia M, Li W, Dai J, Yang KC (2011) A two-reflection divergent differentiating critical angle refractometer. Rev Sci Instrum 82:053108
5. Sarov Y, Sainov S (2002) Absorption sensor based on total internal reflection diffraction grating. J Opt A Pure Appl Opt 4:382–386
6. Robertson J (2002) Diamond-like amorphous carbon. Mater Sci Eng R 37:129–281
7. Meškinis Š, Šlapikas K, Gudaitis R, Tamulevičius S, Kopustinskas V, Guobienė A et al (2008) SiO_x-doped DLC films: charge transport, dielectric properties and structure. Vacuum 82: 617–622
8. Smietana M, Szmidt J, Korwin-Pawlowski ML, Bock WJ, Grabarczyk J (2007) Application of diamond-like carbon films in optical fibre sensors based on long-period gratings. Diamond Relat Mater 16:1374–1377
9. Smietana M, Korwin-Pawlowski ML, Bock WJ, Pickrell GR, Szmidt J (2008) Refractive index sensing of fiber optic long-period grating structures coated with a plasma deposited diamond-like carbon thin film. Meas Sci Technol 19:085301
10. Tamulevičius T, Šeperys R, Andrulevičius M, Tamulevičius S (2011) Total internal reflection based sub-wavelength grating sensor for the determination of refractive index of liquids. Photon Nanostruct Fundam Appl 9:140–148
11. Tamulevičius T, Šeperys R, Andrulevičius M, Kopustinskas V, Meškinis Š, Tamulevičius S et al (2012) Application of holographic sub-wavelength diffraction gratings for monitoring of kinetics of bioprocesses. Appl Surf Sci 258:9292–9296
12. Tamulevičius T, Šeperys R, Andrulevičius M, Kopustinskas V, Meškinis Š, Tamulevičius S (2011) Refractive index sensor based on the diamond like carbon diffraction grating. Thin Solid Films 519:4082–4086
13. Savitzky A, Golay MJE (1964) Smoothing and differentiation of data by simplified least squares procedures. Anal Chem 36:1627–1639
14. The "GSolver" software is available from Grating Solver Development Co. http://www.gsolver.com. Accessed 1 June 2012
15. Moharam MG, Pommet DA, Grann EB, Gaylord TK (1995) Stable implementation of the rigorous coupled-wave analysis for surface-relief gratings – enhanced transmittance matrix approach. J Opt Soc Am A Opt Image Sci Vis 12:1077–1086
16. Meškinis Š, Kopustinskas V, Šlapikas K, Gudaitis R, Tamulevičius S, Niaura G et al. (2006) Optical properties of the undoped and SiOx doped DLC films – art. no. 65961L. In: Ašmontas S, Gradauskas J (eds) Conference on advanced optical materials, technologies and devices, Vilnius, 2006, p L5961.
17. Material Properties – UV-grade synthetic fused silica. Available https://www.cvimellesgriot.com/products/Documents/TechnicalGuide/Material-Properties.pdf. Accessed 1 June 2012
18. Edlén B (1966) The refractive index of air. Metrologia 2:71–80
19. Lide DR (ed) (2010) CRC handbook of chemistry and physics, 90 edn (CD-ROM version 2010). CRC Press/Taylor and Francis, Boca Raton

Chapter 18
Detection and Monitoring of Surface Deformations in Armenia Using INSAR Satellite

G.M. Aleksanyan and M.A. Grigoryan

Abstract This article describes the results of studies conducted as a result of a NATO collaboration linkage grant (CLG): ESP.EAP.CLG.983876, during which we developed components for a future regional monitoring system for those regions of Armenia that the most prone to frequent natural disasters, viz. mud-slides and ground deformation. This system is based on the using of the geological terrain surfaces data, INSAR simulation tools and mathematical interpretation of digital elevation models, GIS technology, mathematical models and computer programs to process satellite's images with a certain probability that allows prediction of onset and developing of disasters. The monitoring results are intended to be used to forewarn, prevent, minimize and mitigate possible adverse effects of such natural disasters.

Keywords InSAR • Geological data • Mudflows • Earthquakes • Topographical maps • DEM • GIS • Processing of satellite images • Modeling

18.1 Introduction

During 2010–2011, joint scientific, Burgas Free University, Bulgaria and Yerevan State University, Armenian team implemented a NATO project № 983876, titled "InSAR Modeling and monitoring of Geological Disaster Phenomena in Caucasus region of Armenia". The main goal of the project is to develop a monitoring system for natural disasters. The object of investigation covers areas of rocks

G.M. Aleksanyan (✉) • M.A. Grigoryan
Geography and Geology Department, Yerevan State University,
1 Alex Manoogian Str., 0025 Yerevan, Armenia
e-mail: gurgenal@ysu.am

A. Vaseashta and S. Khudaverdyan (eds.), *Advanced Sensors for Safety and Security*,
NATO Science for Peace and Security Series B: Physics and Biophysics,
DOI 10.1007/978-94-007-7003-4_18,

of subsidence, landslides, and earthquakes in Armenia. The main research technique comprises Interferometric Synthetic Aperture Radar – (InSAR) processing systems, mathematical instruments for realization of digital models, GIS technologies and mathematical models for handling complex images obtained from ASAR (Advanced Synthetic Aperture Radar) sensors mounted on the satellite ENVISAT ("Environmental Satellite") and Synthetic Aperture Radar (SAR) tools, established on satellites ERS-1 and ERS-2. The developed monitoring system can be used to forecast topographic changes in areas in Armenia under risk to evaluate current situation of them and to perform long-term prediction of probable natural disasters. The basic instruments in this study are methods and algorithms of InSAR technology. SAR is a coherent active sensitive element used in radio vision interferometric SAR technique. SAR interferometry is based on the phase difference information extracted from two complex valued SAR images acquired from different orbit positions and registered in sub-pixel level. This information is useful in measuring several geophysical quantities such as topography, slope, deformation (volcanoes, earthquakes, and ice fields), glacier studies, vegetation growth etc. This methodology has application for defense and security as same principles can be used to study several aspects of battlefield.

18.2 Geologic Features of Armenia

Armenia is situated in the seismically active crescent that stretches from the Alps through the Caucasus and Central Asia to the Russian Federation, along with Turkey and other earthquake prone countries. The substantial earthquake hazard is due to interactions of major tectonic plates: Indian and Arabian plates are moving north, colliding with the Eurasian plates resulting in thrust faulting-an ongoing process that created the major mountain ranges from the Caucasus to the Himalayas.

18.2.1 Landslides and Mudflows in Armenia

Landslide sites in the Republic of Armenia (Fig. 18.1) cover about 122,000 ha, which is 4.1 % of country's total territory; some 35 % of settlements are located on landslide-prone areas [1–4]. 233 communities (≈25 %) are affected by landslides, according to a recent study by the Japan International Cooperation Agency (JICA). Landslides are active in more than 100 communities and have affected hundreds of residential buildings, communication infrastructure, and vital facilities, including 1,744 ha (≈5.2 % of total residential space); 240 km (≈3.2 % of total) of roads/highways; and 4.8 km.(≈0.5 % of the total) of railways.

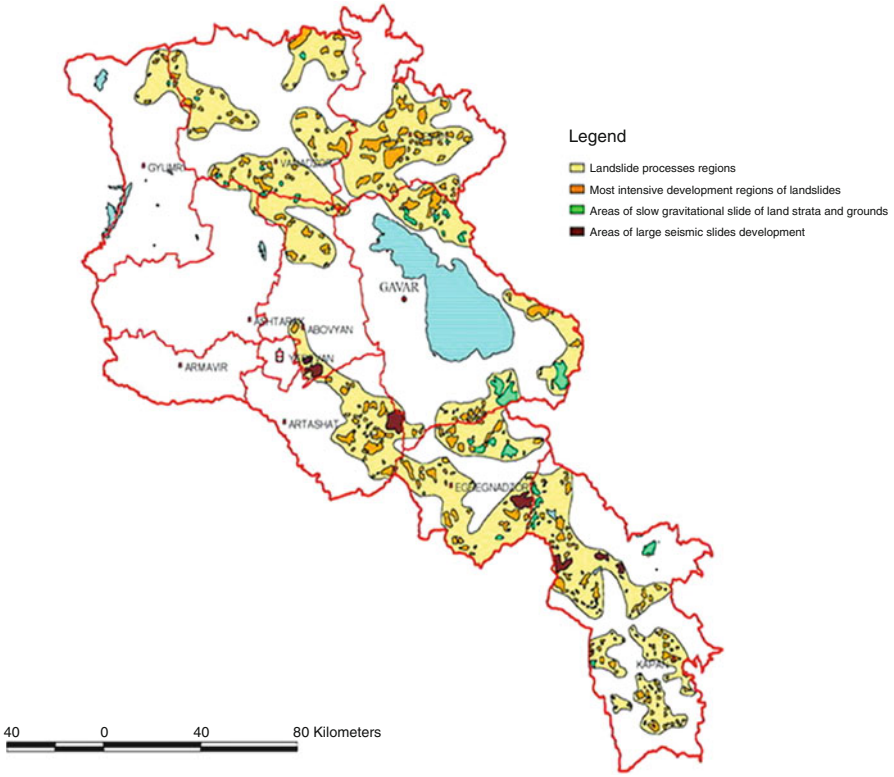

Fig. 18.1 Landslide areas with high level of risk in Armenia

The following activities have been carried out by Armenian principal investigators in the Project.

- Identification and selection of the areas of Armenia which are most exposed to seismic and landslide risk;
- Study of geological and morphological structures of selected areas;
- Study of topographic – geodesic information of risk areas before and after disaster as well as military topographical maps of the former USSR (medium-scales from 1:200,000 to 1:1,000,000 and small-scales less than 1:1,000,000);
- Study of large number of scientific-technical literature, technical reports and geological survey maps.

As a result of this research it was decided that tools ESA, SAR systems are necessary to be used to study the territories having landslides which are the most active and are dangerous for the population and infrastructure of the following

Table 18.1 Coordinates of most active landslides of Armenia

Name of land slip	Latitude (Northern breadth)	Longitude (East longitude)
Voghchaberd	40° 10′ 00″	44° 39′ 10″
Dilijan	40° 45′ 10″	44° 53′ 15″
Ughedzor (Kochbek)	39° 41′ 00″	45° 43′ 00″

areas: Dilijan, Voghchaberd, Ughedzor (Kochbek) – as referred in Table 18.1 and Spitak (a city in northern Armenia) 1988 earthquake zone (also called Leninakan earthquake and Gyumri earthquake).

18.3 Creation of Digital Elevation Models for Selected Risks Territories

The topographic map of 1:100,000 scale of the territory of Armenia was taken as a basis to create digitized maps of the regions with high level of landslides and other ground displacements caused by earthquakes (Dilijan; Voghchaberd; Ughedzor (Kochbek) and the Spitak Earthquake Source Zone). In the map, the vertical shootings of areas were realized during 1950–1958, and the information of plan shooting was refreshed later in 1973–1980. The map has been created with "Gauss Kruger" projection in "Pulkovo 1942" coordinate system. The breaks between horizontals are 20 m. Vertical shooting of the territory of Armenia was not done during last 25–30 years except some local territories. The 1:100,000 scale topographic map of Armenia was used for general orientation, which was inputted into ArcGIS Desktop 9.3 environment by scanning its parts as digital-raster images (Fig. 18.2). The map was geo-referenced with "Gauss Kruger" projection in "Pulkovo 1942" coordinate system. Following that, the Dilijan, Voghchaberd, Ughedzor (Kochbek) landslides and Spitak earthquake source zone areas (100 × 100 km) were separated from the map which have been transformed and presented in the "WGS 1984" [5–8].

For creation of Digital Elevation Model (DEM) of the selected risk areas has been used DEM of Armenia (Fig. 18.3) taken of the Advanced Space borne Thermal Emission and Reflection Radiometer (ASTER) instrument of the Terra satellite (available for 99 % of the globe) which represents elevations at a 30 m resolution [9–11].

DEM of Armenia is also presented in "WGS 1984" Geocentric Coordinate System. Debugging of algorithms and programs for generation of interferograms and differential interferograms for selected areas and signal processing models of SAR (for topographic interferometry) are developed in the framework of the project. DEM of Armenia was selected in accordance with the risk areas using the same principle that was applied in the processing of topographic maps of Armenia.

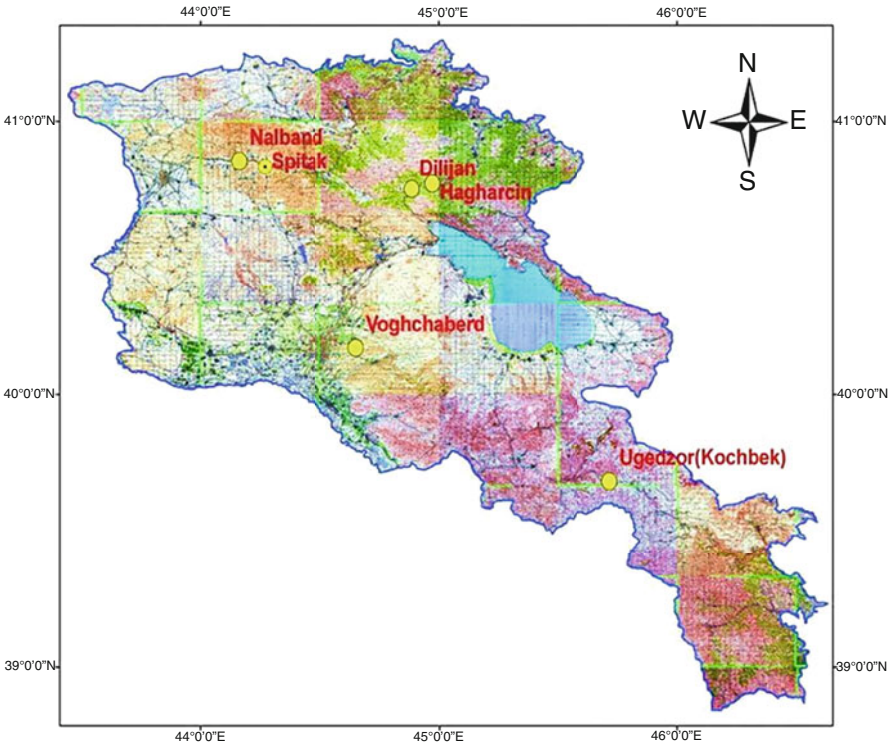

Fig. 18.2 Raster of the 1:100,000 scale topographic map of Armenia

18.4 Simulation Modeling of Land Surface Movement Caused by Natural and Industrial Activities on the Topographical Maps

To generate synthetic interferograms and synthetic differential interferograms simulation modeling of Earth's surface movement caused by natural disasters on the selected areas with high level of risk of surface movements have been simulated. In risk areas we have chosen landslides where depend on relief, local geological structure and composite rocks properties the grounds displacements are possible. Selected landslides of 20 × 20 km areas have been cut from DEM of 100 × 100 km area, because it will be impossible to create modified DEM for the whole territory. All operations have been executed with use of ArcGis Desktop v9.3 and by widely using of ArcMap, ArcToolBox, Spatial Analyst Tools and 3D Analyst Tools. With the help of Spatial Analyst Tools/Surface/Contour tool from the DEM for all

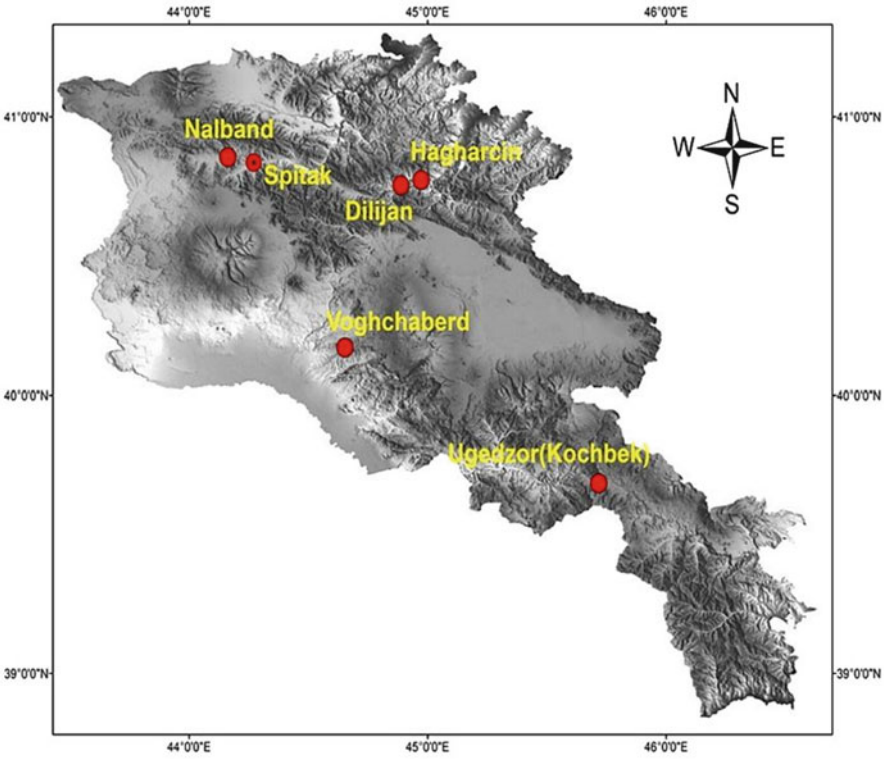

Fig. 18.3 The DEM (with effect hill shade) of Armenia

selected risk areas, the horizontal contours with 10 m intervals (Cell-size) for the areas were obtained. Next, on the base of displaced contours the modified DEMs have been obtained using step by step and with the use of the following tools, as shown in Fig. 18.4 [12].

18.5 Comparison of the Interferograms with Topographical Maps of Risk Areas of Armenia and Correction of the Results

Processing satellite images of 2008–2009 (which were taken from the period 30/08/2008–04/10/2008 and then from 11/07/2009 to 28/11/2009) and topographic information by software package InSAR and Observation Tool IDIOT (InSAR Deformation), and Inspection and Observation Tool (developed by the Computer

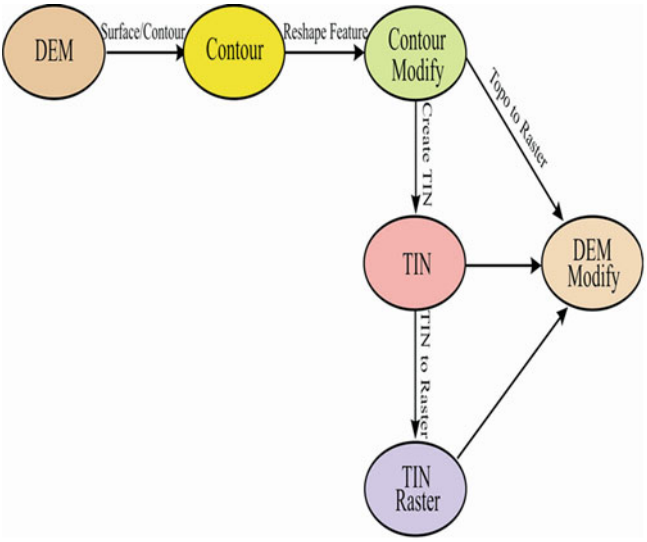

Fig. 18.4 Graph of modified DEM generation

Vision and Remote Sensing Group of the Berlin University of Technology) the Bulgarian research group provided 12 and 4 interferograms and differential interferograms, respectively. On the whole, during 2008–2009, 48 interferograms and differential interferograms were obtained by different combinations of satellite images.

First of all Armenian group made visual examination of all interferograms and differential interferograms; viz. amplitude_master, amplitude_slave, amplitude_rgb, coherence, amplitude_coherence, phase, phase_flat, phase_dinsar, amplitude_dinsar, amplitude_phase, amplitude_topography, coherence_dinsar, etc. were subsequently selected the interferograms (Fig. 18.5) made in 2008–2009 where the most condensations color effected accumulation (or fringe maps -are the typical interference phenomena) were seen; viz. amplitude_coherence, amplitude_dinsar, amplitude_phase, and coherence_dinsar.

The next step of studies were phase, viz. phase_flat and phase_dinsar interferograms on which were selected using parts where interferometric fringes correspond to the inhomogeneous parts on the color images, viz. amplitude_coherence, amplitude_dinsar, amplitude_phase, coherence_dinsar. Then interpreted images of interferograms were selected by visual comparison – amplitude_coherence, amplitude_dinsar, amplitude_phase, coherence_dinsar, phase, phase_flat, phase_dinsar. As Observation Tool (IDIOT) doesn't perform geocoding of the images Armenian group participants' geo-referenced selected images using ArcGIS_9.3 and put them in the WGS 1984 coordinate system.

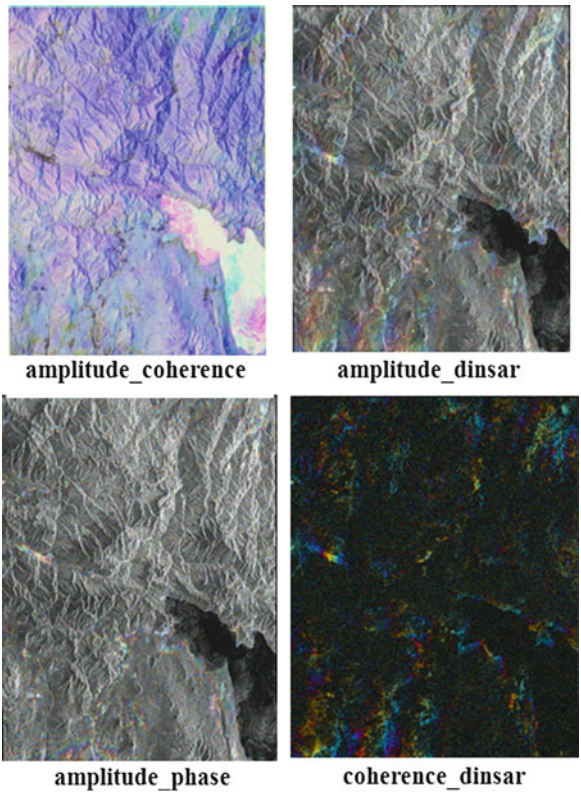

Fig. 18.5 Interferograms with most inhomogeneous color effects

The most comprehensive and accurate studies of the Armenia, in terms of landslides, were done in 2004–2005 by JICA organization. Widely using GIS environment in this stage the participants of the Armenian group compared geo-referenced images and visually selected areas with landslides data that are in "shape" format provided by JICA for the Armenia. As a result of comparison some selected parts of geo-referenced interferograms where fully coincided with the landslides zones really recorded by JICA working team (Fig. 18.6).

Here (Table 18.2) we brought the coordinates of really recorded landslide zones (Selected zones on the Fig. 18.6 were numbered consequently from the top to the down and from the left to the right 1.1, 1.2, … 1.29).

Some areas in the interferograms are located near to the landslide zones and some are far from those zones. The latter can probably be some agricultural or construction areas or of some uncertainties during interferograms processing.

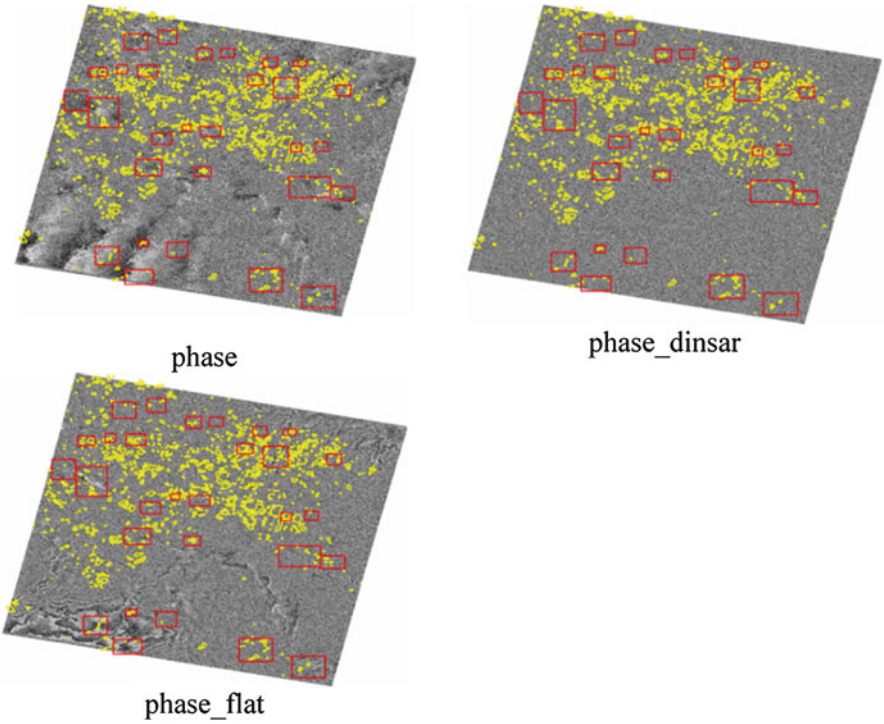

Fig. 18.6 Zones fully match to the landslides areas as recorded by JICA

Table 18.2 The coordinates of landslide zones

#	X-left	Y-bottom	Y-top	X-right	Y-bottom	Y-top
1.1	44.619488	41.037323	41.096781	44.707043	41.037323	41.096781
1.2	44.748207	41.058885	41.109849	44.817467	41.058885	41.109849
1.3	44.892664	40.999514	41.042274	44.949402	40.999514	41.042274
1.4	44.980543	41.007905	41.041619	45.032348	41.007905	41.041619
1.5	45.14164	40.971877	41.007031	45.19437	40.971877	41.007031
1.6	45.253113	40.974653	40.996855	45.301218	40.974653	40.996855
1.7	44.490294	40.935525	40.96929	44.554587	40.935525	40.96929
1.8	44.592935	40.948223	40.98091	44.632406	40.948223	40.98091
1.9	44.67082	40.935577	40.978946	44.743225	40.935577	40.978946
1.10	45.081381	40.904436	40.942056	45.140587	40.904436	40.942056
1.11	45.179832	40.854457	40.931963	45.271871	40.854457	40.931963
1.12	45.415003	40.864105	40.903883	45.468658	40.864105	40.903883
1.13	44.395448	40.809124	40.883043	44.482548	40.809124	40.883043
1.14	44.486289	40.746003	40.855969	44.600274	40.746003	40.855969
1.15	44.723393	40.681075	40.723474	44.798298	40.681075	40.723474
1.16	44.83664	40.732567	40.754238	44.869617	40.732567	40.754238

(continued)

Table 18.2 (continued)

#	X-left	Y-bottom	Y-top	X-right	Y-bottom	Y-top
1.17	44.906179	40.709812	40.747971	44.982969	40.709812	40.747971
1.18	45.24358	40.654046	40.684265	45.28305	40.654046	40.684265
1.19	45.334855	40.655896	40.689816	45.38481	40.655896	40.689816
1.20	44.663643	40.564405	40.624728	44.760539	40.564405	40.624728
1.21	44.88465	40.561428	40.596695	44.945923	40.561428	40.596695
1.22	45.237033	40.482583	40.560599	45.393065	40.482583	40.560599
1.23	45.393421	40.474746	40.522838	45.481768	40.474746	40.522838
1.24	44.512319	40.230316	40.297931	44.600982	40.230316	40.297931
1.25	44.670486	40.29764	40.324108	44.709492	40.29764	40.324108
1.26	44.78037	40.257947	40.314786	44.857708	40.257947	40.314786
1.27	44.622525	40.157048	40.210667	44.728543	40.157048	40.210667
1.28	45.089577	40.129793	40.214706	45.213828	40.129793	40.214706
1.29	45.285508	40.06887	40.148446	45.409759	40.06887	40.148446

18.6 Conclusion

The Digital Elevation Models presented here can be used to generate synthetic interferograms and differential interferograms and to model SAR images of regions of interest as well. The developed DEM mathematical models can be applied in processing steps of satellite SAR image formation, SAR interferogram for topography evaluation and differential interferogram for surface displacement. All above mentioned studies were done for interferograms made in 2009 and also for combined interferograms made in 2008–2009. The inhomogeneous color effected accumulations in the interferograms – amplitude_coherence, amplitude_dinsar, amplitude_phase, coherence_dinsar and phase, phase_flat, phase_dinsarimages where interferometic fringes were seen, were expressed in interferograms of 2008–2009.

References

1. Melkumyan MG (2005) Seismic risk assessment and mitigation strategy in Armenia. Printinfo, Yerevan, p 161
2. Armenia Ministry of Nature Protection (2002) National action program to combat desertification in Armenia, Government of Armenia
3. Boynaghryan VR, Stepanyan VE, Khachatryan DA et al (2009) Landslides in Armenia. Asoghik, Yerevan, p 308 (in Russian)
4. Zohrabyan LN, Sahakyan GD, Karakhanyan AS (1981) Landslide map of Armenian SSR at 1:200 000 scale based on decoding of aero elevation images and geomorphologic investigations (explanation notes for the maps). Institute of Geological Sciences of Academy of Sciences SSRA, Yerevan, p 36 (in Russian)
5. Vardanyan VP, Proshyan AS, Khachatryan DA (1990) Feature of the landslide structure of Fioletovo area in the Dilijan region of Armenian SSR. Sci Notes YSU, Nat Sci 1(172): 133–139 (in Russian)

6. Dorbath K, Arefiev S, Rogozhin E (2004) Seismic tomography constraints on the deep structure of the Spitak earthquake source zone, Izvestiya. Phys Solid Earth 40(8):647–659, Translation from Fizika Zemli 8:41–55
7. Albarede F, Bogachkin B, Oleinik A et al (1980) On a prehistoric strong earthquake in the Spitak area. Dokl Akad Nauk Arm SSR 313(2):397–400
8. Arefiev S, Aptekman Z, Afimina T et al (1991) Catalog of Aftershocks of the Spitak, December 7, 1988 Earthquake. Fiz Zemli 11:60–73 (in Russian)
9. Wise S (2007) Effect of differing DEM creation methods on the results from a hydrological model. J Comput Geosci 33(10):1351–1365
10. Milan D, Heritage G, Large A, Fuller I (2011) Filtering spatial error from DEMs: implications for morphological change estimation. J Geomorphol 125(1):160–171
11. Sorensen R, Seibert J (2007) Effects of DEM resolution on the calculation of topographical indices: TWI and its components. J Hydrol 347(1–2):79–89
12. Grigoryan MA, Aleksanyan GM, Boyakhchyan TN, Navasardyan GKh, Gevorgyan LA, Lazarov A, Minchev D (2011) Digital elevation models of territories under risk in Caucasus region-Armenia. In: International research conference, “Interaction of theory and practice: key problems and solutions”, Burgas, 24–25 June 2011

Chapter 19
Applications of an Effect Based on Electromagnetic Field-Matter Interactions for Investigations of Water

O. Ivanov, Y. Mutafchieva, and Ashok Vaseashta

Abstract A possibility for developing a new method for investigating liquids, water in particular, based on the Surface Photo-Charge Effect has been demonstrated. Due to the strong susceptibility of this effect to the state of the irradiated interface, upon illumination of the interface an easily measurable electric signal arises with magnitude depending on the properties of the liquid. This signal, if properly calibrated, can serve as an express contactless inspecting tool. A variety of sensors for water quality control can be developed using this method. Some examples of the presented experimentally tested sensors based on the effect are for quality control of the chemical composition of water, registering processes in liquids and level sensors.

Keywords Field-matter interactions • Quality control of liquids • Sensors

19.1 Introduction

This report is focused on the possibility to monitor the chemical composition of liquids and in particular of water. The research has been carried out using the Surface Photo-Charge Effect (SPCE). Its essence is that upon irradiation of any liquid and solid with an electromagnetic field one observes an AC potential difference between the solid and common ground of the system with frequency equal to the modulation

O. Ivanov (✉) • Y. Mutafchieva
Institute of Solid State Physics, Bulgarian Academy of Sciences,
72, Tzarigradsko Chaussee Blvd., 1784 Sofia, Bulgaria
e-mail: ogi124@yahoo.com

A. Vaseashta
Norwich University Applied Research Institutes, Herndon, VA, USA

VTT/AVC U.S. Department of State, Washington, DC, USA
e-mail: prof.vaseashta@ieee.org

A. Vaseashta and S. Khudaverdyan (eds.), *Advanced Sensors for Safety and Security*,
NATO Science for Peace and Security Series B: Physics and Biophysics,
DOI 10.1007/978-94-007-7003-4_19,

frequency of the incident field [1–3]. The SPCE is a universal property of any material. The effect has been observed in a very wide range of the electromagnetic spectrum. However, for convenience the experiments presented here are usually conducted in the visible spectrum. A hypothesis presented in [2], for the explanation of the SPCE in conducting media suggests that the incident radiation, attenuating in depth of the medium, generates a force perpendicular to the irradiated surface and redistributes the charges in the conductor. In dielectric media the appearance of SPCE can be attributed to changes provoked by the incident electromagnetic field in the charge accumulated into surface energy states present at any real surface. Other hypotheses for the explanation of the Surface Photo-Charge Effect have also been developed [4–6].

The amplitude of the signal generated by SPCE is strongly influenced by the properties of the irradiated sample which presents opportunities for various practical applications. The method provides information on fluids and processes taking place therein. For example, it is possible to monitor the octane factor of gasoline, impurities in liquids and the concentration of gases [7]. The above effect can also be applied for registration of specific reactions and processes taking place in milk, in particular for instantaneous detection of inhibitors (antibiotics) [8]. Testing of drinking water from the public water distribution system or that distributed to an army in field operations is technically also feasible.

The present work introduces a practical application of SPCE for studying water and liquids on the whole. The investigated liquid is put in contact with an irradiated solid surface. If the characteristics of the setup and the environment are fixed, it is possible to detect changes in the water properties. It can be expected that any changes in the water will cause corresponding changes at the irradiated interface, thus leading to a change in the SPCE signal.

19.2 Experimental Setup

The used experimental setup is illustrated in Fig. 19.1, where (S) is the irradiated solid (generally, it should be a substrate generating a strong SPCE signal, for example a semiconductor), (L) is the studied liquid forming an interface (I) with

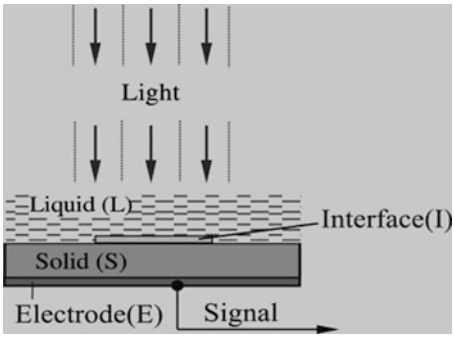

Fig. 19.1 Experimental setup for observation of SPCE: (*S*) solid; (*I*) solid–liquid interface which generates the signal; (*L*) studied liquid; (*E*) electrode

the solid at the point of electromagnetic irradiation. Although it is possible to use white light, it is better to conduct the experiments with monochromatic light that has the appropriate wavelength for obtaining optimum conditions. The most suitable wavelength is determined by various parameters, such as the type of surface states at the interface (I) and the monitored parameters of the liquid (L). The wavelength is not the only feature of the setup that is varied to correlate with the liquid parameters. With different samples, substrates and structure of the setup some features remain fixed and others are varied for obtaining the strongest response signal. Using appropriate equipment the SPCE signal is measured through the electrode (E) [2, 3].

The sensitivity of the proposed method depends on the interface properties but selecting adequate setup characteristics (e.g. irradiation in a suitable spectral range) can make it high enough. The properties of the interface are mostly determined by the properties of the surface states and this defines the correlation between the properties of the water and the surface states. For example, if only the intensity of the light is changed in the setup, there will be a point where the correlation with the water impurities is highest and varying the different parameters can provide more accurate results. The SPCE exists for any type of solid and therefore a suitable solid surface and spectral range of irradiation can always be found for the monitored liquid in order to avoid undesirable effects, such as hysteresis, slow relaxation, etc. The method is universal and can be used to study various liquids under various conditions. It is contactless, express and the results are measured in real time. Most of the equipment for its implementation is off-the-shelf.

19.3 Results and Discussions

Electromagnetic irradiation of all studied liquids induces an AC potential difference, the amplitude of the signal changes for the different liquids and its value is specific for each liquid [7]. In Fig. 19.2 are presented the measured signal values for 15 ml several different liquids. Side effects caused by setup differences were avoided by irradiating at the same point. The vessel where the liquids were monitored was thoroughly rinsed with water and dried by hot air after each of the measurements.

The liquids investigated were selected at random, only to establish that the SPCE signal differs significantly for the various liquids. The results for the three types of water demonstrate that a simple treatment of the liquid induces easily detectable signal changes. Tests monitoring variations in a single liquid property were also conducted. The results for 30 ml of gasoline with a different octane number, with or without lead are shown in Fig. 19.3. Changes in the signal are also observed when mixing two liquids. For example, when only one drop of ammonia solution was added to 200 ml tap water the signal dropped by 15 %, but the signal increased by 10 % when the additive was a drop of acetone.

These results demonstrate the possibility to determine qualitatively if there are any changes in particular characteristics of the investigated liquid, when all other

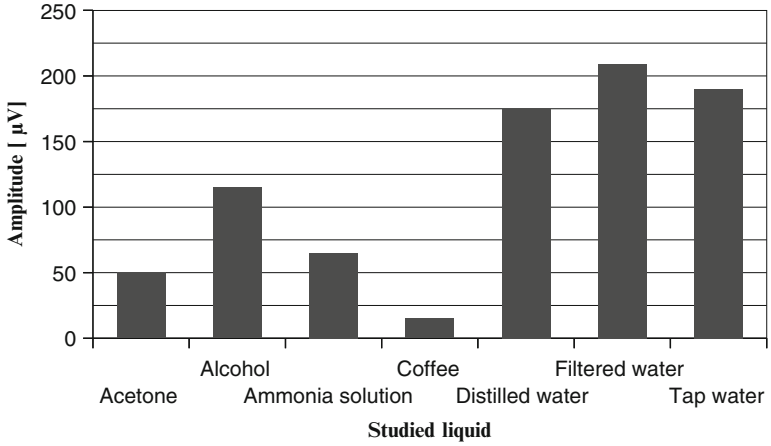

Fig. 19.2 The SPCE signal as a function of different liquids

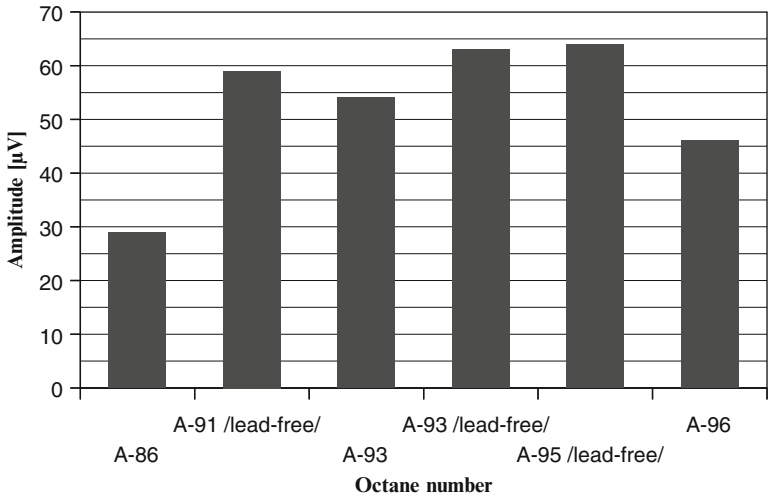

Fig. 19.3 The SPCE signal as a function of the octane number

experimental parameters remain fixed. Further development and more precise calibration will allow definitive quantitative measurements with the presented method.

Other practical applications of this method have been also developed. For instance, a level meter was designed by selecting a suitable electrode and irradiation, so that the signal changes would be determined from the liquid volume [9]. A small laboratory model was constructed in order to establish the feasibility of this application. Levels up to 10 cm of unleaded petrol 95H were measured with it.

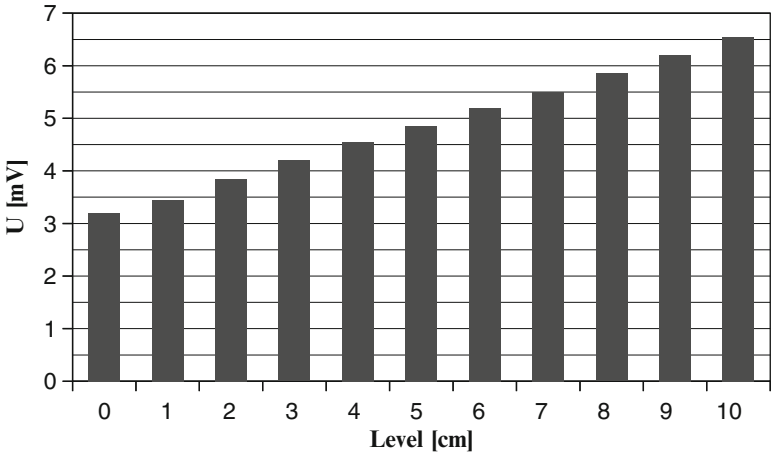

Fig. 19.4 The SPCE signal as a function of the petrol level

The measurement accuracy is 0.4 mm and can be increased by simple technical adjustments. The petrol level to monitored signal ratio is given in Fig. 19.4. It is easy to determine that the dependence is linear. Presently structures suitable for measurements of larger depths using SPCE have not been designed and constructed. The velocity of a flowing liquid could also be controlled by this method, since it has been established that upon certain conditions, the signal is also influenced by this factor.

The SPCE in liquids is probably not an inherent property of the liquid itself but is rather generated at the solid–liquid interface. This is supported by the results of investigations conducted with opaque liquids, when no signal could be measured with sufficient experimental accuracy unless this interface was irradiated. Changes in the parameters of water, for example, will cause changes in the intensity of the contact between the liquid and the solid. This will cause changes in the interface and from there in the measured signal. Thus research and control of water can be carried out.

In order to obtain strongest response signal per unit added impurity it is necessary to select many parameters: the type of the structure that generates the signal; the wavelength of the incident radiation; intensity of the radiation; which parameter of the electrical signal to be measured; the material of the irradiated surface; the method for signal registration; the measurement conditions; any additional influences etc. There are many parameters that need to be optimized. The goal is a minimal change in the controlled variable to cause maximum changes in the measured electrical signal. After the setup for observation of SPCE has been prepared for a specific task it is necessary that all experimental conditions are kept constant.

19.4 Conclusion

The effect presented here has the great potential to complement the already known and used methods for control of water, and liquids in general, with an express and contactless method. The method is universal because the SPCE generated signal exists for all liquids and that allows the various practical applications to be developed. It is possible to monitor even small quantities with suitable measurement setup. The method can easily be implemented in commercial environments.

References

1. Pustovoit VI, Borissov M, Ivanov O (1989) Photon charge effect in conductors. Phys Lett A 135:59–61
2. Pustovoit VI, Borissov M, Ivanov O (1989) Surface photo-charge effect in conductors. Solid State Commun 72:613–619
3. Ivanov O, Mihailov V, Pustovoit VI, Abbate A, Das P (1995) Surface photo-charge effect in solids. Opt Commun 113:509–512
4. Ivanov O, Leyarovski E, Lovchinov V, Popov Chr, Kamenova M, Georgiev M (2007) Photoinduced electrification of solids. III. Temperature dependences, Paper ID – cond-mat/ 0706.3877
5. Ivanov O, Kuneva M (2011) Quality control methods based on electromagnetic field-matter interactions. In: Ivanov O (ed) Application and experience of quality control. INTECH, Vienna, pp 509–536
6. Ivanov O (2006) Sensor applications of field-matter interactions. In: Grimes CA, Dickey EC, Pishko MV (eds) Encyclopedia of sensors, vol 9. American Scientific Publishers, Stevenson Ranch, pp 165–197
7. Ivanov O, Konstantinov L (2002) Investigation of liquids by photo-induced charge effect at solid–liquid interfaces. Sens Actuator B 86:287–289
8. Ivanov O, Radanski S (2009) Application of surface photo charge effect for milk quality control. J Food Sci 74:R79–R83
9. Ivanov O (2001) Level-meter for liquids based on the surface photo-charge effect. Sens Actuator B 75:210–212

Part V
Water Security and Water Contaminations Sensors

Chapter 20
Real-Time Monitoring of Water Contaminants for Situation Awareness Using Electromagnetic Field Sensing System

O. Korostynska, K. Arshak, A. Arshak, A. Mason, Ashok Vaseashta, and A. Al-Shamma'a

Abstract Up to 70,000 known and emerging chemical, biological, and radiological contaminants may be present in various water resources. To assure the safety and quality of water and to guarantee the situational awareness of safe water supplies, efficient real-time measurement methods with superior sensitivity are required. Current measurement methods of pollutants are mostly based on off-line monitoring which implies low frequency data sampling, delays between sampling and results, and additional chemical use. In this study, a novel sensing system where the interaction of the electromagnetic field with the tested fluid reveals its composition is presented. In particular, it is suggested that microwave based sensors are a suitable technology to fulfill the requirement for a real-time water pollution monitoring platform. A prototype microwave sensor in the form of printed Cu pattern on FR4 substrate was designed and tested for its response to air, deionized water, 500 ppm phosphate solution, and cooking oil samples. This sensor operates based upon the interaction of the electromagnetic waves and the material under test, which manifests itself as a unique spectra as measured for each sample due to its specific permittivity. By considering how the reflected microwave signal (in a form of S_{11} parameter) varies at discrete frequency intervals, the change in the signal can be linked to the composition of the object under test.

O. Korostynska (✉) • A. Mason • A. Al-Shamma'a
BEST Research Institute, School of Built Environment,
Liverpool John Moores University, Liverpool, UK
e-mail: o.korostynska@ljmu.ac.uk; olga.korostynska@gmail.com

K. Arshak
Electronics and Computer Engineering Department, University of Limerick, Limerick, Ireland

A. Arshak
Department of Physics and Energy, University of Limerick, Limerick, Ireland

A. Vaseashta
Norwich University Applied Research Institutes, Herndon, VA, USA

VTT/AVC U.S. Department of State, Washington, DC, USA
e-mail: prof.vaseashta@ieee.org

A. Vaseashta and S. Khudaverdyan (eds.), *Advanced Sensors for Safety and Security*,
NATO Science for Peace and Security Series B: Physics and Biophysics,
DOI 10.1007/978-94-007-7003-4_20, © Springer Science+Business Media Dordrecht 2013

Keywords Water sensing • Water quality • Sensors • Microwave sensors

20.1 Introduction

Surface water reservoirs and aquifers are exposed to contamination by thousands of pollutants from industrial, pharmaceutical, agricultural and natural origins. Known [1] and emerging [2, 3] contaminants that might be present in various water resources pose a real threat to humans and require continuous monitoring for situation awareness.

Wastewater also carries such micropollutants as pharmaceuticals and hormonally active substances [4]. So far, there is little scientific evidence as to the detrimental effects of these compounds on aquatic organisms and the quality of water for drinking [5]. However, as these compounds are considered to be harmful, approaches for the removal of micropollutants from wastewater have been developed either at the source or using new end-of-pipe technology [6]. The chemical industry—including the pharmaceutical industry—is becoming progressively more aware of environmental problems and has increased interest in novel real-time water pollutants monitoring systems.

Water quality assessments are based on the analysis of the physical, chemical and bacteriological parameters and require customized apparatus and trained staff. Physical, chemical, biological and radioactive variables vary widely in all types of water and some high concentrations may be difficult to reduce during the treatment process. In conventional end-of-pipe systems, a large part of the pollutants will always be lost to the environment due to leaking, primarily during rain. In the long term, source separation offers the more sustainable solution to the entire wastewater problem, including organic micropollutants. Urine source separation is an elegant solution to the problems of nutrients and pharmaceuticals alike and losses of untreated pollutants to the environment can be minimized [5]. With continuous industrial developments, depleting natural water resources, and increasing population and its corresponding increased demand on domestic and industrial water consumption, it is getting more and more challenging for the water supply industry to maintain water safety.

Another group of human waste contaminants consists of pesticides, which are usually washed with surface water from agricultural regions [7]. There are also various toxic compounds generated by microorganisms (e.g. microcystins) or multicellular organisms existing in the water. In all developed countries, there are defined legislation and regulatory authorities enforcing maximal residual levels of the various contaminants. Microcystins that result from the blooming of toxigenic cyanobacteria [8] can cause severe poisoning episodes in animals and humans when present in drinking water in sufficiently high concentrations.

Notably, most pharmaceuticals compounds are not routinely monitored in drinking, surface, or wastewater; although a large numbers of compounds were detected when such tests were conducted [6].

Traditional methods of water quality control are lab based and include standard UV–vis measurements, mass spectrometry, ion-sensitive electrodes and amperometric sensors. In particular, liquid chromatography tandem mass spectrometry has become a key technique for environmental analysis, allowing the detection of a wide range of polar and non-volatile compounds [6]. On the other hand, a range of modern real-time monitoring approaches exists, for example fiber-optic sensors, MEMs, lab-on-chip sensors and biosensors.

Most of the reported wastewater UV–vis spectrometric applications are based on visual observation and direct comparison of the UV–vis spectra. For example, the main method for phosphorus detection is using a photo sensor which measures the wavelength of a distinct color (e.g. blue or yellow) that results from a chemical reaction between phosphorus and special reagent [9]. The concentration of the resultant dye indicates the concentration of phosphorus in the sample. Sensors based on colorimetric UV spectral measurements are widely used in commercially available systems [10], but they all suffer from a number of limitations. In particular, sample handling is problematic, and the acquisition of a reference spectra and calibration process are necessary for samples of different origin.

Fiber optic sensors are used in combination with the UV–vis methods of water contaminants detection. Normally an optic fiber is suitably doped to produce luminescence when exposed to an excitation light source. Glass fibers are either doped with a rare earth metal or activated with a transition metal. Polymeric fibers are doped with a dye. The fibers have fast response and decay times and can achieve high efficiency through the design of appropriate delivery optics. Fiber optic systems are particularly suitable for harsh and difficult to reach places. The design and selection of the fiber determines the peak wavelength of the output illumination; options exist to span the UV–Vis–NIR spectrum [11].

Amperometric, potentiometric and conductometric sensing approaches are widely used in the measurement of pollution in water [12]. These sensors change their properties as a result of interaction with the component being measured. The species of interest are either oxidized or reduced at the working electrode causing a transfer of electrons, thus generating a measureable signal. This change can be recorded as a change in the output signal, i.e. output voltage, current, change in conductivity, capacitance or dielectric constant – whatever parameter gives the most pronounced sensor response [13]. Potentiometric detection is attractive since it possesses numerous advantages when considering the development of real-time sensing technologies, as the recording instrumentation is cost-effective and highly portable. For example, a portable amperometric three-electrode immunosensor for screening of polycyclic aromatic hydrocarbons (PAHs) in water was recently reported [12]. In particular, amperometric detection is based on the measurement of current when a potential is applied to the working and reference electrodes of the system.

The presence of microorganisms in water is generally assessed with five indicators, such as total coliform, fecal coliform, fecal streptococcus, enterococcus, and Escherichia coli. To protect public health, microbiological standards have to be met at each individual treatment works and service reservoir. Notably, the

presence of various microorganisms in water, including *salmonella*, *campylobacter*, *listeria*, *Bacillus cereus* and *Escherichia coli O157:h7* is a natural and unavoidable occurrence, but the level of these bacteria should be strictly monitored in real time. Infectious doses of these pathogens (as low as ~10 bacterial cells) increase the vulnerability of the elderly, infants, and people with immunological deficiencies or organ transplants [14]. The rise of terrorism has also prompted greater recognition of the importance of *biosecurity* in protecting the environment [15].

Biosensors for the determination of phosphate are normally based on mono- or multi-enzymatic reactions where phosphate acts as an inhibitor or substrate [16]. For example, an amperometric phosphate biosensor, based on a cobalt phthalocyanine screen-printed carbon electrode was recently reported [17] to be successfully applied to the measurement of phosphate in pond water samples and a linear range of 2.5–130 μM with a limit of detection of 2 μM was obtained under optimal conditions, exhibiting a response time of ~13 s. Reportedly, a microelectrode with a tip size ~10 μm fabricated with cobalt wire was designed for in-situ and in vivo environmental analysis of orthophosphate ions (HPO_4^{2-} and $H_2PO_4^-$) that evaluates the wastewater phosphorus removal system and for biological applications [18].

Lab-on-chip and electrochemical sensing-based portable monitoring systems appear well suited to complement standard analytical methods for a number of environmental monitoring applications, including water quality monitoring. The concept of a lab-on-chip type system started from the integration of the various chemical operations involved in conventional analytical processes in a laboratory, such as sampling, preparation, mixing, reaction, and separation into a single unified system, requiring only a tiny volume of chemicals and sample and only a fraction of the time needed for the conventional approach. A modern lab-on-chip is a complex system that combines a amperometric/conductimetric sensor, microelectrodes and MEMs arrays, often along with microfluidics facilities.

Thus, within in the last few years, significant advances have been made in technologies to monitor drinking water quality for source water protection, treatment operations, and distribution system management, in the event of accidental (or deliberate) contamination [19]. Generally speaking, however, no single system available today can fully address the needs of the customers, i.e. industries and regulatory authorities, in its ability to determine on-spot, in real time, the composition of water to the desired sensitivity level, bearing in mind the wish for system portability and cost-effectiveness. This could be partially due to the fact that there is no common chemical feature characterizing all water pollutants, except their solubility to a certain level in water [6].

Therefore, novel real-time monitoring techniques are necessary and they must detect the excess of pollutants established by the official water quality regulations [20]. A promising real-time water quality monitoring technique is that of the electromagnetic wave sensor that works within the microwave region.

Microwave sensing technology has been successfully used as a sensing method for various industrial applications [21–23] including water level measurements [24], material moisture content [25, 26], for continuous process monitoring for biogas

plants [27] and in the healthcare industry; for example, for non-invasive real-time monitoring of glucose in diabetic patients [26, 28–30].

In one study, a microwave sensor in a form of a cavity resonator for accurate measurements of both organic (sugar, alcohol) and inorganic (NaCl, $KMnO_4$) water solutions concentrations was reported [21]. Notably, the sensitivity of the sensor in determination of NaCl was 0.4 dB/(mg/ml) within 0–1 % concentration range. The sensor was able to detect the concentrations of other water solutions, but its sensitivities are strongly dependent on the type of tested chemical ingredient.

Microwave sensors in the form of cavity resonators or in a shape of printed planar antennas of various configurations operate based upon the interaction of the electromagnetic waves and the material, i.e. fluid sample, being tested. This interaction manifests itself as a frequency change, attenuation or reflection of the electromagnetic signal. By considering how transmitted (S_{21}) and reflected (S_{11}) microwave signals vary at discrete frequency intervals, the change in the signal can be linked to the composition/type of the sample under test.

The microwave planar printed antennas for various sensing applications are increasingly used due to their versatility, flat profile and low weight. Their design can be tailored to suit a particular application, coupled with reliability and cost-efficiency, since they are easily manufactured using common methods for printed circuit board production.

20.2 Experimental Procedure

In this work, a sensor in the form of traditional interdigitated electrodes (IDE) was used to provide maximum interaction with the tested fluid samples. Figure 20.1a shows CAD layout of the manufactured IDE sensor along with its dimensions,

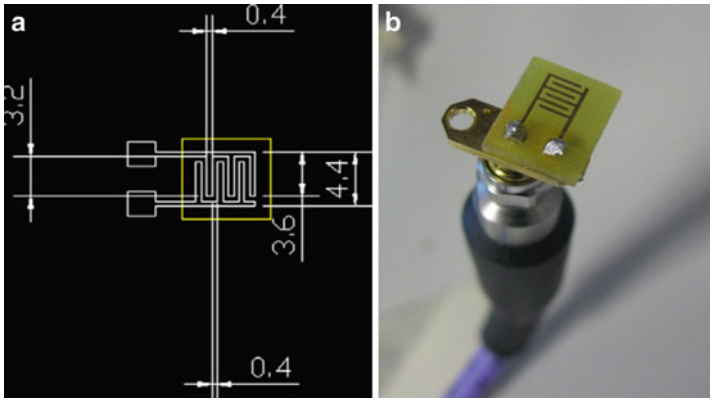

Fig. 20.1 (**a**) CAD layout of Cu IDE pattern; (**b**) Cu IDE on FR4 substrate with SMA connector and N-type cable

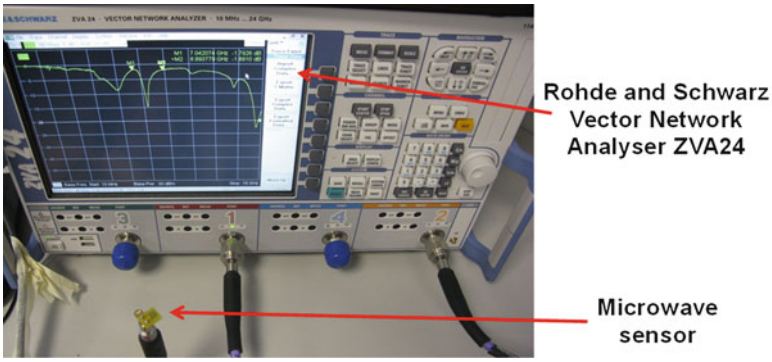

Fig. 20.2 Experimental setup: VNA displays the response of IDE microwave sensor

which are in mm, whereas Fig. 20.1b illustrates the photo of the prototype Cu IDE sensor connected to N-type cable via standard SMA connector. SMA is a very common, popular and easily available connector, which is used to excite a microstrip line or a microstrip antenna. It is mainly 50Ω probe with a central conductor extended to connect the microstrip element. Depending on the size of the antenna or substrate, the connector dimensions may be different [31].

A 1.57 mm thick FR4 substrate (supplied by Mega-UK) covered on one side with 35 μm Cu layer was used. The IDE was subsequently patterned with a Bungarde CNC router. A MOLEX SMA connector was soldered to both arms of IDE antenna to feed the microwave signal. Samples of various fluids, namely deionised water (DIW), 500 ppm phosphate solution (PO_4) and cooking oil (Filippo Berio extra virgin olive oil) were tested (30 μl volume) to verify the applicability of the proposed novel microwave sensor. These were benchmarked against the air spectrum. The experimental setup used to test the IDE response is shown in Fig. 20.2. It comprises a Rohde and Schwarz ZVA24 Vector Network Analyzer (VNA), a microwave sensor and N-type cable to connect the VNA and sensor. The data (60,000 points for each measurement) was captured in the frequency range of up to 15 GHz for the reflected (S_{11}) signal.

20.3 Results and Discussion

Figure 20.3 illustrates the microwave response of IDE in a frequency range up to 15 GHz for air and three different types of fluid, namely deionized water (DIW), 500 ppm phosphate solution (PO_4) and Filippo Berio extra virgin olive oil. From an environmental perspective, the concentration of phosphate in water is crucial due to its role in eutrophication [17]. One can clearly see that the recorded spectra for these samples have unique pattern, with which being accordingly associated the dielectric properties and composition of tested fluid.

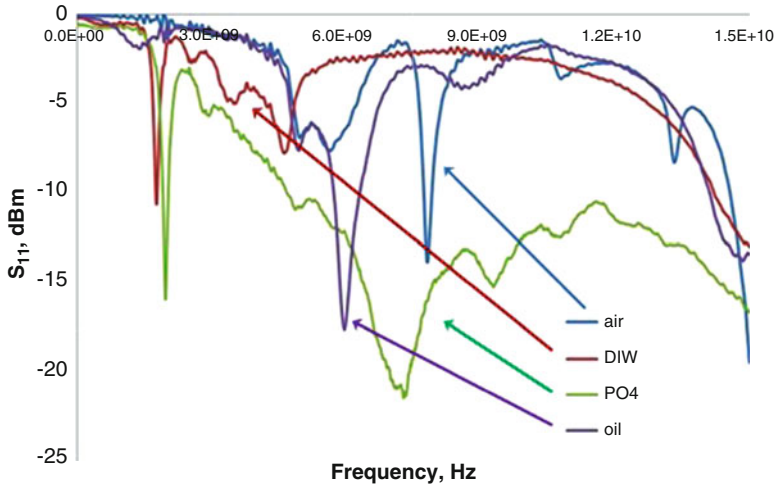

Fig. 20.3 S_{11} spectra for air, deionized water (DIW), 500 ppm phosphate solution (PO_4) and oil (Filippo Berio extra virgin olive oil)

To clarify the principle behind electromagnetic wave sensing suggested in this work for water quality control, it is worth mentioning that microwave sensors in the form of planar IDE sensors operate based upon the fact that an object under test, i.e. fluid, when placed in direct contact with microwave sensor, interacts with the propagating or resonating modes of the electromagnetic field in a unique manner, which can be specifically correlated with the properties of this fluid. Due to this interaction, the dielectric properties of the material can be revealed via frequency change, attenuation, reflection of the signal or its phase shift.

Notably, the sensor dimensions were dictated by a compromise between, on one side, customer requirements for portability and convenience when using the developed water pollution monitoring system, and achieving clearly measurable sensor response with high signal-to-noise ratio to eliminate the need in further signal conditioning and modification.

Importantly, after each sample measurement the sensor response has returned to its original position, namely the air spectrum, which was mostly identical, thus making the sensor reusable for numerous measurements. Small hysteresis could have been caused by a residue cooking oil layer and could be avoided by using an appropriate oil cleaning process between each measurement. Alternatively, new sensor head can be used each time, as the proposed IDE sensor is a cost-efficient solution for real-time monitoring of water pollutants. The observed sensitivity of the developed sensor to various types of fluids suggests that this novel approach can serve as a platform for a cost-effective real-time water contaminants monitoring system.

20.4 Conclusions

There exists a clear need for better on-line monitoring of water systems given that existing laboratory-based methods are too slow to develop operational response and do not provide required level of public health protection. Novel real-time method of water pollutants monitoring is reported. It is based on a microwave sensor system with IDE made from Cu to which a GHz signal is fed via SMA connector and reflected spectra S_{11} is analyzed. Microwave signal experienced a change depending on a type of fluid brought in contact with the sensor. From the database of previously measured test samples, one can determine in real-time what type of water pollutant is present. Other IDE patterns and materials are being explored to achieve the highest sensitivity and selectivity of the sensor response. Moreover, a combination of different sensors into a single system could be an option when a complex mixture of different water pollutants needs to be precisely determined.

Acknowledgments Financial support for this is provided by the European Community's FP7-PEOPLE-2010-IEF Marie-Curie Action project 275201 – Water-Spotcheck.

References

1. Schwarzenbach RP, Escher BI, Fenner K, Hofstetter TB, Johnson CA, Von Gunten U, Wehrli B (2006) The challenge of micropollutants in aquatic systems. Science 313:1072–1077
2. Stuart M, Lapworth D, Crane E, Hart A (2012) Review of risk from potential emerging contaminants in UK groundwater. Sci Total Environ 416:1–21
3. Rodriguez-Mozaz S, Lopez de Alda MJ, Barceló D (2007) Advantages and limitations of on-line solid phase extraction coupled to liquid chromatography–mass spectrometry technologies versus biosensors for monitoring of emerging contaminants in water. J Chromatogr A 1152: 97–115
4. Heberer T (2002) Occurrence, fate, and removal of pharmaceutical residues in the aquatic environment: a review of recent research data. Toxicol Lett 131:5–17
5. Larsen TA, Lienert J, Joss A, Siegrist H (2004) How to avoid pharmaceuticals in the aquatic environment. J Biotechnol 113:295–304
6. Rosen R (2007) Mass spectrometry for monitoring micropollutants in water. Curr Opin Biotechnol 18:246–251
7. Korostynska O, Mason A, Al-Shamma'a AI (2012, March) Monitoring of nitrates and phosphates in wastewater: current technologies and further challenges. Int J Smart Sens Intell Syst 5:149–176
8. Srivastava A, Choi G-G, Ahn C-Y, Oh H-M, Ravi AK, Asthana RK (2012) Dynamics of microcystin production and quantification of potentially toxigenic *Microcystis* sp. Using real-time PCR. Water Res 46:817–827
9. Al-Dasoqi N, Mason A, Alkhaddar R, Al-Shamma'a A (2011) Use of sensors in wastewater quality monitoring – a review of available technologies. In: World environmental and water resources congress 2011: bearing knowledge for sustainability, Palm Springs, 2011, p 354
10. Engblom SO (1998) The phosphate sensor. Biosens Bioelectron 13:981–994
11. Capitán-Vallvey LF, Palma AJ (2011) Recent developments in handheld and portable optosensing—a review. Anal Chim Acta 696:27–46

12. Ahmad A, Paschero A, Moore E (2011) Amperometric immunosensors for screening of polycyclic aromatic hydrocarbons in water. In: 16th conference in the biennial sensors and their applications, Cork, 12–14 Sept 2011
13. Arshak K, Korostynska O (2006) Advanced materials and techniques for radiation dosimetry. Artech House, Boston
14. Van der Star WRL, Abma WR, Blommers D, Mulder J-W, Tokutomi T, Strous M, Picioreanu C, Van Loosdrecht MCM (2007) Startup of reactors for anoxic ammonium oxidation: experiences from the first full-scale anammox reactor in Rotterdam. Water Res 41:4149–4163
15. Velusamy V, Arshak K, Korostynska O, Oliwa K, Adley C (2010) An overview of foodborne pathogen detection: in the perspective of biosensors. Biotechnol Adv 28:232–254
16. Amine A, Palleschi G (2004) Phosphate, nitrate, and sulfate biosensors. Anal Lett 37(1):1–19
17. Gilbert L, Jenkins ATA, Browning S, Hart JP (2011) Development of an amperometric, screen-printed, single-enzyme phosphate ion biosensor and its application to the analysis of biomedical and environmental samples. Sens Actuator B Chem 160:1322–1327
18. Lee WH, Seo Y, Bishop PL (2009) Characteristics of a cobalt-based phosphate microelectrode for in situ monitoring of phosphate and its biological application. Sens Actuator B Chem 137:121–128
19. Storey MV, Van der Gaag B, Burns BP (2011) Advances in on-line drinking water quality monitoring and early warning systems. Water Res 45:741–747
20. Korostynska O, Arshak K, Velusamy V, Arshak A, Vaseashta A (2012) Recent advances in point-of-access water quality monitoring. In: Vaseashta A, Braman E, Susmann P (eds) Technological innovations in sensing and detection of chemical, biological, radiological, nuclear threats and ecological terrorism. Springer, Dordrecht, pp 261–268
21. Kapilevich B, Litvak B (2007) Microwave sensor for accurate measurements of water solution concentrations. In: Asia-Pacific microwave conference APMC, Bangkok, pp 1–4
22. Yunus MAM, Mukhopadhyay S, Punchihewa A (2011) Application of independent component analysis for estimating nitrate contamination in natural water sources using planar electromagnetic sensor. In: ICST 2011 fifth international conference on sensing technology, Limerick, pp 538–543
23. Yunus MAM, Mukhopadhyay SC (2011) Novel planar electromagnetic sensors for detection of nitrates and contamination in natural water sources. Sens J IEEE 11:1440–1447
24. Boon JD, Brubaker JM (2008) Acoustic-microwave water level sensor comparisons in an estuarine environment. In: OCEANS 2008, Quebec City, pp 1–5
25. Jackson B, Jayanthy T (2010) A novel method for water impurity concentration using microstrip resonator sensor. In: Recent advances in space technology services and climate change (RSTSCC), pp 376–379, 13–15 November 2010, in Chennai, India
26. Bernou C, Rebière D, Pistré J (2000) Microwave sensors: a new sensing principle. Application to humidity detection. Sens Actuator B Chem 68:88–93
27. NackeT, Barthel A, Pflieger C, Pliquett U, Beckmann D, Goller A (2010) Continuous process monitoring for biogas plants using microwave sensors. In: 12th biennial baltic electronics conference (BEC), Tallinn, pp 239–242
28. Korostynska O, Arshak A, Creedon P, Arshak K, Wendling L, Al-Shamma'a AI, O'Keeffe S (2009) Glucose monitoring using electromagnetic waves and microsensor with interdigitated electrodes. In: Sensors applications symposium, IEEE SAS 2009, New Orleans, pp. 34–37
29. Mason A, Wylie S, Thomas A, Keele H, Shaw A, Al-Shamma'a A (2010, Sept) HEPA filter material load detection using a microwave cavity sensor. Int J Smart Sens Intell Syst 3:16
30. Al-Shamma'a A, Mason A, Shaw A (2012) Patent: Non-invasive monitoring device, US2012150000 (A1), WO2010131029 (A1), EP2429397 (A1). http://www.google.com/patents/US20120150000
31. Guha D, Antar YMM (2010) Microstrip and printed antennas: new trends, techniques and applications. Wiley, Hoboken

Chapter 21
Development of Polymeric Cryogels as Potential Matrices for Removing Antibiotics from Wastewater

Nimet Bolgen, Didem Demir, and Ashok Vaseashta

Abstract Antibiotics are pharmaceutical compounds used in medical treatment and have been detected worldwide in the aquatic ecosystem. Persistent and continuous existence of these compounds in water/wastewater has raised concerns regarding the toxicity to living organisms and the emergence of antibiotic resistant strains of bacteria. To prevent antibiotic contamination in water, several techniques such as filtration, coagulation, flocculation, sedimentation, adsorption, advanced oxidation, membrane, biological processes and the combination of those methods have been proposed for removal of these substances. The aim of this study is to develop porous polymeric based cryogel matrices for removal of antibiotics from wastewater. This study investigates cryogelation method to prepare matrices by using chitosan and gelatin polymers, as a means to sequester pharmaceuticals in water stream.

Keywords Cryogelation • Chitosan • Gelatin • Antibiotic removal • Wastewater

21.1 Introduction

Recent reports have shown existence of unused pharmaceutical in our water sources. While many factors may contribute to this observation, the factors can be attributed to inadvertent discharge by way of unused regimen by humans and

N. Bolgen • D. Demir
Chemical Engineering Department, Engineering Faculty, Mersin University, Mersin, Turkey
e-mail: nimetbolgen@yahoo.com

A. Vaseashta (✉)
Norwich University Applied Research Institutes, Herndon, VA, USA

VTT/AVC U.S. Department of State, Washington, DC, USA
e-mail: prof.vaseashta@ieee.org

A. Vaseashta and S. Khudaverdyan (eds.), *Advanced Sensors for Safety and Security*,
NATO Science for Peace and Security Series B: Physics and Biophysics,
DOI 10.1007/978-94-007-7003-4_21,

handling and disposal practice of pharmaceuticals by the health care industry. The end result is that water sources now contain antibiotics, steroids, painkillers, and many other over-the-counter (OTC) and prescribed pharmaceuticals in water. Pharmaceutical waste is generated at healthcare facilities during and after patient care. Further improper disposal of expired pharmaceuticals either via drains, landfills, or even incineration contributes to this ever growing issue. The issue is further complicated by publically owned treatment works (POTW), for which the data is not readily available. As a result, the most common pharmaceuticals that exist in water stream include – antibiotics; steroids-fluxoymesterone, methyltestosterone, nandrolone, oxandrolone, oxymetholone, testosterone, and stanozolol; acetaminophen and ibuprofen, to name a few.

Antibiotics are common pharmaceutical compounds that have been used to treat or prevent microbial infections. Their wide usage have drawn a significant attention because of persistent and continuous existence of these compounds in water/wastewater [1]. The introduction of antibiotics into the environment constitutes a potential risk for living organisms in aquatic ecosystem and may cause resistance in bacterial populations, making them ineffective in the treatment of several diseases [2].

The water filtration methods currently in use are not designed to remove pharmaceuticals. To address this concern there are some recent studies to detect such contaminants and study several chemical and/or physical methods to remove, especially antibiotic, from wastewater by using methods such as filtration, coagulation, flocculation, sedimentation, adsorption, advanced oxidation, membrane, biological processes and the combination of those methods [3].

Cryogelation is a method that have been applied to prepare cryogels which have interconnected/supermacroporous structure and exhibit properties including high flexibility, reversible and very rapid size change to external forces and also swellability in aqueous media [4]. Cryogelation have been used to prepare polymeric cryogels from a variety of polymers and applied in many different areas such as chromatographic separation of several biological molecules and cells, carrier matrices for immobilization and scaffolds for tissue engineering applications [5].

Chitosan adsorbents present important advantages, such as their selectivity and they have been used in purification of medicines, cosmetics and foods, previously. In addition, beaded forms of chitosan have been applied to remove amoxicillin in previous studies [6]. Gelatin is a natural polymer produced from denatured collagen and can be processed to porous matrices by different techniques such as cryogelation [7].

The objective of this investigation is to develop several porous polymeric cryogel matrices made of chitosan and gelatin by using cryogelation technique to be used as block type filters for removal of antibiotics and potentially other chemicals from water/wastewater. The method is planned to be used for other pharmaceuticals as different membranes are developed.

21.2 Materials and Methods

Chitosan (highly viscous, Sigma Aldrich), Gelatin (Sigma Aldrich) and acetic acid (glacial, 99–100 %; Merck), were used as received. Glutaraldehyde was obtained from Merck, Germany. Distilled water was used in all steps of the experiments. A cryostat (Wisd WiseCircu, WCL-P12, Daihan, Korea) was used to prepare macroporous cryogels.

21.2.1 Synthesis of Chitosan and Gelatin Cryogels

Chitosan solutions of three different concentrations (0.25; 0.50 and 1 %, w/v) were prepared in (6 %, v/v) acetic acid solution and mixed on a mechanical rotor for 30 min. At the end of mixing, 0.1 ml of glutaraldehyde (25 %, v/v, aqueous solution) was added to 2 ml of prepared chitosan solutions. The whole solution was immediately poured into a 2 ml plastic syringe and transferred into the cryostat. The reaction mixture was incubated in the cryostat at −20 °C for 2 h and then in the fridge (at −16 °C) for 24 h. After the reaction was completed, the frozen samples in the syringe molds were thawed to room temperature. The cryogel blocks were removed from the mold and washed several times to remove the unreacted ingredients. The washed samples were dried at room temperature. In another set of experiments, the concentration of the chitosan solution was kept constant at 0.5 % and the crosslinker (glutaraldehyde) ratio was changed by increasing the volume of the solution, from 0.1 to 1 ml (0.1; 0.5 and 1.0 ml, respectively).

Gelatin solutions of three different concentrations (0.5; 1.0 and 2.0 %, w/v) were prepared in distilled water. 0.5 ml of glutaraldehyde (25 %, v/v, aqueous solution) was added to 2.0 ml of gelatin solution to start the crosslinking reaction. The same cryo-gelation procedure explained previously was applied to prepare gelatin cryogels. In another set of experiments, while the gelatin concentration was kept constant at 1.0 %, the glutaraldehyde concentration was increased from 0.5 to1.0 ml (0.5; 0.8 and 1.0 ml, respectively).

To determine the swelling behavior of chitosan and gelatin cryogels, the samples were dried at room temperature to a constant weight (W_d). Then, completely dried samples were immersed in distilled water to supply swollen cryogels. The excess water on the surface of the cryogels was removed and the samples were weighed (W_s). Swelling ratio was calculated by the following equation [4]:

$$\text{Swelling ratio} = (W_s - W_d)\,/W_d \tag{21.1}$$

21.3 Results and Discussion

For removal of antibiotics from wastewater, our first attempt was to prepare chitosan and gelatin cryogels. During cryogelation process the solvent is frozen at subzero temperatures. The frozen solvent forms crystals, the crystals merge with each other during freezing while the reaction occurs in the non-frozen phase. After the reaction is completed, the whole sample appears like a block. After this block is thawed to room temperature, the frozen solvent melts and leaves the interconnected pores behind, while the walls of the cryogel block is formed as the result of the completed reaction between the monomer, macromers or polymer. The interconnected macroporous cryogels prepared from different polymers find applications in many related biotechnological investigations, such as chromatographic separation.

When a solution is passed through a cryogel block, the interconnected macropores of the cryogel would let the fluid discharge, while adsorbing the required molecule onto the surface of the pore walls. The cryogel block would not be plugged, since it has interconnected supermacroporosity. Our previous studies about synthesis and characterization of polymeric cryogels prompted us to develop cryogel matrices for the removal of antibiotics from waste water [4]. The cryogelation process diagram followed in this investigation is shown in Fig. 21.1.

The interconnected porous wall structure and chemical/physical functionality of the prepared cryogels will allow development of new materials for antibiotic removal from water/wastewater. The concentration of gelatin and chitosan and amount of glutaraldehyde was varied in this study, which affects the chemical, physical, mechanical, morphological and porous structure of cryogels which would result in the separation behavior (amount and rate of the removed antibiotics, kinetics and equilibrium data of antibiotic adsorption) of the material.

A representative figure showing chitosan and gelatin based cryogels in syringe mold after cryogelation reaction is completed (Fig. 21.2a) and cryogel from the syringe mold is removed (Fig. 21.2b) and dried (Fig. 21.2c) is presented below.

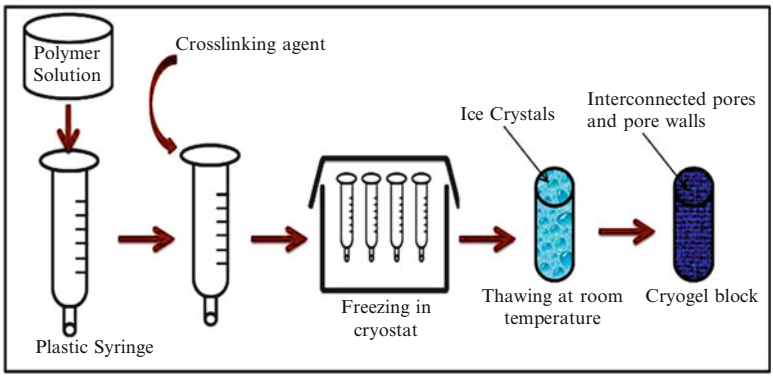

Fig. 21.1 The cryogelation process diagram

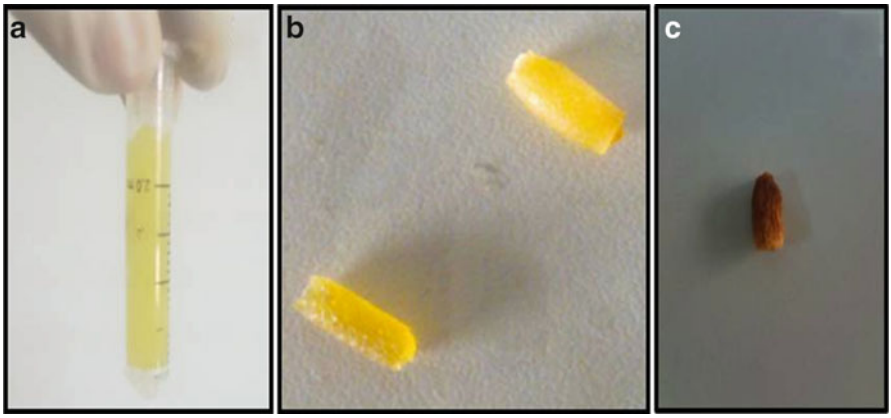

Fig. 21.2 Representative image of chitosan and gelatin based cryogels: (**a**) in syringe mold after reaction is completed, (**b**) after the cryogel is removed from the syringe mold and (**c**) dried form of the cryogel

Table 21.1 Effect of chitosan ratio and glutaraldehyde volume on swelling ratio of the cryogels

Chitosan ratio (%)	Glutaraldehyde solution volume (ml)	Swelling ratio
0.25	0.1	1.649
0.50	0.1	0.964
1.00	0.1	1.069
0.50	0.5	0.4875
0.50	1.0	1.6105

Table 21.1 presents the swelling ratio of the cryogels prepared with different chitosan and glutaraldehyde ratios. Swelling ratio is a significant indicator that gives information about the morphology of the cryogels such as their porosity and pore size distribution. Polymer concentration and the crosslinker ratio has important effects on the swelling ratio profiles of the cryogels which would affect the antibiotic adsorption ability and capacity of them.

When the chitosan ratio increased in the cryogel, the swelling ratio decreased. The decrease was due to the decrease in the pore size of the cryogels, as the polymer concentration increased the pore walls of the cryogel became denser compared to the cryogel prepared with less chitosan ratio.

In Table 21.2, the swelling ratios of cryogels prepared with different gelatin and glutaraldehyde ratios are presented. No cryogel formation occurred when the gelatin ratios were 0.5 and 1.0 % and glutaraldehyde volume was 0.5 ml. Most probably, the content of the crosslinker (glutaraldehyde) and the polymer (gelatin) was not enough to crosslink and hold the whole gel block. However, when the polymer ratio increased to 2.0 % while the glutaraldehyde volume was kept constant at 0.5 ml, cryogel formation was observed. Increasing the glutaraldehyde volume from 0.5 to 0.8 and 1.0 ml, while keeping the gelatin ratio constant at 1.0 %, led to a cryogel

Table 21.2 Effect of gelatin ratio and glutaraldehyde volume on swelling ratio of the cryogels

Gelatin ratio (%)	Glutaraldehyde solution volume (ml)	Swelling ratio
0.5	0.5	[a]
1.0	0.5	[a]
2.0	0.5	1.061
1.0	0.8	2.458
1.0	1.0	3.652

[a]No cryogel formation occurred

structure formation. The swelling ratio increased as the glutaraldehyde volume increased in the reaction mixture. The content of crosslinker was not enough for the reaction in the case of using 1.0 % gelatin and most probably the unreacted gelatin was removed during washing step.

21.4 Conclusion

The introduction of antibiotics into the environment constitutes a potential risk for living organisms in aquatic ecosystem and may cause resistance in bacterial populations, making them ineffective in the treatment of several diseases. Therefore, the antibiotic should be removed from wastewater before entering the environment. In this study, the methodology involves production of porous cryogel matrices from gelatin and chitosan. The interconnected porous wall structure and chemical/physical functionality of the prepared cryogels will allow development of new interconnected macroporous matrices for antibiotic removal from water/wastewater. The type and concentration of the polymer, amount of crosslinking agent and reaction temperature affect the chemical, physical, mechanical, morphological and porous structure of the cryogels which result in the filtration behavior (amount and rate of the removed antibiotics, kinetics and equilibrium data of antibiotic adsorption) of the material. Here, we synthesized a set of chitosan and gelatin based cryogel matrices and presented preliminary results of characterization. Future studies would include the treatment of water containing antibiotics with prepared cryogels. Our investigations are ongoing. In this study, we present the development of chitosan and gelatin cryogels and propose them to be used in antibiotic removal applications from waste water. The development of these porous cryogel matrices may have potential as industrial filter equipment in water treatment plants.

References

1. Klavarioti M, Mantzavinos D, Kassinos D (2009) Removal of residual pharmaceuticals from aqueous systems by advanced oxidation processes. Environ Int 35(2):402–417
2. Caroni ALP, De Lima CRM, Pereira MR, Fonseca JLC (2009) Kinetics of adsorption of tetracycline on chitosan particles. J Colloid Interface Sci 340(2):182–191

3. Homem V, Santos L (2011) Degradation and removal methods of antibiotics from aqueous, matrices – a review. J Environ Manage 92:2304–2347
4. Bölgen N, Plieva F, Galaev IY, Piskin E, Mattiasson B (2007) Cryogelation for preparation of novel biodegradable tissue engineering scaffolds. J Biomater Sci Polym Ed 18:1165–1179
5. Lozinsky V, Plieva FM, Galaev YU, Mattiasson B (2002) The potential of polymeric cryogels in bioseparation. Bioseparation 10:163–188
6. Adriano WS, Veredas V, Santana CC, Gonçalves LRB (2005) Adsorption of amoxicillin on chitosan beads: kinetics, equilibrium and validation of finite bath models. Biochem Eng J 27(2):132–137
7. Kathuria N, Tripathi A, Kar KK, Kumar A (2009) Synthesis and characterization of elastic and macroporous chitosan–gelatin cryogels for tissue engineering. Acta Biomater 5:406–418

Part VI
Radiation Sensors

Chapter 22
On the Concept of System to Detect Unclaimed Inclusions of Fissile and Radioactive Materials in Hand Luggage and Cargo Trucking

A. Lobko, A. Fedorov, M. Korjik, V. Mechinski, and G. Drobychev

Abstract A concept of a system to detect presence of fissile and radioactive materials in cargo and shipping containers is discussed. High energy gamma-radiography of an object may be used to retrieve information on mass and density distribution within it. Important requirement of such a system is the use of appropriate detectors having fast response and large stopping power to high energy gamma-rays along with comparable yields of scintillation and Cherenkov light. We discuss detection by scintillation materials which can be applied to develop such systems.

Keywords Scintillators • Gamma-radiation • Radiation resistance • Detectors

22.1 Introduction

Recently x-ray security system for the inspection of cargo and shipping containers, which apply transmission radiographic techniques, has been proposed [1]. The penetrating x-radiation from the beam that has traversed the object is sensed, generating the detector signal. Information (such as mass absorption coefficient, effective atomic number Z_{eff}, electron density, etc.) with respect to the material composition of the contents of objects may be obtained on the basis of the interaction of x-rays with the material, and, more particularly, by illuminating the material with x-ray beams having energy spectra with more than one distinct energy endpoint (peak energy), or by using energy discriminating detectors. Dual energy methods of material discrimination are used in x-ray inspection systems for security control of hand luggage in customs and other security checkpoints [2]. Novel portable accelerators allow high luminosity and can scan objects moving at

A. Lobko (✉) • A. Fedorov • M. Korjik • V. Mechinski • G. Drobychev
Institute for Nuclear Problems, Belarusian State University, 11 Bobrujskaya Str., Minsk 220030, Belarus
e-mail: lobko@inp.bsu.by

A. Vaseashta and S. Khudaverdyan (eds.), *Advanced Sensors for Safety and Security*, NATO Science for Peace and Security Series B: Physics and Biophysics,
DOI 10.1007/978-94-007-7003-4_22,

relatively high speed. So cargo carriers can be hidden inspected in any appropriate point of interest. Another important requirement to such type of the system is the use of appropriate detector having fast response and large stopping power to high energy x-rays. Here we discuss detecting scintillation materials which can be applied to develop such systems.

22.2 Inspection Method Applying High Energy X-Rays

Typical x-ray transmission inspection system used for interrogating the material composition of matter, such as the contents of containers or vehicles contains source which emits beam of penetrating radiation which traverses an inspected object such as vehicle as shown at Fig. 22.1.

Particular contents of the object may be discriminated and characterized on the basis of the transmission of penetrating radiation through the object and its detection by detector array and its individual detector modules. The discrimination of material characteristics may be improved by the use of x-ray beams with energy spectra having two x-ray peak energies that interact differently with the interrogated matter. For an x-ray beam having peak energy less than 5 MeV, the x-ray radiation will be attenuated mainly by Compton scattering. For an x-ray beam having peak energy more than 5–6 MeV, pair production becomes compatible with the contribution of the Compton scattering. The ratio of the transmitted radiation detected at two energies, for instance 3 and 9 MeV, is indicative of the atomic numbers of the material through which the radiation beam passes. The x-ray source may be an accelerator which has been configured to produce x-ray pulses of appropriate energies. To provide high dynamic range of the detecting system the photon counting may be used. It is advantageous for lower intensities, as it allows rejecting

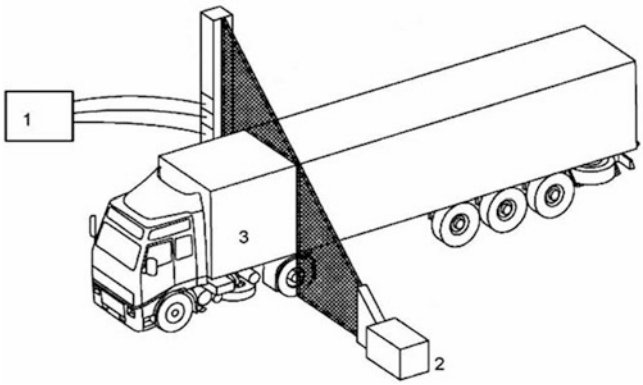

Fig. 22.1 Sketch of x-ray inspection cargo system. *1* – detector and electronics, *2* – source of penetrating beam, *3* – object under inspection

scatter contributions based on the dissemble energy of the individually detected x-ray photons. A Cherenkov or a Scintillation-Cherenkov detector allows rejection of scatter contributions also in integration mode based on its energy discriminating characteristic. Summarising matters discussed above, main requirements to the sensing scintillating material should be as follows:

- material must have sufficient stopping power to detect high energy gamma rays at the reasonable dimensions;
- material must have fast response time to avoid pile-up in intensive radiation beams and further distortion of spectra;
- material should have comparable yields of Cherenkov & scintillating light;
- material must have low optical absorption of the Cherenkov glow and simultaneously provide scintillations in the spectral range suitable for its detecting with the same photo-sensor;
- material must be radiation resistant to provide stability of optical and scintillation parameters during all life time of a detector;
- technology of material production should be developed enough and production cost must be affordable.

In order to obtain sufficiently time resolved data, detectors should be produced on the base of fast respond and heavy scintillators, such as $PbWO_4$ (PWO), or CsI, exhibiting decay times as short as 30 ns. Other detectors, based, for example, on bismuth germanate (BGO) crystals, are less applicable due to their scintillation delay time that equals to 300 ns. Application of PWO crystals for dual readout is described in [3]. Recently, the new modification of PWO crystals doped with molybdenum or PMWO, has been developed [4]. It provides better conditions to detect scintillation and Cherenkov light from the crystal simultaneously. Our preliminary study shows that PWMO, it is $PbWO_4$ crystal doped with Mo and La, is the good candidate to meet most of requirements of the described apparatus.

22.3 PWMO Scintillation Material

PWMO scintillation material has been proposed and tested as the new sensing material for collider experiments [4–6]. It is the PWO based material in which part of the tungsten ions is substituted with Mo ions. Substitution is isomorphic so no defects of the crystal structure occur. PWMO has shift of the scintillation band maximum of about 100 nm toward longer wavelength region in comparison with regular PWO crystal. Cutoff of the absorption spectrum is also shifted from 320 to 350–370 nm depending on Mo concentration ion the crystal. Figure 22.2 shows dependence of crystal absorption spectrum versus Mo concentration in the melt. Scintillation kinetics (timing response) contains three components with $\tau = 10$, 36, 216 ns and fraction 62, 33, 5 % respectively. Room temperature light yield of the $20 \times 20 \times 10$ mm^3 sample is 22 phe/MeV. Figure 22.3 shows radio-luminescence spectra of $PbWO_4$ and $Pb(W_{0.95}-M_{0.05})O_4$:La,Y crystals at room temperature and

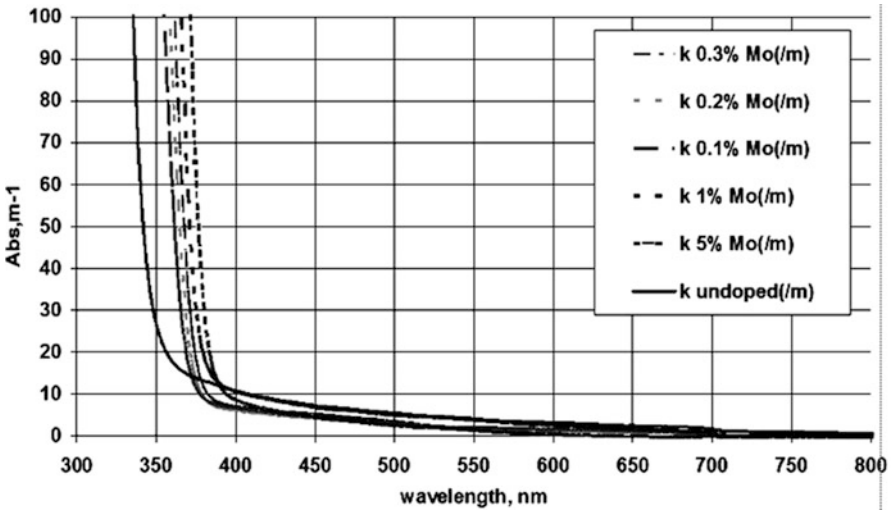

Fig. 22.2 Optical absorption of PWMO crystals with various concentrations of Mo

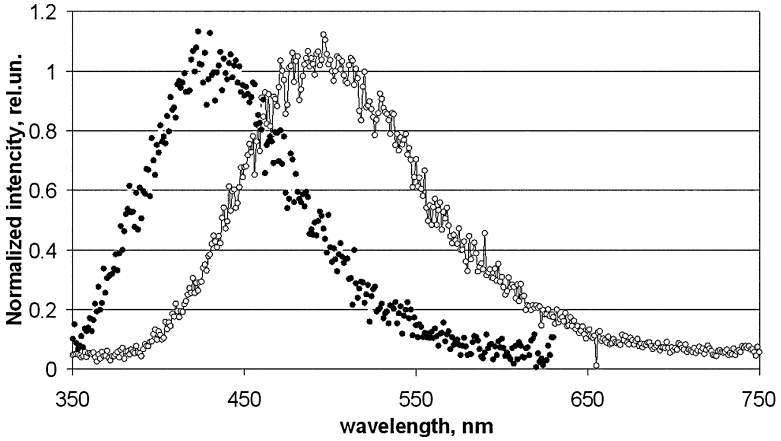

Fig. 22.3 Radioluminescence spectra of $PbWO_4$ (•) and $Pb(W_{0.95}-M_{0.05})O_4$:La, Y (○) crystals at room temperature

Fig. 22.4 is for its scintillation kinetics. Due to shifted scintillation spectrum PMWO crystal allows to detect Cherenkov light in the spectral window between cutoff and scintillation. Yield of scintillation is of one order of magnitude larger than yield of Cherenkov light, however application of the short integration gate (∼5 ns) for Cherenkov light and delayed (∼5 ns) integration of scintillation gives the possibility to achieve better discrimination of Cherenkov light and scintillation. Only 15 % of scintillation is emitted in first 5 ns so, the effective discrimination of scintillation and Cherenkov light becomes possible.

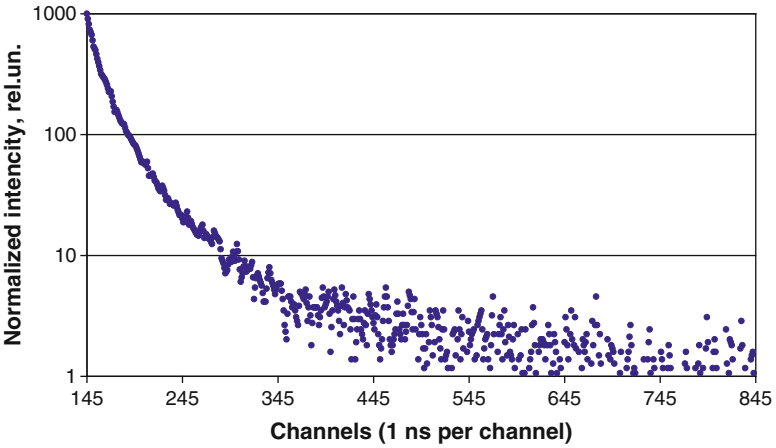

Fig. 22.4 Scintillation kinetics of $Pb(W_{0.95}-M_{0.05})O_4$: La, Y at room temperature

Table 22.1 Comparison of the Cherenkov light yield for large detector elements

Material	Yield of Cherenkov light in 18–20 cm elements, phe/GeV of the deposited energy	Reference
$Bi_4Ge_3O_{12}$ (BGO)	30	[7]
$Bi_4Si_3O_{12}$ (BSO)	48	Ibid
$Pb(W-Mo)O_4$ (PWMO)	55–65	[4, 5]

Some key characteristics of PWO and PWMO materials in compare to other applications and perspective scintillators are summarized in Tables 22.1 and 22.2. As one can see, PWMO scintillator has advantages in comparison with competitors. Industrial production of PWMO can be started quite fast and with no significant additional cost for the R&D.

22.4 Radiation Damage Effects in PWMO Crystals

Stability of the parameters of a detector is crucial requirement to be applied in inspection system. The low damage of the scintillation material by hard x-rays is required.

Due to preliminary research it was determined that crystal optical transmission radiation damage depends on concentration of Mo in the crystal. Figure 22.5a and b shows deconvolution of γ-radiation induced absorption spectra of regular PWO crystal used at CMS experiment and PWMO crystal containing 1 at.% of Mo.

PWMO crystal has two additional induced absorption bands peaked at 3.6 eV (347 nm) and 1.5 eV (830 nm) in comparison with known PWO. UV band appears

Table 22.2 Comparison of some crystals as the Cherenkov emitters and their mass production status

Material	Stokes shift	Window to Cherenkov light	Production status and cost drivers
$Bi_4Ge_3O_{12}$ (BGO)	2.5 eV (20,000 cm^{-1})	1.0 eV (8,000 cm^{-1})	Industrially produced material High cost of Ge oxide
$Bi_4Si_3O_{12}$ (BSO)	2.8 eV (22,400 cm^{-1})	1.25 eV (12,000 cm^{-1})	No industrial production exists. It should have affordable price (similar or less than PWO) if technological problems will be overcome.
$PbWO_4$ (PWO)	0.88 eV (7,000 cm^{-1})	0.5 eV (4,000 cm^{-1})	Industrially produced material in Russia and China. No cost increase is supposed
$Pb(W-Mo)O_4$ (PWMO)	0.96 eV (7,700 cm^{-1})	0.6 eV (4,800 cm^{-1})	Can be industrially produced at PWO production facilities in Russia and China. No cost increase is supposed
CeF_3	0.33 eV (2,600 cm^{-1})	No window in a short wavelength range	Still under development but progress to obtain long crystals (30 cm) has been demonstrated since 1995, see [8]. Target is at least 42 cm long crystals.

due to creation of electron center on the base of $(MoO_4)^{3-}$ impurity center which thermo-activation energy E_{TA} vary in the range 0.3–0.5 eV depending on Mo concentration [9]. The origin of the IR band is not clear yet. However, its appearance correlates with concentration of Mo in the crystal. At low Mo concentration this band becomes already observable while Mo concentration is more than 100 ppm. Its intensity in induced absorption spectra growth proportionally to Mo concentration however, at concentration ~10,000 ppm it starts to fall. This behavior at relatively high concentration is due to the transformation of the electron centre symmetry from axial to cubic. As consequence, the thermo-activation energy of the center is decreased to 0.3 eV. Cubic $(MoO_4)^{3-}$ center is shallow so energy transfer to radiating level of molybdenum oxi-complex becomes faster. Shallow electron centers based on the oxygen vacancies in the crystal are suppressed by additional simultaneous doping of the crystal by La and Y as described in [10]. It should be noted that distance between Mo ions in the heavily doped crystal becomes

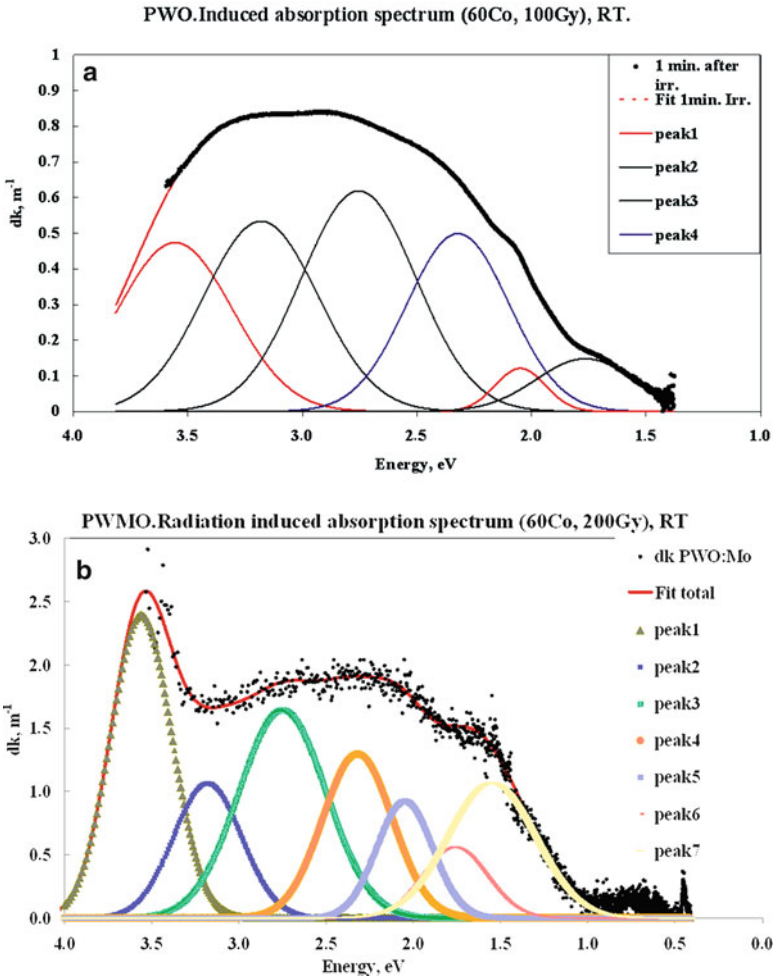

Fig. 22.5 (**a**) Room temperature γ-radiation induced absorption spectra of regular PWO crystal of LHC CMS specification. (**b**) Room temperature γ-radiation induced absorption spectra of PWMO crystal containing 1 at.% of Mo

short, making them interacting. As a consequence, Mo atoms form sub-zone near the bottom of crystal conduction band. It shifts Fermi level in the forbidden zone toward to valence zone making possible the existence of other sorts of the defects combining from vacancies in the vicinity of Mo ion. On a first glance it makes radiation hardness of crystal worse. However, all these possible centers have energy levels which are close to valence band so their recombination becomes faster. The existence of various trends in the behavior of the induced absorption spectra of PMWO crystals and its dependences on the activator concentration is the positive sign that an optimal combination of Mo, Y, La making crystal radiation hard can be developed.

22.5 Conclusion

The results acquired up to date shows that PWMO crystal is the very attractive option to build dual readout system to detect unclaimed inclusions of fissile and radioactive materials in hand luggage and cargo trucking:

- Due to the shifted scintillation band in comparison with that of standard PWO, spectrum of PMWO crystal allows to detect Cherenkov light in the spectral window between cutoff and scintillation;
- Yield of scintillation is the one order of magnitude larger than yield of Cherenkov light, however the application of the short integration gate (∼5 ns) for Cherenkov light and delayed (∼5 ns) integration of scintillation gives the possibility to achieve better discrimination of Cherenkov light and scintillation;
- Only 15 % of scintillation is emitted in first 5 ns so, the effective discrimination of scintillation and Cherenkov light becomes possible;
- Very important: industrial production of PWMO can be started quite fast and with no significant cost for additional R&D.

References

1. Arodzero A et al (2011) Scintillation-cherenkov detector and method for high energy x-ray cargo container imaging and industrial radiography. Patent WO 2011/071759
2. Neale WW et al (1996) Material identification using X-Rays. US Patent No. 5,524,133
3. Korzhik MV, Fedorov AA, Missevitch OV, Auffray E, Lecoq P (2008) Lead tungstate scintillator for the future particle physics detectors. In: Conference program of IEEE 2008 international conference, Dresden, 19–25 Oct 2008, pp N40–N45
4. Akchurin N, Bedeschi F, Cardini A et al (2009) New crystals for dual-readout calorimetry. Nucl Instrum Methods Phys Res A 604:512–526
5. Gaudio G (2010) Optimization of crystals for applications in dual-readout calorimetry. In: CALOR 2010 – XIV international conference for calorimetry in high energy physics, IHEP, Beijing, 10–14 May 2010
6. Hofstaetter A, Oeder R, Scharmann A, Schwabe D, Vitt B (1978) Paramagnetic resonance and thermoluminescence of the $PbWO_4/PbMoO_4$ mixed crystal system. Phys Status Solidi B 89:375–380
7. Akchurin N, Bedeschi F, Cardini A et al (2011) A comparison of BGO and BSO crystals used in the dual-readout mode. Nucl Instrum Methods Phys Res A 640:91–98
8. Dissertori G, Lecomte P, Luckey D et al (2010) A study of high-energy proton induced damage in cerium fluoride in comparison with measurements in lead tungstate calorimeter crystals. Nucl Instrum Methods Phys Res A 622:41–48
9. Annenkov A, Korzhik M, Lecoq P (2002) Lead tungstate scintillation material. Nucl Instrum Methods Phys Res A 490:30–50
10. Dormenev V, Kuske T, Novotny RW, Borisevich A et al (2010) Stimulated recovery of the optical transmission of $PbWO_4$ scintillation crystals for electromagnetic calorimeters after radiation damage. Nucl Instrum Methods Phys Res A 623(3):1082–1085

Chapter 23
New Model of Spectral Analysis of Integral Flux of Radiation

Surik Khudaverdyan, M. Khachatryan, D. Khudaverdyan, S. Caturyan, and Ashok Vaseashta

Abstract In this work we studied a new model of a portable photodetector for the remote spectral analysis of signals using optical information. We studied the applications of the photodetector for identification and quantitative analysis of hazardous mixtures in natural objects with display capability of output of temporal and quantitative data. The new physical principle applied in the photodetector allowed us to carry out the spatial separation and selection of UV and visible waves absorbed in the objects with calculated spectral accuracy of 1 nm. We developed an algorithm of spectral analysis that ensured the operation of the photodetector without any preliminary calibration.

Keywords Algorithm • Visible wave • Spectral analysis • Radiation • Photodetector

23.1 Introduction

Recent studies of the natural objects from a viewpoint of quantitative and qualitative analysis is not satisfactory. One of the advanced methods of studies is the optical spectral analysis. However, even in this case we observe the dispersion of the spectral data of identical objects complicates the correlation between the measured

S. Khudaverdyan (✉) • M. Khachatryan • D. Khudaverdyan • S. Caturyan
Faculties Radio Engineering and Communication Systems, Department Design and Production of Radio Devices, State Engineering University of Armenia, 105, Teryan str., Yerevan 0009, Armenia
e-mail: xudaver13@mail.ru

A. Vaseashta
Norwich University Applied Research Institutes, Herndon, VA, USA

VTT/AVC U.S. Department of State, Washington, DC, USA
e-mail: prof.vaseashta@ieee.org

A. Vaseashta and S. Khudaverdyan (eds.), *Advanced Sensors for Safety and Security*, NATO Science for Peace and Security Series B: Physics and Biophysics,
DOI 10.1007/978-94-007-7003-4_23,

results. The processing of the spectral data is obtained via quantitative analysis. The data accuracy of the analysis depends directly on the parameters of the device under investigation.

To promote the efficiency of remote studies of objects, we need to improve measuring devices (via creating a large number of connections between the object under study and by registering their parameters) and to develop more rational methods of analysis of the results of the experiments. The larger is dataset, more complicated it gets to interpret the measurement results.Since a large number of the parameters of the system does not allow us to find cause-and-effect relations between them [1], it is necessary to highlight and develop;

1. more effective methods of spectral selective sensitivity, and,
2. a more completed algorithm for the registration and analysis of useful information.

23.2 Methods of Spectral Selective Sensitivity

At present, the methods of the registration for separate wavelengths from the interference of light with the help of the prism, and from the spectral distribution of light, have achieved higher accuracy. For registration of photodiode arrays, prisms, diffraction gratings, high accuracy mechanical devices are used which makes the spectrophotometers expensive, hard-to-use and maladjusted to field conditions [2]. Besides, the spectrophotometric systems like that require external computer support.

New structures developed to eliminate above-stated disadvantages, use different depths of absorption to register separate waves from an integral flux of radiation in the solid body [3, 4]. However, in an event that the case where the cascade chain of photoreceivers is used, the technology is complicated and requires an identical output conditions of the operation. In the other case, for the registration of separate waves, the identity of their intensities or the increase towards the long waves are required. There are also problems with the supply of high selective sensitivity.

To solve local problems, the films of porous silicon (PSi) are used [5, 6]. However, the PSi surface is hydrophobic, and the passivation treatment is required to ensure the stability of the surface allowing the bio-probe to bind covalently. Thus, there is an urgent need for the development of a small-size, inexpensive sensor with high selective sensitivity. The sensor will have an embedded computer and will be adjusted to the remote detection in the field conditions.

23.3 Object Under Investigation

Our object under investigation is asemiconductor heterogeneous environment in which the volume registering optical radiation can be widened towards the surface receiving the radiation. It allows us to involve waves with different absorption depths

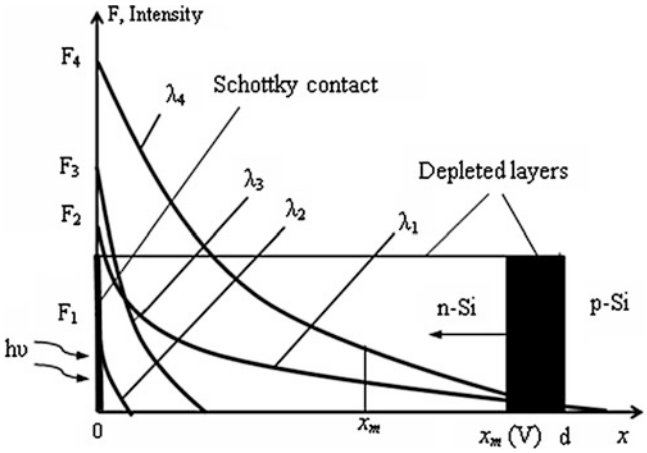

Fig. 23.1 Semiconductor structure showing absorption of differnet waves

into the registering environment. The determination of the lengths and the intensities of these waves with the help of the registering signal is one of our primary issues. For that we need structural and technological solutions, as well as the appropriate algorithm for the information output.

To find a solution of the problem, we propose a semiconductor structure with oppositely directed Schottky barrier and n-p junction, where n-region is the base. It is occupied with the depleted layers of two barriers (Fig. 23.1). In the base the current is drift, and in the p-region is diffusion [7]. The contact point of depleted layers x_m is shifted towards the surface (Schottky contact) by the external voltage. The electromagnetic radiation is absorbed by the Schottky contact. The current is created in the d-x_m section of the d width of the structure base. The photo charge carriers generated in the section from 0 up to x_m do not move into the external circuit and do not create current because of the recombination in the Schottky contact [7, 8]. This shift of x_m towards the surface (towards "0" of Fig. 23.1) involves new waves into the region of the current generation (Fig. 23.1) which leads to the change of the photocurrent. According to Lambert's law, the shorter is the wave, the smaller is the absorption depth. However, in the integral flux of radiation, the shortwave of big intensity (Fig. 23.1, λ_4) can have bigger residual intensity than the long wave of small intensity (Fig. 23.1, λ_1) at the given point of x_m. Thus, the summed photo signal will be partly conditioned by the high intensity wave.

The law of change of the summed photosignal corresponding to two different regions, close to each other in values of x_m will also be conditioned by that wave. The bigger is the contribution of the wave into the summed photosignal and the closer are the two values of x_m, the more accurate will the be response.

23.4 Results of Studies

For determination of the spectral composition of the integral flux of electromagnetic radiation and the definition of its change, we studied outside atmospheric radiation absorption of the Sun (where UV radiation is high). We reduced the wave intensities of radiation so that the penetration depth corresponded to the width of the registering environment. The photocurrent corresponding to the biggest value of x_m was conditioned by the most deeply penetrated wave. Under these conditions the process of the selection of separate waves and their intensities from the integral flux of radiation was the following. Assume the informative signal to be the photocurrent. By the external voltage we can obtain the biggest values of $x_m - x_{m1}$ and x_{m2} with the difference of 1 nm, and the corresponding photocurrents I_1 and I_2. From Lambert's law of the radiation absorption in the homogeneous environment we will have the coefficient of the wave absorption,

$$\alpha_i = \frac{1}{\Delta x_m} \ln \frac{I_2}{I_1} \tag{23.1}$$

where $\Delta x_m = x_{m2} - x_{m1}$

Then, with the help of $\alpha = f(\lambda_i)$ and with the corresponding program we can determine the length of the wave for the initial material of the photodetector, e.g. for silicon (Fig. 23.2).

With the help of the expression [9] for the summed current,

$$\sum_{i,j} I_{Ph.i,j} = \sum_{i,j} I_{dri,j} + \sum_{i,j} I_{diff\ i,j} = S\,q \sum_i \sum_j F_0(\lambda_i) \left(e^{-\alpha_i x_{mj}} - \frac{e^{-\alpha_i d}}{1 + \alpha_i\ w} \right) \tag{23.2}$$

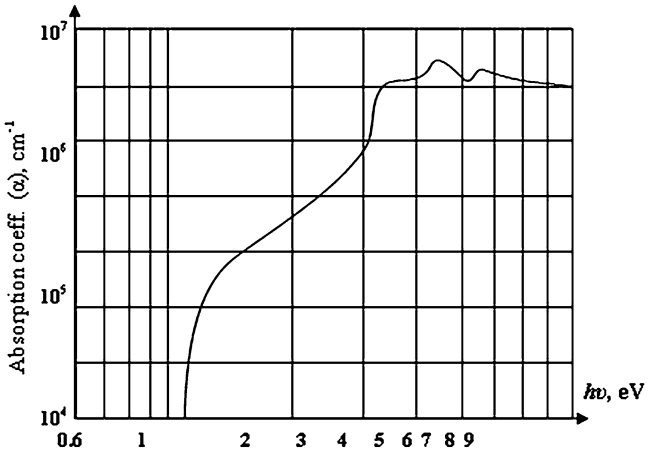

Fig. 23.2 Optical absorption spectrum in pure silicon

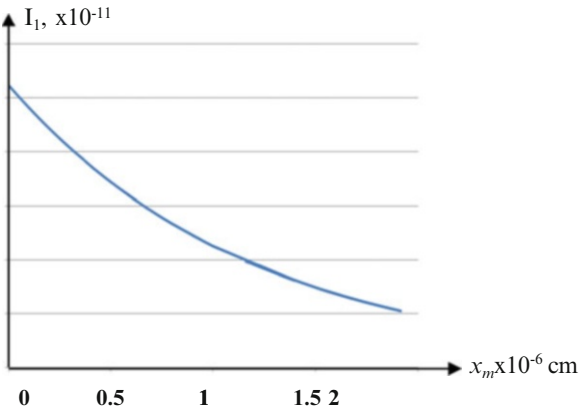

Fig. 23.3 Dependence of the photocurrent created by a separate wave on x_m

we will obtain the intensities of separate waves of the absorption radiation,

$$F_0(\lambda_i) = \frac{I_{Ph.i,j}}{Sq\left(e^{-\alpha_i x_{mj}} - \dfrac{e^{-\alpha_i d}}{1+\alpha_i w}\right)} \tag{23.3}$$

Here, W is the width of the $x > d$ section of the structure (Fig. 23.1), q is the electron charge, and S is the photosensitive surface.

Thus, with the help of (23.1) and (23.3), we determine the absorption coefficient of the most deeply penetrated wave, the wavelength and the intensity of the wave.

Then, with the help of the expression

$$I_{Ph.\,j} = S\,q\,F_0(\lambda)\left(e^{-\alpha x_{mj}} - \frac{e^{-\alpha d}}{1+\alpha \quad w}\right) \tag{23.4}$$

we form the dependence $I_1 = f\,(x_{m1})$ as shown in (Fig. 23.3) and subtract it from the dependence obtained by (23.2) (Fig. 23.4).

As a result, we have a new dependence from the x_m of the summed photocurrent, without the dependence $I_1 = f\,(x_m)$ (Fig. 23.5). By using the corresponding software, this method helps us to successively determine the lengths and the intensities of all the waves in the radiation, and to obtain the dependences of the photocurrent conditioned by those waves on x_m (Fig. 23.6).

Then, we obtain the dependence for the spectrum, for example, in the visible region (Fig. 23.7).

It can be kept in the memory of the device and be used in the identification processes of objects. The following parameters of quantitative determination of some narcotics (Table 23.1, [10]), toxic substances in food (Table 23.2, [7]), harmful substances in water (Table 23.3, [11]) and explosives (Table 23.4, [12]) by means of the UV and visible spectroscopy are known.

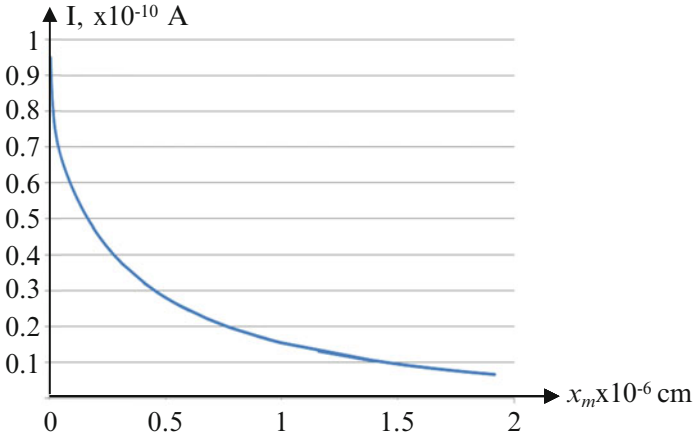

Fig. 23.4 Dependence of the summed photocurrent on x_m

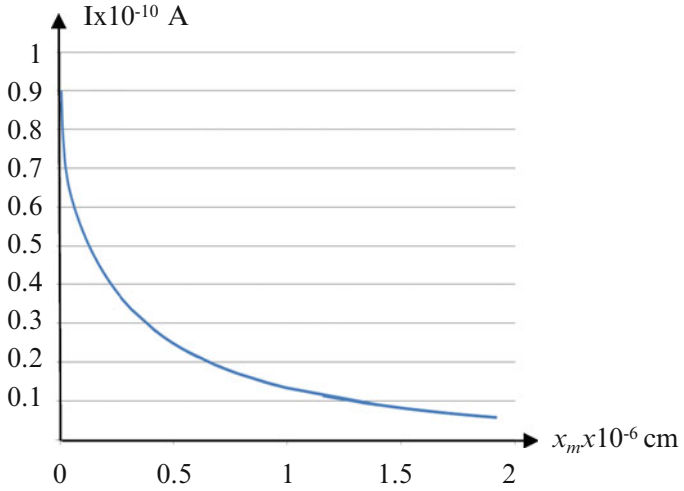

Fig. 23.5 Dependence of the summed photocurrent on x_m, when the determined wave is absent

In the vapors of explosives, NO, N_2 and O_2 molecules excited by laser radiation create luminescence, particularly in the **226** and **236** nm of the wave.

Thus, the optical range of the remote detection of substances brought in Tables 23.1, 23.2, 23.3, and 23.4 includes the UV and visible regions of the spectrum, as well as the sensitive region of the proposed sensor. Figure 23.8 presents the calculated change of the spectral composition in the visible radiation spectrum.

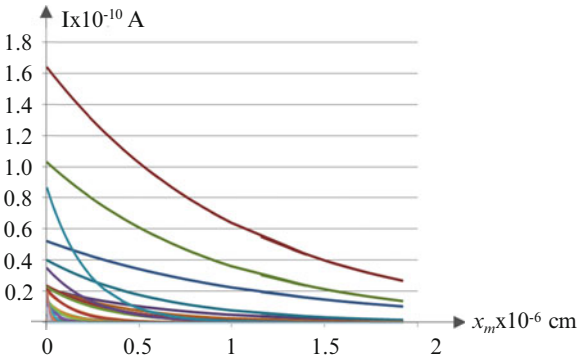

Fig. 23.6 Dependences of the photocurrents of separate waves on x_m

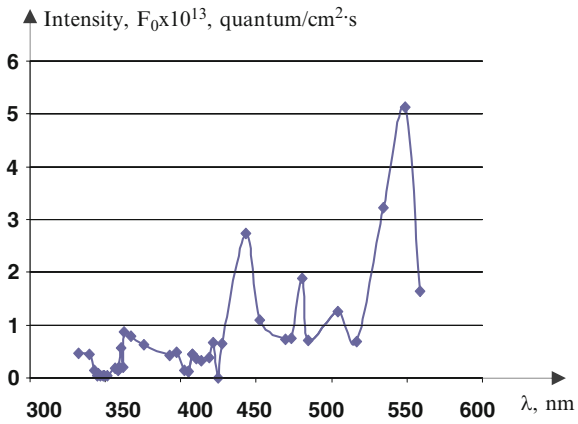

Fig. 23.7 Spectral distribution of radiation intensity

Table 23.1 The following parameters of quantitative determination of some narcotics

Substance	Wavelength in maximum absorption, nm	Concentration range, mg/ml
Cocaine	234	0.01–0.06
Pentazocine	278	0.01–0.20
Buprenorphine	286	0.10–0.40
Methadone	295	0.10–0.60
Phencyclidine	262	0.1–1.5
Methaqualone	227	0.001–0.015

Table 23.2 Toxic substances in food

Substance	Wavelength in maximum absorption, nm	Ultimate number of molecules per gram of substance
Aflatoxin B1	265, 362	$9.6.10^{12}$ molecules
Aflatoxin M1	265, 357	$9.2.10^{12}$ molecules
Sterigmatocystin	208, 249	$9.3.10^{12}$ molecules

Table 23.3 Harmful substances in water

Substance	Wavelength in maximum absorption, nm
Turbidity of water	530
Iron content	400
Ammonium content	470
Nitrite content	500
Fluoride content	590
Manganin content	530

Table 23.4 Various explosives and their vapor densities

	Vapor density of explosives (order of magnitude)		
Type of explosives	Number of molecules of explosives per trillion of molecules of air (ppt)	Number of molecules of explosives/cm^3 of air	Grams of explosives per cm^3 of air
Nitroglycerine (NG)	10^6	10^{13}	10^{-9}
Trotyl (TNT)	10^4	10^{11}	10^{-11}
TEN (PETN)	10^0–10^1	10^8–10^9	10^{-14}–10^{-13}
Cyclonite (RDX)	10^0	10^8	10^{-14}
Explosives C-4 (91 % RDX + 9 % of plastic binder)	10^{-1}	10^7	10^{-15}
Ethylene glycol denitrate (EGDN)	10^8	10^{15}	10^{-7}

23.5 Conclusion

We studied the new model of the portable photosensor developed for remote detection of optical information, and the identification and the quantitative analysis of dangerous substances in the environment. In the radiation spectrum, the waves have different absorption depths, and the process of the selection of these waves is carried out via widening of the registering volume by means of the gradual change of the external voltage applied to the sensor. The developed algorithm allowed us to carry out the spectral analysis without any preliminary calibration.

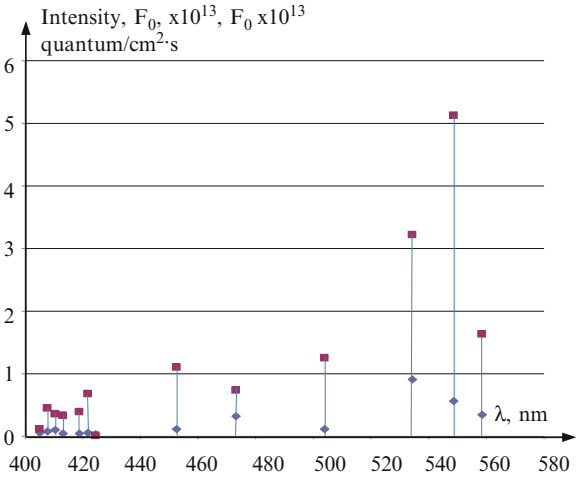

Fig. 23.8 Change of the spectral distribution of the radiation intensity in the visible radiation spectrum. The number of absorbing or emitting molecules in the volume unit is from 10^{12} to $5*10^{12}$

References

1. http://www.dissercat.com/content/razrabotka-i-primenenie-distantsionnykh-spektrometricheskikh-metodov-issledovaniya-prirodnyk
2. http://www.google.ru/search?q=spectrophotometers&hl=ru&newwindow=1&prmd=imvns&tbm=isch&tbo=u&source=univ&sa=X&ei=s7GDUMCMOOmG4gSFhIAw&sqi=2&ved=0CEoQsAQ&biw=1280&bih=885
3. Nader K, Fereydoon N (2004) Filterless Si-based ultraviolet-selective photodetectors. Spire Corp. for Stennis Space Center, Mississippi, Refer to SSC-00072
4. Gergel VA, Lependin AV, Tishin YI et al (2006) Boron distribution profiling in asymmetrical N^+-P silicon photodiodes and new creation concept of selectively sensitive photoelements for megapixel color photoreceivers. Proc SPIE 6260, Micro- and Nanoelectron, 61–64. doi:10.1117/12.677027
5. Stefano L, Arcari P, Lamberti A, Sanges C, Rotiroti L, Rea I, Rendina I (2007) DNA optical detection based on porous silicon technology: from biosensors to biochips. Sensors 7:214–221
6. Lin V, Motesharie Y, Dancil K, Sailor S, Ghadiri M (1997) A porous silicon-bazed optical interferometric biosensor. Science 278:840–843
7. Khudaverdyan S, Dokholyan J, Arustamyan V, Khudaverdyan A, Clinciu D (2009) On the mechanism of spectral selective sensitivity of photonic biosensors. Nucl Instrum Methods Phys Res A 610(1):314–316, Elsevier
8. Khudaverdyan S, Petrosyan O, Dokholyan J, Khudaverdyan D, Tsaturyan S (2012) Modeling of a new type of an optoelectronic biosensor for the monitoring of the environment and the food products.In: Vaseashta A, Braman E, Susmann P (eds) Technological innovations in sensing and detection of chemical, biological, radiological, nuclear threats and ecological terrorism. Springer, Dordrecht, pp 179–184
9. Sze S (1981) Physics of semicondutor devices, 2nd edn. Wiley-Interscience, New York, 450
10. http://www.law7.ru/base33/part3/d33ru3553.htm
11. http://purecology.narod.ru/Work1.htm#_Toc36184872
12. http://www.lavanda-u.ru/Publ/dvv2.html

Chapter 24
Cyclic Amino Acid Derivatives as New Generation of Radioprotectors

A. Boyajyan, A. Poghosyan, T. Hovsepyan, E. Arakelova, L. Zhamharyan, V. Ayvazyan, M. Malakyan, S. Bajinyan, V. Matosyan, and V. Tonoyan

Abstract Recently we synthesized a number of Schiff-base cyclic amino acid derivatives, and their metallic complexes as radioprotectors. Our preliminary investigations revealed four compounds, viz., nicotinyl-L-tryptophan, nicotinyl-L-tyrosine, and copper complexes of nicotinyl-L-tryptophan and picolinyl-L-tryptophan, possessing free radical neutralization capabilities. In the present investigation, we studied the effects of the selected compounds on survival rate, immune and antioxidant systems of the organism in the conditions of IR using animal model of irradiation injury. As the indicators of the immune system state we considered major mediators of the immune response, the complement system and the immune complexes. As the indicators of the antioxidant system functional state, we considered enzymes catalyzing free radical neutralization reactions, CuZn-superoxide dismutase and catalase. The results indicate that nicotinyl-L-tryptophan, nicotinyl-L-tyrosine and copper complex of picolinyl-L-tryptophan increase survival rate and possess immune-modulating and antioxidant system capacity elevating effects in the conditions of IR. These compounds stabilize and reactivate defense biomolecules, regulate the immune response, and increase radiosensitivity threshold, and hence may be considered as a new generation of highly efficient multifunctional radioprotectors targeting native defense systems of the organism.

Keywords Ionizing irradiation • Schiff-base cyclic amino acid derivatives • Multifunctional radioprotectors • Immune system • Antioxidant system

A. Boyajyan (✉) • A. Poghosyan • T. Hovsepyan • E. Arakelova • L. Zhamharyan • V. Ayvazyan
Institute of Molecular Biology, National Academy of Sciences, 7 Hasratyan St.,
0014 Yerevan, Armenia
e-mail: aboyajyan@sci.am

M. Malakyan • S. Bajinyan • V. Matosyan • V. Tonoyan
Scientific Centre of Radiation Medicine and Burns, Davidashen, P.O. Box 25,
0048 Yerevan, Armenia

A. Vaseashta and S. Khudaverdyan (eds.), *Advanced Sensors for Safety and Security*,
NATO Science for Peace and Security Series B: Physics and Biophysics,
DOI 10.1007/978-94-007-7003-4_24,

24.1 Introduction

Harmful effects of ionizing radiation (IR) represent a major public health concern. IR targets all functional systems and organs, destroys blood and bone marrow cells, and damages genes [1–4]. These effects accelerate aging [5], trigger transformation of healthy cells to malignant tumor [6], and, thus, increase risk of cancer [6] and radiation sickness [7].

IR mostly works against our natural protective systems, DNA-repair [2, 8, 9], the antioxidants [10], and the immune system that helps to protect human body from free radicals, repair damaged DNA and destroy malignant cells precursors [10, 11].

Market-available radioprotectors mostly act as free-radical scavengers [12] and cannot overcome free-radical load induced by IR, so are of low efficiency. Therefore, currently there is an urgent need for new generation of radioprotectors, which together with free-radical neutralization capacities may also stabilize the natural protective systems and increase their functional activities.

Recently we synthesized a number of Schiff-base cyclic amino acid derivatives and their metallic complexes. Our preliminary investigations revealed four compounds possessing free radical neutralization capabilities. Those compounds include nicotinyl-L-tryptophan (NLtryp), nicotinyl-L-tyrosine (NLtyr) and copper complexes of NLtryp and picolinyl-L-tryptophan (Cu-NLtryp and Cu-PLtryp, respectively) (Fig. 24.1).

In the present study we investigated the effects of selected compounds on survival rate, immune and antioxidant systems of the organism in the conditions of IR using animal model of irradiation injury. As the indicators of the immune system state we considered major mediators of the immune response, the complement system [13]

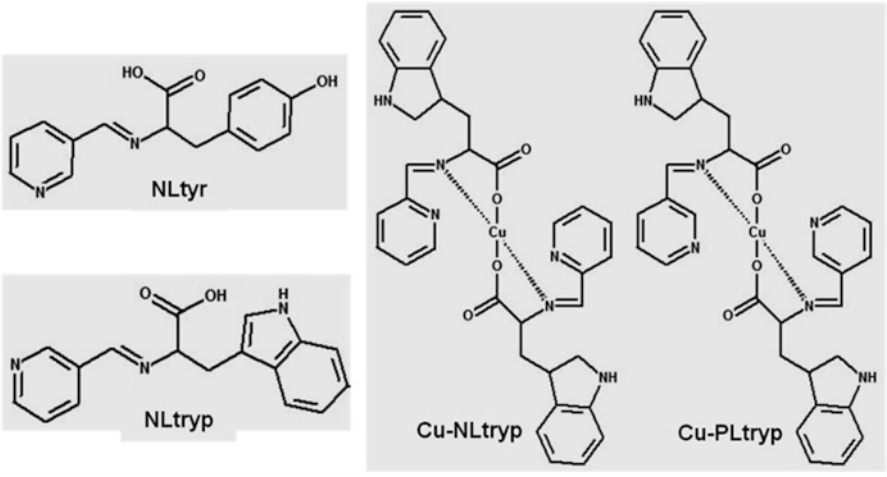

Fig. 24.1 Schiff-base cyclic amino acid derivatives for free radical neutralization

and the immune complexes (IC) [14]. As the indicators of the antioxidant system functional state, we considered the enzymes catalyzing free radical neutralization reactions, Cu, Zn-superoxide dismutase (SOD), and catalase [15].

24.2 Materials and Methods

The study was approved by the Ethics Committee of the Institute of Molecular Biology NAS RA (IRB #00004079) and implemented in accordance with the Helsinki convention related to animal studies. Experiments were performed using albino rates (males; body weight: 160–180 g). We use animal model of irradiation injury by subjecting the experimental rats to single whole body irradiation in a sub-lethal (3.5 and 5.0 Gy) and lethal (8.5 Gy) doses. Animals well divided into three groups: non-irradiated animals, irradiated animals subjected to no treatment, and irradiated animals treated with one of the selected cyclic amino acid derivatives by intra-peritoneal injection (10 mg/kg) 1 h. before irradiation. The compounds were dissolved in 0.01 M phosphate buffered saline, pH 7.4 (PBS) containing 1.4 % polyvinyl alcohol and 4 % propylene glycol. The animals from the first and second groups received only physiological salt solution with polyvinyl alcohol and propylene glycol. The number of animals in each group was 30. Irradiation of animals was performed by the use of "RUM-17" (Russia) X-ray apparatus (without filter; power capacity: 1.78 Gy/min, voltage: 200 KV, current intensity: 20 mA, focal distance: 50 cm).

Blood was collected after decapitation of animals on different time points after irradiation. Blood samples were kept at room temperature until coagulation, then serum was separated from the pellet containing erythrocytes by centrifugation at 3,000 g for 10 min; both the serum and erythrocytes were used in further experiments.

The activities of the classical and alternative pathways of the complement system (CP50 and AP50, respectively) in the blood serum were determined as described earlier [16]. When measuring AP50, rabbit erythrocytes were used as the target cells, while for CP50, sheep erythrocytes sensitized with rabbit anti-sheep bodies were used. Activities were expressed in U/ml of serum. One unit of activity was defined as the amount of serum causing 50 % hemolysis of the erythrocytes in the given incubation medium. Sheep erythrocytes, sensitized by specific rabbit antibodies (5×10^8 cells/ml), and rabbit erythrocytes (1×10^8 cells/ml) were prepared as described above [16]. The activity of the lectin pathway (LP) was measured by the enzyme-linked immunosorbent assay (ELISA) determining C3-dependent cleavage of mannan-binding lectin, and expressed in ng of C3b (the product of C3 proteolytic degradation, formed at activation of the lectin pathway) per 50 μL of serum (ng C3b/50 μL) [17].

Total concentration of IC in the blood serum was determined according to earlier described spectrophotometric assay and expressed in absorbency units at 280 nm (A280) [18]. Testing the presence of pathogenic IC in the serum was

performed as described earlier [19]. The levels of C1q- and C3d-IC were measured by ELISA using commercially available kit (HumanGMBH, Germany) according to manufacturer's instructions and expressed in μg/ml of serum.

SOD activity in hemolyzed erythrocytes was determined using earlier described spectrophotometric assay by estimating the extent of inhibition of auto-oxidation of adrenaline in the alkaline medium by SOD [20]. The activity was expressed in the international units of enzyme activity per 1 ml of hemolyzed suspension of erythrocytes (U/ml). Calculations of the enzymatic activity were based on calibration curve constructed with the use of commercial preparation of purified SOD (Sigma-Aldrich Co. LLC, USA) with known activity. The activity of catalase in hemolyzed erythrocytes was determined using earlier described spectrophotometric assay by estimating the decrease in the content of hydrogen peroxide due to its cleavage by catalase in incubation medium [21]. The activity was expressed in international units of the enzyme activity per 1 ml of hemolyzed erythrocytes suspension or buffer (U/ml). Calculations of the catalase activity were based on calibration curve constructed with the use of commercial preparations of purified catalase (Sigma-Aldrich Co. LLC, USA) with known activity. All measurements were performed on Stat Fax 3,200 microplate reader spectrophotometer (Awareness Technology Inc., USA) in 96-well microplates. Statistical analysis of the data obtained was performed by unpaired Student's one-tailed t-test using SPSS 13.0 (SPSS 13.0 Inc., USA) application package and nonparametric Mann-Whitney U-test (for the complement) using Graphpad Prism 3.0 software (Graphpad Software Inc., USA). P values ≤ 0.05 were considered as statistically significant.

24.3 Results and Discussion

First we assessed the influence of the selected compounds on a survival rate of animals in the conditions of IR. For three of them, namely NLtyr, NLtryp, and Cu-PLtryp, significant increase in the survival rate was detected. However, in case of Cu-NLtryp no effect was observed. The results obtained are presented in Table 24.1. Based on these results in further investigations we focused our attention only on NLtyr, NLtryp, and Cu-PLtryp.

Table 24.1 Survival rates of animals (treated and none-treated with NLtyr, NLtryp, and Cu-PLtryp before irradiation) subjected to different doses of IR

	Survival rate, %		
Group of animals	3.5 Gy	5.0 Gy (LD50[a])	8.5 Gy (LD100[b])
Treated with NLtyr	100 ± 5	90 ± 5	50 ± 5
Treated with NLtryp	100 ± 5	90 ± 5	50 ± 5
Treated with Cu-PLtryp	100 ± 5	90 ± 5	50 ± 5
Treated with Cu-NLtryp	80 ± 5	50 ± 5	0
Non-treated (control)	80 ± 5	50 ± 5	0

[a]Sub-lethal dose
[b]Lethal dose

Table 24.2 Activities (mean ± SD) of the classical, alternative and lectin pathways of the complement system in the blood serum of irradiated animals treated and non-treated with NLtyr, NLtryp, and Cu-PLtryp before irradiation

	Complement pathway activity		
Group of animals	CP50, U/ml	AP50, U/ml	LP, ng C3b/50 μl
Non-irradiated (control)	35.2 ± 4.9^{a}	17.5 ± 0.4^{f}	90.0 ± 19.5^{k}
Irradiated, non-treated	360.0 ± 28.0^{b}	18.0 ± 0.6^{g}	80.0 ± 10.7^{l}
Irradiated, treated with NLtyr	126.0 ± 9.8^{c}	17.3 ± 0.4^{h}	85.4 ± 16.1^{m}
Irradiated, treated with NLtryp	123.0 ± 9.5^{d}	20.0 ± 0.7^{i}	85.0 ± 15.8^{n}
Irradiated, treated with Cu-PLtryp	118.0 ± 9.2^{e}	19.4 ± 0.7^{j}	87.0 ± 16.2^{o}

IR dose – 3.0 Gy, $^{a,b}p < 0.00015$; $^{b,c}p < 0.002$; $^{b,d}p < 0.002$; $^{b,e}p < 0.002$; $^{f–o}p > 0.05$

Next we evaluated the influence of these finally selected compounds on the major mediators of the immune response, the complement system and the IC.

The complement system is a cytotoxic host defense system, a network of more than 30 soluble proteins, regulators and receptors that mediates a variety of interactions in the immune response. Function of the complement is to recognize and destroy foreign pathogens, altered or damaged host cells. The complement system is activated through three pathways, the classical, alternative, and lectin, differed in components and activation mechanisms. Each pathway is a cascade of proteolytic reactions. Up-regulation, uncontrolled hyperactivation of this system is very dangerous, since during the activation many inflammatory mediators and cell damaging agents originate that may cause auto-inflammation and destroy healthy host cells [22].

The results obtained by us upon measuring the activities of the classical, alternative and lectin pathways of the complement system in the blood serum of the experimental animals on day 1 after irradiation are presented in Table 24.2. According to the results obtained, in the conditions of IR a considerable hyper activation of the classical complement cascade was detected. Pre-treatment of animals with NLtyr, NLtryp, and Cu-PLtryp before irradiation significantly diminished this effect.

Regarding IC, their formation is a normal reaction of an organism to foreign or autoantigen. In healthy conditions IC are easily eliminated from the body by phagocytosis [14, 23]. However, in pathologic conditions concentration of IC in circulation increases and the efficiency of their elimination decrease. This leads to a severe tissue lesions caused by IC deposits and promotes inflammation [24–26]. The most aggressive here are called pathogenic IC, which are smaller in size than classic IC, and are hardly recognized by phagocytes and hardly eliminated from the body [19, 25]. Another two subpopulations of IC that reflect structural and functional abnormalities in the immune system are C1q- and C3d-IC containing activation products of the complement system [27, 28].

Our study demonstrated a sufficient increase in the total IC blood levels in rats subjected to IR in comparison to non-irradiated rats. Furthermore, pathogenic ICs were observed in 80 % of irradiated animals, and only in 13 % of non-irradiated.

Table 24.3 Total blood levels of IC (mean ± SD) in irradiated animals treated and non-treated with NLtyr, NLtryp, and Cu-PLtryp before irradiation and a number of animals with pathogenic IC among these groups

Group of animals	[Total IC], A280	Animals with pathogenic IC, % of total
Non-irradiated (control)	0.022 ± 0.004^{a}	13.3 ± 10
Irradiated, non-treated	0.230 ± 0.430^{b}	80 ± 10
Irradiated, treated with NLtyr	0.142 ± 0.028^{c}	63.3 ± 10
Irradiated, treated with NLtryp	0.110 ± 0.022^{d}	53.3 ± 10
Irradiated, treated with Cu-PLtryp	0.130 ± 0.025^{e}	58.5 ± 10

IR dose – 3.0 Gy, $^{a,b}p < 0.00007$; $^{b,c}p < 0.0005$; $^{b,d}p < 0.0004$; $^{b,e}p < 0.0005$

Treatment of animals with NLtyr, NLtryp or Cu-PLtryp before irradiation resulted in sharp decrease in both the total levels of IC and the number of animals with pathogenic population of the IC. The results obtained on day 7 after irradiation, are presented in Table 24.3. The same applies to C1-q and C3d-IC (data not shown).

Finally, we studied the effects of selected cyclic amino acid derivatives on the enzymes catalyzing free radical neutralization reactions, SOD and catalase, which work closely to each other to prevent free radical damage to the body. SOD converts the dangerous superoxide radical to hydrogen peroxide. Catalase converts hydrogen peroxide to harmless water and oxygen preventing the conversion of hydrogen peroxide to hydroxyl radicals, potentially dangerous molecules that can attack and mutate DNA [15].

The results obtained demonstrated that treatment of animals with selected cyclic amino acid derivatives decreased suppression of SOD and catalase activities detected in non-treated irradiated animals (data not shown).

To understand the mechanisms underlying the influence of selected cyclic amino acid derivatives on SOD and catalase, we performed experiments where pure preparations of these two enzymes were used. The results obtained indicated that *in vitro* all three selected compounds demonstrated the ability to increase significantly the activity of SOD, but have no effect on catalase activity (Fig. 24.2). However, when we inactivated catalase by thermal denaturation (56 °C × 20 min), the addition of selected amino acid derivatives resulted in recovery of its activity up to 88 % of its initial level.

24.4 Conclusions

Based upon the results obtained we concluded that NLtyr, NLtryp, and Cu-PLtryp increase survival rate and possess immune-modulating and antioxidant system capacity elevating effects in the conditions of IR. These compounds stabilize and reactivate defense biomolecules, regulate the immune response, and increase

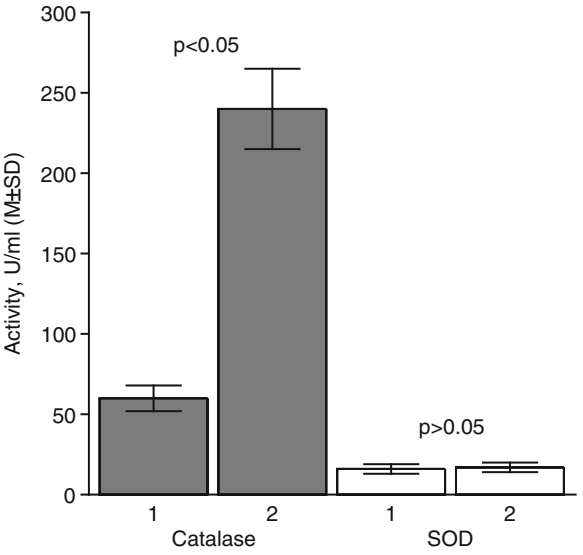

Fig. 24.2 The influence of Cu-PLtryp (20 μg/ml) on the activities (mean ± SD) of pure preparations of catalase (60 U/ml) and SOD (20 U/ml). All components were dissolved in PBS containing 0.1 % dimethyl sulfoxide. The enzymes were incubated with Cu-PLtryp for 10 min at 37 °C. Similar results were obtained in case of NLtyr and NLtryp (data not shown)

radio-sensitivity threshold, thus may be considered as a new generation of highly efficient multifunctional radioprotectors targeting native defense systems of the organism.

Acknowledgment We express our gratitude to the International Science and Technology Centre (ISTC) for the support to this study through the ISTC #A-1321 and #A-1764 grants.

References

1. Bezlepkin VG, Kirillova EN, Zakharova ML, Pavlova OS, Lomaeva MG, Fomenko LA, Antipova VN, Gaziev AI (2011) Delayed and transgenerational molecular and genetic effects of prolonged influence of ionizing radiation in nuclear plant workers. Radiats Biol Radioecol 51:20–32
2. Schanz S, Schuler N, Lorat Y, Fan L, Kaestner L, Wennemuth G, Rübe C, Rübe CE (2012) Accumulation of DNA damage in complex normal tissues after protracted low-dose radiation. DNA Repair (Amst) 11:823–832
3. Kondo T (2012) Radiation-induced cell death. Nihon Rinsho 70:389–393
4. Ryan JL (2012) Ionizing radiation: the good, the bad, and the ugly. J Invest Dermatol 132:985–993
5. Rose H (1976) Acceleration of the ageing process by ionizing radiation. Radiobiol Radiother (Berl) 17:579–588
6. Inaba T (2012) Radiation induced carcinogenesis. Nihon Rinsho 70:421–426
7. Reeves GI, Ainsworth EJ (1995) Description of the chronic radiation syndrome in humans irradiated in the former Soviet Union. Radiat Res 142:242–243
8. Gaziev AI (2011) Low efficiency of repair of critical DNA damage induced by low doses of radiation. Radiats Biol Radioecol 51:512–529

9. Noda A, Hirai Y, Hamasaki K, Mitani H, Nakamura N, Kodama Y (2012) Unrepairable DNA double-strand breaks that are generated by ionizing radiation determine the cell fate of normal human cells. J Cell Sci 125:5280–5287
10. Arakelova E, Ayvazyan V, Zhamgaryan L, Hovsepyan T, Boyajyan A, Malakyan M, Bajinyan S (2010) Influence of ionizing radiation on the immune and antioxidant systems of the organism. Georgia Chem J 10:59–62
11. Kusunoki Y, Hayashi T (2008) Long-lasting alterations of the immune system by ionizing radiation exposure: implications for disease development among atomic bomb survivors. Int J Radiat Biol 84:1–14
12. Greenberge JS (2009) Radioprotection. In Vivo 23:323–336
13. Trouw LA, Daha MR (2011) Role of complementin innate immunity and host defense. Immunol Lett 138:35–37
14. Padlan EA (1994) Antibody-antigen complexes. R.G. Landes Co., Austin
15. Michiels C, Raes M, Toussaint O, Remacle J (1994) Importance of Se-glutathione peroxidase, catalase, and Cu/Zn-SOD for cell survival against oxidative stress. Free Radic Biol Med 17:235–248
16. Doods AW, Sim RB (1997) Complement. A practical approach. Oxford University Press, Oxford
17. Petersen SV, Thiel S, Jensen J, Steffensen R, Jensenius JC (2001) An assay for the mannan-binding lectin pathway of complement activation. J Immunol Methods 257:107–116
18. Tarnacka B, Gromadzka G, Czlonkowska A (2002) Increased circulating immune complexes in acute stroke: the triggering role of *Chlamydia pneumoniae* and cytomegalovirus. Stroke 33:936–940
19. Struchkov PV, Konstantinova NA, Lavrentev VV, Chuchalin AG (1985) Screening test for evaluating the pathogenic properties of immune complexes. Lab Delo 7:410–412
20. Sirota TV (1999) Novel approach to the study of adrenaline auto-oxidation and its use for the measurements of superoxide-dismutase activity. Vopr Med Khim 3:263–272
21. Beers RF, Sizer IW (1952) Spectrophotometric method for measuring the breakdown of hydrogen peroxide by catalase. J Biol Chem 195:133–140
22. Volankis JE, Frank MM (1994) The human complement system in health and disease. Marcel Dekker Inc., New York
23. Hebert LA (1991) The clearance of immune complexes from the circulation of man and other primates. Am J Kidney Dis 17:352–361
24. Theofilopoulos AN, Dixon FJ (1980) Immune complexes in human diseases. Am J Pathol 100:529–594
25. Konstantinova NA (1996) Immune complexes and tissue damage. Medicine, Moscow
26. Shmagel KV, Chereshnev VA (2009) Molecular bases of immune complex pathology. Biochemistry (Mosc) 74:469–479
27. Muso E, Yashiro M, Ito Y, Yoshida H, Sasayama S (1994) Correlations of C1q- and C3d-bearing circulating immune complexes with immunopathological disease activity in lupus nephritis patients. Nippon Jinzo Gakkaishi 36:345–354
28. Moulds JM (2009) Introduction to antibodies and complement. Transfus Apher Sci 40:185–188

Chapter 25
New Polymeric Materials for Medicine and Rehabilitation of Buildings and Different Surfaces Exposed to Radioactive Contamination

V. Sargsyan, L. Hayriyan, G. Harutyunyan, N. Tavakalyan, and P. Voskanyan

Abstract The objective of this investigation is to study kinetics of anesthetic lidocaine release from polymeric gel and film in water and saline. We also investigated the mechanism of binding of non-radioactive compounds of cobalt and cesium from various solid surfaces with water soluble polymeric systems. The participation of the functional units of copolymer in the binding of cobalt and cesium is studied. The efficiency of aqueous polymeric compositions for the treatment of various solid surfaces from radioactive contamination was established.

Keywords Water-soluble copolymers • PVA • Radioactive contamination

25.1 Introduction

The problem of thermal and radiation burns is important in modern medical science. It is relevant in war and in peace, especially during emergencies at nuclear power plants. At present, the development of synthetic polymeric coverings has received a lot of attention. Among others, cotton-gauze products are commonly used, however their sorption capacity remain unsatisfactory. Studies conducted at our Institute are devoted to the development of polymeric coatings, containing a variety of drugs. Polymer film coverings adhere well on the surface of the wound and serve as barrier to infection of the wound surface. The burn trauma is always accompanied by a painful syndrome. It is convenient to introduce drugs in dressing, which mainly act at the sensitive nerve-endings but not through the central nervous system. In first part of this work, we present investigation of polymeric gels and films, containing anesthetic lidocaine. It is further advantageous to introduce

V. Sargsyan (✉) • L. Hayriyan • G. Harutyunyan • N. Tavakalyan • P. Voskanyan
Yerevan Institute "Plastpolymer", 127 Arshakunyats avenue, Yerevan 0007, Armenia
e-mail: vitushs@yahoo.com

A. Vaseashta and S. Khudaverdyan (eds.), *Advanced Sensors for Safety and Security*,
NATO Science for Peace and Security Series B: Physics and Biophysics,
DOI 10.1007/978-94-007-7003-4_25,

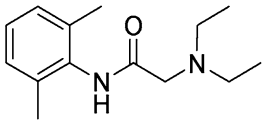

Fig. 25.1 Chemical structure of lidocaine

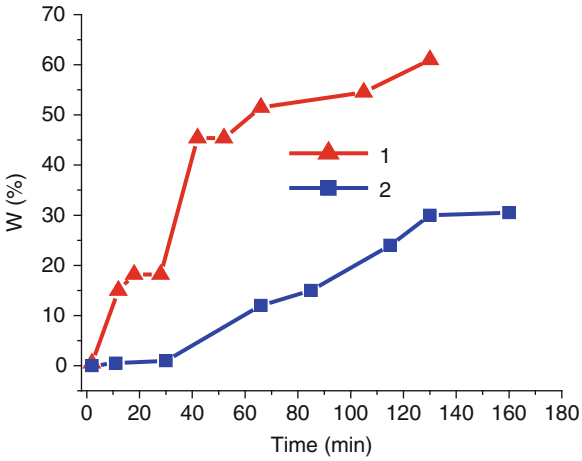

Fig. 25.2 Lidocaine release from polymeric gel to water (*1*) and saline (*2*)

anesthetics into dressing for prolonged action. We prepared polymeric films and gels on the basis of polyvinyl alcohol copolymers, containing carboxylic and amide groups with attached anesthetic 2-(Diethylamino)-N-(2,6-dimethylphenyl)-acetamide hydrochloride or lidocaine hydrochloride (Fig. 25.1).

It was expected that intermolecular interactions of anesthetic and polymer in conjunction with amide, amine and carboxylic groups will provide prolonged action of drug due to moderate release of lidocaine from the polymeric matrix. A degree of lidocaine release in distilled water and saline was studied by increasing of anesthetic absorption band at the wavelength of 275 nm in UV spectrum, where water and saline do not absorb.

We further studied the kinetics of lidocaine release to water and saline from polymeric gel and film with the same functional composition at room temperature and the temperature of the human body ≈37 °C. The content of anesthetic in the polymer varied. Figure 25.2 shows plots of anesthetic release in time from polymeric gel, containing 0.1 % lidocaine in distilled water (1) and saline (2) at 25 °C. The graph shows that the rate of lidocaine release in water is significantly higher than in saline. During the extraction of lidocaine for 66 min to water passes 51.5 % of anesthetic and to saline over the same time period, only 12 % of anesthetic. After 130 min extraction the release of lidocaine in water was 61 % while release in saline was only 30 %. In both cases prolonged release of anesthetic from polymeric gel occurs.

The release rate of lidocaine at the temperature of human body was higher. As for example, at 37 °C gel containing 0.27 % lidocaine, after 1 h release of anesthetic to water was 75 % and to saline 54 %. Generally at the same temperature, the higher the anesthetic content in polymer the higher is its release rate to water and saline.

Table 25.1 Strip-ability of MPVAL films from different surfaces

No.	Sample	Strip-ability (grade)/surface			
		Steel	Polystyrene	Ceramics	Concrete
1	2-09/3-1	5	5	4	2
2	2-09/2	5	5	4	2
3	1/09-5	5	5	4	2
4	1/09-2	5	5	4	2
5	3/09-2	5	5	4	2

Slow release of lidocaine from a polymeric film and gel at the initial stage is caused by gradual swelling of a polymer in water and strong intermolecular interactions between the functional groups of polymer and anesthetic. For the polymeric films containing 2 % of lidocaine, a minimum of 2 h is needed to release 50 % of anesthetic to water. Thus prolonged release of anesthetic from polymeric films and gels containing 0.1–20 % lidocaine hydrochloride was experimentally shown in all experiments. The release rate of anesthetic lidocaine from polymer gel and film depends on its content in the polymer, functional composition of polymer, the nature of the extracting system and temperature.

Another line of researches devoted to the development of deactivating polymeric compositions for the cleaning of concrete, steel and plastics surfaces from the radioactive contamination of ^{60}Co, ^{90}Sr and ^{137}Cs. Currently, spectrum of polymeric compositions on the basis of polyvinyl alcohol solutions and water dispersions Alara 1146, Pentec 604, TLC Stripcoat Bartlett is recommended for deactivation works.

Detailed comparative examination of known polymeric systems as strippable coverings is presented in some reports and patents [1, 2]. Development of polymeric systems for decontamination of different surfaces from radioactive pollutions was performed at the Yerevan Institute "Plastpolymer" under Grants A-1243 and A-1243.2. For this purpose three types of polymeric systems were synthesized and studied. These are modified polyvinyl alcohol (MPVAL), partially neutralized copolymers of vinyl acetate and acrylic acid (VA-AC) and copolymers of acrylamide and acrylic acid (AA-AC). The idea consists in adding of liquid polymeric composition to the solid contaminated surface and after film forming removing it with the captured radionuclides. Tests of deactivating ability of developed products have been conducted at the Armenian NPP (ANPP) and "Scientific Center of Radiation Medicine and Burns" SCRMB. Decontamination Factor (DF) and percent of radionuclides trapping (β_F) was estimated in the following two ways:

- On plates (steel, glass, colored steel and wood) artificially contaminated with isotopes of Co-60, Cs-137, and Sr-90. The activity deposited on the surface was within 800–3,000 Bq/cm^2.
- In real conditions of radioactive contamination: in the premises of the ANPP controlled access area (CAA) (the major radionuclides Co-60, Cs-137, Ag-110, Mn-54).

The main properties to be studied were films formation, strip-ability from different surfaces, deactivating ability (Table 25.1). As samples of comparison one

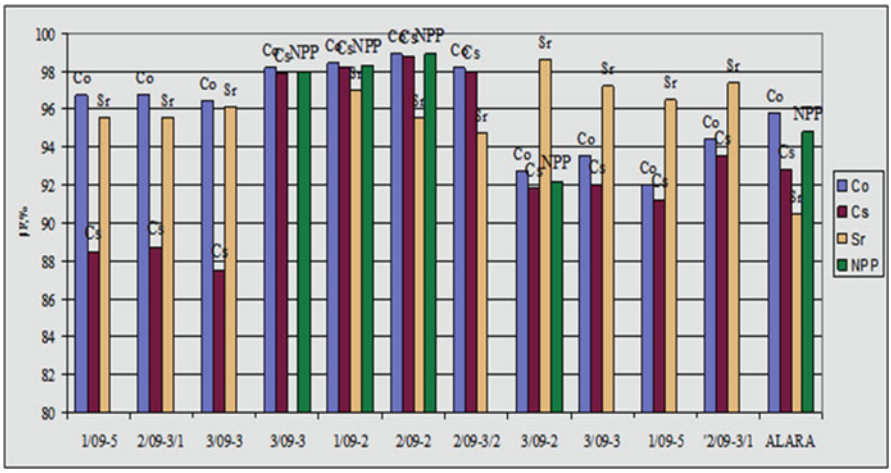

Fig. 25.3 β_F of MPVAL samples, depending on environment conditions (samples 1–3 (30 °C, humidity 32 %, drying time 4–5 h); 4–8 (24 °C, humidity 38 %, drying time 6–9 h); 9–12 (20 °C, humidity 38 %, drying time 6–9 h))

of the best world analogues-water dispersion ALARA-1146 were used. MPVAL-s is water-soluble powders, containing chelate-forming groups. Viscosity of 10 % solutions – 100–500 cP Brookfield, surface tensions – 45–65 mN/m (strongly depend on concentration).

In Fig. 25.3 data of β_F are plotted to compare deactivating abilities of some investigated samples of MPVAL, depending both on copolymers characteristics and environment conditions (temperature, humidity) [3]. As follows from data above, percentage of contamination removed, β_F depend on functional content, molecular characteristics and on experiments conditions (temperature and humidity of environment). These systems provide selectivity towards different radionuclides (Co-60, Cs-137 and Sr-90). These polymeric systems have shown high efficiency as films, in cleaning of all mentioned radioactive isotopes from the steel surface (proportion of removed pollutions β_F was 87–99 %).

25.2 The Mechanism of Binding of Radio Nuclides with Polymers

The influence of functional compositions and properties of polymeric films in terms of ability to deactivate polymeric systems was studied. Three types of polymeric systems were used: modified polyvinyl alcohol with different content of carboxylate groups (MPVAL[1] and MPVAL[2]), partially neutralized copolymers of VA-AC and copolymers of AA-AC. Major air and facilities pollutants at the Armenian NPP are

radionuclides ^{137}Cs, ^{134}Cs and ^{60}Co. The mechanism of binding of radionuclides with polymers from the different solid surfaces was studied in the lab experiments with using non-radioactive isotopes of Co and Cs.

25.3 The Methodology and Experimental Part

The methodology of research of the binding mechanism of metals includes adding the known amount of a metal compound solution (cobalt or cesium) to a variety of solid surfaces and then, after drying of solid surface, adding a certain amount of the polymer composition for binding. After formation of polymer film with the captured metal (usually 24 h) we determine by analysis the degree of metal binding with polymer. To establish the functional groups of polymer responsible for the binding of cobalt, IR spectra of metal containing polymeric films are studied. The polymeric composition containing 10–12 % by mass of polymers is applied using an amount of 0.2 ml/cm^2 surface, which gives a film thickness of 150–250 μm.

In experiments with cesium to low porous concrete surface with an area of 15–18 cm^2, 0.02 mg of cesium is added and after drying 2 ml of the polymer composition. A day after polymer films were removed from the surface dissolved in a mixture of HNO_3 and HF acids in a ratio of 1:3 by weight and analyzed for Cs content. Determination of cesium was performed by atomic absorption spectrometry (AAS) after appropriate treatment of polymeric films containing cesium. In this case, the test sample solution containing cesium is introduced into the flame. As an analytical spectral line for cesium the wavelength of 852.11 nm was used. Cesium concentration is calculated from the intensity of the spectral wave from the calibration curve. The analysis is performed on the device AAS −30 by atomic – emission method in an air-propane flame.

Cobalt was determined by complexometric titrations after dissolving of polymeric film in water with using a standard solution of trilon B with a concentration of 0.05 M in the presence of 0.1 % solution of xylenol orange as indicator in buffer solution at pH 5.5–6.0. At the equivalence point the color of violet solution change to yellow-orange. Hence, it is possible to determine 0.2–0.3 mg of Co^{2+} ions in the presence of 1.0–1.5 g of polymer in 100 ml of the analyzing solution. So the method used is very sensitive.

25.4 Analysis and Conclusion

For concrete surfaces, cobalt and cesium penetrate deeper into the pores of concrete and therefore removal of metal ions by polymeric compositions was less effective than in the experiments with the steel surface. The results (Table 25.2) indicate that the amount of cesium removed from low porous concrete surface by copolymer

Table 25.2 Binding of cobalt and cesium from solid surfaces by polymeric compositions

No.	Polymer composition	Degree of neutralization of AC (%)	pH of comp.	Viscosity VS-1 (5, 4), s	Surface	Mass of bonded Co (%)	Mass of bonded Cs (%)
1	VA-AC 30:70	20	5.9	270	Tile, plastic	100	–
2	VA-AC 30:70	80	6.9	55	Tile, plastic	100	–
1	VA-AC 30:70	20	5.9	270	Duralumin	99	–
1	VA-AC 30:70	20	5.9	270	Steel	90	4
2	VA-AC 30:70	80	6.9	55	Concrete	67	6.5
2	VA-AC 30:70	80	6.9	55	Steel	89	–
3	MPVAL1		6	–	Steel	90	–
4	MPVAL2		6	–	Steel	92	–
5	AA-AC	30	4.5	–	Concrete	–	4
6	AA-AC	80	6.8	500	Concrete	–	10

No. 2 was 6.5 % and by copolymer No. 6 was 10 %. These copolymers both contain 80 % neutralized acid units in contrast to copolymers No. 1 and 5 with low content of carboxylate groups. With increasing degree of neutralization of the acid groups in the copolymers VA-AC and AA-AC viscosity of solution is reduced, which contributes to a better penetration of the polymer into the concrete pores and trapping cesium.

Thus with the increasing of carboxylate groups content in the copolymers of VA-AC and AA-AC level of removed cesium from the concrete surface is increased. However as a result of the improving of adhesion of polymer macromolecules to concrete surface and greater penetration into the concrete pores strip-ability of polymeric film becomes difficult. The results of our modeling studies indicate that, apparently, the binding of cesium ions occurs by ion exchange, i.e. the exchange of cations in carboxylate groups of the copolymer to cesium ions from the pores of the concrete. Partially neutralized AA-AC and VA-AC copolymers are polyelectrolytes and thus increasing the content of easily ionizable carboxylate groups in these polymers provides high concentration of metal cations in the polymer solution and, therefore, increases removal of cesium from concrete pores by ions exchange. It is also possible that the mechanism of cesium binding by investigated copolymers is close to the action of cation-exchange resins. Therefore, the presence in the copolymers carboxylate groups with metal ions, where the size is close to cesium ions size, can indeed increase the efficiency of cesium removal.

Removal of cobalt ions from the surface of duralumin by copolymer solutions VA-AC is 99 %. In case of steel surface the degree of extraction of cobalt by polymer compositions is reduced due to the partial reduction of Co^{2+} ions in iron surface, which is observed visually on the plate surface. Galvanic cell is formed and the following reaction occurs $Fe + Co^{2+} = Fe^{2+} + Co$. Given the standard electrode potentials $E°\ (Fe^{2+}/Fe°) = -0.44V$ and $E°\ (Co^{2+}/Co°) = -0.277$ V, indicating that the iron electrode is negative and cobalt is positive. In this case is expedient to determine cobalt remaining on the metal surface, rather than jumping into the

polymer film. According to this analysis the removal of Co^{2+} ions is 90 % for a solution of the copolymer VA-AA. If the steel plate is painted, the degree of removal of cobalt up to 100 %, as the steel surface does not corrode.

It is known that the fixation of radio nuclides on the surface and in the bulk of the polymer coating can occur by different mechanisms, including adhesion, chemisorption, and ion exchange [4, 5]. According to the literature data the carboxyl groups of polyacrylic acid reacts with Co^{2+} ions to form monodentate complexes, which absorb in the 500–700 cm^{-1}, with a major band at 615 cm^{-1} [6, 7]. In order to study the nature of the binding of cobalt by copolymer VA-AA, we prepared films with a thickness of 0.03 mm of pure copolymer and cobalt containing copolymer. IR spectra data of cobalt-containing copolymers VA-AC suggest the formation of complexes between the carboxylic groups of the copolymer and Co^{2+} ions. According to IR spectroscopy data the intensity ratio of the absorption bands D_{3350}/D_{615} (OH/complex), D_{1714}/D_{615} (C = O/complex) and D_{1565}/D_{615} (COO^-/complex) 2–3.5 times less than in the IR spectrum of the copolymer, which does not contain cobalt. The greatest decrease is observed for the ratio of bands D_{3350}/D_{615}, which means that in the complex with cobalt are most involved hydroxyl groups of copolymer acid units.

In conclusion, prolonged release of anesthetic from polyvinyl alcohol copolymers films and gels, containing 0.1–20 % lidocaine hydrochloride, to water and saline was experimentally shown. Polymeric compositions based on modified polyvinyl alcohol MPVAL and partially neutralized copolymers of VA-AC provide effective decontamination of non-radioactive cobalt from the surface of the steel, duralumin, tiles, plastic and low porous concrete. They were effective also in cleaning of radioactive isotopes Co-60, Cs-137 and Sr-90 from the different solid surfaces in experiments performed at Armenian NPP. When using the VA-AC copolymers, complex formation occurs between the carboxylic groups and cobalt ions according to IR spectroscopy data. It was shown that binding of Co occurs by carboxylic groups of polymers while in binding of Cs crucial role have carboxylate groups of partially neutralized vinyl copolymers.

References

1. US Department of Energy, Office of Science and Technology (2000) ALARA™ 1146 Strippable Coating, Innovative Technology Summary Report
2. James RR, Willenberg ZJ, Fox RV, Drake J (2008) Isotron Corp.Orion™ Radiological Decontamination Strippable Coating, Technology Evaluation Report EPA/600/R-08/100
3. Harutyunyan G, Farmazyan Z et al. (2012) Advanced polymeric deactivating coatings: modified polyvinylalcohol. In: Proceedings of the radiation safety challenges in the 21st century, Yerevan, 40–42 June 2012
4. Slugin VA et al. (2009) Some aspects of physical and chemical processes of radioactive contamination and decontamination of polymeric coatings. Report FTUP THREAD after A.P. Alexandrov. Sosnovy Bor
5. Gorodinskiy SM, Goldstein DS (1981) Deactivation of polymeric materials. Energoizdat 28:28–30

6. Zhdankovich EL, Annenkov VZ, Abzaeva KA, Strashnikova NV, Brodskaya EI, Voronkov MG (1995) Structure and properties of water-swell able cobalt salts of polyacrylic acid. Rep Acad Sci 340(2):204–205
7. Zhdankovich EL, Azarova IN, Erofeev LG, Abzaeva KA, Sherstyannikova LV, Annenkov VZ, Voronkov MG (1997) Synthesis and properties of cobalt containing water absorbing salts of polyacrylic acid. J Appl Chem 70(3):505–507

Chapter 26
Application of New Heavy Scintillation Crystals for Remote Detection of Fissile Materials

G.Yu. Drobychev, A.E. Karneyeu, and V.A. Mechinsky

Abstract An approach for development of high effective systems for remote detection of fissile materials and devices based on them is proposed. A use of the new generation of heavy scintillators to measure gammas in energy region above 3 MeV have several advantages.

Keywords PWO • Scintillation detector • Fissile materials detection

26.1 Introduction

Threat of terrorism is permanently increasing worldwide during recent decades. According to IAEA Illicit Trafficking Data Base (ITDB), 2,164 incidents involving unauthorized possession and related criminal activities of radioactive and nuclear materials were registered from 1993 to 2011 [1]. Most radioactive or nuclear materials can be dangerous, but it must be noted that fissile (nuclear) materials, such as enriched uranium and plutonium can provoke especially significant damage to health of people and economic losses [2]. High volatility and tendency to form aerosols [3] of plutonium make it easy to distribute over large areas and allow lungs penetration through inhalation. Uranium and plutonium emit alpha particles that determine their high radiological toxicity [4, 5]. IAEA experts warn that it is very difficult to prevent illicit trafficking of radioactive or nuclear materials in case when such action is prepared by professional group [1]. We have to admit that there is

G.Y. Drobychev (✉) • A.E. Karneyeu • V.A. Mechinsky
Institute for Nuclear Problems (INP), Belarusian State University,
11 Bobrujskaya Str., Minsk 220030, Belarus
e-mail: gleb@inp.bsu.by

A. Vaseashta and S. Khudaverdyan (eds.), *Advanced Sensors for Safety and Security*,
NATO Science for Peace and Security Series B: Physics and Biophysics,
DOI 10.1007/978-94-007-7003-4_26,

permanent non-zero probability of attempt of terrorist action involving radioactive or fissile materials. The probability of an event of this may seem small; however its consequences can be very significant. Hence, an improvement of technique for fissile materials detection is of significant importance.

26.2 Short Review of Methods for Fissile Materials Detection

Detection methods may be classified as active and passive. The idea of active methods corresponds to irradiation of inspecting cargo or transport facility with powerful beam of neutrons or gamma or X-rays. This irradiation provokes a secondary neutron or gamma emission from fissile material, even if hidden inside. Active methods allow detection of even small quantities of materials regardless of their shielding. However, active methods have two drawbacks: (1) necessary equipment is heavy and bulky, hence it can be installed as stationary unit only; (2) active methods cannot be applied for examination of people or animals. Passive methods use detectors that register radiation naturally emitting by seeking materials. Passive methods are safe for personnel and other people and necessary equipment is generally more compact and lightweight up to portable models. However, an efficiency of passive methods is much lower as compare to the active ones, especially when illicit materials are shielded or masked. Most of radiation of concern from nuclear materials is alpha, which cannot be detected.

Nuclear materials are detected by emission of gamma or neutrons. Unfortunately, gamma or neutron radiation from uranium or plutonium has rather low intensity, which can be further reduced by shielding of nuclear materials. Therefore, a simple gamma counting technique is inefficient; rather neutron detection or gamma spectroscopy technique seems preferable. A neutron detection method has widely been used for detection of ^{239}Pu. The method of fissile materials remote detection with an intrinsic *n*-radiation was applied in practice, within the framework of the Nunn-Lugar program for realization of expert control of exportation and proliferation of nuclear weapons, as carried out by experts from the U.S.A., Russia and Belarus in the early 1990s [6].

Neutrons passing through air undergo multiple scattering; hence neutron flux loses intrusiveness after few tens of centimetres. The γ-channel detection, which permits acquiring information about secret characteristics of a nuclear device, was earlier prohibited. However, in the framework of anti-terrorist activities, an intrusiveness of the detection through γ-channel became an additional positive factor allowing discerning a radiation from devices based on fissile materials and radiation of separately carried fissile materials or radioactive substances or materials used in medicine or industry. A detailed review of gamma spectroscopy detection methods is given in [7], while various problems of detection and identification are discussed in [8–13].

Spectroscopic method of detection and identification of isotopes includes the following steps:

- Registration of spectra of gamma emission from object under examination;
- Detection of peaks in spectra;
- Calculation of peak centers and their FWHM;
- Comparison of FWHM of registered peaks with expected values;
- Comparison of registered peak centers with data from library;
- Seek of correspondence of registered gamma-ray line to appropriate isotope or composition of isotopes.

For example, detection of ^{235}U and ^{239}Pu is often carried out through a registration of 185 and 0.769 keV gammas respectively. Unfortunately, use of spectroscopic methods also meets with several difficulties. One of the problems is a complex composition of fissile material due to both: (1) incomplete purification, and (2) contamination of initial material with fission products. Every component has its own radiation spectrum, so the resulting spectrum has a complex structure. From other side, some isotopes of additives presenting in nuclear material emit intensive gamma or neutron radiation, which can be used for their detection by spectroscopic technique. For example, some quantity of ^{238}U always exists in ^{235}U, and ^{238}U can be detected through 1.001 MeV emissions by protactinium-234m – a product of ^{238}U decay. And a spontaneous decay of ^{240}Pu, which always presents in the ^{239}Pu, gives an emission of 910 neutrons per gram in second, which is five orders of magnitude higher, that the emission from ^{239}Pu itself.

Masking of nuclear material also can seriously decrease a probability of detection. A principle of masking is a use of some of wide used isotopes whose spectra have peaks close to characteristic peaks of fissile materials. A lot of isotopes appropriate for masking are in wide use in nuclear medicine (^{125}I, ^{131}I, ^{99m}Tc, ^{198}Au) and industry (^{60}Co, ^{113}Ba, ^{137}Cs, ^{152}Eu ^{226}Ra) [8]. The characteristic gamma peaks of nuclear materials registered in 0.1–3 MeV region, are suppressed by natural radioactivity background. Figure 26.1 presents a typical spectra registered during the first joint Soviet Union – USA experiment on detection of nuclear weapons, which was carried out aboard of "Slava" battle-cruiser at the Black Sea in 1989 [6, 12].

Estimations of data acquisition time are necessary for detection of various compositions on a basis of nuclear materials made in [11]. Some measurements can take tens of hours, which are unacceptable and can be economically not viable. Taking into account problems listed above, we can state a necessity to develop equipment with increased detection efficiency and signal-to-noise ratio.

26.3 Application of Heavy Scintillators for Nuclear Materials Detection

We propose to apply heavy scintillators for detection of nuclear materials through a characteristic gamma emission in a region above 3 MeV. Two processes in ^{235}U and ^{239}Pu cause gamma emission. The first one is a spontaneous decay that provokes

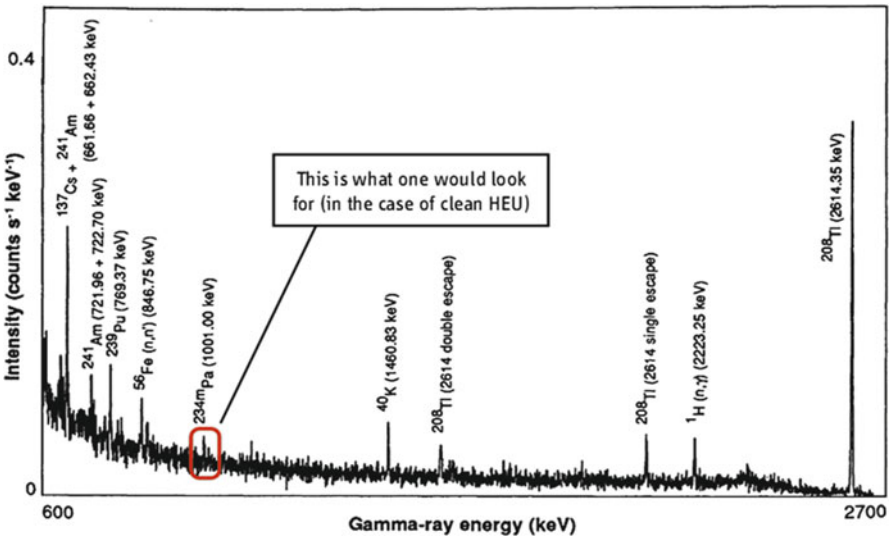

Fig. 26.1 Typical spectra registered during the first joint Soviet Union – USA experiment on detection of nuclear weapons, which was carried out aboard of "Slava" battle-cruiser at the Black Sea in 1989 (Fig. is quoted from [12])

emission of gammas with energies in a region 0.3–7 MeV. The second one is a secondary emission of gammas appearing due to a radiation capture of thermal neutrons by atoms of ^{14}N in surrounding air. The second process causes an emission in a region of 4.5–12 MeV [8]. The attractiveness of detection of gamma – radiation is in a range from 3 to 12 MeV, stipulated by a lack of natural radioactive sources, masking medical and industrial sources in this energy range. Also, a penetrating ability of high-energy gamma quanta is higher, which reduces an efficiency of possible shielding.

Till recently, use of high energy gamma-channel was rather problematic due to absence of scintillation material which possesses a complex yet necessary parameters. In case of conventional scintillator use, a volume of detector has to be significantly large for registration of 3–12 MeV gammas. An increase of detector volume causes an increase of registered background, so the overall performance of detector could even decrease.

However, a new heavy scintillator was developed recently by a collaboration of scientists from European Laboratory for Particle Physics (CERN – Geneva, Switzerland), Laboratory of Particle Physics (Annecy-le-Vieux, France), Institute for Nuclear Problems (Minsk, Belarus) and Bogoroditsk Techno-Chemical Plant (Bogoroditsk, Russia) [14]. Lead tungstate $PbWO_4$ (PWO) scintillator was developed for applications in high-energy physics experiments, however its characteristics allow extension of its field of application. Preliminary estimations of PWO applicability for nuclear materials detection were presented in [15, 16].

26.4 Development of Models for Simulation of Detectors and Sources

We propose a preliminary concept of detector, which includes the following parts:

- Main detecting unit on a basis of one or several PWO single crystals;
- Background monitor using bismuth germinate ($Bi_4Ge_3O_{12}$, BGO) scintillator;
- Active shielding on a basis of large plastic of NaI(Tl) scintillators;
- Tungsten collimator;
- Passive lead shielding.

We plan to perform a series of simulations in order to define a more exact design of detector, in particular, to check a necessity of collimator and lead shielding. First, sufficient detector directivity can be provided at the account of main scintillator segmentation without collimator use. Second, a future detector will operate in a higher energy region where background is low and determined mainly by a secondary cosmic radiation. To our preliminary estimations, a use of background monitor and active shielding will be sufficient to suppress a secondary cosmic radiation and residual background without lead shielding use.

26.5 Simulations and Results

GEANT4 package was applied in simulations [17]. At the current stage we simulated simplified models of sources maid on a basis of nuclear materials: Cubic shape samples of high enriched uranium (HEU) and weapon plutonium (WP). A size of each sample is $4 \times 4 \times 4$ cm. Densities of HEU and WP are 19.1 and 19.86 g/cm^3, so simulated samples have mass 1222.4 and 1268.2 g, respectively. Considered isotopes and activities are summarized in Table 26.1.

Table 26.1 Calculation of list of nuclear materials and devices for simulations

Nuclear material	Isotope	Contribution to total mass (%)	Mass of isotope (g)	Specific activity (Bq/g)	Activity (Bq)	Specific spontaneous decay rate (n/(s*g))	Spontaneous decay rate (n/(s*g))
HEU	^{234}U	1.1	13.4	2.30E+08	3.09E+09	7.80E−03	1.05E−01
	^{235}U	93.3	1140.5	8.00E+04	9.12E+07	1.11E−05	1.27E−02
	^{236}U	5.6	68.5	2.39E+06	1.64E+08	4.37E−03	2.99E−01
WP	^{238}Pu	0.005	0.063	6.34E+11	4.02E+10	2.61E+03	1.66E+02
	^{239}Pu	93.3	1183.3	2.30E+09	2.72E+12	2.22E−02	2.63E+01
	^{240}Pu	6.0	76.1	8.40E+09	6.39E+11	1.09E+03	8.29E+04
	^{241}Pu	0.44	5.6	3.62E+12	2.02E+13	4.80E−02	2.68E−01
	^{242}Pu	0.255	3.2	1.46E+08	4.72E+08	1.72E+03	5.56E+03

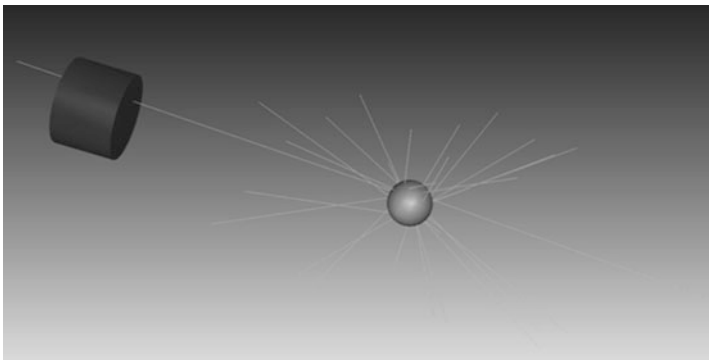

Fig. 26.2 Geometry of simulated setup: *grey sphere* – source, *dark grey cylinder* – detector, *light grey lines* – gamma quanta

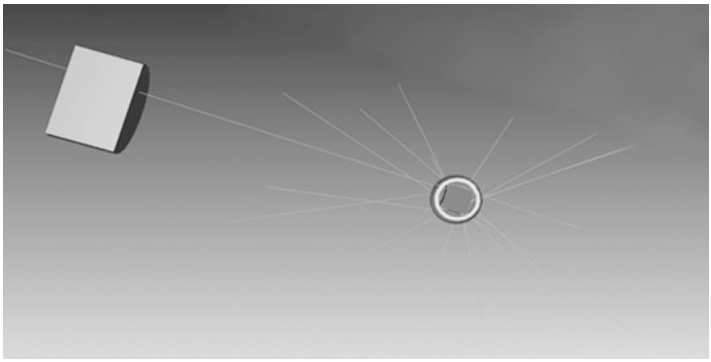

Fig. 26.3 A cross section of simulated setup: *dark grey cube* – nuclear material, *light grey sphere* – lead shielding, *light grey cylinder* – scintillation material, *light grey lines* – gamma quanta

A sphere made of lead of 50 mm thickness surrounds nuclear material for shielding. Two different types of detecting materials were simulated: $PbWO_4$ and NaI(Tl), which is one of the most wide used scintillator up to date. Simulated scintillators had cylindrical shape of 15 cm diameter and 10 cm length. A 0.5 m distance between source and scintillator was currently chosen. Geometry of simulated setup is shown in Figs. 26.2 and 26.3.

Two processes: gamma emission from radioactive decay and spontaneous fission were simulated separately in order to simplify a process of calculation. Numbers of events were selected to correspond to 10 min of acquisition. Noise from natural sources was not implemented into simulation model up to date. Gamma spectra produced by radioactive decay (U and Pu source) and spontaneous fission (Pu source only) registered by both NaI(Tl) and $PbWO_4$ scintillators are presented in Figs. 26.4 and 26.5.

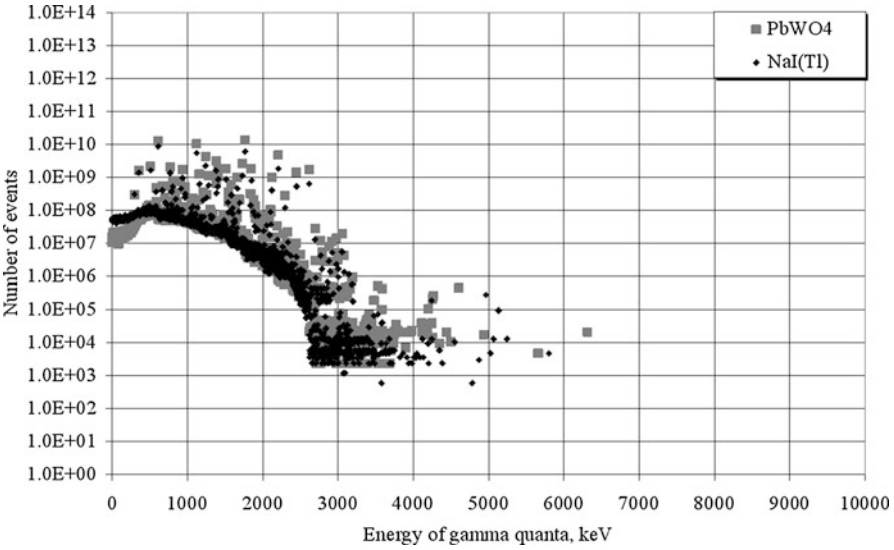

Fig. 26.4 NaI(Tl) vs $PbWO_4$ comparison of deposited energy. HEU source

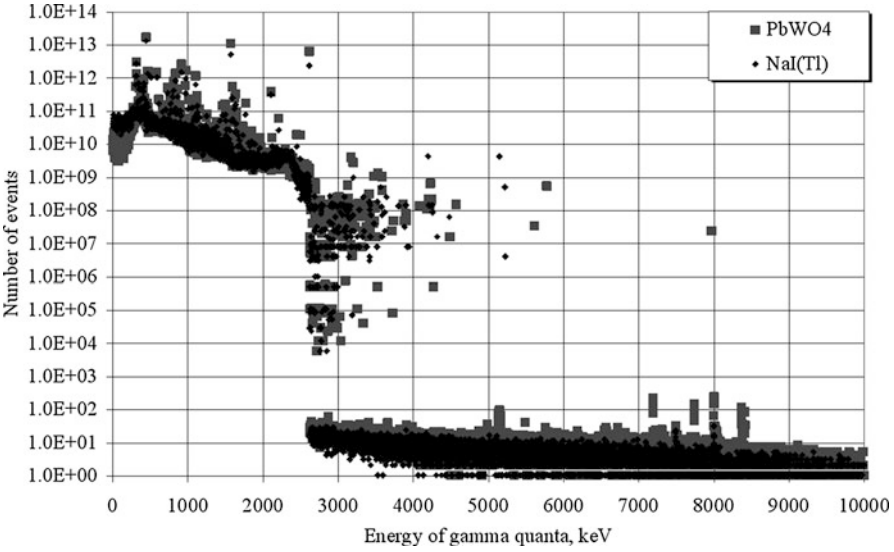

Fig. 26.5 NaI(Tl) vs $PbWO_4$ comparison of deposited energy. WP source

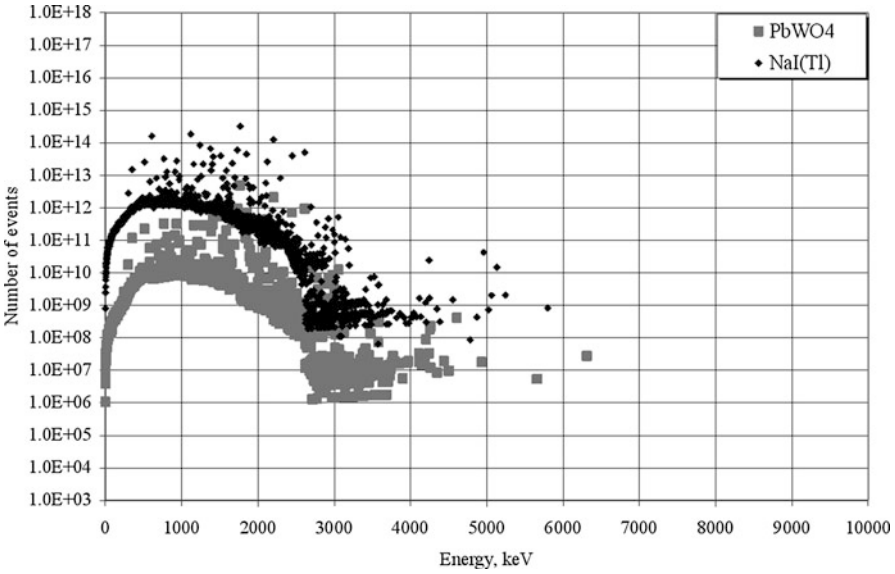

Fig. 26.6 NaI(Tl) vs $PbWO_4$ comparison of deposited energy. HEU sources. Calibration on a scintillator light yield is applied

As one can see, $PbWO_4$ gives significantly more intensive peaks compare to NaI(Tl). What is especially important is that, $PbWO_4$ detector discovers clear peaks in a region above 5.5 MeV, which are practically invisible by NaI detector. They are 6.3 MeV peak in HEU spectrum and multiple peaks are in 7–8.5 MeV region in WP spectrum.

Unfortunately, a low light yield is a serious limitation of $PbWO_4$ scintillator. This factor is not important in high energy (tens of GeV region) physics application, but can be decisive in low energies. To verify applicability of $PbWO_4$ for our application we calibrated calculated spectra by light yield of scintillators. We consider a light yield of $PbWO_4$ to be 200 photons per MeV (standard second generation PWO scintillator for high energy physics experiment) and light yield of NaI(Tl) as 30,000 photons per MeV. The results of calibration are presented in Figs. 26.6 and 26.7.

As one can see, a NaI(Tl) signal from HEU source is about one order of magnitude higher a $PbWO_4$ signal. However, we have to take into account that a noise from natural radioactivity will affect results of real measurements and we can expect that a signal to noise ratio will be better in a region above 3 MeV in case of $PbWO_4$ scintillator use. Also, $PbWO_4$ scintillator gives a clear indication of HEU presence through a 6.3 MeV peak. We can conclude that neither NaI(Tl) nor $PbWO_4$ have an absolute advantage in HEU detection.

In case of WP source an advantage of $PbWO_4$ scintillator is more obvious. $PbWO_4$ provides well resolved peaks in a region above 5 MeV.

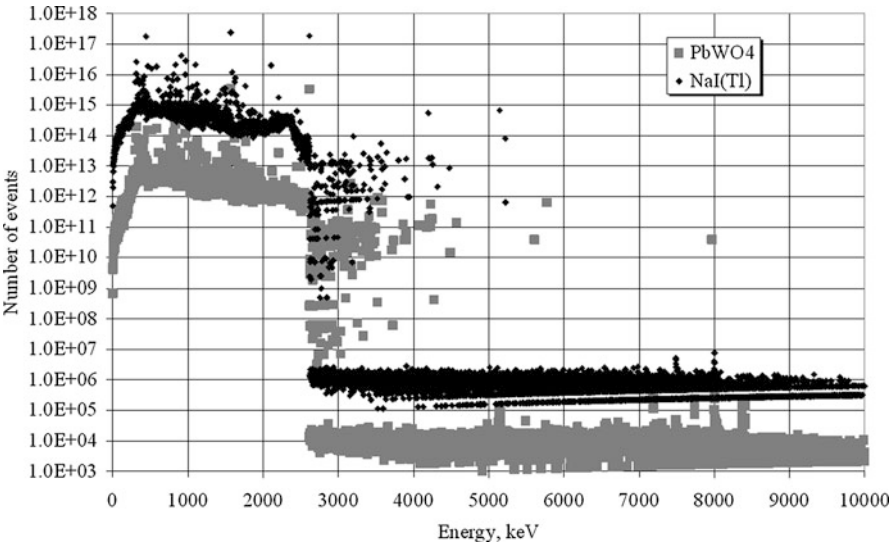

Fig. 26.7 NaI(Tl) vs $PbWO_4$ comparison of deposited energy. WP source. Calibration on a scintillator light yield is applied

26.6 Conclusion

The results of simulations presented above prove an attractiveness of application of heavy high energy scintillators for nuclear materials detection. $PbWO_4$ scintillator have clear advantage in comparison to conventional NaI(Tl) scintillator in detection of WP, however it shows no significant advantage in detection of HEU.

The factor limiting applicability $PbWO_4$ is its very low light yield. According to our understanding of $PbWO_4$ scintillation mechanisms some technological measures allow increasing light yield by several times, which can be a good improvement. However, such kind of R&D requires an additional financial support for research. Another solution can be in a choice of other types of heavy scintillator with higher light yield.

References

1. IAEA (2011) IAEA Illicit Trafficking Database (ITDB) fact sheet 1993–2011. IAEA, Vienna
2. The Non-proliferation Review (1993) Program for Non-proliferation studies. Monterey Institute of International Studies, 1(1):162–164
3. Knunyants IL et al (eds) (1965) Pyrometallurgy – brief chemical encyclopedia, vol 4. Soviet Encyclopedia, Moscow, pp 90–92 (in Russian)
4. Bekman IN (2009) Plutonium. Tutorial. Moscow State University, Moscow
5. Nadykto BA, Timofeeva LF (eds) (2003) Plutonium. Fundamental problems. VNIIEF, Sarov

6. Baryshevsky VG (ed) (2001) Basic and applied physical research. 1986–2001. Collected articles. Belarus State University Press, Minsk. ISBN 985-445-545-9
7. Fetter S, Mozly R, Prilutsky OF, Radionov SN, Sagdeev RZ, Miller M (1989) Detecting nuclear weapons. FAS, Washington, DC, pp 1–200
8. Reinhard MI, Prokopovich D, Van der Gaast H, Hill D (2006) Detection of illicit nuclear materials masked with other gamma-ray emitters. 2006 IEEE nuclear science symposium conference record. N14-21. San Diego, 29 October–5 November 2006. http://173.21.69.124/classwork/ecrd/reference/IEEE-2006-san-diego/czt/n14-21.pdf
9. Martin R (1973) A direct-reading arithmetic unit for non-destructive assay of nuclear materials. Nucl Instrum Methods 109:439–444
10. Sampson EA, Parker JL (1990) Application of gamma-ray spectrometry in the quantitative non destructive assay of special nuclear material. Nucl Instrum Methods A 299:327–334
11. Fetter S, Frolov VA, Miller M, Mozley R, Prilutsky OF, Rodionov SN, Sagdeev RZ (1990) Detecting nuclear warheads. Sci Global Secur 1(3–4):225–253
12. Glaser A (2007) Detection of special nuclear materials, WWS556d, Revision 6. Princeton University, Princeton
13. Khrutchinsky AA, Baryshevsky VG, Moroz VI, Dezhurko MD (1992) Gamma-ray spectrometric system for remote detection and control of fissile materials. IEEE Trans Nucl Sci 1(4):971–976
14. CMS (1997) The electromagnetic calorimeter technical design report, CERN/LHCC 97-33, CMS TDR4
15. Drobychev GYU, Baryshevsky VG, Fedorov AA, Khruschinsky AA, Korjik MV, Lecoq P, Missevitch OV (2005) Application of PWO crystals for detection of low activity gamma-radiation in the energy range above 3 MeV. Nucl Instrum Methods Phys Res A 537:439–442
16. Drobychev GYu, Baryshevsky VG, Fedorov AA, Khruschinsky AA, Korjik MV, Missevitch OV (2009) Development of a new generation of scintillation detectors for remote control of fissile materials and devices based on them. In: Proceedings of the technical workshop in response to chemical, biological, and radiological/nuclear terrorist attacks, Ottawa, 28–30 Apr 2009, pp 636–651
17. GEANT 4. http://geant4.cern.ch/

Part VII
Synthesis/Processing

Chapter 27
Inorganic Nanotubes and Fullerene-Like Nano-particles: From the Lab to Applications

R. Tenne

Abstract Recent progress in the synthesis and the applications of inorganic nanotubes and fullerene-like nanoparticles of layered compounds is reviewed in short brief. New synthetic pathways have been developed for this purpose. Thus, the use of heavy metal catalysts, like lead and bismuth, allowed the synthesis of nanotubes from the "misfit" SnS/SnS_2 superstructure; WSe_2 and other compounds. Scaling up of the synthesis of multiwall WS_2 nanotubes is also briefly discussed. The use of such nanotubes to reinforce polymer matrices, and for humidity sensors, is described.

Keywords Inorganic nanotubes • WS_2 • Solid lubrication • Sensors

27.1 Introduction

This short brief to underline the principles, synthesis, characterization and some of the numerous applications of fullerene-like (IF) nanoparticles (NP) [1].

27.2 Characteristics and Scaling Up

Figure 27.1a shows a transmission electron microscope (TEM) image of IF-MoS_2 NP, while Fig. 27.1b shows TEM image of inorganic nanotubes (INT-WS_2). While the high temperature synthesis and study of IF materials and INT from layered metal dichalcogenides, like WS_2 and MoS_2 remain a major challenge, progress

R. Tenne (✉)
Department of Materials and Interfaces, Weizmann Institute of Science, Rehovot 76100, Israel
e-mail: reshef.tenne@weizmann.ac.il

A. Vaseashta and S. Khudaverdyan (eds.), *Advanced Sensors for Safety and Security*,
NATO Science for Peace and Security Series B: Physics and Biophysics,
DOI 10.1007/978-94-007-7003-4_27,

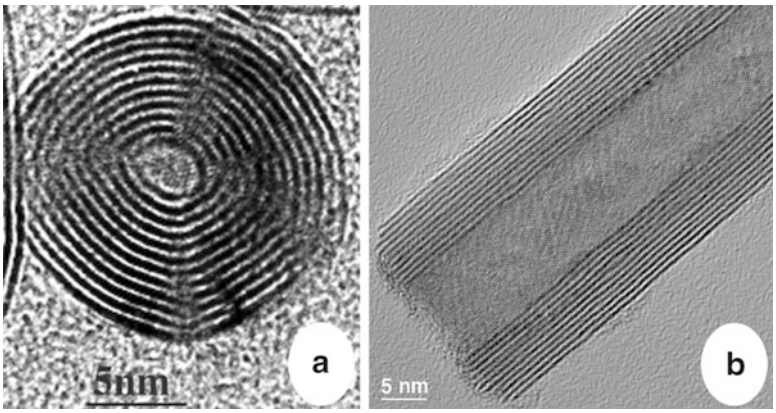

Fig. 27.1 TEM images of IF-MoS_2 nanoparticle (**a**) and INT-WS_2 (**b**)

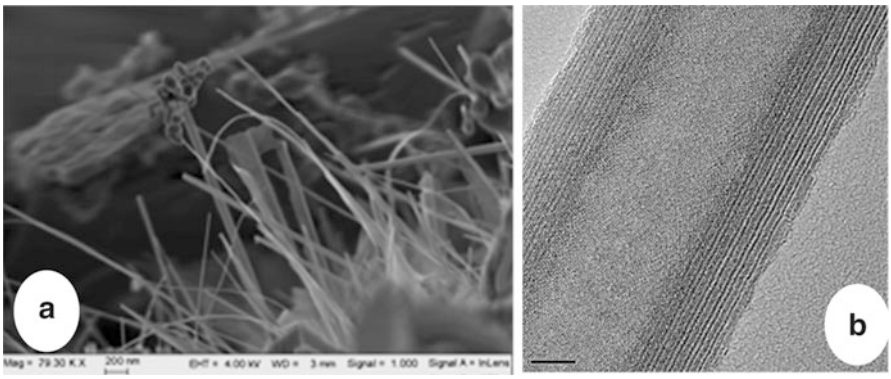

Fig. 27.2 (**a**) SEM image of WSe_2 nanotube which were obatined by solar ablation and Pb as the growth promoter; (**b**) TEM image SnS/SnS_2 ("misfit") nanotube with a clear repeating superstructure of SnS and SnS_2 layers

with the synthesis of such nanostructures from various other compounds has been realized, as well. For example, solar ablation has been used together with metal catalysts (Pb) in order to promote the growth of different nanotubes, like those of WSe_2 (see Fig. 27.2a) [2]. The recent synthesis of "misfit" SnS/SnS_2 nanotubes with a repeating SnS and SnS_2 layers (superstructure) in substantial amounts has been also demonstrated (see Fig. 27.2b) [3]. Scaling-up the synthesis of multiwall WS_2 nanotubes to 500g/batch were recently accomplished (Fig. 27.3). Scaling-up efforts in collaboration with "Nanomaterials" resulted in multi kilogram production of (almost) pure multiwall WS_2 nanotube phases and commercial production of "industrial grade" IF-WS_2 nanoparticles (Fig. 27.4) [4].

IF-MS_2 (M = W, Mo, etc.) were shown to be superior solid lubricants in variety of forms, including an additive to various lubricating fluids/greases and

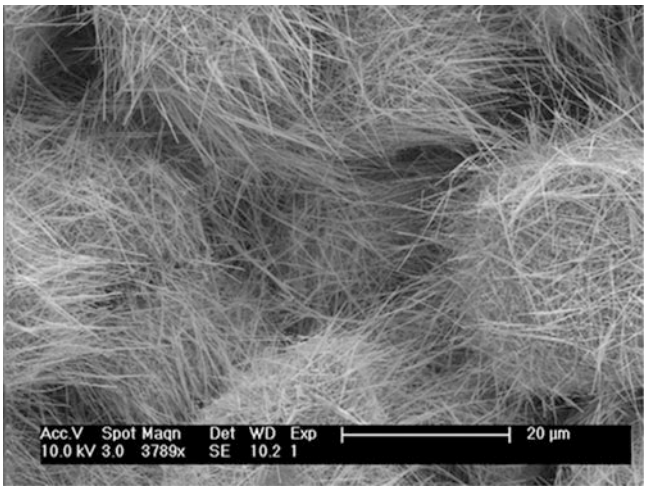

Fig. 27.3 SEM image of WS_2 nanotubes produced in multi kg and used for reinforcing polymer nanocomposites

Fig. 27.4 Production facility for 20 g/batch (*left*) of IF-WS_2 erected in 2000 and a pilot for 150 kg/batch of industrial grade IF-WS_2 nanoparticles (*right*) in "NanoMaterials" site

for various self-lubricating coatings. Doping of the IF nanoparticles with Re atoms produced negatively-charged IF nanoparticles which exhibit very low friction and wear [5]. Following scaling-up efforts, initial commercialization of products based on this technology have taken place in the automotive, aerospace, food, machining and other industries. New potential applications have been realized, e.g. in the field of medical technology [6]. Major progress has been recently reported with polymer nanocomposites reinforced with both carbon nanotubes and IF-WS_2 nanoparticles [7].

27.3 Applications and Path Forward

New sensorial applications for WS_2-based FET have been demonstrated recently [8a, 8b]. Thus a photodetector with high figure of merit [8a] and humidity sensor [8b] have been studied. Numerous other potential applications using IF and INT of various kinds in the field of sensors are expected to be realized in the next few years.

In conclusion, the development of new synthetic routes to obtain inorganic nanotubes of different compounds with layered structure has enriched the field of chemistry of materials and produced numerous opportuinties for new applications, including in sensors of various sorts.

References

1. Tenne R (2006) Inorganic nanotubes and fullerene-like materials. Nat Nanotechnol 1:103–111
2. Brontvein O, Stroppa DG, Albu-Yaron A, Levy M, Feuerman D, Houben L, Tenne R, Gordon JM (2012) New high-temperature Pb-catalyzed synthesis of inorganic nanotubes. J Am Chem Soc 134:16379–16386
3. Radovsky G, Popovitz-Biro R, Staiger M, Gartsman K, Thomsen C, Lorenz T, Seifert G, Tenne R (2011) Synthesis of copious amounts of SnS_2 and SnS_2/SnS nanotubes with ordered superstructures. Angew Chem Int Ed 50:12316–12320
4. Zak A, Sallacan Ecker L, Efrati R, Drangai L, Fleischer N, Tenne R (2011) Large-scale synthesis of WS_2 multiwall nanotubes: update. J Sens Transducers 12:1–10
5. Yadgarov L, Rosentsveig R, Leitus G, Albu-Yaron A, Moshkovith A, Perfilyev V, Vasic R, Frenkel AI, Enyashin AN, Seifert G, Rapoport L, Tenne R (2012) Controlled doping of MS_2 (M = W, Mo) nanotubes and fullerene-like nanoparticles. Angew Chem Int Ed 51:1148–1151
6. Adini AR, Redlich M, Tenne R (2011) Medical applications of inorganic fullerene-like nanoparticles. J Mater Chem 21:15121–15131
7. Díez-Pascual AM, Naffakh M, Marco C, Ellis G, Gomez-Fatou MA (2011) High-performance nanocomposites based on polyetherketones. Prog Mater Sci 56:1106–1190

8a. Zhang C, Wang S, Yang L, Liu Y, Xu T, Ning Z, Zak A, Zhang Z, Tenne R, Chen Q (2012) High-performance photodetectors for visible and near-infrared lights based on individual WS2 nanotubes. Appl Phys Lett 100:243101

8b. Zhang C, Ning Z, Liu Y, Xu T, Guo Y, Zak A, Zhang Z, Wang S, Tenne R, Chen Q (2012) Electrical transport properties of individual WS2 nanotubes and their dependence on water and oxygen absorption. Appl Phys Lett 101:113112

Chapter 28
Porous Silicon by Galvanostatic Electrochemical Anodisation of Epitaxial Silicon, Polycrystalline Silicon and Silicon on Insulator Layers

M. Ivanda, M. Balarin, O. Gamulin, V. Đerek, D. Ristić, S. Musić, M. Ristić, and M. Kosović

Abstract Porous silicon (PSi) samples were prepared by galvanostatic electrochemical anodization of epitaxial silicon, polycrystalline silicon and silicon on insulator layers. Structural and optical properties of prepared samples were investigated by Raman and photoluminescence (PL) spectroscopy, field emission scanning electron microscopy (FE-SEM) and energy dispersive x-ray spectroscopy (EDS). Epitaxial silicon layers of n-type and {111} orientation grown on n-type {111} oriented silicon substrates were anodized as a function of concentration of 48 % HF in ethanol solution and anodization time. Electrical resistivities of the epitaxial layers and of the silicon substrate were ∼2 and ∼0.015 Ω cm, successively. Within the epitaxial layer and on the substrate surface, micro- and nano-pores of different sizes in dependence on HF concentration and anodization time were obtained. For anodization times longer than 30 min epitaxially grown layer detached from the substrate. A high density of micrometer sized pores with regions of three-dimensional photonic crystal expressed in an intersecting <113> oriented macropore lattice on {111} oriented crystal was observed. After detaching the epitaxial layer, the black colored substrate consisted of fine nanometer sized cobweb-like silicon structures whose morphology and density depended on HF concentration and anodization time was found. The Raman spectra of such structures show broadened and red-shifted optical phonon band O(Γ), depending on the size of silicon nanostructures. The intensity of PL of such fine porous substrate shows the sensitivity on the level of the optical phonon confinement.

M. Ivanda (✉) • V. Đerek • D. Ristić
Division of Materials Physics, Ruđer Bošković Institute, Bijenička cesta 54, Zagreb, Croatia
e-mail: ivanda@irb.hr

M. Balarin • O. Gamulin • M. Kosović
Department of Physics and Biophysics, University of Zagreb, School of Medicine, Šalata 3b, Zagreb, Croatia

S. Musić • M. Ristić
Division of Materials Chemistry, Ruđer Bošković Institute, Bijenička cesta 54, Zagreb, Croatia

A. Vaseashta and S. Khudaverdyan (eds.), *Advanced Sensors for Safety and Security*,
NATO Science for Peace and Security Series B: Physics and Biophysics,
DOI 10.1007/978-94-007-7003-4_28, © Springer Science+Business Media Dordrecht 2013

Polycrystalline *p*-type silicon film were prepared by low pressure chemical vapor deposition (LPCVD) and anodized in aqueous hydrofluoric acid (HF)/ethanol electrolyte. The FE-SEM images showed preferential anodization and macro-PSi formation along grain boundaries. Weak PL signal was detected in all samples, while Raman measurements indicated minimal or no confinement effects. The anodization of silicon on insulator layers was performed by direct and alternating currents at 50 Hz. Raman spectra of DC samples showed no significant shift of c-Si peak while PL spectra showed intensive luminescence over the entire surface. When etched with AC, a very intensive PL was observed at the circular edge of the sample that exhibited micrometer sized island-like porous structures, while the center of the sample showed moderate PL signal similar to DC samples. The formation of such island-like structures was interpreted as stress due to difference of the piezoelectric effect of silicon and quartz layers (buried SiO_2). Micro-Raman spectra of islands show strong phonon confinement in the range 1.4–3.5 nm.

Keywords Micro and nano PSi • Anodization • Raman • Sensors

28.1 Introduction

Porous silicon (PSi) was established as a promising optoelectronic material since Canham's discovery of intense pSi photoluminescence (PL) at room temperature in the visible light spectrum in 1990 [1]. Silicon can be electrochemically anodised in hydrofluoric acid (HF) solutions and at specific current densities, local dissolution of silicon atoms occurs such that low density porous crystalline silicon is formed. pSi properties can be engineered by careful control of anodization parameters such as current density, electrolyte composition and substrate doping (concentration and type, n, p), light intensity and temperature. Research has mostly been focused on donor and acceptor doped monocrystalline silicon substrates for PSi preparation. High quality PSi films with good reproducibility can be prepared on such substrates, due to their outstanding purity and crystalline perfection.

The fabrication of PSi is simple, cheap, flexible and compatible with Si-technology. Depending on the set of parameters completely different types of porous silicon may result. The extremely large specific surface of 3–300 m^2/g is the most important property with respect to sensor and other applications. Strong sensitivity to environmental conditions allow construction of simple environmental sensors with possible uses in science, industry, medicine, environmental applications, etc. The porous silicon active element has been already used for gas, humidity and chemical/biological sensing as well as for the therapeutic and diagnostic applications in medicine [2]. In sensor applications specific materials are adsorbed and can fill in the pores, changing materials physical/chemical properties (dielectric constant and index of refraction). The readout is usually electrical (capacitive and conductive) or optical (reflectivity and photoluminescence). Current research and potential applications are in development of microcavities, broadband AR coatings, LEDs for

THz, chemical sensors, smart dust, pressure sensors, photonic crystals, biosensors for pathogen and toxin detection [3, 4]. For the case of gas sensors with electrical readout, the design is similar for all types of sensors. The main goal is in achieving rapid, reversible, sensitive, selective and low voltage (1–10 mV) detection. Beside the changes in electrode assembly and in measurement of conductivity/capacitance, the main road in improving the sensor properties is in preparation of specific active porous silicon layer. This investigation focuses on novel methods for preparation of active porous silicon by anodization of epitaxial silicon, polycrystalline silicon and silicon on insulator layers.

28.2 Experimental

A specially designed electrochemical anodization cell schematically shown on Fig. 28.1a was used for preparation of pSi samples. Three type of silicon substrates were used in anodization processes:

(a) Commercially available silicon-on-insulator wafers, consisting of 20–24 μm thick *n*-type (phosphorus doped) silicon epitaxial {111} layer grown on a 280 μm thick n-type (Sb doped) silicon substrate. The FE-SEM image of epitaxial layer is shown on Fig. 28.1b. Electrical resistivity of the epitaxial layer is 2 Ω cm. Silicon substrate is a much better conductor with resistivity of 0.015 Ω cm. The bottom of the wafers was coated with gold for electrical contact with the bottom part of the anodization cell. Three samples were prepared by varying the concentration of 48 % HF in 96 % ethanol solution in the electrochemical anodization cell. Concentrations of 50 and 25 % of 48 % HF in 96 % ethanol solution were used at constant current density of 13 mA/cm^2 provided for 30 min for the samples S_1 and S_2, respectively, and concentrations of 50 % of 48 % HF in 96 % ethanol solution for 80 min at the

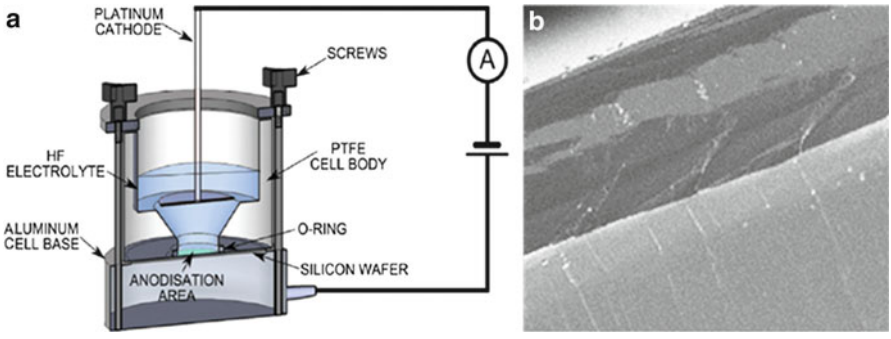

Fig. 28.1 Cross section of the cell for anodization (**a**), and FE-SEM image of cleaved wafer with 24 μm thick epitaxial layer (**b**)

current density ~16 mA/cm^2 for the sample S_3. After anodization samples were dried in air. It was immediately noticed that the porous top epitaxial layer had detached from the rest of the wafer, and was easily removed. This was caused by different anodization process between the top epitaxial layer and the much better conducting substrate layer.

(b) Thin polycrystalline Si films deposited by low pressure chemical vapor deposition (LPCVD) method on top of 2-in. monocrystalline silicon {111} oriented wafers. The wafers were *n*-type, double-layered, consisting of 280 μm thick Sb-doped substrate ($\rho = 0.015$ Ω cm) and epitaxially grown and polished top layer (phosphorus doped, 4.2–5.3 μm thick, $\rho = 0.8$–1.0 Ω cm). Poly-Si with thickness of 6.5 μm was deposited and boron delta doped by LPCVD process. The deposited samples were annealed for 30 min at 1,050 °C in nitrogen gas flow at atmospheric pressure. Film resistivity measured by four-point probe method ranged from 3 to 14 Ω cm, which corresponds to the positive charge carrier density of 10^{17} cm^{-3}. Anodization was conducted in the dark. Electrolyte composition was 5 % w/w solution of HF in ethanol prepared from 40 % aqueous HF acid, constant for all samples. Anodic contact was accomplished with aluminum foil pressed between the back sample side and electrochemical cell base made of aluminum. Cathode was a platinum spiral wire inserted in electrolyte. Variable voltage source was connected to anodization cell. Current passing through the cell and potential drop on the cell were measured continuously during the anodization. Current was kept constant during the process. It is well established that electro-polishing of silicon begins for the current density $j > j_{crit}$ [5]. For this reason the current–voltage characteristics of anodization cell with poly-Si substrates were taken in order to determine the electro-polishing current j_{PS} (6 mA/cm^2 < j_{PS} < 8 mA/cm^2 for prepared samples). During sample preparation anodization current was kept at 3.4 mA/cm^2, which is about half of average j_{PS} while anodization time was varied from 3 to 75 min.

(c) The commercially available silicon on insulator (SOI) wafers consisting of 40 μm thick device layer with resistivity $\rho = 20\,\Omega$ cm, separated from the 460 μm thick handle with resistivity $\rho = 10\,\Omega$ cm, with 1.5 μm thick SiO_2 layer. The active layer and the substrate has {110} and {100} orientation, respectively. The anodization process was carried out in an ethanoic solution of HF acid with volume concentration 1:1, by using different DC and AC current densities and anodization time. The samples S_1 (AC) and S_2 (AC) were anodized using the current density of 13 and 15 mA/cm^2 for duration of 5 and 10 min respectively. The samples S3 (AC) and S_4 (AC) were anodized using the current density ~30 mA/cm^2 during 15 and 7.5 min, respectively. Following the anodization process, the electrolyte from the anodization cell was exchanged with ethanol.

After anodization all samples were once more rinsed in ethanol and twice in pentane. Final pentane rinse was continued for 5 min in order to reduce the capillary stress during sample drying, since pentane has a very low surface tension [6]. Pentane was removed and samples were left to dry in air. Porous poly-Si surface morphology and cross-section were explored with FE-SEM using JEOL

JSM 7,000 F field-emission FE-SEM. Photoluminescence and Raman spectra in micro-Raman mode were recorded with Jobin Yvon T64000 triple spectrometer using excitation from 514.5 nm wavelength argon-ion laser. The special care was taken to avoid the laser heating effects on the O(Γ) silicon Raman mode. For this reason the laser beam power at the surface of the sample was kept at 1 mW and in special cases of recording Raman and PL spectra from silicon islands, the laser power on the sample was 0.01 mW. Raman and photoluminescence spectra were recorded from the same spot at the top of the samples.

28.3 Results and Discussion

28.3.1 Porous Epitaxial Layers

Here we show the results of preparation of porous silicon samples prepared from n-type silicon epitaxial layer grown on more conductive n-type silicon substrate. By varying the concentration of 48 % HF in ethanol solution micro- and nano-pores of different sizes within the epitaxial layer in dependence on HF concentration were obtained.

Figure 28.2a shows the FE-SEM images of the cleaved cross section of the etched thin epitaxial layer of the samples S_1–S_3. It is evident that the layers were detached from the substrate. A dramatic difference between the top Fig. 28.2b and the bottom side Fig. 28.2c of the detached epitaxial layer was observed. Figure 28.2d shows the fine porous structure of the substrate after removing of the detached epitaxial layer.

Figure 28.3a shows the cleaved epitaxialy layer on the substrate with fine cobweb silicon structure that is better visible at higher magnification on Fig. 28.3c. Visually and by optical microscopy this structure is completely black. Some further work is necessary to compare the properties of such nanostructured silicon with so called "black silicon" of Mazur et al. [7]. This material has found commercial applications in a number of photodetectors for various imaging and night vision applications as well as for high-efficiency solar cells [8]. Figure 28.3b shows in more detail the cross section of the cleaved epitaxial layer of S_1. A three-dimensional photonic crystal expressed in intersecting <113> oriented macropore lattice on {111} silicon plains is formed.

The FE-SEM images of the top of samples S_1–S_3, Fig. 28.2b, shows numerous macropores with dislocation like shape that are entry points of F^- ions along the <113> direction of silicon crystal. The bottom side of epitaxial layer shown on Fig. 28.2c exhibits a large number of micrometer-sized and homogeneously distributed pores. The anodization process at defects like dislocations is much faster when compared to bulk silicon. Therefore, the substrate acts effectively as a barrier for the penetration of F^- ions. For this reason the epitaxial layer was cut from the substrates by the effective lateral anodization at the boundary surface and, therefore, was completely detached from the rest of the wafer (substrate). With further anodization the porous structure is formed in the substrate.

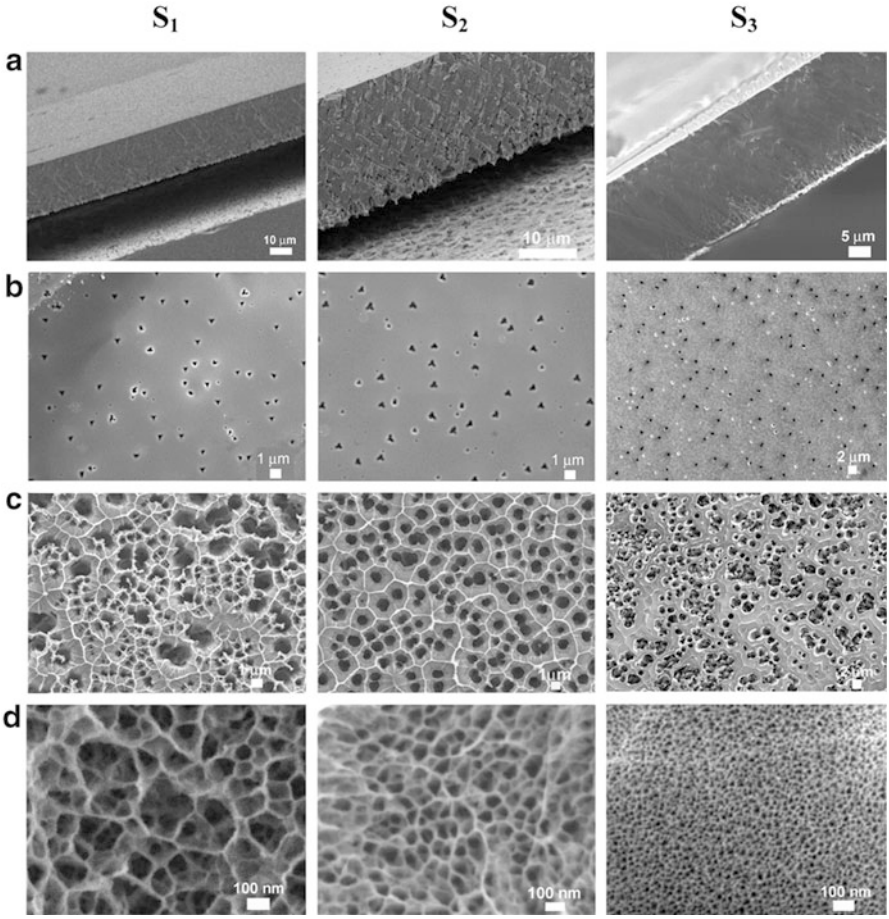

Fig. 28.2 FE-SEM images of the sample S1–S3 at different magnifications: (**a**) cleaved cross section with detached epitaxial layer from the substrate, (**b**) top of the epitaxial layer, (**c**) bottom side of the epitaxial layer, (**d**) substrate layer

Figure 28.2d shows FE-SEM images obtained at high magnification of the cobweb-like silicon structures of the samples S_1–S_3 recorded after longer period of time exposed to air denoted in Table 28.1. Within this time the porous silicon was oxidized by the process of native oxidation. The estimated mean value of diameters $D_{FE\text{-}SEM}$ and standard deviation of the wire-like-shapes of such porous structure is presented in Table 28.1. The concentrations of silicon and oxygen atoms of such structures determined by EDS are shown in Table 28.1. The EDS spectra were taken from the same part of the samples and at the same magnification as shown on Fig. 28.2d. The thickness of the native oxide presented in Table 28.1 is calculated by the formula of Graf et al. [9].

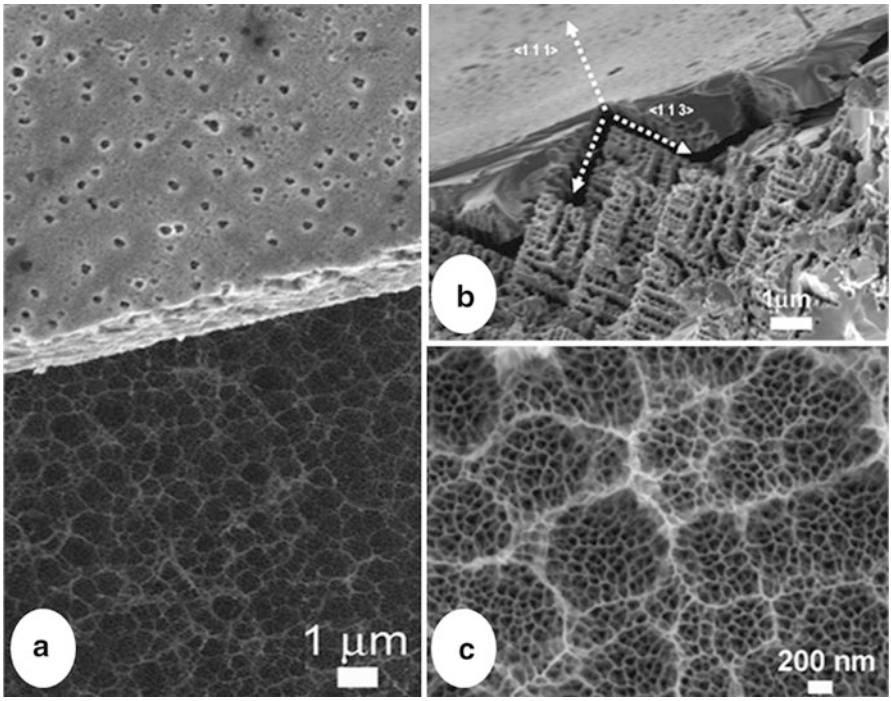

Fig. 28.3 FE-SEM images of the sample S1: (**a**) *top view* of partially cleaved epitaxial layer with substrate layer visible, (**b**) cleaved epitaxial layer that shows anodization paths that intersect {111} silicon plains with <113> channels forming photonic crystal, (**c**) high magnification of substrate layer showing cobweb like silicon nanostructures

Table 28.1 Comparison of sizes of basic structural units of anodized epitaxial Si substrates – samples S1–S3 after detachment of epitaxial layers

Sample	S_1	S_2	S_3
t [min] exposure to air	2.00×10^6	2.30×10^6	5.57×10^5
N_{Si}/N_0 (by EDS)	3.13	1.49	2.39
$D_c(SiO_2)$ [nm] thickness of native oxide layer (calculated)	2.93	2.96	2.68
$D_c(Si)$ [nm] (calculated)	23.4	6.9	14.7
$D_c = D_c(Si) + 2D_c(SiO_2)$ [nm]	29.2	12.9	20.1
$D_{FE\text{-}SEM}$ [nm] – by FE-SEM	28.0 ± 6.6	14.6 ± 3.3	18.3 ± 3.3
D(Si) [nm] – by Raman	6.0	5.5	3.8

The sizes were determined by FE-SEM micrographs and Raman spectroscopy and calculated using oxidized Si cylinder model

$$d\ (\text{nm}) = 0.1 + 0.45^* \log\left[\text{t}\,(\text{min}) - 10,000\right] \tag{28.1}$$

Using the model of silicon cylinder oxidation, the diameter of silicon core $D_c(Si)$ as well as a total diameter of the oxidized cylinder D_c was calculated. The D_c values

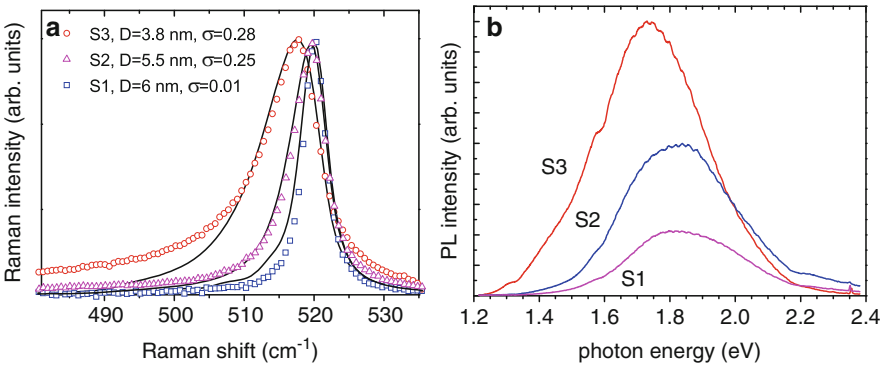

Fig. 28.4 Raman spectra of the samples S1–S3 with mean particle diameter D and size distribution width σ as found from the fit by Eq. 28.5 (**a**). Photoluminescence spectra from the porous substrates of the samples S1–S3 (**b**)

shown in Table 28.1 agree well with those observed by FE-SEM ($D_{FE\text{-}SEM}$). Another way to find size of silicon nanostructures is by confinement effects of O(Γ) silicon Raman spectroscopy mode.

Raman spectroscopy is recognized as a powerful technique for characterization of nanostructures. Figure 28.4a shows Raman spectra in the spectral range of O(Γ) vibrational band at 520 cm^{-1} of the substrate layers for the freshly prepared samples S_1–S_3 (30 min after anodization). The broadening and redshift of the c-Si optical O(Γ) vibrational band at 520 cm^{-1} occurs due to the phonon confinement effects. In order to determine the size of phonon confinement, the spectra were fitted by the procedure described below. The final results are shown on Fig. 28.3a. The corresponding PL spectra are shown on Fig. 28.3b. The PL bands of 0.40 eV linewidth have the maxima at 1.85, 1.82 and 1.73 eV for the samples S1-S3, respectively. The observed PL intensity increases with the increase of phonon confinement, but instead of expected blue shift of PL, the red shift is observed. This indicates that another competitive mechanism, probably connected with creation of non-radiative recombination centers is involved in the process of silicon anodization.

Effect of quantum confinement on the optical phonon peak manifests in its red shift and broadening [10, 11]. Spatial confinement of the vibration leads to the breakdown of the momentum conservation rule which causes the Raman scattering from all the phonons down the phonon branch to contribute to the Raman spectrum. To calculate the Raman spectrum the phonon dispersion relation $\omega(k)$ must be known. Here we used the Brout sum phonon dispersion relation [12]. The phonon confinement function must also be specified, and in this work the following confinement relation is used [13]:

$$W(r, D) = \frac{\sin(2\pi r/D)}{2\pi r/D} \tag{28.2}$$

which corresponds to phonons in a spherical potential well. Raman intensity of optical phonon peak for an isotropic medium is given as [10, 11]:

$$I(\omega, D) = \frac{n(\omega)+1}{\omega} 4\pi \int \frac{\left|C(\vec{k}, D)\right|^2}{[\omega - \omega(k)]^2 + (\Gamma_o/2)^2} k^2 dk \tag{28.3}$$

where the integration is carried out over the entire Brillouin zone, $n(\omega)$ is the Bose-Einstein distribution, Γ_o is the intrinsic optical phonon peak width and the coefficients are the Fourier transform of the confinement function:

$$C(\vec{k}, D) = \int W(\vec{r}, D) d\vec{r} \tag{28.4}$$

The final Raman intensity is given by the convolution of $I(\omega, D)$ with size distribution of nanoparticles $N(D)$:

$$I(\omega) = \int I(\omega, D) N(D) dD \tag{28.5}$$

where size distribution for the small nanoparticles is best described by log-normal distribution:

$$N(D) \propto \exp\left[-\frac{(\ln(D/D_0)^2}{2\sigma^2}\right] \tag{28.6}$$

Here, D_0 is diameter that corresponds to the maximum of distribution and σ the parameter of distribution width.

Figure 28.4a shows the results of fit on the optical mode of silicon with mean particle diameter D and size distribution width σ as free parameters. It is interesting that this procedure gives three to four times smaller dimension for the correlation length of phonon confinement when compared to the wires diameter directly measured by FE-SEM as shown on Fig. 28.3d. This suggests that silicon cobweb-like wires have substructure that are not visible by FE-SEM. To better understand this effect the high resolution TEM images have to be performed on the samples.

28.3.2 Porous Poly-Si Layer

PSi can also be prepared on polycrystalline silicon substrates. Poly-Si consists of Si grains which are crystalline over the grain size. Grains of different crystal orientation are separated by grain boundaries. Such material inhomogeneity can make reproducibility in porous poly-Si samples hard to obtain, hence poly-Si has not been the favorite substrate for PSi preparation. Literature search shows that only about 1 % of all research papers regarding PSi focus on porous poly-Si. However,

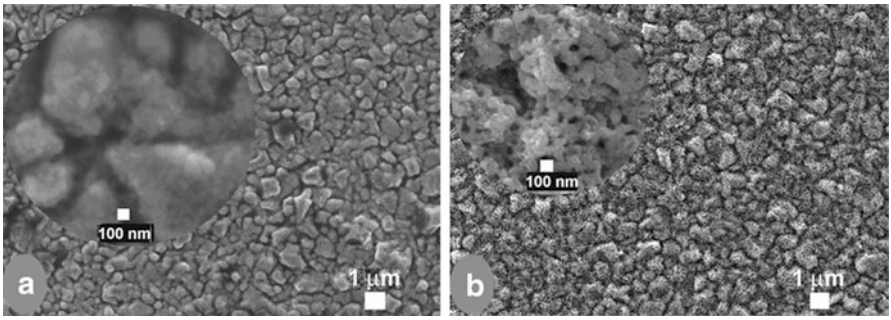

Fig. 28.5 FE-SEM micrograph of poly-Si sample surface with inset at higher magnification (**a**), FE-SEM micrograph of the sample anodized for 3 min with *inset* at higher magnification showing porous poly-Si surface morphology (**b**)

use of poly-Si has been expanding due to its lower cost of production as compared to semiconductor-grade monocrystalline silicon, especially in photovoltaic industry. Thin poly-Si films can easily be deposited on most solid surfaces and electrochemically processed into porous poly-Si. This opens possibilities for industrial applications of porous poly-Si films in cases where their properties are found interesting.

FE-SEM micrograph of poly-Si sample surface consisting of partially fused grains is shown in Fig. 28.5a. Least-squares Gaussian fit to Feret's diameter of selected sample of grains gives a value of $d = (1.1 \pm 0.4)$ μm. High magnification inset on Fig. 28.5a shows surface morphology of several poly-Si grains. Features about 50 nm in diameter can be distinguished on grain surfaces. This is indicative of polycrystalline grains which consist of multiple fused silicon nanocrystals.

The Raman spectra of poly-Si samples in comparison with monocrystalline silicon showed a slight broadening of silicon O(Γ) Raman vibrational band at 520 cm^{-1} that could be due to phonon confinement in small crystallites, and crystal defects which are abundantly present in poly-Si in grain boundaries or created due to thermal relaxation in grains after annealing [14–17]. Statistical analysis of peak positions for all samples shows small shift towards the lower wavenumbers (0.1–0.3 cm^{-1}). Such small observed Raman shifts can be attributed to phonon confinement effect in silicon nanocrystals sized from 30 to 50 nm in diameter that is also consistent with FE-SEM micrographs. No measurable photoluminescence was observed from bare poly-Si samples.

Six porous poly-Si samples with different anodization times (3–75 min) were prepared, keeping other parameters constant. Voltage drop on electrochemical cell was measured during anodization under constant current density conditions. During the first 10 min of anodization the voltage was constant. About 25 min into anodization a sharp voltage peak was observed. This peak was explained as pore growth through depletion layer in *p*-*n* junction present between *p*-type poly-Si and

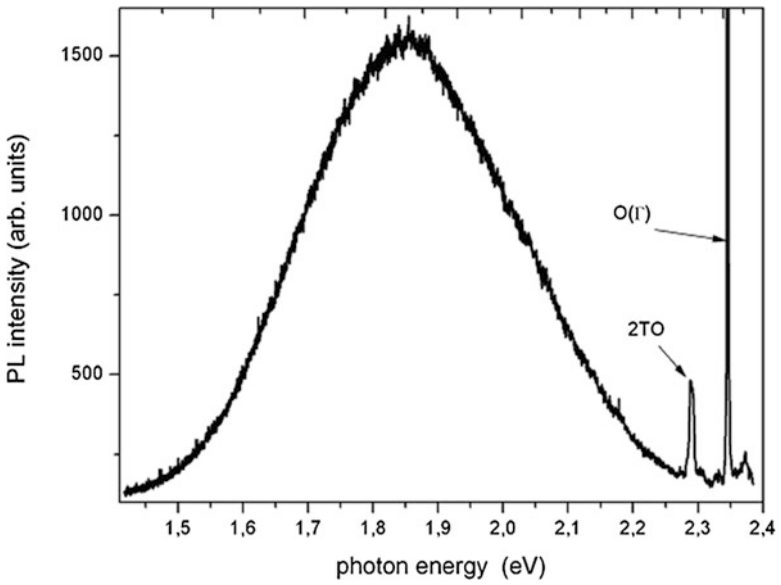

Fig. 28.6 Photoluminescence spectrum of porous poly-Si anodized for 3 min

n-type substrate. This feature can be helpful in determining the pore growth speed, and could also be used as a stop condition for anodization process.

Porous poly-Si surface appears visually matte compared to poly-Si shiny surface. Samples anodized for up to 10 min appear black, following with blue-green (10–20 min) and yellow-orange surface color for samples etched for 30 and 75 min. Color effects are attributed to interference effects due to different porous layer thickness. A typical porous poly-Si surface morphology observed by FE-SEM is shown on Fig. 28.5b, showing large macropores along the poly-Si grain boundaries and mesopores on the grains themselves. The average distance between pores of around 50 nm is an indication that the main anodization path is by the grain boundaries. For longer anodization time general morphology stays the same, with more material etched away. The Raman spectra showed no band downshifting in comparison to poly-Si samples. Such result indicates absence or very low concentration of silicon nanocrystalites created by anodization.

Figure 28.6 shows a weak PL observed in all porous poly-Si samples that are Gaussian in profile, cantered at 1.85 eV with linewidth of 0.4 eV. PSi photoluminescence can be attributed to quantum confinement (QC) effect [18]. QC model relates silicon crystallite size to PL peak energy [19, 20], giving crystallite diameter of 3.3 nm for 1.85 eV PL peak. Most intense observed PL peak intensity was only 6 % of the peak intensity of silicon Raman line at 520 cm^{-1}, while in some crystalline porous silicon samples PL peak intensity was up to 100 times the peak intensity of the said Raman line. This can be attributed to assumed small concentration of silicon nanocrystals in samples. Inefficient PL from inhomogeneous material of low porosity has previously been attributed to microscopic areas of high porosity

[21]. Proposed low density of small (∼3 nm) nanocrystals showing high PL external quantum efficiency is consistent with no observable O(Γ) Raman band shift.

The PL could be improved by introducing high porosity in poly-Si samples, which could be obtained by pore widening using longer anodization times and higher current densities or by prolonged HF acid bath after anodization. Another way of increasing porosity and obtaining small nanocrystals in PSi samples is increasing *p*-doping level in poly-Si substrate, since formation of mesoporous layers is favored in highly *p* doped samples (*p*+) [21], in contrast to macroporous structures obtained in prepared samples. Unfortunately, in $p+$ doped PSi samples the PL intensity is reduced by orders of magnitude compared to low doped *p*-type samples of the same porosity [21]. In order to obtain increased PL intensity in porous poly-Si further attention should be addressed to careful optimization of mentioned anodization parameters.

28.3.3 Porous SOI Layers

Anodization of silicon-on-insulator (SOI) wafers is of scientific and technological challenge due to the nature of anodization process itself, as well as due to the possible application of such silicon in development of new sensors. Here we present the results of preparation of PSi samples using silicon-on-insulator wafers electrochemically etched using direct and alternated currents (DC and AC).

Samples S_1(DC) and S_2(DC) were etched with direct current densities of 4 and 13 mA/cm^2 and time interval of 60 and 30 min, respectively. The porous silicon samples of color that is a mixture of dark brown, old gold and red were produced. Rogriguez-Perez and colleagues [22] showed that the preparation of silicon on insulator in the silicon (active) and SiO_2 layers produces large amounts of defects. In the active layer the defects are mainly dislocations, while in SiO_2 layer these defects are mainly silicon islands located near the upper and lower boundaries of silicon and SiO_2. In our case, it is possible that the current passes through the insulator layer by these islands resulting in electrochemical anodization of active layer forming the pore size of average diameter of ∼50–500 nm in S_1(DC) and 5–50 μm in S_2(DC) samples as shown on Fig. 28.7a and b, respectively.

The density of these pores is greater at the edge of the sample, and decreases as it goes towards the center. Effects of geometry i.e. of the electric field that are larger at the edge [23], resulting in larger current density which causes larger pores. Argument in favor is larger pores in observed on the sample S_2(DC) etched with larger current. X-ray energy dispersive spectra show that the bottom of the pores contains, beside silicon, also oxygen atoms whose origin is from the broken down SiO_2 insulator layer. Figure 28.7c shows the visible red PL recorded by digital camera with long pass filter (455 nm) and diffuse blue light (405 nm) illumination. The PL is centered at 1.9 eV (650 nm) and is of 0.4 eV width. The PL peak intensity is about 20 times peak intensity of the O(Γ) silicon Raman peak.

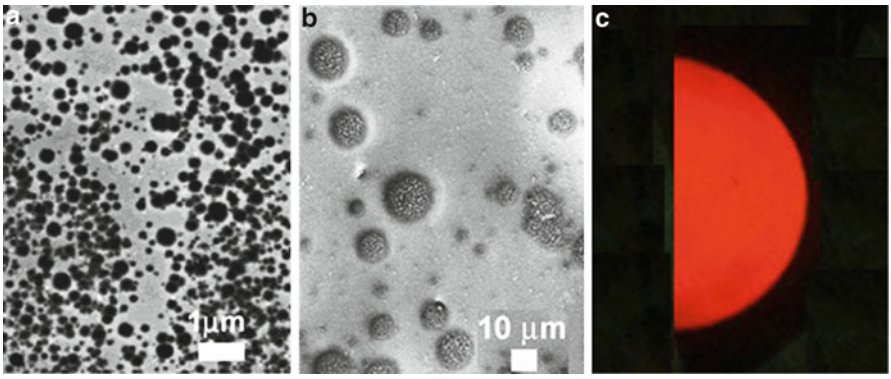

Fig. 28.7 FE-SEM image of the surface of anodised SOI sample prepared by using direct current of 4 mA (**a**) and 13 mA (**b**) showing the surface covered with regular circular cavities that mainly consists of silicon and oxygen atoms in ratio 1:2. Homogenous visible red PL on the half of the etched region of 2 cm in diameter excited with diffuse blue light of 405 nm illumination and recorded by digital camera with long pass filter of 455 nm (**c**)

Very strong PL was found in the samples prepared by anodization with mains frequency AC (50 Hz). The samples S_1(AC) and S_2(AC) were anodized under the current density of 13 and 15 mA/cm^2 in a time of 5 and 10 min, respectively. The samples S_3(AC) and S_4(AC) were anodized under the current density of 30 mA/cm^2 in a time of 15 and 7.5 min, respectively. While the intensity of the PL in the center of the samples was similar to those observed on DC samples, a very strong PL was observed at the edge of two cm in diameter anodization region of SOI wafer. Figure 28.8a shows the image of strong red PL from the sample S_1(AC) excited with diffuse green light of 514.5 nm laser. The photo was recorded through green laser light filter of 10^5 attenuations. Figure 28.8b shows the visible red PL recorded by digital camera with long pass filter (455 nm) and diffuse blue laser light (405 nm) illumination. Figure 28.8c shows the red PL emission from the silicon islands illuminated with microscope white light filtered with standard blue microscope filter. The silicon islands are red due to luminescence, while the blue color is blue light of filtered microscope light reflected from the SiO_2 layer. Figure 28.8d shows the FE-SEM images of these islands, Fig. 28.8e FE-SEM image of one island and Fig. 28.8f high magnification of the same shows that the surface consist of a large number of small (3–50 nm) pores. Figure 28.8g–i shows the similar FE-SEM images of the sample S_2(AC). Here, the highest magnification shows that the surface consists of more homogeneous pores of sizes 50–200 nm.

Figure 28.9a shows the intensive PL spectra recorded from the mentioned islands of the samples S_1(AC) and S_2(AC) with maxima at 1.86 and 1.81 eV and linewidth of 0.311 and 0.342 respectively. Figure 28.9b shows the corresponding Raman spectra in the range of O(Γ) mode with the spectrum of crystalline silicon for a comparison. It is evident that O(Γ) modes of the both samples are broadened which is an indication of a strong phonon confinement. The O(Γ) mode of the sample

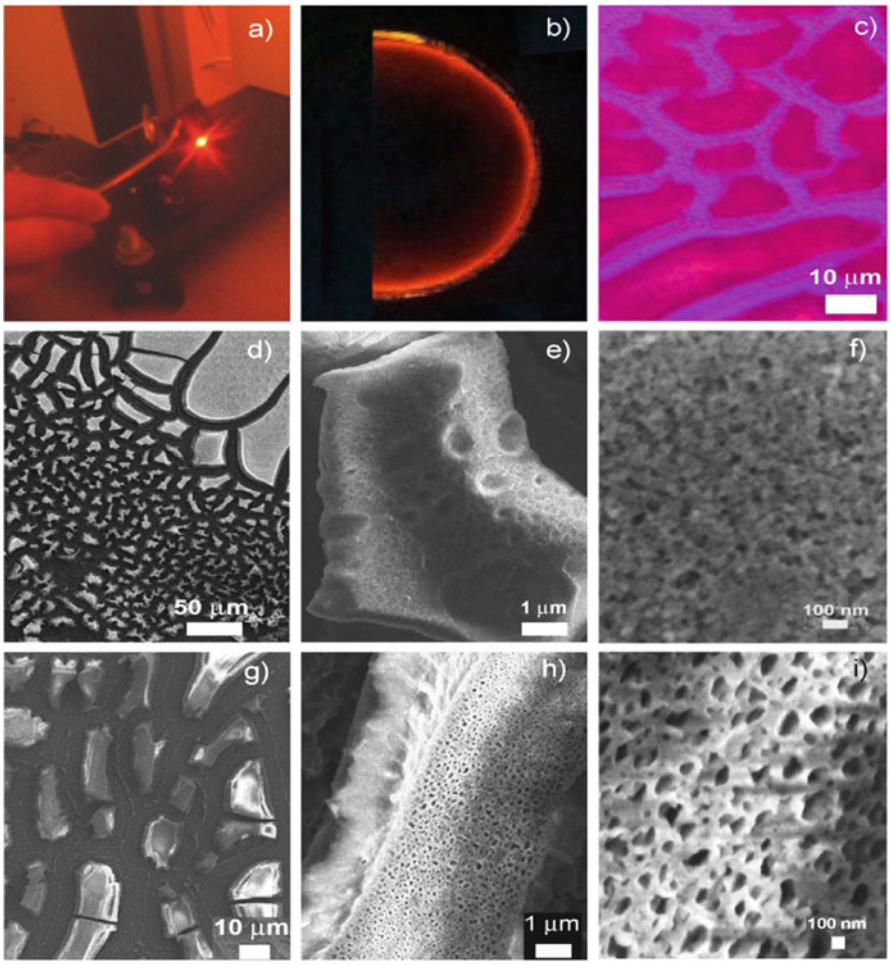

Fig. 28.8 Strong visible red photoluminescence from the edge of anodized SOI sample (**a**). The strongest visible red PL recorded at the edge of etched region of 2 cm in diameter excited with diffuse blue light of 405 nm illumination and recorded by digital camera with long pass filter of 455 nm (**b**). The strong visible red PL recorded from the islands observed by optical microscope at the edge of anodized region. The PL was excited with diffuse microscope light filtered with blue filter (**c**). The FE-SEM images of the same islands under the different magnifications (**d–f**). The FE-SEM images of the similar islands from the edge of anodized SOI sample prepared by using alternating current of 15 mA in duration of 10 min under the different magnifications (**g–i**)

S_1(AC) has a maximum at 518.9 cm^{-1} and linewidth of 8.7 cm^{-1}. The Raman spectrum of the sample S_2(AC) consists of two peaks – one at 518.4 cm^{-1} and linewidth of 4.7 cm^{-1} and another at 512.8 cm^{-1} and linewidth of 19.2 cm^{-1}. For comparison the c-Si has a peak at 521.5 cm^{-1} and of 4.6 cm^{-1} linewidth. The Raman peak of the sample S_1(AC) could be interpreted with phonon confinement on silicon

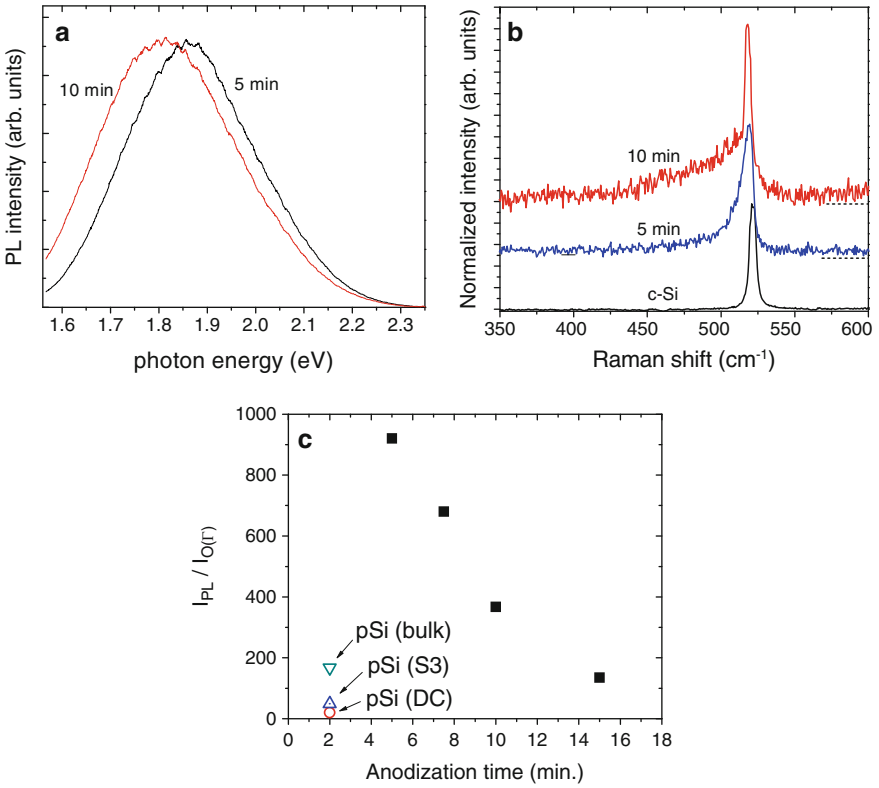

Fig. 28.9 Photoluminescence spectra recorded from the surface of the samples S1(AC) and S2(AC) with peak value at 1.87 and 1.82 eV, respectively (**a**); the corresponding Raman spectra with spectrum of crystalline silicon for comparison (**b**); dependence of ratio of peak intensity of PL band and O(Γ) phonon mode in dependence on anodization time (**c**); PL band and O(Γ) phonon mode in dependence on anodization time

nanostructures of ∼3.5 nm mean size. The two Raman peaks observed at S_2(AC) could be due to two phases – one with domains of sizes larger than 50 nm (also observed by FE-SEM) that are (due to observed Raman red shift of ∼3 cm^{-1}) under the tensile stress and another of sizes of 1.4 nm. It is evident (from Raman spectra and FE-SEM micrographs) that longer anodization time increases size of the voids but also reduce the size of the silicon nanostructures. However, this is not followed with the blue shift of the PL band, moreover, the slight red shift was observed.

The bulk silicon exhibits up to five orders of magnitude weaker PL than PSi as a material with indirect energy band-gap [2]. Despite the large number of investigations devoted to understand the origin of PL in Si nanocrystal systems, neither experimental nor theoretical studies have clearly demonstrated the dominance of one of these particular processes in observed PL spectra. Although the most promising candidates were quantum confinement models [24], other mechanisms also found to originate from, such as for example interface states [25, 26], luminescent defect

states [27] and oxygen vacancy states at the $Si = SiO_2$ interface [28]. However, two mechanisms of radiative recombination in Si nanocrystal systems are known to dominate in PL emission. After the creation of the exciton inside the nano-crystal, radiative recombination can occur either in the nanocrystal (quantum confinement) or outside at an interface state. The relative contribution of each mechanism is not known [25, 29, 30] and their respective efficiency as a function of nano-crystal size is poorly understood. The high photoluminescence efficiency of porous silicon is due to the small probability of finding a nonradiative recombination center in silicon nanocrystallites or on its surface. It has been found that the presence of only one dangling bond at the surface of a crystallite in porous silicon can destroy its luminescent properties above 1.1 eV by producing a luminescence below 1.1 eV due to a radiative capture on the dangling bond [31].

Figure 28.9c shows the decrease of the peak intensity of PL normalized to the peak intensity of O(Γ) mode with anodization time. The possible explanation of such decrease is production of more dangling bonds with AC anodization time. For the comparison, the largest values of $I_{PL}/I_{O(\Gamma)}$ of anodized bulk silicon, epitaxial silicon and DC anodized SOI was also shown on the same figure. The shortest used AC anodization time of 5 min (S_{1AC}) resulted with very strong PL that is six times intensive when compared to the best value we obtained for anodized bulk silicon. Because of such strong PL observation, the AC anodization of silicon on insulator could be promising route in development of silicon light emitting diode.

28.4 Conclusion

Porous silicon (PSi) samples were prepared by galvanostatic electrochemical anodization of epitaxial silicon, polycrystalline silicon and silicon on insulator layers. Porous silicon (PSi) samples prepared by anodization of thin epitaxial silicon layers results in two type of porous silicon structures: (a) detached porous silicon layers of 24 μm thick with reach micrometer sized porous structure with some regular regions of photonic crystal that resulted from the intersection of {111} silicon and (b) plains with <113> anodization channels. After detaching the epitaxial layers, the substrate layers showed high density of nanometer sized cobweb-like silicon structures whose morphology and density depended on the HF concentration and anodization time. The Raman spectra of such structures show optical O(Γ) phonon bands that broaden and red-shift depending on the size of silicon nanostructures. By applying the phonon confinement model, the size of the silicon nanostructures in the range 3.8–6.0 nm where determined. A strong PL at ∼1.8 eV of such nanostructures was observed. After longer exposition to air the FE-SEM and EDS showed that the produced nano-porous cobweb-like silicon consists of silicon wires covered with the native oxide. When Raman results are compared to the FE-SEM diameters of observed wires, they are 3–4 times smaller indicating the existence of silicon substructure not observable by SEM microscopy that have to exist in the wire-like silicon structure.

The ability to prepare porous poly-Si samples on LPCVD boron delta-doped poly-Si substrates was also demonstrated. Useful range of anodization parameters for preparation of porous poly-Si samples was determined. While the properties of prepared samples leave somewhat to be desired in the photoluminescence intensity, it is believed that PL efficiency can be significantly improved with careful choice of anodization parameters.

The anodization of silicon on insulator was also performed by direct and alternating currents of the 50 Hz frequency. The SOI etched with DC current showed the surface covered with circular cavities of different sizes composed mainly of SiO_2. Raman spectra of these samples showed no significant shift of c-Si peak while PL spectra showed intense luminescence over the entire surface. When SOI was etched with AC, the extremely strong PL was observed at the circular edge of anodized region. It was shown that such PL comes from micrometer sized island-like porous structures with while the moderate PL similar to DC samples was observed in the center of the samples. The intensity of PL peak from the islands on the samples edge showed dependence on the anodization time. It has been assumed that island-like structures were produced by stress caused by difference of the piezoelectric effect of silicon on insulator and quartz layers (buried SiO_2). Micro-Raman spectra of islands show strong phonon confinement of O(Γ) silicon mode in the range 1.4–3.5 nm.

References

1. Canham LT (1990) Silicon quantum wire array fabrication by electrochemical and chemical dissolution of wafers. Appl Phys Lett 57:1046
2. Perelman LA (2011) Macromolecular coatings on porous silicon: applications in drug delivery, biosensing, and composites, ProQuest, UMI Dissertation Publishing, 184 p
3. Sailor MJ (2011) Porous silicon in practice – preparation, characterization and applications. Wiley-VCH, Weinheim
4. Florinel-Gabriel B (2012) Chemical sensors and biosensors: fundamentals and applications. Wiley, Chichester, 541 p
5. Rauscher M, Spohn H (2001) Porous silicon formation and electropolishing. Phys Rev E 64:031604
6. Gamulin O, Balarin M, Ivanda M, Kosović M, Đerek V, Mikac L, Serec K, Furić K, Ristić D, Krilov D (2012) Micro and nano structure of electrochemically etched silicon epitaxial wafers. Croat Chem Acta 85:101
7. Serpengzel A, Kurt A, Inanc I, Careyand JE, Mazur E (2008) Luminescence of black silicon. J Nanophoton 2:021770
8. Oh J, Yuan H-C, Branz HM (2012) An 18.2%-efficient black-silicon solar cell achieved through control of carrier recombination in nanostructures. Nat Nanotechnol 7:743
9. Graf D, Grunder M, Schulz R (1990) Oxidation of HF-treated Si wafer surfaces in air. J Appl Phys 68:5155
10. Campbell IH, Fauchet PM (1986) The effects of microcrystal size and shape on the one phonon Raman spectra of crystalline semiconductors. Solid State Commun 58:739
11. Richter H, Wang ZP, Ley L (1981) The one phonon Raman spectrum in microcrystalline silicon. Solid State Commun 36:625
12. Brout R (1959) Sum rule for lattice vibrations in ionic crystals. Phys Rev 113:224

13. Fauchet PH, Campbell IH (1988) Raman spectroscopy of low-dimensional semiconductors. Critical Rev Solid State Mat Sci 14:S79
14. Zi J, Büscher H, Falter C, Ludwig W, Zhang K, Xie Y (1996) Raman shifts in Si nanocrystals. Appl Phys Lett 69:200
15. Kawamura H, Tsu R, Esaki L (1972) Disorder-activated acoustic mode in Raman spectrum of $Ga_xAl_{1-x}As$. Phys Rev Lett 29:1397
16. Nakano N, Marville L, Reif R (2009) Raman scattering in polycrystalline silicon doped with boron. J Appl Phys 72:3641
17. Nguyen NV, Maslar JE, Kim JY, Han JP, Park JW, Chandler-Horowitz D, Vogel EM (2009) Crystalline quality of bonded silicon-on-insulator characterized by spectroscopic ellipsometry and Raman spectroscopy. Appl Phys Lett 85:2765
18. Kwok HL, Ho KH (1982) A three-dimensional model for the transport properties of polycrystalline silicon. J Phys D: Appl Phys 15:2271
19. Cooke DW, Muenchausen RE, Bennett BL, Jacobsohn LG, Nastasi M (2004) Quantum confinement contribution to porous silicon photoluminescence spectra. J Appl Phys 96:197
20. Ledoux G, Gong J, Huisken F, Guillois O, Reynaud C (2002) Photoluminescence of size-separated silicon nanocrystals: confirmation of quantum confinement. Appl Phys Lett 80:4834
21. Gaburro Z, Daldosso N, Pavesi L (2005) Encyclopedia of condensed matter physics: porous silicon. Elsevier Ltd., Amsterdam
22. Perez-Rodriguez A, Cornet A, Morante JR, Jimenez J, Hemment PLF, Homewood KP (1991) Raman scattering and photoluminescence analysis of silicon on insulator structures obtained by single and multiple oxygen implants. Appl Phys 70:1678
23. Foss SE (2005) Doctoral thesis: graded optical filters in porous silicon for use in MOEMS applications. University of Oslo, Oslo
24. Yoffe AD (1993) Low-dimensional systems: quantum size effects and electronic properties of semiconductor microcrystallites (zero-dimensional systems) and some quasi-two-dimensional systems. Adv Phys 42:173
25. Wang XX, Zhang JG, Ding L, Cheng BW, Ge WK, Yu JZ, Wang QM (2005) Origin and evolution of photoluminescence from Si nanocrystals embedded in a SiO_2 matrix. Phys Rev B 72:195313
26. Luppi M, Ossicini S (2005) Ab initio study on oxidized silicon clusters and silicon nanocrystals embedded in SiO_2: beyond the quantum confinement effect. Phys Rev B 71:035340
27. Kanemitsu Y, Fukunishi Y, Kushida T (2000) Decay dynamics of visible luminescence in amorphous silicon nanoparticles. Appl Phys Lett 77:211
28. Degoli E, Ossicini S (2000) The electronic and optical properties of Si/SiO2 superlattices: role of confined and defect states. Surf Sci 470:32
29. Wolkin MV, Jorne J, Fauchet PM (1999) Electronic states and luminescence in porous silicon quantum dots: the role of oxygen. Phys Rev Lett 82:197
30. Qin GG, Li YJ (2003) Photoluminescence mechanism model for oxidized porous silicon and nanoscale-silicon-particle-embedded silicon oxide. Phys Rev B 68:085309
31. Delerue C, Allan G, Lannoo M (1993) Theoretical aspects of the luminescence of porous silicon. Phys Rev B 48:11024

Chapter 29
Advanced Materials for IR Sensors

A.I. Belogorokhov, I.A. Denisov, A.G. Milvidskaya, S.N. Knyazev, K.E. Anoshin, and A.B. Danilin

Abstract The brief review of the results achieved by Giredmet in the field of semiconductor materials for infra-red (IR) sensors is presented.

Keywords IR sensors • Semiconductor materials • Zinc Selenide • Germanium • Indium Antimonide • Indium Arsenide • $Cd_xHg_{1-x}Te$

29.1 Introduction

The key parameters of IR sensors are strongly dependent on the properties of materials used for their preparation. State Research and Design Institute of Rare-Metal Industry Giredmet is engaged in technology development, as well as in direct laboratory production of wide range of materials including materials for IR sensors and optics. Technology of the following materials is ready to be transferred to from the laboratory level to the industrial one. Below, we present a brief report of the most important Giredmet achievements in this area.

29.2 Zinc Selenide

Zinc Selenide (ZnSe) is used for different IR optical components as prisms, lenses, windows, mirrors, optical blanks. ZnSe is transparent material in wide spectral range from yellow (visible) to far IR.

A.I. Belogorokhov • I.A. Denisov • A.G. Milvidskaya • S.N. Knyazev • K.E. Anoshin
A.B. Danilin (✉)
State Scientific-Research and Design Institute of Rare-Metal Industry "Giredmet" JSC,
Building 5-1, B. Tolmachevsky lane, Moscow 119017, Russian Federation
e-mail: danilin.ab@giredmet.ru; adanilin@xbond.ru

A. Vaseashta and S. Khudaverdyan (eds.), *Advanced Sensors for Safety and Security*,
NATO Science for Peace and Security Series B: Physics and Biophysics,
DOI 10.1007/978-94-007-7003-4_29,

Our latest research is focused on the physical properties of ZnSe nanocrystals. Highly monodisperse ZnSe nanocrystals were deposited on porous Al_2O_3 free-standing layer substrates as composite films containing isolated quantum dots. Optical phonons confined in nearly spherical ZnSe nanocrystals have been studied theoretically and experimentally. Spatially quantized phonon modes are considered in the framework of a continuum model. Raman scattering and absorption of far-infrared radiation in ZnSe nanocrystals have been studied. Experimental FTIR transmittance spectra of porous Al_2O_3 free-standing layers containing nearly spherical ZnSe nanocrystals show a broad band between the bulk TO and LO phonon frequencies. These measurements agree with theoretical predictions and thereby confirm the influence of electrostatic and mechanical boundary conditions on the phonon modes of semiconductor nanocrystals.

In recent years, several advanced technologies permit the growth of semiconductor nanocrystals (NCs) with quasi-zero-dimensional properties. The diameter of these NCs is in the range of a few nanometers.

Novel physical properties appear which suggest a broad range of device applications. While the electronic and optical properties of NCs are well understood based on the effective mass theory and have received considerable attention during the last decade, the vibrational properties (phonons confined in pherical NCs of several nanometers in size) of NCs have received much less attention until the last few years [1–4].

An accurate description of the vibrational modes of a NC is of fundamental interest and is also required to understand the coupling of vibrational modes to electronic charge. Recently it has been shown theoretically that mechanical confinement becomes important both for infrared and Raman- active phonons in the limit of small QDs size [5].

We studied a series of ZnSe NCs embedded in free-standing layers of porous Al_2O_3 with varying pore sizes. The size of the ZnSe NCs ranges from 2.1 to ∼20 nm and was determined from the photoluminescence and AFM study. The luminescence spectra of ZnSe NCs were blue-shifted to the visible spectral region compared with that of the bulk ZnSe. This energy shift allowed us to estimate the average size of NCs.

The frequencies of the coupled phonon modes with angular momentum $L_p = 1$ are interesting because they represent a more general solution with both LO and TO components including a surface mode contribution. The TO components converge to a value of 207 cm^{-1}, and the LO components to 246 cm^{-1} in the limit of large NC radii.

The vibrational modes were studied experimentally using FTIR spectroscopy. The FTIR spectra were measured with an IFS-113v Bruker Fourier – IR spectrometer at temperature 300 K. It was observed that a broad peak between the bulk TO and LO phonon frequencies, centered at (226–231) cm^{-1} dominates the spectrum. We assign the peak in the FTIR spectrum to the coupled LO-TO modes with $L_p = 1$ on the basis of our theoretical calculations for the frequencies of the coupled phonon modes.

We also recorded the Raman spectra (RS) in a backscattering configuration with the 488 nm line of an Ar-ion laser at low power to avoid darkening of the quantum dots. In the RS spectra the LO-phonon peak in ZnSe NCs was shifted to lower frequency relative to the frequency of bulk ZnSe. The IR and RS spectra of pure porous Al_2O_3 free-standing layers were made to ensure that the observed features were not due to the host material.

Two-peak behavior of the RS spectrum was observed that may be due to the presence of the of the electrostatic Frohlich mode corresponding to a uniform polarization of the ZnSe nanosphere [6]. The results show that the lattice dynamics of very small ZnSe NCs are similar to that of bulk ZnSe crystals. It is confirmed by the data obtained in [5, 7] for CdTe QDs and CdS QDs embedded in porous Al_2O_3 free-standing layers.

29.3 Germanium

Germanium (Ge) is highly transparent for the light in the range of 2–15 μm. In particular Ge lenses because of high refraction index are widely used as components for IR systems for infrared imaging systems. Typically this systems works in two spectra ranges 3–5 and 8–12 μm.

Over last several years, we constantly attempted to improve the quality of Germanium (Ge) monocrystals as per our customers' requirements. A special attention is paid for Ge manufactured for aspherical optics. Aspherical optics is free from the main traditional disadvantages of usual optics. It is possible to avoid most of distortion as well as spherical aberration. The only one Ge aspherical lens may replace 3–4 spherical lenses.

29.4 Indium Antimonide

Indium Antimonide (InSb) is the only semiconductor material which can be used for three types of photodetectors: photoconductive (photoresistance), photovoltaic and photoelectromagnetic. It is one of the main materials for photodetectors which operates in the range of 3–5 μm. The unique properties of InSb make possible to use it in the broad band of civil applications including medicine and ecological monitoring.

In our labs we are able to grow undoped InSb crystals with the following parameters:

- majority carrier concentration $2.0*10^{14}$–$2.0*10^{15}$cm^{-3} (77K), and
- mobility $5 \cdot 10^5$cm^2/V $\cdot$ s.

Table 29.1 Characteristics of InSb monocrystals

Doping	Type	Conc., cm^{-3} (77K)	Carrier mobility, $sm^2/V \cdot s$ (77K)	Dislocation density, cm^{-2}
Undopped	n-type	$2.0 \cdot 10^{14}$–$2.0 \cdot 10^{15}$	$(5.5–2.5) \cdot 10^5$	$\leq 10^2$
Dopped with Te	n-type	$2.0 \cdot 10^{15}$–$1.5 \cdot 10^{18}$	$2.5 \cdot 10^5$–$1.0 \cdot 10^4$	$\leq 10^2$
Dopped with Te	n-type poly	10^{19}–10^{22}	$\leq 7 \cdot 10^2$	–

Fig. 29.1 InSb ingot (Ø 2′)

As a result of the latest research we are happy to report our ability to make highly doped InSb wafers. We have developed a laboratory technology for production of the InSb with parameters presented in the Table 29.1 (Fig. 29.1).

29.5 Indium Arsenide

Indium Arsenide (InAs) is used for optoelectronic devices as optical filters, sources of IR emission and many other applications [8]. The range of optical activity is 3–5 μm. Devices made from InAs are tolerant to radiation and magnetic fields [9].

We use Czochralski method to pull out InAs monocrystals. The ingots diameter is 2 and 3 in. and crystallographic orientations are <100> and <111>, n and p-type crystals are doped with S or Sn up to carrier concentration not more $2.0*10^{17}$ cm^{-3}. Dislocation density for 2′ diameter is on the level of $2.0*10^4$ cm^{-2}, and for 3′ diameter is on the level of $5.0*10^4$ cm^{-2} [1].

S is more effective doping impurity than Sn in terms of the process cost and doping uniformity. Because S is highly volatile impurity it can't be used directly. We have developed sulfur compound with precise content of S. The compound content and technology of doping gave us required uniformity of crystal doping and high reproducibility of the process.

Fig. 29.2 3′ diameter ingot of monocrystal InAs (100)

Another problem of InAs (100) monocrystals growing is effect of twining. The fundamental reason of this effect is very low specific energy of the staking faults in the crystal lattice. The main provocative factor of twinning is nonstoichiometry of the melt. This problem was solved by the use of reversible materials (heap) rather than direct polycrystalline alloy of InAs. With the growth technology developed we have designed laboratory production line of (100) InAs monocrystals of 3′ diameter. The production yield is >85 % (Fig. 29.2).

29.6 $Cd_xHg_{1-x}Te$

It is well known that solid solution of $Cd_xHg_{1-x}Te$ has the most specific and important position among other IR detecting materials. Because the unique possibility of gradual change of the band gap by changing the chemical content of this solution the range of spectral sensitivity of photodetectors overlaps absorption band of the majority atmospheric gases. It also includes all the main windows of atmospheric transparency in IR range as shortwave (1–3 μm), middle wave (3–5 μm) and long wave (8–14 μm).

Giredmet has more than 30 years' experience in the fields of $Cd_xHg_{1-x}Te$ material science and technology of growth. During the last years because of the rapid growth of optoelectronic devices of far IR range our main efforts were focused on the development of the $Cd_xHg_{1-x}Te$ liquid phase epitaxy (LPE) processes and technology of $Cd_{1-y}Zn_yTe$ substrate growth. We should make a point that all these works were accompanied by development of the techniques and methods of deep purification of all the components and environments used in the processes as well as design of the special technological and test equipment.

The role of $Cd_{1-y}Zn_yTe$ substrates is crucially important. For $Cd_xHg_{1-x}Te$ layers growth by MBE and MOCVD not expensive widely available GaAs, Si or

Ge substrates can be used. But for LPE only substrates based on CdTe can be used. $Cd_{1-y}Zn_yTe$ is the best material which provides the chemical and structural compatibility of substrate and epitaxial layer. The only disadvantage of the material is its price.

We have finished a set of research works to optimize the substrate growth process, controlling structural, electrical and optical properties of material in the strong relation with content and external treatments [10, 11]. Special chamber for material growth was designed. Mathematical model of the $Cd_{1-y}Zn_yTe$ crystal growth by Bridgmen method was developed [12]. The effect of Te precipitation in $Cd_{1-y}Zn_yTe$ matrix was studied. Processes of wafer cutting, grinding and CMP of epi-ready wafers for LPE $Cd_xHg_{1-x}Te$ were developed [13].

The main parameters of $Cd_{1-y}Zn_yTe$ wafers which today are under production you can find on the site www.giredmet.ru. These days our specialists work on the technology of $Cd_xHg_{1-x}Te$ multilayer heterostructures growth. Implementation of such a technology will give us possibility to develop and produce two-range IR matrix which are expected to be the next generation of photodetectors. At the same time we are focused on the development of new perspective IR materials. One of such materials supposed to be a four component solid solution $Cd_xHg_{1-x-y}Zn_yTe$. So far we have developed technological principals for LPE this system [14].

29.7 Conclusions

We intend to bring our technologies and elaborations in IR sensors manufacturing, as well as our skills and experience to the open world market with an objective of seeking partners and customers.

References

1. Chamberlain MP, Trallero-Giner C, Cardona M (1995) Theory of one-phonon Raman scattering in semiconductor microcrystallites. Phys Rev B 51:1680–1693
2. Vasilevskiy MI, Rolo AG, Artemyev MV, Filonovich SA, Gomes MJM, Rakovich YP (2001) FIR absorption in CdSe quantum dot ensembles. Phys Status Solid B 224:599–604
3. Belogorokhov AI, Belogorokhova LI (2001) Optical phonons of circular wires in porous GaP. Phys Solid State 43:1765–1769
4. Rolo AG, Vasilevskiy MI, Gaponik NP, Rogach AL, Gomes MJM (2002) Confined optical vibrations in CdTe quantum dots and clusters. Phys Stat Sol B 229:433–437
5. Vasilevskiy MI (2002) Dipolar vibrational modes in spherical semiconductor quantum dots. Phys Rev B 66:195326–195334
6. Belogorokhov AI, Gavrilov SA, Belogorokhova LI (2003) Coupled polar optical vibrational modes of CdS semiconductor nanocrystals embedded in porous Al_2O_3. Phys Stat Sol A 197:204–207
7. Anisimova ID, Vikulin IM, Zaitov FA, Kurmashev SD (1984) Semiconducting photoreceptors – the ultraviolet, visible, near-infrared, ranges of the spectrum. Izdatel'stvo Radio i Sviaz', Moscow, 216 p (In Russian)

8. Uillardson P (1970) Optical properties of semiconductors. Mir, Moscow
9. Milvidskiy MG, Osvensky VB (1984) Structural defects in semiconductor monocrystals. Metallurgy, Moscow
10. Filachev AM, Taubkin II, Trishenkov MA (2010) The current state and the main directions of development of photoelectronic. Fizmatkniga, Moscow. ISBN 978-5-89155-191-6
11. Shmatov NI, Smirnova NA, Belov AG, Oransky VA, Shlensky AA (2006) Solid solutions of $Cd_{1-y}Zn_yTe$ – material for substrates for epitaxial structures $Cd_xHg_{1-x}Te$. Mater Electron Tech 3:28–32
12. Levonovich BN, Shmatov NI, Shlensky AA, Smirnova NA, Pashkova NV (2008) Study of electrical and optical inhomogeneities in $Cd_{1-x}Zn_xTe$ ($x \leq 0.04$) crystals, grown by VGF method. Mater Electron Tech 1:28–32
13. Averichkin PA, Andrusov JB, Grishechkin MB, Denisov IA, Smirnova NA (2011) Production of CdZnTe substrates using polyhedral methylsilsesquioxane. Mater Electron Tech 1:28–32
14. Belogorokhov AI, Belov AG, Denisov IA, Lakeenkov VM, Smirnova NA (2001) Optical properties of semiconductor solid solutions $Cd_xHg_{1-x-y}Zn_yTe$. Mater Electron Tech 4:62–66

Chapter 30
Small Carbon Molecules and Quasi-Fullerenes as Products of New Method of Hydrocarbons Pyrolysis

Oleksii Kharlamov, Ganna Kharlamova, Marina Bondarenko, and Veneamin Fomenko

Abstract Previously small carbon molecules C_2–C_{13} were detected only in hot carbon plasma as cations and anions. From clusters, smaller than C_{60}, revealed in mass spectra of carbon vapor only C_{20} and C_{36} were synthesized. Therefore the problem of establishment of methods for synthesis of carbon molecules is considered extremely important. Our new method of pyrolysis of hydrocarbons, particularly benzene, created the products which contain small carbon molecules, quasi-fullerenes and their hydrides. A distinctive feature of this method is the opportunity of separate localization of condensed products and soot. Firstly the substances are synthesized which mass spectra of toluene solutions contain intensive peaks with m/z values appropriate to anions of small molecules (C_3–C_{20}), their hydrides (C_5H_2, $C_{10}H_4$, $C_{14}H_4$, $C_{16}H_8$, $C_{18}H_2$) and cations of C_6, C_7, C_{15}, C_{17}, C_7H, C_8H, C_9H, $C_{11}H$, $C_{18}H$. Firstly, quasi-fullerenes C_{21}, C_{23}, C_{33}, C_{40}, C_{48}, C_{52} and C_{54} are found out in products of pyrolysis. Thus, small carbon molecules, quasi-fullerenes and C_{60} can be formed in reactionary conditions excluding carbon evaporation.

Keywords Pyrolysis • Fullerenes • Quasi-fullerenes • Pyridine • Benzene

O. Kharlamov (✉) • M. Bondarenko • V. Fomenko
Frantsevich Institute for Problems of Materials Science of NAS, 3 Krzhyzhanovsky st., dep. 73, 03142 Kyiv, Ukraine
e-mail: akharlamov@ukr.net

G. Kharlamova
Taras Shevchenko National University of Kyiv, 64/13, Volodymyrs'ka Str., 01601 Kyiv, Ukraine

A. Vaseashta and S. Khudaverdyan (eds.), *Advanced Sensors for Safety and Security*, NATO Science for Peace and Security Series B: Physics and Biophysics,
DOI 10.1007/978-94-007-7003-4_30,

30.1 Introduction

After discovery of fullerene C_{60} [1] and its higher homologues (C_{70}, C_{76}, C_{78}, C_{84} and more) [2, 3] the synthesis of quasi-fullerenes (smaller-sized fullerenes C_n ($20 < n < 60$), in which isolated pentagons are absent, and small carbon molecules C_n ($n < 20$)) is considered as the basic challenge to modern chemical community. The fate of small carbon molecules C_2–C_{20} and quasi-fullerenes found out simultaneously with clusters C_{60} and C_{70} in carbon vapors [1, 2] by means of a mass spectrometric method [4] has appeared less bright in comparison with fullerenes C_{60} and C_{70}. Only C_{20} [5] of more than 20 quasi-fullerenes detected in mass – spectra [6, 7] was synthesized in preparative amounts. Quasi-fullerenes C_{28} and C_{50} are obtained only as their derivative: endohedral metal-fullerene (MC_{28}) [8] and decachlor-fullerene ($C_{50}Cl_{10}$) [9]. It is should be noted that the nature of cluster C_{36} synthesized by Piskoti [10] by arc-discharge method is still unclear because in another experiment [11] only the hydrides ($C_{36}H_4$, $C_{36}H_6$) and oxyhydrides ($C_{36}H_4O$, $C_{36}H_6O$) as main products were revealed under the same reactionary conditions. Despite intensive signals in mass spectra [6, 7], neither molecular clusters C_{26}, C_{30}, C_{34}, C_{38}, C_{42}, C_{46}, C_{48}, C_{52}, C_{54}, C_{56}, C_{58} nor their endohedral derivative were found out yet. Moreover, assumed as most stable clusters C_{32} and C_{44}, as well as C_{50}, which are referred to the category «magic» in a molecular form as well are not synthesized yet.

The small carbon molecules such as C_2 and C_3, C_4 and C_5 are found out together with polyynes (HC_nN) ($n \leq 11$) only in the circumstellar medium [12]. In laboratory conditions these carbon molecules were isolated only in solid argon at about 15 K [13–17], but time of life of such frozen clusters is extremely small ($\backsim$10 ms). Even and odd ions of small carbon molecules are detected only in laboratory conditions in mass spectra of carbon vapor. It is considered [18] that the hot carbon plasma contains linear chains C_1–C_{10}, where C_3 cluster is contained in the greatest amount ($\backsim$70 %) [19]. These chains C_1–C_{10} as any chemical radicals are extremely inclined to radical polymerization and can be stabilized owing to the interaction of trailer atoms of carbon with H, N or CN with formation of relatively more stable polyynes or cyanopolyynes [18, 20]. Therefore research into creation of a new method for synthesis of carbon molecules is considered extremely important. The absence of appreciable progress in synthesis C_n ($n < 20$) and quasi-fullerenes is probably determined by domination of hypothesis that the atoms of carbon are always in need for growth of carbon molecules, and their generation is possible only under carbon sublimation.

This research presents essentially another method of generation of small carbon molecules and quasi-fullerenes as well as fullerene C_{60} and fullerenes hydrides, in which the stage of high-temperature sublimation of carbon is completely excluded. Within this work, a new method of benzene pyrolysis is developed, in which products the ions of all kinds of carbon molecules are found out:

- small carbon molecules (C_3–C_{20});
- quasi – fullerenes C_{21}, C_{23}, C_{33}, C_{40}, C_{48}, C_{52} and C_{54};

- fullerene C_{60};
- hydrides of small carbon molecules, for example, C_5H_2, $C_{10}H_4$, $C_{14}H_4$, $C_{16}H_8$ and $C_{18}H_2$;
- hydrides of quasi – fullerenes ($C_{25}H_2$–$C_{27}H_2$–...–$C_{31}H_4$–$C_{33}H_4$–... $C_{37}H_6$–$C_{39}H_6$–... $C_{43}H_8$–...–$C_{45}H_8$ ... $C_{47}H_{10}$–$C_{49}H_{10}$).

30.2 Results and Discussion

Shortly after discovery [1] and synthesis C_{60} by the electro-arc method [2], the method of heat treatment of hydrocarbons was used as an alternative [21, 22]. However, fullerenes are formed only in microamounts under usual method of pyrolysis (continuously flowing pyrolysis, CFP) [22] and under burning of hydrocarbons [21]. Products, obtained at heat treatment (<1,200 °C) of naphthalene $C_{10}H_8$, its dimer and corannulene [22, 23] as well as benzene, cyclopentadiene [24], ethylene and acetylene [25], contain only up to ∽1 % C_{60}. In the latter process of pyrolysis fullerene C_{70} is formed only at the presence of metallic (nickel) catalyst [26]. Hence, known methods of hydrocarbons pyrolysis are low effective. Though the obtained experimental results convincingly demonstrate that the formation of C_{60} and C_{70} can be realized in the absence of atoms (or clusters) of carbon from hot carbon gas.

Earlier, we proposed [27, 28] the polycondensation mechanism of carbon molecules and nanostructures growth at hydrocarbons pyrolysis according to which the escalating of bonds C–C with formation of graphene net can be fulfilled due to a reaction of dehydropolymerization (polycondensation) mainly of benzene molecules and products of their partial decomposition. The curvature of graphene net is created at the expense of trailing, peripheral sp^3 – hybridization atoms of carbon. At the pyrolysis (as well as at cracking) of hydrocarbons the escalating of bonds C–C is realized also according to reaction of polymerization with formation of polyaromatic hydrocarbons. The reactions of polycondensation and polymerization are competitive in the given process and therefore one of them is obviously possible for optimizing by means of the variation of reactionary conditions.

Under the systematic investigation [27–30] we have studied the influence of various technological parameters and reactionary factors on obtained product composition and, in particular, on the composition of a condensation product. As a result of this research, the new method of heat treatment of organics vapours was developed. This method differs from two already known processes of pyrolysis that are used long ago and for different purposes. Flash vacuum pyrolysis (FVP) [31, 32] is used mainly to prepare small size, highly reactive objects. CFP [22, 31] is employed for obtaining both carbon nanostructures of different morphologies and large polyaromatic molecules. Novel method of pyrolysis allows obtaining simultaneously not only carbon nanostructures but as well fullerene C_{60}, and fullerenes hydrides [30, 33–35].

The distinctive feature of our method is the possibility of partial division of products of deposition and condensation, their subsequent localization in different

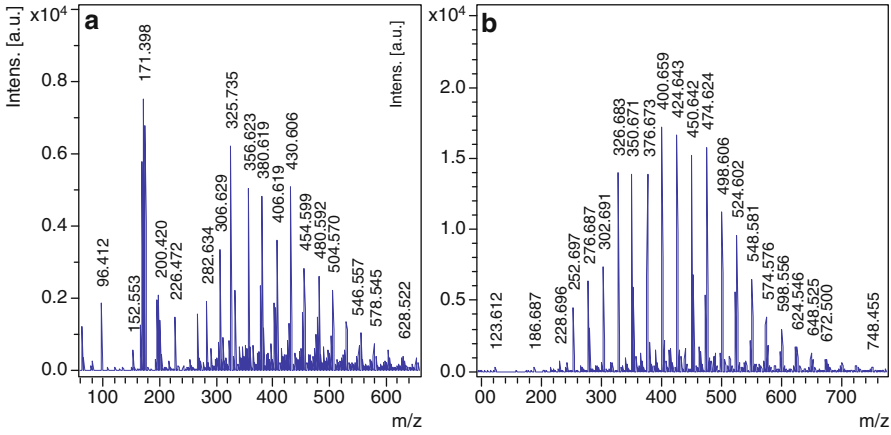

Fig. 30.1 Anions (**a**) and cations (**b**) mass spectra of toluene extract from the product B_1

zones of reactionary space. Besides the time of standing of reagents in the most high-temperature (∽1,000 °C), zone A of reaction can be varied in a wide interval that allows in the certain moment to interrupt a course of reaction and to obtain the intermediate products. A part of condensation substances and pyrolytic soot are taken out in a gas reactionary flow from a zone A and are located in more low temperature zone B. Another part of vapour-like products (sometimes along with very small amount of pyrolytic soot) is condensed in the special zone C – cooled reactionary space. Depending on temperature in a zone A and time of standing in this zone, reagents vary as a composition of products in zones B and C but as well as their amount. The results of study of two products (B_1 and B_2) of heat treatment of benzene vapours condensed in zones B and one product (C_1) condensed in a zone C are submitted.

B_1 product is obtained at lower temperature zone A, than product B_2. The reaction of polymerization in comparison with competitive reaction of polycondensation in the thermodynamic relation should be more preferable at lower temperature. Therefore according to the mechanism, we assume the product B_2 should contain mainly carbon clusters and product B_1 – hydrides of carbon clusters. Toluene extract from B_1 was investigated by method of mass spectrometry matrix-assisted laser desorption/ionization (MALDI) (Bruker Daltonics flexAnalysis). It is visible (Fig. 30.1) that mass spectra of positive and negative ions cardinally differ.

In a group of positively charged clusters (Fig. 30.1b), beginning from the cluster with value m/z 252 and finishing cluster with value m/z 648, there is a precise periodicity in growth of their size. Every subsequent cluster grows on 24 or 26 units only. Clusters with values m/z 228, 252, 276, 480, 624 and 648, probably, correspond to molecules C_{19}, C_{21}, C_{23}, C_{40}, C_{52} and C_{54}. (Usually it is believed that clusters C_{52}, C_{54} and C_{56}, C_{58} which detected in mass spectra of C_{60} are products of its decomposition) [36]. Peaks with m/z from 302 up to 598 can belong both as to a little hydrogenated odd ($C_{25}H_2$–$C_{27}H_2$–…–$C_{31}H_4$–$C_{33}H_4$–… $C_{37}H_6$–

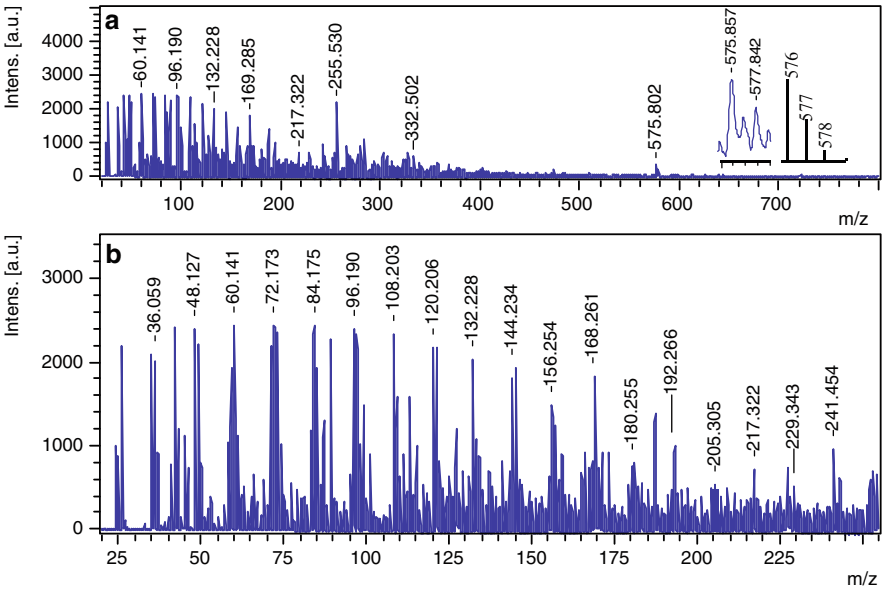

Fig. 30.2 Anions mass spectrum of toluene extract from the product B_2 with the expansions of the experimental and theoretical isotope distributions for C_{48} in the inset (**a**); m/z 20–250 region (**b**)

$C_{39}H_6$–... $C_{43}H_8$–...–$C_{45}H_8$–... $C_{47}H_{10}$–$C_{49}H_{10}$) as to even clusters, but with the large contents of hydrogen ($C_{24}H_{12}$–$C_{26}H_{12}$–...–$C_{48}H_{22}$). The last one in the given group of peaks is a cluster with m/z 748 which corresponds to hydride $C_{60}H_{28}$. It is possible, that positively charged cluster with m/z 124 corresponds to hydride ($C_{10}H_4$) of small molecule C_{10}.

In a spectrum of negative ions (Fig. 30.1a) peaks with m/z 172 and 326 considerably dominate and they can correspond to partially hydrogenated molecules $C_{14}H_4$, and $C_{27}H_2$. The less intensive peaks with m/z 62, 200 and 96, probably, also display presence of hydrides C_5H_2, $C_{16}H_8$ and molecule C_8 at a product B_1. Also there is a group of peaks at a spectrum, which m/z values differ from 24 to 26 units. Among them there is a distinct peak with value m/z 480 that can correspond to quasi-fullerene C_{40}. Only cluster $C_{27}H_2$ is detected in both spectra. Positively charged cluster C_{52} (m/z 624) is shown in a spectrum of negative ions as hydride $C_{52}H_4$ (m/z 628). It is noted that negatively charged clusters ($C_{30}H_{20}$ and $C_{34}H_{22}$) are, as a rule, more hydrogenated than appropriate positively charged ($C_{30}H_{16}$ and $C_{34}H_{16}$).

Soluble in toluene substances were extracted and deposited by ethanol from a product B_2 obtained at the minimal concentration of benzene vapours in a zone A. Deposited powder B_2 was again dissolved in toluene and mass spectra of this solution are submitted in Figs. 30.2 and 30.3. In a spectrum of negative ions (Fig. 30.2) there is a group of peaks, in which the periodicity of change of m/z values makes 12 units. Such m/z values as 36, 48, 60, 72, 84, 96, 108, 120, 132, 144, 156, 168, 180 and 204 (Fig. 30.2b), undoubtedly, concern to small carbon molecules

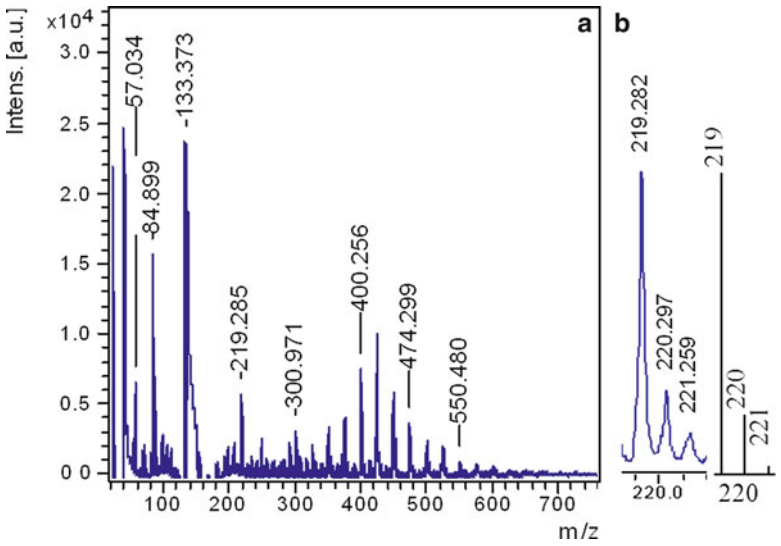

Fig. 30.3 Cations mass spectrum of toluene extract from the product B_2 (**a**), the expansions of the experimental and theoretical isotope distributions for $C_{18}H_3$ (**b**)

C_3, C_4, C_5, C_6, C_7, C_8, C_9, C_{10}, C_{11}, C_{12}, C_{13}, C_{14}, C_{15} and C_{17} accordingly. It is considered [37, 38] that there are a line and a ring C_n $(2 > n < 20)$ clusters with carbon atoms in the sp-hybridization formed in the carbon vapour. Clusters with m/z 193, 217, 229, 241, 255 and 326 can correspond to anions $C_{16}H$, $C_{18}H$, $C_{19}H$, $C_{20}H$, $C_{21}H_3$, $C_{27}H_2$ which under the ionization by laser of minimally hydrogenated cyclic molecules (or linear polyynes [39] $C_{16}H_2$ … $C_{27}H_2$ are formed).

In the spectrum of negative ions the peak 576 is present, which may correspond to quasi-fullerene C_{48}. The peak with m/z 326 ($C_{27}H_2$) was also detected in the mass spectrum of the product B_1 (Fig. 30.1). Note, that in the mass spectrum of high-resolution (Fig. 30.2a, inset) it can be seen that the molecule C_{48} is hydrogenated, because the ratio in this molecule is garbled in comparison to characteristic one for the natural isotopic distribution of carbon molecule [40]. The formation of small carbon clusters as a result of degradation of C_{60} is unlikely. It is likely that the clusters C_3–C_{15} and their hydrides are new products of the pyrolysis of benzene, which are formed at a temperature of 1,000 °C, eliminating the evaporation of carbon.

Spectrum of positive ions (Fig. 30.3a) contains three intensive peaks with m/z 84, 133 and 219, which can display molecules C_7, C_{11} (or $C_{11}H$) and $C_{18}H_3$. Just these clusters detected by mass spectrometric method as cations as anions, are, probably, most stable among small carbon molecules. Cation mass spectra of high resolution (Fig. 30.3b) demonstrates that cluster with number carbon atoms ($n = 18$) is hydrogenated.

So, the products B_1 and B_2 deposited together with soot contain small carbon molecules from C_3 up to C_{15}, quasi-fullerenes C_{21}, C_{23}, C_{40}, C_{48}, C_{52}, C_{54}, fullerene

C_{60} and hydrides of carbon molecules of different sizes, particularly, $C_{14}H_2$, $C_{16}H_8$, $C_{18}H_2$, $C_{20}H_2$. If the small carbon molecule can only be a cyclic structure with polyynic (even molecules C_{2n}) or cumulenic bonds (Fig. 30.4a, inset), the dihydrides of these molecules can be both cyclic and linear (polyynes) structures.

Product of C represents white crystalline transparent plates which are formed under any regimes of heat treatment of benzene vapors. Sometimes these plates are located on a surface of deposited soot in reactionary C zone. Anions mass spectrum of an ethanol solution of this product is submitted in Fig. 30.4. It is visible that the spectrum of negative ions (Fig. 30.4b) contains mainly a group of the most intensive peaks, which, as well as in mass – spectrum of a product B_2, correspond to anions of small carbon molecules from C_3 up to C_{20}. At the spectrum there are also peaks with m/z 720 and 846, characteristic for C_{60} and $C_{70}H_6$.

At mass spectrum of positive ions peaks with m/z 85, 97 and 109 are present, which can correspond to ionizing by proton molecules C_7, C_8 and C_9. Four distinct peaks at m/z 72, 120, 180 and 204 correspond to minimally hydrogenated molecules C_6, C_{10}, C_{15} and C_{17}. Hence, the small carbon molecules are detected mainly as anions but their hydrides are as cations. Only molecules C_6, C_{10}, C_{15} and C_{17} are detected in both spectra.

It is unlikely that in the products B_2 and C there is containing of practically the full spectrum of small carbon molecules. It is possible that the product B_2 contains mainly molecule C_7, C_{11} and C_{18}, which are recorded in the mass spectra in the form of cations (Fig. 30.3) and anions (Fig. 30.2). Under the impact of the laser from these molecules anions mostly of smaller molecules of carbon are formed. In a product C mainly molecules C_{15}, C_{17}, C_{18} and C_{20} can break up at laser ablation.

30.3 Conclusions

In this chapter, we report the experimental results obtained under the realization of the novel method of benzene pyrolysis. For the first time, it is demonstrated that the small carbon molecules (C_3–C_{20}), quasi-fullerenes C_{21}, C_{23}, C_{40}, C_{48}, C_{52}, C_{54} can be obtained in reactionary conditions excluding evaporation of carbon. Earlier such carbon molecules were detected only as ions in hot carbon plasma. First solid substances are synthesized, in which mass-spectra clusters are present that are appropriate to small carbon molecules. Before such molecules were detected in circumstellar medium and in a matrix of solid argon at the temperatures ∽15–24 K. One of distinctive features of the novel method of pyrolysis is the opportunity to separate localization of a part of the condensed products and soot formed at the heat treatment (∽1,000 °C) of benzene. First, the method of joint synthesis of carbon molecules and their hydrides is developed. Usually the hydrides fullerenes were obtained exclusively by hydrogenation of carbon molecules.

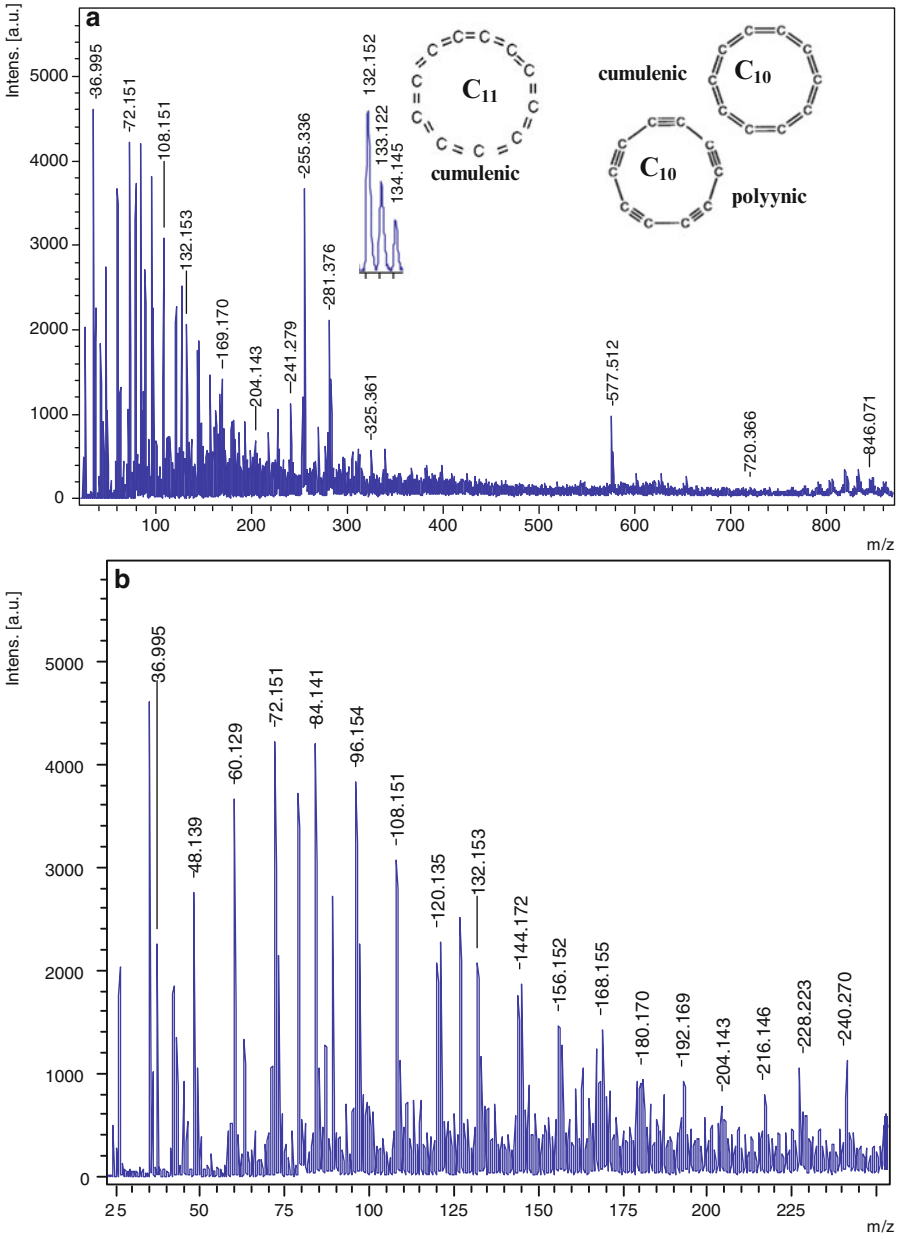

Fig. 30.4 Anions mass spectrum of toluene extract from the product C with the expansions around m/z 132 peak and molecules C_{10}, C_{11} schemes in the inserts (**a**); m/z 35–250 region of anions mass spectrum of the product C (**b**)

References

1. Kroto HW, Heath JR, O'Brien SC et al (1985) C60: buckminsterfullerene. Nature 318:162–163
2. Kratschmer W, Lamb LD, Fostiropoulos K, Huffman DR (1990) Solid C60: a new form of carbon. Nature 347:354–358
3. Kroto HW (1990) C60: fullerenes, giant fullerenes and soot. Pure Appl Chem 62:407–415
4. Rohlfing C, Kaldor J (1984) Production and characterization of supersonic carbon cluster beams. Chem Phys 81:3322–3330
5. Prinzbach H, Weiler A, Landenberger P et al (2000) Gas-phase production and photoelectron spectroscopy of the smallest fullerene, C_{20}. Nature 407:60–63
6. Kietzmann H, Rochow R, Ganteför G, Eberhardt W (1998) Electronic structure of small fullerenes: evidence for the high stability of C_{32}. Phys Rev Lett 81:5378–5381
7. Kroto HW (1987) The stability of the fullerenes C_n (n = 24, 28, 32, 50, 60 & 70). Nature 329:529–531
8. Guo T, Diener MD, Chai Y et al (1992) Uranium stabilization of C_{28}: a tetravalent fullerene. Science 257:1661–1664
9. Xie SY, Gao F, Lu X et al (2004) Capturing the labile fullerene [50] as $C_{50}Cl_{10}$. Science 304:699
10. Piskoti C, Yarger J, Zettl A (1998) A new carbon solid, C_{36}. Nature 393:771–774
11. Koshio A, Inakuma M, Sugai T, Shinohara H (2000) A preparative scale synthesis of C_{36} by high temperature laser vaporization: purification and identification of $C_{36}H_6$ and $C_{36}H_6O$. J Am Chem Soc 122:398–399
12. Cataldo F (2004) Cyanopolyynes: carbon chains formation in a carbon arc mimicking the formation of carbon chains in the circumstellar medium. Int J Astrobiol 3:237–246
13. Weltner WJ, Walsh PN, Angell CL (1964) Spectroscopy of carbon vapor condensed in rare-gas matrices at 4° and 20°K. I. J Chem Phys 40:1299–1305
14. Maier JP (1997) Electronic spectroscopy of carbon chains. Chem Soc Rev 26:21–28
15. Wakabayashi T, Krätschmer W (2006) Chapter 1: Carbon chain molecules in cryogenic matrices. In: Cataldo F (ed) Polyynes synthesis, properties, and applications. Taylor & Francis Group, New York, pp 1–15
16. Presilla-Márquez JD, Sheehy JA, Mills JD et al (1997) Vibrational spectra of cyclic C_{60} in solid argon. Chem Phys Lett 274:439–444
17. Cermak I, Förderer M, Kalhofer S et al (1998) Laser–induced emission spectroscopy of matrix–isolated carbon molecules: experimental setup and new results on C3. J Chem Phys 108:10129–10142
18. Cataldo F (2003) Simple generation and detection of polyynes in an arc discharge between graphite electrodes submerged in various solvents. Carbon 41:2653–2689
19. Zavitsanos PD, Carlson GA (1973) Experimental study of the sublimation of graphite at high temperatures. J Chem Phys 59:2966–2973
20. Heath JR, Zhang Q, O'Brien SC et al (1987) The formation of long carbon chain molecules during laser vaporization of graphite. J Am Chem Soc 109:359–363
21. Howard JB, McKinnon JT, Makarovsky Y et al (1991) Fullerenes C_{60} and C_{70} in flames. Nature 352:139–141
22. Taylor R, Langley GJ, Kroto HW, Walton DRM (1993) Formation of C_{60} by pyrolysis of naphthalene. Nature 366:728–731
23. Crowley CJ, Taylor R, Kroto HW et al (1996) Pyrolytic production of fullerenes. Synth Met 77:17–22
24. Osterodt J, Zett A, Vögtle F (1996) Fullerenes by pyrolysis of hydrocarbons and synthesis of isomeric methanofullerenes. Tetrahedron 52:4949–4962
25. Jenkins GM, Holland LR, Maleki H, Fisher J (1998) Continuous production of fullerenes by pyrolysis of acetylene at a glassy carbon surface. Carbon 36:1725–1727
26. Conley NR, Lagowski JJ (2002) On an improved pyrolytic synthesis of [60]- and [70]-fullerene. Carbon 40:949–953

27. Kharlamov AI, Loythenko SV, Kirillova NV et al (2004) Toroidal nanostructures of carbon. Single-walled 4, 5 and 6 hedrons and nanorings. Rep Natl Acad Sci Ukraine 1:95–100
28. Kharlamov AI, Ushkalov LN, Kirillova NV et al (2006) Synthesis of onion nanostructures of carbon at pyrolysis of aromatic hydrocarbons. Rep Natl Acad Sci Ukraine 3:97–103
29. Kharlamova G, Kharlamov A, Kirillova N, Skripnichenko A (2008) Novel transparent molecular crystals of carbon. In: Vaseashta A, Mihailescu I (eds) Functionalized nanoscale materials, devices, and systems. Springer, Dordrecht, pp 373–379
30. Kharlamov AI, Kirillova NV (2009) Fullerenes and hydrides of fullerenes as products transformation (polycondensation) of molecules of aromatic hydrocarbons. Rep Natl Acad Sci Ukraine 5:110–118
31. Brown RFC (1980) Pyrolytic methods in organic chemistry: application of flow and flash vacuum pyrolytic techniques. Academic, New York
32. Plater MJ, Praveen M, Schmidt DM (1997) Buckybowlsynthesis: a novel application of flash vacuum pyrolysis. Fuller Sci Technol 5:781–800
33. Kharlamov A, Kharlamova G, Khyzhun O, Kirillova N (2011) New substances: red carbon suboxide, red N-doped fullerene $(C_{50}N_{10})O_3H_{10}$ and red carbon. In: Zaginaichenko S, Schur D, Skorokhod V (eds) Carbon nanomaterials in clean – energy hydrogen systems. Springer, Dordrecht, pp 257–268
34. Kharlamov O, Kharlamova G, Kirillova N et al (2012) Synthesis of new carbon compounds: N-doped fullerene (C50N10)O3H10 and "Pyridine" nanocarbon. In: Vaseashta A, Braman E, Susmann P (eds) Technological innovations in sensing and detection of chemical, biological, radiological, nuclear threats and ecological terrorism. Springer, Dordrecht, pp 245–253
35. Kharlamov AI, Bondarenko ME, Kirillova NV (2012) New method for synthesis of fullerenes and fullerene hydrides from benzene. Russ J Appl Chem 85:233–239
36. Whetten RL, Alvarez MM, Anz SJ et al (1991) Spectroscopic and photophysical properties of the soluble C_n molecules, $n = 60, 70, 76/78, 84$. Mater Res Soc Symp Proc 206:639–650
37. Jones RO (1999) Density functional study of carbon clusters C_{2n} $2 < n < 16$. I. Structure and bonding in the neutral clusters. J Chem Phys 110:5189–5200
38. Yang S, Taylor KJ, Craycraft MJJ et al (1988) UPS of 2-30-atom carbon clusters: chains and rings. Chem Phys Lett 144:431–436
39. Cataldo F (2004) Synthesis of polyynes in a submerged electric arc in organic solvents. Carbon 42:129–142
40. Beynon JH (1960) Mass spectrometry and its applications to organic chemistry. Elsevier, New York

Chapter 31
Hetero-Carbon: Heteroatomic Molecules and Nano-structures of Carbon

Ganna Kharlamova, Oleksii Kharlamov, Marina Bondarenko, Nadezhda Gubareni, and Veneamin Fomenko

Abstract The hetero-carbon as hetero-fullerenes, hetero-graphene and hetero-nanotubes are considered as unique nanosensors which properties essentially differ from properties of undoped molecules and nanostructures of carbon. Products of a new method of pyrolysis (NMP) of pyridine by mass – spectrometric method are investigated. Fullerene C_{60} and its hydrides ($C_{60}H_6$), small carbon molecules C_3–C_{11}, quasi-fullerene C_{48} and new heteroatomic fullerene-like molecules such as functionalized polyazafullerenes $(C_{35}N_5)H_9$, $(C_{45}N_5)(OH)_3H_{14}$ and $(C_{49}N_{11})(OH)_5H_{18}$ with the large contents of nitrogen are basic substances formed at NMP of pyridine. The formation of undoped molecules C_{60}, $C_{60}H_6$ and C_{48} could be carried out only from fragments C_2H_2, C_3H_3, C_4H_4 and C_5H_5 of destruction of C_5NH_5 molecules. The growth of heteroatomic molecules is carried out with participation of pyridine molecules or the product of their dehydrogenation (C_5N).

Keywords Nanosensors • Pyrolysis • Fullerenes • Azafullerenes • Quasi-fullerenes • Pyridine • Benzene

31.1 Introduction

The opening of a unique state of carbon as closed spheroidal molecules and nanostructures and tremendous interest of the experimentalists and "chemical modelers" (simulate virtual or already existing objects) to study and forecasting properties

G. Kharlamova (✉)
Taras Shevchenko National University of Kyiv, 64/13, Volodymyrska Str., 01601 Kyiv, Ukraine
e-mail: akharlamova@ukr.net

O. Kharlamov • M. Bondarenko • N. Gubareni • V. Fomenko
Frantsevich Institute for Problems of Materials Science of NAS, 3 Krzhyzhanovsky st., dep. 73, 03142 Kyiv, Ukraine

A. Vaseashta and S. Khudaverdyan (eds.), *Advanced Sensors for Safety and Security*,
NATO Science for Peace and Security Series B: Physics and Biophysics,
DOI 10.1007/978-94-007-7003-4_31,

of these objects, was stimulated by new attempts to obtain "in a similar state" various nanoforms of hetero-carbon. What is Hetero-Carbon? Hetero-Carbon are heteroatomic molecules (fullerenes, single-walled nanotubes) and nanostructures (graphene, multi-walled nanotubes, onions, and another) of carbon in graphene layer in which one or several atoms of carbon are replaced with atoms of other element such as boron, nitrogen and silicon. The atoms of nitrogen and boron as the donors and acceptors of electrons, are the most typical replacing elements (dopants) in carbon materials. Basically, the replacement of atoms of carbon with formation of hetero-carbon can be carried out practically in all known allotropic modifications and nanostructural forms of carbon. However, the greatest interest represents the obtaining of hetero-carbon as hetero-graphene, hetero-fullerene and hetero-nanotubes. By replacing carbon atoms in fullerene cage with atoms of nitrogen and boron, there is formation of BN-doped fullerene or azaborafullerene. A question than arises – what, if any, are other interesting nanoforms of hetero-carbon? It is supposed that these derivatives, because of brightly expressed asymmetry of distribution of electronic density in graphene layer will have the unusual electronic and optical characteristics, which will allow creation of new effective catalysts and supports, functional active adsorbents and perspective nanomaterials for application in chemistry, medicine and nanoelectronics.

The first results on the use of some nanoforms of hetero-carbon in quality of nanosensors seemed to appear extremely important. So according to [1], the molecule of BN-doped fullerene (azabora [60] fullerene) serve as a nanoscale sensor to differentiate of adenine and its rare isomer Cu(II) complexes which their chemical identification practically impossible. The molecule of adenine by atom of nitrogen is fixed on the boron atom of azabora [60] fullerene. (As a reminder, adenine ($C_5H_5N_5$) is a part of many vital compounds in living organisms, such as adenosine, a adenosine triphosphate (ATP), adenosine phosphoric acids, nucleic acids, adenine nucleotides, etc.). In [2], it is noted that N-substituted carbon nanotubes (CNTs) show significant advantages over undoped nanotubes for gas sensor applications for detection various gases (NH_3, NO_2, O_2, N_2, CO_2, CH_4, H_2O, H_2, Ar) and solvents vapors (ethanol, acetone, chloroform, gasoline, pyridine, benzene) (Fig. 31.1).

Sensors based on N-doped CNTs showed advantages over undoped nanotubes because they have higher sensitivities and response times (0.1–1 s) [2]. A sensor on a basis monolayer N-graphene is capable of detecting rhodamine B (RhB), to which usual undoped graphene is tolerant [3]. (RhB – Rhodamine B ($C_{28}H_{31}ClN_2O_3$) is an indicator and a dye. It is often used as a tracer, a biomarker in oral rabies vaccines.) Application of water-soluble fullerene derivatives, for example $C_{60}O$ (fullerene epoxide), to medical biology is considered also extremely perspective [4]. Effective gene delivery in vitro and in vivo on mice with tetra (piperazino) fullerene epoxide (TPFE) and its superiority to Lipofectin have been successfully implemented and described. No toxicity of TPFE was found for the liver and kidney, although Lipofectin significantly increased liver enzymes and blood urea nitrogen. The delivery of an insulin gene to female mice increased plasma insulin levels and reduced blood glucose concentrations, indicating the potential of TPFE-based gene

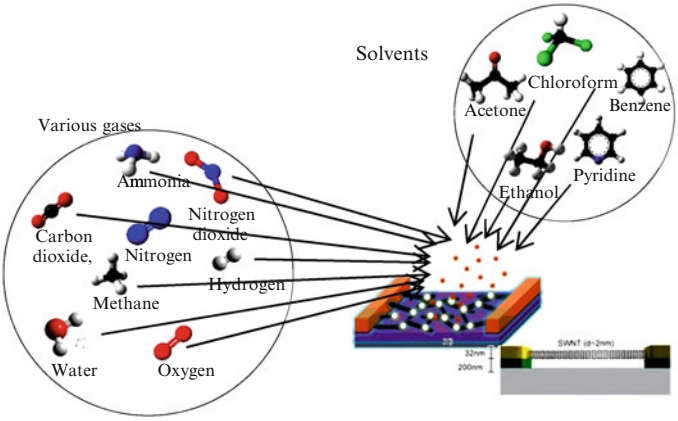

Fig. 31.1 Application of N-substituted carbon nanotubes as various gases and solvents vapours nanosensors

delivery for clinical application. In conclusion, this study demonstrated effective gene delivery in vivo for the first time using a water-soluble fullerene.

In the present communication all known forms of hetero-carbon are described, the ways of their preparation, and for the first time perfectly new monoatomic and heteroatomic molecules of carbon are discussed, which can be perspective objects for creation of selective and highly effective nanosensors.

31.2 Hetero-Fullerenes

Having researched the opening of spheroidal molecules and nanostructures of carbon as well as a graphene and development of ways of synthesis of these objects in preparative amounts, research in the area of nanochemistry of carbon is now concentrated on development of methods of synthesis of their derivative. In contrast to nanotubes and grapheme, for fullerenes there are three basic derivatives.

1. Endohedral fullerenes are fullerene derivatives that have atoms, ions, clusters or molecules incapsulated within fullerene cage.
2. Exohedral fullerenes can be as fullerene salts and exohedral adducts:
   - fullerene salts are fullerene with adducts (other atoms, molecules, functional groups) situated outside the fullerene cage;
   - exohedral adducts are fullerene on-ball addition due to opening C = C bond other atoms, molecules, functional groups.
3. Hetero-fullerenes are fullerenes in which cage one or more of the carbon atoms are replaced by other atoms.

31.2.1 Azafullerenes

N-endohedrally doped fullerene is formed, in particular, at the introduction of atom (or molecule) nitrogen, molecule of ammonia or some consistently «enclosed» (built – in) each other molecules (so-called 'Russian-doll' fullerenes) in a cavity of fullerene cage. The example N-doped endohedral fullerenes can be molecules $N@C_{60}$ [5], $N_2@C_{60}$ [6], $(NH_3)2@C_{60}$ [7], $N_2@Sc_4@C_{60}$ [8] $Sc_3@NC@C_{80}$ [9].

N – hetero-fullerene or azafullerene contains one or several atoms of nitrogen in fullerene cage instead of atoms of carbon: $(C_{59}N)_2$, $C_{57}N_3$.

For synthesis of azafullerenes, as well as for obtaining of hetero-graphene and hetero-nanotubes, as a rule, two basic approaches are used:

- introduction of atoms of nitrogen in graphene nets of different nanoforms of carbon during their heat treatment in nitrogen-containing atmosphere: nitrogen or ammonia;
- direct synthesis of nanoforms of carbon with participation of nitrogen-containing compounds such as acetonitrile, melamine, methane, pyridine, iron phtalocyanine, dimethylformamide.

The first attempts of obtaining of N-doped carbon were carried out 50 years back [10, 11] when the carbon containing up to 0.5 at of % N was obtained. Later works [12] showed that the degree of replacement by atoms of nitrogen of atoms of carbon in graphene sheets essentially depends on a method of nitrogenation and structure of carbon nanoform. At use of a catalyst, the degree of nitrogenation of carbon structure usually raises, however formed product, thus, substantially becomes soiled by the catalyst.

The first publication [13] about possible synthesis of hetero-fullerene had appeared already after 1 year after the preparation of fullerene C_{60} in a solid [14] (or after 6 years after its opening [15]). Rao [13] on the basis of the analysis of mass – spectra of toluene extracts from fullerene soot had concluded that the peaks with m/z from 722 up to 768 correspond to heteroatomic molecules of carbon: $C_{59}N_2$, $C_{59}N_4$, $C_{59}N_6$ и $C_{70}N_2$. Analyzed fullerene soot at arc evaporation of graphite in the presence of nitrogen (or ammonia) was obtained. In spite of the fact that down to the present time these data have not found yet confirmation (any of these heteroatomic molecules of carbon is not obtained yet), the interest to hetero-fullerenes has appeared extremely huge. An ion monoreplaced azafullerene $C_{59}N^-$ was for the first time [16] is found out in mass – spectrum of toluene extract of fullerene soot obtained by an arc method in an atmosphere of nitrogen. The peak at m/z 722 in mass – spectra of products of bombardment by ions of nitrogen (N^+) a mix of vapors of C_{60} and C_{70} also was identified in [17] as an ion of hetero-fullerene $C_{59}N^+$. Later [18] peaks at m/z 723 and 724 were identified as ions dihydroazafullerene $C_{59}NH^+$ и $C_{59}NH_2^+$. The ion of hetero-fullerene $C_{59}N^+$ was found out also in mass – spectra of products formed at electro-arc

evaporation of graphite at presence of pyrrole vapors [19] and at bombardments N-methoxyethoxy methyl ketolactam [20, 21]. The values m/z 722 and 842, which are identified with ions $C_{59}N^+$ and $C_{69}N^+$, were found out also in mass – spectra of the products formed at laser ablation of graphite in an atmosphere heated up азота [22]. Experiments with an isotope $^{15}N_2$ and the data of XPS convincingly have confirmed, as considered in [22], existence in analyzed products of N-containing molecules of carbon. In [22], it is shown that the value of energy of bond N1s in heteroatomic molecules makes 400.7 eV that almost on 1 eV is higher, than for nitrogen atom in pyridinic or pyrrolic states. It is necessary to mention that as compared to borafullerenes, azafullerenes by laser ablation in a nitrogen-containing target (for example, composite C/BN) are not formed [23].

However numerous attempts by several experts in area of gas-phase transformations of carbon to isolate carbon from heteroatomic vapor molecules were unsuccessful. Undoubtedly, it is connected to extremely high reaction ability of molecules, as for example, NC59 has no coupled electron with carbon or nitrogen atom. The small carbon molecules of polyynic or polycumulenic structure, which also are detected in mass – spectra carbon vapor, isolate owing to freezing in firm neon (or argon) [24] or as a result of connection to trailer atoms of carbon of atoms of nitrogen, hydrogen or CN with formation concerning more stable polyynes or cyanopolyynes [25]. (Please be reminded that cyanopentaacetylene ($HC_{11}N$) usually is present at interstar space [26]).

The problem of azafullerenes preparation, which ions are convincingly detected in mass – spectra of carbon vapor, was decided essentially by other method. Practically simultaneously, two groups of the authors [21, 27] have developed a liquid-phase route of obtaining of azafullerenes and their derivatives from fullerenes. For the first time in 1995 by group Hummelen [21] from fullerene C_{60} was synthesized N-methoxyethoxy methyl ketolactam from which further was prepared in microamounts dimer $(C_{59}N)_2$ [21] of ion monoazafullerene $(C_{59}N)^+$. Synthesis begins with a 1,3-dipolar cycloaddition methoxyethoxy methyl azide (MEM-N_3) to fullerene C_{60}. A little bit later (in 1996) Nuber and Hirsh developed a new liquid-phase route of synthesis from fullerenes dimers $(C_{59}N)_2$ and $(C_{69}N)_2$. The authors [27] synthesized $(C_{69}N)_2$ at heating butylamino adducts of diazafullerenes with toluene-*p*-sulfonic acid. Bisadducts of diazafullerene (for example C_{60}-N-methoxyethoxy methyl (MEM)-bisadduct) were also obtained by interaction of appropriate fullerene with MEM-azide [28].

In [29], the study reported obtaining in microamounts triazafullerene $C_{57}N_3$ fixed on a surface of the platinum catalyst. A polycyclic aromatic molecule $C_{57}H_{33}N_3$ as precursor for synthesis $C_{57}N_3$ was prepared by means of complex (11 stages) process. A molecule $C_{57}H_{33}N_3$, besieged on a surface of the platinum catalyst, cyclodehydrogenated at temperature 750 K. The energy of bond N1s in obtained $C_{57}N_3$/Pt makes 400.7 eV that in opinion [29], testifies to interaction of atom of nitrogen with atom of carbon in sp^2-hybridization.

Attempts to obtain azafullerenes with plenty of atoms of nitrogen in fullerene cage were unsuccessful. In 1999 Tobe by mass – spectrometric method has found out an ion $C_{58}N_2^-$at a laser irradiation of macrocyclic polyynes, containing pyridinic cycle (pyridinophanes) of composition $C_{58}H_4N_2$ [30]. However diazafullerene $C_{58}N_2$ and its derivatives were not synthesized subsequently.

It is necessary here to mention work [31], in which on the basis of the data electronic microscope and spectroscope of losses of electrons energy, the opportunity of existence of azafullerene $C_{48}N_{12}$ in a core of onion-like carbon structure formed in C- and N-containing films is discussed. These films at magnetron sputtering of a graphite target in an atmosphere of nitrogen were prepared. However azafullerene of composition $C_{48}N_{12}$ as individual substance till now is not synthesized yet. Thus, it is possible to sum up that now only mono-replaced azafullerenes as dimers $(C_{59}N)_2$ and $(C_{69}N)_2$ are synthesized in preparative amounts.

31.2.2 Borafullerenes

The first information on an opportunity of formation of heteroatomic molecules of fullerene has appeared in 1991 [32, 33], when in carbon plasma obtained at laser ablation of a target from a composite graphite/BN, by mass – spectrometric method were detected borafullerenes $C_{60-n}B_n$ (n = 1–6). In 1996 the ions of mono-replaced borafullerenes ($C_{59}B^-$, $C_{69}B^-$) were found out in mass – spectra of pyridine [34] and toluene [35] of extracts from products of arc synthesis. Graphite electrodes contained boron, BN or B_4C. A photo-electronic spectrum (the peak 188.8 eV) [34] has shown the presence of a boron in an analyzed product. The ions of borafullerenes with the large contents of boron atoms ($C_{60\text{-}n}B_n$ (n = 1, 2, 3)) were detected in mass – spectra of an *o*-xylene extract from fullerene soot [36], obtained at use as electrodes of a graphite or B_4C/graphite composite. Extraction of a product, as especially it is marked in [36], carried out at absence of access of oxygen and moisture of air (in an atmosphere of nitrogen).

Monosubstituted borafullerenes C_{60} and C_{70} also were found out by mass-spectrometric method in products of plasma chemical synthesis of fullerenes at presence at reactionary space of boron oxide (B_2O_3) [37, 38]. (Boron was inputted into arc as powdery B_2O_3). Synthesis carried out in a high-frequency arch (into HF-arc) at atmospheric pressure. Monoborafullerene $C_{59}B$ was allocated as a solid solution $C_{59}B^{\bullet}C_{60}$ (contents $C_{59}B$ -11 %). The authors [38, 39] believe, that borafullerene in $C_{59}B^{\bullet}C_{60}$ forms dimer $(C_{59}B)_2$, as the signal from radical $C_{59}B^{\bullet}$ was not registered in a EPR-spectrum of a product. By a method HPLC the authors [39] managed to isolate a fraction of borafullerene in a solution of benzene and to investigate by its methods by emission spectroscopy, NMR and IR-spectroscopy.

Data of NMR and emission spectroscopy have confirmed a boron presence in the analyzed product. Some deviation of an experimental IR-spectrum from settlement, in opinion of the authors [39], is a consequence of dimerisation $C_{59}B$. It is necessary to note, that any attempts to allocate a borafullerene in the crystal form from their solutions (in toluene [35], ortho-xylene [36], pyridine and tetrahydrofuran

[34]) have appeared unsuccessful, as resulted in complete decomposition of a product. When taken from a solution, a product has appeared extremely unstable and sensitive to a moisture, that results in its decomposition with formation of boron oxide or boron acid [34].

31.2.3 Azabora [60] Fullerenes

Azabora[60]fullerene $C_{58}BN$ for the first time was obtained in conditions of high-temperature laser ablation of a graphite target [40], containing or BN (BC_2N – rods), or boron (B_4C-rods) in an atmosphere of nitrogen. The research of the obtained product by methods of mass – spectrometry and photoelectron spectroscopy has shown [40] that the formation $C_{58}BN$ is proceeded parallel with formation C60. In [41, 42] the more productive method of obtaining $C_{58}BN$ is described: the synthesis is carried out at laser ablation of a solution C_{60} in hexane at the presence of a powdery BN. After removal of a hexane from a reactionary mix a product extracts by three portions pyridine (on 3 ml). Then a pyridine evaporates dry at the lowered pressure. Azabora[60]fullerene $C_{58}BN$ of a high degree of cleanliness obtain by means of use of a method of high performance liquid chromatography ((HPLC), eluent is a toluene). The cleared product was certificated by methods of mass – spectrometry [41, 42] (laser desorption/ionization, p-nitrobenzyl alcohol is a matrix), photoelectron spectroscopy [41] and NMR (^{13}C and ^{11}B) [42]. On the basis of the analysis of the obtained spectra in [43] the conclusion was made, that the product has a fullerene structure, in which two next atoms of carbon are replaced with atoms B and N. In [43] also have assumed, that in $C_{58}BN$ the atoms B and N are located between two hexagons, and two monomers $C_{58}BN$ form a dimer $(C_{58}BN)_2$.

31.2.4 Si-, P-, As- and Ge-Doped Fullerenes

The interest to synthesis Si-doped fullerenes has led to the possible prospect of creation of a new route of polymerization of heterofullerenes. It is supposed [44] that the stability of fullerene cage can be kept at replacement by atoms of silicon up to 12 atoms of carbon. However contrary to the forecasts [44] data on obtaining of Si-fullerenes are still absent [45]. In [46] there is mention of detection in mass – spectra of vapors generated during laser ablation of C/Si targets. These are ions, corresponding to Si-fullerenes from composition $C_{60-n}S_{in}$ ($n = 1, 3$). The ions P-fullerenes such as $C_{59}P$ and $C_{69}P$ also were detected in mass – spectra of vapors of phosphorus and carbon, which simultaneous evaporation is carried out in radiofrequency furnaces [47].

As- and Ge-fullerenes as against Si-fullerenes as radioactive As^*C_{59}, As^*C_{69} ($As^* = {}^{71}As$, ^{72}As, ^{74}As), $^{69}GeC_{59}$ by using radiochemical and radio chromatographic techniques were detected [48]. However reports about isolated As -, Ge -, P- heterofullerenes are absent.

31.3 New Monoatomic and Heteroatomic Carbon Molecules

We develop new, distinct from two already known [49], method for pyrolysis of organics vapors [50, 51]. As is established by our earlier work [50, 51] at a new method of pyrolysis, (NMP) of benzene can be formed not only fullerene C60 (detected in products of a usual method of benzene pyrolysis [52]), but also carbon molecules with the smaller contents of carbon as well as hydrides of fullerenes. For the first time in products of NMP of pyridine vapors, the hetero-carbon as heteroatomic molecules and nanostructures of carbon with large (more than 15 %) contents of nitrogen [53, 54] was found. Earlier heterofullerenes among products of pyridine pyrolysis as at usual, continuous flow pyrolysis (CFP) [55, 56] and rather seldom used flash pyrolysis (FP) [57] methods were not found out. It is necessary to remember that the method FP is used basically for obtaining of the small size objects with high activity. CFP is applied for generation, in particular, from hydrocarbons both carbon nanostructures, and large polyaromatic molecules.

So, according to [56] in flow systems at the temperature range of 677–1,127 °C, the major products of pyridine pyrolysis are acrylonitrile (C_3H_3N), benzonitrile (C_7H_5N), methane, hydrogen, acetylene and hydrogen cyanide. The largest amount of nitrogen-containing product is formed at 985 °C and most nitrogen-free products are formed at 1,025 °C. Besides, in [56], it is noted that hydrogen cyanide presences are always found as an additional product in the pyrolysis of organic nitrogen compounds. In [55], the attempt was undertaken to find out whether heterofullerens might be synthesized directly in CFP of pyridine. It was shown convincingly that among 25 identified products of CFP of pyridine at 900 °C heterofullerenes were not revealed. Major products in this CFP of pyridine are N-heterocycles like quinoline, isoquinoline, and indole. According to [55, 57], the synthesis of different N-heterocycles is initiated by formation of pyridyl radicals and soot formation is realized by oligomerization reaction. It is important to note that the products of the reactions of polymerization and polycondensation in pyrolizates were not revealed.

In [58], it is marked that at FP of pyridine on the Fe/Al_2O_3-catalyst are formed N-heterofilaments with the contents of nitrogen no more than 2.5 %. The basic products at FP of pyridine in an atmosphere of argon [59] are cyanoacetylene ($HC \equiv C–C \equiv N$) at the lowest temperatures and hydrogen cyanide ($HC \equiv N$) at the highest temperatures as well as acetylene and hydrogen. FP is extremely nonequilibrum process with high gradients on temperature and pressure. The shock wave in reactionary tube is created by means of single pulses of laser radiation. At action of a laser pulse with a shock wave in the reactor during 450–600 μs, the temperature raises up to 1,200–1,800 K and the pressure – up to 175–359 kPa.

In the present report, the experimental results demonstrating features of NMP of pyridine are presented. Distinctive technological feature of NMP of pyridine is the possibility of partial division of products (under deposition and condensation), subsequent its localization in different zones of reactionary space. The time of stay of reagents in the most high-temperature zone **A** of reaction can be changed in a wide interval that allows in the certain moment to interrupt course of reaction and

to obtain intermediate products. A part of condensed substances and pyrolytic soot are taken out in a gas reactionary flow from vicinities of a zone **A** and are located in more low-temperature zone **B**. Some part of vapor-like products is condensed in the least heated up zone **C** of reactionary space. Depending on duration of test, temperature in a zone **A** and time of stay in **A** reagents changes not only composition of products in zones **B** and **C**, but also its amount. Results of the study of two product $\mathbf{B_1}$ and $\mathbf{B_2}$, product $\mathbf{C_1}$ of heat treatment of pyridine vapors located in zones **B** and **C** accordingly here are submitted. The products $\mathbf{B_1}$ and $\mathbf{C_1}$ are obtained at lower temperature of synthesis, than product $\mathbf{B_2}$. It is important to note, that earlier [53, 54] our work discussed results of study by different methods (except for mass – spectrometric analysis), the product of a zone **C**. Here a toluene extracts from products **B** and **C** by method of mass spectrometry matrix-assisted laser desorption/ionization (MALDI) (Bruker Daltonics flexAnalysis) was investigated.

31.3.1 Products of Zone B

From a products located in a zone **B** soluble in toluene, condensed substances $\mathbf{B_1}$ and $\mathbf{B_2}$ were extracted. In addition to concentrated toluene, extracts of ethanol red – brown powders $\mathbf{B_1}$ and $\mathbf{B_2}$ were deposited. Then $\mathbf{B_1}$ and $\mathbf{B_2}$ were again dissolved in toluene. Mass – spectra of these solutions are represented on Figs. 31.2, 31.3, 31.4 and 31.5.

It is visible, that the spectra of anions (Fig. 31.2) and cations of $\mathbf{B_1}$ essentially differ. Only spectrum of anions contains two peaks with values m/z 666 and 726 (close to C_{60}). From structure of a thin spectrum of peak with m/z 726 (Fig. 31.2, inset) it follows that the ratio of intensities of first (726) and second (727) (including an isotope ^{13}C) peaks perfectly coincides with accounted ratio corresponding to a natural isotope distribution of carbon in the molecule $C_{60}H_6$ (Fig. 31.2, inset). From the analysis of thin structure of peak with m/z 666 (Fig. 31.2, inset) it follows that this (666) value also can corresponds to molecule $C_{54}H_{18}$ (Fig. 31.2, inset) (or $C_{55}H_6$). The formation of a molecule $C_{60}H_6$ at pyridine pyrolysis convincingly testifies that the growth of a carbon molecule is realized from carbon fragments C_2H_2, C_3H_3, C_4H_4 and C_5H_5 formed at destruction of a molecule of precursor.

In a mass-spectrum of cations it is necessary, first of all, to allocate peak with m/z 576 which can corresponds to a molecule of quasi-fullerene C_{48}. For the first time, we found the molecule C_{48} in products of benzene NMP. Peaks with smaller values m/z, their clear periodicity (through 24 and 26 units), probably, correspond to hydrides of some more unknown carbon molecules or molecules of polyaromatic hydrocarbons.

Two peaks with m/z 576 and 720 are contained in a spectrum of anions of product B2 (Fig. 31.3). From thin structure (Fig. 31.3, inset) of peaks with m/z 576 and 720 it follows, that the ratio of intensities of first and second (including an isotope 13C) peaks absolutely coincides with an accounted ratio corresponding to natural isotope distribution of carbon in molecules of quasi-fullerene C_{48} and fullerene

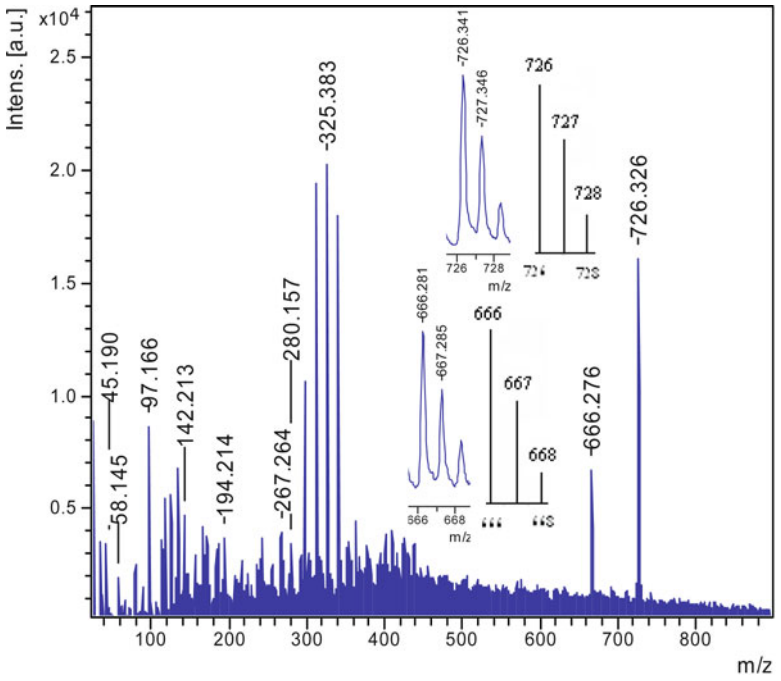

Fig. 31.2 Anions mass spectrum of toluene solution of product B_1 with the expansions of the experimental and theoretical isotope distributions for molecules $C_{60}H_6$ and $C_{54}H_{18}$ in the inset

C_{60} accordingly. The spectrum of negative ions also contains a group of the most intensive peaks (Fig. 31.4) with m/z, differing on 12 units, which can correspond to small carbon molecules from C_3 up to C_{20}. From thin spectra (Fig. 31.4, inset) it also follows that for each of small molecules, for example C_{11}, partially hydrogenated clusters ($C_{11}H_2$) are characterized.

In a spectrum of cations of a product **B_2** (Fig. 31.5) the group of peaks with m/z from 424 up to 550 is visible which also are characteristic for a spectrum of cations of a product **B_1**. It is possible that these peaks concern to hydrides of such molecules as C_{46}, C_{44} and C_{42}.

The most intensive peak with m/z 133 can correspond to a protonated ($C_{11}H^+$) molecule C_{11}, detected in a spectrum of anions. The intensive peaks with m/z 61, 85 and 219, probably, also correspond to protonated molecules C_5H^+, C_7H^+ and $C_{18}H_3^+$ (Fig. 31.5, inset) accordingly. It is known that the molecule C_{60} under action of the powerful laser shows appreciable fragmentation [60], therefore in mass – spectra of anions and cations not only fragments from C_{58} up to C_{52}, but also small clusters from C_3 up to C_9 are sometimes detected. It is possible that the molecules C_{11} and C_{18} are easily exposed to the destruction with the formation of negatively charged clusters from C_3 to C_{10}. Thus, a fullerenization of pyridine molecules with formation fullerene C_{60}, quasi-fullerene C_{48} and small

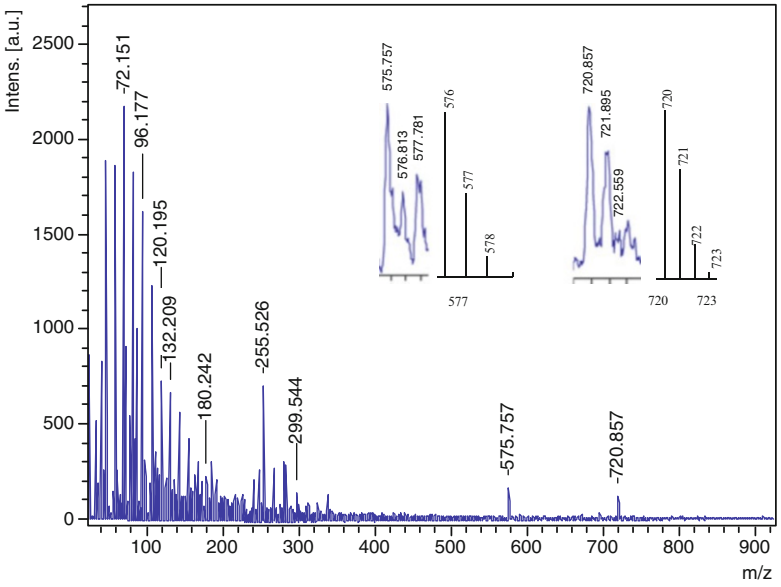

Fig. 31.3 Anions mass spectrum of toluene solution of product B_2 with the expansions of the experimental and theoretical isotope distributions for molecules C_{60} and C_{48} in the inset

carbon molecules (C_6–C_{11}), as well as partially hydrogenated molecules ($C_{60}H_6$) show participation in their growth. Detected clusters greater, than C_{11}, size from C_{12} up to C_{20}, and probably, are intermediate towards the formation of fullerene C_{60} and quasi-fullerene C_{48}.

31.3.2 Products of Zone C

The products of pyridine NMP located in zone **C** were dissolved in toluene and the resulting brightly red solutions $\mathbf{C_1}$ is investigated by mass – spectrometric method.

The structure and intensity of spectra of negative (Fig. 31.6) and positive ions of a solution C1 essentially differ. The peaks corresponding to positively charged clusters are located mainly in the field of small values m/z. The most intensive peaks with m/z 60 and 139 are typical for products of benzene pyrolysis. According to thin structure of these peaks it is possible to believe, that they correspond to molecules C_5 and $C_{11}H_7$.

Mass spectrum of negative ions (Fig. 31.6a) contains the most intensive peaks with m/z 152 and 329, which can correspond to intermediate polyaromatic hydrocarbons. Is remarkable, that in the anions spectrum there is a peak with m/z 720, for which completely coincides with for a thin film containing molecule C_{60}. However peaks with m/z 499, 675 and 845 are most interesting. Basically, these

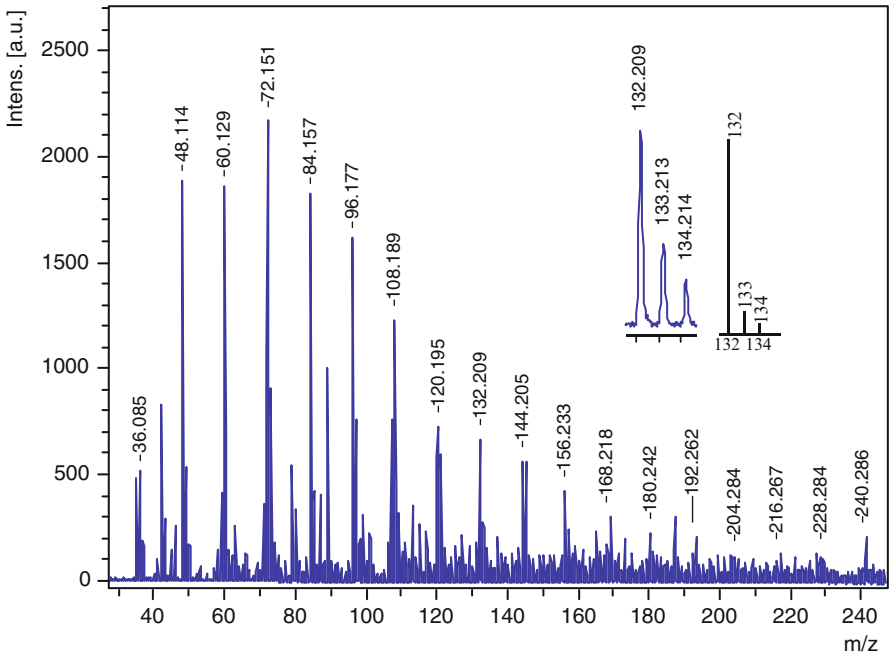

Fig. 31.4 Anions mass spectrum of toluene solution of product B_2 in m/z 25–245 region with the expansions of the experimental and theoretical isotope distributions for molecule C_{11} in the inset

mass can correspond to hydrides molecules $C_{40}H_{19}$ (Fig. 31.7c), $C_{56}H_3$ (Fig. 31.7f) and $C_{70}H_5$ (Fig. 31.8d) accordingly. However from thin structure of these peaks (Figs. 31.7a, d and 31.8b) it follows, that the experimental isotope distribution is differed very strongly from that marked for each of given hydrides molecules. The similar discrepancy between experimental and natural isotope distribution can be explained that detected molecules are heteroatomic ones. Against monoatomic molecules of fullerene C_{60} and quasi-fullerene C_{48} the growth of heteroatomic molecules can be carried out with participation of molecules C_5NH_5 (or C_5N) and; hence, detected in mass spectrum heteroatomic molecules can be azafullerenes. An opportunity of formation N-doped fullerenes appeared in the literature after Rao et al. [13] research by an arc method at the presence of nitrogen (or ammonia) in mass spectra of toluene extract from soot after which peaks with m/z from 722 up to 728 were found. It was offered, that these m/z meanings concern not to hydrides ($C_{60}H_2$, $C_{60}H_4$ and $C_{60}H_8$) but to N-doped fullerenes C_nN_m. On the basis of the analysis of a thin spectrum of peaks with m/z 722 and 1,445 in [21] the formation of azafullerene (as dimer $(C_{59}N)_2$), instead of hydride of fullerene $C_{60}H_2$ with same molecular mass, is reasonable. In [61] it was shown, that the isotope distribution in mass spectrum of a molecule with m/z 360 corresponds to heterofullerene $C_{16}N_{12}$, instead of C_{30}, as it would be possible to expect.

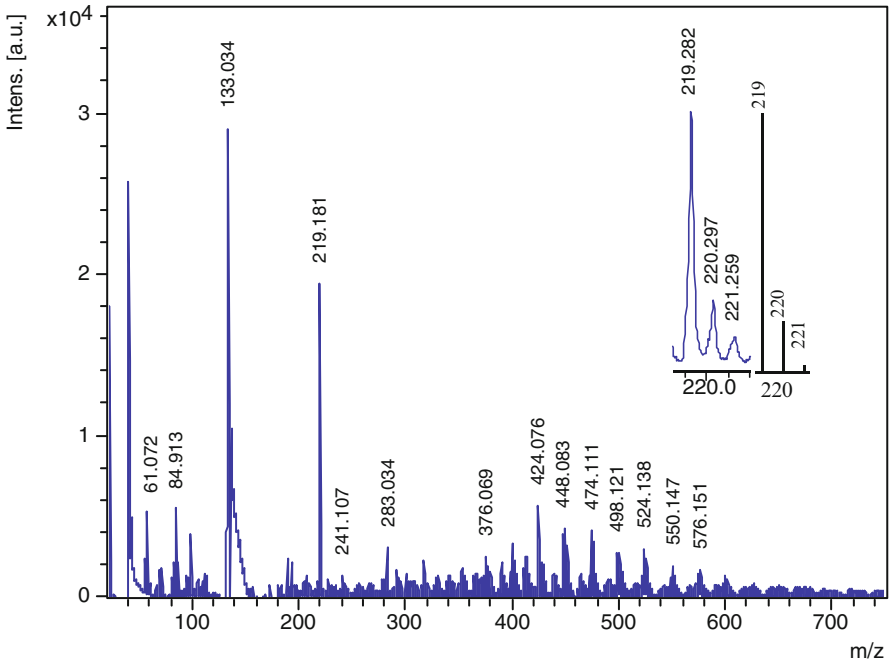

Fig. 31.5 Cations mass spectrum of toluene solution of product B_2 with the expansions of the experimental and theoretical isotope distributions for molecule with m/z 219 in the inset

According to the chemical analysis, a powdery product $\mathbf{C_2}$, obtained at evaporation of toluene solution $\mathbf{C_1}$, contains nitrogen (12.0 %) and carbon (83.3 %) in the ratio approximately 7:1, and also oxygen (4 %) and hydrogen (0.7 %). From XPS-spectrum (Fig. 31.9a) it is visible that this substance, really, except for carbon (83.5 %) contains as well nitrogen (9.2 %) and oxygen (7.3 %). The lines C1s (284.5 eV) spectrum (Fig. 31.9c) and N1s (399.1 eV) spectrum (Fig. 31.9d) are asymmetrical and, hence, not all atoms C and N are equivalent in the given substance. The value N1s 399.1 eV is essentially less value (400.7 eV) which is determined for nitrogen in ions $C_{59}N^+$ and $C_{69}N^+$ [22], and also in $C_{57}N_3$/Pt [29]. The value N1s 399.1 eV, as usual is considered, corresponds to pyridinic atom of nitrogen in graphite N-doped net.

Believing, that detected in mass spectrum of anions, molecules contain carbon and nitrogen approximately as well in the ratio 7:1, the optimal formula for a molecule with m/z 499 is $(C_{35}N_5)H_9$, for a molecule with m/z 675 is $(C_{45}N_5)O_3H_{17}$ and for a molecule with m/z 845 is $(C_{49}N_{11})O_5H_{23}$. Accounted distribution of isotopes in all three of these heteroatomic molecules (Figs. 31.7b, e and 31.8c) practically completely coincides with an experimental ratio of isotopes in the appropriate peaks. The atoms of oxygen and hydrogen can form exohedral bonds with one of atoms monoazafullerene net always having not coupled electron

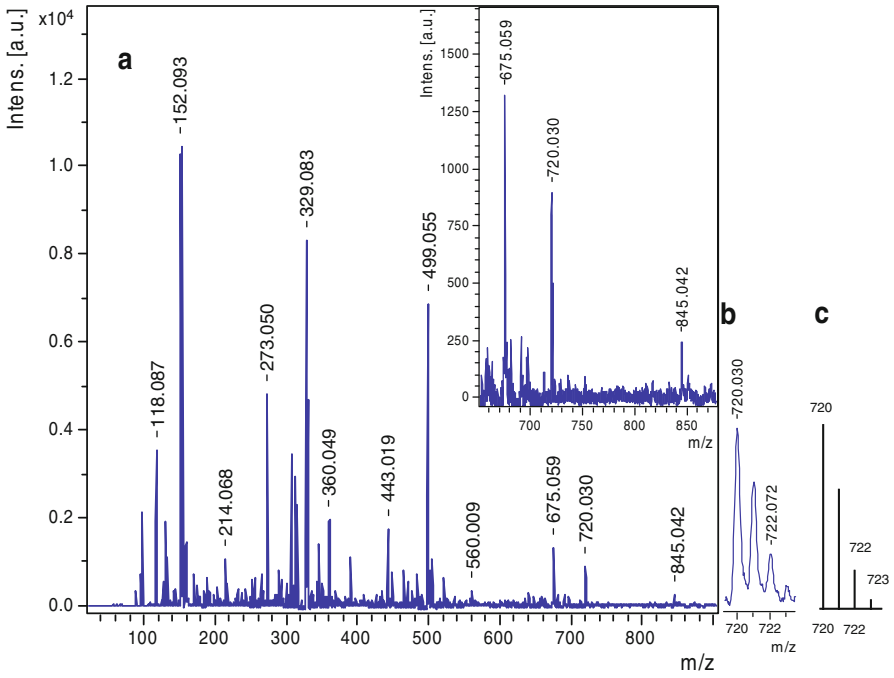

Fig. 31.6 Anions mass spectrum of the toluene solution of the product C_1 with m/z 650–880 region in the inset (**a**), the expanded patterns of the 720 m/z peak (**b**), the calculated isotope mass ratios for fullerene C_{60} molecule (**c**)

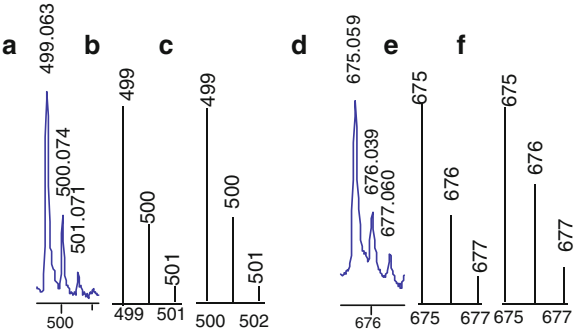

Fig. 31.7 The expanded patterns of the 499 m/z peak (**a**), the calculated isotope mass ratios for $(C_{35}N_5)H_9$ (**b**) and $C_{40}H_{19}$ (**c**) molecules; the expanded patterns of the 675 m/z peak (**d**), the calculated isotope mass ratios for $(C_{45}N_5)(OH)_3H_{14}$ (**e**) and $C_{56}H_3$ (**f**) molecules

because of formation of bonds between trivalent nitrogen with nearest quaternary atoms of carbons. In polyazafullerene net the amount of not coupled electrons should coincide with number of substituted atoms of nitrogen. Depending on localization not coupled electrons on atoms of carbon or nitrogen can be obtained by functionalized exohedral azafullerenes of different structure. Therefore it is very important to find out on what of atoms (carbon or nitrogen) azafullerene net not

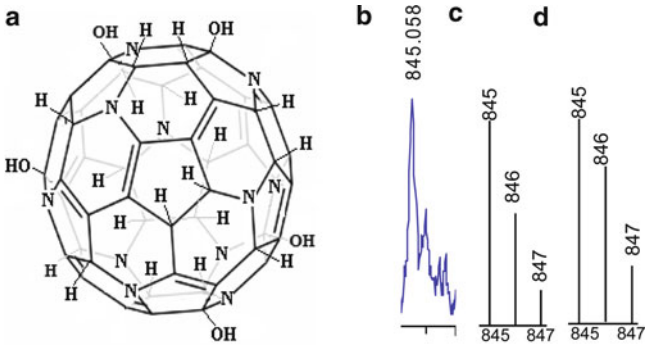

Fig. 31.8 Scheme of molecule $(C_{49}N_{11})(OH)_5H_{18}$ (**a**), the expanded patterns of the 845 m/z peak (**b**), the calculated isotope mass ratios for $(C_{49}N_{11})(OH)_5H_{18}$ (**c**) and $C_{70}H_5$ (**d**) molecules

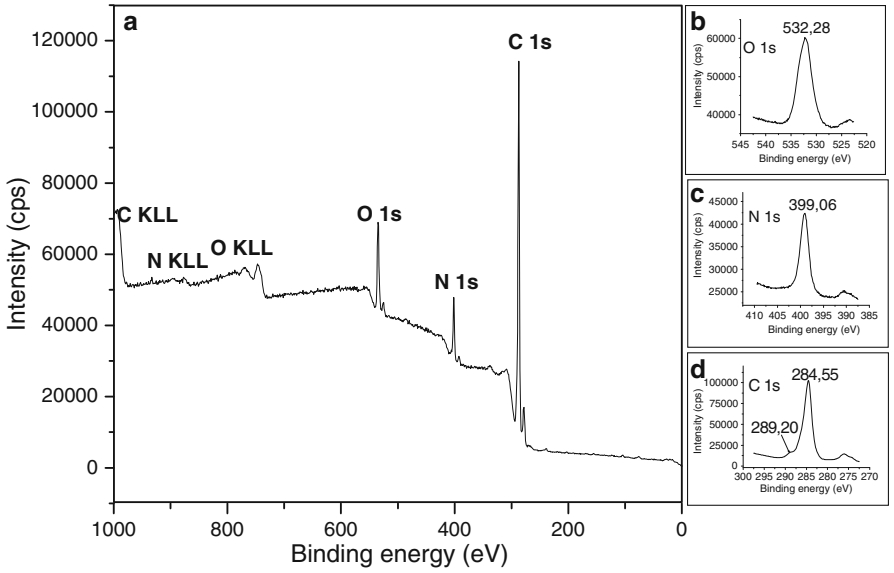

Fig. 31.9 XPS survey (**a**) and core level spectra O 1 s (**b**), C 1 s (**c**), N 1 s (**d**) of the product C_2

coupled electron is located. It was considered [58] that the atoms of nitrogen in graphite N-doped net can be in pyridinic (sp^2), pyrrolic (sp^3) and quaternary states.

On quaternary atom of nitrogen having four bonds with three next atoms of carbon, should be located free electron. It is established also, that monoazafullerene exists in a gas phase and in a liquid solution, as well as in a solid solution with C_{60} ($C_{59}N^{\bullet}$ C_{60}) in the form of a radical with possible localization of electron or on atom of carbon ($NC_{59}^{\bullet}$) – if the atom of nitrogen is accepted trivalent one, or on atom of nitrogen ($C_{59}N^{\bullet}$) – if the atom of nitrogen is considered quaternary one. The synthesis of monosubstituted azafullerenes in solutions as dimers $(C_{59}N)_2$

and $(C_{69}N)_2$ according to methods Hummelen [21] and Nuber–Hirsh [27] from heteroatomic organic molecules is carried out also through a stage of formation of ions of intermediate products such as monoazafullerenes $(C_{59}N)^+$ and $(C_{69}N)^+$. Bonds C–C between monomers of dimer $(C_{59}N)_2$ include a lot of alkaline metals that can collapse with the formation $(C_{59}N)^+$ in a solution of ions, that specifies convertibility of a reaction

$$2(C_{59}N)^+ = (C_{59}N)_2.$$

It is remarkable, that the radicals $C_{59}N$ in a gas phase (as against ions $(C_{59}N)^+$ in a solution) are not dimerizated. However at the presence of hydrogen of monomers $C_{59}N^{\bullet}$, generated at thermal evaporation and dissociation of dimer $(C_{59}N)_2$, with formation of hydromonoazafullerene $C_{59}NH$ are hydrogenated [62, 63]. The distinctive (from dimer $(C_{59}N)_2$) feature of $C_{59}HN$ is the presence at its electronic oscillatory and ^{13}C NMR spectra of signals sp^3 (C–H) carbon [64] and, hence, electron in a radical $C_{59}N^{\bullet}$ is located on atom of carbon. Therefore it is possible to assume, that a dimerization in a gas phase the monomers $C_{59}N^{\bullet}$ is not realized because of its low concentration. Hydromonoazafullerene $C_{59}NH$ in contrast to fullerene C_{60} (C_{60} is hydrogenated at ultra-high pressures [65]) can be easily hydrogenated by hydrogen generated under the decomposition of hydride of fullerene $C_{60}H_{36}$, up to $C_{59}NH_5$ [62, 63].

We believe, that in an hydrogen containing atmosphere of pyridine pyrolysis the opportunity for interaction of atoms of hydrogen (or groups -OH) to atom of carbon with formation of functionalized polyazafullerenes $(C_{35}N_5)H_9$, $(C_{45}N_5)(OH)_3H_{14}$ and $(C_{49}N_{11})(OH)_5H_{18}$ is created. Superfluous concerning an amount of atoms of nitrogen (or tertiary atoms of carbon) in azafullerene net the hydrogen, probably, characterizes a degree of hydrogenation of formed exohedral polyazafullerene.

31.4 Conclusions

1. Hetero-carbon (azafullerenes, BN-fullerene, N-graphene, N-nanotubes) as nanosensors can have significant advantages in comparison to undoped (monoatomic) carbon nanostructures.
2. The new substances as possible perspective sensitive elements are obtained at realization of a new method of pyridine pyrolysis.
3. Firstly quasi-fullerene C_{48}, fullerene C_{60}, $C_{60}H_6$ and heteroatomic functionalized exohedral polyazafullerenes $(C_{35}N_5)H_9$, $(C_{45}N_5)(OH)_3H_{14}$ and $(C_{49}N_{11})(OH)_5H_{18}$ are detected by mass – spectrometric method in products of pyridine pyrolysis. The formation of molecules C_{60}, $C_{60}H_6$ and C_{48} only from fragments C_2H_2, C_3H_3, C_4H_4 and C_5H_5 of destruction of C_5NH_5 molecules could be fulfilled. The growth of heteroatomic fullerene-like molecules with participation of molecules C_5NH_5 is realized.
4. Process of fullerenization of pyridine with formation of fullerene C_{60}, quasi-fullerene C_{48} and small carbon molecules C_3–C_{15} is carried out for the first time.

References

1. Krainara N, Illas F, Limtraku J (2012) Interaction of adenine Cu(II) complexes with BN-doped fullerene differentiates electronically equivalent tautomers. Chem Phys Lett 537(1):88–93
2. Sandoval LM, Martinez H, Terrones M (2004) Fabrication of vapor and gas sensors using films of aligned CN_x nanotubes. Chem Phys Lett 386:137–143
3. Lv R, Li Q, Botello-Méndez AR et al (2012) Nitrogen-doped graphene: beyond single substitution and enhanced molecular sensing. Sci Rep 2:586
4. Maeda-Mamiya R, Noiri E, Isobe H et al (2010) In vivo gene delivery by cationic tetraamino fullerene. Proc Natl Acad Sci USA 107:5339–5344
5. Weidinger A, Waiblinger M, Pietzak B et al (1998) Atomic nitrogen in C_{60}:N@C_{60}. Appl Phys A: Mater Sci Process 66(3):287–292
6. Suetsuna T, Dragoe N, Harneit W et al (2002) Separation of N_2@C_{60} and N@C_{60}. Chem Eur J 8(22):5079–5083
7. Erkoc S, Turker L (2003) Ammonia deposition in fullerene: (NH_3)N@C_{60}. J Mol Struct (THEOCHEM) 640:57–61
8. Yang S, Liu F, Chen C (2011) Fullerenes encaging metal clusters—clusterfullerenes. Chem Commun 47:11822–11839
9. Wang TS, Feng L, Wu JY et al (2010) Planar quinary cluster inside a fullerene cage: synthesis and structural characterizations of Sc_3NC@C_{80}-Ih. J Am Chem Soc 132:16362–16364
10. Zanchetta J, Marchand A (1965) Electronic properties of nitrogen doped carbons. Carbon 3:332
11. Marchand A, Zanchetta JV (1966) Proprietes electroniques d'un carbone dope a l'azote. Carbon 3:483–491
12. Belz T, Baue A, Find J et al (1998) Structural and chemical characterization of N-doped nanocarbons. Carbon 36:731–741
13. Pradeep T, Vijayakrishnan V, Santra AK, Rao CNR (1991) Interaction of nitrogen with fullerenes: nitrogen derivatives of C_{60} and C_{70}. Phys Chem 95:10564–10568
14. Kratschmer W, Lamb LD, Fostiropoulos K, Huffman DR (1991) Solid C_{60}: a new form of carbon. Nature 347:354–358
15. Kroto HW, Heath JR, O'Brien SC et al (1985) C_{60}: buckminsterfullerene. Nature 318:162–163
16. Yu R, Zhan M, Cheng D et al (1995) Simultaneous synthesis of carbon nanotubes and nitrogen-doped fullerenes in nitrogen atmosphere. J Phys Chem 99:1818–1819
17. Christian JF, Wan Z, Anderson SL (1992) $N^+ + C_{60}$ reactive scattering: substitution, charge transfer and fragmentation. J Phys Chem 96:10597–10600
18. Averdung J, Luftmann H, Schlachter I, Mattay J (1995) Aza-dihydro[60]fullerene in the gas phase – a mass-spectrometric and quantum chemical study. Tetrahedron 51:6977–6982
19. Glenis S, Cooke S, Chen X, Labes MM (1994) Photophysical properties of fullerenes prepared in an atmosphere of pyrrole. Chem Mater 6(10):1850–1853
20. Lamparth I, Nuber B, Schick G et al (1995) $C_{59}N^+$ and $C_{69}N^+$: isoelectronic heteroanalogues of C_{60} and C_{70}. Angew Chem Int Ed 34:2257–2259
21. Hummelen JC, Knight B, Pavlovich J et al (1995) Isolation of the heterofullerene $C_{59}N$ as its dimer $(C_{59}N)_2$. Science 269:1554–1556
22. Ying ZC, Hettich RL, Compton RN, Haufler RE (1996) Synthesis of nitrogen-doped fullerenes by laser ablation. J Phys B: At Mol Opt Phys 29:4935–4942
23. Smalley RE (1992) Doping the fullerenes. ACS Symp Ser 481:141–159
24. Weltner WJ, Walsh PN, Angell CL (1964) Spectroscopy of carbon vapor condensed in rare-gas matrices at 4° and 20° K. I. J Chem Phys 5:1299–1305
25. Heath JR, Zhang Q, O'Brien SC et al (1987) The formation of long carbon chain molecules during laser vaporization of graphite. J Am Chem Soc 109:359–363
26. Cataldo F (2004) Cyanopolyynes: carbon chains formation in a carbon arc mimicking the formation of carbon chains in the circumstellar medium. Int J Astrobiol 3:237–246
27. Nuber B, Hirsh A (1996) A new route to nitrogen heterofullerenes and the first synthesis of $(C_{69}N)_2$. Chem Commun 12:1421–1442

28. Reuther U, Hirsch A (2000) Synthesis, properties and chemistry of aza[60]fullerene. Carbon 38:1539–1549
29. Otero G, Biddau G, Sanchez-Sanchez C et al (2008) Fullerenes from aromatic precursors by surface-catalysed cyclodehydrogenation. Nature 454:865–869
30. Tobe Y, Nakanishi H, Sonoda M et al (1999) Pyridine analogue of macrocyclic polyyne $C_{58}H_4N_2$ as a precursor to diazafullerene $C_{58}N_2$. Chem Commun 17:1625–1626
31. Hultman L, Stafström S, Czigány Z (2001) Cross-linked nano-onions of carbon nitride in the solid phase: existence of a novel $C_{48}N_{12}$ aza-fullerene. Phys Rev Lett 87:225503–225507
32. Guo T, Jin C, Smalley RE (1991) Doping bucky: formation of boron doped buckminsterfullerene. J Phys Chem 95:4948–4950
33. Chai Y, Guo T, Jin C et al (1991) Fullerenes with metals inside. J Phys Chem 95:7564–7568
34. Muhr HJ, Nesper R, Schnyder B, Kotz R (1996) The boronheterofullerenes C59B and C69B: generation, extraction, mass spectrometric and XPS characterization. Chem Phys Lett 249:399–405
35. Piechota J, Byszewski P, Jablonski R, Antonova K (1996) Characterization of fullerenes obtained from boron nitrite containinggraphite-electrodes – electronic-structure of C_{60}-X-YBXNY and deformed C_{60}. Fuller Sci Technol 4:491–507
36. Cao BP, Zhou XH, Shi ZJ, Jin ZX (1997) Synthesis and characterization of boron-doped fullerenes [J]. Acta Phys Chim Sin 13(03):204–206
37. Churilov GN (2000) Plasma synthesis of fullerenes. PTE 1:5–15
38. Churilov GN, Alikhanyan AS, Nikitin MI, Glushenko GA et al (2003) Synthesis and characterization of boron- and scandium-containing fullerenes. Tech Phys Lett 29(2):168–170
39. Bulina NV, Glushchenko GA, Novikov PV et al. (2003) Study of boron substituted fullerene. In: Schur DV, Zaginaichenko SYu, Veziroglu TN (eds) Hydrogen materials science and chemistry of carbon nanomaterials ichms, VIII international conference, sudak, Crimea, 2003, pp 538–541
40. Nakamura T, Ishikawa K, Yamamoto K et al (1999) Synthesis of heterofullerenes by laser ablation. Phys Chem Chem Phys 1:2631–2633
41. Nakamura T, Ishikawa K, Goto A, Ishihara M (2001) BN substitution reaction of fullerene using an excimer laser irradiation. Diamond Relat Mater 10:1228–1230
42. Nakamura T, Ishikawa K, Goto A, Ishihara M (2003) Synthesis of heterofullerene using a direct BN substitution reaction of fullerene. Diamond Relat Mater 12:1908–1911
43. Krainara N, Luksirikul P, Sirijaraensre J et al (2007) Conduction properties of BN-doped fullerene chain obtained by density functional calculations. Nanotechnology 1:508–511
44. Pellarin M, Ray C, Lerme J et al (1999) Production and stability of silicon-doped heterofullerenes. Eur Phys J D 9:49–54
45. Fan X, Zhu Z, Liu L et al (2010) Theoretical study on structural stability of alloy cages: a case of silicon-doped heterofullerenes. Commun Comput Phys 8:289–303
46. Ray C, Pellarin M, Lerme JL et al (1998) Synthesis and structure of silicon-doped heterofullerenes. Phys Rev Lett 80:5365–5368
47. Moschel C, Jansen M (1999) Generation of stable phosphorus heterofullerenes in a radiofrequency furnace. Z Anorg A C 625(2):175–177
48. Ohtsuki T, Ohno K, Shiga K et al (1999) Formation of As- and Ge-doped heterofullerenes. Phys Rev B 60:1531–1534
49. Brown RFC (1980) Pyrolytic methods in organic chemistry: application of flow and flash vacuum pyrolytic techniques. Academic, New York
50. Kharlamov AI, Kirillova NV (2009) Fullerenes and hydrides of fullerenes as products transformation (polycondensation) of molecules of aromatic hydrocarbons. Rep Acad Sci Ukraine 5:110–118
51. Kharlamov AI, Bondarenko ME, Kirillova NV (2012) New method for synthesis of fullerenes and fullerene hydrides from benzene. Russ J Appl Chem 85:233–239
52. Crowley C, Taylor R, Kroto HW, Walton DRM (1996) Pyrolytic production of fullerenes. Synth Met 77:17–22

53. Kharlamov AI, Kirillova NV (2011) New substance: molecular crystals of fullerene-like N-containing molecule of carbon – $(C_{50}N_{10})O_3H_{10}$. Rep Acad Sci Ukraine 6:156–163
54. Kharlamov O, Kharlamova G, Kirillova N et al (2012) Synthesis of new carbon compounds: n-doped fullerene (C50N10)O3H10 and "pyridine" nanocarbon synthesis of new carbon compounds. In: Vaseashta A, Braman E, Susmann P (eds) Technological innovations in sensing and detection of chemical, biological, radiological, nuclear threats and ecological terrorism, NATO science for peace and security series, a: chemistry and biology. Springer Science+Business Media B.V., Dordrecht, Chap. 27, pp 245–253
55. Winkler JK, Karow W, Rademacher P (2000) Gas phase pyrolysis of heterocyclic compounds, flow pyrolysis and annulation reactions of some nitrogen heterocycles. Arkivoc 3:576–602
56. Houser TJ, McMarville ME, Biftu T (1980) Kinetics of the thermal decomposition of pyridine in a flow system. Int J Chem Kinet 12:555–558
57. Mackie JC, Colket MB, Nelson PF (1990) Shock tube pyrolysis of pyridine. J Phys Chem 94:4099–4106
58. Teddy J (2009) CVD synthesis of carbon nanostructures and their applications as supports in catalysis. ethesis, Toulouse University, Toulouse, pp 1–113
59. Colket MB, Hall RJ, Sangiovanni JJ, Seery DJ (1990) In: Hartford E (ed) The determination of rate-limiting steps during soot formation. United Technologies Research Center, East Hartford, pp 1–437
60. Kong Q, Zhao L, Zhuang J et al (2001) Formation of odd-numbered fullerene-related species and its relation to the formation of metallofullerenes. Int J Mass Spectrom 209(1):69–79
61. Vaziri M (2006) Synthesis of small carbon-nitride heterofullerenes. Mater Lett 60(7):926–928
62. Vasil'ev YV, Hirsch A, Taylor R, Drewello T (2004) Hydrogen storage on fullerenes: hydrogenation of $C_{59}N$ using $C_{60}H_{36}$ as the source of hydrogen. Chem Commun 7(15): 1752–1753
63. Vasil'ev YV, Abzalimov RR, Tuktarov RF et al (2002) In situ hydrogenation of $C_{59}N$ and resonant electron capture of $C_{59}NH_x$ ($x = 0$, 1 and 5). Chem Commun Lett 354(5–6):361–366
64. Keshavarz-K M, González R, Hicks RG et al (1996) Synthesis of hydroazafullerene $C_{59}HN$, the parent hydroheterofullerene. Nature 383(6596):147–150
65. Jin C, Hettich R, Compton R et al (1994) Direct solid phase hydrogenation of fullerenes. J Phys Chem 98(16):4215–4217

Chapter 32
A Preliminary Analysis of Wind-Hydrogen System in Bulgaria

M. Ali, D. Kirova, and K. Petrov

Abstract We present system design and analysis to use the produce electricity from wind generator to power an electrolyzer, which in turn splits water into hydrogen and oxygen. The system has applicability to be used as a stand-alone unit for many safety and security related applications.

Keywords Wind-energy • Stand-alone systems • Electrolyzer

32.1 Introduction

Renewable energy sources, such as energy from water, wind, sun, geothermal and biomass sources are increasingly studied as alternatives to the conventional fossil fuels. The problem occurs with the fact that they are not constant over time. This appears to be a problem for energy distributors in defining the share of the energy consumption that could be covered from renewable energy sources. For example during night hours when electricity consumption is low wind farms continue producing energy which in most cases remains unused. Transformation and storage of this energy under different form can reduce losses and solve the problem. In this study we will examine the possibility of conversion and storage of wind energy under the form of hydrogen for wing generator installed on the Black Sea coast of Bulgaria.

M. Ali • K. Petrov (✉)
Institute of Electrochemistry and Energy Systems, Bulgarian Academy of Sciences, Acad. G. Bonchev Str., Bl. 10, Sofia 1113, Bulgaria
e-mail: kmavrodiev55@abv.bg

D. Kirova
Department of Mathematics, Technical University of Varna, 1 Studentska Str., 9010 Varna, Bulgaria

A. Vaseashta and S. Khudaverdyan (eds.), *Advanced Sensors for Safety and Security*, NATO Science for Peace and Security Series B: Physics and Biophysics,
DOI 10.1007/978-94-007-7003-4_32,

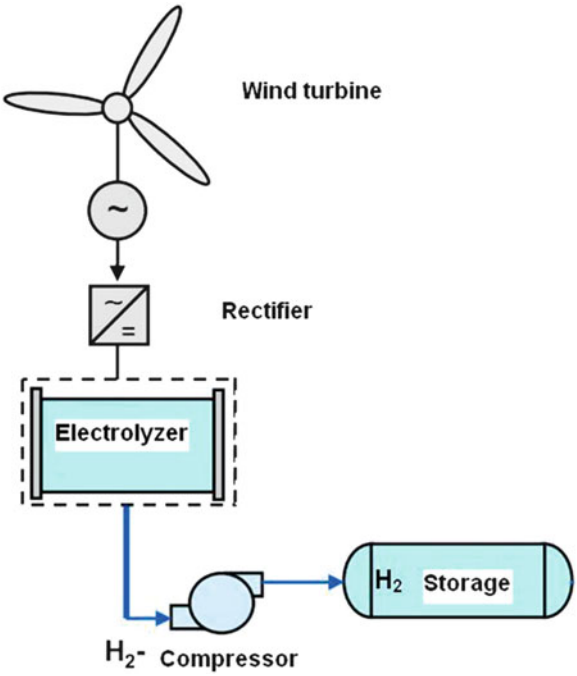

Fig. 32.1 Elements of the system. Wind turbine – electrolyzer – hydrogen storage and transport

Hydrogen is one of the most abundant elements on Earth and the Universe. However, since it readily forms compounds with most elements, it is rarely found in pure form. Hydrogen occurs in water and in most organic compounds. Being the lightest element and having the highest caloric value compared to typical fossil fuels, together with its ability to be stored and transported, leads us to believe that in the future hydrogen will become the main source of energy [1, 3–5].

The main purpose of project is to use the produce electricity from wind generator to power an electrolyzer, which in turn splits water into hydrogen and oxygen. The produced hydrogen can be transported through the existing pipeline network or by auto transportation to reach end users. At that point hydrogen can be used to produce electricity through fuel cells, burned directly in internal combustion engines, or used for industrial needs [2, 7, 8]. The elements of the system for the purpose of this study are presented schematically in Fig. 32.1 and they are as follows:

Our analysis is limited to a wind turbine and an electrolyzer.

32.2 Design of Wind-Hydrogen System

For the purpose of this study, measurements of the potential of the wind were made by a 50 m high meteorological mast at Kaliakra cape, for a period of 1 year at 10 min averages. The wind characteristics were measured with anemometers mounted at

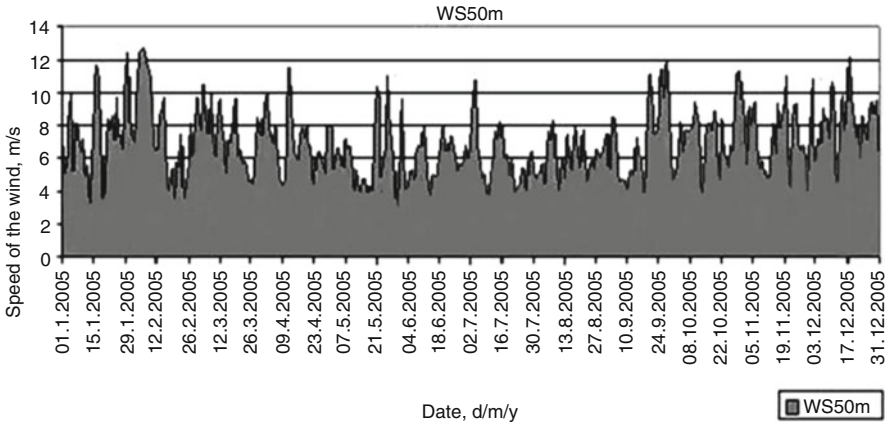

Fig. 32.2 Speed of the wind during one calendar year

50, 40, 20 m, and wind vanes at 50 and 35 m. There are also sensors for measuring air temperature, barometric pressure and humidity. All the data have been collected by "Inis Ltd", Bulgarian – Japanese company, who has built and exploits a wind park of 38 MW power. Figure 32.2 represents the values of wind speed during one calendar year at cape Kaliakra.

In order to determine the wind potential of the site the data were processed using the program for wind farm designing – WindPRO and more particularly its METEO module. The METEO module has two functions: (i) input, analysis and presentation of the data; and (ii) calculation of the annual production of a single turbine based on these data.

All figures regarding wind energy assessment have been derived from WindPRO. Figures 32.3 and 32.4 represent the turbulence intensity of the wind and mean wind speed, respectively, versus their daily averages at 50, 40, 20 m. The observations show that a turbine would not be very productive during the day. At night, when the energy consumption is lower, winds at 40 and 50 m blow harder and are less turbulent. The problem is how to accumulate energy during these peak night hours.

The first step in the analysis of wind potential is the estimation of the wind speed distribution – the relative frequency of a specific wind speed versus the wind speed. It is usually approximated by the two-parametric Weibull probability density function:

$$f(x) = \begin{cases} \left(\frac{k}{A}\right)\left(\frac{x}{A}\right)^{k-1} e^{-\left(\frac{x}{A}\right)^{k}}, & x \geq 0 \\ 0, & x \geq 0 \end{cases}$$

where $k > 0$ is the shape parameter and A > 0 is the scale parameter.

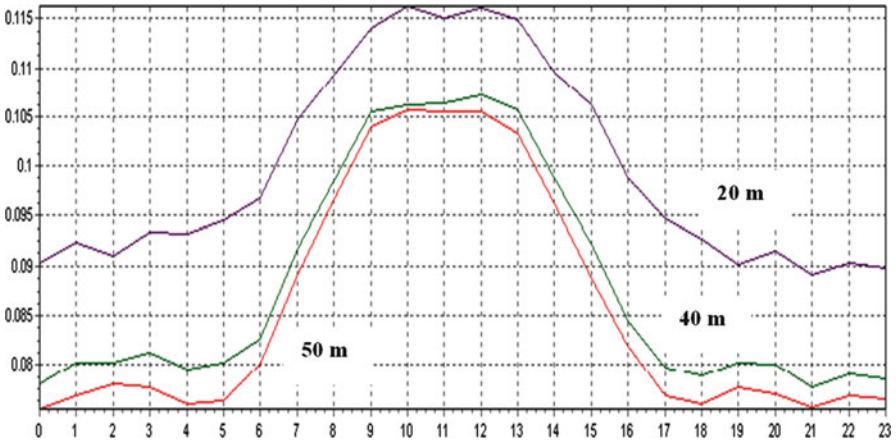

Fig. 32.3 Turbulence intensity of the wind at 50, 40, 20 m measured at Kaliakra cape – daily averages [m/s]

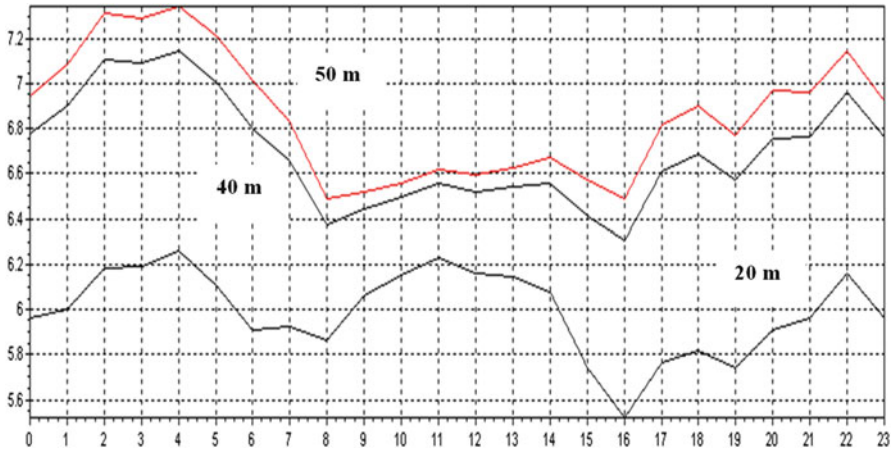

Fig. 32.4 Mean wind speed at 50, 40, 20 m measured at Kaliakra cape – daily averages [m/s]

After a vertical extrapolation based on the measured data the wind profile at a desired height can be obtained. The wind energy output at a specific time is calculated with the following equation (Fig. 32.5):

$$E = \frac{1}{2}\rho v^3 A_r C_e \ \text{(W/s)}$$

where,

ρ – the Air Density ($= 2.70$ kg/m^3)
v – the Wind Speed

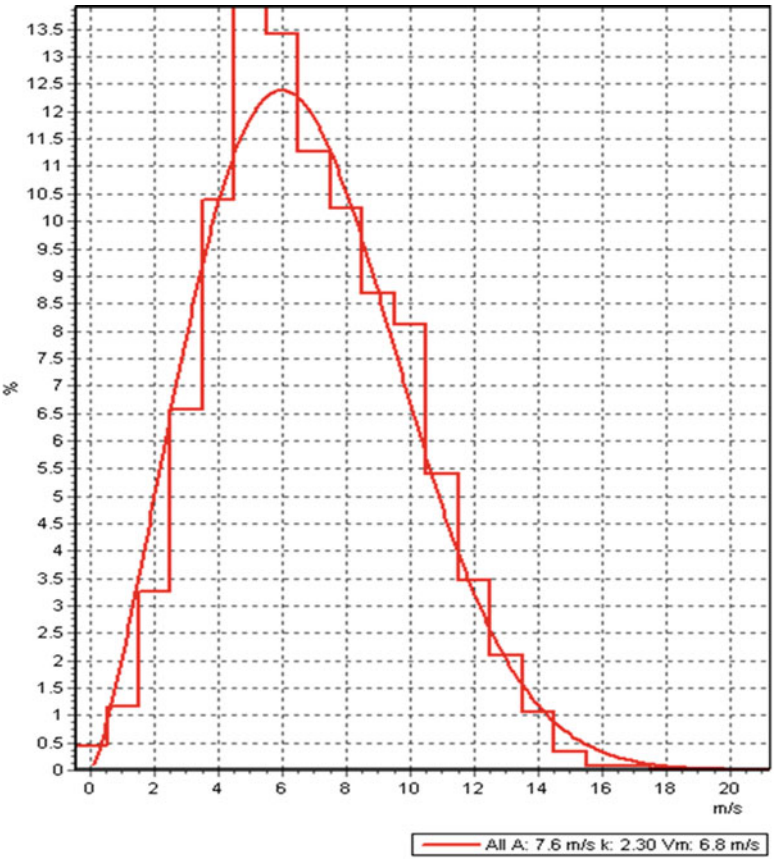

Fig. 32.5 Weibull distribution for the wind speed at 50 m height

A_r – the Area Swept of the Rotor
C_e – the total efficiency of the wind turbine at the given wind speed
A = 7.6 m/s, k = 2.30

The model of the turbine selected for an energy assessment is Gemesa G90/2000 with capacity of 2,000 kW, rotor diameter of 90 m, located at 78 m height from the surface of the ground. It has CPA (capacity factor) of 43 % at an average wind speed of 7.6 m/s at hub height. The graph of the power and the Ce curves are given below. The power curve describes the electric power output from a specific wind turbine versus the wind speed at hub height.

The final step is to make an estimation of the annual production of a single turbine using the wind speed distribution and power and Ce curves of this turbine (Fig. 32.6).

Figure 32.7 represents the yearly produced energy depending on wind speed. Similar to this is Fig. 32.8, which shows the production of electricity with time for

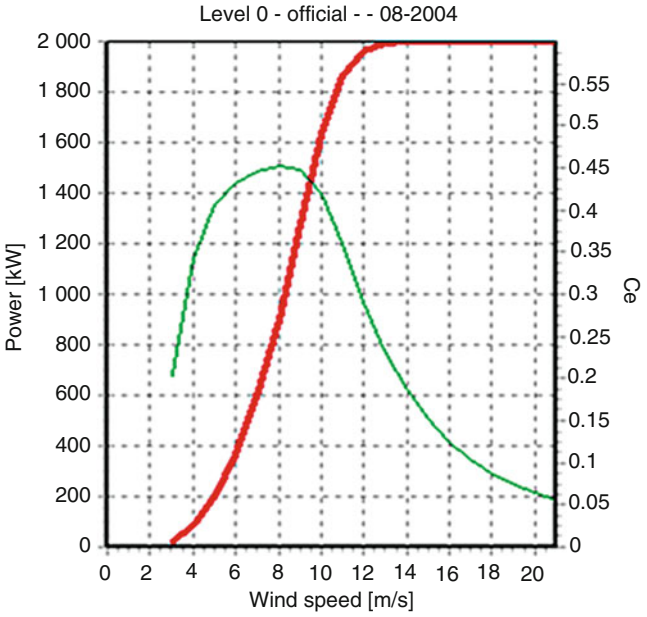

Fig. 32.6 Power and Ce curves of the selected turbine

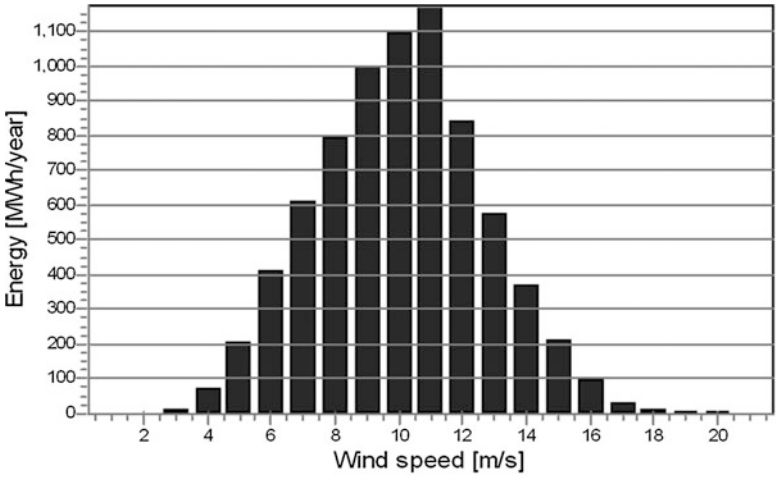

Fig. 32.7 Energy versus wind speed based on the measurements at Kaliakra cape

a calendar year. From both curves we can estimate the total possible electricity for this wind turbine. The actual produced electricity is much lower depending on the demand in the area, local distributor, etc.

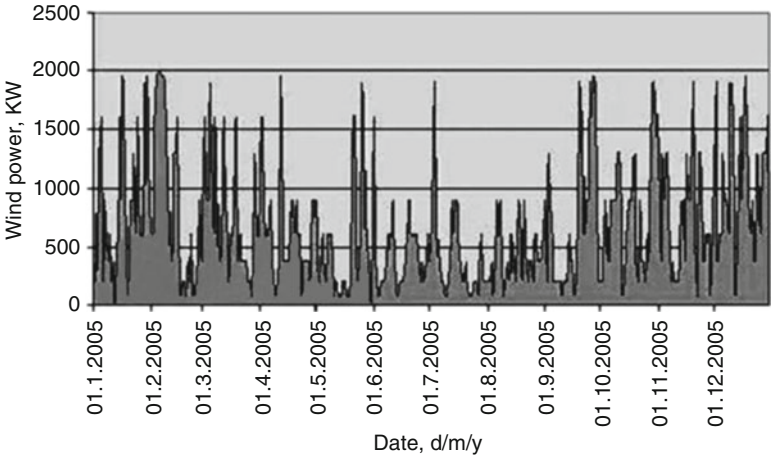

Fig. 32.8 Production of electrical energy in time

From the above figures follow that the estimated amount of electrical energy which could be produced from the selected generator for a period of 1 year equals to 7,522 MWh [6, 9]. We have selected an alkaline electrolyzer, with 80 % efficiency, electrolyte temperature of 70–90 °C, the current density of 2,000–3,000 A/m^2 and electrical energy consumption of 4–5 kWh/N m^3 hydrogen.

Given the efficiency of the selected electrolyzer and energy density of the hydrogen, the production of 1 kg of hydrogen will require about 42 kWh of electrical energy. Obviously, the energy produced only during the low demand periods, such as during the nights, could be used for hydrogen production or the whole amount of energy obtained could be used solely for the production of hydrogen. If we choose to use the whole amount of energy (7,522 MWh/year) for the production of hydrogen for the given period of 1 year we would acquire approximately 179,095 kg of hydrogen.

The produced hydrogen can be then transported to urban regions and end consumers and then again converted into electrical energy through fuel cells. The concept has wide applications to be used as a stand-alone unit for applications requiring energy generation in areas with no easy access to electricity grid, such as border patrol, remote austere locations for homeland protection, and many similar applications. Therefore, in case many projects of this kind are put into practice, many negative impacts on the environment would be avoided.

References

1. Ulleberg Ø, Nakken T, Ete A (2004) The wind/hydrogen demonstration system at Utsira in Norway: evaluation of system performance using operational data and updated hydrogen energy system modeling tools. Int J Hydrog Energy 35(5):1841–1852

2. Malkovic T (2008) The quest to make hydrogen the fuel of the future. Australian Academy of Science, Canberra. http://www.science.org.au/nova/111/111key.html. Accessed on 20 Sept 2012
3. Gross BK, Sutherland IJ, Mooiweer H (2007) Hydrogen fueling infrastructure assessment. General Motors Corporation R&D Center, Warren. http://www.renewableenergyworld.com/assets/documents/2008/10Things.pdf. Accessed on 20 Sept 2012
4. Lilov E (2009) Hydrogen is the energy of the future. http://www.dw.de/dw/article/0,,3927012,00.html. Accessed on 20 Sept 2012
5. Herranz DS, Rahbar MT, Li A, Ezpelta AS, Ramon LS (2008) Renewable energy. Wind power. http://www.exergy.se/goran/hig/re/08/wind.pdf. Accessed on 20 Sept 2012
6. Nenov I (1989) Fundamentals of electrochemistry. Technical Publishing House, Sofia
7. Ball M, Wietschel M (2009) Hydrogen economy: opportunities and challenges. Cambridge University Press, Cambridge
8. Shishkov D, Dimitrov M (1986) Technology of ammonia and urea. Technical Publishing House, Sofia
9. Stojić DL, Grozdić TD, Umićević AB, Maksić AD (2008) A comparison of alkaline and proton exchange membrane electrolyzers. Russ J Phys Chem A Focus Chem 82(11):1958–1960

Photographs

ARW Group Photograph

NATO Advanced Research Workshop on Technological Advances in Chemical, Biological, Radiological, Nuclear, Explosives – (CBRNE) Sensing and Detection for Safety, Security, and Sustainability. Yerevan, Armenia Sept 29–Oct 02 2012

A. Vaseashta and S. Khudaverdyan (eds.), *Advanced Sensors for Safety and Security*,
NATO Science for Peace and Security Series B: Physics and Biophysics,
DOI 10.1007/978-94-007-7003-4,

ARW Selected Photographs


Classification of the Biologic
agents


One of the advanced methods of quantitative and qualitative studies of natural objects is the optical spectral analysis. Nevertheless, the large number of connections between the object under study and registered parameters complicates the detection of cause-and-effect relations between them.
Thus we highlighted:
The necessity to develop more efficient methods of spectral selective sensitivity;
The necessity to develop a more completed algorithm for registering and analizing of useful information


Why Multy Walled CNT ?
- MWCNT can be grown longer than SWCNT or DWCNT
- the MWCNT have a larger diameter (SWCNT<2nm).
- the MWCNT are stiffer and more resistant

Index

A
Absorption, 43
Aleksanyan, G.M., 213
Algorithm, 261
Ali, M., 359
Al-Shamma'a, A., 233
Anodization, 304
Anoshin, K.E., 321
Antibiotic removal, 243
Antioxidant system, 271
Arakelova, E., 271
Aroutiounian, V., 105
Arshak, A., 233
Arshak, K., 233
Azafullerenes, 339

B
Balázsi, C., 125
Balázsi, K., 125
Ballistic electron resonance, 27
Benzene, 329, 339
Biological Weapons Convention, 67
Biomimetic, 3
Bisio, C., 43
Blood-sampling, 163
Bolgen, N., 243
Bondarenko, M., 329, 339
Boyajyan, A., 271
Brain injury, 193
Buha, A., 163
Bulat, Z., 163

C
Capitani, F., 55
Carbon nanotubes (CNTs), 105, 125, 151
Carboxyhemoglobin, 163
Carniato, F., 43
Caterinciuc, N., 75
Caturyan, S., 261
CBRN agents, 43
CdxHg1-xTe, 321
Charge fluctuation, 139
Chitosan, 243
CNTs. *See* Carbon nanotubes (CNTs)
Combustion, 56
Complex refractive index, 203
Convergence, 3
Conversion disorder, 94
Counter-measures, 3
Cryogelation, 243

D
Decontamination, 43
DEM, 213
Denisov, I.A., 321
Đerek, V., 303
Detectors, 253
Diffraction grating, 203
Dimitrov, A., 151
Discogenic radiculopathy, 94
DLC, 203
Drobychev, G., 253
Drobychev, G.Yu., 287

E
Earthquakes, 213
Ecosystem of innovations, 3
Electrolyte-insulator-semiconductor, 139
Electrolyzer, 359
Electron emission, 173

A. Vaseashta and S. Khudaverdyan (eds.), *Advanced Sensors for Safety and Security*,
NATO Science for Peace and Security Series B: Physics and Biophysics,
DOI 10.1007/978-94-007-7003-4, © Springer Science+Business Media Dordrecht 2013

Electronic alert, 75
Emergency system, 75
Emerging security challenges, 3

F
Field-emission, 27
Field-matter interactions, 225
Fissile materials detection, 287
Foresight, 83
Fullerenes, 329, 339

G
Gamma-radiation, 253
Gas and radiation sensor, 173
Gas chromatography, 163
Gasparyan, F.V., 139
Gas sensor, 105, 125
Gatti, A.M., 55
Gelatin, 243
Geological data, 213
Germanium, 321
Gheorghita, S., 75
GIS, 213
Gražulevičiūtė, I., 203
Grigoryan, M.A., 213
Grozdanov, A., 151
Gubareni, N., 339
Guidotti, M., 43

H
Hartnagel, H.L., 27
Harutyunyan, G., 279
Hayriyan, L., 279
Health surveillance, 75
Heterogeneous catalysis, 43
Hexagonal tungsten oxide, 125
Hodgkin's lymphoma, 56
Hovsepyan, T., 271
Hydrogen, 105

I
Immune system, 271
Indium antimonide, 321
Indium arsenide, 321
Inorganic nanotubes, 299
Inorganic oxides, 43
InSAR, 213
International Health Regulations, 67
Ionizing irradiation, 271
IR sensors, 321
Ivanda, M., 303
Ivanov, O., 225

K
Karneyeu, A.E., 287
Kharlamova, G., 329, 339
Kharlamov, O., 329, 339
Khudaverdyan, D., 183, 261
Khudaverdyan, S., 183, 261
Korjik, M., 253
Korostynska, O., 233
Kosović, M., 303
Krumpane, D., 173

L
Leukaemia, 56
Lobko, A., 253
Lukács, I.E., 125

M
Mason, A., 233
Matosyan, V., 271
Matović, V., 163
MB, 203
Metal-oxide, 105
Micro and nano PSI, 304
Microwave sensors, 234
Military firing range, 56
Modeling, 213
Montanari, S., 55
mTBI, 94
Mudflows, 213
Multifunctional radioprotectors, 271
Mutafchieva, Y., 225

N
Nanocomposites, 151
Nanodosimetry, 173
Nanomaterials, 83
Nanoparticles, 56
Nanosensors, 339
Nanotechnology, 3
Nanotoxicity, 163
Near infra-red spectroscopy, 193

O
Optical mixing, 27

P
Paiziev, A., 193
Perkins, D., 67
Perovicha, K., 173
Petrov, K., 359
Photodetector, 183, 261
Photogeneration, 183
Poghosyan, A., 271
Point-of-care, 193
Porous and layered materials, 43
Porous silicon, 105
Processing of satellite images, 213
PTSD, 94
PVA, 279
PWO, 287
Pyridine, 329, 339
Pyrolysis, 329, 339

Q
Quality control of liquids, 225
Quasi-fullerenes, 329, 339

R
Radiation, 261
Radiation resistance, 253
Radioactive contamination, 279
Raman, 304
Ranghieri, M.C., 43
Reisfeld, R., 173
Risk-assessment, 83
Ristić, D., 303
Ristić, M., 303
Romanova, M., 173

S
Saraidarov, T., 173
Sargsyan, V., 279
Schiff-base cycle amino acid derivatives, 271
Science convergence, 83
Scintillation detector, 287
Scintillators, 253
Security, 27
Semiconductor materials, 321
Sensors, 139, 151, 225, 233, 299, 304
Sidorenko, I., 93
Sidorenko, L., 93
Sidorenko, S., 93
Smith, J.E., 83
Smokers, 163
Solid lubrication, 299
Spectral analysis, 261
Spectral sensitivity, 183
Stand-alone systems, 359
Surkova, I., 173
Synthetic-biology, 3

T
Tamulevičius, S., 203
Tamulevičius, T., 203
Tavakalyan, N., 279
Technology nexus, 3
Tenne, R., 299
THz, 27
Tomova, A., 151
Tonoyan, V., 271
Topographical maps, 213
Toxic gas, 105

U
UN SCR 1540, 67

V
Vaseashta, A., 3, 83, 93, 163, 183, 225, 233, 243, 261
Visible wave, 261
Voskanyan, P., 279

W
Wastewater, 243
Water quality, 234
Water sensing, 234
Water-soluble copolymers, 279
Wind-energy, 359
WS2, 299

Z
Zinc selenide, 321